Transactions of the ASME®

Transactions of the ASME, Journal of Engineering for Gas Turbines and Power (ISSN 0022-0825) is published quarterly (Jan., Apr., July, Oct.) for $95 per year by The American Society of Mechanical Engineers, 345 East 47th Street, New York, NY 10017. Second class postage paid at New York, NY and additional mailing offices. POSTMASTER: Send address change to The Journal of Engineering for Gas Turbines and Power, c/o The AMERICAN SOCIETY OF MECHANICAL ENGINEERS, 22 Law Drive, Box 2300, Fairfield, NJ 07007-2300.

CHANGES OF ADDRESS must be received at Society headquarters seven weeks before they are to be effective. Please send old label and new address.

PRICES: To members, $27.00, annually; to nonmembers, $95.00. Add $12.00 for postage to countries outside the United States and Canada.

STATEMENT from By-Laws. The Society shall not be responsible for statements or opinions advanced in papers or ... printed in its publications (B 7.1, para. 3).

INDEXED by Applied Mechanics Reviews and Engineering Information, Inc.

Journal of Engineering for Gas Turbines and Power

Published Quarterly by The American Society of Mechanical Engineers
VOLUME 110 • NUMBER 2 • APRIL 1988

TECHNICAL PAPERS

ANNOUNCEMENTS

A. Lyngfelt

P. Stenberg[1]

Dept. of Energy Conversion,
Chalmers University of Technology,
412 96 Göteborg, Sweden

Wet Peat Power Processes: A Thermodynamic Study

The efficiencies of four power processes for wet peat have been studied. These include gas turbine cycles, steam power cycles, and combinations thereof. It is concluded that wet peat can be used in power processes with reasonable efficiency. The paper suggests that wet peat power processes could be cost competitive relative to conventional power production.

Introduction

The main complication at the utilization of wet fuels is the drying of the fuel. A wet fuel that could be of great importance is peat. The problems concerned with the drying of peat, especially in cold and rainy climates, lead to the question: Is it possible to make use of peat without previous extensive drying? This study is concerned with one aspect of this question: the study of different power cycles for wet peat and the efficiencies of these. Contrary to conventional steam power processes, the processes treated here are concerned with the recovery of the energy used for evaporating the fuel moisture. The difficulty of recovering this energy has resulted in the defining of the lower fuel heating value H_i, which is the calorimetric, or higher, heating value H_s, less the condensation heat of the flue gas vapor resulting from hydrogen and moisture in the fuel. The efficiency of a process may be calculated as energy produced divided by the lower heating value of the fuel consumed. This suitable for comparing processes using different fuels, where one process should not be handicapped for using an inferior fuel. For this study, however, it is proper to define the efficiency as energy produced divided by the *calorimetric* heating value of the fuel consumed. If the condensation heat of the flue gas vapor is not recovered the efficiency will be reduced by a factor H_i/H_s (see Fig. 1). The possibility of recovering the heat of evaporation of the fuel moisture for power production is, however, restricted by the second law of thermodynamics. If combustion is accomplished at atmospheric pressure the evaporation of fuel moisture involves a loss of exergy due to the low boiling temperature. The exergy loss is, accordingly, reduced if combustion is accomplished at a higher pressure. Thus, pressurized combustion of the peat renders possible the recovery of the heat of evaporation of the fuel moisture for power production. Possible ways to produce power with pressurized combustion are gas turbine power cycles, steam power cycles, and combinations thereof. This report examines two "unmixed" cycles and also two combined cycles. The four processes treated are:

- A simple gas turbine process
- A gas turbine process with steam admixture
- A combined gas turbine/steam power process
- A two-pressure steam power process

In the *simple gas turbine process* the vapor resulting from fuel mosture increases the volume flow through the gas turbine and thus contributes to the power production. The heat in the exhaust gases from this process can be utilized for the generation of steam, which can be expanded along with the flue gases, thus raising the efficiency of the process. This process is called the *gas turbine process with steam admixture*. Still higher efficiency is obtained if the generated steam is expanded in a separate steam turbine, which gives a *combined gas turbine/steam power cycle*. The *two-pressure steam power cycle* shows an alternative means of utilizing the fuel moisture heat of evaporation. The fuel moisture is condensed under pressure, generating low-pressure steam. To obtain good thermal efficiency this low-pressure steam cycle is combined with a high-pressure steam cycle.

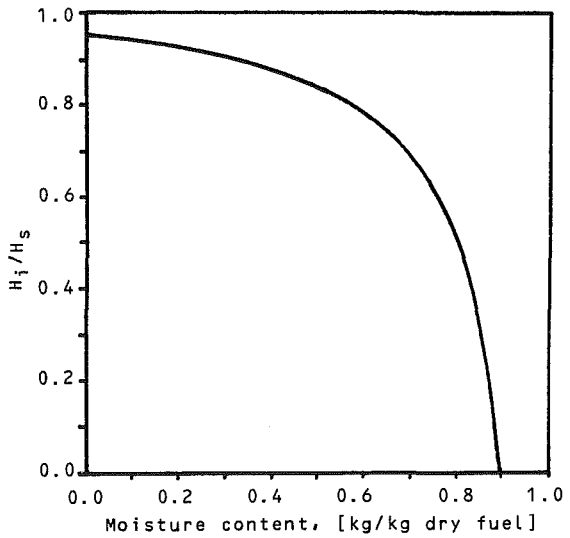

Fig. 1 Ratio of the lower and higher heating values, H_i/H_s, as a function of moisture content

[1]Present address Götaverken Energy, Göteborg, Sweden.

Contributed by the Power Division for publication in the JOURNAL OF ENGINEERING FOR GAS TURBINES AND POWER. Manuscripts received by the Power Division July 1985.

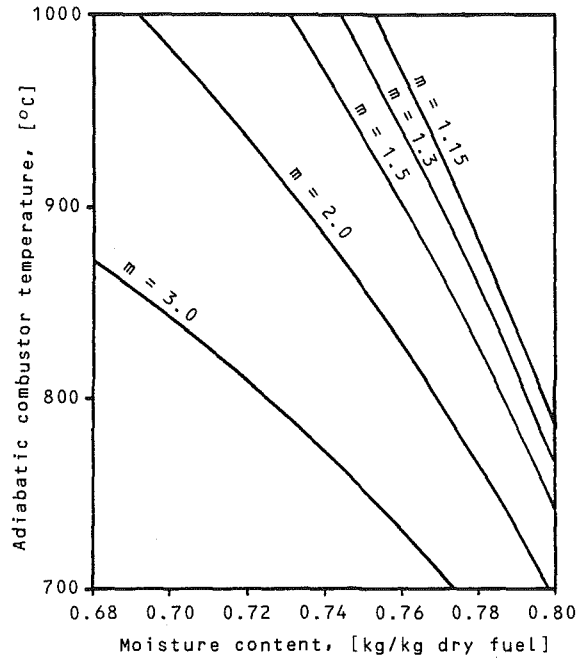

Fig. 2 Adiabatic combustor temperature as a function of peat moisture content and excess air ratio (m) if the air is preheated to 405°C, which corresponds to a compression to 15 bar

Combustion of Peat Under Pressure

The combustion of wet peat in a pressurized fluidized bed is readily accomplished according to Tiberg (1984). Peat is a reactive fuel, and complete combustion can be obtained at low temperatures, i.e., at a bed temperature down to 800 to 850°C (1472–1562°F) (Leckner and Åmand, 1985). The adiabatic combustor temperature is a function of air preheat temperature, fuel moisture content, and excess air ratio (see Fig. 2). If these parameters are properly matched it is possible to use an adiabatic fluidized bed, thus simplifying the process and eliminating potential bed tube erosion problems.

Simple Gas Turbine Process

If the moisture content, the air temperature rise in the compressor, and the excess air ratio are matched to give an adiabatic combustor, the gas turbine process will indeed be a simple one (see Fig. 3*a*). The process will have no heat transfer surfaces and the essential difference from a common oil-fired gas turbine process is the more complex handling and feeding of fuel and bed material and the necessity to separate dust before admittance to the turbine. The efficiency of the process for different pressures and moisture contents is shown in Fig. 4(*a*).

Gas Turbine Process With Steam Admixture

The simple gas turbine process gives a flue gas of high temperature. A simple way of utilizing the sensible heat in this gas is to append a flue gas boiler and a superheater. The superheated steam is then added to the flue gases before entering the gas turbine (see Fig. 3*b*), thus raising the power output and the efficiency (see Fig. 4*b*).

Combined Gas Turbine/Steam Power Cycle

If the steam is expanded to a lower pressure than that of the gas turbine steam admixture process, more power will be generated. This can be accomplished with a separate steam cycle. This leads to a combined gas turbine/steam power cycle (see Fig. 3*c*). Consistently the efficienc;y of this process is higher than those of the simpler processes treated before (see Fig. 4*c*). This process is, however, more complex, and also requires a substantial amount of cooling water for the condenser.

Two-Pressure Steam Power Cycle

For this process it is presupposed that no net power will be produced from, nor delivered to, the gas turbine/compressor steam. The thermal energy is instead used in two steam power cycles. It is desirable that the heat be delivered to the steam power cycles at the highest temperature possible in order to attain a high thermal efficiency. The role of the gas turbine/compressor system is to create a high pressure for the flue gases so that the vapor in these will condense at a high enough temperature to be of use for power production. It is not sufficient to have a steam cycle with only one pressure. A high-pressure steam cycle would exclude the possibility of recovering the vapor condensation energy, whereas a low-pressure steam cycle would give a very low mean temperature difference for the steam process, i.e., poor thermal efficiency. The solution is to use a two-pressure steam cycle: a low-pressure cycle to recover the condensation energy of the fuel moisture and a high-pressure cycle to recover the high temperature sensible heat of the flue gases. The process layout in Fig. 3(*d*) shows the compressors (1*a*, 1*b*) and gas turbines (4*a*, 4*b*) needed to keep a high pressure in the flue gas vapor condenser (13). Considering the low temperatures of the gas entering the low-pressure gas turbine (4*a*), it is obvious that the pressure rise in the low-pressure compressor (1*a*) will be less than the pressure drop in the low-pressure turbine, provided no external energy is supplied. This pressure deficit, as well as other pressure drops, is made up for in the high-pressure compressor (1*b*), due to the higher temperature and larger mass flow (vapor) in the high-pressure gas turbine (4*b*). Thus the sole purpose of the high-pressure turbine/compressor is to eliminate the power deficit for condensing the flue gas vapor at a high pressure. The flue gases are cooled in the low and high-pressure steam superheaters (11) and the high-pressure steam boiler (12), and then the flue gas vapor is condensed (13) while boiling low-pressure steam and preheating the feed water. It is assumed in the layout that the fluidized bed (2) is adiabatic. It may, however, be cooled if part of the high-pressure steam boiling (12) is placed in the fluidized bed. The efficiency of the process is shown in Fig. 4(*d*) as a function of combustion pressure and moisture content. For low moisture contents it is not reasonable to have an adiabatic bed since the high excess air ratio would dilute the vapor in the flue gas and thus lower the vapor condensation temperature. The graphs show the efficiency for a fixed excess air ratio of 1.3, which means that the bed will have to be cooled for moisture contents less than 0.76–0.78 depending on the pressure. The resulting efficiency for an adiabatic bed is indicated by the dotted line.

Conventional Process

The processes studied here are compared to a fictitious conventional steam power process with wet peat as fuel. The efficiency of this process has been calculated as

$$\eta = 0.34 \cdot H_i / H_s$$

The value of 0.34 was obtained using the same steam data and component efficiencies as for the two-pressure steam process, except that reheat was at 15 bar (218 psi). The value also includes an assumed boiler efficiency of 0.92.

Calculations and Input Data

The efficiencies of the processes have been studied by means of computer programs including data for air, water, and flue gases. A more thorough presentation of the results obtained in these calculations is given by Stenberg and Lyngfelt (1985a, 1985b). The validity of the results is of course dependent on the choice of input data such as efficiencies of components, pressures, temperatures, etc. Most input data are common to all or some of the processes while others are specific for one process. Most of these input data appear in Table 1, column Ref. The rest of the data will be shown here, accompanied by some comments.

Common Input Data for the Four Processes. The analysis of the peat on a moisture-free basis is C 0.547, H 0.049, O 0.333, N 0.006, S 0.002, and ash 0.063. Moisture content varies between 0.68 and 0.8, and is 0.75 when not otherwise stated.

The excess air ratio is at lowest 1.3, but is increased when necessary to keep the adiabatic combustor temperature at 880°C (1616°F). This does not apply to the two-pressure steam process as mentioned earlier. The radiation heat loss is zero. The pressure at the inlet of the fluidized bed is 15 bar (218 psi) if not otherwise stated.

Input Data for the Steam Admixture Process. The pressure of the admixed steam is 108 percent of the flue gas pressure at the point of injection. The temperature of the admixed steam is set by a chosen pinch point temperature difference in the superheater (see Table 1), and thus depends on the flue gas temperature.

Input Data for the Combined Process. The steam pressure is restricted by the pinch point temperature difference between the boiling feed water and the flue gases (see Table 1). There is, however, an upper limit of 58 bar (841 psi). The

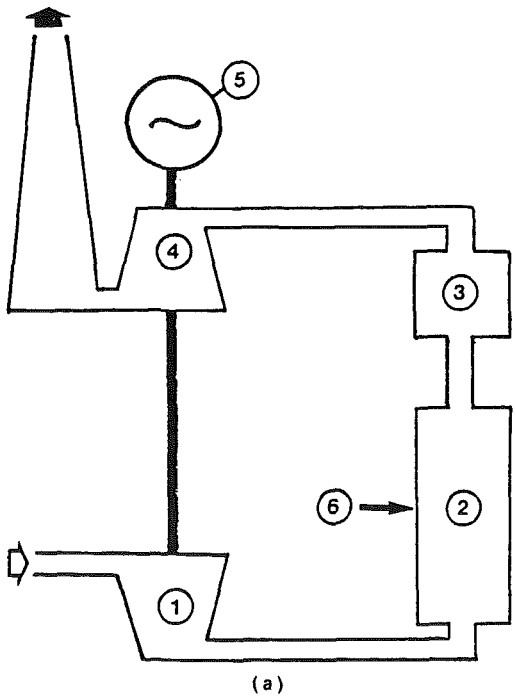

(a)

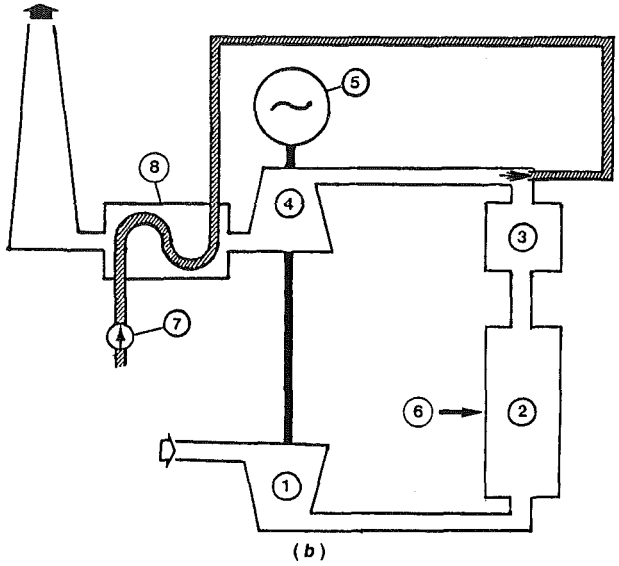

(b)

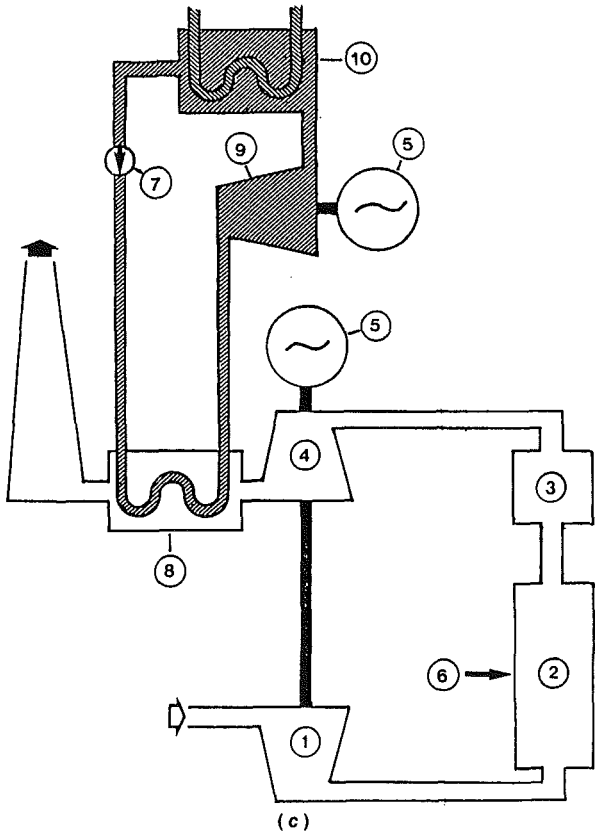

(c)

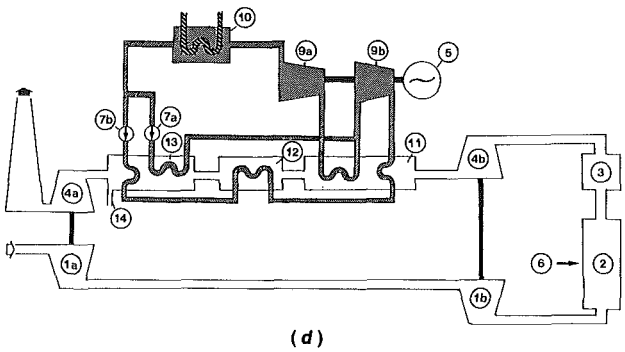

(d)

Fig. 3 Process layout of (*a*) the simple gas turbine process, (*b*) the gas turbine process with steam admixture, (*c*) the combined process, and (*d*) the two-pressure steam power process: (1) compressor, (2) combustor, (3) dust separator, (4) gas turbine, (5) generator, (6) fuel feed, (7) feed water pump, (8) flue gas boiler, (9) steam turbine, (10) condenser, (11-13) see text, (14) condensate outlet; *a* and *b* indicate low and high pressures, respectively

superheating of the steam is also restricted by a pinch point temperature difference (see Table 1).

Input Data for the Two-Pressure Steam Power Process. The steam pressure and temperature of the high-pressure steam are 75 bar (1088 psi) and 540°C (1004°F), respectively. The pressure of the low-pressure part of the steam cycle is set by a pinch point temperature difference that is lower than that of the two previously treated processes (see Table 1). This is realistic since a low pinch point temperature difference here is important for the thermal efficiency and since the heat transfer is high because of the high pressure and the condensing vapor. The low-pressure steam and the steam from the high-pressure turbine are superheated/reheated to 200°C (392°F). This is done to avoid high moisture in the low-

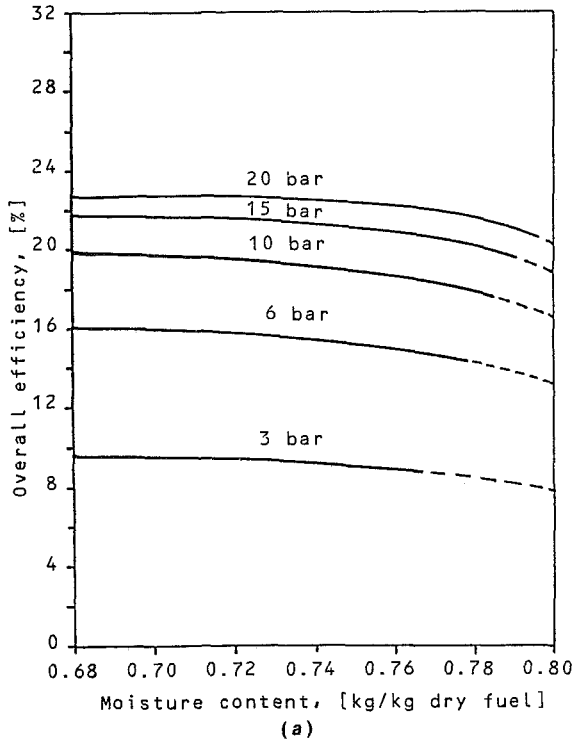

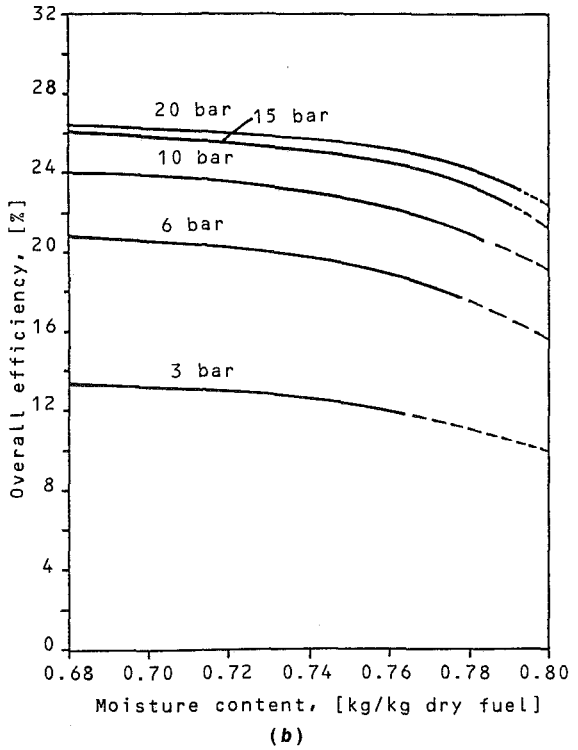

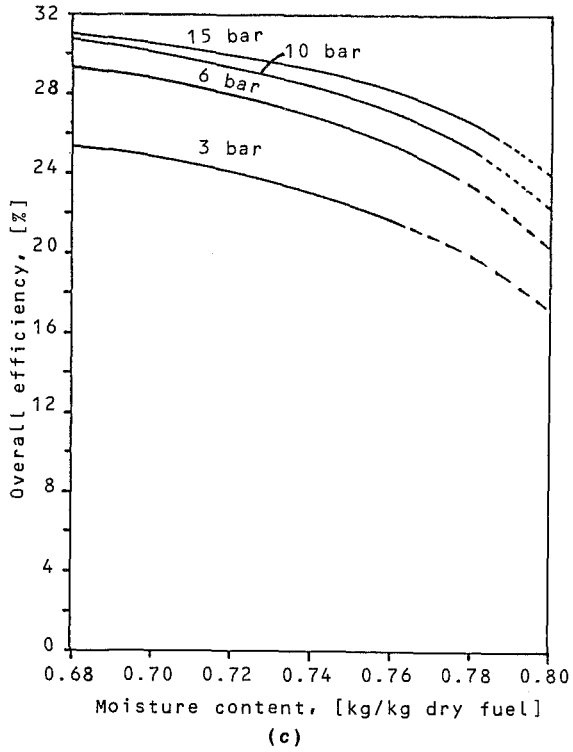

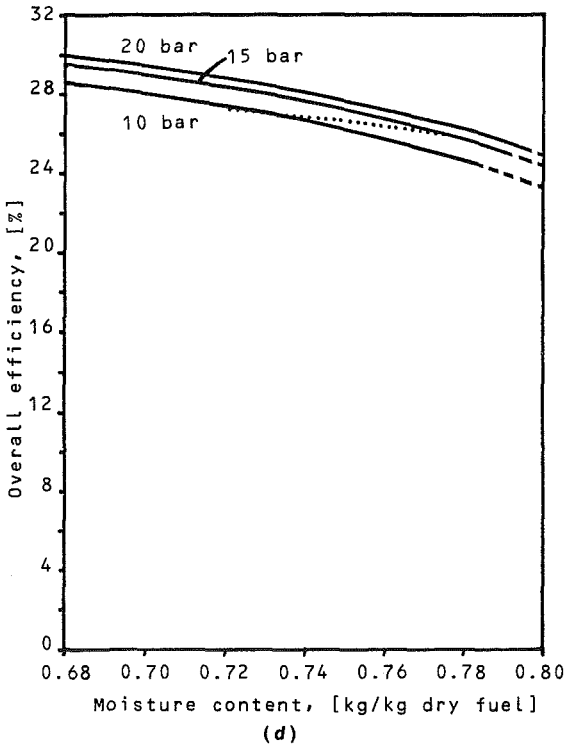

Fig. 4 Efficiency of (a) the simple gas turbine process, (b) the gas turbine process with steam admixture, (c) the combined process, and (d) the two-pressure steam power process as a function of fuel moisture content at various pressures; broken lines indicate an adiabatic combustor temperature below a limit of 800°C; the two-pressure steam power process combustor is not adiabatic; the excess air ratio is fixed at 1.3; the dotted line, however, shows the adiabatic process for a pressure of 15 bar

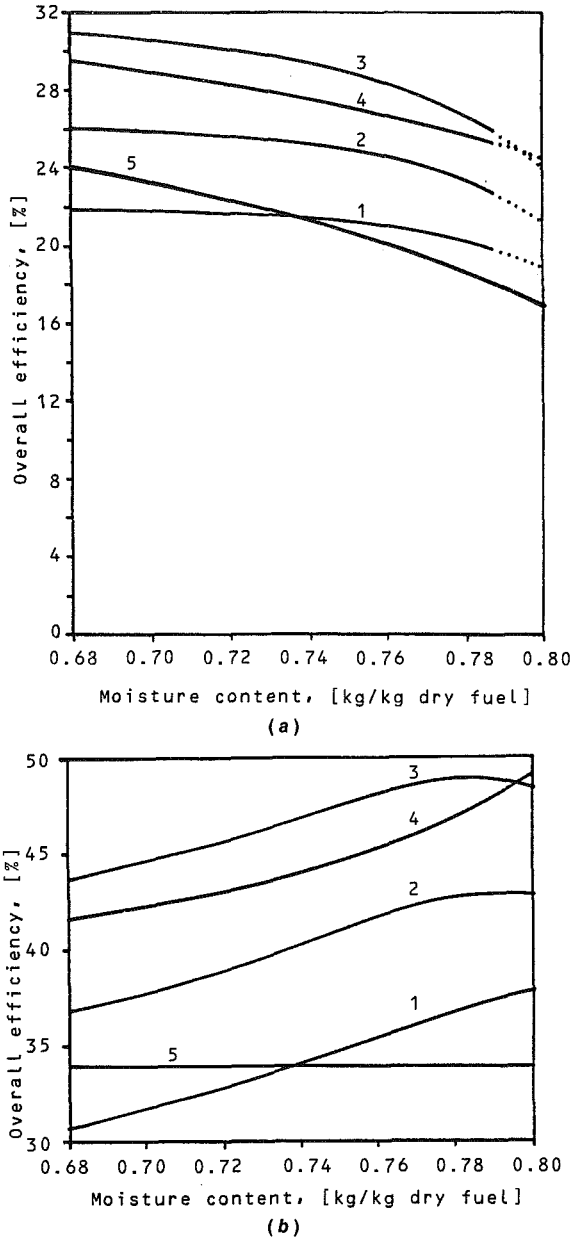

Fig. 5 A comparison of the four processes and the conventional process: (*a*) the different lines show the efficiencies of the simple gas turbine process (1), the gas turbine process with steam admixture (2), the combined process (3), the two-pressure steam power process (4), and the conventional process (5); (*b*) efficiency is here calculated as energy produced divided by the *lower* heating value of the supplied fuel

pressure steam turbine outlet and does not improve the thermal efficiency of the process.

The temperature at the low-pressure gas turbine inlet is chosen as 110°C (230°F), which gives a high process efficiency for a process with a pressure of 15 bar (218 psi) (Stenberg and Lyngfelt, 1985b).

Comparison

The calculated efficiencies of the four processes are shown in Fig. 5(*a*). These are compared with the estimated efficiency of a conventional steam power process that does not recover any heat of evaporation of the fuel moisture. The efficiency of this process decreases more rapidly with growing moisture content, if compared to the four processes studied here, which shows that these processes do recover the heat of evaporation of the fuel moisture. This is easier to see if the efficiency is calculated as energy produced divided by the lower heating value of the fuel supplied (see Fig. 5*b*). The comparison shows that the efficiencies of the four processes studied rise with higher complexity as is to be expected. The two-pressure steam process is, however, an exception. It is the most complex of the four processes but does not show the highest efficiency.

Table 1 Parameter study. The value in column Ref is substituted for the value in column New. The change results in a new overall efficiency indicated by the following columns, where η_1, η_2, η_3, and η_4 are the efficiencies of the simple gas turbine process, the gas turbine process with steam admixture, the combined process, and the two-pressure steam process, respectively. The reference efficiencies are given at the top of these columns.

parameter	ref	new	η_1	η_2	η_3	η_4
Reference	-	-	0.2099	0.2465	0.2863	0.2656
Lower heating value of dry peat [MJ/kg]	20.9	23.0	0.2132	0.2518	0.2947	0.2753
Pressure at compressor inlet [bar]	0.95	1.0	0.2140	0.2505	0.2899	0.2673
Temperature at compressor inlet [°C]	20	0	0.2166	0.2519	0.2899	0.2647
Pressure at gas turbine outlet [bar]	1.2	1.0	0.2316	0.2657	0.2991	0.2710
Isentropic expansion efficiency of gas turbine	0.87	0.95	0.2471	0.2768	0.3081	0.2741
Isentropic compression efficiency of compressor	0.90	0.95	0.2172	0.2530	0.2919	0.2691
Efficiency of generator including mechanical losses	0.95	0.98	0.2166	0.2543	0.2954	0.2740
Combustor outlet temperature [°C]	880	950	0.2167	0.2570	0.3019	0.2714
Pressure drop in combustor and dust separator [bar]	0.7	0.3	0.2133	0.2495	0.2885	0.2673
Flue gas temperature at outlet [°C]	180	160	-	0.2492	0.2891	-
Pinch point temperature difference [°C]	15 5	5 0	- -	0.2469 -	0.2889 -	- 0.2627
Isentropic efficiency of steam turbine	0.85	0.92	-	-	0.2926	0.2828
Steam condensing temperature [°C]	22	18	-	-	0.2875	0.2709
Total effect of all above listed changes	-	-	0.3055	0.3428	0.3784	0.3284

Parameter Study

In order to examine the influence of the input data on the calculated efficiencies, a parameter study has been made (see Table 1). A conclusion of the parameter study is that none of the cycles show any marked or unexpected sensitivity to any of the parameters varied. This suggests that the estimated efficiencies of the processes are realistic since the input data cannot, on the whole, be considered either very optimistic or very conservative.

Practical Aspects

There are many practical aspects of the processes that have not been considered in this study. These concern the demand for cooling water, possible locations of the plant, startup, control, etc. Some of these will be briefly discussed here.

The two "high-efficiency" processes, i.e., the two-pressure steam power cycle and the combined cycle, have the disadvantage that they demand a substantial amount of cooling water for the condenser. This means that many locations are unsuitable for such plants.

The gas turbine process with steam admixture demands feed water for the boiler. The water consumption is in the same order as the amount of moisture added to the process as fuel moisture (Stenberg and Lyngfelt, 1985a), and is very small compared to the cooling water demand mentioned above. This water has to be treated in order not to foul the boiler. A lower purity of this water, compared to the feed water of conventional steam power stations, may be compensated for by a larger extent of boiler blowdown.

A possible location for a plant involves a sufficient supply of peat within a reasonable distance for transportation. That supply should last the entire lifetime of the plant, provided that the plant is not movable.

An important part of the volume flow through the gas turbine is made up of the vapor from the fuel moisture. Different moisture contents will thus entail different ratios of flue gas mass flow to incoming air mass flow. This is important for the coupling of the gas turbines and compressors. If peat with varying moisture content is fed to the process this, however, can be compensated for by water injection. Water injection in the bed is also a possible means of regulating the bed temperature.

Part load is of little interest since the plant is intended to be part of a power grid that either does or does not demand power from the plant.

Discussion

This report is concerned with fuel moisture contents of approximately 0.7–0.8. Figure 1 shows that peat with moisture contents of more than approximately 0.8 is not suitable for these processes. Wet air oxidation provides a possibility to burn wet peat of much higher moisture contents. Dewatering of peat is, however, readily accomplished at such high moisture contents. Furthermore, a wet air oxidation power process is rather complex, and will also have an efficiency that is markedly lower than those of the processes studied here (Lyngfelt and Leckner, 1982).

This study is made on the presupposition that wet peat is substantially less expensive than dry peat. An estimation of the price of wet peat lies outside of the scope of this study. Estimations of others, for instance Schuster (1979), suggest very low costs. It should be noted that there is no market for wet peat and that wet peat thus is not produced on a commercial basis. Since no wet peat harvesting technique has been developed it is hard to validate any estimations concerning its costs.

As mentioned the efficiency of a conventional power process is assumed to be $0.34 \cdot H_i/H_s$. This gives an efficiency of approximately 28 percent for a peat with a moisture content of 50 percent, which is a realistic value for sun-dried peat. As can be seen in Fig. 5(*a*), the complex processes have an efficiency of the same order. The lower efficiencies of the two simpler processes means that they will have a peat consumption per produced unit of electrical energy approximately 20–50 percent greater than that of the conventional process. It is assumed that the price difference between dry peat and wet peat is greater than that, which, if correct, leads to the conclusion that the processes studied here will have lower fuel costs than the conventional process. As for the less complex of the processes it is also assumed that they will have lower specific investiment costs. This study suggests that wet peat power processes will produce power at lower cost than a conventional peat power process. If, as presupposed, the cost of wet peat is very low, there are good reasons to make a careful study of the cost of these processes, to see whether they are cost competitive compared to power production with conventional fuels.

Acknowledgments

This work has been financially supported by the Swedish National Energy Administration.

References

Leckner, B., and Åmand, L.-E., 1985, "Emissions From Combustion of Peat in Fluidised Bed" [in Swedish], Report No. A85-141, Department of Energy Conversion, Chalmers University of Technology, Göteborg, Sweden.

Lyngfelt, A., and Leckner, B., 1982, "A Thermodynamic Study of a Wet Air Oxidation Power Process," *Proceedings, 17th Intersociety Energy Conversion Engineering Conference*, IEEE, New York, Vol. 1, pp. 445–449.

Schuster, R., 1979, "Wet Air Oxidation of Wet Fuels" [in Swedish], AB Fjärrvärme, Trosa (available from the National Swedish Board for Energy Source Development as NE/TO-79/12).

Stenberg, P., and Lyngfelt, A., 1985a, "Three Gas Turbine Power Cycles for Wet Peat" [in Swedish], Report No. A85-144, Department of Energy Conversion, Chalmers University of Technology, Göteborg, Sweden.

Stenberg, P., and Lyngfelt, A., 1985b, "A Power Cycle for Wet Peat With Recovery of the Heat of Evaporation of the Fuel Moisture" [in Swedish], Report No. A85-143, Department of Energy Conversion, Chalmers University of Technology, Göteborg, Sweden.

Tiberg, L., 1984, "The Bioturbo—a Status Report," *Proceedings, Bioenergy 84*, H. Egneus and A. Ellegård, eds., Elsevier Applied Science Publishers, London, Vol. 4, p. 127–130.

N. W. Brown
Astro-Space Division.

G. L. Gyorey
Advance Nuclear Technology.

B. K. Genetti
Advance Nuclear Technology.

M. A. Smith
Astro-Space Division.

General Electric Company,
San Jose, CA 95153-5354

An Innovative Approach to Nuclear Reactor Design Certification

General Electric has proposed that the US Nuclear Regulatory Commission (NRC) consider adding an Appendix to 10CFR50 that would specifically address NRC Safety Review and Design Certification of advanced reactors through use of an experience building test program. The proposal was made in conjunction with the Department of Energy (DOE)-sponsored review of the General Electric advanced Liquid Metal Reactor (LMR) concept, Power Reactor Inherently Safe Module (PRISM). This paper provides a description of the proposed new 10CFR50 Appendix. It also provides the basis for the proposed new approach to Design Certification and outlines the plans that are in place for further review and consideration by the NRC.

Introduction

General Electric Company has undertaken an effort to introduce an innovative technological approach to reactor design that, when combined with changes in NRC practice, will lead to safe and economically competitive fast breeder reactor electric power plants. This paper discusses the proposed changes to the NRC Regulations, the basis for these changes, and plans for their application to General Electric's PRISM [1]. The changes are procedural and are intended to be applicable generally to any advanced concept that lacks a substantial experience base.

The conceptual design of PRISM and the NRC review of the design are sponsored by the DOE, as is the proposed change to the NRC Regulations. The principal document being reviewed is the Preliminary Safety Information Document (PSID). This document is prepared in the same format as Safety Analysis Reports, but with significantly less detail. In parallel with this document, General Electric has submitted a draft of a proposed new Appendix to 10CFR50. This Appendix, if incorporated in the NRC Regulations, would provide assurance of a relatively simple and direct path to Design Certification of first-of-a-kind advanced reactor designs. The approach is intended for application to advanced concepts that are not based on evolutionary changes to designs with substantial operating experience.

Plant standardization and NRC Design Certification are being given a great deal of attention by the United States nuclear power community. Recognition that standardization and NRC Design Certification can reduce cost and schedule uncertainty and improve safety have given impetus to the movement toward standardization. These potential benefits have been recognized for some time; however, it has not been possible to fully realize the potential. Reference [2] reports the results of an Atomic Industrial Forum (AIF) study group evaluation of future application of standardization in the US. One of the conclusions of this study was:

"The pre-approval of designs which can be referenced in individual plant applications, must be the cornerstone of any standardization policy. In order to provide a means for additional regulatory stability, the Commission has indicated that it will grant Design Certifications in addition to Preliminary and Final Design Approvals. Design Certifications will not be subject to challenge in individual licensing hearings. We believe that, ultimately, certified designs will become the most favored by the industry."

General Electric's Light Water Reactor (LWR) experience and our recent LMR evaluations for the DOE support this conclusion. The stability that NRC Design Certification will bring to the regulatory process is what is required to realize the benefits of standardization. It is this conclusion that provided the focus for this approach to licensing an advanced LMR design such as PRISM. It appears that a revitalized nuclear industry will be based on NRC Design Certified concepts. For any new design to be accepted ultimately for use by the utility industry, it must exhibit standardization and be capable of obtaining NRC Design Certification. The intermediate steps of a Preliminary Design Approval (PDA) or Final Design Approval (FDA) lack the commitment of licensing stability necessary to compete with certified designs. Thus a designer of an advanced reactor must include in his development plan a consideration of how best to obtain NRC Design Certification.

New Approach

The proposed 10CFR50 Appendix, "Certification of Standard Designs for Advanced Nuclear Power Plants Applying Demonstrated Performance" (Appendix A), is based on recognized changes in the regulatory and business environment. When first-of-a-kind advanced reactors are introduced to the utilities, the demand is likely to be for designs that can be NRC Design Certified. The procedures and data base re-

Contributed by the Nuclear Engineering Division and presented at the Joint Power Generation Conference, Miami, Florida, October 1987. Manuscript received at ASME Headquarters August 7, 1987. Paper No. 87-JPGC-NE-3.

quired to accomplish Design Certification of these advanced designs is not well defined. The proposed 10CFR50 Appendix would remove the procedural uncertainty and provide a format for addressing the data base uncertainty prior to making major financial commitments to development of such an advanced design.

The proposed 10CFR50 Appendix is a new appendix that has been developed using Appendix 0 as a starting point. The specific modifications and additions to Appendix O that are considered to be important are discussed under four topical headings: (*a*) specific recognition of advanced reactor designs, (*b*) Certification Basis Agreement, (*c*) Certification Test Plan and Test Report, and (*d*) procedural updates based on existing or proposed Regulatory Position Statements that follow. It is intended that the new Appendix would be a stand-alone alternative to Appendix O.

Recognition of Advanced Reactor Designs. There is significant uncertainty concerning the intended applicability of Appendix O to advanced reactor designs that have little or no operating experience. There are no specific statements in Appendix O that would exclude its application but neither are there statements that make it clearly applicable to first-of-a-kind advanced designs. Admittedly this is an area where judgment is based on past experience and interpretation of related activities in the area of standardization and regulatory reform. The NRC's application of rules and judgments on the legality of the rules is the only firm basis and this experience must be obtained by trial and error.

It is our judgment that there is good reason not simply to assume that Appendix O is applicable to advanced reactors, especially for LMRs. The Policy Statement on Standardization that led to Appendix M, N, and O and the proposed licensing reform bills supported by NRC tend to indicate that Design Certification is intended for those LWR plants that have substantial closely related design and operating experience. Proceeding with a less experienced advanced design and licensing it in the usual two-step construction/operation approach by proceeding through some poorly defined process to Design Certification appears to involve considerable up-front risk. The addition of the proposed new Appendix would significantly reduce this risk and contribute to encouraging advanced design development efforts.

Certification Basis Agreement. The proposed 10CFR50 Appendix requires the NRC, supported by the applicant, to issue a Certification Basis Agreement. This document would allow the Applicant and the NRC to document the specific rules and guidelines that would be adhered to in the design. The content of the document would be negotiated and issued by the NRC prior to initiation of NRC's formal review of the applicant's Design Report. The Certification Basis Agreement focuses on design and analysis rules but also identifies the need for the Certification Test Plan. The details of testing and verification of the design are left to the Design Report and the Certification Test Plan and Test Report. The Design Report is essentially a Final Safety Analysis Report (FSAR) but this nomenclature is not used to avoid unnecessary application of Regulatory rules that are specifically applicable to FSARs. It may be found appropriate to submit preliminary design information to the NRC to permit completion of the Certification Basis Agreement. It is anticipated that neither the applicant nor the NRC would be required to commit major resources prior to completing the Certification Basis Agreement.

Certification Test Plan and Test Report. The proposed Appendix requires the applicant to submit a Certification Test Plan and Test Report. The Certification Test Plan would also be reviewed and approved by the NRC early in the review process. The Certification Test Plan would identify all testing that would be completed to support the Design Certification. It would also identify criteria for acceptance of test adequacy and need for possible new or expanded tests if criteria are not satisfied. Following completion of the identified testing, a Certification Test Report would be submitted for review and approval. The test plan is intended to detail the specific experience basis that will be developed to support Design Certification. It is anticipated that test plans could vary considerably from design to design. In the case of PRISM, although not specifically called for in the Appendix, a full-scale prototypical reactor module test is planned as a major element of the Certification Test Plan.

Procedural Updates. The proposed 10CFR50 Appendix was developed recognizing a number of NRC changes that have been made since the incorporation of Appendix O into 10CFR50. Specifically, the NRC Backfit Rule [3], Severe Accident Policy [4], Standardization Policy [5] (and industry comments thereto), Advanced Reactor Policy [6], and pending licensing reform legislation [7] have all been considered. A number of the provisions of the pending reform legislation have been implemented in the proposed 10CFR50 Appendix. The combined construction/operating license was not one of these. The importance placed on having one-step licensing embodied in the law rather than simply in regulation continues to be valid.

Application of the proposed 10CFR50 Appendix assumes that licensing reform legislation will be implemented and will permit application of the one-step Construction/Operating License procedures to advanced reactor designs, including LMRs. Some of the reform legislation that has been proposed restricts application to thermal neutron reactors. This type of restriction would not be acceptable for application of the new Appendix to LMRs.

Need and Alternatives

The need for the proposed 10CFR50 Appendix is primarily driven by the desire to reduce uncertainty at the front end of an expensive development activity. Without the proposed 10CFR50 Appendix there are essentially two alternatives: (1) don't focus on Design Certification, or (2) assume the untested 10CFR50 Appendix O can be applied to first-of-a-kind advanced reactor designs. The first approach implies that one would undertake an expensive development project with standardization so far in the future as to not be a concern. The current economic environment makes this a highly unlikely alternative. The second approach includes considerable uncertainty associated with application of Appendix O to first-of-a-kind designs. This uncertainty will be reduced to some extent once an LWR standard design has been certified. Residual uncertainty will remain depending on the extent the advanced design is innovative or introduces new technologies. This approach requires an expensive commitment to obtain an unspecified but "sufficient" level of experience to allow the NRC to certify the standard plant design.

It is clearly desirable to avoid an open-ended commitment. That is one of the primary purposes for introducing the proposed new 10CFR50 Appendix. With the conceptual and preliminary advanced reactor designs activity supported by DOE, it should be possible to develop sufficient insight to establish the procedural basis for assuring that first-of-a-kind advanced reactor designs can be certified with a specified program prior to commitment to their construction. A second equally important basis for introducing the proposed 10CFR50 Appendix is to provide a procedural approach to acknowledge the unique demonstrable safety characteristics of advanced reactor designs. The potential for advanced reactor designs to demonstrate enhanced safety and to provide a suitable data base for Design Certification needs to be given

encouragement. The proposed 10CFR50 Appendix would do this by providing an opportunity to identify and specify an approach to Design Certification prior to major construction commitments.

Plans for Review and Implementation

Following an introductory discussion with the NRC staff reviewing PRISM, a draft of the proposed 10CFR50 Appendix was sent to the NRC on March 7, 1986.

The NRC response was to encourage continued development of the proposed approach through the DOE program supporting advanced reactor interactions. It is General Electric's plan to conduct these interactions by preparing draft versions of two key documents required by the proposed 10CFR50 Appendix: the Certification Basis Agreement and the Certification Test Plan. The new appendix requires that the NRC concur on these documents prior to completing review of the Design Report and prior to conduct of the testing necessary to design certify the plant. Review of these draft reports during the current time period is intended to provide an interaction that simulates what would take place if the proposed 10CFR50 Appendix were implemented and applied to PRISM. Through this experience and the review of the PRISM PSID the NRC and DOE will obtain a measure of the usefulness of the proposed 10CFR50 Appendix and will also assess the benefit of proceeding with a rule change that implements it. Both of the draft documents are in preparation and will be submitted for review and discussion during the last half of FY1987. If DOE and NRC concur on the usefulness of the approach, the follow-on activity will be to prepare, for DOE's submittal, the proposed rule adding the new 10CFR50 Appendix and supporting justification. It is anticipated that this action would take place in the second half of FY1988.

The rule making action that would follow the anticipated DOE proposal would proceed along a normal schedule for public comment and interaction and can reasonably be expected to be completed in less than a year.

Application to PRISM

The proposed 10CFR50 Appendix does not specify the contents of the Certification Test Plan, nor does it characterize the facilities required for the necessary testing. These are left open for the applicant to identify and negotiate with the NRC. The plans are expected to be dependent on the reactor plant type and design characteristics. If a full-scale prototype is used, it could be a licensed test facility or it could be placed on one of the Government reservations used for nuclear reactor testing. General Electric has selected the latter approach for PRISM.

The PRISM design was developed on the basis of providing the capability to test a prototypic module to the fullest extent practical. This early commitment has produced a design that is well suited for obtaining operational experience and safety test data to support NRC Design Certification. The small size of the module and the small safety-related envelope support construction of a single module safety test that uses a minimum amount of heat rejection hardware. The inherent response characteristics in the PRISM design permit a scope of testing that includes full-scale demonstration of safety response to Anticipated Transient Without Scram (ATWS) events and to station blackout.

Both the hardware scope and a test plan for PRISM have been developed conceptually. The PRISM safety test is comprised of three testing phases—conventional testing, benchmark testing, and safety testing. The conventional testing phase is made up of preoperational testing, baselining of in-service inspections, hot functional testing, fuel loading, and startup testing. The conventional testing is very similar to the tests completed by Experimental Breeder Reactor (EBR-II) and Fast Flux Test Facility (FFTF) prior to startup. The benchmark testing phase consists of tests to measure the inherent response of the reactor, such as neutronic performance and performance of the decay heat removal system. The safety testing phase is the key to the PRISM safety test and is to demonstrate the inherent safety of PRISM under postulated design basis and beyond design basis events. Tests covering design basis events envelop design duty cycles, anticipated scram events, and unlikely accident conditions to demonstrate PRISM's longer term decay heat removal capabilities. Tests covering beyond design basis events are directed to those without scram and include rod withdrawal, loss of intermediate heat transport system (IHTS) cooling, and loss of primary circulation flow to demonstrate PRISM's inherent response to maintain core and structural temperatures to well below safe limits. Testing of the seismic isolation system is also being planned.

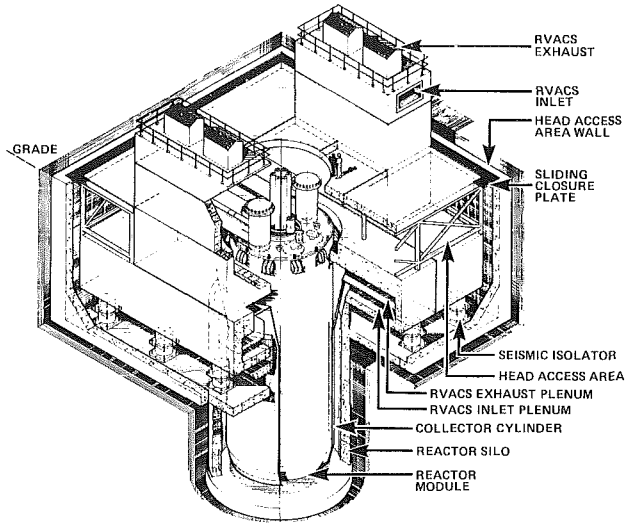

Fig. 1 Safety-related test module

The test article is a full-scale, prototypic PRISM reactor module and its support structure and seismic isolation system (see Fig. 1). It also includes the air ducts and flow path structures that comprise the passive decay heat removal system for the reactor and any safety-related equipment, such as the scram system and the pump coastdown power supplies.

Fuel handling equipment and methods for the test facility are prototypic of those for the PRISM plant. New and reprocessed fuel are brought to the PRISM test facility by direct transfer from the host fuel cycle facility. Fuel is transferred between the reactor and reactor service building by a cask with transporter. Spent fuel is held in storage at the reactor service building for eventual transfer to the fuel cycle facility.

The enhanced safety performance capability of PRISM combined with the safety test is believed capable of providing the information necessary for supporting NRC Design Certification of a first-of-a-kind design. Additional feature testing, reliability testing, and safety phenomenological testing will be required, but the extent of the additional testing as well as the operational experience base is believed to be considerably reduced with the PRISM approach.

General Electric is developing a plan that would encourage the DOE to proceed with the PRISM test program on one of the reactor test sites. A standard reference plant final design (see Fig. 2) would be prepared in parallel with the test project and would be submitted for NRC review. A Safety Evaluation Report (SER) would be issued following review of the Design Report. Following completion of the test program and review

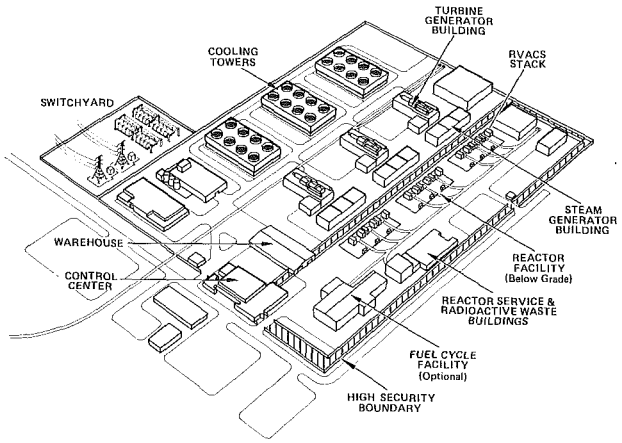

Fig. 2 PRISM reference plant

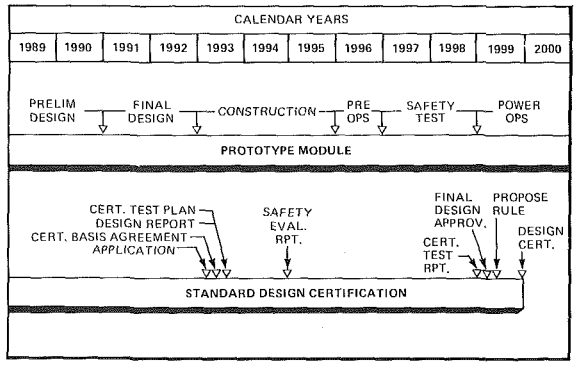

Fig. 3 PRISM certification schedule

with the NRC, an FDA would be issued. The FDA would be the basis upon which a Design Certification would be issued (see Fig. 3).

Summary

The General Electric proposed 10CFR50 Appendix "Certification of Standard Designs for Advance Nuclear Power Plants Applying Demonstrated Performance" provides an innovative procedural approach to Design Certification of first-of-a-kind advanced designs. The PRISM plant is being developed to take advantage of this approach and proceed in a cost-effective manner to Design Certification.

References

1 Tippets, F. E., et al., "Progress on PRISM, an Inherently Safe, Economic and Testable Advanced Liquid Metal Reactor," presented at the American Power Conference, Chicago, IL, Apr. 1987.

2 Atomic Industrial Forum, Inc., *Standardization of Nuclear Power Plants in the US*, Nov. 1986.

3 Nuclear Regulatory Commissions' Backfit Rule 35 FR 5318, Mar. 31, 1970.

4 Nuclear Regulatory Commission's Policy Statement on Severe Reactor Accidents Regarding Future Designs and Existing Plants, 50 FR 32138, Aug. 8, 1985.

5 Nuclear Regulatory Commission's Current Revisit to Supersede the Standardization Policy Statement issued in Aug. 1978.

6 Nuclear Regulatory Commission's Policy Statement on Regulation of Advanced Nuclear Power Plants, 50 FR 24643, July 8, 1986.

7 Proposed Licensing Reform Legislation (S836 Simpson, April 2, 1985) HR 1447 Udall, Mar. 6, 1985 ("Nuclear Power Plant Licensing and Standardization Act of 1985"). Additional more recently proposed bills are pending.

APPENDIX

Draft of Proposed New Appendix to 10CFR50—Certification of Standard Designs for Advanced Nuclear Power Plants Applying Demonstrated Performance

This appendix sets out procedures for the filing, staff review, referral to the Advisory Committee on Reactor Safeguards (ACRS), and the certification through rulemaking of standard designs for advanced nuclear power reactors of the type described in § 50.22 or major portions thereof.

This appendix is similar to Appendix O but differs principally from Appendix O in that the staff review, ACRS referral, and the certification rulemaking emphasize the use of demonstrated performance (for example a prototypical safety test) supplemented by analysis rather than the degree of reliance on traditional analysis in response to 10CFR50 and Reg. Guide 1.70.

1 Any person may submit a proposed final standard design for a nuclear power reactor of the type described in § 50.22 to the regulatory staff for its review. Such a submittal may consist of either the final design for the entire reactor facility or the final design of major portions thereof.

2 The submittal for review of the standard design shall be made in the same manner and in the same number of copies as provided in § 50.36 (*a*), (*c*), (1) and (3) for license applications.

3(*a*) The submittal for review of the standard design shall include the information described in § 50.33 (*a*)-(*d*) and the applicable technical information required by §§ 50.34 (*a*) (except that the preliminary safety analysis report shall be designated as a "design report"), and (*b*), as appropriate, and 50.34*a* (other than that required by §§ 50.34 (*a*) (6) and (10), 50.34 (*b*) (1), (6) (*i*), (*ii*), (*iv*), and (*v*), 50.34 (*b*) (7) and (8) and 50.34 (*f*)[1]). The submittal shall also include a description, analysis, and evaluation of the interfaces between the submitted design and the balance of the nuclear power plant. The submittal shall describe how certain testing will be used to supplement or replace safety analysis and include a certification test plan along with a description and evaluation of the test site. With respect to the requirements of § 50.34 (*a*) (1), the submittal for review of a standard design shall include the site parameters postulated for the design, and an analysis and evaluation of the design in terms of such postulated site parameters. The information submitted pursuant to § 50.34 (*a*) (7) shall be limited to the quality assurance program to be applied to the design, procurement, and fabrication of the structures, systems, and components for which the design review has been requested and the information submitted pursuant to § 50.34 (*a*) (9) shall be limited to the qualifications of the person submitting the standard design to design the reactor or major portion thereof. The submittal shall also include information pertaining to design features that affect plans for coping with emergencies in the operation of the reactor or major portion thereof. The submittal for the review of the standard design shall also include a proposed certification basis document identifying regulatory criteria against which the standard design might be measured.

3(*b*) Review and approval of the certification test plan and identification of additional information to be provided to satisfy Commission policy and regulatory practice will be

[1]The regulatory staff will advise the certification applicant as to the appropriateness of this technical information and such additional information as may be required by the Commission's Policy Statement on Severe Reactor Accidents Regarding Future Designs and Existing Plants (50 F. R. 32138 Aug. 8, 1985). Some of the information cannot be made available on a standard design. Other information may be substituted and/or supplemented with demonstrated performance. Finally, some information may not be applicable to a particular type of reactor.

completed prior to conduct of the certification tests. The design review will be based on this pretest determination of test scope and applicable regulatory practice and shall not be subject to revision unless it is determined on the basis of significant information that a revision is required to protect public health and safety or common defense and security.

3(*c*) Before initiating the technical review, the regulatory staff shall prepare and issue the certification basis document. The certification basis document shall be based on the applicant's proposed certification basis document of paragraph 3(*a*).

4 Review and approval of the test facilities used in the demonstration tests shall be completed in accordance with applicable regulations.

5 On completion of the approved certification test program the applicant will submit a final test report for review.

6 Once the regulatory staff has initiated a technical review of a submittal under this appendix, the submittal will be referred to the ACRS for a review and report.

7 Upon completion of their review of a submittal under this appendix, the regulatory staff shall publish in the Federal Register a determination as to whether or not the final design is acceptable, subject to such conditions as may be appropriate, and make available in the Public Document Room an analysis of the design in the form of a Final Design Approval (FDA).

8 A design determined to be acceptable pursuant to the foregoing paragraphs shall be used and relied upon by the regulatory staff and the ACRS in their review of any individual facility license application which incorporates such design by reference, unless there exists significant new information that substantially affects the earlier determination or other good cause. The determination and report by the regulatory staff shall not, however, constitute a commitment to issue a design certification, or in any way affect the authority of the Commission, Atomic Safety and Licensing Appeal Board, atomic safety and licensing boards, and other presiding officers in any proceeding under Subpart G of Part 2 of this chapter.

9 Certification of the design will be obtained in a rulemaking proceeding following completion of the staff and ACRS review. The Commission may, on its own initiative or in response to a petition for rulemaking by a certification applicant, institute a certification rulemaking proceeding. An environmental impact statement may be prepared, for such a rulemaking action in accordance with § § 51.20 (*b*) (13) and 51.85 of this chapter. If an environmental impact statement is prepared, the Commission may require the applicant for certification to submit information to the Commission to aid the Commission in the preparation of the environmental impact statement.

10 Upon completion of the rulemaking proceedings, the Commission shall issue a certification if it determines based on the record thereof that such certification will not be inimical to the health and safety of the public or to the common defense and security.

11 Any design certification issued by the Commission under this Appendix may be referenced in an application for a facility license which meets the conditions of the design certification and is filed within the period during which the design certification remains valid.

12(*a*) Following the issuance of a design certification hereunder, in any subsequent Commission proceeding involving a facility design for which a design certification has been granted hereunder, the certified design will be subject to challenge only as provided in § 2.758 of this chapter.

12(*b*) Any person may petition the Commission at any time for an amendment to a design approval; provided, however, that the Commission shall not modify any final determination of an issue that has been considered and decided in a design certification proceeding unless it determines, based on significant new information, that a modification is required to protect the public health and safety or the common defense and security and that the modification proposed will substantially enhance the public health and safety or the common defense and security by improving overall safety or security of facility operation.

13(*a*) The Commission shall approve an amendment to a design certification issued hereunder upon application by the holder of the design certification if the Commission determines that the amendment will comply with the Atomic Energy Act and the Commission's regulations.

13(*b*) Any amendment approved by the Commission under this paragraph shall not apply to an application for a facility license referencing the certification for which the amendment has been granted that is filed before the effective date of such amendment unless (1) the license applicant requests that such amendment apply to the application, or (2) the requirements of § 12(*b*) are satisfied with respect to the amendment.

14 Any application for a facility license, or any amendment to such license, referencing a design certification issued hereunder may include a request for a variance from one or more elements of the design certification. Such requests shall be granted if the Commission determines that the variance will comply with the Atomic Energy Act and the Commission's regulations. Any variance issued hereunder shall be limited to the facility license for which such variance has been requested.

E. Yasni
Engineer,
Electricity Corporation,
Wellington, New Zealand

C. G. Carrington
Associate Professor,
Department of Physics,
University of Otago,
Dunedin, New Zealand

Off-Design Exergy Audit of a Thermal Power Station

A second-law state analysis procedure, having on-line capability, has been implemented at a fossil-fueled power station at Huntly, N.Z. The analysis fully integrates the combustion and steam processes in order to provide a viable understanding of the influence of operating parameters on the distribution of losses within the plant. The procedures do not rely significantly on manufacturer's performance data and the validity of the audit is substantially verifiable. Examples of audit data are presented, including operation with and without the top heater and a comparison of throttle and sliding pressure control.

(A) Introduction

The generation cost in thermal power stations comprises three principal components: fuel charges, operating and maintenance expenses, and capital costs. The relative importance of these factors depends on the maturity of the station and its role in the generation network. The goal of the plant engineers, after ensuring that the station operates safely and reliably, is to minimize these costs. Many power stations are now equipped with data acquisition systems to assist the operators in securing these goals, although this is far from universal. However where it is in use the impact of on-line monitoring and analysis on the station is widespread. It creates an enhanced consciousness of unit efficiency and this influences both short-term operating strategies and long-term planning.

The procedures adopted for the analysis and presentation of plant data are important because they affect the significance and utility of the information. But at the present time no single form of analysis has received general acceptance. This paper examines the practical application of second-law auditing, a procedure in which thermodynamic efficiency is analyzed in terms of the flow and loss within the plant of mechanical work potential, known as thermodynamic availability or exergy. As distinct from an energy audit alone this procedure is particularly relevant because work is the primary product of the power station. Indeed the merit of employing second-law criteria for assessing power station efficiency has been acknowledged for more than fifty years, particularly since the work of Keenan (1932); references to recent related work are contained in the bibliography compiled by Liu and Wepfer (1980). Yet to a large extent second-law auditing is regarded as an academic preoccupation having theoretical significance only. While some claim that the techniques are employed within the thermal power industry "where appropriate," in the experience of the authors the concepts have not been widely adopted as routine instruments of management even though they are considered by many to offer considerable utility to plant engineers (Began, 1982; Haywood, 1980; Gaggioli, 1975; Bosnjakovic, 1963). The method has failed to achieve general usage on a day-to-day basis. On the contrary, tasks for which second-law auditing has the potential to provide real practical benefits, such as component performance monitoring, have been performed in other ways, some of which entirely avoid the use of second-law criteria. The heat-rate deviation analysis method introduced originally by Salisbury (1958, 1959, 1961) is an example of the kind which has been based solely on considerations of enthalpy balance and plant modeling. This approach is unable explicitly to evaluate the loss due to irreversibility within any specified control volume, an important feature of the exergy audit.

The failure of second-law analysis to acquire acceptance as a regular monitoring tool implies questions about the practical relevance and applicability of the method. These have been raised already in another context by Linnhoff (1983) who has described the difficulties in the use of second-law criteria to achieve optimal designs for chemical process networks. In these situations, as in others, the value of the second law is restricted because of the limitations imposed by existing technology. Linnhoff has carefully distinguished avoidable and unavoidable thermodynamic losses in order to manage these constraints. More generally, however, many engineers view second-law analysis as a rather impractical procedure. Thus while it is often regarded as appropriate to use second-law criteria to analyze novel plants and processes, it is considered that "practical considerations" will ultimately dominate design details and operating procedures. In addition the procedures themselves present conceptual problems for some, a difficulty noted by Salisbury (1958) who suggested that the concepts necessary to appreciate irreversibility losses "lack tangibility."

The view of the present authors is that second-law auditing has more practical utility for the thermal power industry than is generally accepted. This belief is based on the experience of the authors with second-law analysis methods in conjunction

Contributed by the Power Division for publication in the JOURNAL OF ENGINEERING FOR GAS TURBINES AND POWER. Manuscript received by the Power Division January 8, 1987.

with the on-line data acquisition system in a power station newly commissioned by the Electricity Corporation of New Zealand. The station is located at Huntly, N.Z. Software has been developed to perform this analysis and the program has been commissioned, complete with on-line acquisition of data. The results presented here, most of which employ data obtained during acceptance heat-rate tests, illustrate the application of the analysis. The purpose of this paper is to present some of the experiences since implementing it.

(B) Background

During the 1950s and 1960s power cycle analysis procedures were developed by Salisbury (1958, 1959, 1961) under the sponsorship of Bailey Meter Co. An important feature of this methodology was the use of analytic descriptions for the turbine cycle, both to reduce the required quantity of input data and to minimize computational demands, an important consideration at the time. In this procedure the performance of components was characterized by representative performance parameters. The deviations of these parameters from values obtained under reference conditions were used to calculate the additional heat rejected at the condenser as a consequence of the deviation, the calculation being entirely of first-law character. The work of Salisbury formed the basis for a plant monitoring system that has since been widely used. However the success of the method depends on the existence and validity of certain input data relating to the performance of particular items of the plant. These data, which are needed in order to determine the contribution of a component to the heat-rate deviation, include manufacturers' correction curves. The heat-rate deviation method thus invokes a rather specific model of the plant which depends, in part at least, on prior information of plant performance. The validity of these data is not generally open to verification.

Second-law analysis also relies on a model for the evaluation of processes, but it is one of considerable generality. In common with other procedures it is assumed that a steady-state, steady flow representation is applicable and that the intensive properties of material flows at the boundaries of defined control volumes are those of equilibrium states. Other more specific assumptions used in this work are listed in section (C) below. The detailed calculations used in this study have utilized essentially the same computational procedures used by Petit and Gaggioli (1980) and by Rodriguez (1980).

The physical foundations of second-law analysis are well documented. Here we take the Reversible Work and Lost Work Theorems of Haywood (1980) as the basis of our procedures. These theorems lead to the use of a fully reversible process as the standard against which the efficiency of a process is measured, a limit in which both energy and entropy are conserved in the control volume of interest. The specific *exergy* of material in steady flow, having a known thermodynamic state, is defined as the output shaft work that would be produced during a hypothetical reversible steady flow process which reduces one unit of mass of the material to a state of full thermodynamic equilibrium with the environment. The *lost work* in a process is defined as the additional work that would be produced by a reversible process compared with the actual process, while maintaining the same process boundary states. In general such an ideal process will involve reversible heat exchange with the environment.

It is occasionally claimed that a fully reversible process is an unrealistically high performance standard for the assessment of real processes, so that it is irrelevant for practical purposes. Instead it is suggested that detailed process models provide more realistic goals for plant improvement. However this attitude ignores a number of aspects of second-law analysis.

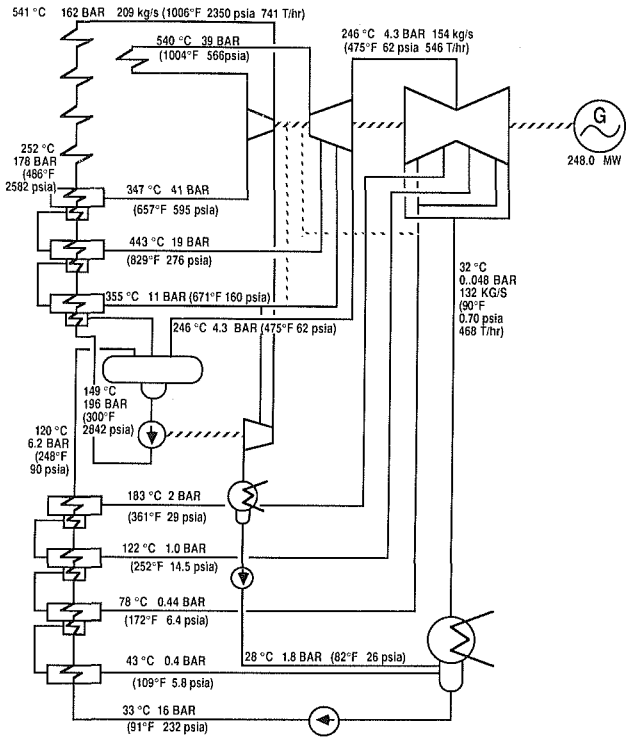

Fig. 1 Huntly unit 4, schematic steam cycle with gas firing, throttle control, and top heater intact. English units are given in parentheses: temperature in °F, pressure in lb/in.^{2}, steam flow in t/hr.

First, in most subprocesses within a generating plant the exergetic efficiency is not low, and consequently second-law performance criteria can be very realistic indeed. The exergetic efficiency of noncondensing turbines is typically 90 percent or more. Second, as a plant management tool, the second-law audit is complementary to process models. The viewpoint offered by the exergy audit should help to provoke questions that the process model may subsequently help answer, whereas a process model alone admits to only trial and error procedures. In addition an exergy audit involves a minimal set of assumptions of component behavior so that it creates a particularly faithful representation of the state of the plant. Further, it provides a means for locating and quantifying the thermodynamic losses of individual subprocesses within the plant, all expressed on an equivalent and consistent basis. This is valuable because in a multistage process the losses are not independent of each other: Subprocesses cannot generally be independently optimized in order to optimize the entire plant. A system change which reduces total losses may actually increase those in some subprocesses while reducing them in others. The use of a common base for assessing losses is therefore important because it allows the connection between losses within different subprocesses to be understood.

We note that second-law procedures do not exclude the use of deviation methods, the objective of which is to identify the cause of extra heat rejected at the condenser due to inefficiency in the plant. On the contrary the second-law audit is especially suited to deviation analysis because the change in the heat rejected at the condenser due to a variation in a process is simply the change in the lost work in the process. This may be determined from the boundary states of the process alone. By comparison, when applying first-law deviation procedures using the intensive parameters of a process, a complete plant simulation is required to calculate the resulting extra heat rejected at the condenser.

(C) Implementation

The host unit for the tests described in section (D) is Huntly, Unit 4, the steam cycle for which is shown schematically in Fig. 1. The turbogenerator is a three-cylinder single reheat unit with seven stages of regenerative feed heating, operating at 3000 rpm and rated at 250 MW. The steam generator has a controlled water circulation single radiant furnace designed for pulverized coal, fuel oil, or natural gas firing to maximum continuous rating. River water cooling is employed and the unit includes Ljungstrom air heaters. The plant is fitted with instrumentation for automatic data acquisition, but this is not suitable for heat-rate acceptance test purposes.

The exergy audit has involved all significant processes throughout the unit, thus providing an estimation of the lost work associated with each identified process. In the analysis, the plant is divided into control volumes, chosen, in most cases, so that the thermodynamic boundaries coincide with existing data acquisition instruments. The total data available are usually more than sufficient to permit a full heat balance of the plant, including major auxiliaries, thus allowing both the state condition of all the thermodynamic walls to be determined and the thermodynamic consistency of the input data to be examined. The lost work is then calculated for each control volume and aggregate performance parameters, such as the second-law efficiency of the unit, are then calculated as functions of these individual losses. In addition the procedure provides a mechanism for internally checking the audit by the use of Haywood's Second Lost Work Theorem (Haywood, 1980) which shows that the loss resulting from a process linking a particular set of boundaries with fixed intensive state parameters is the sum of the losses for the individual subprocesses within those boundaries.

In principle the accuracy of the plant thermodynamic representation created by this procedure is limited by the precision of the measuring instruments alone. However in order to reduce the amount of input data the following assumptions have been made:

(*a*) Processes occurring within insulated components are adiabatic unless otherwise specified.

(*b*) Kinetic energy differences between the input and output of control volumes are negligible, apart from the low-pressure turbine exhaust.

(*c*) Velocities are subsonic.

(*d*) Steam leaving the steam drum to the superheater is dry saturated.

(*e*) Water flowing in the downcomers and the boiler circulating pump is saturated liquid.

(*f*) Pressure drops in the main condensate line and main feed line are uniformly distributed among the low-pressure and high-pressure heaters, respectively.

(*g*) All steam leaks are attributed to one location before the secondary superheater, the soot-blowing steam takeoff point. For the sake of performance calculations soot-blowing is treated as a leak.

(*h*) Auxiliary electric driven machinery is excluded from the analysis apart from the condensate pump.

(*i*) Pressure changes within the gas side of the boiler are ignored and the temperature of flue gas is taken to be uniform over boiler cross sections perpendicular to the gas velocity.

(*j*) Dissociation and ionization of the flue gas is not included in the analysis and the Gibbs–Dalton law is assumed to represent the mixture of the flue gases adequately.

In the first computational step energy balance is used to establish steam flows using the enthalpy at the boundary of control volumes, such as feed-water heaters, together with one major measured flow, in this case the flow of feedwater entering the economizer. The steam properties are calculated using the equations of the 1967 IFC Formulation for Industrial Use (Schmidt, 1982). Additional considerations are needed to determine both flow and enthalpy in the case of wet steam, such as the low pressure turbine exhaust and, under certain conditions, low pressure turbine bled steam 1. This is accomplished by using an iterative procedure to solve the coupled energy and mass balance equations for the feedwater heaters while treating additional flows due to glands and auxiliary machinery (e.g., air ejectors) as perturbations. The kinetic energy at the low pressure turbine exhaust, which dissipates downstream at the condenser, is evaluated as a separate term since the resulting loss is not regarded as a turbine loss. At the first iteration bled steam 1 is assumed to be saturated dry and the stagnation enthalpy of the exhaust steam is determined by utilizing energy balance around the turbine set. This allows the kinetic energy of the exhaust steam to be found by numerical solution and hence permits the state of the low pressure turbine exhaust to be found. The state of bled steam 1 is then redetermined by interpolation and the iteration procedure is repeated until specified convergence criteria are satisfied. One shortcoming of this approach is that it assumes that the turbine expansion curve is smooth, whereas the aim of the analysis, in part, is to determine the turbine characteristic.

The analysis of the boiler is made complicated by the lack of detailed measured data, flue gas temperatures particularly. Consequently the exergy audit of boiler processes is less robust than that for the turbine and other steam systems. First the thermal efficiency of the boiler is calculated using the loss method by stoichiometric analysis, based on the chemical composition of the fuel (natural gas in the tests described here), its calorific value (determined daily), together with the flue gas excess oxygen and the stack temperature. An adjustment was necessary to correct for the effect of air leaks in the rotary regenerative heaters. The magnitude of the leak was established by comparing the measured air mass flow rate with that calculated by stoichiometry and energy balance. The required gas properties were calculated from JANAF data (Stull and Prophet, 1971). The measured fuel flow rate was not used as a primary input variable; instead it was computed from the boiler thermal efficiency and the steam flows obtained from the energy analysis of the power cycle. The exergy losses within identified sections of the boiler depend principally on the relevant gas temperatures, many of which are not measured. However since the boiler is the seat of more than 50 percent of the exergy losses in the plant it is important to establish how these are distributed. Temperatures have therefore been estimated using energy balance criteria applied to a plug flow model for points downstream of the furnace. To establish the temperature of flue gas entering the superheaters a radiation heat transfer model has been used together with energy balance over the superheaters. The relevant dimensional parameters were selected to secure agreement with existing test data.

The determination of exergetic losses in the boiler employs the procedures described by Petit and Gaggioli (1980) including the use of the same reference state used by those authors for the chemical contributions. The inlet temperature of the condenser cooling water is used as the dead state temperature both for the boiler and the steam cycle. In fact the analysis should treat the boiler, power-cycle, and atmospheric-cooling water subsystems separately (Wepfer and Gaggioli, 1980). However we took the view that the temperature of the conceptual environment with which the plant exchanges heat is established by the river, the exhaust to the atmosphere being regarded as a stray loss. This is a reasonable approach because approximately 90 percent of the exergy lost in boiler processes is ultimately dissipated as heat to the cooling water. We note here that the first and second-law efficiencies of the boiler can vary independently, which emphasizes the irrelevance of the first-law efficiency of the boiler as it indicates incidental losses only.

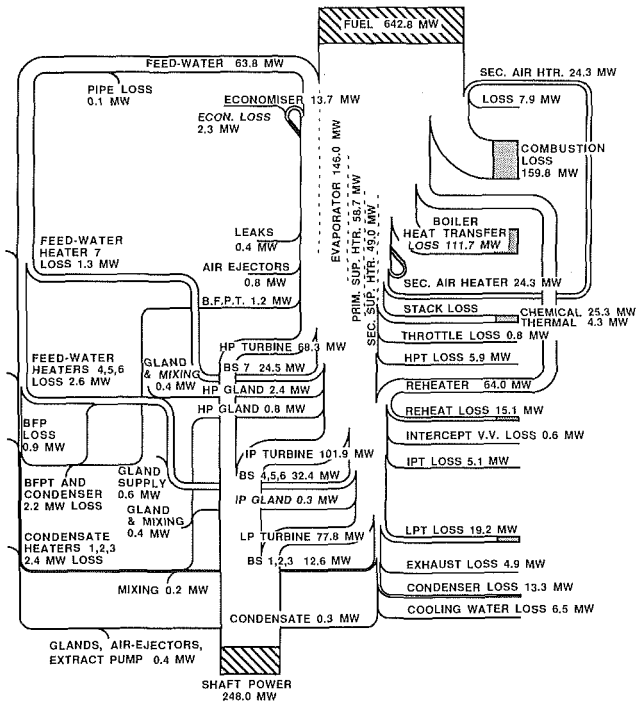

Fig. 2 Exergy audit of Huntly unit 4. Conditions as in Fig. 1. Details of feedwater heater flows have been removed.

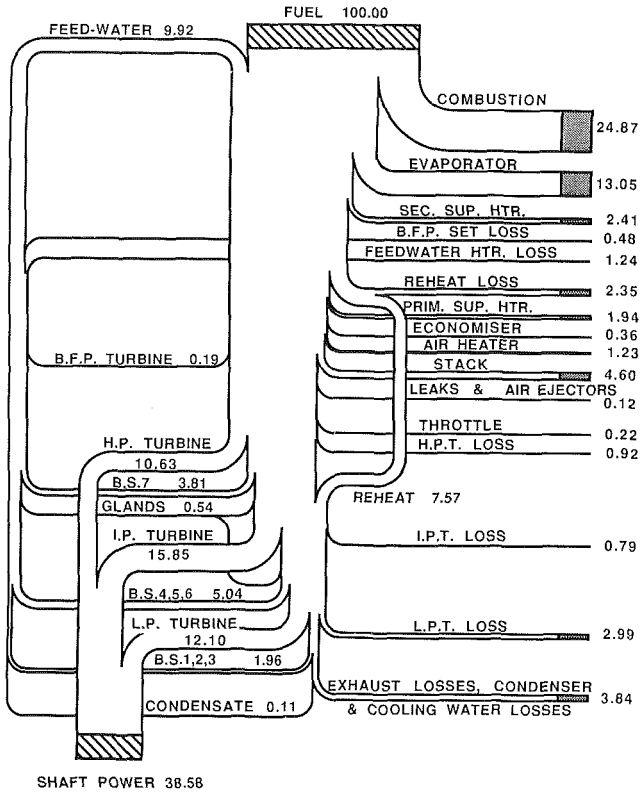

Fig. 3 Exergy audit of Huntly unit 4, expressing all flows as a percentage of the fuel exergy; shaft power 248 MW

(D) Illustrative Exergy Audits

The exergy audits presented here are based on data acquired while turbine heat-rate tests were being carried out on the host unit. The tests included both design and nonstandard modes of operation and we focus here on two comparisons involving the latter:

(*a*) Unit operating first with and second without the top heater (H.P.7 in Fig. 1) at a nominal load of 250 MW.

(*b*) Unit operating first with throttle control mode and second with sliding pressure control mode at a nominal load of 150 MW.

The heat-rate acceptance tests involved only the steam cycle and consequently no special instruments were provided for the boiler and flue-gas system. In this situation the station data acquisition system for the boiler, which is known to be in good condition from previous boiler tests, has been used to supply the necessary boiler data. Also the flow of water into the main desuperheaters was established using commercial, rather than test instruments, but even a large error (e.g., 10 percent) here would have had a negligible effect on the results presented. Apart from this tests were conducted in accordance with the British Standards institution test code BS752, which specifies instrumentation quality and test procedures. Natural gas firing was used in the tests described here, each being conducted over a 2-h period during which all measurements were averaged. However it was necessary to make adjustments to come of the recorded data. For example during one test the values obtained for two temperatures (bled steam 2 and 3) yielded state conditions with entropy lower than that for the steam entering the low pressure turbine. Errors in these temperatures would affect estimates of the performance of individual turbine stages, but would not significantly influence estimates of the overall low pressure turbine parameters. For the sake of completeness these bled steam temperatures have therefore been estimated by extrapolation from design data. In addition suspicions attach to the value for the boiler feed pump condensate flow rate in one test. However it has been established by sensitivity analysis that this particular uncertainty also does not affect the validity of the illustrative audits.

Figure 2 shows the principal exergy pathways for the host unit at 248 MW shaft power under natural gas firing with the system intact. The cooling water entry temperature was 12.4°C. To avoid unnecessary detail the exergy flows in the condensate and feed water heater chain have been simplified. This figure clearly illustrates the well-known fact that the most exergy losses in the unit, 83 percent of all losses in this case, are due to the combustion, stack, and heat transfer processes in the boiler. Internal turbine losses, on the other hand, amount to less than 8 percent of the plant loss, while exhaust, condenser, and cooling water losses represent 6 percent. Most of the remaining losses are associated with the condensate return process for which mixing, heat transfer, and boiler feed pump losses account for 2.5 percent of all losses. Finally gland, throttle, air ejector, and pipe losses amount to approximately 1 percent of the total losses. We note too that most of the stack losses are due to chemical rather than thermal nonequilibrium, the principal contributors being the combustion products CO_2 and H_2O together with residual combustible material, which was assumed to be methane.

The removal of the feed-water heater H.P.7 was carried out while keeping all boundary intensive properties and the load as close as possible to those used in the first test so that the shaft power output dropped only marginally, from 248.0 to 245.2 MW. The major readjustments were: a reduction in main steam flow by 19.6 kg/s (i.e., 10 percent), which is approximately the same as the bled steam 7 flow in the first test; an increase in the steam flow to the intermediate-pressure and low pressure turbines by approximately 3.3 kg/s; and an increase in the steam pressure downstream of the governor valves of 3.5 percent. The removal of heater H.P.7 resulted in an increase in the steam cycle heat rate of 76 kJ/kWh. The redistribution of thermodynamic losses within the unit is

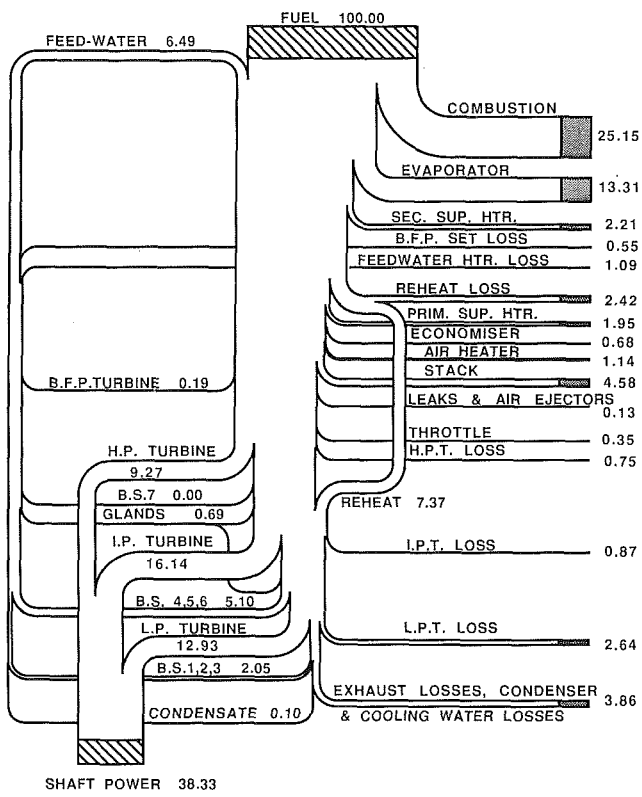

Fig. 4 Exergy audit with the top heater out of service. Conditions otherwise as in Fig. 3, shaft power 245 MW.

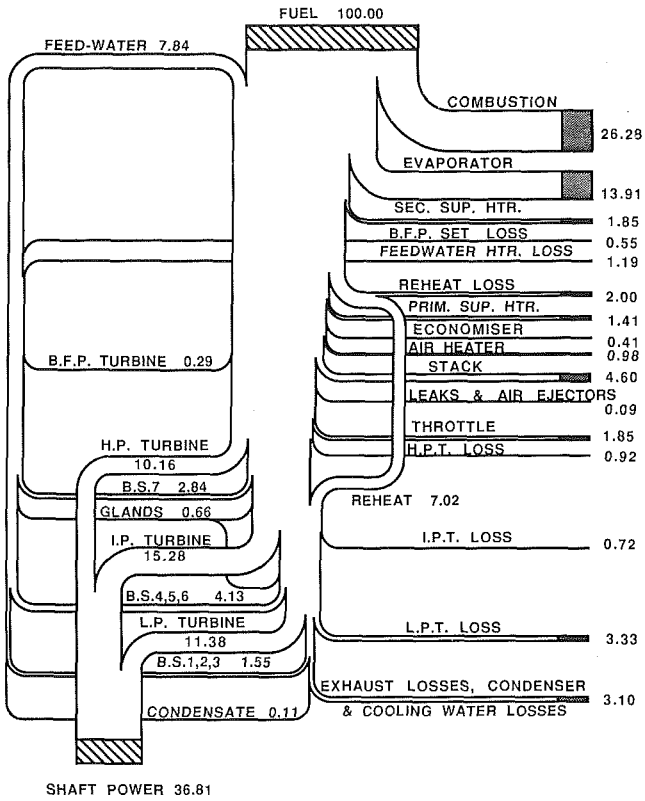

Fig. 5 Exergy analysis as percentage of fuel exergy; Huntly unit 4 at 152 MW shaft power with throttle control

therefore of some interest because it reveals the reasons for this deterioration in terms of the exergy audit. These are illustrated in Figs. 3 and 4, which show reduced representations of the major exergy flows in the unit. To assist the comparison of the two tests all flows have been expressed as a percentage of the fuel exergy in these figures. We comment now on significant differences shown here.

It is apparent that boiler losses, condenser losses and feedwater heater losses increased from 56.49 to 57.07 percent of the fuel exergy input as a result of removing heater H.P.7 from service, whereas turbine losses decreased from 4.70 to 4.26 percent. This trend in boiler losses is to be expected. For instance small increases occurred in the evaporator and economizer losses due to heat transfer to the colder return feedwater (43°C colder at the economizer inlet, 28°C colder at the outlet). These are, however, partly offset by a decrease in secondary superheater and feedwater losses due to the reduced main feed flow in the absence of heater H.P.7. Also because of the reduced main steam flow the shaft output of the H.P. turbine is reduced by 1.36 percent (of the fuel exergy rate) but the high pressure turbine efficiency remains almost constant. On the other hand, the governor valves were partly closed in order to reduce the steam flow and this had the effect of increasing throttle losses by 0.13 percent. While only small changes are seen in the low pressure turbine performance, a significant increase in exergetic efficiency of the low pressure turbine, from 80.12 to 83.04 percent, is evident. This increase partly compensates for the increase in boiler and throttle losses so that the overall effect is a small reduction in the exergetic efficiency of the unit by 0.25 percent, representing 0.66 percent of shaft output. This is the same as the decrease in the unit thermal efficiency from 37.05 to 36.81 percent.

It is noteworthy that whereas the steam cycle heat rate deteriorated by 76 kJ/kWh the exergetic efficiency of the turbines showed the opposite trend, increasing from 89.16 to 90.00 percent. The reason for the increase in the heat rate is the added unavailable energy at the turbine cycle terminals. However the first-law analysis does not contain the information that the extra energy is bound to be rejected, thereby giving a deterioration in the heat rate. The second-law analysis does include this information and therefore reflects more faithfully the machinery performance, namely the increase in the low pressure turbine efficiency. The ability of the exergy audit to disaggregate losses without the use of a detailed process model is an important aspect of this analysis.

The results of the second pair of tests, to compare throttle with sliding pressure control at part load operation, are presented in Figs. 5 and 6. These also show the exergy flows as a percentage of fuel exergy, first with throttle control at 152 MW shaft power (Fig. 5) and second (Fig. 6) with sliding pressure control at 155 MW output. The second set of measurements were taken immediately after the first, allowing time for the system to settle to a steady-state condition, while preserving the values of all boundary intensive properties, apart from the steam drum pressure which was reduced from 168 to 112 bar in order to keep the governor valves wide open.

Examination of the exergy flows shows that there is an increase in the evaporator heat transfer loss (1.54 percent of the input fuel exergy), which is attributable to the reduction in evaporation temperature from 352°C to 320°C. However there is a compensating reduction of 1.64 percent in throttle loss. In addition there are significant reductions in the reheater loss (0.29 percent) and in the economizer loss (0.10 percent). The reason for the reduction in reheater loss is that the cold reheat steam temperature is higher in the sliding pressure mode than in the throttle mode, so that heat transfer losses in the reheater are smaller because of the reduced temperature difference. In addition the reheater heat transfer rate is lower in the sliding pressure mode. Heat transfer losses in the economizer are similarly down in the sliding pressure mode

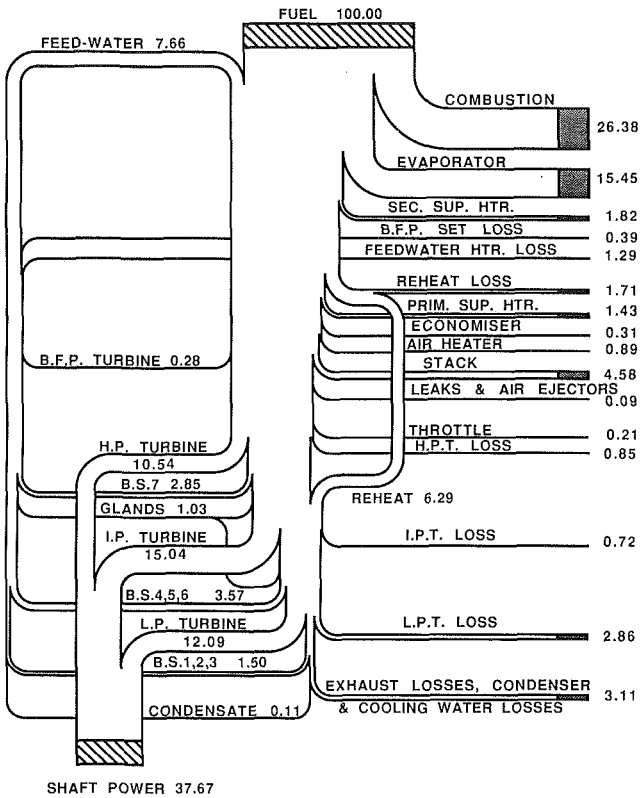

Fig. 6 Analysis for comparison with Fig. 5, using sliding pressure control at 155 MW shaft power

because the flue gas temperature is lower at that stage. Furthermore boiler feed pump losses, including the boiler feed pump turbine, are down by 0.16 percent in the sliding pressure mode, principally because the pumping power is down by 0.33 percent (of the fuel exergy). In total, losses not directly associated with the main turbines are reduced by 0.31 percent of fuel exergy. However the turbine output increased by 0.86 percent, which is considered more, because of an additional increase in turbine efficiency. Thus the improvement associated with sliding pressure control in this particular situation is largely due to an increase in the exergetic efficiency of the low pressure turbine, from 77.34 to 80.91 percent. We emphasize again that not all measurements complied fully with the BS752 specification, and we note that these efficiency changes are a matter for ongoing investigation.

It is evident that the sliding pressure mode of control offers some improvement in unit efficiency over the throttle mode. However the principal change in this particular case is related to the low pressure turbine while the nonturbine component involves a close competition between increased evaporator heat transfer losses and decreased throttle losses. We note that the gain in performance achieved by reducing the head pressure of the boiler feed pump in sliding pressure mode is much less than the change in associated heat transfer losses and is offset in this example by other small increases in steam losses. For instance gland leak losses, which are here included with feedwater heater losses, increased by 0.07 percent in the sliding pressure mode. Thus the change in the load of the boiler feed pump turbine (BFPT) had relatively little impact on the efficiency of the unit, although other authors (Silvestri et al., 1972; Riley et al., 1984) have given this aspect some emphasis. Here the reduction in reheater, economizer, and air heater losses contributed more to the improvement in performance in the sliding pressure mode than the reduction in BFPT load. The reason is connected with the exergetic efficiency of the boiler feed pump set, being approximately 55 percent in the throttle mode dropping to 53 percent in the sliding pressure mode. This means that slightly more than half the exergy flow into the BFP set is reinvested in the feed water. Consequently while the BFPT steam demand is down by 0.39 percent of fuel exergy, the BFPT and pumping losses decrease by only 0.16 percent. No general conclusion should be drawn from this result on the economy of an electric motor rather than a turbine-driven feed pump. However in this particular example the exergetic efficiency of the pump increased in the sliding pressure mode while the turbine efficiency decreased. As a result there would be an economic advantage from the use of electric pump drive, but only in the sliding pressure mode.

This comparison of throttle and sliding pressure control indicates the existence of an optimal steam-drum pressure in the case of sliding pressure control and shows the potential for additional savings through the use of combined nozzle and pressure control. Such hybrid control modes avoid much of the throttle loss while maintaining higher evaporation temperatures, therefore avoiding the enhanced evaporator losses of the sliding pressure mode. Economizer losses would remain as in the throttle control mode, as would BFPT losses. The maximum potential for improvement in unit efficiency, excluding the possibility of the turbine efficiency changing significantly, is approximately 1.9 percent of the fuel exergy.

(E) Closure

The point we wish to emphasize is not that one particular plant configuration or control mode offers higher efficiency than another. Rather we stress the impact of the exergy audit on our understanding of changes in the performance of the unit and which elements of the plant determine these changes. The examples presented have shown that some commonly accepted views on the causes of the losses illustrated could give an inappropriate emphasis. The very limited influence of the boiler feed pump turbine on the unit efficiency in the sliding pressure control mode is an example. More importantly, the results illustrate the need for the exergy audit to include both the boiler and steam cycle in an integrated way in order to provide a comprehensive and valid account of plant losses. The current work is restricted to an audit of the status of the plant at the time of measurement so that a process model would be required to make the analysis a predictive one. Yet in the present form the exergy audit provides much more information of the plant losses than an analysis confined to the energy flows and heat rate. The significance of individual item losses is quantified and a consistent understanding of the causes of the changes of these losses is made possible in a way which first-law process models of the plant do not provide.

Acknowledgments

Permission to publish this paper has been granted by the Electricity Corporation of New Zealand, formerly a Division of the N.Z. Ministry of Energy, whose cooperation and support for this work is gratefully acknowledged. We also wish to thank the staff of Huntly power station of their practical assistance, in particular: Mr. T. Weaver for software support, Mr. R. Woulf and Mr. R. Smale for data preparation and organization, and Mr. R. Jordan and his staff for generously accepting many inquiries and providing valuable information.

References

Began, A., 1982, *Entropy Generation Through Heat and Fluid Flow*, Wiley, New York.

Bosnjakovic, F., 1963, *Technical Thermodynamics*, Holt, Rinehart and Winston, New York.

Gaggioli, R. A., Yoon, J. J., Patulski, S. A., Latus, A. J., and Obert, E. F., 1975, "Pinpointing the Real Inefficiencies in Power Plants and Energy Systems," *Proc. Amer. Power Conf.*, Vol. 37, pp. 671-679.

Haywood, R. W., 1980, *Equilibrium Thermodynamics for Engineers and Scientists*, Wiley, Chichester.

Keenan, J. H., 1932, "A Steam Chart for Second-Law Analysis," *Mechanical Engineering*, Vol. 54, pp. 195–204.

Linnhoff, B., 1983, "New Concepts in Thermodynamics for Better Chemical Process Design," *Proc. Royal Society*, London, Vol. A386, pp. 1–33.

Liu, Y. A., and Wepfer, W. J., 1980, "Bibliography," *Efficiency and Costing; Second Law Analysis of Processes*, ACS Symposium Series Vol. 235, pp. 415–446.

Petit, P. J., and Gaggioli, R. A., 1980, "Second Law Procedures for Evaluating Processes," *Thermodynamics: Second Law Analysis*, ACS Symposium Series, Vol. 122, pp. 15–37.

Riley, J. F., Schumacher, R. L., and Bary, M. R., 1984, "When Sliding Pressure Operation Can Boost Cycling-Unit Efficiency," *Power*, pp. 45–48.

Rodriguez, L., 1980, "Calculation of Available-Energy Quantities," *Thermodynamics: Second Law Analysis*, ACS Symposium Series Vol. 122, pp. 39–59.

Salisbury, J. K., 1958, "Analysis of the Steam-Turbine Reheat Cycle," ASME JOURNAL OF ENGINEERING FOR POWER, Vol. 80, pp. 1629–1642.

Salisbury, J. K., 1959, "A New Performance Criterion for Steam-Turbine Regenerative Cycles," ASME JOURNAL OF ENGINEERING FOR POWER, Vol. 81, pp. 389–402.

Salisbury, J. K., 1961, "Power-Plant Performance Monitoring," ASME JOURNAL OF ENGINEERING FOR POWER, Vol. 83, pp. 409–422.

Schmidt, E., 1982, *Properties of Water and Steam in S.I. Units*, U. Grigull, ed., 3rd edn., Springer-Verlag and R. Oldenbourg, New York, pp. 179–190.

Silvestri, G. J., Aanstad, O. J., and Ballantyne, J. T., 1972, "A Review of Sliding Throttle Pressure for Fossil-Fueled Steam Turbine-Generators," *Proceedings of the American Power Conference*, Vol. 34, pp. 438–453.

Stull, D. R., and Prophet, H., 1971, *JANAF Thermochemical Tables*, 2nd ed., U.S. Dept. of Commerce, National Standard Reference Data System – NBS37.

Wepfer, W. J., and Gaggioli, R. A., 1980, "Reference Datums for Available Energy," *Thermodynamics: Second Law Analysis*, ACS Symposium Series Vol. 122, pp. 77–92.

ERRATA

Correction to "A Correlation for the Burning Velocity of Methane–Air Mixtures at High Pressures and Temperatures," by T. J. Al-Himyary and G. A. Karim, published in the October 1987 issue of the ASME JOURNAL OF ENGINEERING FOR GAS TURBINES AND POWER, pp. 439–442.

Equation (2) had a sign reversed. The correct equation should read as follows:

$$S_u = A - (F_1 \cdot F_2) \cdot (F_3 + F_4 \cdot f + F_5 \cdot f^2)$$

B. J. Huang
Professor.

R. H. Yen
Associate Professor.

W. S. Shyu
Graduate Assistant.

Department of Mechanical Engineering,
National Taiwan University,
Taipei, Taiwan 10764

A Steady-State Thermal Performance Model of Fire-Tube Shell Boilers

A nonlinear steady-state thermal performance model of a fire-tube shell boiler was developed in the present study. The model consists of two semi-empirical equations for the radiative heat flux from the combustion gas to the boiling water and the heat loss flux from the body surface to the ambient. Using this model, we can simulate the boiler performance under standard conditions and draw standard performance curves from which the thermal performance comparison between different boilers can be made on a common basis.

Introduction

The fire-tube shell boiler is probably one of the most widely used boilers in process industries. Unfortunately, it was found that the average boiler efficiency is relatively low, approximately 65–70 percent (Cheng et al., 1983a).

The heat input-output or the heat loss method, based on ASME *Power Test Codes*, has been widely used in the computation of steady-state thermal efficiency, using on-site test data (Cheng et al., 1983b). The computation itself does not require a performance model but is merely an energy balance calculation at an operating point. Moreover, the computed efficiencies were found to be scattered due to the variation of operating conditions, which can hardly be fixed at the same values for all boilers during field tests. Therefore, the problem of comparison of efficiency between different boilers by using on-site test data alone arises, unless a thermal model is available for computing and drawing performance curves at a fixed operating condition. Unfortunately, unlike the water-tube boiler which has been studied extensively (Chien et al., 1958; Nicholson, 1964, 1965, 1966; Anderson, 1969; Kwan, 1970; McDonald and Kwatny, 1973), research on thermal performance models of the fire-tube shell boiler is sparse.

Some researchers have developed simple lumped models to study domestic water heater performance (Claus and Stephan, 1985; Malmstrom et al., 1985; Lebrun et al., 1985). However, these models are not suitable for steam boiler analysis since they assume several known variables other than the measurable ones, such as combined heat transfer coefficients, solid phase temperature, etc. It is known that heat transfer from the combustion gas to the boiling water via a heating surface in a shell steam boiler is very complicated as radiative, convective, and boiling processes are all involved. The assumed unmeasured variables are thus unreliable since accurate prediction of them is extremely difficult. In addition, these models are mainly for water heaters without boiling.

In the present study, a nonlinear semi-empirical steady-state model is developed, based on a lumped hypothesis, for the heat transfer from the combustion gas to the boiling water and the heat loss from the boiler body to the ambient. The model then can be used to compute the performance curves of a shell boiler under given standard conditions and thus allow comparison of performance between different boilers to be correctly made on a common basis.

Development of Performance Model

The present study focuses on a residual fuel-oil fire-tube shell boiler (see Fig. 1). The boiler as a whole can be divided into three phases in accordance with the heat-carrying media: (1) gaseous phase (a heat source), (2) boiling-water phase (a heat sink), and (3) solid phase (including heating surface metal and insulating material of shell). The gaseous phase includes the combustion gas products in the firing chamber and the interior space of the tube bundle (i.e., fire tubes). Radiative and convective heat are then transmitted from the gaseous phase via a metallic wall (the solid phase) to the boiling water where boiling and evaporation take place. Heat loss also occurs from

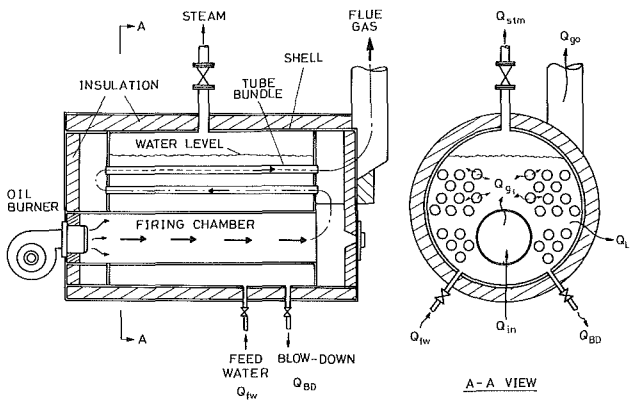

Fig. 1 Schematic diagram of a fire-tube shell boiler

Contributed by the Power Division for publication in the JOURNAL OF ENGINEERING FOR GAS TURBINES AND POWER. Manuscript received by the Power Division October 24, 1986.

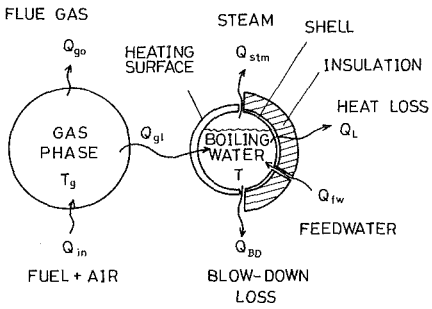

Fig. 2 Schematic diagram of steady-state heat flow of a shell boiler

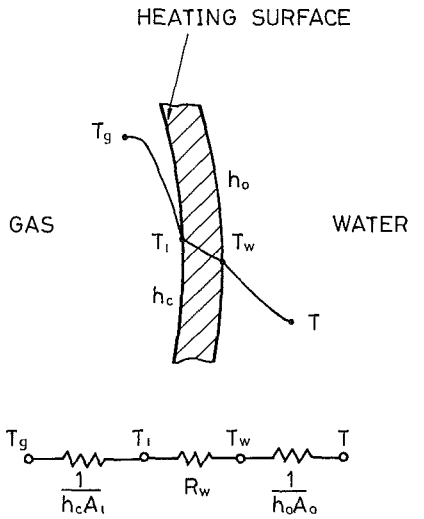

Fig. 3 Thermal network from combustion gas to boiling water

the boiling water via the shell wall and the insulation layer to the ambient. A schematic steady-state heat flow diagram is shown in Fig. 2.

In conventional boiler efficiency tests, a complete data set, as presented in Table 1, is first collected from a field test run following a standard measurement procedure; these data are then used to compute the efficiency using the mass and energy balance equations given by the ASME *Power Test Code Steam Generating Units PTC 4.1* (McLean and Murdock, 1972) or similar ones (Cheng et al., 1983b). Derivation of the set of performance equations in the present study basically requires that the equations should contain variables that can be either measured directly or computed exactly from raw test data, and unknown parameters that can be determined analytically.

The steady-state performance model developed here includes a radiative heat flux equation q_{g1} (from gas to heating surface) and a body surface heat loss flux equation q_L (from boiling water to ambient). It should be noted here that these two equations are semi-empirical. The derivation to be presented in the following sections is based on a simplified lumped model.

1 Radiative Heat Flux Equation. In deriving the radiative heat flux equation, the following assumptions are made:

1 The gaseous and boiling-water phases are at the equivalent uniform temperatures T_g and T, respectively.

2 The metallic wall surface, which is in contact with the gaseous phase, is at an equivalent uniform temperature T_1.

3 The radiative heat transfer process approaches the well-stirred model of Lobo and Evans (1939), Hottel and Sarofim (1967), Lihou (1977), and Sarofim and Hottel (1978). Therefore, the temperature of flue gas is assumed to be $T_{go} = T_g - D$, where D is a temperature drop defined by the well-stirred model.

From the above assumptions, the steady-state radiative heat transfer from gas phase to heating surface Q_{g1} (W) can be written as

$$\begin{aligned} Q_{g1} &= f_r A_1 \sigma (T_g^4 - T_1^4) + h_c A_1 (T_g - T_1) \\ &= f_r A_1 \sigma [(T_{go} + D)^4 - T_1^4] + h_c A_1 [(T_{go} + D) - T_1] \end{aligned} \quad (1)$$

where $f_r A_1 = \overline{GS}_1$, which is a total-exchange area, m^2, as defined by Hottel and Sarofim (1967); f_r represents the absorptance-emittance factor between combustion gas product and metallic wall; σ is the Stefan–Boltzmann constant, 5.669×10^{-8} W/m^2 K^4; A_1 is the heating surface area, m^2. The temperature drop D can be further written as, according to the well-stirred model

$$D = \phi \frac{Q_{g1}}{Q_{in}} \frac{T_{af} - T_o}{T_{af}} = \phi \frac{q_{g1}}{q_{in}} \frac{T_{af} - T_o}{T_{af}} \quad (2)$$

$$T_{af} = Q_{in}/m_a C_g \quad (3)$$

$$q_{g1} = Q_{g1}/A_1, \quad q_{in} = Q_{in}/A_1 \quad (4)$$

where T_{af} is the pseudo-flame temperature, K; m_a is the mass flow rate of combustion air, kg/s; C_g is the mean specific heat of the combustion gas, J/kg K; T_o is the ambient temperature, K; Q_{in} is the total energy input rate by fuel combustion and preheating of fuel and air, if any; q_{g1} is the radiative heat flux, W/m^2; q_{in} is the energy input rate to the gaseous phase, W/m^2, based on the heating surface area A_1; ϕ is a parameter to be determined experimentally. The last term in equation (1) represents the effect of convective heat transfer.

It is noticeable that the heating surface temperature T_1 is just a hypothesized uniform variable and thus is an unmeasurable quantity. However, a useful relation for T_1 can be derived intuitively by use of the thermal network as shown in Fig. 3

$$T_1 = \left(r_w + \frac{A_1}{h_o A_o}\right) q_{g1} + T \quad (5)$$

where r_w ($\equiv R_w A_1$) is an effective total thermal resistance of the heating wall, K m^2/W; R_w ($= r_w/A_1$) represents the thermal resistance based on heating surface area A_1, K/W; h_o is the boiling heat transfer coefficient adjacent to the heating

Nomenclature

A_s = inner surface area of shell, m^2
h_s = heat transfer coefficient, W/m^{2}K
q_e = net heat flow carried away by steam based on heating surface area, W/m^2
q_{go} = heat loss from flue gas based on heating surface area = Q_{go}/A_1, W/m^2
Q_{BD} = boiler blowdown loss, W
Q_L = boiler body surface heat loss rate, W
Q_{stm} = rate of energy carried out by steam, W
Q_{fw} = rate of energy carried in by feedwater, W
R_b = thermal resistance from boiler body to ambient, K/W
T_f = fuel temperature, °C
T_{fw} = feedwater temperature, °C
T_s = temperature at inner surface of shell, K

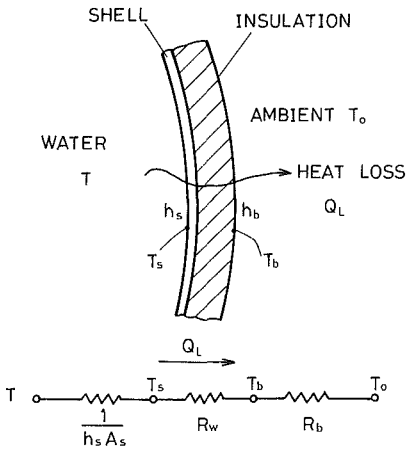

Fig. 4 Thermal network from boiling water to ambient

surface, W/m^2 K; A_o is the total heating surface area in contact with the boiling water, m^2.

It can easily be shown from many experimental results that the boiling heat transfer coefficient h_o in fire-tube shell boilers is proportional to the power of the heat flux (Rohsenow, 1952; Levy, 1959; Cryder and Finalborgo, 1937; Gorenflo, 1968; Collier, 1981; Leong and Cornwell, 1979; Nelson and Burnside, 1985; Hwang and Yao, 1986), i.e.,

$$h_o \sim q_{g1}^{n'} \tag{6}$$

where n' is an exponential constant. Using this relation and substituting equation (5) into equation (1), we obtain

$$q_{g1} = f_r\, \sigma[(T_{go}+D)^4 - (r_w\, q_{g1} + C\, q_{g1}^n + T)^4] + h_c[(T_{go}+D) - (r_w\, q_{g1} + C\, q_{g1}^n + T)] \tag{7}$$

where C and n are the parameters related to boiling heat transfer phenomenon; D is defined through equations (2)–(4). This is nonlinear semi-empirical relation for radiative heat flux.

For easy understanding, equation (7) can be written as a function of two groups, the unknown parameters and the measurable operating variables

$$q_{g1} = q_{g1}(f_r,\ \phi,\ C,\ n,\ r_w,\ h_c;\ T,\ T_{go},\ T_o,\ m_a,\ q_{in}) \tag{8}$$

In practice, the steam and the boiling water inside the shell can be assumed to be at thermodynamic equilibrium. That is, the evaporation of steam from the boiling water is very fast so that both of them have equal temperature and pressure. This assumption is true, typically for fire-tube shell boilers, due to three facts: (1) the boiling in the shell is severe and always associated with high agitating effect; (2) all the combustion heat is directly transferred to water; i.e., the shell does not only serve as an evaporation device as in water-tube boilers; (3) the hold-up water quantity in the shell is relatively large in design and there is a long retention time for feedwater; hence the heat storage effect dominates. Therefore, the temperature T in equation (7) or (8) can approximate the measurable steam supply temperature. The effect of steam load or feedwater crossflow on the boiling heat transfer coefficient h_o can be neglected and thus does not appear in equations (6) and (7) since the dominating process in the shell is pool boiling and the feedwater crossflow is low.

The six parameters, f_r, ϕ, C, n, r_w, and h_c defined in equation (7) can be assumed to be fixed for a given boiler, irrespective of the operating conditions. This can be proved by the results of many investigations, which have shown that the physical properties such as the emissivities of surface and gas and the constants defined in the boiling transfer correlations for tube bundles are approximately constant over a wide range of operating conditions (Haigh and Chojnowski, 1975; Morgan, 1974; Guruz, 1977; Dombrowski and Johns, 1969).

2 Heat Loss Flux Equation. The heat loss from boiler body surface Q_L usually includes both radiative and convective transfers. Since field operation has shown that the heat loss from body surface increases with increasing steam load or fuel firing rate, the total energy loss rate Q_L can be hypothesized to be in an exponential relation

$$Q_L = C_b m_f A_b (T_b - T_o)^{n_L} \tag{9}$$

where C_b is the overall heat transfer coefficient from body surface per unit fuel rate, J/kg m^{2}K; T_b is an assumed uniform body surface temperature, K; A_b is the body surface area, m^2; here, m_f is the fuel firing rate, kg/h; n_L is an empirical constant.

Using the thermal network from T to T_b as shown in Fig. 4, we obtain

$$T_b = T - r_L\, q_L \tag{10}$$

where r_L $(\equiv A_1/h_s A_s + A_1 R_w)$ is an effective thermal resistance from boiling water to the boiler body surface, including conductive resistances of shell and its insulation; q_L $(\equiv Q_L/A_1)$ is the heat loss flux based on the heating surface area A_1, W/m^2.

Substituting equation (10) into (9) and noting $Q_L = q_L A_1$, we obtain

$$q_L = U_o (m_f/A_1)[T - T_o - r_L q_L]^{n_L} \tag{11}$$

where U_o $(= C_b A_b)$, r_L, and n_L are the three parameters to be determined experimentally. Again, the functional relation can be written as

$$q_L = q_L(U_o,\ r_L,\ n_L;\ T,\ m_f) \tag{12}$$

where the latter group represents the measurable operating variables; the former one represents the unknown parameters. Similarly, the effect of steam or feedwater crossflow is also neglected here.

Parameter Determination

1 Nonlinear Least-Square Fit. Equations (7) and (11) form the basic performance model of the shell boiler in which nine unknown parameters in total are defined. They are derived from several hypotheses and can be used for the correlation between the heat fluxes (radiative and heat loss) and field test data. The validity of this semi-empirical model thus relies mainly on experimental verification.

Substituting the measured operating variables into the model and performing a least-squares fit, we can solve for the parameters, by minimizing the residual sum of squares for the radiative flux S_{g1}, and heat loss flux S_L

$$S_{g1} = \sum_{i=1}^{N} [q_{g1i} - f_i(f_r,\ \phi,\ C,\ n,\ r_w,\ h_c)]^2 \tag{13}$$

$$S_L = \sum_{i=1}^{N} [q_{Li} - g_i(U_o,\ r_L,\ n_L)]^2 \tag{14}$$

where q_{g1i} and q_{Li} are the heat fluxes determined at the ith experiment; the functional relations for the ith test data set, $f_i(\ldots)$ and $g_i(\ldots)$, follow equations (7) and (11); and N is the total number of test data sets. It should be noted here that the heat fluxes q_{g1} and q_L are measurable or can be computed from measurable operating variables by use of the equations as given by the ASME *Power Test Code PTC 4.1* mentioned above.

As can be seen, equations (13) and (14) are highly nonlinear and thus a nonlinear programming method has to be used. Here, the Polak-Ribere conjugate gradient method was employed to solve the above equations numerically (Reklaitis

Table 1 Data collected from efficiency testing

Type	Descriptions and Notations
Temperature	steam or boiling water (T), flue gas (T_{go}), feedwater (T_{fw}), fuel (T_f) (after preheating), combustion air (T_a) (preheated), ambient(T_o).
Pressure	steam (P), ambient (P_a), flue gas (P_{go}) firing chamber (P_c).
Flowrate	fuel (m_f), supplied steam (m_s), feedwater (m_w), combustion air (m_a) (optional).
Flue gas composition	O_2, CO_2, CO, SO_2, NOx.
Quality	supplied steam (x).
Fuel composition	carbon, hydrogen, oxygen, nitrogen, sulphur, water, ash.
Humidity	ambient (Z).

Table 2 Specifications of the testing shell boiler

	BOILER A	BOILER B
Boiler Type:	3-pass shell boiler (Model HTH-5)	4-pass shell boiler (Model S4-2000)
Evaporation Rate:		
maximum	600 kg/hr	2400 kg/hr
normal	500 kg/hr	2000 kg/hr
Rating Capacity:	29 kW	120 kW
Actual Total Heating Surface Area:	14.5 sq. m	60.0 sq. m
Inside Diameters		
Shell:	1.36 m	1.65 m
Firing Chamber:	0.38 m	0.58 m
Fire Tubes:	0.0483 m	0.0508 m
No. of Fire Tubes:	40	104
Length of Fire Tubes:	2.0 m	3.36 m
Thickness of Fire Tubes:	0.0095 m	0.0095
Operating Pressure:		
(guage) maximum	10 kg/sq. cm	10 kg/sq. cm
normal	7 kg/sq. cm	7 kg/sq. cm
Fuel Type:	heavy fuel oil #6	heavy fuel oil #6
Fuel Consumption Rate:		
maximum	36.2 kg/hr	123.0 kg/hr
normal	30.2 kg/hr	100.kg/hr
Body Insulation:	75 mm fibre	350 mm fibre

Table 3 Operating ranges of Boilers A and B at steady state

Descriptions	Boiler A	Boiler B
Steam load, kg/hr	140 - 500	1000 - 2700
Fuel consumption rate, kg/hr	10 - 50	50 - 220
Steam temperature, °C	140 - 160	155 - 160
Ambient temperature, °C	16 - 28	24 - 28
Flue gas temperature, °C	170 - 380	170 - 220

et al., 1983; Vanderplaats, 1984). A computer package was developed and can be run on an IBM PC or is compatible with an 8087 math coprocessor. It takes about 30 min CPU to finish a nonlinear minimization job.

2 Experimental Determinations of q_{g1} and q_L. To determine q_{g1} and q_L, we obtain from a steady-state energy balance of the gaseous phase of the shell boiler

$$Q_{g1} = Q_{in} - Q_{go} \tag{15}$$

where Q_{go} is the total rate of energy carried away by the flue gas, including sensible heat and water vapor formation heat losses.

From the energy balance of boiling water as shown in Fig. 2, we obtain, without blowdown and at steady state

$$Q_L = Q_{g1} - Q_E \tag{16}$$

where $Q_E (= Q_{stm} - Q_{fw})$ is the net rate of energy carried out by steam. Therefore Q_L can be computed if Q_{g1} and Q_E are known.

Apparently, Q_{in}, Q_{go}, and Q_E can be easily determined using the available test data of Table 1 and the standard equations given in the ASME *Power Test Code PTC 4.1* or other similar references, such as Japan Industrial Standard (JIS) or Chinese National Standard (CNS) (Cheng et al., 1983b). Here,

Table 4 Model fitting of Boiler A for q_{g1}

TEST DATA kW/m²	FITTED VALUE kW/m²	DEVIATION* %
20.779	19.703	-1.2614
8.451	8.344	-1.2614
13.666	13.995	2.4023
8.234	8.457	2.7179
17.130	17.197	.3880
13.256	13.357	.7611
8.359	8.398	.4711
15.267	15.357	.5922
18.857	18.513	-1.8265
23.838	23.771	-.2800
28.305	27.851	-1.6033
17.433	17.355	-.4438
16.184	16.689	3.1166
23.683	24.660	4.1289
9.334	9.565	2.4752
19.185	19.363	.9270
18.145	18.142	-.0195
23.521	23.509	-.0515
17.575	17.820	1.3913
28.501	28.656	.5431
10.455	10.157	-2.8494
10.504	10.102	-3.8247
11.261	10.793	-4.1572
11.657	11.371	-2.4528
13.694	13.356	-2.4637
12.040	12.330	2.4147
12.261	11.984	-2.2568
12.223	12.491	2.1915
12.943	13.124	1.4030
11.869	11.967	.8286
12.546	12.718	1.3729

STANDARD DEVIATION : .402 kW/m²

f_r = .38567; ø = 1123.09 K; C = 865.11

n = -0.0019912; h_c = 13.990 W/m² K

r_w = 3.078E-04 m² K/W

* DEVIATION ≡ 100 x (FITTED - TEST)/TEST, %

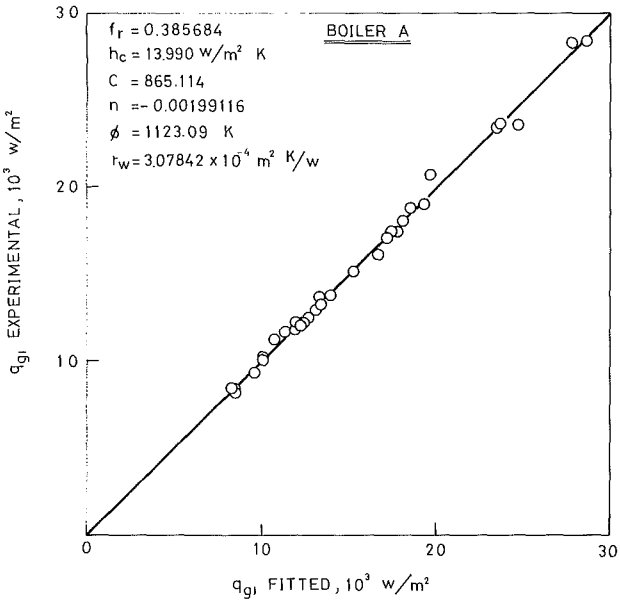

Fig. 5 Model fitting of Boiler A for q_{g1}

the heat fluxes q_{g1}, q_{in}, and q_L are all based on the heating surface area A_1 and can be obtained as well.

3 Experiments. Two shell boilers (Boiler A and Boiler B) were used in the present experiment. Boiler A is a mini-size (29 kW) experimental boiler installed in the laboratory with well-equipped instruments for this study, while Boiler B is a small size (120 kW) shell boiler already installed and in use in a factory. The basic design data of these two boilers are listed in Table 2.

T-type thermocouples were used to measure temperature in

Table 5 Model fitting of Boiler B for q_{g1}

TEST DATA kW/m²	FITTED VALUE kW/m²	DEVIATION* %
16.1119	16.1974	.5308
24.6529	24.5854	-.2737
19.1505	19.1049	-.2384
24.9552	24.6101	-1.3828
14.4172	14.4741	.3945
16.1322	16.0732	-.3659
18.1542	18.0868	-.3714
21.2911	21.2240	-.3149
25.8892	25.7206	-.6512
22.8838	22.8893	.0240
35.7674	35.6239	-.4012
12.7977	12.9142	.9099
22.2522	22.2729	.0933
23.7325	23.6996	-.1387
15.4550	15.4748	.1279
18.1300	18.0796	-.2781
20.3610	20.2755	-.4202
13.2252	13.2484	.1761
16.0729	16.1948	.7581
17.1049	18.2570	6.7351

STANDARD DEVIATION : .3344 kW/m²

f_r = .465143; ϕ = 1329.80 K; C = 1078.05;

n = -.00330086; h_c = 744.788 W/m² K;

r_w = 2.64578E-04 m² K/W.

* DEVIATION ≡ 100 x (FITTED - TEST)/TEST, %

Table 6 Model fitting of Boiler A for q_L

TEST DATA kW/m²	FITTED VALUE kW/m²	DEVIATION* %
2.68857	2.78845	3.7148
1.19154	1.21485	1.9562
1.89015	1.94788	3.0545
1.19644	1.31794	10.1555
2.70373	2.59030	-4.1950
2.14568	1.93259	-9.9312
1.07096	1.23582	15.3943
2.38742	2.15273	-9.8302
3.11208	2.58618	-16.8987
2.94948	3.13900	6.4257
4.53566	3.75561	-17.1982
3.21335	2.60425	-18.9551
2.46335	3.18199	29.1733
1.82600	1.35237	-25.9384
2.39977	2.66716	11.1425
2.58217	3.27432	26.8047
2.43023	2.58217	6.2518
3.52861	3.81477	8.1096
1.72794	1.55338	-10.1022
1.25112	1.33202	6.4667
1.08354	1.37556	26.9502
1.42118	1.60289	12.7860
1.59605	1.69062	5.9253
2.06205	1.74212	-15.5151

STANDARD DEVIATION : .3857 kW/m²

r_L = .120019E-01; U_o = .999991E+01

n_L = .105682E+01

* DEVIATION ≡ 100 x (FITTED - TEST)/TEST, %

the shell, the flue gas, and the ambient, with ±0.7°C uncertainty. Two rotary-type integrating flow meters were used to measure the flow rates of fuel and feedwater with ±3 percent uncertainty, and a carefully calibrated flue gas analyzer was used to measure the volume concentrations of O_2 and CO with uncertainties of ±1.5 percent and ±10 percent, respectively.

The experiments were run at various conditions as listed in Table 3. The test data of Boiler B were taken on site in the factory when the boiler was operational. Since we were unable to install a precision throttling meter to measure the quality of the exhausted steam for the calculation of Q_L, the verification of the heat loss modal, equation (11), for Boiler B was omitted.

4 Analytical Results. For the radiative heat flux q_{g1}, it was found in the present study that the experimental data for both Boiler A and B can be fitted very well to equation (7), for

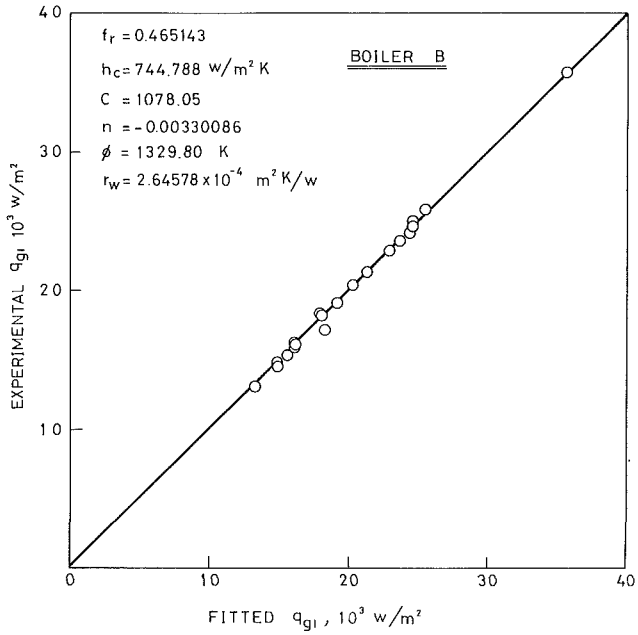

Fig. 6 Model fitting of Boiler B for q_{g1}

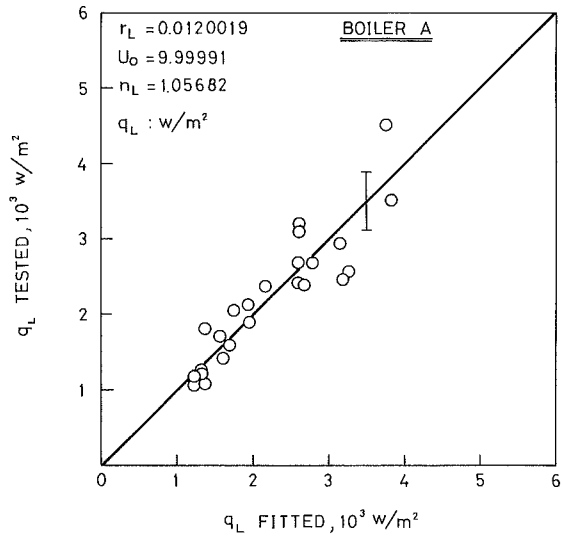

$$q_L = U_o\left(\frac{m_f}{A}\right)\left[T - T_o - r_L\, q_L\right]^{n_L}$$

r_L = 0.0120019, U_o = 9.99991, n_L = 1.05682

q_L : w/m², T, T_o: °C, m_f/A_f: kg/hr m²

Fig. 7 Model fitting of Boiler A for q_L

the parameters determined by the nonlinear least-squares technique.

For Boiler A, all the deviations are surprisingly within ±4.2 percent, and mainly within ±3 percent (see Table 4 and Fig. 5). For Boiler B, the deviation is always within ±6.8 percent, primarily within ±2 percent (see Table 5 and Fig. 6).

For the heat loss model q_L, the test data collected from Boiler A were found to fit equation (11) with larger diviations, mainly less than ±15 percent, although some are even higher (see Table 6 and Fig. 7). The higher deviation is attributed to the errors in the measurement of steam flow rates and exit steam quality. Since the body heat loss is small, as compared

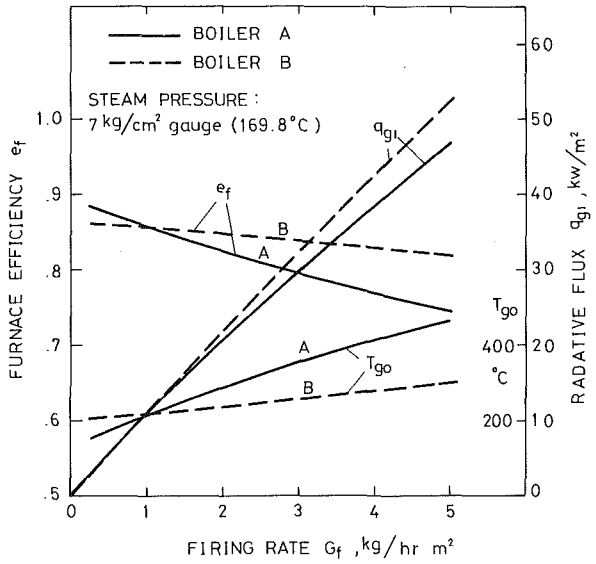

Fig. 8 Standard performance curves of Boiler A and B at 7 kg/cm²

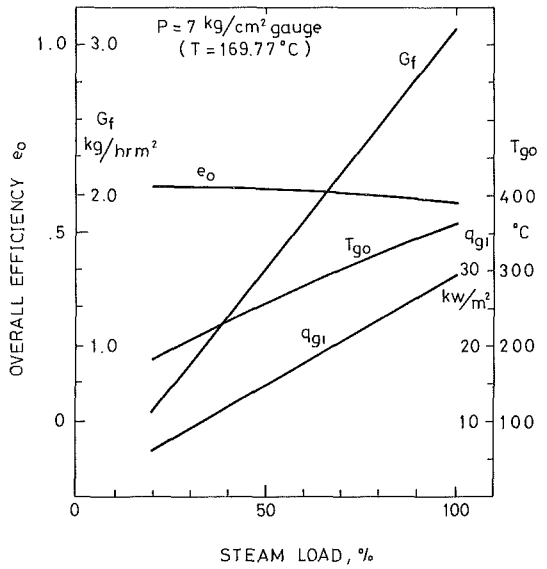

Fig. 9 Standard overall performance curves of Boiler A at 7 kg/cm²

to the total heat loss of the shell boiler, usually less than 15 percent (or less than 3 percent of total energy input rate), the deviations are still in engineering tolerable range. Therefore, the heat loss model q_L still provides fair agreement with the experimental measurements.

Performance Curves and Design Evaluation of Shell Boiler

The proposed model has been verified over a wide operating range and thus allows us to simulate the boiler performance accurately at any operating condition. This simulation can be considered as interpolation of performance to a fixed operating condition that is not controllable during field test run. This method can then be used to solve problems associated with scattering of the measured efficiencies due to variations or fluctuations of the operating conditions, such as steam temperature and pressure, amount of excess air, ambient conditions, etc.

If we define a common or standard operating condition, the performance curves simulated from the model can be used to evaluate the thermal performance of different boilers correctly on a common basis. We define a standard condition at: 20 percent excess air, $T_o = T_{fw} = T_f = 25°C$, and ambient humidity $Z = 0.02$ kg vapor/kg air. This is an average condition for most boilers, except T_f may vary depending on burner design. Besides, the properties of the fuel oil used for the simulation, including chemical composition and heating value, also must be designated. Here, the fuel oil used in the present experiment (with heating value of 10,289 kcal/kg) is chosen as the standard fuel. Then for a given steam pressure or temperature, the standard performance curves can be computed and drawn.

For heat transfer in the boiler, we further define a furnace efficiency e_f as the fraction of the rate of total input energy transmitted to the boiling water

$$e_f = Q_{g1}/Q_{in} = q_{g1}/q_{in} \tag{17}$$

For overall performance, we define an overall efficiency e_o as the fraction of the rate of total input energy carried out by steam

$$e_o = Q_E/Q_{in} \tag{18}$$

The performance thus can be represented by the above two efficiencies, e_f and e_o, which will vary with fuel firing rate and steam load.

Assuming that no entrained water is carried away with outflow steam and using the performance equation, equation (7), the furnace efficiency e_f can be simulated with respect to various fuel firing rates (per unit heating surface area), $G_f (= m_f/A_1)$, for a given steam pressure or temperature. It should be noted that for fixed fuel oil and common operating conditions mentioned above, furnace efficiency e_f and firing rate G_f are equivalent to the reduced efficiency and the reduced firing density, respectively, which are the universal dimensionless characteristic variables for furnace operation defined by Hottel and Sarofim (1967) in the stirred model. Thus, the simulated standard furnace efficiency curves can be used to evaluate the thermal performance of different boilers. One of the results is shown in Fig. 8.

It is seen from Fig. 8 that at 7 kg/cm² gage Boiler B is, in general, superior to Boiler A except at very low fuel firing rate ($G_f < 1.0$ kg/h m²), which corresponds to low load condition and is not desirable. This coincides with the fact that Boiler B is designed in patented four-pass tube bundles and with a corrugated cylindrical firing chamber, which may enhance both radiative and convective heat transfer processes.

The overall standard performance curve is simulated for Boiler A only in the present study, using equations (7) and (11). To avoid interpolation from charts and to facilitate the computation, we used the empirical equations of the steam table (Steltz and Silvestri, 1958; Irvine and Liley, 1984) for the present study.

Figure 9 shows the variations of overall efficiency, fuel firing rate, radiative flux, and flue gas temperature with the steam load, which is defined as the ratio of actual to rated steam flow rates. It is seen that the steam load would affect the overall performance because the fuel firing rate varies with steam load and in turn affects the total rate of heat input Q_{in} as well as the radiative heat flux q_{g1}. No overall performance comparison and evaluation can be made with Boiler B here since the heat loss flux model, equation (11), was not identified for Boiler B due to the lack of necessary field test data. However, it would not have been a problem if data were available.

Discussion and Conclusions

A semi-empirical performance model for fire-tube shell boilers was developed in the present study. With this model, we can further simulate the boiler performance at standard conditions and compare the thermal performance of different

boilers on a common basis. Action then can be taken to improve the boiler design in order to achieve better performance. Since we are only concerned with the development of a useful technique for thermal performance evaluation, the study of boiler thermal design technique to improve performance is not included in the present paper.

To determine performance of different shell boilers, we summarized the following efficiency test procedures:

Step 1: Follow the ASME *Power Test Code PTC 4.1* or similar standards to obtain a field test data set as listed in Table 1, under various steam pressures or temperatures, and fuel firing rate or steam loads.

Step 2: Search for the optimum parameters in equations (7) and (11), using field test data and the nonlinear programming technique.

Step 3: Simulate the performance curves at a standard condition, which is suggested to be: $T_f = T_{fw} = T_o = 25°C$, 20 percent excess air, 0.02 kg vapor/kg air humidity. Fuel with fixed chemical composition and heating value must be designated for the simulation. Two standard performance curves have to be simulated and plotted: furnace efficiency versus fuel firing rate and overall efficiency versus steam load.

Step 4: Evaluate the design and performance of different boilers using the standard performance curves.

The data shown in Figs. 5–7 for Boiler A were taken following Steps 1 and 2. Figures 8 and 9 are the simulated performance curves following Step 3.

Finally, it should be emphasized again that the present performance model for shell boilers is semi-empirical and was developed from several hypotheses such as lumped temperatures of heating surface and combustion gas, uniform heat fluxes, etc. Thus, the physical significance of equations (7) and (11) is limited to the correlation between the heat fluxes (radiative and heat-loss) and the measurable operating variables or field test data only. No physical significance can be exactly given to the magnitudes of the lumped variables and the parameters defined in equations (7) and (11).

Acknowledgments

The authors are very grateful to the Energy Committee at the Ministry of Economic Affairs, the Republic of China, for supporting this study. Technical support from Mr. Y. C. Cheng at the Energy Research/Service Organization of the Industrial Technology Research Institute during the field test of Boiler B is also very much appreciated.

References

Anderson, J. H., 1969, "Dynamic Control of a Power Boiler," *Proc. IEE*, Vol. 116, No. 7, pp. 1257–1268.

Cheng, Y. C., Huang, C. L., and Lee, M. Y., 1983a, "Survey of Industrial Boiler Efficiency in Taiwan Area," Technical Report No. ERL-022, Energy Research Laboratory, Industrial Technology Research Institute, Taipei, Taiwan.

Cheng, Y. C., Chuan, S., and Lee, M. Y., 1983b, "A Study on Calculation Method of Boiler Efficiency," Technical Report No. ERL-024, Energy Research Laboratory, Industrial Technology Research Institute, Taipei, Taiwan.

Chien, K. L., Ergin, E. I., Ling, C., and Lee, A., 1958, "Dynamic Analysis of a Boiler," *Trans. ASME*, Vol, 80, pp. 1809–1819.

Claus, G., and Stephan, W., 1985, "A General Computer Simulation Model for Furnaces and Boilers," *ASHRAE Trans.*, Vol. 91, Pt. 1.

Collier, J. G., 1981, "Thermal-Hydraulic Fundamentals and Designs: Two-Phase Boiling and Evaporation," in: *Heat Exchanger*, S. Kakac, A. E. Bergles, and F. Mayinger, eds., McGraw-Hill, New York.

Cryder, D. S., and Finalborgo, A. C., 1937, "Heat Transmission From Metal Surfaces to Boiling Liquids," *Trans. AIChE*, Vol. 33, pp. 346–352.

Dombrowski, N., and Johns, W. R., 1969, "Thermal Properties of Combustion Gases From a Residual Fuel-Oil-Fired High Intensity Combustion Chamber," *J. Inst. Fuel*, pp. 194–199.

Gorenflo, D., 1968, "Zur Druckabhangigkeit des Warmeubergangs an Siedende Kaftemittel bei freier Konvektion," *Chem. Ing. Techn.*, Vol. 40, pp. 757–762.

Guruz, H. K., 1977, "A Simple Method for Predicting the Overall Performance of Fuel-Oil Fired Boilers," *Comb. Sci. and Tech.*, Vol. 17, pp. 163–168.

Haigh, C. P., and Chojnowski, B., 1975, "Hemispherical Emissivity of Clean Furnace Tubes," *J. Inst. of Fuel*, pp. 139–141.

Hottel, H. C., and Sarofim, A. F., 1967, *Radiative Transfer*, McGraw-Hill, New York, Chaps. 8 and 14.

Hwang, T. H., and Yao, S. C., 1986, "Forced Convective Boiling in Horizontal Tube Bundles," *Int. J. Heat Mass Transfer*, Vol. 29, No. 5, pp. 785–795.

Irvine, T. F., Jr., and Liley, P. E., 1984, *Steam and Gas Tables With Computer Equations*, Academic Press, New York.

Kwan, H. W., 1970, "A Mathematical Model of a 200 MW Boiler," *Int. J. Control*, Vol. 12, No. 6, pp. 977–998.

Lebrun, J. J., Hannay, J., Dols, J. M., and Morant, M. A., 1985, "Research of a Good Boiler Model for HVAC Energy Simulation," *ASHRAE Trans.*, Vol. 91, Pt. 1.

Leong, L. S., and Cornwell, K., 1979, "Heat Transfer Coefficients in a Reboiler Tube Bundle," *The Chemical Engineer*, No. 343, pp. 219–221.

Levy, S., 1959, "Generalized Correlation of Boiling Heat Transfer," ASME *Journal of Heat Transfer*, Vol. 810, pp. 37–42.

Lihou, D., 1977, "Review of Furnace Design Methods," *Trans. Ind. Chem. Eng.*, Vol. 55, pp. 225–242.

Lobo, W. E., and Evans, J. E., 1939, "Heat Transfer in the Radiant Section of Petroleum Heaters," *Trans. AIChE*, Vol. 35, p. 743.

Malmstrom, T. G., Mundt, B., and Bring, A. G., 1985, "A Simple Boiler Model," *ASHRAE Trans.*, Vol. 91, Pt. 1.

McDonald, J. P., and Kwatny, H. G., 1973, "Design and Analysis of Boiler-Turbine-Generator Controls Using Optimal Linear Regulator Theory," *Trans. IEEE*, Vol. AC-18, No. 3, pp. 202–209.

McLean, W. G., and Murdock, J. W., 1972, *ASME Power Test Code Steam Generating Units PTC 4.1*, ASME, New York.

Morgan, E. S., 1974, "Errors Associated With Radiant Heat Flux Meters When Used in Boiler Furnaces," *J. Inst. Fuel*, Vol. 47, pp. 113–116.

Nelson, P. J., and Burnside, B. M., 1985, "Boiling the Immiscible Water/*n*-Nonane System From a Tube Bundle," *Int. J. Heat Mass Transfer*, Vol. 28, No. 7, pp. 1257–1267.

Nicholson, H., 1964, "Dynamic Optimization of a Boiler," *Proc. IEE*, Vol. 111, No. 8, pp. 1479–1499.

Nicholson, H., 1965, "Dual-Mode Control of a Time-Varying Boiler Model With Parameter and State Estimation," *Proc. IEE*, Vol. 112, No. 2, pp. 383–395.

Nicholson, H., 1967, "Integrated Control of a Nonlinear Boiler Model," *Proc. IEE*, Vol. 114, No. 10, pp. 1569–1576.

Reklaitis, G. V., Ravindran, A., and Ragsdell, K. M., 1983, *Engineering Optimization, Methods and Applications*, Wiley, New York.

Rohsenow, W. M., 1952, "A Method of Correlating Heat Transfer Data for Surface Boiling Liquids," *Trans. ASME*, Vol. 74, p. 969.

Sarofim, A. F., and Hottel, H. C., 1978, "Radiative Transfer in Combustion Chambers: Influence of Alternative Fuels," presented at the 6th International Heat Transfer Conference, Canada.

Steltz, W. G., and Silvestri, G. J., 1958, "The Formulation of Steam Properties for Digital Computer Application," *Trans. ASME*, pp. 967–973.

Vanderplaats, G. N., 1984, *Numerical Optimization Techniques for Engineering Design With Applications*, McGraw-Hill, New York.

L. E. Sanchez-Caldera[1]

P. Griffith
Fellow ASME

E. Rabinowicz
Fellow ASME

Department of Mechanical Engineering,
Massachusetts Institute of Technology,
Cambridge, MA 02139

The Mechanism of Corrosion-Erosion in Steam Extraction Lines of Power Stations

Corrosion-erosion occurs in steam extraction piping made of low carbon steel that conveys wet steam. The rate of metal removal peaks at 150°C and is most severe on the inside and outside of bends and in the vicinity of fittings. A theory is presented by which three processes are shown to give rise to the observed peak in the metal removal rate: (1) the oxidation reaction, (2) the mass transfer process, which governs at 150°C, and (3) the diffusion resistance of the oxide layer, which governs at higher temperatures. The results of the derived model agree well with the available experimental data in predicting wear rates and in establishing the temperature and the location of maximum material removal.

1 Introduction

The high material removal rate (wear rate) experienced in the elbows of steam extraction lines of several nuclear power stations was the specific problem that generated the current work. In 1982, Vu described the problem in detail. He showed wall thickness data for several pipe bends taken from power stations. These pipes, which experienced wear rates of the order of one mm per year (0.04 in./y), operated at around 90 percent quality (10 percent humidity) and at 0.4 MPa (60 psi). The most severe wear was sometimes on the inside of the bend and sometimes on the outside.

Vu's experimental work showed that, as a result of the secondary flow in an elbow (see Fig. 1), a water film flows along the inside of a bend. The mass transfer to this film was found to be responsible for the removal of ferrous ions from the inside of a bend. This phenomenon in many cases leads to greater material loss than that caused on the outside of the bend by water droplet impact.

In order to understand the above process, it is necessary to investigate the chemical aspects linked to the phenomenon of corrosion-erosion in single-phase water. Since the regions of high wear were those where the liquid film was found, this investigation has dealt only with single-phase corrosion-erosion. Other studies in the area of corrosion-erosion in two-phase flow have been undertaken by other researchers (Berkow, 1984; Freitas, 1986).

To develop an understanding of the corrosion-erosion process, the specific goals of the research were to characterize the wear, under a common range of operating conditions, of a typical material from which steam extraction lines are made (SA 155 Grade C) and to propose a method for estimating the wear rate as a function of velocity, temperature, and pH. To achieve these goals, a high-temperature-high-pressure loop was designed and constructed. Its use has helped evaluate the performance of our specific material for different temperatures from 300 to 450 K (100 to 320°F) and for different velocities from 0.5 m/s to 10 m/s (30 ft/sec).

2 Corrosion-Erosion Model Derivation

This section gives background on corrosion-erosion and describes how the model used to predict wear rates was derived.

2.1 Corrosion-Erosion Background. Water conditions in a power station are such that the dissolved oxygen concentration is very low, of the order of 100 ppb. Under these conditions, the final product during the oxidation of steel is a porous oxide layer of magnetite (Fe_3O_4) (Castle and Thomson, 1967). The pores in the film are associated with the dissolution of iron at the metal-oxide interface and its transport into solution in the ferrous form.

Experiments with low-carbon steel in water at a temperature above 150°C have shown that the first step in the oxidation of steel is the formation of the hydroxide of iron $Fe(OH)_2$. The following reactions, which take place at the metal-oxide inter-

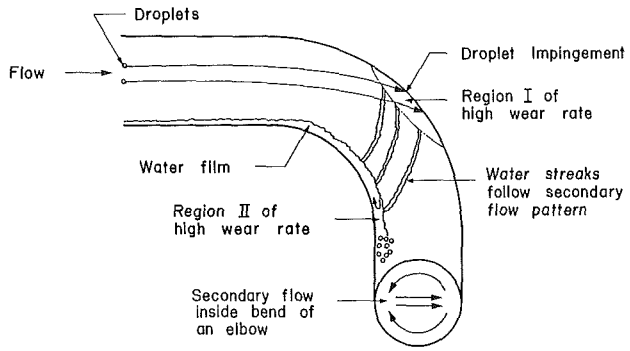

Fig. 1 Wear regions in an elbow of a steam extraction line

[1]Presently at Mixalloy Corp., Hudson, MA 01749.

Contributed by the Power Division for publication in the JOURNAL OF ENGINEERING FOR GAS TURBINES AND POWER. Manuscript received by the Power Division December 24, 1986.

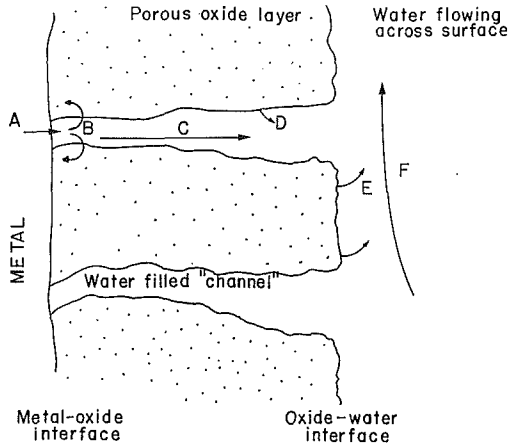

Fig. 2 Phenomena occurring during corrosion-erosion:
(A) Iron hydroxides are generated: $Fe + 2H_2O \rightarrow Fe(OH)_2 + H_2$.
(B) Magnetite is formed according to the Schikorr reaction: $3(Fe(OH)_2) \rightarrow Fe_3O_4 + H_2 + 2H_2O$.
(C) A fraction of the hydroxides formed in step (B) and hydrogen generated in steps (A) and (B) diffuses through pores in the oxide.
(D) Magnetite can dissolve in the pore.
(E) Magnetite dissolves at the oxide-water interface.
(F) Water flow removes the soluble species by a convection mass transfer mechanism.

face, account for the generation of this hydroxide (Berge, 1972; Gadiyar, 1980; Heitman and Kastner, 1982):

Component reactions:

$$Fe \rightarrow Fe^{2+} + 2e^- \quad (1)$$

$$2H_2O \rightarrow 2H^+ + 2OH^- \quad (2)$$

$$2H^+ + 2e^- \rightarrow H_2 \quad (3)$$

$$Fe^{2+} + 2OH^- \rightarrow Fe(OH)_2 \quad (4)$$

Overall reaction:

$$Fe + 2H_2O \rightarrow Fe(OH)_2 + H_2 \quad (5)$$

The hydroxide produced during the first step of the oxidation of iron can form magnetite through the Schikorr reaction (Schikorr, 1933)

$$3(Fe(OH)_2) \rightarrow Fe_3O_4 + H_2 + 2H_2O \quad (6)$$

The rate of the above reaction increases greatly at temperatures close to 175°C (350°F) (Heitman and Kastner, 1982).

Important research was carried out by Sweeton and Baes (1970). They showed that the presence of the oxide magnetite can lead to the formation of the following species: Fe^{++}, $Fe(OH)^+$, $Fe(OH)_2$, $Fe(OH)_{3-}$, which are soluble in water. Their experimental data on the solubility of magnetite as a function of temperature, hydrogen concentration, and pH allowed them to compute thermodynamic data (ΔS, ΔH) needed for calculating the equilibrium constant K ($\log K = (T\Delta S - \Delta H)/(2.3\,RT)$) for the following reaction:

$$Fe_3O_4 + 3(2-b)H^+ + H_2\,(g) \rightarrow 3(Fe(OH)_b^{(2-b)+}) + (4-3b)H_2O \quad (7)$$

where b can have the values of 0, 1, 2, and 3.

The work of Sweeton and Baes provides a method for determining the concentrations of the soluble hydroxide species in equilibrium, and it suggests that the formation of hydroxides of iron is the mechanism by which iron is lost in a dynamic system (flowing water). The net iron removal rate will depend on the concentration of soluble iron species at the oxide-water interface and on the physicochemical characteristics of the water.

2.2 Recent Work on Corrosion-Erosion. In order to study the phenomenon of corrosin-erosion, researchers have made use of laboratory rigs or have inserted their specimens inside the pipes of power plants. A summary of these methods can be found in Berge (1982).

Some investigators have tried to develop models for estimating corrosion-erosion damage. The model of Keller (1974) is empirical, and its main disadvantage is that it does not include the influence of the chemistry of the water (pH, oxygen concentration). The models of Bignold et al. (1981) and Berge (1982) fail to provide values of the essential constant needed to estimate the rate of wear from their relations.

One reason for the inadequacy of these attempts is the lack of physically realistic model that expresses clearly the influence of both the hydrodynamics and the kinetics of the chemical reactions involved. This problem, in turn, is linked to the fact that experimental work has made use of very complicated geometries (bends, impinging plates, orifices). In these cases, the hydrodynamic parameters by themselves are difficult to establish, making it even more difficult to determine the way in which the hydrodynamics influence the reaction kinetics.

The influence of the wear rate of velocity, oxygen, pH, and temperature of the water was described in detail by Sanchez (1984). It is important to note that experimental data on corrosion-erosion show that the wear follows a linear law with time. A constant wear rate implies that the oxide layer provides a constant resistance to corrosion by maintaining constant thickness and porosity.

2.3 Corrosion-Erosion Model Assumptions and Derivation. As described earlier, the removal of material by corrosive-erosive wear is the result of several phenomena, including the initial reaction of pure iron with water and the final step of mass transport of hydroxides into the bulk flow of water. The oxide layer, formed on the iron, plays an important role by restricting the flow of water to the metal and the flow of hydroxides by diffusion from the iron surface to the water flow; those factors in turn affect the hydroxide concentration at the iron-oxide and oxide-water interfaces. The various effects that take place in the neighborhood of the metal surface are shown in Fig. 2.

As can be inferred from the figure, the process of corrosion-erosion includes complicated chemical kinetics and fluid mechanics. It is difficult to incorporate all the process laws in the derivation of the model; instead, we looked for the minimum number of variables necessary to explain the experimental data. These data indicated that (*a*) the wear is a linear function of time, (*b*) the wear rate is maximum at a temperature near 150°C (300°F) and (*c*) the wear increases with velocity.

With the above ideas in mind the following equation was derived[1]:

$$\frac{dm}{dt} = \frac{\theta(C_e - C_\infty)}{(1/k) + (1-f)[(1/h_d) + (d/D)]} \quad (8)$$

where dm/dt = wear rate in mol/cm²s (to be determined); C_e = equilibrium concentration of iron species in mol/cm³; this concentration depends on temperature, hydrogen concentration, and pH (obtained from Sweeton and Baes, 1970); θ = porosity in cm² of open area/cm² of metal or cm³ H_2O/cm³ (some values reported by Surman, 1969); h_d = mass transfer coefficent in cm/s (obtained from a known relation for the specific geometry being considered, Berger and Hau, 1977); $k = Aexp(-E/RT)$, the reaction rate constant in cm/s (our experiments described later in Section 3, provided the data required to determine the value of this constant); f = fraction of oxidized metal converted into magnetite at the

[1] Typical values of the variables of equation 8 applicable to our experimental setup and conditions were: $\theta = 0.005$, $f = 0.5$, $C_e = 4.5$E-5 mol/cm³, $D = 2.85$E-5 cm², $h_d = 9.9$E-3 cm/s, $d = 1$ micron, $C_\infty < 1$E-7, i.e., approximately 0.0 when compared to C_e.

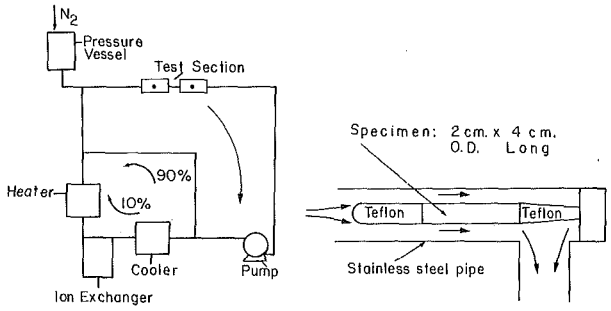

Fig. 3 Corrosion-erosion rig: (*a*) components of the corrosion-erosion rig (in addition to the components shown, the rig had the necessary instrumentation to measure pH temperature, O_2 content, pressure, and flow rate); (*b*) detail of the test section

metal-oxide interface (constant $f = 1/2$); D = diffusion coefficient of iron hydroxides in water, in cm^2/s (obtained from Rohsenow and Choi, 1961); d = oxide thickness in cm (to be obtained experimentally); C_∞ = iron species concentration in the bulk of the fluid, in mol/cm^3.

The assumptions made to derive equation (8) were the following:

Assumption 1. A steady state is considered. The oxide layer has been developed, and its thickness (d) and porosity (θ) have attained a constant value as a function of time. This first hypothesis assumes that corrosion brings about the formation of magnetite with the same porosity as the remainder of the oxide layer. Simultaneously, the layer is assumed to remain at a constant thickness by producing magnetite on the metal oxide interface. This assumption also makes reference to the amount of hydroxides being formed in the pore. If the resistance to corrosion is constant, we have assumed that neither the porosity nor the layer thickness can change. The amount of magnetite formed at the metal base has to be the same as that being dissolved in the pore and on the oxide-water interface. The assumption in the model is that the major part of the dissolution takes place on the oxide surface, where the hydrogen ion concentration is the greatest; as a result, the diffusion through the pores remains unaffected by dissolution through the pores.

It is important to note that the oxide layer is constant as a function of time. It will be shown later that in order for the model to predict the experimental data observed, the porosity has to vary as a function of temperature.

Assumption 2. Of the amount of iron oxidized at the metal-oxide interface, a fraction f is converted into magnetite; this is the same amount being removed at the oxide-water interface. It has been assumed that f has a fixed value of 0.5. This value is based on static experiments of the corrosion of steel; where, in general, two oxide layers are formed and the outside oxide layer has the same amount of iron as the inner layer (Berger, 1976).

Assumption 3. There is no net circulation or flow of water inside the oxide layer; therefore, the simulation of the transport of species inside the layer can be considered as a concentration diffusion problem.

Assumption 4. The water is oxygen free (<200 ppb), and the only oxide present is magnetite.

Assumption 5. The reaction rate at the metal-oxide interface proceeds at a rate equal to

$$\frac{dm}{dt} = k\theta(C_e - C_o) \tag{9}$$

where k is equal to $A\exp(-E/RT)$. This implies that the reaction rate at the metal surface is proportional to the potential created by the concentration difference between C_e, the equilibrium concentration of hydroxides (their solubility), and C_o, the actual concentration of hydroxides at the metal-oxide interface. This assumption is verifiable through experimentation; our data will show that the assumption is valid.

Assumption 6. The hydroxides diffuse through the pores due to differences in concentration from the metal to the water. The diffusion path length is considered to be equal to the oxide thickness.

$$(1-f)\frac{dm}{dt} = \frac{D\theta}{d}(C_o - C_1) \tag{10}$$

Assumption 7. At the oxide-water interface, the concentration at the pores is C_1, but everywhere else it is different. The mass transfer rate from the pores to the water is considered to be equal to $h_d\theta(C_1 - C_\infty)$, and the mass transfer rate from the nonporous oxide is equal to the rate of magnetitie formed at the metal-oxide interface.

The above assumption permits the use of the following equations to represent the wear rate dm/dt:

$$\frac{dm}{dt} = k\theta(C_e - C_o) \text{ (see assumption 5)} \tag{9}$$

$$(1-f)\frac{dm}{dt} = \frac{D\theta}{d}(C_o - C_1) \text{ (see assumption 6)} \tag{10}$$

$$(1-f)\frac{dm}{dt} = h_d\theta(C_1 - C_\infty) \text{ (see assumption 7)} \tag{11}$$

This system of three equations with three unknowns dm/dt, C_1, and C_0, can be solved for dm/dt, yielding equation (8).

3 Experimental Studies

The experimental work, aimed at generating wear-rate data, was used to verify the derived model and to measure the missing values of constants.

3.1 Description of Experimental Apparatus. A high-pressure-high-temperature water loop of 2.5 cm (1 in.) type 316 stainless steel pipe was constructed. Its design focused on operating at temperatures between 100 and 200°C (200 to 370°F), with a pH of 5 to 10, with low oxygen water contents (<200 ppb), and with velocities of up to 10 m/s (30 ft/sec); see Fig. 3.

An annulus, a simple geometry that allowed mass transfer coefficients to be estimated, was used as a test section; see Fig. 3. The inside of the annulus was the surface being tested. It was machined from a plate of A155 Grade C55 steel (also equivalent to SA 285 Grade C steel), a common material used in steam extraction lines (ASME Standards, 1974).

3.2 Experimental Procedure. The tests lasted a minimum of 200 h, the period believed necessary for a constant wear rate to be developed (Heitman and Kastner, 1982; Berger, 1976); during this time, pH, velocity and temperature were maintained constant.

From the weight of the specimen at the beginning of a test, the descaled weight at the end of the test, the surface area available for wear, and the period of the test, the wear rate was calculated for every flow velocity and temperature chosen. The oxide was removed by dissolving it in a solution of water and hydrochloric acid; the specifics of the method are described by Sanchez-Caldera (1984).

In addition to recording the weight at the beginning and end of a test, on various occasions, the weight of a speicmen was recorded several times during the course of a test. The measurements were carried out to verify that although the initial wear rate was variable, after 200 h of operation, it was a constant function of time.

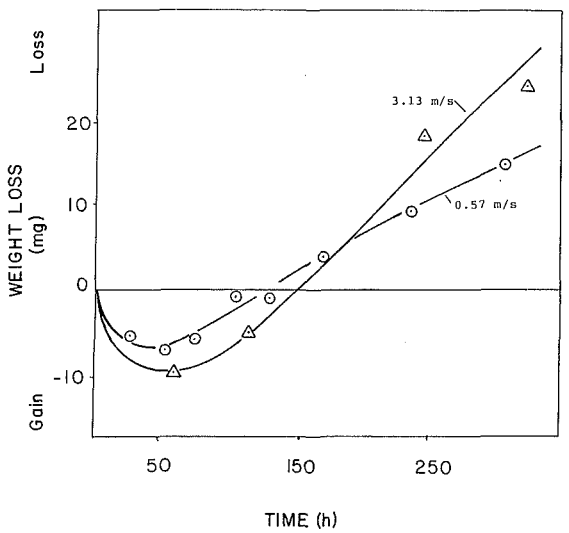

Fig. 4 Specimen at 395 K (250°F), pH of 5.5, ⊙ 0.57 m/s (1.9 ft/sec) and △ 3.13 m/s (10.3 ft/sec)

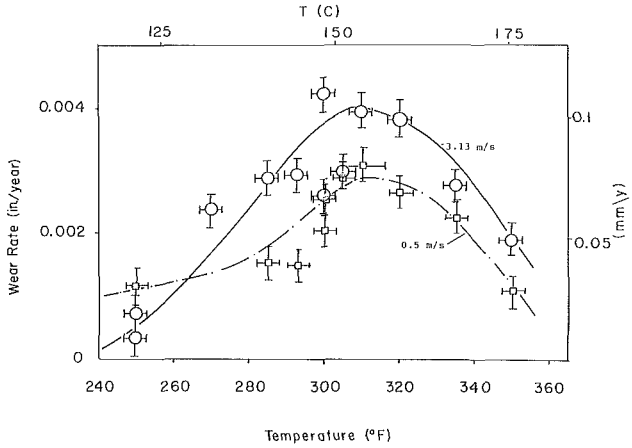

Fig. 5 Descaled wear rate versus temperature for low-velocity specimens (0.5 m/s) and high-velocity specimens (3.1 m/s); pH = 5.5

Specimens were also analyzed using a scanning electron microscope (SEM). The thickness of the oxide was directly measured from the pictures taken at specific magnifications.

3.3 Experimental Results. Typical data of weight loss as a function of time are shown in Fig. 4. The figure verifies that the wear rate becomes a constant in time after about 150 h, and that high-velocity tests lead to a greater wear than do those at low velocity.

Wear rates calculated in the manner described previously are shown in Fig. 5. There was a maximum wear rate close to 150°C (300°F); and except at low temperatures higher velocities yield higher wear.

SEM micrographs, not shown here, revealed oxide layer thickness of close to 1 μm. No particular trend of oxide thickness with respect to velocity or temperature was found.

4 Discussion of Results

With the data presented above, it is possible to verify the assumptions made during the derivations of the model as well as to obtain values for the unknown constants.

First, it is important to notice that equation (8) shows that in the limit when the terms $1/h_d$ and d/D are small compared to $1/k$ the wear rate becomes equal to $k\theta(C_e - C_o)$. This means that the wear is independent of velocity. This result agrees well with the data presented previously, where at low temperatures the rates of high and low-velocity specimens yield approximately the same wear rates.

Perhaps the most critical assumption in the model is that the wear rate is equal to $k\theta(C_e - C_o)$, where k, the reaction rate constant, is assumed to equal the Arrhenius expression $A\exp(E/RT)$.

From the data gathered in our experiment, it has been possible to plot values of k versus $1/T$ and verify the above assumption.

In equation (8), with values of dm/dt, h_d, θ, D, d, and C_e established, a value of k can be calculated for every temperature, pH, and velocity. Values of h_d, D, C_e, and θ were obtained as described previously under the explanation of the terms in equation (8). The experimental values of d and dm/dt were used in determining k.

Figure 6 is a plot of log k versus $1/T$. The figure shows that k tends to follow an Arrhenius expression and that the activation energy constant E was equal to 35,380 cal/g°C, which agrees well with activation energy values obtained by other

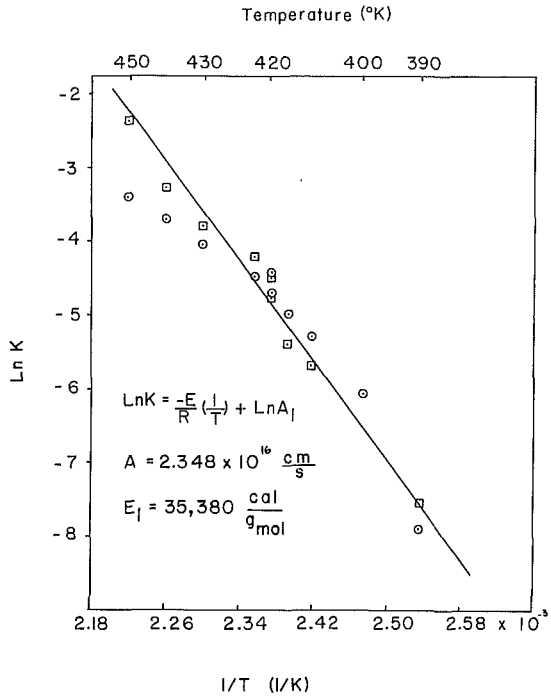

Fig. 6 Plot of natural logarithm of the reaction rate constant k versus the inverse of temperature

authors for the corrosion of steel /(Surman, 1969, cites an activation energy value of 30,000 cal/g°C).

The alignment of the data to a straight line is very good considering that the analysis covers three orders of magnitude for k; nevertheless, there seems to be some discrepancy at high temperatures (low $1/T$).

The values of the parameters used for h_d, D, d, and θ were verified and calculated by different relations. From this parametric study, it was found that the only variable that affects the outcome of Fig. 6 is the porosity θ.

From this result, the following conclusion was derived and the model of corrosion-erosion for this application evolved. The hypothesis is that at high temperatures the fast chemical reactions lead to a decrease in porosity. The complete model therefore takes the following form:

$$\frac{dm}{dt} = \frac{\theta(C_e - C_o)}{(1/k) + (1-f)(1/h_d + d/D)} \tag{12}$$

where $k = 2.35\text{E}14 \exp(-35{,}380/RT)$, in SI units, and

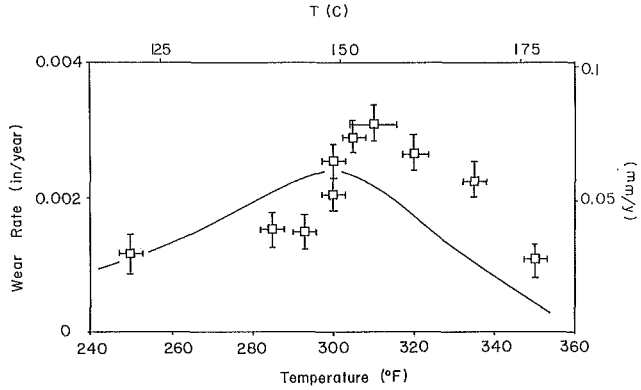

Fig. 7 Comparison between the wear rate data and the results of the corrosion-erosion model, equation (12), for the low-velocity specimens; pH = 5.5

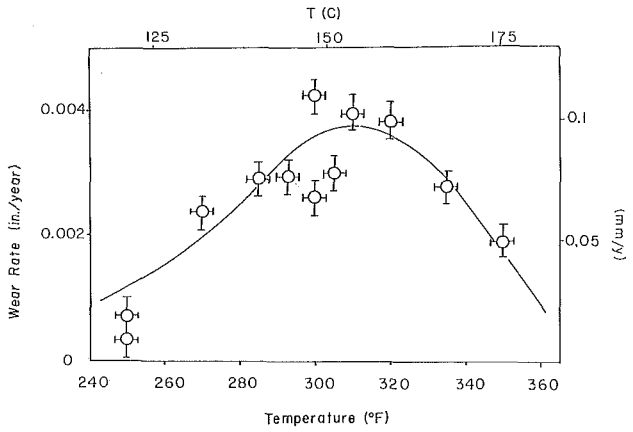

Fig. 8 Comparison between the wear-rate data and the results of the corrosion-erosion model, equation (12), for the high-velocity specimens; pH 5.5

$\theta = 0.05$ percent at $T < 422$ K (300°F) or $\theta = 6.75\text{E-}3 - 1.48\text{E-}5T$ (K), for $422 < T < 449$ K.[2]

With this last equation a procedure to estimate the wear rate is available. Figures 7 and 8 show the wear rate calculated versus the experimental values. Agreement between experimental and theoretical values is good. Specifically, at high velocity where the original data have less scatter than at low velocity, the calculated values are within 30 percent of the original data.

5 Summary of Conclusions

Systematic measurements were performed to evaluate material wear due to corrosion–erosion of specimens in single-phase liquid water with a pH of 5.5 and two different velocities. In particular, the effects of the fluid temperature on a low-carbon steel, A155 Grade C55, were analyzed.

During the work two goals were pursued. The first goal was to study the state of the art regarding the phenomenon of corrosion–erosion. Achieving this first objective led to the conclusion that the problems resulting from corrosive–erosive wear can be considerably diminished or even eliminated if the systems are properly designed and constructed. This includes the use of higher alloying metal concentration in the steel, the use of higher steam quality, the reduction of the flow velocity, an increase in the pH value from 5.5 to 9, avoidance of operation of carbon steels at temperatures around 150°C (300°F) and good workmanship in the connections of pipe fittings.

Since the improvement of material composition is an expensive design solution, it may be good practice to use alloy steels only for the critical temperature range. For plants already in operation and experiencing corrosion-erosion problems, further work to suggest inexpensive protective material combinations with low risk of galvanic corrosion will be necessary.

The second goal was to develop a model to estimate wear rates. The model was developed on the basis of the description of the corrosion of iron given by Heitman and Kastner (1982); its final form is given in equation (12). It is a simple model that uses a minimum number of variables and phenomenological laws to explain the experimental findings.

With our experimental data, the model has been subjected to initial verification. The study has shown that the most important assumptions made, i.e., a constant wear rate, and a reaction rate constant following an Arrhenius function with temperature, have been proven appropriate.

Further validation of the model by obtaining wear rate data for different velocities, oxygen contents, pH, and other geometries is now required.

[2]Typical expressions used to calculate the value of h_d, D, d, and C_e were outlined in Section 2.3 under the explanation of the terms in equation (8); a detailed explanation of each expression can be found in Sanchez-Caldera (1984).

Acknowledgments

We thank Boston Edison for having sponsored this research, as well as CONACYT and the Instituto de Investigaciones Electricas, Mexico for their financial assistance.

References

ASME Standards, *Annual Book of Standards*, 1974, Section II, Part H; 1981, Part 10-G1.

Berge, Ph., 1972, "Mécanisme de l'Oxydation des Aciers dans l'Eau à Haute Temperature et de al Formation des Depots d'Oxides," *Congress d'Ermenoville*, Ermenoville, France.

Berge, Ph., Ribon, C., and Saint Paul, P., 1976, "Effect of Hydrogen on the Corrosion of Steels in High Temperature Water," *Corrosion—NACE*, Vol. 32, No. 6, pp. 223–228.

Berge, Ph., and Khan, F., 1982, "Corrosion-Erosion of Steels in High Temperature Water and Wet Steam," *Reunion E.D.F.*, Les Renardiers.

Berger, F. P., and Hau, K., 1977, *Heat and Mass Transfer*, Vol. 20, p. 1185.

Berkow, M. J., 1984, "The Use of Novel Bend Geometries to Reduce or Eliminate Erosive-Corrosive Wear in Steam Extraction Lines," M.E., M. Sc. Thesis, MIT, Cambridge, MA.

Bignold, G. J., Garbett, K., Garnsey, R., and Woolsey, I. S., 1981, "Tackling Erosion-Corrosion in Nuclear Steam Generating Plants," *Nuclear Engineering International*, Vol. 26, No. 314.

Castle, J., and Thomson, R., 1967, "Stability of Ferrous Hydroxide in Aqueous Suspension at 300°C," *J. Appl. Chem.*, Vol. 17, pp. 177–178.

Gadiyar, H. S., and Elayathu, N. S. D., 1980, "Corrosion and Magnetite Growth on Carbon Steels in Water in 310°C," *Corrosion—NACE*, Vol. 36, No. 6, pp. 306–312.

Germano de Freitas, 1986, "Dissolution Rate in the Water of a Welding Backup Ring," M.E. Engineering Degree Thesis, MIT, Cambridge, MA.

Heitman, H. G., and Kastner, W., 1982, "Erosion-Corrosion in Water-Steam Cycles, Causes and Counter Measures," *VGB Kraftwerkstechnik*, Vol. 62, No. 3, pp. 211–219.

Keller, H., 1974, "Erosion–Corrosion in Wet Steam Turbines," *VGB Kraftwerkstechnik*, Vol. 54, No. 5, pp. 12–21.

Rohsenow, W., and Choi, H. 1961, *Heat, Mass, and Momentum Transfer*, Prentice Hall, Canada.

Sanchez-Caldera, L. E., 1984, "Corrosion–Erosion in Steam Extraction Lines of Power Stations," M.E. Ph.D. Thesis, MIT, Cambridge, MA.

Schikorr, G. Z., 1933, *Anorg. allg. Chem.*, Vol. 212, p. 533.

Surman, P. L., 1969, "Gas Phase Transport in the Oxidation of Fe and Steel," *Corrosion Science*, Vol. 9, pp. 771–777.

Sweeton, F., and Baes, C., 1970, "The Solubility of Magnetite and Hydrolysis of Ferrous Ion in Aqueous Solutions at Elevated Temperatures," *J. Chem. Thermodynamics*, Vol. 2, pp. 479–500.

Vu, H., 1982, "Erosive-Corrosive Wear in Steam Extraction Lines of Power Plants," M.E., M.Sc. Thesis, MIT, Cambridge, MA.

Refinery Process Heater NO_x Control by Staged Combustion Air Lances

S. C. Hunter
Principal Engineer
KVB, Inc.,
A Research-Cottrell Company,
Irvine, CA
Mem. ASME

R. E. Hall
Chief, Combustion Research Branch
U.S. Environmental Protection Agency,
Air and Energy Engineering Research
Laboratory,
Research Triangle Park, NC
Mem. ASME

A vertically fired natural-draft petroleum-refinery crude-oil process heater was modified to reduce oxides of nitrogen (NO_x) emissions by installing staged combustion air lances. Baseline NO emissions firing refinery gas before modification were measured to be 100 to 125 parts per million by volume, dry, corrected to 3 percent oxygen. Staged combustion air lances were installed to bypass combustion air around the burners to achieve staged combustion. With the modification, an average reduction of 64 percent in NO emissions was observed over a 30-day test period, with NO emissions of 25 to 50 ppm, dependent on the excess air. This method of combustion modification can be applied to most vertically fired process heaters where flame length increased by a factor of 2 to 4 would not cause flame impingement.

Introduction

Emissions of oxides of nitrogen (NO_x) from petroleum industry stationary sources are estimated (Hunter and Cherry, 1979) to be about 1,300,000 tons (1,201,000 metric tons) per year based on 1975 data. This emission rate is about 6 percent of the total stationary and mobile NO_x emissions from all sources in the United States. Petroleum refining operations produce 22 percent of total petroleum industry NO_x emissions. Natural draft process heaters are the prevalent source of NO_x in refineries, contributing about 10 percent of total petroleum industry NO_x emissions.

There are currently no New Source Performance Standards for NO_x from petroleum process heaters. However, the U.S. Environmental Protection Agency regularly reviews the NSPS for refineries and has a need to understand the potential for controlling process heater NO_x emissions. In the State of California the South Coast Air Quality Management District has adopted limitations on NO_x emissions from petroleum refineries, and other areas of the U.S impose limits, including new source review requirements for Best Available Control Technology. These various needs have resulted in research to investigate NO_x controls for process heaters.

This paper summarizes research conducted under contract to the Combustion Research Branch at the U.S. Environmental Protection Agency's Air and Energy Engineering Research Laboratory in Research Triangle Park, NC. Research involving evaluation of combustion modifications on a variety of industrial process combustion equipment was performed under this contract. This paper concentrates on the process heater portions of the research, summarizing results that have been reported in detail (Tidona et al., 1983).

Contributed by the Environmental Control Division for publication in the JOURNAL OF ENGINEERING FOR GAS TURBINES AND POWER. Manuscript received by the Environmental Control Division September 12, 1986.

Petroleum Refinery Process Heater Characteristics

Process heaters are of two basic types: natural draft and mechanical draft (forced, induced, or balanced draft). These draft types result in basic differences in combustion characteristics that are reflected in NO_x emission levels and feasibility of combustion modification. Some mechanical draft units are equipped with combustion air preheating that, in general, is expected to increase NO_x emissions because of higher flame temperatures. There are two basic forms of heater construction: horizontal box and vertical cylindrical. Horizontal tubes are most common in box heaters, but some have vertical tubes. Burners are usually mounted in the floor firing upward, but may also be located in the side. Box units can have from 3 to over 100 burners arranged in one or more rows. Two or more box furnaces may be connected to a single convection section. Vertical-cylindrical units all have vertical tubes, and one or more burners are mounted in the floor firing upward.

The refining process performed is important. Uniformity in heat distribution required varies with process type, and this influences the flexibility of the combustion system. Process heater tests reported here encompass only one process: crude oil heating. The heater made available for testing did not involve the most critical processes where the unknown effects of combustion modifications might result in process disruption or heater damage, primarily product tube internal coke formation.

These details are important in application of combustion modifications because process heater construction differs from that of steam boilers. Burners for heaters also differ from steam boiler burners. Heater burners form round, conical, or flat flames to produce the proper heat distribution necessary to avoid tube coking, which is not a problem in steam boilers. These differences imply that combustion modifications developed on steam boilers, and reductions in NO_x achieved, may not be directly applicable to process

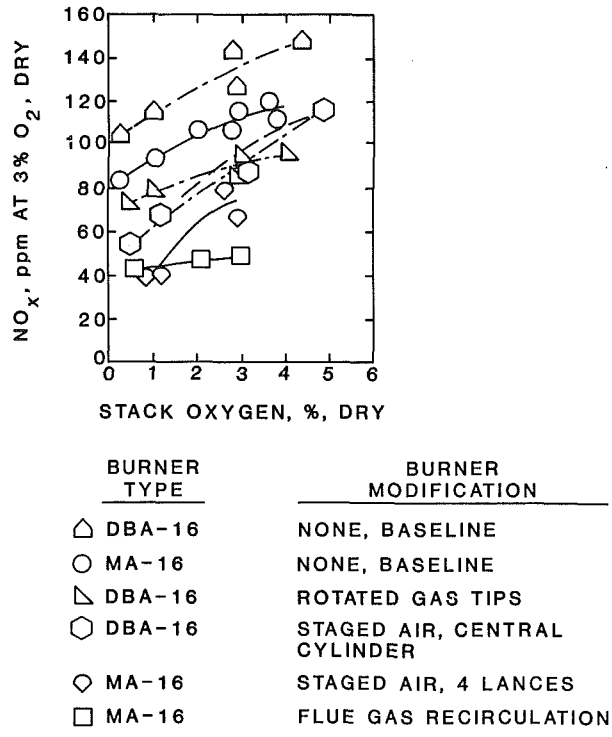

Fig. 1 Summary of NO_x emissions as a function of stack oxygen for subscale natural-draft furnace firing natural gas

heaters. Therefore, specific research is necessary to tailor these techniques to process heaters.

Combustion Modifications on a Subscale Research Heater

Prior to attempting hardware modifications on a refinery heater, several potential modifications were evaluated in a subscale research furnace at the factory of a major manufacturer of process heater burners. The furnace was a refractory lined, uncooled, rectangular, box-type furnace 8 ft (2.4 m) wide by 6 ft (1.8 m) deep by 32 ft (9.8 m) high.

A single natural-draft burner was installed in the furnace floor firing vertically upward. The nominal firing rate for the tests was 5×10^6 Btu/hr (1.5 MW). Furnace draft was controlled manually with a damper in the stack. View ports were provided for observing flame shape.

The furnace had the capability of firing either oil or natural gas. Both flows were measured with flowmeters. Thermocouples were installed in the side of the furnace to measure the vertical thermal gradient and the temperature/time behavior during furnace heat-up.

The modifications evaluated included:

1 Lowered excess air
2 Redesigned burners (low-NO_x burners)
3 Flue gas recirculation
4 Steam injection
5 Altered fuel injection geometry
6 Staged combustion air lances

The results obtained have been reported previously in detail (Hunter et al., 1979). Figure 1 shows the NO_x emissions for the various modifications as a function of stack oxygen while firing natural gas. At low stack oxygen levels (1 percent), flue gas recirculation and staged combustion air lances both produced similar reductions. At higher stack oxygen levels, flue gas recirculation was superior to staged combustion air lances, showing less sensitivity to variation of excess air.

An analysis of cost/effectiveness ratio, expressed as annual cost per unit mass of NO_x (as NO_2) reduced, indicated that staged combustion air lances had a significantly lower cost/effectiveness ratio compared with flue gas recirculation. Therefore, the staged combustion air lance method was selected for installation in an operating refinery process heater as discussed below. Based on the research furnace tests, a reduction in NO_x of 40 to 67 percent was anticipated for a pilot-scale system firing gas fuel.

Pilot-Scale Test Heater

The pilot-scale test unit was a natural draft, vertical-cylindrical crude-oil process heater, which is used to supply a partially vaporized charge to a crude oil distillation column. A maximum load of 16,250 bbl/d (108 m^3/h) can be sent through the heater in two passes. The maximum firing rate of the heater is 55×10^6 Btu/hr (16.1 MW) thermal input. It is fired by six natural-draft DBA-type burners arranged in a circle in the heater floor. The burners are combination gas/oil burners rated at a maximum of 9.14×10^6 Btu/hr (2.68 MW) each with a turndown ratio of 3:1.Although combination gas/oil burners are used, some gas must always be fired because the unit is base loaded at constant oil firing rate, and an automatic temperature controller adjusts the gas fuel flow to maintain crude oil outlet temperature.

Staged Combustion Air Lance System Description

A staged combustion air lance system flow schematic is presented in Fig. 2. The purpose of the system is to bypass a portion of the combustion air around the burners and inject the air into the flame above the fuel injection plane of each burner. The air is injected into the firebox through tubular lances, which penetrate through the floor of a vertically fired unit. The introduction of air above the burners permits fuel-rich operation at the burners with as little as 50 percent of the theoretical air required for complete combustion, achieved by closing the burner air registers. The combustion air injected through the lances provides the remainder of the theoretical air requirement plus the amount of excess air necessary to eliminate combustibles in the flue gas and provide a good flame.

A prototype system was constructed of polyvinylchloride pipe, fittings, and valves, connected through flexible tubing to 24 stainless steel lances made from 3.2 cm (1.25 in.) 316 stainless tubing. The lances were arranged on a 3-ft (1-m) diameter around each burner, four lances per burner at 90 degrees, two lances on the burner centerline circumference and two on each burner radial line. The system was designed to provide flexibility for the adjustment and control of air flow, including the capability to control the lance air flow to each burner by means of ball valves. The lance height above the furnace floor was adjustable from floor level up to 8 ft (2.4m) above the floor. The ability to adjust flows and lance position, although desirable for testing, should not be necessary in a permanent system.

Emissions Sampling Instrumentation

The gaseous and particulate emissions were monitored with an EPA-furnished mobile laboratory. Continuous gaseous emissions analyzers measure volumetric concentrations of O_2, CO_2, CO, SO_2, NO, NO_x, and HC (as methane) in the flue gas. Particulate total mass and size were measured. SO_3 measurement was by a controlled condensation technique using a Goksoyr–Ross type coil. The sampling system and test methods are discussed in detail in the final project report (Tidona et al., 1983). All NO and CO emissions discussed in this paper are expressed in parts per million (ppm) by volume,

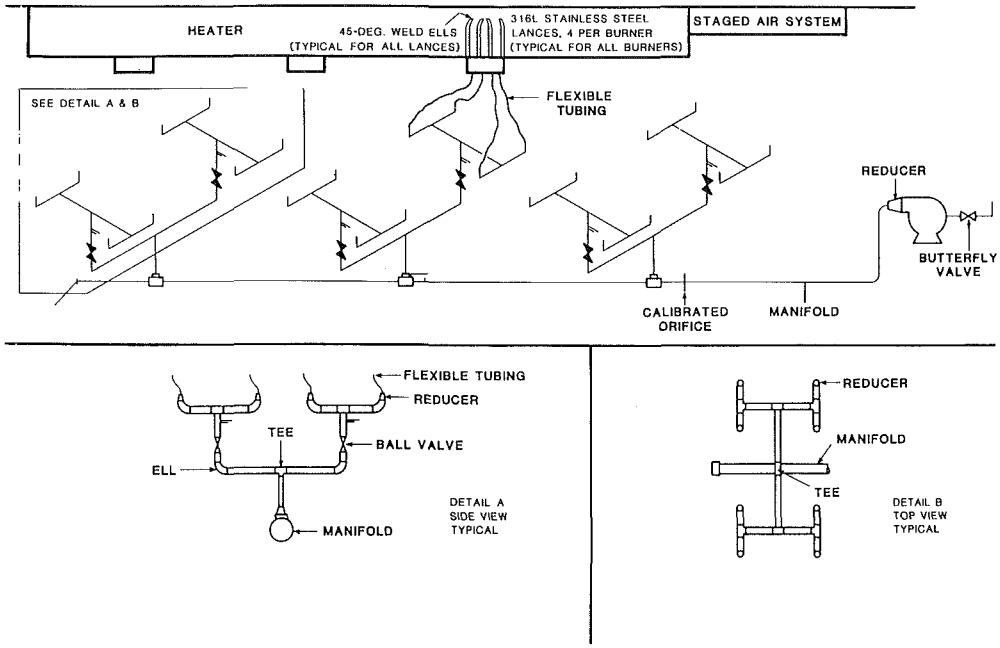

Fig. 2 Flow schematic of staged combustion air system for a natural-draft process heater

dry basis, corrected to 3 percent oxygen. Only NO data are presented. NO_2 was found to be from 0 to 10 ppm, with an average value of 3 ppm, which is below the accuracy of the measurement method.

Staged Combustion Air Lance Testing

Evaluation of the staged combustion air system included the variation of three important parameters: (1) burner theoretical air ratio, (2) stack oxygen level, and (3) staged air lance insertion height.

The NO emission is graphed as a function of burner theoretical air ratio in Fig. 3. The staging height for this test series was 4 ft (1.2 m) and the load was 9600 bbl/d (64 m^3/h), 60 percent of rated capacity. At each overall stack 0_2 level, burner air was decreased in steps to a minimum value determined by the limitations of the staged combustion air fan. At 4 percent O_2, the minimum burner theoretical air ratio (maximum staging) was 0.74, which decreased NO emissions 35 percent below the baseline of 105 ppm. At 2 percent O_2 and burner theoretical air ratio of 0.65, the NO concentration dropped to 51 ppm. This represented a reduction of 51 percent below the 4 percent O_2 baseline condition and a reduction of 43 percent below the 2 percent O_2 level with no staged air. These results generally confirmed the research furnace tests using a single burner, indicating little influence of a multiple burner arrangement.

Staging the combustion air while firing a mixture of No. 6 oil and adsorber gas at intermediate load did not produce as large a percentage decrease in NO emissions as when firing adsorber gas only. The absolute amount of NO concentration reduction, however, was about the same with combined fuel firing as it was with gas alone. For example, the NO level firing oil decreased from a baseline of 219 ppm to 166 ppm, a reduction of 53 ppm. Firing adsorber gas, the reduction was 46 ppm. This indicates that fuel oil nitrogen conversion to NO was responsible for approximately half of the baseline NO emission firing oil with gas, and the other half was due to thermal NO formation. The estimated fuel nitrogen conversion efficiency is approximately 19 percent, based on the ratio of oil to gas in the fuel and the fuel nitrogen content (~0.8 percent) of the oil.

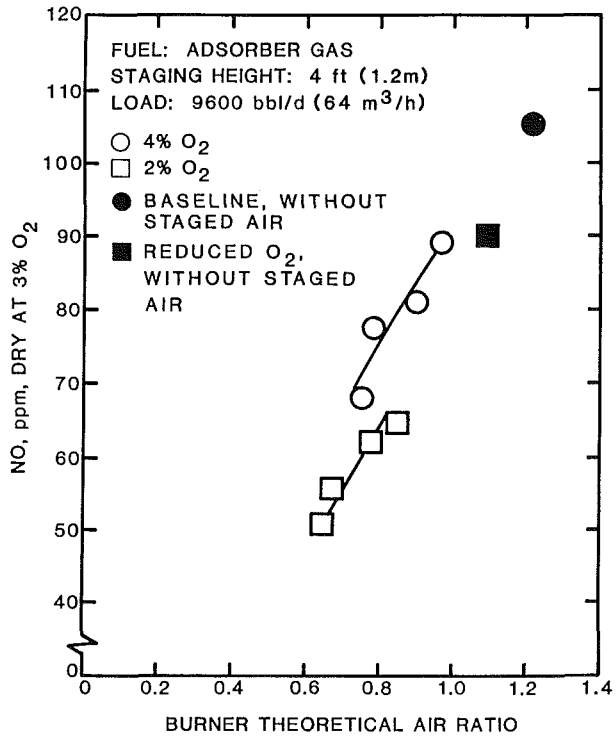

Fig. 3 NO emissions as a function of burner equivalence ratio at two stack oxygen levels with constant staged air insertion height

NO emissions decreased slightly as staging height was increased while firing oil together with gas. However, very little decrease was observed at heights greater than 4 ft (1.2 m).

During all testing, the flame and furnace draft were observed carefully. There did not appear to be any problems with coking of the process tubes and at no time was there any measurable emission of CO or unburned HC, even at 2 percent stack oxygen. In certain instances, the draft in the convection section became slightly positive at the low O_2 condition with maximum staging; however, flashback was never observed. A general lengthening of the flame was observed, in-

Table 1 Summary of 24-hr average gaseous emissions data

Petroleum Process Heater, Staged Combustion Air, Refinery Gas Fuel
24-Hour Data
Dry Stack Gas Concentration

Date	Load B/D	O_2 Vol % Meas.	CO_2 Vol % Meas.	CO ppmv 3% O_2	NO ppmv 3% O_2	CO ng/J	NO ng/J
5/01/81	10717.0	1.6	12.3	7	32	2	17
5/02/81	10717.0	2.1	12.0	10	40	3	22
5/03/81	10717.0	2.3	11.9	10	43	3	23
5/04/81	10717.0	2.2	11.9	12	42	4	22
5/05/81	10717.0	2.3	11.9	26	40	8	21
5/06/81	10717.0	2.5	11.7	8	42	2	23
5/07/81	10717.0	2.7	11.6	27	42	9	22
5/08/81	10717.0	2.2	11.9	5	37	1	20
5/09/81	10717.0	1.9	11.8	12	33	4	18
5/10/81	10717.0	1.6	12.3	12	29	3	16
5/11/81	11178.7	1.6	12.3	39	29	13	16
5/12/81	10717.0	1.4	12.4	8	27	2	14
5/13/81	10717.0	1.7	12.2	4	29	1	16
5/14/81	10717.0	1.6	12.2	11	30	3	16
5/15/81	10717.0	1.6	12.1	11	29	3	16
5/16/81	10717.0	3.9	10.5	73	57	24	31
5/17/81	10717.0	6.8	8.9	8	100	2	54
5/18/81	10717.0	3.6	10.8	216	49	71	26
5/19/81	10717.0	3.3	10.8	96	49	31	27
5/20/81	10717.0	1.6	11.9	51	28	16	15
5/21/81	10717.0	2.4	11.7	10	34	3	18
5/22/81	10717.0	2.5	11.7	46	34	15	18
5/23/81	10717.0	4.4	10.5	21	54	7	29
5/24/81	10717.0	2.1	12.0	19	41	6	22
5/25/81	10717.0	3.3	11.3	99	43	32	23
5/26/81	10717.0	4.2	10.7	7	48	2	26
5/27/81	10717.0	4.2	10.6	8	48	2	26
5/28/81	10717.0	4.1	10.4	5	49	1	26
5/29/81	10717.0	3.8	10.8	10	53	3	28
5/30/81	10717.0	3.9	10.8	13	51	4	27
5/31/81	10717.0	3.9	10.8	12	47	4	25
6/01/81	10717.0	3.7	10.8	8	46	2	25
6/02/81	10717.0	3.9	10.6	6	48	2	26

Table 2 Cost/effectiveness ratio ($/Mg) of combustion modification applied to three natural draft process heater sizes

Modification	Heater Size* 16.1 MW	29.3 MW	147 MW
Staged Combustion Air at 4% O_2	2636**	2362	1934
Staged Combustion Air + Lowered Excess Air (2% O_2)	1089	700	(40)
Lowered Excess Air, Firing Gas	(5843)	(6853)	(4813)
Lowered Excess Air, Firing Oil and Gas	(1459)	(1712)	(2189)

* 10^6 Btu/hr = MW x 3.42
** $/ton = $/Mg x 0.907
( ) indicates cost savings

creasing by a factor of 2 to 4, but this did not result in flame impingement on the internal surfaces.

Extended Duration Test of Staged Combustion Air Lance System

An endurance test was conducted while firing refinery gas to evaluate the staged air lance system during normal refinery operations. The objective of the test was to collect data continuously for 30 days. The actual test period was 33 days. The load was constant at 10,717 bbl/day (71 m^3/h) throughout the test, except for one upset day.

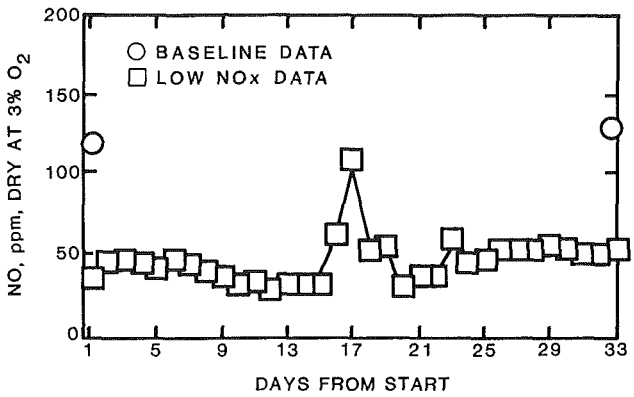

Fig. 4 NO_x emissions variation during 30-day test

A mobile laboratory was used to measure the gaseous emissions. The monitoring system was certified in accordance with Performance Specifications 2 (PS2) and 3(PS3) of 40 CFR 60. These specifications establish minimum performance that the NO monitoring system must meet in terms of eight parameters: accuracy, calibration error, 2- and 24-h zero drifts, 2- and 24-h calibration drifts, response time, and operational period.

Gaseous emissions data were measured continuously and recorded on an automatic data logger, strip chart recorders, and a magnetic tape recorder. Fifteen-minute averages of NO, O_2, CO_2, and CO emissions were recorded on tape. The data were processed on a computer, and 15-min averages were compiled. These data were then used to compile 24-h averages for the entire test period. The 24-h averages compiled from the 15-min averages for the 30-day test period are summarized in Table 1, showing O_2 and CO_2 as measured, CO and NO corrected to 3 percent O_2, and CO and NO expressed in ng/J using the gaseous fuel sample analyses.

Baseline emissions with no staged air were measured before and after the 30-day test. The NO emissions before and after the test were 120 and 130 ppm, dry, corrected to 3 percent O_2, respectively. On a heat input basis, the baseline emissions were 0.144 and 0.156 lb/10^6 Btu (62 and 67 ng/J), respectively.

After conducting baseline tests, the staged air system was activated and the stack oxygen was lowered to approximately 2 percent with the concurrence of the refinery operating personnel. The heater was then operated in this mode steadily for 15 days. After approximately 15 days, a change in the crude oil charge required an increase in firing rate. Since the heater was not controlled automatically, the increase in fuel flow resulted in a deficiency in oxygen and high CO values. The operators responded by opening the dampers, resulting in high values of stack oxygen. The highest 24-h average CO emission rate was 216 ppm, dry, corrected to 3 percent O_2 (71 ng/J). On the other 32 days, CO averaged 22 ppm and never exceeded 100 ppm, as shown in Table 1. Peak values of CO were approximately 1300 ppm.

The day following the crude oil change, efforts were made to reduce O_2 to the previous 2 percent level. Due to changing conditions and lack of automatic controls, it was decided to operate the remainder of the test at about 4 percent oxygen.

The NO emission rate as a function of days from the start of testing is presented in Fig. 4. The peak occurred during the upset condition when O_2 was increased. Even under the high O_2 condition, with the staged air system operating, the NO emission rate was lower than the baseline level. The NO emission rate data were divided into two groups corresponding to 2 and 4 percent stack oxygen. The mean value of NO emission

for the 2 percent O_2 setting was 35 ppm, and the mean value for the 4 percent O_2 setting was 49 ppm.

The results of this test, relative to the average baseline NO emission of 125 ppm, were 60 percent reduction at 4 percent O_2, 71 percent reduction at 2 percent O_2, and an overall average NO reduction of 64 percent. Upon completion of the tests, inspection of the staged air lances did not reveal any corrosion or damage to the lance material.

The cost/effectiveness ratio, based on a permanent system, of the staged combustion modification was evaluated for the gaseous fuel and for combination fuel, and also at two levels of stack oxygen. Cost/effectiveness ratio is defined as the total annual cost, including capital charges and operating costs, divided by the annual reduction of NO_x, expressed as dollars/megagram (dollars per ton). The cost/effectiveness ratios are shown in Table 2 for three heater sizes. The values for low excess air and for staged combustion with low excess air on the largest heater are negative, indicating a cost savings in addition to an NO reduction. This is a desirable situation; however, one must realize that a modification that saves money yet produces only a small NO reduction will have a large negative cost/effectiveness ratio. This may not be the most desirable modification if the NO reduction is less than is necessary to achieve compliance with regulations or to offset future emissions from plant expansions.

Guideline Manual

A manual (Tidona, 1983) has been prepared, documenting the procedures for implementing process heater combustion modifications investigated in this program. The manual is intended for use by heater manufacturers and operators.

Conclusions

On the basis of the work reported, it was concluded that:

- Based on research furnace tests with a single burner, staged combustion air injection and flue gas recirculation appear to be the most promising combustion modifications for reduction of gas-fired process-heater NO emissions, with a potential of up to 67 percent reduction.
- Installation of staged air lances through the floor of a vertically fired process heater appears to be a lower cost approach, compared with burner replacement or flue gas recirculation.
- Staged combustion using air lances was accomplished with no apparent detrimental effect on heater performance or structural integrity.
- Parametric test results with staged air lances firing gas fuel reduced NO emissions by 35 to 51 percent from a baseline level of 105 ppm, dry, corrected to 3 percent O_2.
- Test results with staged air lances firing combined No. 2 oil and gas reduced NO emissions by 24 percent from the baseline level of 219 ppm, dry, corrected to 3 percent 0_2.
- NO emissions firing No. 2 oil and gas were higher than from gas alone due to oil nitrogen content of 0.8 percent by weight, indicating that about 19 percent of the oil nitrogen was converted to NO.
- Staged air lances produced about the same absolute reduction in NO concentration (about 50 ppm) while firing gas alone or combined No. 2 oil and gas.
- During an extended 30-day test of staged combustion air lances, while firing gas fuel, NO was reduced an average of 64 percent from a baseline of 125 ppm, dry, corrected to 3 percent O_2.
- Based on an examination of many process heaters in refineries, the staged air lance system should be applicable to most vertically fired heaters. The exceptions are heaters where the flames are already near the internal surfaces, in which cases lengthened flames could result in flame impingement.

Acknowledgments

The following KVB employees contributed to the research reported here: H. J. Buening, W. A. Carter, S. S. Cherry, J. R. Hart, A. Frohoff, M. Gabriel, and R. J. Tidona.

Numerous persons at the petroleum refinery where the tests were conducted assisted KVB during the program.

Disclaimer

The research described in this article has been funded by the United States Environmental Protection Agency through Contract 68-02-2645 to KVB, Inc. It has been subjected to the Agency's required peer and policy review and has been cleared for publication.

References

Hunter, S. C., and Cherry, S. S., 1979, "NO_x Emissions From Petroleum Industry Operations," American Petroleum Institute, Publication No. 4311.

Hunter, S. C., Tidona, R. J., Carter, W. A., and Buening, H. J., 1979, "Application of Advanced Combustion Modifications to Industrial Process Equipment—Process Heater Subscale Tests," in: *Proceedings of the Third Stationary Source Combustion Symposium*, Vol. III pp. 3-36, EPA-600/7-79-050c, NTIS Order Number PB-292-541.

Tidona, R. J., 1983, "Guidelines for the Reduction of Emissions and Efficiency Improvement for Refinery Process Heaters," EPA-600/8-83-017, NTIS Order Number PB83-206995.

Tidona, R. J., Carter, W. A., and Buening, H. J., 1983, "Refinery Process Heater NO_x Reductions Using Staged Combustion Air Lances," EPA-600/7-83-022, NTIS Order Number PB83-193946.

Computer Simulation of Transport Phenomena in Evaporative Cooling Towers

D. J. Benton

W. R. Waldrop

Tennessee Valley Authority,
Engineering Laboratory,
Norris, TN 37828

A computer model of the simultaneous heat, mass, and momentum transfer processes occurring throughout an entire cooling tower is described in this paper. The model includes the flexibility to analyze the several configurations, fill arrangements, and flow distributions commonly used by the power industry. The fundamental governing equations are solved using a finite-integral technique to provide a quasi-two-dimensional description of the flow and cooling process within the tower. The model has been successfully compared with field data from cooling towers at three TVA power plants as well as data from other utilities. Each of these towers was significantly different in design, thereby demonstrating the versatility of the model for correctly predicting the cooling performance of mechanical and natural draft towers, as well as crossflow and counterflow orientations, for a range of meteorological and plant operating conditions.

Introduction

To comply with environmental regulations, many power plants constructed since the early 1970s use cooling towers in the recirculating loop of the condenser cooling water. The thermal efficiency of these power plants is directly dependent upon the efficiency of the cooling towers. Inefficiency in the cooling process of these towers will result in a continuous loss of power generation. Even the loss of a few megawatts, representing a fraction of a precent of the total plant generation, may amount to millions of dollars per year. This continuous power loss may be insignificant in comparison to load reductions which may be required to achieve an internal temperature limit during extremely hot meteorological conditions. A recent survey of utilities by Boroughs (1983) revealed that most evaporative cooling towers do not deliver the design cooling capacity. Consequently, there is a heightened interest in cooling tower performance throughout the power industry.

Evaporative cooling towers are based upon a very simple principle—energy is removed from the hot water by facilitating contact with relatively cool, dry air. The two key factors in this transer of energy are interfacial area and contact time between the air and water, the product of which is defined as the activity. The numerous configurations of cooling towers represent different approaches to increase the activity with minimum resistance to airflow. In addition, this must be accomplished for the lowest possible capital and operating cost.

Although evaporative cooling towers appear quite diverse in design, they generally can be described with a few classifications. The direction of the airflow relative to the waterflow distinguishes whether the tower is of the crossflow or counterflow type. A fill material is used to increase the contact time and interfacial area. There are two major classifications of fill—splash-bar and film. Splash-bar fill is designed to break the waterflow into droplets as it cascades and is often used in crossflow towers. Film fill breaks the waterflow into thin sheets. Because of its typically vertical orientation, it is used predominantly in counterflow towers. Towers are also classified by the mechanism used to induce airflow. Mechanical draft towers use fans to force airflow, whereas natural draft towers rely upon the buoyancy of the moist air to draw through tall chimneys. Regardless of the classifications or the combinations thereof, the physical phenomena within the tower are similar.

The simultaneous heat, mass, and momentum transfer processes occurring throughout a cooling tower are difficult to analyze. Scale modeling of these processes throughout an entire tower is infeasible because the necessary similitude, which includes two-phase flow, cannot be achieved. However, physical modeling of segments of individual components of the tower, such as a block of fill or a cluster of spray nozzles, has produced empirical heat and mass transfer coefficients for the various components of a tower (e.g., Lowe and Christie, 1961).

Perhaps the first attempt at modeling the processes taking place in an evaporative cooling tower was made by Merkel in 1962. Merkel made several simplifying assumptions which reduce the governing relationships for a counterflow tower to a single separable ordinary differential equation; this Merkel integrated numerically using the four-point Chebyshev method. Lowe and Christie (1961) performed laboratory studies on several types of counterflow fill, employing Merkels' method in the data reduction. The Cooling Tower Institute (CTI) still employs the method developed by Merkel

Contributed by the Power Division for publication in the JOURNAL OF ENGINEERING FOR GAS TURBINES AND POWER. Manuscript received by the Power Division February 3, 1987.

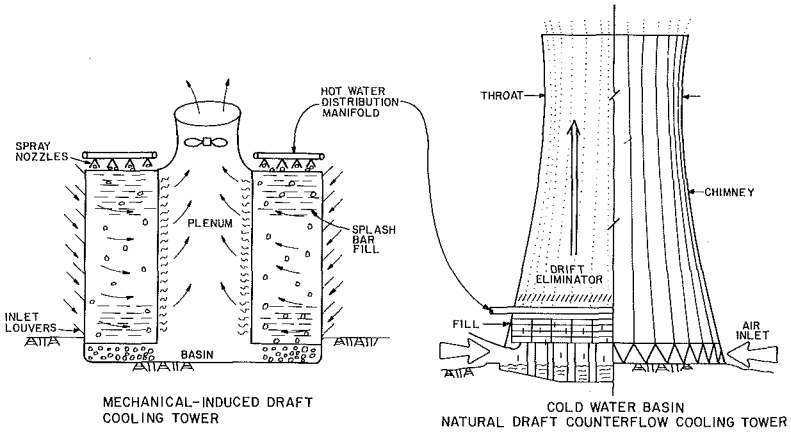

Fig. 1 Evaporative cooling towers

(CTI, 1977). Zivi and Brand (1956) extended the analysis of Merkel to crossflow towers. Kelly (1976) used the model of Zivi and Brand along with laboratory data to produce a volume of crossflow cooling tower characteristic curves to be used in graphical solutions and design calculations. Cross et al. (1976) and Bourillot (1983) also developed models with transfer equations similar to Zivi and Brand. None of these models included any variation in airflow throughout the fill. Penney and Spalding (1979) introduced a model for natural draft cross- and counterflow towers that attempted to solve for the air velocity field within the tower using a finite-difference method. This model was extended to mechanical draft towers by Majumdar and Singhal (1981). Some difficulty was experienced with this model in attempting to fit field data.

A computer model of the simultaneous heat, mass, and momentum transfer processing occurring throughout a cooling tower has been developed based on the finite-integral method (Benton, 1984a, 1984b). This model uses heat and mass transfer, and pressure loss coefficients available in the literature (e.g., Lowe and Christie, 1961; Kelly, 1976; CTI, 1977). Consequently, model calibration is necessary only for cases where these coefficients are unavailable.

The model was verified by comparing predicted results with test data from Tennessee Valley Authority (TVA) cooling towers as well as data from other utilities. These test data not only cover a range of operational and ambient meteorological conditions, but also represent a wide spectrum of fundamentally different tower and fill configurations. A mathematical description of the physical phenomena, the numerical scheme for solution of the equations, and the model verification are presented.

Equations Describing the Physical Processes

In an evaporative cooling tower, the water acts as both the heat transporting medium and the source of evaporative mass. The evaporation process which occurs in a cooling tower when hot water contacts cooler air has two effects: Heat is extracted from the water, and the density of the air is decreased, which makes the cooling tower effluent buoyant relative to the ambient air. Since the latent heat of vaporization of water at atmospheric pressure is three orders of magnitude greater than the specific heat, evaporation of even a small fraction of the water produces significant cooling. The buoyancy of the air can assist the flow of air through the tower in the case of mechanical draft towers which employ fans; or drive the flow of air, as in the case of natural draft towers which rely solely upon a chimney to utilize this buoyant force (see Fig. 1).

The analysis of cooling towers is complicated by the interrelationship of the heat transfer, mass transfer, and two-phase

Nomenclature

a = interfacial area per unit volume 1/m
A = outward normal area vector, m^2
A_i = interfacial area, m^2
B = mass transfer driving potential
C_{pa} = constant pressure specific heat of air, J/kg/°C
C_{pw} = constant pressure specific heat of water, J/kg/°C
D = air/water vapor diffusion coefficient, m^2/s
E = evaporative mass flux, $kg/m^2/s$
g = acceleration of gravity, m/s^2
g_c = Newton's constant, Nt-m/kg/s^2
G = dry airflow rate, kg/s
h_a = enthalpy of moist air (per unit mass dry air), J/kg dry air
h_g = enthalpy of saturated water vapor, J/kg
H = sensible heat tranfer coefficient, $W/m^2/°C$
K = mass transfer coefficient, $kg/m^2/s$
L = waterflow rate, kg/s
Le = Lewis number
p = absolute pressure, Nt/m^2
Q_e = evaporative heat flux, W
Q_s = sensible heat flux, W
Q_t = total heat flux, W
s = distance along a streamline, m
T = water temperature, °C
T_{db} = dry-bulb temperature, °C
T_{dbo} = ambient dry-bulb temperature, °C
T_h = inlet water temperature, °C
T_{wb} = wet-bulb temperature, °C
T_{wbo} = ambient wet-bulb temperature, °C
v = air velocity, m/s
V = vector velocity, m/s
W_{fan} = fan power input, W
x = horizontal distance, m
y = vertical distance, m
z = lateral distance, m
η_{fan} = fan efficiency
κ = thermal conductivity of air, W/m/°C
λ = headloss coefficient (velocity heads per unit length of air travel), 1/m
ρ = density of moist air, kg/m^3
ω = absolute humidity
ω_i = absolute humidity at interface

flow, the two phases being liquid water and moist air. As in most analysis of transport phenomena, the processes are described by the conservation of mass, momentum, and energy. Because the evaporative process changes the phase of a portion of the water passing through the tower, the conservation of mass of the dry air and water vapor, and the conservation of energy of the gas and water phases are considered individually. These equatons are applied in their steady-state, steady-flow form.

The independent variables for the analysis are: x, y, z, L, T_h, T_{wbo}, and T_{dbo}. The dependent variables in the conservation equations are: v, ω, h_a, T, and p.

The auxiliary quantities (T_{db}), (T_{wb}), and (ρ) are computed throughout the tower from thermodynamic relationships for air–water vapor mixtures from computed values of ω, h_a, and p. These relationships are presented in Van Wylen and Sonntag (1973) and ASHRAE (1977), and the properties are tabulated in Keenan et al. (1969) and ASHRAE (1977).

Conservation of momentum of the gas-phase flow is approximated by the Bernoulli equation. For two points (1) and (2) along a streamline of length Δs, this is expressed as (Streeter and Wylie, 1975)

$$P_1 + \frac{\rho_1 v_1^2}{2g_c}(1+\omega_1) = P_2 + \frac{\rho_2 v_2^2}{2g_c}(1+\omega_2) + \frac{\rho_1 v_1^2 + \rho_2 v_2^2}{4g_c}\lambda \Delta s + \left(\frac{\rho_1+\rho_2}{2}\right)\frac{g}{g_c}(y_2 - y_1) \quad (1)$$

where λ is the headloss coefficient having units of velocity heads per unit length along the streamline. Using headloss coefficients λ for the various components of the tower (i.e., fill, spray, rain zones), the pressure distribution may be computed throughout. The flowrate between streamlines is controlled by the exit boundary condition, which requires the head at a common point (such as the plenum) to be equal across streamlines. This approach is therefore somewhat analogous to a branched pipe flow analysis.

The total heat transfer may be expressed in terms of sensible and evaporative (or latent) heat transfer. The differential sensible heat transfer rate dQ_s from the water to the air is expressed as the product of the local heat transfer coefficient H; the temperature difference between the local water temperature T; the local air dry-bulb temperature T_{db}; and the differential interfacial area dA_i

$$dQ_s = H(T - T_{db})dA_i \quad (2)$$

To establish an equivalent heat transfer rate for evaporation dQ_e, it is convenient first to develop an expression for the mass transfer rate. The differential evaporative mass transfer rate dE is defined in terms of the driving potential B, and the mass transfer coefficient K, by (Kays, 1966)

$$dE = B\,K\,dA_i \quad (3)$$

In the case of mixtures of air and water vapor, Kays defines the mass transfer driving potential B in terms of the absolute humidity ω as

$$B = \frac{\omega_i - \omega}{1+\omega} \quad (4)$$

where ω_i is the absolute humidity at the interface and is assumed to be at saturation. The differential evaporative mass transfer rate dE may then be expressed in terms of the absolute humidity as

$$dE = K\frac{(\omega_i - \omega)}{(1+\omega)}dA_i \quad (5)$$

The differential mass transfer rate is related to the differential latent heat transfer rate dQ_e through the enthalpy of saturated water vapor h_g

$$dQ_e = h_g\,dE \quad (6)$$

The differential interfacial area dA_i within a differential volume $dx\,dy\,dz$ of fill is expressed as

$$dA_i = a\,dx\,dy\,dz \quad (7)$$

where a is the interfacial area per unit volume.

The three transfer equations of interest are then

$$dQ_s = H\,a(T - T_{db})dx\,dy\,dz \quad (8)$$

$$dE = K\,a\frac{(\omega_i - \omega)}{(1+\omega)}dx\,dy\,dz \quad (9)$$

$$dQ_e = h_g K\,a\frac{(\omega_i - \omega)}{(1+\omega)}dx\,dy\,dz \quad (10)$$

For cylindrical coordinates, $dx\,dy\,dz$ is replaced with $r\,dr\,d\theta\,dy$.

The differential total heat transfer rate dQ_t is the sum of the sensible and evaporative transfers

$$dQ_t = dQ_s + dQ_e \quad (11)$$

These three transfer equations can now be used to express the conservation of mass and energy within a control volume by including the advective terms. The *conservation of mass of the water vapor* can be expressed as

$$\iiint K\,a\frac{(\omega_i - \omega)}{(1+\omega)}dx\,dy\,dz = \iint \frac{\omega}{(1+\omega)}\rho V \cdot dA \quad (12)$$

where $V \cdot dA$ is the dot product of the vector velocity V and the outward normal area vector dA. This simply says that the net efflux of water vapor from each cell through advection must be equal to the evaporaton within the cell.

A *conservation of mass of the air* within each cell is formulated upon the concept that the net efflux of dry air from each cell is zero, or

$$\iint \left(\frac{1}{1+\omega}\right)\rho\, V \cdot dA = 0 \quad (13)$$

The *conservation of energy for the air* within a control volume similarly includes the addition of energy from the sensible and latent heat transfer. This can be expressed as

$$\iiint \left[h_g K\,a\frac{(\omega_i - \omega)}{(1+\omega)} + H\,a(T - T_{db})\right]dxdydz = \iint \frac{1}{(1+\omega)}h_a\,\rho V \cdot dA \quad (14)$$

Note that by convention h_a is the energy of the moist air per unit mass dry air.

The *conservation of energy for the water* within a control volume uses a slightly different formulation for the advective component. The total heat transfer rate dQ_t may be expressed in terms of the change in the product of the mass flowrate of water L; specific heat C_{pw}; and the temperature T; or

$$dQ_t = -d(L\,C_{pw}\,T) \quad (15)$$

Combining equations (8), (10), (11), and (15) yields

$$d(L\,C_{pw}\,T) = -\left[h_g\,K\,a\frac{(\omega_i - \omega)}{(1+\omega)} + H\,a(T - T_{db})\right]dx\,dy\,dz \quad (16)$$

A sensible heat transfer coefficient H and a mass transfer coefficient K are required for this analysis. In the event that only one is available, the Lewis analogy, expressed as

$$H = C_{pa}\mathrm{Le}\,K \quad (17)$$

is applied (Lewis, 1922). The local Lewis number Le is deter-

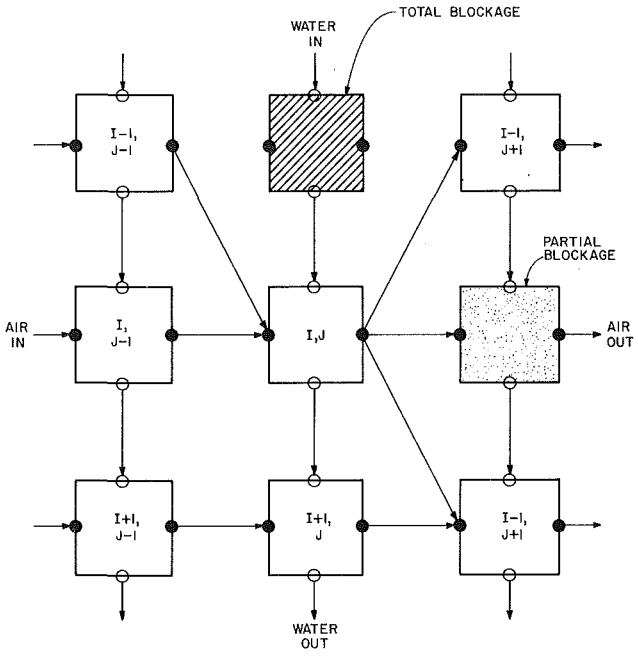

Fig. 2 Cell and node notation in crossflow fill and flowpaths in crossflow fill with blockage

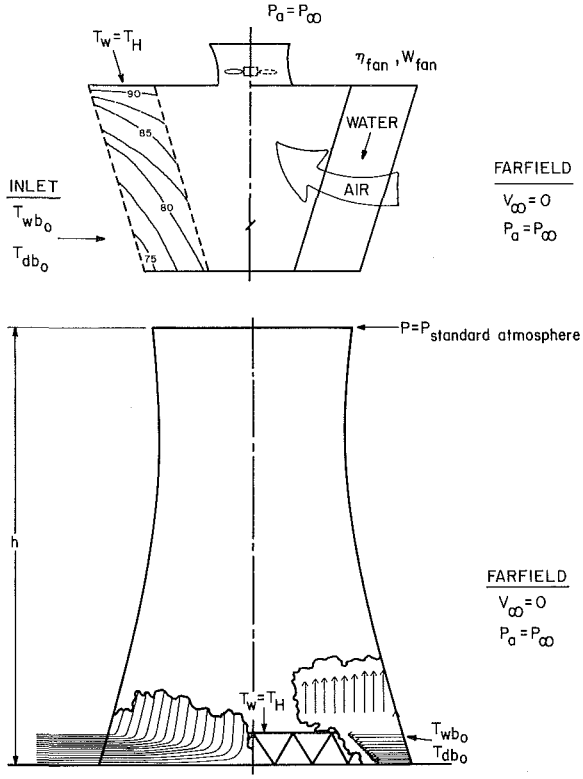

Fig. 3 Boundary conditions, streamlines, and internal distributions

mined from the local values of molecular thermal conductivity κ, density ρ, diffusion coefficient D, and specific heat C_{pa}

$$\text{Le} = \frac{\kappa}{\rho D C_{pa}} \tag{18}$$

The local values of κ, ρ, and C_{pa} are functions of temperature and absolute humidity; the diffusion coefficient D is a function of temperature.

Certain assumptions are implicit in the simplified form of the governing equations being used. The steady-state, steady-flow assumption precludes the analysis of transients associated with plant operations or meteorology. The wet-bulb temperature is assumed equal to the adiabatic saturation temperature, the difference being negligible for these computations. Two-dimensional symmetry is also assumed. This is expressed as either lateral symmetry in Cartesian coordinates or circumferential symmetry in cylindrical coordinates, depending upon the tower geometry. Therefore, the model in its present form cannot address asymmetric airflow resulting from winds or multiple tower interference.

Solution of the Governing Equations

Simulation of the mass, momentum, and heat transfer processes in the cooling tower requires that the tower be discretized, or divided into computational cells. Each cell is treated as a control volume, and the governing equations are applied to each. At each cell the computed dependent variables from adjacent upstream cells are utilized. These variables (e.g., enthalpy, velocity, water temperature, absolute humidity, and pressure) are defined at nodes located at the midpoints of the cell boundaries. The use of boundary nodes assures conservation of mass and energy from cell to cell (e.g., the mass leaving the east face of one cell enters the west face of the adjacent cell by virtue of common storage of the variables, see Fig. 2). Applying the Bernoulli equation and conservation equations to each cell results in a set of nonlinear simultaneous equations (five for each cell) implicitly relating the dependent variables h_a, v, T, ω, and p. These implicit nonlinear simultaneous equations are solved using the Gauss–Seidel method (i.e., point-by-point successive substitution). A finite-integral formulation of the conservation equations (1), (12), (13), (14), and (16) was used. This method is described in detail by Benton (1984b).

Although natural and mechanical draft towers are quite different in appearance, much of the solution procedure is similar. For natural draft towers, flow through the chimney must be computed based upon the buoyancy of the moist air. For mechanical draft towers, the flow is computed by replacing the chimney with a fan. The pressure rise across the fan Δp_{fan} is computed using the following relationship:

$$\Delta p_{\text{fan}} = \frac{\eta_{\text{fan}} W_{\text{fan}}\ \rho_{\text{fan}}}{G(1+\omega_{\text{fan}})} \tag{19}$$

The fan efficiency is an implicit function of airflow, air density, input power, and the pressure drop across the fill. The functional relationship for fan efficiency must be determined from field or laboratory measurements and supplied to the model. The model uses a cubic iteration to solve the pressure balance at the fan for the dry airflow G and the fan efficiency η_{fan}.

The differences between counterflow and crossflow towers are more significant to the computation than the differences between mechanical and natural draft towers. The differences in the boundary conditions (illustrated in Fig. 3) make the formulation and solution of the finite-integral equations somewhat different. For this reason, these two cases will be discussed separately.

Crossflow Towers

Computation of the transport phenomena within crossflow towers is the simpler of the two cases. The finite-integral formulation of the conservation equations for this case, expressed in rectangular coordinates, becomes

Conservation of Mass for the Dry Air

$$\frac{\rho_w v_w A_w}{1+\omega_w} = \frac{\rho_e v_e A_e}{1+\omega_e} \tag{20}$$

Conservation of Mass for the Water Vapor

$$\frac{\omega_e \rho_e v_e A_e}{1+\omega_e} - \frac{\omega_w \rho_w v_w A_w}{1+\omega_w} = 1/2\ Ka\left(\frac{\omega_{in}-\omega_e}{1+\omega_e} + \frac{\omega_{is}-\omega_w}{1+\omega_w}\right)\Delta x \Delta y \Delta z \tag{21}$$

where n, s, e, and w refer to north, south, east, and west, respectively (see Fig. 2); and ω_{in} and ω_{is} are the saturated absolute humidities evaluated at the north and south water temperatures, respectively.

Conservation of Energy for the Air

$$\frac{\rho_e v_e A_e h_{ae}}{1+\omega_e} - \frac{\rho_w v_w A_w h_{aw}}{1+\omega_w} = \left(1/2\ Ka\left(\frac{\omega_{in}-\omega_e}{1+\omega_e} + \frac{\omega_{is}-\omega_w}{1+\omega_w}\right)h_{ge} + 1/2\ Ha((T_n - T_{dbe}) + (T_s - T_{dbw}))\right)\Delta x \Delta y \Delta z \tag{22}$$

where T_n and T_s are the water temperatures at the north and south nodes, respectively; and T_{dbe} and T_{dbw} are the dry-bulb temperatures at the east and west nodes, respectively.

Conservation of Energy for the Water

$$C_{pw}(L_n T_n - L_s T_s) = \frac{\rho_e v_e A_e h_{ae}}{1+\omega_e} - \frac{\rho_w v_w A_w h_{aw}}{1+\omega_w} \tag{23}$$

Bernoulli's Equation

$$P_w + \frac{\rho_w v_w^2}{2g_c}(1+\omega_w) = P_e + \frac{\rho_e v_e^2}{2g_c}(1+\omega_e) + \frac{\rho_w v_w^2 + \rho_e v_e^2}{4g_c}\lambda\ \Delta x \tag{24}$$

These five equations are solved throughout a two-dimensional network of cells representing the fill region. The properties of the fill do not have to be homogeneous; consequently, the model will accommodate obstructions, voids, and hybrid fill as demonstrated by Benton (1984a). The entering waterflow distribution at the top row of cells and a distribution of inlet wet- and dry-bulb temperatures can also be arbitrarily specified.

The iterative solution process is initiated by solving a simplified point model to obtain initial values for the airflow rate and wet- and dry-bulb temperature at the exit of the cooling tower. The results are used to provide an initial distribution of the absolute humidity, enthalpy, and wet- and dry-bulb temperatures throughout the tower. Linear interpolation from entrance to exit is used to obtain initial values at intermediate locations.

The computation of sensible and latent heat transfer rates starts in the *upper lefthand corner* cell as shown in Fig. 3, and proceeds one column at a time. The computation for each cell is an iterative process since the driving potential for the transfer utilizes the conditions at the exit. After the energy transfer in the cells located in the fill has been computed, the air is assumed to be thoroughly mixed as it flows through the chimney (or fan) without further heat or mass transfer. Exit conditions of the two-dimensional analysis of the rain, fill, and spray zones are numerically integrated to establish initial conditions for the one-dimensional computation through the chimney. In the absence of heat or mass transfer, a one-dimensional distribution of cells is assumed to be sufficient in the chimney region of natural draft towers and in the fan and stack region of mechanical draft towers.

With the temperatures and absolute humidities established based on a trial airflow estimate, an evaluation of the airflow distribution is undertaken. The Bernoulli equation and the conservation of mass of dry air is applied to each cell. The airflow distribution is solved in the same manner as a branched pipe network having interconnecting paths which permit crossflow. This solution of the Bernoulli and the conservation of mass of air equations provides values of velocity and pressure at the exit face of each cell within the fill. An average velocity is computed for the plenum, and the Bernoulli equation is used through the chimney or fan. The fan and recovery stack in mechanical draft towers are each modeled as a single cell. In natural draft towers the chimney is discretized into a number of cells.

Based on the new flow distribution, revised values of temperature, enthalpy, and humidity ratio are computed. These values reflect vertical mixing between adjacent cells in the fill as indicated in Fig. 3. The sensible and latent heat tranfer rates in the various cells are recomputed using the temperatures, densities, and velocities from the preceding step.

The iterative process is considered to have converged when the computed pressure at the exit plane corresponds to the ambient pressure.

Counterflow Towers

Computations for counterflow towers are more complicated than those for crossflow towers because of the nature of the boundary conditions. Also the transport phenomena must be calculated in four separate zones: the rain, fill, spray, and chimney (or fan) zones. Each zone is treated separately, but obviously the dependent variables at the boundaries of the zones must match. The finite-integral approximation to the governing equations is slightly different from that of the crossflow towers because the direction of flow is different. For counterflow towers, the finite-integral equations expressed in cylindrical coordinates are:

Conservation of Mass for the Dry Air

$$\frac{\rho_s v_s A_s}{1+\omega_s} = \frac{\rho_n v_n A_n}{1+\omega_n} \tag{25}$$

Conservation of Mass for the Water Vapor

$$\frac{\omega_n \rho_n v_n A_n}{1+\omega_n} - \frac{\omega_s \rho_s v_s A_s}{1+\omega_s} = 1/2\ Ka\left(\frac{\omega_{in}-\omega_n}{1+\omega_n} + \frac{\omega_{is}-\omega_s}{1+\omega_s}\right)2\pi r \Delta r \Delta y \tag{26}$$

Conservation of Energy for the Air

$$\frac{\rho_n v_n A_n h_{an}}{1+\omega_n} - \frac{\rho_s v_s A_s h_{as}}{1+\omega_s} = \left(1/2\ Ka\left(\frac{\omega_{in}-\omega_n}{1+\omega_n} + \frac{\omega_{is}-\omega_s}{1+\omega_s}\right)h_{gn} + 1/2\ Ha((T_n - T_{dbn}) + (T_s - T_{dbs}))\right)2\pi r \Delta r \Delta y \tag{27}$$

Conservation of Energy for the Water

$$C_{pw}(L_n T_n - L_s T_s) = \frac{\rho_n v_n A_n h_{an}}{1+\omega_n} - \frac{\rho_s v_s A_s h_{as}}{1+\omega_s} \tag{28}$$

Bernoulli's Equation

$$P_s + \frac{\rho_s v_s^2}{2g_c}(1+\omega_s) = P_n + \frac{\rho_n v_n^2}{2g_c}(1+\omega_n) + \frac{\rho_s v_s^2 + \rho_n v_n^2}{4g_c}\lambda\ \Delta y + \frac{(\rho_n + \rho_s)}{2}\frac{g \Delta y}{g_c} \tag{29}$$

Boundary conditions for this case (shown in Fig. 3) require an iterative procedure. The iterative solution process is initiated by solving a simplified point model to obtain initial

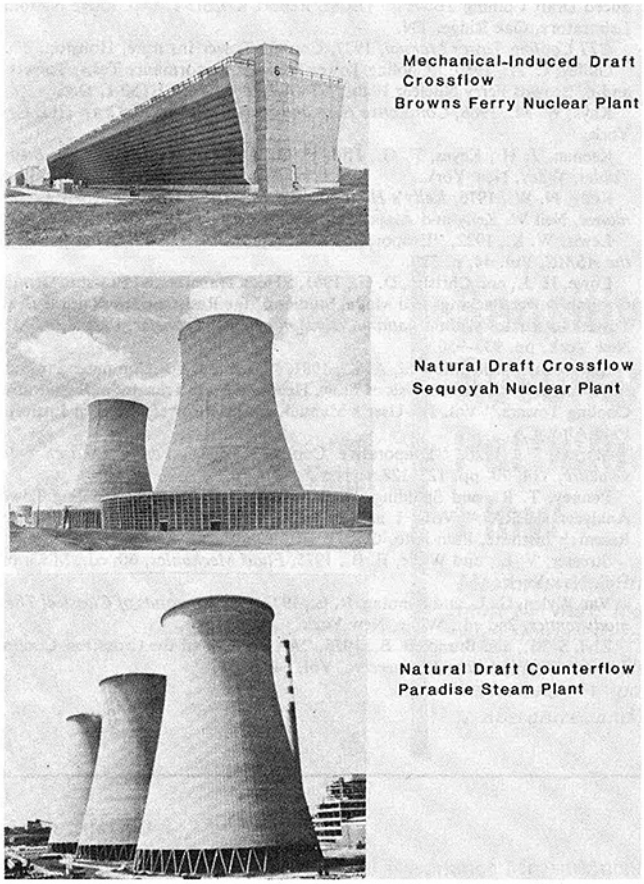

Fig. 4 TVA evaporative cooling towers used for model verification

values for the airflow rate and wet- and dry-bulb temperature at the exit of the cooling tower. The results are used to provide an initial distribution of the absolute humidity, enthalpy, and wet- and dry-bulb temperatures throughout the tower. Linear interpolation from entrance to exit is used to obtain initial values at intermediate locations. An initial estimate of the airflow distribution is computed based on uniform radial velocity at the inlet.

The solution procedure is initiated in the rain zone and is based on an assumed cold water temperature so that heat transfer computations can proceed. Flows through the fill zone are confined to the vertical direction, which is a logical assumption for sheet fill. When the computations are advanced to the spray nozzles, a check is made to determine whether the computed hot water temperature corresponds to the specified hot water temperature. If the computed and specified hot water temperatures do not agree, the cold water temperature at the base of the tower is adjusted and the heat transfer is recomputed. When the computed and specified hot water temperatures agree, the pressure computations are performed. The airflow within the rain and fill zones is redistributed among the assumed pathlines (Fig. 3) according to the Bernoulli equation such that dynamic pressure (i.e., $p+(1+\omega)\rho v^2/2g_c$) at the top of the fill is uniform in the radial direction. The computed pressure at the exit plane is then compared to the specified ambient pressure. If the pressures are not in agreement, the airflow is appropriately adjusted and the heat transfer computations restarted. This series of computations continues until the computed hot water temperature and exit pressure correspond with the values prescribed as boundary conditions.

The entering waterflow can be arbitrarily distributed for these computations. Likewise, an arbitrary distribution of inlet wet- and dry-bulb temperatures can be specified. The

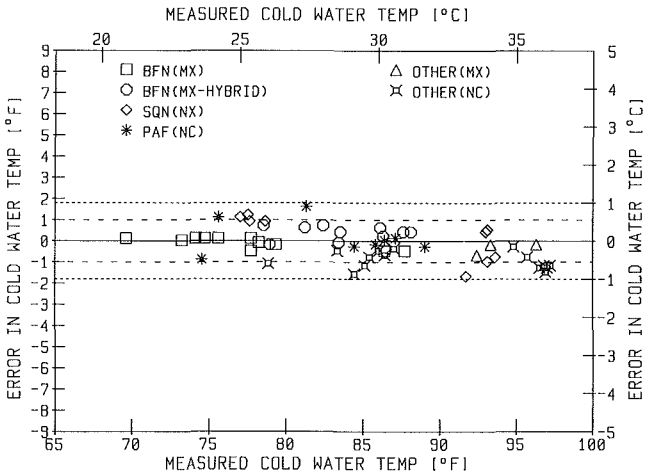

Fig. 5 Comparison of measured and computed cold water temperature

model can also analyze nonhomogeneous or unevenly distributed fills so long as they retain circumferential symmetry.

Comparison of Model Results With Field Data

The validity of the model has been tested by comparing model results with field data collected on cooling towers at three TVA power plants as well as data from other utilities. These towers are each fundamentally different in design as shown in Fig. 4, providing data on natural draft counterflow, natural draft crossflow, and rectangular mechanical draft crossflow towers. In addition, field data are also available on one of the mechanical draft towers modified by adding hybrid fill (Gidley, 1980; Benton, 1984a).

Each application was initiated by specifying the geometry of the tower, the fill characteristics, meteorology, and plant operating data (i.e., water temperature and flowrate). The fill characteristics used in the model for these comparisons were taken from Majumdar and Singhal (1981). The results of the comparison are presented in Fig. 5. It is important to note that no calibration of the model was used in making the predictions. Although only the global results of these computations are shown in Fig. 5, the model also provides distributions of dependent variables throughout the tower for each case as illustrated in Fig. 3. Such distributions are important in providing insight into the internal transport phenomena, which is essential to correcting deficiencies.

Model Statistics

The present model has been developed into a FORTRAN coded computer program. The program is comprised of a main program and 38 subprograms in approximately 7000 statements. The computer program requires 109K bytes (1 byte = 8 binary bits) of memory. However, only 33K bytes are required for any one geometry (i.e., mechanical-crossflow). The execution time is approximately 30 s on an HP-1000F minicomputer, 90 s on an IBM-XT, or 1 s on an IBM-3031.

The computer program models mechanical draft crossflow (rectangular), mechanical draft counterflow (round or rectangular), natural draft crossflow (round), and natural draft counterflow (round) towers.

Summary

Complex and complete solution of heat, mass, and momentum processes cannot be described in their most basic form. However, a cooling tower can be subdivided into components,

with heat, mass, and momentum described using empirical coefficients.

A mathematical model, which can be run economically on a minicomputer or a microcomputer, has been developed to solve equations describing these processes. The solutions to these equations provide a two-dimensional description of the flow and cooling processes throughout the tower. Results from the mathematical model compare favorably with data from field tests of TVA cooling towers as well as those of other utilities under a variety of operating conditions.

References

ASHRAE Handbook: Fundamentals, 1977, American Society of Heating, Refrigerating, and Air-Conditioning Engineers, New York.

Benton, D. J., 1984a, "Computer Simulation of Hybrid Fill in Crossflow Mechanical-Induced-Draft Cooling Towers," Proceedings ASME Winter Annual Meeting, New Orleans, LA.

Benton, D. J., 1984b, "Development of the Finite-Integral Method," TVA Report No. WR28-2-900-148.

Boroughs, R. D., and Terrell, J. E., 1983, "Survey of Utility Cooling Towers," TVA Report OP/EDT-83/13.

Bourillot, C., 1983, TEFERI, "Numerical Model for Calculating the Performance of an Evaporative Cooling Tower," translated by J. A. Bartz, EPRI Report CS-3212-SR, Electric Power Research Institute, Palo Alto, CA.

Cross, K. E., Park, J. E., Vance, J. M., and van Wie, N. H., 1976, "Theory and Application of Engineering Models for Cross-flow and Counterflow Induced Draft Cooling Towers," ORNL Report K/CSD-1, Oak Ridge National Laboratory, Oak Ridge, TN.

CTI Cooling Tower Manual, 1977, Cooling Tower Institute, Houston, TX.

Gidley, C. A., 1980, "Cooling Tower Thermal Performance Tests, Towers 5 and 6, Browns Ferry Nuclear Plant," TVA Report No. SET80-1, Dec.

Kays, W. M., 1966, *Convective Heat and Mass Transfer*, McGraw-Hill, New York.

Keenan, J. H., Keyes, F. G., Hill, P. G., and Moore, J. G., 1969, *Steam Tables*, Wiley, New York.

Kelly, N. W., 1976, *Kelly's Handbook of Crossflow Cooling Tower Performance*, Neil W. Kelly and Associates, Kansas City, MO.

Lewis, W. K., 1922, "Evaporation of a Liquid Into a Gas," *Transactions of the ASME*, Vol. 44, p. 329.

Lowe, H. J., and Christie, D. G., 1961, "Heat Transfer and Pressure Drop in Cooling Tower Packings and Model Studies of the Resistance of Natural-Draft Towers to Airflow," *International Division of Heat Transfer*, Part V, ASME, New York, pp. 933–950.

Majumdar, A. K., Singhal, A. K., 1981, "VERA2D—A Computer Program for Two-Dimensional Analysis of Flow, Heat and Mass Transfer in Evaporative Cooling Towers," Vol. II—User's Manual, Electric Power Research Institute, Palo Alto, CA.

Merkel, F., 1926, "Evaporative Cooling," *Zeits. Verein Deutscher Ingenieure*, Vol. 70, pp. 123–128.

Penney, T. R., and Spalding, D. B., 1979, "Validation of Cooling Tower Analyzer (VERA)," Vols. 1 and 2, EPRI Report FP-1279, Electric Power Research Institute, Palo Alto, CA.

Streeter, V. L., and Wylie, E. B., 1975, *Fluid Mechanics*, 6th ed., McGraw-Hill, New York.

Van Wylen, G. J., and Sonntag, R. E., 1973, *Fundamentals of Classical Thermodynamics*, 2nd ed., Wiley, New York.

Zivi, S. M., and Brand, B. B., 1956, "An Analysis of the Crossflow Cooling Tower," *Refrigeration Engineering*, Vol. 64, p. 31.

Sensitivity of the Acoustical Resonance Measurement of Particle Loading in Gas-Solids Flow

A. A. Vetter
Humbug Mountain Research Laboratories,
Duarte, CA 91010

Measurement of the frequency of transverse acoustic resonances of a duct can determine the mass loading and size of particles fluidized by a gas phase. A first-order perturbation-iteration acoustic analysis is applied to determine the sensitivity of this two-phase flow measurement, termed the Acoustical Resonance Measurement, to variations in particle size, particle size dispersion, particle heat capacity, temperature, and pressure for the application of pulverized coal fluidized by air.

Introduction

In previous work, the Acoustical Resonance Measurement was shown to determine the ratio of mass density of solid particles to the mass density of the gas phase by measurement of the sound speed in a gas-solids mixture (Vetter and Culick, 1987). When particles are added to a gas to form a dispersed two-phase flow, the sound speed in the mixture is lower than the sound speed of the gas phase alone. Acoustic resonances occur in fixed geometries, with the frequency at which the resonances occur being proportional to the sound speed of the two-phase mixture. The particle loading is determined by the frequency shift of a single transverse resonance, defined as the decrease in the resonance frequency divided by the resonance frequency with the gas phase alone

$$s = (f_0 - f)/f_0 \tag{1}$$

and the particle size is determined by the ratio of the frequency shifts of first to second transverse resonances.

The sensitivity of the Acoustical Resonance Measurement is examined for the application of pneumatically conveyed pulverized coal. The nominal conditions have a temperature of 334 K, pressure of 1 atm, absolute humidity of 4.5 percent, particle dispersion parameter of 0.8, particle specific heat of 1.255 kJ/kg, particle shape factor of 0.75, and a pipe diameter of 0.5 m (Vetter and Culick, 1987). The sensitivities of the frequency shift and the ratio of shifts are calculated numerically with a first-order perturbation-iteration acoustical analysis applied to the geometry of an infinitely long circular pipe. The details of this analysis are given by Vetter and Culick (1985). Relationships between the frequency shift and the mass loading and the shift ratio and between the particle fineness parameter were determined previously (Vetter and Culick, 1987).

Particle Sizing

The distribution of sizes of pulverized coal, as well as larger-sized coal, has been found to fit a two-parameter (fineness and dispersion) Rosin-Rammler distribution (Shotts, 1968). Samples obtained in coal transport piping at a power plant were found to fit distributions with dispersion parameters of approximately 0.8 (Vetter, 1982). With a dispersion parameter of 0.8, the mean particle size is approximately ⅔ of the fineness parameter.

Uncertainty in the particle size converts to uncertainty in the experimentally determined mass loading via the uncertainty in the frequency shift. The influence coefficient of the frequency shift of the lowest transverse resonance with respect to fineness parameter, which is defined by

$$\Delta s/s = a_x(\Delta x/x) \tag{2}$$

and represents the instantaneous relationship in the power form $s = x^a$, is presented in Fig. 1 as a function of fineness

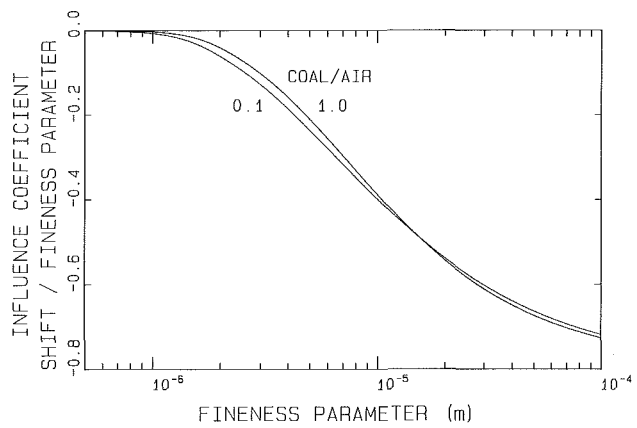

Fig. 1 The influence coefficient of the resonance frequency shift with respect to the particle fineness parameter, as defined in equation (2), as a function of particle size for coal/air mass density ratios of 0.1 and 1.0

Contributed by the Power Division for publication in the JOURNAL OF ENGINEERING FOR GAS TURBINES AND POWER. Manuscript received by the Power Division January 21, 1987.

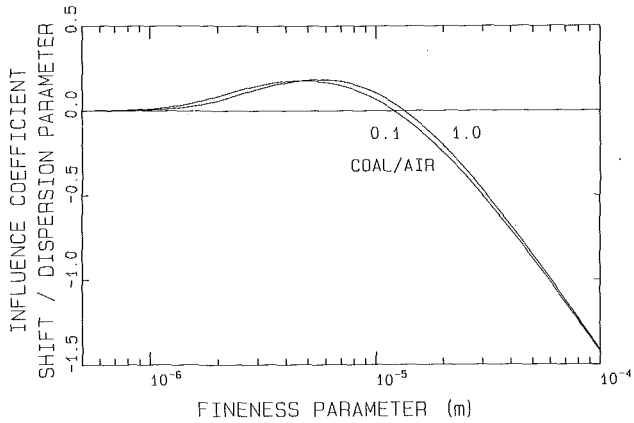

Fig. 2 The influence coefficient of the resonance frequency shift with respect to the particle dispersion parameter

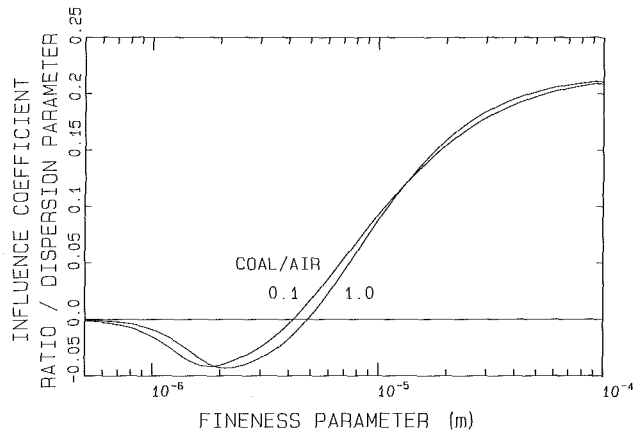

Fig. 3 The influence coefficient of the ratio of the shifts of the first to second transverse resonances with respect to the particle dispersion parameter

parameter with parametric variations of mass loading. The influence coefficient is nearly independent of mass loading, due to the main influence of mass loading occurring as nearly equal factors in both the numerator and denominator in the definition of the influence coefficient. For small particles, the Acoustical Resonance Measurement is near the no-slip limit where the particles fully follow the acoustical waves, and the frequency shift is independent of particle size. This behavior is shown on the left-hand side of Fig. 1 where the influence coefficient approaches zero. For larger particles the influence coefficient obtains significant values, approximately an inverse square root dependence (-0.5) at a value of the fineness parameter of 10 to 20 μm, and approaches a value of -0.8 for fineness parameters greater than 0.1 mm.

The ratio of the shifts of the first to second transverse resonance frequencies was previously determined to be nearly independent of particle mass loading (Vetter and Culick, 1987). The influence coefficient of the ratio with respect to the particle mass loading is zero at both the large and small particle limits, has a minimum for a value of the fineness parameter of 4 μm, passes through zero at approximately 13 μm, and has a maximum at approximately 40 μm. For a particle mass loading of 0.1 the minimum value of the influence coefficient is -1.4×10^{-3} and the maximum is 0.6×10^{-3}. For a loading of 1.0, the minimum is -4.0×10^{-3} and the maximum is 1.8×10^{-3}.

The influence coefficients of the frequency shift and the shift ratio with respect to the dispersion parameter are given in Figs. 2 and 3 as a function of fineness parameter for particle mass loadings of 0.1 and 1.0. Both of these influence coefficients are nearly independent of mass loading. The shift influence coefficient is zero at the small particle limit, then increases as the fineness parameter increases to reach a maximum of approximately 0.2 at a fineness parameter of approximately 5 μm. The influence coefficient then has another zero at approximately 12 μm, before steadily decreasing with increasing fineness parameter. The influence coefficient steadily decreases at large values of the fineness parameter because large particles have only a small effect on the sound speed and distributions with increased dispersion (smaller dispersion parameter) have a larger number of smaller particles.

The influence coefficient of the shift ratio with respect to the dispersion parameter is zero at the small particle limit,

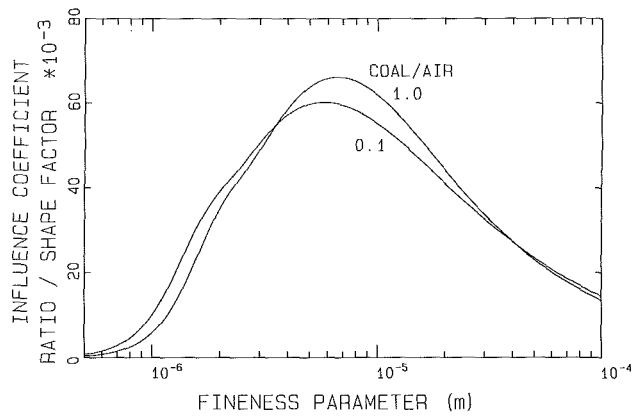

Fig. 4 The influence coefficient of the shift ratio with respect to the particle shape factor.

reaches a minimum of approximately -0.04 at 2 μm, passes through a zero at approximately 5 μm, before reaching a value of approximately 0.21 at the large particle limit.

A shape factor is required to relate the coal particle sizes to the spherical particle sizes from which theoretical expressions are derived. Due to the irregular shape, the coal particle has a higher drag per mass than would a sphere with the same density and mass. From the standpoint of the Acoustical Resonance Measurement, the coal particles act as if they are less dense because the larger drag allows the particles to follow the acoustic waves more closely. From the definition of the shape factor, the influence coefficient of the frequency shift with respect to the shape factor has the same values as the influence coefficient of the frequency shift with respect to the fineness parameter given in Fig. 1. The influence coefficient of the shift ratio with respect to the shape factor is given in Fig. 4 as a function of fineness parameter for particle mass loadings of 0.1 and 1.0. The influence coefficient is small, with a maximum value of less than 0.07, and is almost independent of mass loading. The small value of this influence coefficient is due to both frequency shifts being affected nearly equally by the shape factor.

Nomenclature

a = influence coefficient
f = resonance frequency
s = resonance frequency shift due to particles
x = Rosin–Rammler fineness parameter
X = mole fraction of water vapor in the gas phase
z = any parameter

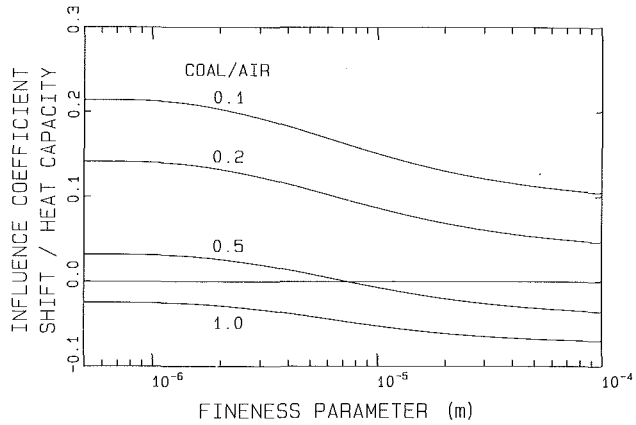

Fig. 5 The influence coefficient of the resonance frequency shift with respect to the particle heat capacity for coal/air mass density ratios from 0.1 to 1.0

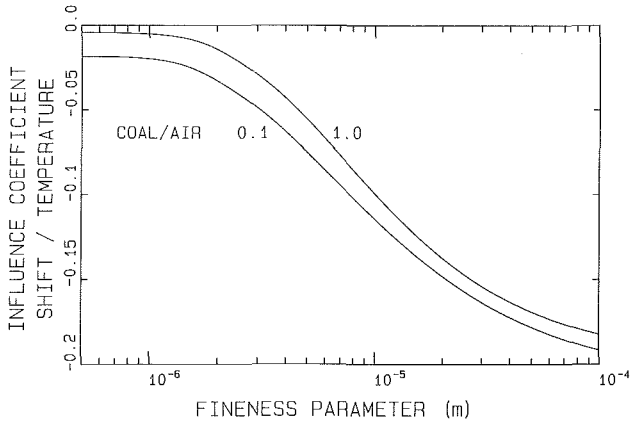

Fig. 6 The influence coefficient of the resonance frequency shift with respect to the absolute temperature

Heat Capacity

The heat capacity of the coal particles was varied over a range from 0.8 to 1.6 kJ/kg, corresponding to the range for U.S. coals (McCabe and Boley, 1945). For a mass loading, of 0.05, the frequency shift changes by 20 percent over the range of heat capacity from 0.8 to 1.6 kJ/kg. As the mass loading increases, the effect of changing heat capacity is decreased, and even changes its direction. At a mass loading of 1.0, the frequency shift changes only 3 percent over the entire range of heat capacities.

The influence coefficient of the frequency shift with respect to the particle heat capacity is presented in Fig. 5 as a function of fineness parameter for particle mass loadings from 0.1 to 1.0. The influence coefficient is largest for light mass loadings, but is smaller at higher mass loadings.

The influence coefficient of the shift ratio with respect to the particle heat capacity is small for all particle sizes and particle mass loadings. This influence coefficient is zero at both the small and large particle limits and has a maximum near 5 μm, which is approximately 9×10^{-3} for a particle mass loading of 0.1 and decreases with increasing loading to a maximum of 4×10^{-3} for a loading of 1.0. The small influence of the heat capacity on the shift ratio is due to both shifts being influenced by approximately the same amount.

Humidity

The water that is removed from the coal in the pulverizing process enters the air as vapor, changing the molecular weight and the heat capacity of the conveying gas. The change in molecular weight affects the mass loading ratio and the speed of sound in the gas phase. Change in heat capacity affects the thermal contribution to the sound speed shift and also changes the isentropic constant, i.e., the ratio of specific heats, which in turn affects both the sound speed in the gas phase alone and the thermal contribution to the sound speed shift.

The properties of air and water vapor are well known, so that a measurement of the humidity is sufficient to make the humidity correction accurately. The effect of the change in resonance frequency by the air humidity can be approximated by using the ideal gas law and assuming an ideal mixture. The resonance frequency of dry air divided by the resonance frequency of air with a water vapor mole fraction X is given by

$$(f_d/f_X)^2 = (1+0.167X)/((1+0.233X)(1-0.379X)) \quad (3)$$

Equation (3) represents the zero frequency correction. Minor adjustments to account for nonideal effects at other frequencies can be obtained from measurements at 293 K (Evans and Bass, 1972).

The influence coefficients for the humidity are small. The influence coefficient of the frequency shift with respect to the water vapor mole fraction varies from -0.5×10^{-3} at the small particle limit to -2.0×10^{-3} for a fineness parameter of 0.1 mm. The absolute value of this coefficient increases with coal loading, and is almost constant for all particle sizes at -8×10^{-3}. The influence coefficient of the shift ratio with respect to the water vapor mole fraction is small for all particle sizes and particle mass loadings. This influence coefficient is zero at the small particle limit and varies between zero and 1×10^{-4} before approaching zero at the large particle limit.

Temperature

Although the speed of sound in the gas phase varies as the square root of the absolute temperature, the resonance frequency shift defined in equation (1) is almost independent of temperature. There is only a minor dependence due to the changes in heat capacity and isentropic constant. Thus, the Acoustical Resonance Measurement is valid over a large temperature range.

The influence coefficient of the frequency shift with respect to the temperature is presented in Fig. 6 as a function of fineness parameter for particle mass loadings of 0.1 and 1.0. The absolute temperature is often known to within a fraction of a percent, so that temperature uncertainty adds very little uncertainty to the measurement. The influence coefficient of the shift ratio with respect to the temperature is small for all particle sizes and particle mass loadings. This influence coefficient is zero at the small particle limit and has a maximum near 6 μm of 0.014 for a particle mass loading of 0.1 and increases with increasing loading to a maximum of 0.016 for a loading of 1.0. The influence coefficient is less than 4×10^{-3} at a fineness parameter of 0.1 mm.

Pressure

The sound speed of a perfect gas is independent of the pressure. The sound speed is not a function of pressure until very high pressures are reached so that the ideal gas law no longer applies. Even in that limit, the Acoustical Resonance Measurement will provide a frequency shift. Consequently, the Acoustical Resonance Measurement is applicable to all pressures found in pneumatic conveying applications, and pressure changes do not affect the measurement.

Example

The experimental uncertainty of the determination of the shift can be determined by

$$(\Delta s/s)^2 = \sum_z (a_z(\Delta z/z))^2 \quad (4)$$

where the sum is over the parameters. Taking a specific example with the values of the parameters as given in the Introduction, a fineness parameter of 20 μm, and a mass loading ratio of 0.4, the influence coefficients for the frequency shift are: fineness parameter, -0.54; dispersion parameter, -0.23; shape factor, -0.54; heat capacity, -4.6×10^{-4}; humidity, -3.7×10^{-3}; and temperature, -0.14. If the uncertainties of the fineness parameter, dispersion parameter, shape factor, and heat capacity are each 10 percent and the uncertainties in the humidity and temperature are each 1 percent, then the uncertainty of the frequency shift would be 8.0 percent. The influence coefficient of the mass loading with respect to the frequency shift for this example is 1.56, which leads to an estimate for the uncertainty in the determination of the mass loading with the Acoustical Resonance Measurement of 12.4 percent.

A relation similar to that described in equation (4) can be written for the ratio of shifts. The influence coefficients are: mass loading, 9.8×10^{-4}; dispersion parameter, 0.16; shape factor, 0.043; heat capacity, 4.1×10^{-3}; humidity, 5×10^{-5}; and temperature, 0.010. Using the same uncertainties for each of the parameters, then the uncertainty of the shift ratio is 1.6 percent. The influence coefficient of the fineness parameter with respect to the shift ratio is 24. The estimate for the uncertainty in the determination of the coal fineness parameter with the Acoustical Resonance Measurement for this example would be 38 percent.

The particular example chosen is not one that is best for the Acoustical Resonance Measurement. Smaller particle size, which is becoming more important for more efficient combustion, or larger diameter piping would yield better conditions for the Acoustical Resonance Measurement. For example, choosing a fineness parameter of 1 μm, near the small particle limit, the following influence coefficients for the frequency shift: fineness parameter, -0.0050; dispersion parameter, -0.0077; shape factor, -0.0050; heat capacity, 0.056; humidity, -0.0032, and temperature, -0.0011. Uncertainties as before in each of these parameters yield a 0.6 percent uncertainty in the frequency shift. The influence coefficient of the mass loading with respect to the frequency shift is 1.61, which leads to an estimate for the uncertainty in the determination of the mass loading with the Acoustical Resonance Measurement of only 0.9 percent. At the small particle limit, the frequency shifts for both resonances are equal and the particle size cannot be determined from the ratio of the shifts (Vetter and Culick, 1987).

Conclusions

The sensitivities of the determination of mass loading and particle sizing to the variation of all of the important parameters for the Acoustical Resonance Measurement have been evaluated with a first-order perturbation-iteration acoustic analysis. The sensitivity to particle size and dispersion of particle sizes is shown to be significant. The heat capacity of the particles has been shown not to be an important factor for the coal/air mass ratios found in coal piping. The temperature and humidity of the fluidizing gas have effects on the resonance frequency that can be accounted for by measuring the temperature and humidity. The Acoustical Resonance Measurement is independent of the pressure of the fluidizing gas.

Even at off-optimum conditions, the Acoustical Resonance Measurement can provide reasonable estimates of particle mass loading. However, determination of the particle sizing by the ratio of the frequency shifts is sensitive to experimental uncertainties.

References

Evans, L. B., and Bass, H. E., 1972, "Tables of Absorption and Velocity of Sound in Still Air at 68°F," Report No. WR72-2, Wyle Labs, Huntsville, AL.

McCabe, L. C., and Boley, C. C., 1945, "Physical Properties of Coals," in: *Chemistry of Coal Utilization*, Wiley/Chapman & Hall, New York, Vol. 1, Chap. 7, pp. 310–336.

Shotts, R. Q., 1968, "Screening," in: *Coal Preparation*, 3rd ed., American Institute of Mining, Metallurgical, and Petroleum Engineers, New York, Chap. 8.

Vetter, A. A., 1982, "Theoretical Calculations for Balancing the Two-Phase Fuel Flows in the Coal Transport Piping of the Coronado Generating Station," Report No. HMRL-R-32A:1, Humbug Mountain Research Laboratories, Duarte, CA.

Vetter, A. A., and Culick, F. E. C., 1985, "Evaluation of the Acoustical Resonance Measurement of Particle Loading in Two-Phase Flow," Report No. DOE/ER/80193-1, U.S. Department of Energy, Washington, DC.

Vetter, A. A., and Culick, F. E. C., 1987, "Acoustical Resonance Measurement of Particle Loading in Gas–Solids Flow," ASME JOURNAL OF ENGINEERING FOR GAS TURBINES AND POWER, Vol. 109, pp. 331–335.

GASCAN—an Interactive Code for Thermal Analysis of Gas Turbine Systems

M. A. El-Masri
Associate Professor of Mechanical Engineering,
Massachusetts Institute of Technology,
Cambridge, MA 02139

A general, dimensionless formulation of the thermodynamic, heat transfer, and fluid-dynamic processes in a cooled gas turbine is used to construct a compact, flexible, interactive system-analysis program. A variety of multishaft systems using surface or evaporative intercoolers, surface recuperators, or rotary regenerators, and incorporating gas turbine reheat combustors, can be analyzed. Different types of turbine cooling methods at various levels of technology parameters, including thermal barrier coatings, may be represented. The system configuration is flexible, allowing the number of turbine stages, shaft/spool arrangement, number and selection of coolant bleed points, and coolant routing scheme to be varied at will. Interactive iterations between system thermodynamic performance and simplified quasi-three-dimensional models of the turbine stages allow exploration of realistic turbine-design opportunities within the system/thermodynamic parameter space. The code performs exergy-balance analysis to break down and trace system inefficiencies to their source components and source processes within the components, thereby providing insight into the interactions between the components and the system optimization tradeoffs.

1 Introduction

The thermodynamic analysis of a modern gas turbine cycle is a highly complex undertaking. Calculating cooled-turbine performance requires simultaneous solution of models describing stage fluid dynamics, heat transfer, and thermodynamic cooling-penalty losses. This calculation is coupled to the other cycle components since the cooling flows are usually extracted from several bleed sources in the compressor, thereby influencing compressor work and flow rates as well as combustor flow rate. The necessary cooling flow rates are functions of the turbine gas temperatures, which depend on the rate of work-extraction set by the fluid-dynamic design as well as on the thermal dilution of the hot gases by the cooling flows themselves. The cooling flows also depend on the coolant temperatures, which are functions of compressor efficiency and bleed-point pressures. Since the cooling flows in a modern high-temperature gas turbine are typically in the range of 20–30 percent of compressor inlet airflow, they play a major role in cycle optimization. Thus accurate modeling of those flows and their interaction with the rest of the cycle is a necessary task in performance studies, whether directed at improving current systems, designing novel cycles, or assessing the benefit/cost relationship of proposed advances in materials, component, or system technology.

Most gas turbine manufacturers have developed proprietary computer codes that perform the abovementioned calculations reliably and accurately. Based upon the author's observations, and to the best of his knowledge, such codes tend to reflect the practices, procedures, and design expertise representative of the manufacturers' product lines rather than focusing on the general fundamentals. Those features make them unwieldy as tools for wide-ranging studies of novel systems, which may require consideration of hundreds (or thousands) of cases, particularly if uncommon features such as intercooling, regeneration, gas turbine reheating, steam injection, or steam or water-cooling are considered. One code with wider availability that was written to analyze advanced power cycles is the EPRI-GATE program [1] which, while capable of accurate cycle assessment, requires considerable effort and expertise for input preparation. Some modifications to this code and examples of its application are presented in [2].

The GASCAN code was written to circumvent such limitations. It is a symbiosis of earlier cycle calculation procedures developed by the author and his colleagues [3–5] with the second-law methodolgy of cycle analysis and generalized dimensionless formulation of the turbine-cooling problem presented in [6–8]. The emphasis is on fundamental physical description of all thermodynamic, fluid-dynamic, and heat transfer processes in a general dimensionless formulation. Within the code, all temperatures and pressures are nondimensionalized by the reference ambient values $T_a = 289$ K and $p_a = 1.013$ bar. All velocities are nondimensionalized by the speed of sound at T_a; all molar specific heats, entropies, and ϕ functions by the universal gas constant R; and all molar

Contributed by the Advanced Energy Systems Division and presented at the ASME Winter Annual Meeting, Anaheim, California, December 1986. Manuscript received at ASME Headquarters November 1987.

specific enthalpies, exergies, work, and heat quantities, by RT_a. Conversion to dimensional variables is relegated to the user interface. All solutions and results are thus obtained for a generalized system of arbitrary size, then a single dimensional variable is used to select a physical scale, thereby establishing all dimensional attributes of the system. In calculations where algebraic solutions are possible, they are used rather than numerical iterations to provide speed, compactness, and robustness. The number of required inputs is kept to a minimum consistent with obtaining accurate system thermodynamic performance results. Every effort is made to exclude superfluous information. The code is completely interactive and menu-driven, with prompts for all user-inputs. Sufficient generality and flexibility are incorporated in the inputs to enable the code to reflect accurately the characteristics and duplicate the performance of the corresponding real engines. Once the inputs have been tuned to reflect the design features and component characteristics of an engine, the code can be used as a spreadsheet to rapidly answer "what if . . . ?" questions about the impact of any proposed change or improvement on the performance and state points throughout the system. In addition, the code performs second-law exergy balances for all components and identifies and quantifies the sources of system inefficiency. Printouts of all mass, energy, and exergy streams of the system are produced to aid in understanding the interactions between the different components and system design tradeoffs. The compact formulation of the code, which consists of approximately 2500 BASIC statements in 35 subroutines, results in a portable execution file (produced with the Microsoft QuickBasic Compiler) that occupies about 120 KB and executes in a few seconds on an IBM AT or comparable microcomputer.

Some key aspects of the calculation model are described below; then the code is demonstrated by an analysis of the advanced intercooled/reheat gas turbine system illustrated in Fig. 1. Reference to the inputs and results for this example presented in the Appendices should facilitate reading the paper.

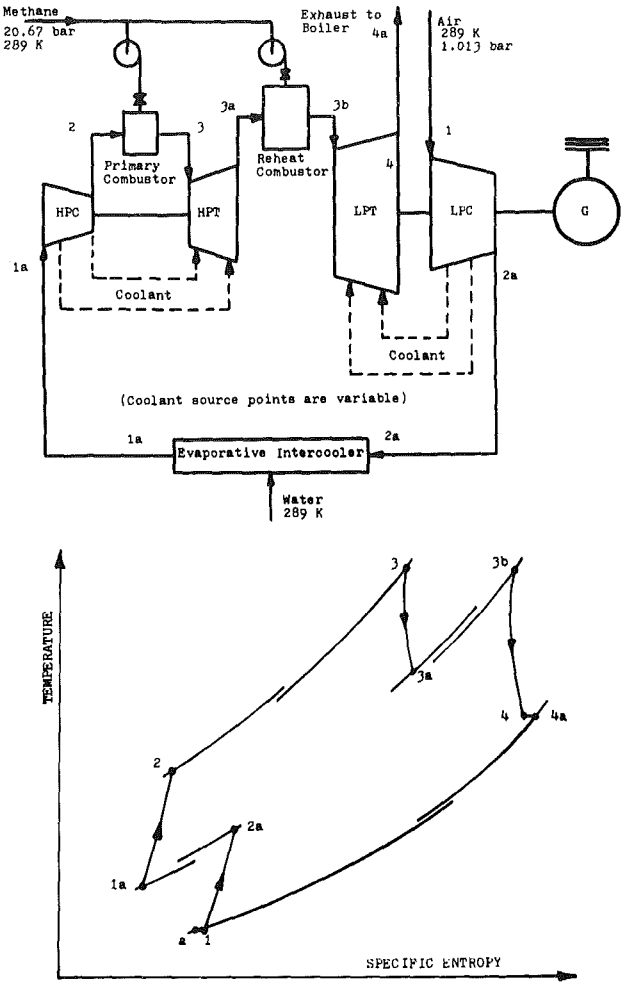

Fig. 1 The cycle analyzed in the illustrative example

Nomenclature

a = coefficient in equation (4) (ARC in Appendix)
b = coefficient in equation (4) (PWR in Appendix)
Cp = molar constant-pressure specific heat
c = absolute velocity
e = compressor polytropic efficiency
h = molar specific enthalpy*
MW = molecular weight
M = Mach number
m = mass flow rate
n = mole flow rate
p = pressure
R = universal gas constant
$\Re$ = degree-of-reaction parameter
T = temperature
T.I.T. = turbine inlet temperature
u = blade pitchline velocity
w = rotor-relative velocity
Y = main gas momentum loss parameter, defined in equation (9)
ZP = wheelspace purge flow volume fraction
ZL = coolant leakage flow volume fraction
α = absolute flow angle
β = rotor-relative flow angle
γ = specific heat ratio
η = stage adiabatic total-to-total efficiency
ϑ = stage flow coefficient $= c_x/u$
ξ = ratio of hub radius to tip radius
Φ = cooling effectiveness
ϕ = thermodynamic property function $= \int_{T_a}^{T} Cp \cdot dT/T$
ψ = stage loading parameter $= \Delta h_w/u^2 \cdot \mathrm{MW}$
Ω = availability or exergy
$\bar{\omega}$ = profile-loss coefficient

Subscripts

A, B, C, D = stage state points defined on Fig. 3
1, 2, 3 = stator-inlet, rotor-inlet, rotor-exit
a = reference ambient air at 289 K, 1.013 bar
b = blade or metal
c = coolant
d = downstream
g = gas
m = mixing
rr = rotor-relative
s = static thermodynamic state*
u = upstream
w = work-extraction
x = axial

Superscripts

~ = dimensionless as defined in the Introduction

*All unsubscripted properties refer to stagnation states.

2 Model Description

2.1 Gas Properties. A semi-perfect gas model is used to allow the specific molar properties Cp, h, and ϕ of all gas mixtures to be expressed in terms of composition and temperature only. The compositions of the gas mixtures are expressed by their mole fractions of three "components," which are themselves mixtures. These are air (77.44 percent N_2, 20.76 percent O_2, 0.92 percent Ar, 0.85 percent H_2O, 0.03 percent CO_2); water; and stoichiometric products whose composition depends on the type of fuel used. For methane this is 70.16 percent N_2, 19.58 percent H_2O, 9.43 percent CO_2, and 0.83 percent Ar. The influence of presence of products of incomplete combustion on the specific heat and sensible enthalpy of the mixture is neglected. When the combustion efficiency is specified to be less than 100 percent, the unburned fuel is treated as having the same Cp and h per mole as for the stoichiometric products. The specific heat ratio γ is calculated from the ratio of R/Cp.

In drawing up the exergy balances, the convention adopted is to assign all gas mixtures zero thermomechanical availability at the reference ambient state of 289 K, 1.013 bar. Exergies of all gas mixtures are based on their total pressures

$$\Omega = \Sigma n_i h_i - T_a \Sigma n_i \phi_i + T_a R (\Sigma n_i) \ln (p/p_a) \tag{1}$$

rather than on the partial pressures of their constituents

$$\Omega = \Sigma n_i h_i - T_a \Sigma n_i \phi_i + T_a R [\Sigma n_i \ln (p_i/p_a)] \tag{2}$$

Equation (1) gives the maximum work that can be extracted from the gas mixture without separating it into its pure constituents. It exceeds the exergy defined by equation (2) by the theoretical work necessary to separate the mixture. The former definition is more relevant to thermal power-plant engineering, since one is not usually interested in separating the exhaust gases into their individual constituents or in condensing water vapor present in the flue gases prior to their discharge.

2.2 Compressor. For a compressor spool with a specified inlet state and polytropic efficiency, the temperature is expressed in terms of the local pressure by integrating

$$dT/T = (R/e \cdot Cp) dp/p \tag{3}$$

Thus the temperatures, specific enthalpies, and specific exergies may be determined at the bleed ports and at compressor delivery once their pressures have been specified. After the turbine cooling flow calculations have been performed, one may determine the mass flows extracted from each bleed port and thus at all points within the compressor. Energy and exergy balances then give the compressor work and exergy lost.

2.3 Evaporative Intercooler. Given the air and water inlet states and the pressure and relative humidity at the exit, the mass and energy balances may be solved to obtain the exit temperature and ratio of water/air flow rates. In LHV analysis consistent with the gas-property model, pure liquid water at 289 K is assigned an enthalpy of -2465 kJ/kg. The exergy balance is then applied to solve for the lost availability, defined as the difference between the maximum work that may be extracted from the streams entering the intercooler and that extracted from the intercooler discharge stream without recondensing the water vapor. Pure liquid water at 289 K is assigned zero availability. The theoretical work that may be extracted per mole of ambient-temperature water in the presence of unsaturated air, $RT_a \ln (p/p_a)$, appears as a reduction of the exergy lost in the intercooler as discussed in [9].

2.4 Combustor. For a specified fuel type, combustion efficiency, inlet state, and discharge pressure and temperature, the fuel flow rate and exit gas composition may be computed from the chemical-reaction equation and the mass and energy balances in the standard manner. With the inlet and exit states and flow rates known, one may compute the exergy streams entering and leaving the combustor and thereby determine the lost availability. This may be further broken down into its constitutive irreversibilities: fuel throttling loss, mainflow pressure drop loss, incomplete combustion loss, and fundamental or "thermal degradation" loss as shown in Appendix 2 for the illustrative example. The equations for deriving these quantities are given in [10].

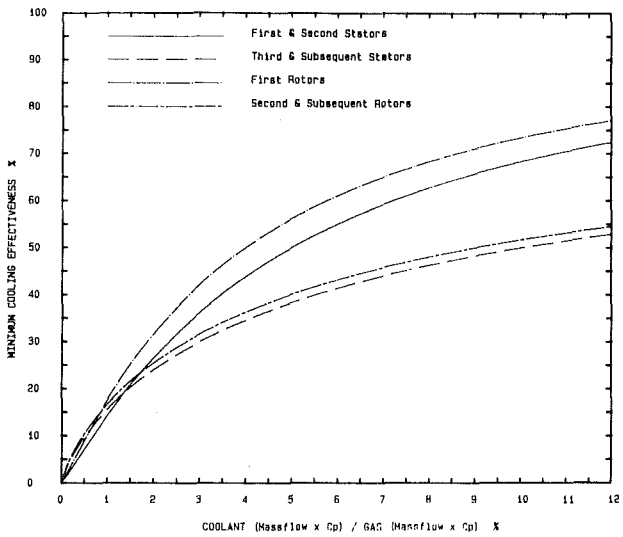

Fig. 2 Cooling-effectiveness curves used in the example

2.5 Turbine

Cooling Flow Calculations. Each stage is allocated four cooled elements: stator row, rotor row, forward wheelspace, and aft wheelspace. The endwall cooling flows are included with their associated blade rows. Transition piece leakage flows are included with the first-stage nozzle flow.

The cooling flows to each blade row are found from a semi-empirical cooling-effectiveness relation derived in [11] and illustrated in Fig. 2

$$\frac{(n \cdot Cp)_c}{(n \cdot Cp)_g} = a \left(\frac{\Phi}{\Phi_\infty - \Phi} \right)^b \tag{4}$$

where Φ denotes the cooling effectiveness

$$\Phi = \frac{T_{g,\max} - T_{b,\max}}{T_{g,\max} - T_c} \tag{5}$$

and Φ_∞ its asymptotic value at large coolant flow rates. The theoretical value of Φ_∞ is 1 for film cooling and $1/(1 + \mathrm{Bi})$ for convection cooling, where Bi is the Biot number based on blade skin conduction [11]. The three-parameter family of effectiveness curves described by equation (4) enables most experimental curves to be well represented in the code. The maximum gas temperature in equation (5) is the stagnation temperature, absolute or rotor-relative, since the recovery factor is assumed to be unity. To account for the nonuniform gas temperature profile, provision is made for this temperature to exceed its mixed-mean value by specifying a pattern factor for each blade row

$$\lambda = [T_{g,\max} - T_{g,\mathrm{mean}}]/\Delta T_{\mathrm{comb}} \tag{6}$$

In addition to the cooling flow rates computed from equation (4), an amount of coolant is assumed to leak from the machine clearances of each cooled blade row. This is specified as a volumetric fraction (ZL) of the local main-gas flow rate.

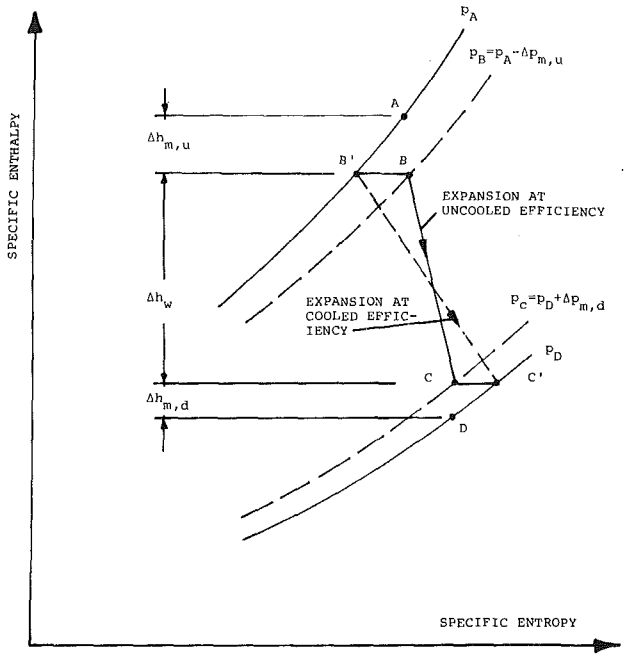

Fig. 3 Thermodynamic states of the stage model

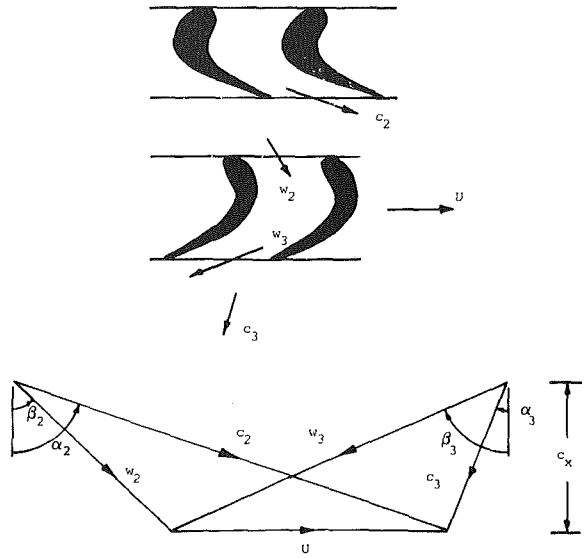

Fig. 4 Stage velocity triangles

Wheelspace purge flows are specified as a volumetric fraction (ZP) of the local main gas flow. The quantities ZP furnished by the user for each wheelspace may at his option be treated as "hard" values, invariant throughout the computation, or as reference values corresponding to a hub-to-tip radius-ratio ξ of 0.8. In the latter case, the code will vary ZP for each wheelspace according to the proportionality

$$\mathrm{ZP} \propto \xi/\vartheta(1+\xi)^2(1-\xi) \tag{7}$$

based upon holding the ratios of wheel-clearance/hub-radius and purge-flow-radial-velocity/hub-peripheral-velocity constant.

Stage Model. Figures 3–5 illustrate the model of the cooled turbine stage. The total enthalpy (or temperature) drop consists of cooling components A-B and C-D, which can be computed from coolant mixing enthalpy balances alone, and a work-extraction component B-C, which can be calculated from the total pressure ratio after accounting for the mainflow stagnation pressure losses incurred by coolant mixing. Figure 3 illustrates two alternative approaches for performing the latter calculation. The solid line B-C on that figure represents a model where the effective total pressure ratio across the rotor is reduced by an upstream total pressure loss $\Delta p_{m,u}$ arising from the mixing stator and forward wheelspace coolants and a downstream loss $\Delta p_{m,d}$ due to mixing rotor and aft wheelspace coolants. The stage total-to-total efficiency η is then assumed unaltered as it operates at the reduced pressure ratio; thus,

$$T_B - T_C = \eta T_B \{1-(p_C/p_B)^{(\gamma-1)/\gamma}\} \tag{8}$$

This model is adopted in the program and the mixing pressure losses are calculated by specifying a momentum-loss parameter Y for each cooled element

$$\left(\frac{\Delta p}{p}\right)_i = Y_i \frac{n_{c,i}}{n_g}\left(1+\frac{\mathrm{MW}_{c,i}}{\mathrm{MW}_g}\right) \tag{9}$$

The dotted line $B'-C'$ on Fig. 3 illustrates an alternate model where the total pressure ratio is assumed unaffected by cooling, whose effects are manifested as decrements to stage efficiency given by correlations of the form

$$\Delta\eta = \sum C_i \frac{m_{c,i}}{m_g} \tag{10}$$

where C_i represents an empirical coefficient for cooling flow i. This method is used in the GATE program [1]. While the two approaches are equivalent, the method illustrated by the solid line B–C on Fig. 3 and equation (8) is used since it reflects the fundamental fluid dynamics of mixing and accounts for the effect of different molecular weights. This would be important if steam or air/steam mixtures were used as coolants. The momentum loss parameter Y for the case of mixing a small amount of quiescent fluid into a stream flowing at a Mach number M is

$$\gamma \mathrm{M}^2/2\left\{1+\frac{\gamma-1}{2}\mathrm{M}^2\right\}^{\gamma/(\gamma-1)} \tag{11}$$

In turbine blading, the coolant is injected with a substantial streamwise velocity, and portions of it are discharged from the trailing edges into the wakes. This results in much lower pressure losses than for injecting a quiescent fluid into a stream with the same Mach number. For the case of identical coolant and mainflow, the parameter Y for a blade row can be related to the cooling component of the profile-loss coefficient

$$\bar{\omega}_c = \Delta p/(p-p_{s,\mathrm{out}}) \tag{12}$$

by

$$Y = \frac{\bar{\omega}_c}{2(m_c/m_g)}\left\{1-\left(1+\frac{\gamma-1}{2}\mathrm{M}^2\right)^{\gamma/(1-\gamma)}\right\} \tag{13}$$

References [12, 13] present relations between cooling flow rates and cascade-loss coefficients for full-coverage film cooling. The values of the momentum-loss parameters used in the illustrative cycle calculation are estimated, in part, from the data presented in [14] for a model film-cooled stage.

As shown by the flow-chart of Fig. 6, the stage model is invoked from the main program with a specified inlet state A and total pressure ratio p_A/p_D. Whereas the stator cooling flow may be computed directly, the remaining cooling flows depend on the stage thermofluid dynamics illustrated in Figs. 4 and 5. The gas static thermodynamic states may be computed only after the corresponding stagnation states and Mach numbers have been found. The static states are needed for the determination of properties such as γ for use in equation (8), and the density for determining the gas volumetric flow rates, which are needed to compute the wheelspace purge flows. Calculation of the rotor cooling flow requires knowledge of the gas rotor-relative total temperature for use in equation (5).

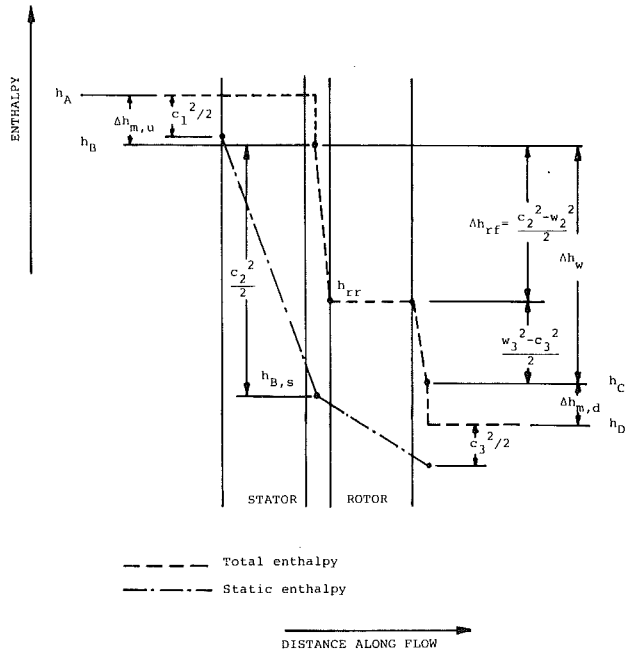

Fig. 5 Thermo/fluid dynamics of the stage model

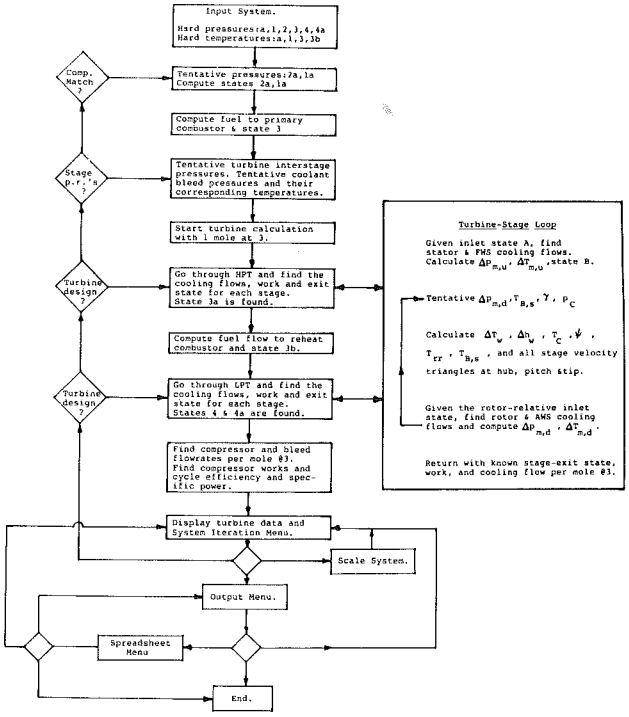

Fig. 6 Program flow hart

This is found from the rotor-relative total enthalpy, which is related to its absolute value by

$$h_{rr} = h_B - \mathrm{MW}_g (c_2^2 - w_2^2)/2 \tag{14}$$

The two velocity triangles shown in Fig. 4 are completely specified by five independent quantities. Assuming the flow coefficient ϑ to be the same at rotor inlet and exit, those reduce to four. GASCAN requires the user to input the flow coefficient ϑ, blade speed u, and rotor-exit absolute flow angle α_3 at the pitchline of each turbine stage.[1] The fourth quantity needed for the complete specification of the velocity triangles is derived from the relation between the work-extraction rate and the velocities

$$\Delta\tilde{h}_w = \frac{\mathrm{MW}_g}{\mathrm{MW}_a} \gamma_a \tilde{u}^2 \vartheta (\tan\alpha_2 + \tan\alpha_3) \tag{15}$$

Since the stage model is nonlinear, numerical iterations between the cooling flows and stage thermofluid dynamics are used as indicated in the flow chart of Fig. 6. The procedure is structured to converge rapidly, and the stage exit state, work, cooling flows, and velocity triangles are found. The pitchline loading parameter and degree of reaction are calculated from

$$\psi = \frac{\Delta\tilde{h}_w}{\gamma_a} \frac{\mathrm{MW}_a}{\mathrm{MW}_g} \frac{1}{\tilde{u}^2} \tag{16}$$

$$\mathfrak{R} = 1 + \vartheta \tan\alpha_3 - \psi/2 \tag{17}$$

With the stage pitchline characteristics found, the velocity triangles may be computed at other radii. The current version of GASCAN is limited to free-vortex designs. The user is asked to specify the hub-to-tip radius ratio for the last rotor on each shaft. GASCAN then uses the volume flow rates to compute the hub-to-tip ratios for the remaining stages as well as the ratios of the rotational speeds of all shafts to one another. The velocities, Mach numbers, and flow angles at the inlet and exit of each rotor are then computed in both the absolute and relative frames at the hub, pitch, and tip radii. The degree of reaction at the hub and tip of each stage is also found.

The availability lost in each turbine stage can be found as the difference between the maximum work that may be extracted from all fluid streams supplied to the stage and the sum of its actual work and that which may be extracted from its exit stream. The cooling irreversibility arises from three processes: coolant throttling from the bleed-point total pressure to that downstream of the blade row where it is assumed to mix, thermal degradation due to introduction of the coolant into the hot gas path, and loss of main flow total pressure due to coolant mixing. Those quantities are computed independently for each cooling flow. The equations used are similar to those presented in [7] for the constant-property continuous-turbine model. The results calculated in GASCAN are broken down by cooled components and by loss mechanism as illustrated in Appendix 2 under the heading "Component Irreversibilities Breakdown." Stage irreversibility arising from fluid friction and leakage, unrelated to cooling, is calculated as the difference between the total exergy lost by the stage and that lost in its cooling. This quantity is also computed independently, as a check, from equation (18) of [7] based on the stage adiabatic efficiency. The discrepancy between the two calculations, rising from the nonlinearity of the model, is found to be negligible.

[1] This implies specification of the pitchline slope for each turbine spool.

3 Results and Discussion

The code is illustrated by applying it to analyze the intercooled, reheated gas turbine cycle shown in Fig. 1. This is similar in general layout to the AGTJ-100A "Moonlight Project" under development in Japan [15–18]. Other analyses of reheat gas turbine cycles are given in [2, 19–24].

The inputs to the present calculation are given in Appendix 1, which is a printer-echo of the computer screen during the run. This shows the prompts from the code as well as the user's responses. The program has built-in demonstration values for all required inputs, which may be accepted or rejected and replaced by the user in response to prompts from the code. As shown in Appendix 1, the run starts by selecting a system of units followed by choosing between Higher and Lower Heating value as a basis for the analysis. Those options are easily accommodated by the generality of the formulation. This is followed by prompts to input other system parameters as shown.

System configuration is specified by selecting the number of

shafts, total number of turbine stages, and their number upstream of the reheat. Shaft-splits, which may or may not coincide with the reheat, are specified by entering the number of the last turbine stage on each shaft. Current configuration is then displayed. It may be accepted as "hard," tentative, or reselected. The example presented is a two-shaft system with four turbine stages, two on each shaft, with the reheat after two stages.

The maximum allowable metal temperatures, temperature pattern factors, cooling-effectiveness-curve parameters, leakage and wheelspace purge flow parameters, momentum pressure loss parameters, and TBC (Thermal Barrier Coating) thickness parameters are then determined for each turbine element. This is followed by a specification of the coolant bleed points and coolant routing to the different cooled elements. Finally, the pitch speed, flow coefficient, exit angle and adiabatic efficiency are specified for each turbine stage and the hub-to-tip radius-ratio for the last stage on each shaft.

With the inputs complete, the code computes through the cycle and displays the tabulated turbine parameter summary and "System Iteration Menu" shown. This allows reselection of stage pressure ratios or other turbine design parameters to avoid unacceptable loadings, negative reactions, or excessive tip speeds. When those parameters appear satisfactory, the code can be instructed to vary the intercooling pressure until the net work of the high-pressure spool is zero. Throughout this process, the compressor bleed pressures are automatically adjusted to keep each at the desired multiple of the inlet pressure of the highest blade row it serves. At any round of this iteration, the user may elect to scale the current system by entering any one of the four dimensional quantities: last-shaft rotational speed, last-rotor annulus area, gas turbine power output, or compressor inlet mass flow rate. Those quantities will then be displayed together with speeds of the remaining shafts and last-stage pitch radius as shown. When those iterations are complete, the user may elect to exit to the output menu. The computational heat and mass balance errors are then displayed as shown, followed by a menu to choose an output device and any of eight outputs. All eight are shown in Appendix 2.

The first output in Appendix 2 is the "System Description," which summarizes the component and system parameters, followed by a "Performance Summary" showing the sample cycle to achieve 55.25 percent gross thermal efficiency and 53.83 percent net electric efficiency after mechanical, electrical, and plant-auxiliary losses. With a 3600 rpm drive shaft and the turbine parameters selected, this corresponds to 187 kg/s inlet air flow, 92 MW gross gas turbine output, and 139 MW combined cycle net output. The combined-cycle calculations are based on the relation between the efficiency of an optimized, dual-pressure steam bottoming cycle and turbine exhaust gas temperature presented in [25], which also presents the detailed exergy balances for those steam cycles. The third output, "Cycle State Points," provides a summary of the pressure, temperature, composition, and relative mass flow rate at each state point in the system. The next table, "Turbine Pitchline Characteristics," displays cooling effectiveness and cooling mass flow fractions for each blade row and wheelspace. The upper values in the fifth column of that table are the cooled stage efficiencies, defined by the expansion B′-C′ on Fig. 3. The lower values in the same column are the second-law effectivenesses defined as the ratio of work output to exergy consumption by each stage. The sixth column shows stage specific power per unit rotor inlet flow and per unit compressor inlet flow for each stage.

The next output, "Energy and Exergy Balances," presents the overall cycle energy balance per unit inlet air flow in the first column and as a percentage of the fuel enthalpy in the second. Although the intercooler is adiabatic, it shows an energy loss due to the introduction of liquid water, whose enthalpy is negative with respect to the LHV-analysis datum. If HHV-analysis is selected, the intercooler shows zero energy loss. The intercooler exergy loss shown in the third column, however, is identical on either basis. The third through fifth columns present the overall breakdown of cycle irreversibilities per unit airflow and as percentages of fuel exergy and enthalpy, respectively. Work output represents specific power in the first and third columns, second-law efficiency in the fourth column, and first-law efficiency in the second and fifth. The irreversibilities in the fifth column can be regarded as the decrements to cycle efficiency arising from each component. The combustors are the prime source of irreversibility, followed by the turbine. The detailed breakdown of the component irreversibilities by source-process is presented in the next table, "Component Irreversibilities Breakdown." The dominant combustion irreversibility mechanism is seen to be the thermal-degradation loss as discussed in [10]. Roughly 70 percent of the turbine exergy losses, representing 4 percent of the total fuel enthalpy, are cooling related. The intercooler irreversibility (0.75 percent) is small in this example since intercooling takes place at a moderate inlet pressure (2.5 bar) and inlet temperature (382 K). In similar cycles with a single turbine stage on the high-pressure spool, resulting in high intercooler inlet pressures and temperatures, the intercooler irreversibility is significantly higher, reaching 3 percent in some cases, but the turbine irreversibilities are decreased by lowering the cooling-air temperature to the first turbine stages [24].

The thermodynamic state, relative mass flow, energy and exergy fluxes of all main flow and cooling streams are presented in the table "Cycle Energy and Exergy Streams."

The last output, "Turbine Gaspath," lists all angles, velocities, and corresponding Mach numbers for the velocity triangles of Fig. 4 at the hub, pitch, and tip radius of each stage. The current version of GASCAN can only perform this calculation for free-vortex designs. This table also lists the static temperatures, blade speeds, degree of reaction parameters, and physical radius at hub, pitch, and tip. The rotational speed of each stage is also given.

The code structure allows any of the eight outputs shown in Appendix 2 to be accessed for screen viewing during the system iteration procedure to investigate the interrelationships between those outputs and the user's selections.

Once a system has been analyzed, the user can access a "spreadsheet menu" that allows rapid change in any of the system inputs and recomputation of the cycle. As an example, raising the allowable metal temperatures of all blade rows by 50 K was found to decrease cooling flow from 29.3 to 24 percent, raising gross efficiency from 55.24 to 56.58 percent, and gross specific power from 765 to 798 kJ/kg. Reducing all metal temperatures by 50 K gives 35.4 percent, 53.36 percent, and 702 kJ/kg for cooling flow, gross efficiency, and gross specific power, respectively. Application of thermal barrier coatings with constant thickness of all blades corresponding to a Biot number of 0.5 on the first stator [26] was found to reduce cooling flow to 26.3 percent and increase efficiency and specific power to 55.8 percent and 756 kJ/kg. If this is combined with the 50 K increase in metal temperature, the cooling flow is reduced to 21.4 percent and the cycle achieves 57 percent gross efficiency with 786 kJ/kg gross specific power.

4 Conclusions

1 A compact, general, and flexible procedure for representing and computing the performance of complex gas turbine systems has been developed and incorporated in the GASCAN code.

2 The energy-balance analysis built into the code allows the

sources of system inefficiency to be identified and quantified.

3 Application of the code to the intercooled, reheated gas turbine combined cycle shows it to offer potential for significant advances in electric power generation. The performance calculated for the example given is close to the projections of [15]. The results presented, however, are specific to the cycle inputs used in the calculations, and do not represent a systematic design or optimization study of this class of systems.

References

1 Waters, M., and Associates Inc., "Gas Turbine Evaluation (GATE) Computer Program. Thermodynamic Cycles, Methods and Sample Programs," EPRI Report AP-2871-CCM, Feb. 1983.

2 Giglio, R. S., "A Thermodynamic Performance Analysis of a Combined Cycle Engine," S.M. Thesis, M.I.T. Dept. of Mechanical Engineering, June 1986.

3 El-Masri, M. A., Kobayashi, Y., and Louis, J. F., "A General Performance Model for the Open-Loop Water-Cooled Gas Turbine," ASME Paper No. 82-GT-212.

4 Louis, J. F., Hiraoka, K., and El-Masri, M. A., "A Comparative Study of Different Means of Turbine Cooling on Gas Turbine Performance," ASME Paper No. 83-GT-180; *Int. J. Turbo and Jet Eng.*, Vol. 1, No. 2, pp. 123-137.

5 Wu, C. S., and Louis, J. F., "A Comparative Study of the Different Means of Turbine Cooling on Performance of Combined Cycles," ASME JOURNAL OF ENGINEERING FOR GAS TURBINES AND POWER, Vol. 106, No. 4, 1984, pp. 750-755.

6 El-Masri, M. A., "On Thermodynamics of Gas Turbine Cycles—Part 1: Second-Law Analysis of Combined Cycles," ASME JOURNAL OF ENGINEERING FOR GAS TURBINES AND POWER, Vol. 107, 1985, pp. 880-889.

7 El-Masri, M. A., "On Thermodynamics of Gas Turbine Cycles—Part 2: A Model for Expansion in Cooled Turbines," ASME JOURNAL OF ENGINEERING FOR GAS TURBINES AND POWER, Vol. 108, 1986, pp. 151-159.

8 El-Masri, M. A., "On Thermodynamics of Gas Turbine Cycles—Part 3: Thermodynamic Potential and Limitations of Cooled Reheat-Gas-Turbine Combined Cycles," ASME JOURNAL OF ENGINEERING FOR GAS TURBINES AND POWER, Vol. 108, 1986, pp. 160-170.

9 El-Masri, M. A., "Exergy Analysis and Optimization of the Recuperated Gas Turbine Cycle," presented at Winter Annual Meeting, Anaheim, CA, Dec. 1986.

10 El-Masri, M. A., "Exergy Analysis of Combined Cycles—Part 1: Air-Cooled Brayton Cycle Gas Turbines," ASME JOURNAL OF ENGINEERING FOR GAS TURBINES AND POWER, Vol. 109, 1987, pp. 228-236.

11 El-Masri, M. A., and Pourkey, F., "Prediction of Cooling Flow Requirements for Advanced Utility Gas Turbines—Part 1: Analysis and Scaling of the Effectiveness Curve," ASME Paper No. 86-WA/HT-43.

12 Ito, S., Eckert, E. R. G., and Goldstein, R. J., "Aerodynamic Loss in a Gas Turbine Stage With Film Cooling," ASME JOURNAL OF ENGINEERING FOR POWER, Vol. 102, 1980, pp. 964-970.

13 Hempel, H., and Friedrich, R., "Profile Loss Characteristics and Heat Transfer of Full Coverage Film-Cooled Blading," ASME Paper No. 78-GT-98.

14 McDonel, J. D., and Eiswerth, J. E., "Effects of Film Injection on Performance of a Cooled Turbine," AGARD-CP-229, Ankara, Turkey, Sept. 1977.

15 Hori, A., and Takeya, K., "Outline of Plan for Advanced Research Gas Turbine," ASME JOURNAL OF ENGINEERING FOR POWER, Vol. 103, No. 4, 1981.

16 Teshima, K., et al., "A Report for the Engineering Status of Some Confirmation Tests in the Development of the AGTJ-100A," ASME Paper No. 84-GT-53.

17 Takeya, K., Oteki, Y., and Yasui, H., "Current Status of Advanced Reheat Gas Turbine AGTJ-100A (part 3) Experimental Results of Shop Tests," ASME Paper No. 84-GT-57.

18 Arai, M., et al., "Results From the High Temperature Turbine Tests on the HPT of the AGTJ-100A," ASME Paper No. 84-GT-235.

19 Rice, I. G., "The Combined Reheat Gas Turbine/Steam Turbine Cycle: Part 1—A Critical Analysis of the Combined Reheat Gas Turbine/Steam Turbine Cycle," ASME Paper No. 79-GT-7.

20 Rice, I. G., "The Combined Reheat Gas Turbine/Steam Turbine Cycle: Part 2—The LM 5000 Gas Generator Applied to the Combined Reheat Gas Turbine/Steam Turbine Cycle," ASME Paper No. 79-GT-8.

21 Rice, I. G., "The Reheat Gas Turbine With Steam Blade Cooling—A Means of Increasing Reheat Pressure, Output and Combined Cycle Efficiency," ASME JOURNAL OF ENGINEERING FOR POWER, Vol. 104, No. 1, 1982.

22 Rice, I. G., and Jenkins, P. E., "Comparison of the HTTT Reheat Gas Turbine Combined Cycle With the HTTT Non-Reheat Gas Turbine Combined Cycle," ASME JOURNAL OF ENGINEERING FOR POWER, Vol. 104, No. 1, 1982.

23 Rice, I. G., "The Reheat Gas Turbine Combined Cycle," Turbomachinery International, July-Aug., 1981.

24 El-Masri, M. A., "Exergy Analysis of the Reheat Gas Turbine Combined Cycle," Proceedings 1987 Joint ASME/JSME Thermal Engineering Conference, Honolulu, Mar. 1987, Vol. 2, pp. 117-126.

25 Chin, W., and El-Masri, M. A., "Exergy Analysis of Combined Cycles—Part 2: Analysis and Optimization of Two-Pressure Steam Bottoming Cycles," ASME JOURNAL OF ENGINEERING FOR GAS TURBINES AND POWER, Vol. 109, 1987, pp. 237-243.

26 El-Masri, M. A., "Prediction of Cooling Flow Requirements for Advanced Utility Gas Turbines—Part 2: Influence of Ceramic Thermal Barrier Coatings," ASME Paper No. 86-WA/HT-44.

APPENDIX 1

Inputs for Illustrative Example

```
GASCAN version 5.4     07-23-1986    19:33:10

SELECT A SYSTEM OF UNITS:
   ------------------------------------------------------------
     # Temperature  Pressure  Energy  Mass  Length  Time  Power
   ------------------------------------------------------------
     1      F         PSIA      BTU     LB     FT      S     MW
     2      K         BAR       KJ      KG     M       S     MW
     3      C         ATM       KCAL    KG     M       S     MW
   ------------------------------------------------------------
Default is #2. Enter your choice? 2
Default is LHV basis for energy & exergy balances. Enter h to select HHV?
  REFERENCE AMBIENT IS :  Pamb= 1.013 BAR    Tamb= 289 K
  CURRENT AMBIENT IS :  Pamb= 1.013 BAR    Tamb= 289 K
Is that OK ? (y/n)? y
Current setting is 2 - shaft system. OK? (y/n)?
? y
Current fuel is CH4. Combustion efficiency EQ = .99
Will you use this value ? (y/n)? y
Current LP & HP compressor polytropic efficiencies: ECL= .92  ECH= .91
Will you use those values ? (y/n)? y
Enter e for evaporative intercooler, s for surface, n for none? e
Default evaporative intercooler saturation effectiveness is .9
Is that OK ? (y/n)? y
Current pressure drops for inlet, primary combustor, reheat combustor,
and exit diffuser are:
dpi= .0075  dpq= .04  dprh= .04  dpd= .06
Will you use these values ? (y/n)? y
Current pressure drops for intercooler, boiler gas side are:
dpic= .03  dpb= .035
Will you use these values ? (y/n)? y
Current overall pressure ratio= 48   T.I.T.= 1500 K
Reheat temperature = 1500 K
Will you use those values ? (y/n)? y
Overall turbine pressure ratio= 40.01917
Is a 4 stage turbine OK? (y/n)?
? y
 2 stages before the reheat. OK? (y/n)
? y
Current configuration of 2 - shaft system as follows:
Last turbine stage on shaft 1 is # 2
Last turbine stage on shaft 2 is # 4
Is that OK (y/n)? y
Current stage-pressure-ratios are:
          STAGE     SHAFT     P,in BAR      P,out BAR    Pressure Ratio
          ------------------------------------------------------------
            1         1        45.7344       18.1834        2.5152
            2         1        18.1834        7.2295        2.5152
          Reheat
            3         2         6.9403        2.7594        2.5152
            4         2         2.7594        1.0971        2.5152
Enter i to impose those values, t to keep them tentative, r to re-select? t
Current maximum metal temperatures are:
            Stage  1        STATOR 1085 K      ROTOR  1040 K
            Stage  2        STATOR 1035 K      ROTOR  1000 K
            Stage  3        STATOR 1085 K      ROTOR  1040 K
            Stage  4        STATOR 1035 K      ROTOR  1000 K
Will you use those temperatures (y/n)? y
Current temperature pattern factors are :
                    STATOR 1 : 0.1000
                    ROTOR  1 : 0.0562
                    STATOR 2 : 0.0360
                    ROTOR  2 : 0.0250
                    STATOR 3 : 0.1000
                    ROTOR  3 : 0.0562
                    STATOR 4 : 0.0360
                    ROTOR  4 : 0.0250
Will you use those values ? (y/n)? y
The current gaspath cooling parameters are:
-------------------------------------------------------------------------------
ELEMENT          EFFECTIVENESS CURVE PARAMETERS                  LEAK     MOM.
--------  ------------------------------------------------       VOL.     LOSS
          TYPE        BH50%    PHIMAX    PWR      ARC          FRAC.    PARM.
          ------------------------------------------------     ------   -----
STATOR 1  Film        0.050    1.000     0.900    0.050        0.002    0.200
ROTOR  1  Film        0.040    1.000     0.900    0.040        0.002    0.250
STATOR 2  Film        0.050    1.000     0.900    0.050        0.002    0.200
ROTOR  2  Convection  0.090    0.850     1.250    0.058        0.002    0.250
STATOR 3  Film        0.050    1.000     0.900    0.050        0.002    0.200
ROTOR  3  Film        0.040    1.000     0.900    0.040        0.002    0.250
STATOR 4  Film        0.050    1.000     0.900    0.050        0.002    0.200
ROTOR  4  Convection  0.090    0.850     1.250    0.058        0.002    0.250
-------------------------------------------------------------------------------
Will you use those values (y/n)? y


The current (or default) wheelspace purge flow parameters are :
                Wheelspace    Volume Fraction   Momentum Loss Parm.
                ------------------------------------------------
                Fwd.WS 1          0.0035            0.3500
                Aft WS 1          0.0035            0.3000
                Fwd.WS 2          0.0035            0.3500
                Aft WS 2          0.0035            0.3000
                Fwd.WS 3          0.0035            0.3500
                Aft WS 3          0.0035            0.3000
                Fwd.WS 4          0.0035            0.3500
                Aft WS 4          0.0035            0.3000
Enter y to fix those, yv to use those as reference values and allow the code
to vary them with hub-to-tip ratios, n to reselect? y

Current first-stator Thermal Barrier Coating Biot Number is 0
Will you use this value ? (y/n)? y
Current no. of coolant sources is 4 .Their extraction points are 1.3
*Inlet pressure of highest row they serve (but<=p2). i.e.,
SOURCE # 1  Highest turb row STATOR 1  Tentative bleed pressure= 48.25932 BAR
SOURCE # 2  Highest turb row STATOR 2  Tentative bleed pressure= 23.94577 BAR
SOURCE # 3  Highest turb row STATOR 3  Tentative bleed pressure= 9.139722 BAR
SOURCE # 4  Highest turb row STATOR 4  Tentative bleed pressure= 3.633842 BAR
The code will readjust those pressures; enter y to approve, r to revise this
scheme; i to enter and impose fixed bleed pressures? y
The default coolant source for all rotors is that for the inlet-stator of its
spool; for all stators it is the lowest appropriate source; and for all wheel-
spaces same as the adjacent stator row.
```

APPENDIX 2

Outputs for Illustrative Example

```
Current coolant sourcing is summarized below:
              Stage  1   STATOR cooled from Source # 1
              Stage  1   ROTOR  cooled from Source # 1
              Stage  1   Fwd.WS cooled from Source # 1
              Stage  1   Aft WS cooled from Source # 2

              Stage  2   STATOR cooled from Source # 2
              Stage  2   ROTOR  cooled from Source # 1
              Stage  2   Fwd.WS cooled from Source # 2
              Stage  2   Aft WS cooled from Source # 3

              Stage  3   STATOR cooled from Source # 3
              Stage  3   ROTOR  cooled from Source # 3
              Stage  3   Fwd.WS cooled from Source # 3
              Stage  3   Aft WS cooled from Source # 4

              Stage  4   STATOR cooled from Source # 4
              Stage  4   ROTOR  cooled from Source # 3
              Stage  4   Fwd.WS cooled from Source # 4
              Stage  4   Aft WS cooled from Source # 4


Will you use current coolant sourcing (y/n)? y
Current turbine-stage pitchline velocities, flow coefficients, absolute rotor-
exit flow angles and stage uncooled adiabatic efficiencies are:
        STAGE   Vpitch M/S    Vaxial/Vpitch     Alpha 3          EtaS
        ------------------------------------------------------------
          1        392           0.5000         19.4806         0.9100
          2        412           0.5000          4.8702         0.9200
          3        392           0.5000         19.4806         0.9100
          4        412           0.5000          4.8702         0.9200
Will you use those values (y/n)? n
Enter your Vpitch, Vaxial/Vpitch, Alpha3, EtaS  for stage  1
? 400,.5,21,.91
Enter your Vpitch, Vaxial/Vpitch, Alpha3, EtaS  for stage  2
? 420,.5,8,.92
Enter your Vpitch, Vaxial/Vpitch, Alpha3, EtaS  for stage  3
? 400,.5,21,.91
Enter your Vpitch, Vaxial/Vpitch, Alpha3, EtaS  for stage  4
? 420,.5,8,.92
Enter Hub/Tip radius-ratio for last turbine stage on each shaft:
Shaft 2  stage 4  Hub/Tip radius-ratio? .7
Shaft 1  stage 2  Hub/Tip radius-ratio? .7
ROUND # 1
-------------------------------------------------------------------------------
STG SHAFT REL.RPM  HUB/TIP   P.R.   LOADING  PTCH.REAC HB.REAC   WORK    TIP VEL
-------------------------------------------------------------------------------
 1   1     2.787    0.834    2.515   1.928    0.228    0.067    268.4    436.2
 2   1     2.787    0.700    2.515   1.510    0.315   -0.010    249.8    494.1
 3   2     1.000    0.830    2.515   2.008    0.188    0.014    328.6    437.1
 4   2     1.000    0.700    2.515   1.540    0.300   -0.032    295.1    494.1
-------------------------------------------------------------------------------
HPC: PR= 6.928203 Work= 291.107     LPC: PR= 7.142477 Work= 240.4893
GT Work= 610.2515   Efficiency= .3652649   Cooling Flow= .2610165

ROUND # 1
-------------------------------------------------------------------------------
STG SHAFT REL.RPM  HUB/TIP   P.R.   LOADING  PTCH.REAC HB.REAC   WORK    TIP VEL
-------------------------------------------------------------------------------
 1   1     2.787    0.834    2.515   1.928    0.228    0.067    268.4    436.2
 2   1     2.787    0.700    2.515   1.510    0.315   -0.010    249.8    494.1
 3   2     1.000    0.830    2.515   2.008    0.188    0.014    328.6    437.1
 4   2     1.000    0.700    2.515   1.540    0.300   -0.032    295.1    494.1
-------------------------------------------------------------------------------
HPC: PR= 6.928203 Work= 291.107     LPC: PR= 7.142477 Work= 240.4893
GT Work= 610.2515   Efficiency= .3652649   Cooling Flow= .2610165
* SYSTEM ITERATION MENU * Select one of the following options:-
   1. Keep current turbine and let code match compressor split.
   2. Re-select turbine hub-to-tip ratios.
   3. Manually re-set turbine stage pressure ratios.
   4. Manually re-set compressor spool pressure ratios.
   5. Re-select turbine pitchline design.
   6. Scale system by specifying last-shaft RPM
   7. Scale system by specifying last-rotor exit-annulus area,SQ.M.
   8. Scale system by specifying gross G.T. power in MW
   9. Scale system by specifying compressor inlet massflow,KG/S
  10. ******* EXIT TO OUTPUT MENU *******
Make a choice? 1
Iteration to match compressor continuing.......

ROUND # 3
-------------------------------------------------------------------------------
STG SHAFT REL.RPM  HUB/TIP   P.R.   LOADING  PTCH.REAC HB.REAC   WORK    TIP VEL
-------------------------------------------------------------------------------
 1   1     2.808    0.837    2.515   1.822    0.281    0.135    237.2    435.4
 2   1     2.808    0.700    2.515   1.454    0.343    0.032    228.9    494.1
 3   2     1.000    0.830    2.515   1.947    0.219    0.050    306.4    437.1
 4   2     1.000    0.700    2.515   1.499    0.321   -0.001    275.8    494.1
-------------------------------------------------------------------------------
HPC: PR= 20.08031 Work= 462.6798     LPC: PR= 2.464331 Work= 94.14966
GT Work= 491.5048   Efficiency= .3550318   Cooling Flow= .2929398
Iteration to match compressor continuing.......
Compressor matched.
Make a choice? 6
Enter RPM? 3600
    Shaft 1 RPM= 10110     Shaft 2 RPM= 3600 .
Last stage exit annulus area= 2.752455 SQ.M.  ; pitch radius= 1.114104 M
Gross G.T. power= 91.89758 MW.       Compressor inlet airflow= 186.9719 KG/S
Make a choice? 10

HEAT BALANCE ERRORS % ARE :-
Compressor/Intercooler :-5.328147E-06
Primary Combustor :-9.536743E-07    Reheat Combustor : 9.536743E-06
Turbine Stage 1 :  1.46066E-05
Turbine Stage 2 :  1.357836E-02
Turbine Stage 3 : -5.132427E-06
Turbine Stage 4 :  1.53678E-05
GT Cycle:  9.030029E-03
Cycle mass balance error = 3.011199E-02 %
Enter any key to continue.?

Enter an identifying comment or run number? Example
Enter p to output to printer; s to screen; f to file? p
Output shall be to lpt1:


                    ******* OUTPUT MENU *******

Select desired output:-
      1. System Description.
      2. Performance Summary.
      3. Cycle State Points Summary.
      4. Turbine Pitchline Characteristsics.
      5. Cycle Energy and Exergy Balances.
      6. Cycle Mass, Energy and Exergy Streams.
      7. Component Irreversibility Breakdowns.
      8. Turbine Free-Vortex Gaspath.
      9. All of the above (printer or file only).
     10. ***** TO RE-SELECT OUTPUT DEVICE *****
     11. **** TO EXIT TO SPREADSHEET MENU *****
     12. ****** TO EXIT & MAKE NEW RUN ********
     13. * TO RETURN TO SYSTEM ITERATION MENU *
     14. **** TO EXIT & TERMINATE SESSION *****
```

```
                    SYSTEM DESCRIPTION

Ambient :Pressure= 1.013 BAR  Temperature= 289 K
Overall pressure ratio = 48
Primary Comb. disch. temp.(TIT) = 1500 K Reheat to 1500 K

Fractional total pressure losses :-
Inlet: .0075  Primary Combustor: .04  Reheat Combustor: .04  Diffuser: .06
Intercooler: .03  Boiler gas-side: .035

CH4 fuel, standard enthalpy of reaction = 50187.34  KJ/KG LHV
Standard Gibbs function of reaction (availability) = 50086.97  KJ/KG
Combustion efficiency = 99 %
Evaporative Intercooler. Saturation effectiveness= .9
LPC pressure ratio= 2.447934   Polytropic efficiency= .92
HPC pressure ratio= 20.21481   Polytropic efficiency = .91


First Stator TBC Biot Number= 0
                    BLADE ROW      PATTERN FACTOR    tct/tct,1
                    ------------------------------------------
                    STATOR 1           0.100           1.000
                    ROTOR  1           0.056           1.000
                    STATOR 2           0.036           1.000
                    ROTOR  2           0.025           1.000
                    STATOR 3           0.100           1.000
                    ROTOR  3           0.056           1.000
                    STATOR 4           0.036           1.000
                    ROTOR  4           0.025           1.000
        STAGE   Vpitch M/S   Vaxial/Vpitch    Alpha 3          EtaS
        ------------------------------------------------------------
          1        399           0.5000         21.0000         0.9100
          2        420           0.5000          8.0000         0.9200
          3        399           0.5000         21.0000         0.9100
          4        420           0.5000          8.0000         0.9200


4 Air extrac. pts. Bleed press.= 1.3 x Pin of highest row served (but<=P2)
    COOLANT      HIGHEST BLADE     EXTR.PRESS     EXTR.TEMP.      H20 moles
    SOURCE #     ROW SERVED          BAR              K              %
    ------------------------------------------------------------------------
          1      STATOR 1           48.26          788.25          3.84
          2      STATOR 2           23.95          643.45          3.84
          3      STATOR 3            9.14          482.43          3.84
          4      STATOR 4            3.63          363.49          3.84


ELEMENT     Trow K  SOURCE#  Tc K     ARC      PWR      ZL       ZP       Y
-------------------------------------------------------------------------------
STATOR 1    1085      1      788    0.0500   0.9000   0.0020             0.2000
ROTOR  1    1040      1      788    0.0400   0.9000   0.0020             0.2500
Fwd.WS 1              1      788                                0.0035   0.3500
Aft WS 1              2      643                                0.0035   0.3000
STATOR 2    1035      2      643    0.0500   0.9000   0.0020             0.2000
ROTOR  2    1000      1      788    0.0576   1.2500   0.0020             0.2500
Fwd.WS 2              2      643                                0.0035   0.3500
Aft WS 2              3      482                                0.0035   0.3000
STATOR 3    1085      3      482    0.0500   0.9000   0.0020             0.2000
ROTOR  3    1040      3      482    0.0400   0.9000   0.0020             0.2500
Fwd.WS 3              3      482                                0.0035   0.3500
Aft WS 3              4      363                                0.0035   0.3000
STATOR 4    1035      4      363    0.0500   0.9000   0.0020             0.2000
ROTOR  4    1000      3      482    0.0576   1.2500   0.0020             0.2500
Fwd.WS 4              4      363                                0.0035   0.3500
Aft WS 4              4      363                                0.0035   0.3000


                  PERFORMANCE SUMMARY LHV

Cooling air mass % of comp inlet= 29.29398
CH4 supply line @  20.67351 BAR &  289 K. Boost comp. work= 5.527554  KJ/KG al
Primary fuel massflow= 1.368841 %al , Reheat fuel = 1.38273 %al.
Compressor work = 556.8295  KJ/KG  al : LP= 94.14966 , HP= 462.6798
Turbine work    = 1048.334  KJ/KG  al
GT gross work= 491.5048  KJ/KG  al          GT gross efficiency = 35.50318 %
ST gross work= 273.2567  KJ/KG  al          SC gross efficiency = 33.42746 %
CC gross work= 764.7615  KJ/KG  al          CC gross efficiency = 55.2415 %
CC NET ELECTRIC KJ/KG = 743.2964
CC APPARENT NET ELECTRIC EFF.= 53.82537 %LHV

Compressor Inlet massflow= 186.9719 KG/S
GT gross power output= 91.89758  MW
CC Net Electric output= 138.9756  MW


GASCAN 5.4

                    CYCLE STATE POINTS

-------------------------------------------------------------------------------
     POINT          PRESSURE   TEMPERATURE K          MASS      MOLE COMPOSITION %
                      BAR    Absolute  Rotor-        FLOW      air     water  st.gas
                                       Relative      % al
---------------  -------  --------  --------  -------  -------  -------  -------
Air Inlet   (a)     1.013    289.0                100.00   100.00     0.00     0.00
Comp. Inlet (1)     1.013    289.0                100.00   100.00     0.00     0.00

LPC Disch. (2A)     2.478    382.0                100.00   100.00     0.00     0.00

Interc. Dis(1A)     2.403    319.7                102.49    96.16     3.84     0.00

HPC Disch.  (2)    48.259    788.2                 72.47    96.16     3.84     0.00

Comb. Disch.(3)    46.329   1500.0                 73.85    62.12     3.72    34.16

Inlet STATOR 1     46.329   1500.0                 73.43    62.12     3.72    34.16
Inlet ROTOR  1     44.504   1441.5     1301.0      80.74    65.14     3.73    31.13

Inlet STATOR 2     18.420   1192.1                 85.58    66.87     3.74    29.39
Inlet ROTOR  2     18.161   1174.9     1048.5      88.61    67.85     3.74    28.41

Reheater Inlet      7.323    961.8                 90.80    68.53     3.74    27.73

Inlet STATOR 3      7.031   1500.0                 92.62    42.05     3.65    54.30
Inlet ROTOR  3      6.867   1451.1     1299.7      98.09    45.01     3.66    51.34

Inlet STATOR 4      2.795   1194.3                101.49    46.68     3.66    49.65
Inlet ROTOR  4      2.767   1176.3     1047.0     104.08    47.89     3.67    48.44

Turb. Exit  (4)    1.111    962.3                105.28    48.43     3.67    47.90
Diffuser Ex(4A)     1.048    962.3                105.28    48.43     3.67    47.90
```

TURBINE PITCHLINE CHARACTERISTICS

BLADE ROW	COOLING EFFECT%	COOLANT % OF ROW INLET			STAGE EFF.%	STAGE WORK	CHARACTERISTICS	
		Gaspath Compnts	Gaspath w/Lekge	Dnstrm Whspce		KJ/KG R.I. KJ/KG al	Reaction	Loading
STATOR 1	0.621	9.203	9.464	0.482	78.5	293.858		
ROTOR 1	0.545	5.327	5.544	0.462	91.7	237.247	0.281	1.822
STATOR 2	0.318	2.925	3.156	0.374	87.3	258.288		
ROTOR 2	0.238	1.920	2.096	0.379	94.3	228.857	0.343	1.454
STATOR 3	0.438	5.139	5.452	0.454	82.9	312.374		
ROTOR 3	0.342	2.745	3.006	0.457	91.8	306.406	0.219	1.947
STATOR 4	0.210	1.904	2.183	0.378	88.9	265.000		
ROTOR 4	0.105	0.582	0.795	0.351	94.7	275.824	0.321	1.499

GASCAN 5.4

ENERGY & EXERGY BALANCES LHV

	ENERGY		EXERGY		
	KJ/KG al	% of Fuel Enthalpy	KJ/KG al	% of Fuel Exergy	% of Fuel Enthalpy
FUEL SUPPLY LINES	1384.397	100.000	1393.884	100.000	100.685
ATMOSPHERE	0.000	0.000	0.000	0.000	0.000
G.T. CYCLE NET WORK	491.505	35.503	491.505	35.262	35.503
LOSSES :-					
Inlet pressure loss	0.000	0.000	0.627	0.045	0.045
Compressor	0.000	0.000	29.941	2.148	2.163
Intercooler	61.496	4.442	10.296	0.739	0.744
Primary Combustor	6.870	0.497	190.587	13.673	13.767
Reheat Combustor	6.940	0.503	182.835	13.117	13.207
Turbine	0.000	0.000	78.162	5.608	5.646
Exit diffuser loss	0.000	0.000	5.284	0.379	0.382
TURBINE EXIT GAS STREAM	817.462	59.048	404.649	29.030	29.229
STEAM CYCLE WORK	273.257	19.738	273.257	19.604	19.738
COMBINED CYCLE WORK	764.762	55.242	764.762	54.866	55.242
PLANT NET ELECTRIC WORK	743.296	53.691	743.296	53.326	53.691

COMPONENT EFFECTIVENESS

Compressor :- 94.623 %

Primary combustor :- 73.06661 % Fuel enthalpy 72.58015 % Fuel exergy
Reheat combustor :- 74.35349 % Fuel enthalpy 73.83643 % Fuel exergy

Turbine Stage 1 :- 91.66166 %
Turbine Stage 2 :- 94.29118 %
Turbine Stage 3 :- 91.82419 %
Turbine Stage 4 :- 94.69823 %
Turbine as a whole :- 93.06149 %

SC work= 33.42746 % of turbine exit energy.
SC work= 67.52935 % of turbine exit exergy.

GASCAN 5.4

TURBINE GASPATH - FREE VORTEX

	ABSOLUTE			RELATIVE				Reaction /Blade	Static
	Velocity M/S	Angle deg	Mach Number	Velocity M/S	Angle deg	Mach Number	Radius M	Velocity M/S	Temp. K
				ROTOR # 1 10110 RPM					
INLET :-									
Hub	728.5	74.1	1.06	384.3	58.6	0.56	0.35	0.135	1240.5
Pitch	681.9	73.0	0.98	321.7	51.6	0.46	0.38	0.281	1265.4
Tip	641.7	71.8	0.92	270.4	42.3	0.39	0.40	0.393	1285.6
EXIT :-									
Hub	217.0	22.8	0.32	491.4	66.0	0.73	0.34	364.6	1196.9
Pitch	214.2	21.0	0.32	517.0	67.2	0.76	0.38	400.0	1197.4
Tip	212.1	19.4	0.31	544.0	68.4	0.80	0.41	435.4	1197.7
				ROTOR # 2 10110 RPM					
INLET :-									
Hub	700.9	72.6	1.14	369.2	55.3	0.60	0.34	0.032	981.9
Pitch	617.8	70.1	0.98	264.7	37.5	0.42	0.40	0.343	1025.0
Tip	555.0	67.8	0.87	213.5	10.4	0.34	0.45	0.526	1053.9
EXIT :-									
Hub	213.0	9.7	0.35	435.7	61.2	0.72	0.33	345.9	948.9
Pitch	212.1	8.0	0.35	496.1	65.0	0.82	0.40	420.0	949.0
Tip	211.5	6.8	0.35	560.1	68.0	0.93	0.47	494.1	949.1
				ROTOR # 3 3600 RPM					
INLET :-									
Hub	784.4	75.2	1.15	436.8	62.8	0.64	0.98	0.050	1225.7
Pitch	729.9	74.1	1.06	362.2	56.5	0.52	1.06	0.219	1255.9
Tip	683.2	73.0	0.98	299.9	48.2	0.43	1.14	0.346	1280.1
EXIT :-									
Hub	217.2	22.9	0.32	490.2	65.9	0.72	0.96	362.9	1198.7
Pitch	214.2	21.0	0.32	517.0	67.2	0.76	1.06	400.0	1199.1
Tip	212.0	19.4	0.31	545.4	68.5	0.81	1.16	437.1	1199.5
				ROTOR # 4 3600 RPM					
INLET :-									
Hub	722.4	73.1	1.18	388.4	57.3	0.63	0.97	-0.001	977.1
Pitch	635.6	70.7	1.01	276.6	40.6	0.44	1.11	0.321	1022.1
Tip	570.1	68.4	0.90	217.0	14.6	0.34	1.26	0.509	1052.3
EXIT :-									
Hub	213.0	9.7	0.35	435.7	61.2	0.72	0.92	345.9	950.1
Pitch	212.1	8.0	0.35	496.1	65.0	0.82	1.11	420.0	950.2
Tip	211.5	6.8	0.35	560.1	68.0	0.92	1.31	494.1	950.3

GASCAN 5.4

CYCLE ENERGY & EXERGY STREAMS LHV

STREAM	THERMODYNAMIC STATE				FLUXES		
	P BAR	T K	h KJ/KG	omega KJ/KG	Mass KG/S	Enthalpy KW	Exergy KW
Atmosphere inlet	1.013	289.00	0.0	0.0	187.0	0.0	0.0
Compr. Inlet (1)	1.005	289.00	0.0	-0.6	187.0	0.0	-117.2
LPC into IC (2A)	2.478	382.04	94.1	87.0	187.0	17603.3	16265.8
LPC power input							17603.3
H2O inj. into IC	N/A	289.00	-2465.1	0.0	4.7	-11498.0	0.2
IC into HPC (1A)	2.403	319.67	31.9	74.8	191.6	6105.3	14340.9
HPC into Comb(2)	48.259	788.25	527.3	545.0	135.5	72497.9	74925.9
HPC power input							86508.1
Bleed port # 1	48.259	788.25	535.0	553.0	25.5	13641.9	14098.8
Bleed port # 2	23.946	643.45	374.4	398.2	6.3	2376.2	2527.1
Bleed port # 3	9.140	482.43	201.4	233.2	17.9	3607.3	4177.3
Bleed port # 4	3.634	363.49	76.8	116.4	6.4	490.2	742.4
Prmry. fuel line	68.075	395.93	50439.8	50777.9	2.6	129093.1	129958.3
Comb. Disch. (3)	46.329	1500.00	1450.6	1225.7	138.1	200306.5	169249.8
STAGE # 1							
Main Gasflow in	46.329	1500.00	1458.9	1232.7	137.3	200306.5	169249.8
STATOR coolant	48.259	788.25	535.0	553.0	13.0	6952.5	7185.4
ROTOR coolant	48.259	788.25	535.0	553.0	8.4	4477.5	4627.5
Fwd.WS coolant	48.259	788.25	535.0	553.0	0.7	354.3	366.1
Aft WS coolant	23.946	643.45	374.4	398.2	0.7	261.0	277.6
Stage power output							44358.5
STAGE # 2							
Main Gasflow in	18.420	1192.07	1044.7	829.0	160.0	167993.2	133312.6
STATOR coolant	23.946	643.45	374.4	398.2	5.1	1891.0	2011.1
ROTOR coolant	48.259	788.25	535.0	553.0	3.5	1857.6	1919.8
Fwd.WS coolant	23.946	643.45	374.4	398.2	0.6	224.2	238.4
Aft WS coolant	9.140	482.43	201.4	233.2	0.6	126.4	146.4
Stage power output							42789.9
Stage 2 into R/H	7.323	961.77	758.0	540.9	169.8	129279.2	92247.7
Reheat fuel line	20.674	289.00	50187.3	50538.8	2.6	129750.2	130658.8
STAGE # 3							
Main Gasflow in	7.031	1500.00	1488.3	1089.8	173.2	257732.0	188721.5
STATOR coolant	9.140	482.43	201.4	233.2	9.4	1901.0	2201.4
ROTOR coolant	9.140	482.43	201.4	233.2	5.5	1110.1	1285.5
Fwd.WS coolant	9.140	482.43	201.4	233.2	0.8	158.1	183.1
Aft WS coolant	3.634	363.49	76.8	116.4	0.8	64.4	97.5
Stage power output							57289.3
STAGE # 4							
Main Gasflow in	2.795	1194.26	1073.4	685.6	189.8	203676.3	130098.7
STATOR coolant	3.634	363.49	76.8	116.4	4.1	318.3	481.9
ROTOR coolant	9.140	482.43	201.4	233.2	1.5	311.6	360.9
Fwd.WS coolant	3.634	363.49	76.8	116.4	0.7	55.1	83.4
Aft WS coolant	3.634	363.49	76.8	116.4	0.7	52.5	79.5
Stage power output							51571.3
Turbine exit (4)	1.111	962.34	776.5	389.4	196.8	152842.4	76645.9
Diff to HRSG(4A)	1.048	962.34	776.5	384.4	196.8	152842.4	75658.0

GASCAN 5.4

COMPONENT IRREVERSIBILITIES BREAKDOWN

SOURCE OF IRREVERSIBILITY	EXERGY LOSS % OF FUEL ENTHALPY AND MECHANISM					
	coolant throttling	mainstream pressure losses	thermal degradation	cooling totals	friction &aerodynamic	STAGE TOTAL
STATOR 1 cooling	0.0331	0.1697	0.2714	0.4741		
ROTOR 1 cooling	0.2623	0.3084	0.0846	0.6553		
Fwd.WS 1 cooling	0.0017	0.0152	0.0130	0.0300		
Aft WS 1 cooling	0.0060	0.0138	0.0138	0.0335		
Totals	0.3030	0.5070	0.3829	1.1930	0.3660	
TOTAL STAGE # 1						1.5590
STATOR 2 cooling	0.0452	0.0618	0.0977	0.2047		
ROTOR 2 cooling	0.2135	0.1278	0.0085	0.3498		
Fwd.WS 2 cooling	0.0054	0.0138	0.0100	0.0292		
Aft WS 2 cooling	0.0046	0.0124	0.0135	0.0305		
Totals	0.2686	0.2158	0.1298	0.6142	0.3867	
TOTAL STAGE # 2						1.0009
STATOR 3 cooling	0.0871	0.1187	0.5246	0.7304		
ROTOR 3 cooling	0.2126	0.2000	0.2149	0.6276		
Fwd.WS 3 cooling	0.0073	0.0182	0.0425	0.0680		
Aft WS 3 cooling	0.0072	0.0166	0.0500	0.0738		
Totals	0.3143	0.3534	0.8320	1.4997	0.4709	
TOTAL STAGE # 3						1.9707
STATOR 4 cooling	0.0365	0.0478	0.2446	0.3289		
ROTOR 4 cooling	0.1063	0.0462	0.0364	0.1890		
Fwd.WS 4 cooling	0.0064	0.0166	0.0419	0.0648		
Aft WS 4 cooling	0.0264	0.0135	0.0287	0.0687		
Totals	0.1756	0.1241	0.3516	0.6513	0.4641	
TOTAL STAGE # 4						1.1155
TURBINE TOTAL						5.6459

	fuel throttling	mainflow pressure loss	thermal degradation	incomplete combustion	COMBUSTOR TOTAL
PRIMARY COMBUSTOR	0.0510	0.1865	13.0341	0.4952	
REHEAT COMBUSTOR	0.1553	0.2359	12.3154	0.5003	
					26.9736

	mainflow pressure loss	thermal degradation	INTERCOOLER TOTAL
INTERCOOLER	0.1831	0.5606	
			0.7437

E. Wiederuh
Mannesmann Demag,
Duisburg, Federal Republic of Germany

An Attempt to Standardize the Use of Isentropic Exponents for Compressor Calculations

1 Introduction

Isentropic changes of state are generally the basis for the calculation of thermodynamic processes that can be regarded approximately as adiabatic. The exact way to calculate an isentropic change of state between state 1 and state 2 is the satisfaction of the condition $s_1 = s_2$ using an equation of state. In most cases p_1, T_1, and p_2 are known, while T_2 is the value to be found. Since for real gases the equations for entroy have the form $s = s\ (T, p)$, the temperature T_2 can only be calculated iteratively. Today computers are mostly available for this calculation so that complicated equations of state can also be handled. Nevertheless isentropic exponents, which give less exact results but which simplify these calculations and which were used for this reason in former times, are still used in many fields. Domains of isentropic exponents are the calculation of labyrinth leakages [1] and the measurement of fluid flows by orifice plates and nozzles [2, 3]. Isentropic exponents are still used in power test codes [4, 5] and, of course, for approximate calculations and checks. Because the pressure and temperature ranges in which these calculations are made enlarge more and more so that the real gas properties can no longer be neglected, it is important to be aware of the validity of the different isentropic exponents. Only the correct use of these exponents can guarantee good approximations and reliable checks and thus avoid redundant discussions.

It is the objective of this paper to summarize the derivations of the different isentropic exponents and to point out the differences and the limits. Another objective is to plead for *uniform marking* to enable comparison of exponents of different sources and to recognize the way they were calculated. Those comparisons have rarely been possible up to now because of differing and unclear definitions.

2 Isentropic Exponents for Perfect and Ideal Gases

The starting point for the derivation of the isentropic exponent is the well-known Second Law of Thermodynamics because this law combines the entropy and the quantities which are measurable and of interest for practical applications

$$Tds = dh - vdp \tag{1}$$

For an ideal gas, the enthalpy is a function only of temperature

$$dh = c_p^0(T)dT \tag{2}$$

The combination of equations (1) and (2) and the demand for an isentropic change of state realized by the condition $ds = 0$ result in

$$\frac{c_p^0(T)}{T}\,dT = \frac{v}{T}\,dp \tag{3}$$

General integration of equation (3) implies that the functions $c_p^0 = f\ (T)$ and $v/T = f\ (p)$ are known. Because ideal gases are being considered here, the equation of state for ideal gases can be used

$$\frac{v}{T} = \frac{R}{p} \tag{4}$$

A general function $c_p^0 = f\ (T)$ for ideal gases does not exist because this function varies for different gases. A general integration of equation (3) however is possible for so-called perfect gases; i.e., ideal gases for which the additional restriction

$$c_p^0 = \text{const} \tag{5}$$

applies.

Introducing equations (4) and (5) into equation (3), the integration yields

$$\frac{T_2}{T_1} = \left[\frac{p_2}{p_1}\right]^{\frac{R}{c_p^0}} \tag{6}$$

To realize the meaning of the term "isentropic exponent," we replace the temperature T by the equation of state for ideal gases and obtain

$$\frac{v_2}{v_1} = \left[\frac{p_2}{p_1}\right]^{\frac{R}{c_p^0}-1} \tag{7}$$

Using the following equation, which is valid for *perfect and ideal gases*

$$c_p^0(T) - c_v^\infty(T) = R \tag{8}$$

and introducing the abbreviation valid for *perfect gases*

$$\frac{c_p^0}{c_v^\infty} = \kappa = \text{const} \tag{9}$$

equation (7) can be written in the well-known form

$$\frac{p_2}{p_1} = \left[\frac{v_1}{v_2}\right]^\kappa \tag{10}$$

or

$$p_1 v_1^\kappa = p_2 v_2^\kappa = \text{const}$$

which illustrates why κ is called the "isentropic exponent."

Contributed by the Gas Turbine Division for publication in the JOURNAL OF ENGINEERING FOR GAS TURBINES AND POWER. Manuscript received at ASME Headquarters May 26, 1987.

Similarly we can derive the two further equations

$$\frac{T_2}{T_1}=\left[\frac{p_2}{p_1}\right]^{\frac{\kappa-1}{\kappa}} \tag{11}$$

$$\frac{T_2}{T_1}=\left[\frac{v_2}{v_2}\right]^{\kappa-1} \tag{12}$$

This paragraph was intended to show that equations (10)–(12) are strictly valid for perfect gases only. Calculations for ideal gases are possible using the isentropic exponent $\kappa_1 = \kappa(T_1)$ or an average value $\bar{\kappa} = \kappa(T_x)$ whereby $T_1 < T_x < T_2$ but it is obvious that those calculations are approximate whereby the quality of the approximation depends on the extent of the change of the specific heats between states 1 and 2.

3 Isentropic Exponents for Real Gases

Starting again with the Second Law of Thermodynamics, it must be taken into account that, for real gases, the specific heat c_p and specific enthalpy are functions not only of temperature but also of pressure. So, equation (1) comprises an additional term

$$Tds=c_p(T, p)dT+\left(\frac{\partial h}{\partial p}\right)_T dp-vdp \tag{13}$$

Using the generally valid equation

$$\left(\frac{\delta h}{\delta p}\right)_T=v-T\left(\frac{\delta v}{\delta T}\right)_p \tag{14}$$

and paying attention to the condition $ds = 0$ results in

$$\frac{c_p(T, p)}{T}\,dT=\left(\frac{\delta v}{\delta T}\right)_p dp \tag{15}$$

The specific heat c_p is usually split into two parts

$$c_p(T, p)=c_p^0(T)+\Delta c_p(T, p) \tag{16}$$

whereby c_p^0 is the specific heat of the ideal gas and Δc_p comprises the real gas properties

$$\Delta c_p(T, p)=-T\int_0^p\left(\frac{\delta^2 v}{\delta T^2}\right)_p dp \tag{17}$$

It is evident that general integration of equation (15) is not possible for real gases because the term $(\delta v/\delta T)_p$ and the departure Δc_p of the specific heat can be calculated only by using special equations of state. Equation (15) can be solved numerically for a special gas but it is not possible to define an isentropic exponent for real gases in this way.

Because the calculation of isentropic changes of state is very easy and comfortable using the simple equations (10)–(12), derived for perfect and ideal gases, an attempt has been made to see whether it is possible to define isentropic exponents and to elaborate similar equations for real gases in another way.

The starting point is equation (10)

$$pv^\kappa=\text{const}$$

We have seen that κ is not constant for a finite change of state except for perfect gases. Therefore an infinitely small change of state is considered to define an isentropic exponent for real gases. To do this, we have to differentiate equation (10)

$$\frac{dp}{p}+\kappa_{pv}\frac{dv}{v}=0 \tag{18}$$

It is proposed here to use the index 'pv' because this exponent is valid for the combination of p and v only. On the other hand, the index shows that this exponent is calculated by real gas rules.

Equation (18) defines the isentropic exponent κ_{pv}

$$\kappa_{pv}=-\frac{v}{p}\left(\frac{\delta p}{\delta v}\right)_s \tag{19}$$

Because the calculation of the term $(\delta p/\delta v)_s$, which includes the entropy, is very complicated to handle, it is more convenient to replace this term by the generally valid equation

$$\left(\frac{\delta p}{\delta v}\right)_s=\frac{c_p(T, p)}{c_v(T, v)}\left(\frac{\delta p}{\delta v}\right)_T \tag{20}$$

So equation (19) can be written in the final and more practical form

$$\kappa_{pv}(T, p)=-\frac{v}{p}\left(\frac{\delta p}{\delta v}\right)_T\frac{c_p(T, p)}{c_v(T, v)} \tag{21}$$

Compared with the isentropic exponent for the ideal gas, κ_{pv} is not only a function of temperature but also of pressure and very different from the quotient of the specific heats c_p/c_v, a matter which is often overlooked.

With the definition of the acoustic velocity

$$a^2=\left(\frac{\delta p}{\delta \rho}\right)_s=-\frac{1}{\rho^2}\left(\frac{\delta p}{\partial v}\right)_s$$

and using equation (19) we get

$$a^2=\kappa_{pv}pv$$

and for a real gas with the equation of state $pv = zRT$

$$a^2=\kappa_{pv}zRT$$

The equations for the isentropic exponents, which combine p and T or T and v can be derived in a similar manner.

Starting with equation (11)

$$pT^{\frac{\kappa}{1-\kappa}}=\text{const}$$

we again differentiate

$$\frac{dp}{p}+\frac{\kappa_{pT}}{1-\kappa_{pT}}\frac{dT}{T}=0 \tag{22}$$

and obtain

$$\left(\frac{\delta p}{\delta T}\right)_s=-\frac{\kappa_{pT}}{1-\kappa_{pT}}\frac{p}{T} \tag{23}$$

To facilitate the calculation of κ_{pT} we use equation (15)

$$\left(\frac{\delta p}{\delta T}\right)_s=\frac{c_p(T, p)}{T\left(\frac{\delta v}{\delta T}\right)_p} \tag{24}$$

Nomenclature

a = acoustic velocity
c_p^0 = specific heat at constant pressure of the ideal gas
c_p = specific heat at constant pressure of the real gas
c_v^∞ = specific heat at constant volume of the ideal gas
c_v = specific heat at constant volume of the real gas
f = polytropic work factor
h = specific enthalpy
p = pressure
R = gas constant
s = specific entropy
T = absolute temperature
u = energy
v = specific volume
w_s = specific isentropic work, marking of PTC 10
w_t = specific work
z = compressibility factor
ρ = density

so that the definition of κ_{pT} has the final form

$$\kappa_{pT}(T, p) = \frac{1}{1 - \frac{p}{c_p(T, p)}\left(\frac{\delta v}{\delta T}\right)_p} \tag{25}$$

Because most of the equations of state are explicit in p, it is more convenient to use in addition the generally valid equation

$$\left(\frac{\delta v}{\delta T}\right)_p = -\left(\frac{\delta p}{\delta T}\right)_v \Big/ \left(\frac{\delta p}{\delta v}\right)_T \tag{26}$$

To obtain the definition for κ_{Tv} we start with equation (12)

$$Tv^{\kappa - 1} = \text{const}$$

We differentiate this equation

$$\frac{dT}{T} + (\kappa_{Tv} - 1)\frac{dv}{v} = 0 \tag{27}$$

and obtain

$$\left(\frac{\delta T}{\delta v}\right)_s = -\frac{T}{v}(\kappa_{Tv} - 1) \tag{28}$$

Using the Second Law of Thermodynamics in the form

$$Tds = du + pdv \tag{29}$$

yields

$$\left(\frac{\delta T}{\delta v}\right)_s = -\frac{T}{c_v(T, v)}\left(\frac{\delta p}{\delta T}\right)_v \tag{30}$$

so we can write κ_{Tv} in the following form:

$$\kappa_{Tv}(T, v) = 1 + \frac{v}{c_v(T, v)}\left(\frac{\delta p}{\delta T}\right)_v \tag{31}$$

It was the objective of this section to call to mind that, for real gases, three different isentropic exponents can be defined, which are functions of temperature and pressure or specific volume. Therefore it is proposed here to use definite indices to make clear which isentropic exponent is used and to add the temperature and the pressure or specific volume for which the exponent is calculated (κ_{xy} $(T, p) = \ldots$). Only on these premises is a comparison of isentropic exponents possible.

Two additional remarks are necessary. It can easily be shown that the three isentropic exponents for real gases are combined by the following equation:

$$\kappa_{pT} = \frac{1}{1 - \frac{\kappa_{Tv} - 1}{\kappa_{pv}}} \tag{32}$$

Furthermore it should be mentioned that the well-known equation (8), which is valid for ideal gases, is not valid for real gases and must be replaced by

$$c_p(T, p) - c_v(T, v) = -T\frac{\left(\frac{\delta p}{\delta T}\right)_v^2}{\left(\frac{\delta p}{\delta v}\right)_T} \tag{33}$$

To point out the differences between the isentropic exponents and the quotient c_p/c_v often falsely used, Fig. 1 shows these properties for a natural gas.

The calculation was made using the BWRS equation (8). Figure 1 shows that there are great differences especially at high pressure. For $p = 0$ the state of the ideal gas is reached; therefore the differences between the different properties, of course, disappear.

The above derivations show that the isentropic exponents can be exactly defined for a definite temperature and pressure

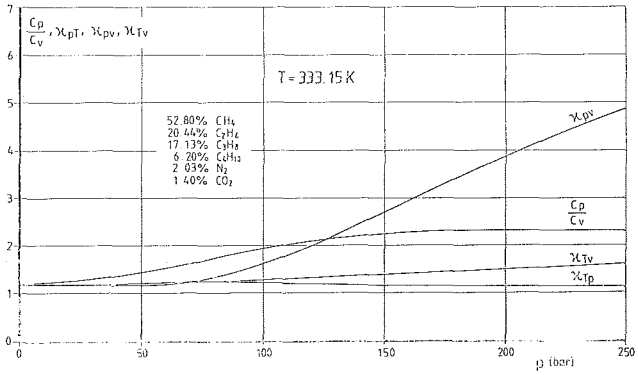

Fig. 1 Comparison between κ_{Tv}, κ_{pv}, κ_{Tp}, and C_p/C_v for a natural gas

or specific volume only and for the combination of two of the thermal properties p and T, p and v, or T and v. In practice, however, finite isentropic changes between state 1 and state 2 have to be calculated. State 1 and one thermal property of state 2 are known. The missing properties of state 2 can be calculated approximately by using κ_{pv}, κ_{pT}, or κ_{Tv} of state 1 together with the modified equations (10)–(12).

$$\frac{p_2}{p_2} = \left[\frac{v_1}{v_2}\right]^{\kappa_{pv_1}} \tag{34}$$

$$\frac{T_2}{T_1} = \left[\frac{p_2}{p_1}\right]^{\frac{\kappa_{pT_1} - 1}{\kappa_{pT_1}}} \tag{35}$$

$$\frac{T_2}{T_1} = \left[\frac{v_1}{v_2}\right]^{\kappa_{Tv_1} - 1} \tag{36}$$

The quality of the approximate properties of state 2 depends on the change in the isentropic exponents between state 1 and 2 whereby the deviations will not in general be equal for the different properties because of the different slopes of κ_{pv}, κ_{pT}, and κ_{Tv}. The consequence is that, if p_2 is given, T_2 and v_2 calculated by equations (34)–(36) will not in general fulfill the equation of state for state 2. In other words, the thermal properties of state 2 will not be consistent.

An improvement of the results is possible by using mean values for the isentropic exponents, which must be found iteratively.

If only the isentropic exponent κ_{pv} is known, the isentropic temperature of state 2 can be calculated in principle in the following manner. Starting with equation (34) and using the equation of state for the real gas

$$pv = zRT \tag{37}$$

we obtain

$$\frac{T_2}{T_1} = \left[\frac{v_1}{v_2}\right]^{\kappa_{pv_1} - 1}\frac{z_1}{z_2} \tag{38}$$

or, for the combination of T and p,

$$\frac{T_2}{T_1} = \left[\frac{p_2}{p_1}\right]^{\frac{\kappa_{pv_1} - 1}{\kappa_{pv_1}}}\frac{z_1}{z_2} \tag{39}$$

The disadvantage of this method is that z_2 must be known, which is not the case because T_2 and v_2 are the figures we are interested in. Therefore iteration is necessary. Contrary to the statement made by Scholz [6], it is important to mention that the temperature T_2, calculated by equation (35), will not be the same as the temperature T_2 calculated by equation (39), which follows from the above explanations.

Besides p, T, and v, the specific work w_t is necessary in practice. Because the specific work is defined

$$w_t = \int_{p_1}^{p_2} v dp \tag{40}$$

the isentropic exponent κ_{pv} must be used, so that for real gases we obtain

$$w_t = \frac{\kappa_{pv}}{\kappa_{pv}-1} z_1 R\, T_1 \left[\left(\frac{p_2}{p_1} \right)^{\frac{\kappa_{pv}-1}{\kappa_{pv}}} - 1 \right] \tag{41}$$

whereby κ_{pv} can be κ_{pv_1} or an average value.

The question is how to obtain the isentropic exponents for approximate calculations. κ_{pv} diagrams have been published for some gases [5, 7] while diagrams for κ_{pT} and κ_{Tv} have been missing up to now. Here modern pocket calculators open new possibilities, because they are powerful enough to calculate the isentropic exponents using equations of state of the van der Waals type; e.g., the Redlich-Kwong [9], the Redlich-Kwong-Soave [10], or the Peng-Robinson [11] equations. As long as iterative procedures overtax such calculators, isentropic exponents can be a useful aid and will therefore be of renewed interest at the project stage where approximate but speedy results are needed [12, 13].

4 Isentropic Exponents in Compressor Data Sheets

In the modern compressor industry, exact calculation of isentropic changes of state is made by using equations of state and computers. However, customers still ask for isentropic exponents in the data sheets. These exponents are used to check the consistency of the given data or to compare the exponents of different compressor producers. As we have seen in the preceding sections, such a comparison can be problematic because of the different definitions of the isentropic exponents. In many data sheets, the value c_p/c_v is asked for, facts which add to the confusion. Because those exponents are only used for checks, it is proposed here to use the definition of the isentropic exponent contained in the ASME Power Test Code for Compressors and Exhausters (PTC 10)

$$n_s = \frac{\ln \dfrac{p_2}{p_1}}{\ln \dfrac{v_1}{v_2}} \tag{42}$$

This exponent can only be calculated when the data of state 2 are already known, whereas normally the isentropic exponent is used to find the data of state 2. Therefore n_s, is a pseudo-isentropic exponent. But, because the PTC 10 is internationally acknowledged and because this exponent yields the correct value v_2, which is of interest, the agreement on the use of n_s would give a common and uniform basis for the definition of an isentropic exponent in data sheets.

The isentropic temperature T_2 can easily be calculated using equations (38) or (39) because z_2 is already known

$$\frac{T_2}{T_1} = \left[\frac{v_1}{v_2} \right]^{n_s - 1} \frac{z_1}{z_2} \tag{43}$$

or

$$\frac{T_2}{T_1} = \left[\frac{p_2}{p_1} \right]^{\frac{n_s - 1}{n_s}} \frac{z_1}{z_2} \tag{44}$$

The exponent n_s gives the correct value of v_2 but all the values of v between v_1 and v_2 are not correct, so that equation (40), together with the isentropic exponent n_s, cannot yield the correct specific work. Therefore, PTC 10 defines what is known as the "polytropic work factor" f using the exact value of the enthalpy h_2 calculated before

$$f = \frac{h_2 - h_1}{\dfrac{n_s}{n_s - 1}(p_2 v_2 - p_1 v_1)} \tag{45}$$

With this factor we get the correct specific work

$$w_s = \frac{n_s}{n_s - 1} f \cdot p_1 v_1 \left[\left(\frac{p_2}{p_1} \right)^{\frac{n_s - 1}{n_s}} - 1 \right] \tag{46}$$

For the calculation of the polytropic work and the exact derivation of the polytropic work factor f see [14, 15].

So, to check the isentropic specific work w_s, the statement of f is also necessary in the data sheets.

Sometimes, instead of f, another pseudo-isentropic exponent κ_h is defined iteratively, which yields the correct isentropic specific work

$$w_t = \frac{\kappa_h}{\kappa_h - 1} z_1 R\, T_1 \left[\left(\frac{p_2}{p_1} \right)^{\frac{\kappa_h - 1}{\kappa_h}} - 1 \right] = h_2 - h_1$$

This exponent κ_h can be used instead of n_s and f but this definition is not as well known as the definition contained in PTC 10.

5 Summary

Isentropic changes of state are generally used in thermodynamic calculations. Often isentropic exponents are used for these calculations, a method which is not without risk especially if these calculations are being made for real gases. Therefore, the objective of this paper is to summarize the definitions of the different isentropic exponents as well as the preconditions and restrictions which must be given due consideration. This paper is intended to make the use of isentropic exponent more transparent and to plead for uniform marking of the exponents. This is of particular interest when addressing people engaged in the compressor business.

Acknowledgments

This paper was written when I was a member of the Mannesmann Demag Compressor Division. I thank Mannesmann Demag for the support and the authority to publish this paper.

References

1 Trutnovsky, K., and Komotori, K., *Berührungsfreie Dichtungen*, VDI-Verlag, 1980.

2 "Measurement of Fluid Flow by Means of Orifice Plates and Nozzles," ISO Recommendation R 541, 1967.

3 "Durchflussmessung mit genormten Düsen, Blenden und Venturidüsen," DIN 1952, 1971.

4 "Compressors and Exhausters," Power Test Code 10, ASME, New York, 1974.

5 "Abnahme- und Leistungsversuche an Verdichtern," VDI Richtlinie 2045, 1973.

6 Scholz, R., "Verschiedene Definitionen und Verwendung des Isentropenexponenten bei realen Gasen," *Gas Wärme International*, Vol. 23, No. 12, 1974.

7 Baehr, H. D., "Der Isentropenexponent der Gase H, N, 0, CH, CO, NH_3 und Luft für Drücke bis 300 bar," *BWK*, Vol. 19, No. 2, 1967.

8 Starling, K. E., *Fluid Thermodynamics Properties for Light Petroleum Systems*, Gulf Publishing Company, Houston, TX, 1973.

9 Redlich, O., and Kwong, J. S., *Chem. Rev.*, Vol. 44, 1949, p. 233.

10 Soave, G., *Chem. Eng. Science*, Vol. 27, 1972, p. 1197.

11 Peng, D.-Y., and Robinson, D. B., *Ind. Eng. Chem. Fundam.*, Vol. 15, 1976, pp. 1, 59.

12 Wiederuh, E., "Calculation of Real Gas Data With a HP41C," unpublished.

13 Wiederuh, E., "Estimated Compressor Calculation With a HP41C," unpublished.

14 Schultz, J. M., "The Polytropic Analysis of Centrifugal Compressors," ASME JOURNAL OF ENGINEERING FOR POWER, Vol. 91, 1969.

15 Huntington, R. A., "Evaluation of Polytropic Calculation Methods for Turbomachinery Performance," ASME Paper No. 85-GT-13, presented at the 30th International Gas Turbine Conference and Exhibit, Houston, Texas, March 17-21, 1985.

J. L. Catina

H. J. Fortune, Jr.

Virginia Power,
Richmond, VA 23261

G. E. Soroka

Bechtel Eastern Power Corporation,
Gaithersburg, MD 20877

Repowering Chesterfield 1 and 2 With Combined Cycle

Introduction

Virginia Power has recently completed a detailed study for repowering two retired units at the Chesterfield Station with 300 to 400 MW (300,000-400,000 kW) of combined cycle power as required by the 1985 load growth forecast. The study involved economic and technical assessments of combined cycle equipment and integration of existing facilities.

Evaluations of peaking and base load characteristics, fuels, and steam cycles were performed to establish the optimum performance and cycle configuration. An integrated coal gasification plant was also sited and evaluated but is not discussed in this paper. During the progress of this study, certain external factors were changing and have been noted where appropriate.

Existing Facilities

The Chesterfield Station is located 15 miles (24 km) south of Richmond, VA on the James River and consists of four active coal-fired units of 1250 MW (1,250,000 kW) generating capacity and two inactive units of 63 and 69 MW (63,000 and 69,000 kW). These latter two units, originally constructed in 1944 and 1945 and retired in 1981, are proposed for repowering. Figure 1 illustrates the plant general arrangement and location of the two units. The site is constrained on the north by the river, on the east by the administration building, and on the west by Unit 3.

Repowering Versus New Construction

Prior to initiating the study, a comparison of the advantages and disadvantages of repowering versus new construction was performed and the results are shown in Table 1. One obvious incentive for repowering over new construction is the savings in capital investment. These are derived mainly from the reuse of existing equipment and structures, the use of owned land, existing transmission capacity, and the sharing of infrastructure with other units. Other important advantages are lower operation and maintenance costs resulting from sharing existing support facilities and staff, and shorter and less complicated relicensing by designing within the station's existing thermal discharge permits and intake structures.

There are also several disadvantages to repowering. One is the added complexity that can result when matching old equipment with modern, high-efficiency equipment. A second is the potential for increased maintenance frequency of refurbished equipment.

The weight of the incentives over disincentives provided the basis to study repowering rather than construction.

Table 1 *Repowering versus new construction*

ADVANTAGES:

- LOWER CAPITAL INVESTMENT
- LOWER OPERATING AND MAINTENANCE COSTS
- LOWER ENVIRONMENTAL IMPACT
- SHORTER LICENSING PERIOD

DISADVANTAGES:

- INCREASED CYCLE COMPLEXITY
- LOWER RELIABILITY OF REFURBISHED EQUIPMENT

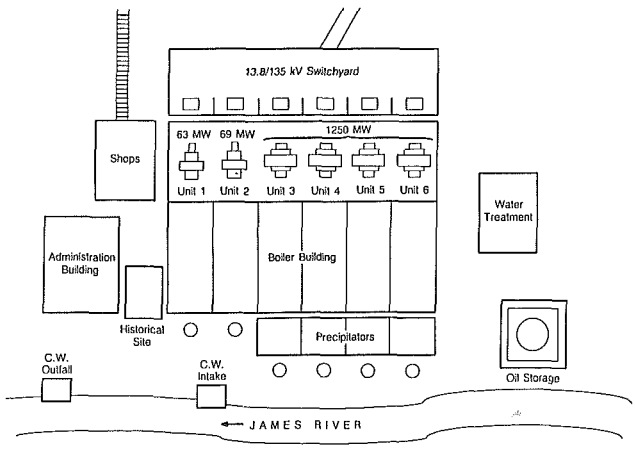

Fig. 1 Plant layout

Contributed by the Gas Turbine Division of THE AMERICAN SOCIETY OF MECHANICAL ENGINEERS and presented at the 32rd International Gas Turbine Conference and Exhibit, Anaheim, California, May 31–June 4, 1987. Manuscript received at ASME Headquarters January 30, 1987. Paper No. 87-GT-12.

Repowering With Combined Cycle

Virginia Power's load growth projection indicated that the next increment of power required would be 300 to 400 MW (300,000-400,000 kW) beginning in 1991.[1] A unit that could be used initially for intermediate and later for base load operation would be suitable for the projected growth. In addition, the new plant would have to fit in the space occupied by the present Units 1 and 2, be available by 1991,[2] and not exceed the thermal emissions limits established for the original units. It would also have to meet atmospheric emission limits for the site.

A comparison between the expected performance of combined cycle and conventional cycle repowering for this application is summarized in Table 2.

Station Output. A significantly higher station output, 400 MW versus 130 MW (400,000 kW versus 130,000 kW), can be achieved by the combined cycle for the same amount of thermal discharge as with the conventional coal-fired unit.

Station Auxiliary Load. A combined cycle requires approximately 5 percent of its output for auxiliary power (and losses) compared to approximately 15 percent for a coal-fired unit.

[1] 1986 load growth indicated a need for two 200 MW (200,000 kW) units, 2 years apart.
[2] 1986 load growth indicated 1989.

Table 2 Repowering options

	CONVENTIONAL CYCLE	COMBINED CYCLE
Station Output	130 MW(1)	400 MW(2)
Station Auxiliary Load	15%	5%
Station Heat Rate	10,800 Btu/kWh	7,500 Btu/kWh
Capital Cost(3)	1,600 kW	$500 kW
Availability	85%	92%
Construction Duration	48 Mos.	24 Mos.
Peaking Capability	Fair	Good
Reuse of Existing Equipment	Limited	Limited
Reuse of Existing Structures	Limited	Good
Use of Available Space	Marginal	Good
Cost of Fuel(4)	Low	Intermediate

(1) THERMAL DISCHARGE LIMIT
(2) INCLUDES 130 MW STEAM CYCLE
(3) 1986 DOLLARS
(4) NO. 2 FUEL OIL REFERENCE

Station Heat Rate. Because of the inherently higher efficiency of the Brayton-Rankine cycle over the Rankine cycle alone (45 percent versus 31 percent) and the lower station auxiliary load, the combined cycle exhibits about a 30 percent advantage in net heat rate.

Capital Cost. The capital investment required for a combined cycle is significantly less than for an equivalent conventional plant.

Availability. Combustion turbines historically provide a higher availability than conventional coal-fired units because of the reduced outage durations required for maintenance and the shorter downtime and restart time required with unscheduled outages.

Procurement and Construction Duration. Combined cycle equipment, including heat recovery boilers, in this size range can be installed and operational in about half the time required for a conventional field-erected boiler.

Intermediate Capability. The starting and loading characteristics of the combined cycle make it superior to a coal-fired unit for cycling duty.

Reuse of Existing Structures. Since the combined cycle is smaller and lighter than conventional cycle equipment, it is more adaptable to siting on existing foundations and in the available space.

Cost of Fuel. The single disadvantage of the combined cycle is that it does not burn coal and therefore has higher fuel costs. However, it is capable of burning medium-Btu gas produced by a coal gasification facility.

Combustion Turbine Market

A survey of both foreign and domestic manufacturers of combustion turbines was conducted to determine the equipment available for repowering and their characteristics.

The size of the units was established by the size of the existing steam turbines, since the thermal discharge limits established for Units 1 and 2 could not be exceeded (135 MW, or 135,000 kW). Since in a combined cycle the Rankine cycle constitutes one third of the output, the combined combustion turbine output could be approximately 270 MW (270,000 kW) without exceeding these limits. The existing space could accommodate up to three gas turbines; therefore, only combustion turbines 90 MW (90,000 kW) and larger were considered acceptable. The equipment selected for consideration is listed

Table 3 Combined cycle equipment survey

	OPEN CYCLE		COMBINED CYCLE					
Manufacturer and Model	Output MW	Heat Rate Btu/kWh	Estimated Output MW	Estimated Heat Rate Btu/kWh	Press. Ratio/ Drive End	Comb. Type	Year Introduced	No. In Service
Westinghouse W501D5	104.4	10,290	147.3	7190	14.2/ Compr.	Can-Annular	1980	17
Kraftwerk Union V84	98	10,435	134.0	7180	10.4/ Compr.	Dual External Silos	1985	0
General Electric Frame 7E	75	10,760	118.1	7310	11.7/ Turbine	Can-Annular	1976	370
Brown-Boveri Type 11	72.5	10,765	115.9	7446	9.0 Compr.	Single Integral Silo	1971	110
General Electric Frame 7F	135	---	205	7003	--/ Compr.	Can-Annular	1988	Prototype

(1) Based on 100% load, ISO conditions
(2) Heat rates based on LHV of Natural Gas

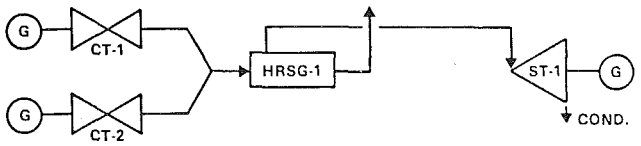

2 COMBUSTION TURBINES/1 HRSG/1 OR 2 STEAM TURBINES

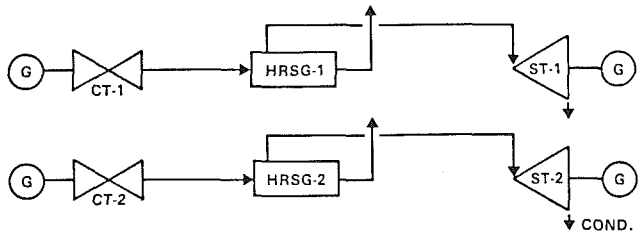

2 COMBUSTION TURBINES/2 HRSGs/1 OR 2 STEAM TURBINES

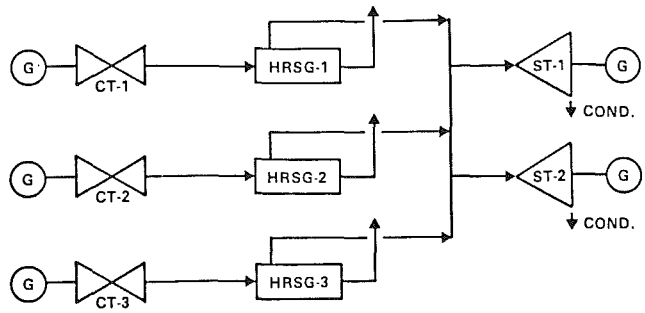

3 COMBUSTION TURBINES/3 HRSGs/1 OR 2 STEAM TURBINES

Fig. 2 Alternative configurations

in Table 3 along with expected performance and principal features.

Both the Westinghouse 501D and Kraftwerk V84 can supply the required output with two supplementally fired units. The GE Frame 7F can supply the required output with two units without supplemental firing. The Westinghouse and Kraftwerk units required three units each to provide the required output in an unfired mode.

The pressure ratio is significant in that it establishes the required fuel pressure and NO_x abatement steam injection pressure.

The "drive end" refers to the end of the machine to which the generator is connected. If connected to the compressor end, the shaft extends through the inlet duct, which must enter at a right angle to the air flow. The exhaust from this type of machine discharges directly into the HRSG. When the generator is connected to the turbine end, the shaft extends through the exhaust duct, which must exit at a right angle to the through-flow. The inlet to this type of machine is unobstructed.

The "combustor type" is significant from layout considerations in that the silo type requires more head room and width than the can-annular type.

The "year introduced" and "number in service" influence the availability assessment of the equipment.

Combined Cycle Arrangements

Based on the equipment selected from the survey, a number of alternate cycle configurations were available. Several of these are illustrated in Fig. 2.

Figure 2-1 illustrates the use of a single heat recovery steam generator (HRSG) serving two (or three) combustion turbines.

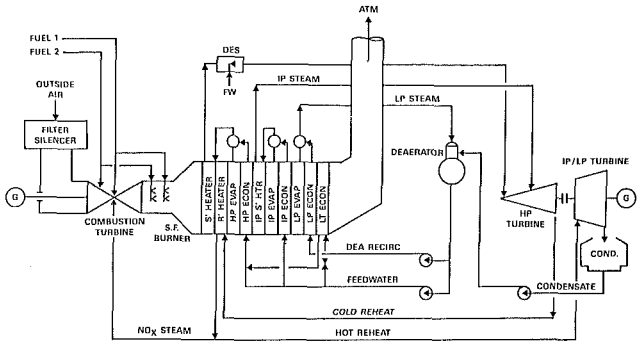

Fig. 3 Fully developed combined cycle

The chief advantage of this scheme is economy. The chief drawback is that the entire plant is down when the HRSG is down. If a HRSG diverter is installed, 2/3 of the power would be available from the unit. The steam turbine efficiency is also reduced when only one combustion turbine is operating.

Figure 2-2 illustrates the multitrain arrangement consisting of two trains of combustion turbines, HRSGs, and steam turbines. This arrangement provides for the greatest degree of flexibility, especially when main steam lines are interconnected, and the heat rate is not affected when one unit or component is down. Interconnection of reheat units is not recommended due to steam distribution control problems. A single turbine can also be used when this arrangement with some loss of flexibility and a higher heat rate when one HRSG or combustion turbine is down. Of course, both trains are down when the steam turbine is down. Again, a diverter damper would add to flexibility.

Figure 2-3 illustrates an arrangement with three combustion turbines, three HRSG arrangements, and two steam turbines. It can also be configured with a single turbine; however, this arrangement improves system availability by not having the entire output dependent on the operation of a single steam turbine. Part-load operation (when one combustion turbine or HRSG is down) is more likely to occur with this arrangement because of the high number of components and higher likelihood that one will be down. This arrangement, however, presents problems in staged construction and may only be appropriate for a unit constructed in one stage.

Topping cycles with and without reheat have also been considered and evaluated, but are not included because the existing turbines (over 40 years old) are not considered salvageable at a lesser cost than new equipment.[3]

Since two steam turbine pedestals are already in place at Chesterfield, along with major elements of the circulating water system that can be salvaged, a two-steam-turbine arrangement is favored. This arrangement has the additional advantage of allowing the installation to be constructed in two phases, should the need develop.

Concurrent with this preference, a two-combustion-turbine arrangement is preferred over a three-combustion-turbine arrangement if staged construction is desired.[4]

The three-HRSG, two-turbine arrangement would be preferred over the single turbine arrangement if the smaller units are selected.

Therefore, a two-train configuration appears to offer the most advantages for Chesterfield.

Various Cycle Arrangements

Table 4 summarizes the expected performance of a typical

[3]This determination was made based upon maintenance records and Virginia Power's experience with similar vintage turbines.

[4]Due to the change in predicted need for capacity, the two-unit arrangement now has preference.

Table 4 Case summary

CASE NO.	DESCRIPTION	No. Cts	HP	RH	IP	LP	Percent SF	Output MW	Heat Rate Btu/kWH
1A	Existing Turbines	2	800	--	--	35	0	301	Base
1B	Existing Turbines	2	800	--	--	35	25	340	+664
2	Intermediate Pressure Turbines	2	1450	--	600	35	0	301	- 50
3	Intermediate Pressure Turbines	3	1450	--	600	35	0	452	- 50
4	High Pressure Turbines with Reheat	2	1800	800	600	35	0	301	-338

combustion turbine matched with high and intermediate-pressure steam cycles, and single and multiple pressure HRSGs with and without reheat. All heat rates are expressed in the lower heating value (LHV) of the fuel. This table illustrates the trade off between efficiency and cycle complexity.

Case 1A illustrates an 800 psig (5516 kPa) boiler, dual pressure HRSG without supplemental firing suitable for repowering the existing turbines. The output is 301 MW (301,000 kW) at a heat rate of 7240 Btu/kWh (7639 kJ/kWh).

Case 1B reflects the improvement in output attainable with light supplemental firing and resulting increase in heat rate. This arrangement might be very suitable for both base load and peaking service.

Case 2 reflects the improvement in efficiency achieved with a higher pressure, multipressure HRSG, and turbine.

Case 3 illustrates the maximum output achieved with three of these combustion turbines.

Case 4 represents the fully developed very high-pressure, multipressure combined cycle with reheat.

Combined Cycle Options

A fully developed combined cycle containing all the elements required to achieve the minimum heat rate is shown in Fig. 3. It consists of combustion turbine, HRSG, steam turbine, condenser, deaerator, deaerator recirculation, feedwater, and condensate systems. The HRSG consists of a superheater, reheater, main steam evaporator and economizer, intermediate pressure evaporator and economizer, low-pressure evaporator and economizer, and low-temperature economizer. Not all of these are required for a given installation. The relative merits of each, in relation to Chesterfield's needs, are discussed in the following paragraphs.

Reheat Versus Nonreheat. A reheat combined cycle provides the optimum in waste heat recovery and cycle efficiency. Although one is yet to be built, there appears to be nothing inherent in the design that would preclude its construction. Without supplemental firing, the superheater and reheater would be in parallel. With supplemental firing and attemperation, a series configuration is possible. Other elements include an HP economizer, an intermediate-pressure evaporator and economizer for secondary steam admission, and a low-pressure evaporator and economizer for deaerator steam and feedwater heating.

A deaerating condenser is an option which could reduce equipment costs. Also, NO_x steam can be obtained directly from the HRSG.

It should be noted that the GE7F is the only studied CT capable of producing an effective reheat cycle without supplementary firing.

Supplemental Firing. Supplemental firing is used to raise the temperature and increase the steam production of smaller units. It involves injecting and burning fuel in the exhaust of the gas turbine before it enters the HRSG. It is made possible by the approximately 400 percent excess air in the turbine exhaust. Since the exhaust is already at 1000°F (538°C), its temperature can be raised to 1400°F (760°C) or 1600°F (871°C) and higher without significant losses except for minor moisture and radiation. Although not as efficient as the combined cycle itself, it is, nevertheless, a very efficient method for extending the HRSG performance.

When used with reheat, the reheater can be positioned downstream of the superheater requiring desuperheating of the main steam.

Table 5 Fuel comparisons

		FUEL OILS		
	Nat. Gas	No. 2	No. 6	MBtu Gas
Heating Value B/lb	21,500	18,500	18,500	6,250
Derating Required	NO	NO	YES	NO
Special Equipment	NO	NO	YES	YES
Pretreatment Req'd	NO	NO	YES	NO
Heating Req'd	NO	NO	YES	NO
Fouling Potential	NO	NO	YES	NO
Corrosion Potential	NO	NO	YES	NO (2)
SF Firing	YES	YES (1)	Not Recommended	YES
NO_x Steam Ratio	0.2:1	0.8:1	0.8:1	0.5:1

(1) CORROSION POTENTIAL IN HRSG
(2) CORROSION POTENTIAL VARIES WITH PROCESS

Single Pressure Versus Multipressure HRSG. To achieve the optimum heat recovery from the gas turbine exhaust, a multiple-pressure HRSG may be required. The additional heat removal sections permit the lowering of the stack (exit) temperature from about 400°F to 300°F (204 to 149°C) and below. A low-pressure evaporator and economizer is also necessary for deaerator steam and feedwater heating. Therefore, at least two pressures are recommended. A third, intermediate, pressure may be required if there is a significant difference between the high and low-pressure ratings. The disadvantage is in the added complexity of the feedwater circuit, including pump and level control systems. For peaking duty, a single-pressure HRSG is quicker starting and simpler to maintain in hot standby condition. For both base load and intermediate duty, a dual-pressure unit appears most appropriate.

High-Pressure Versus Low-Pressure HRSG. The pressure of the HRSG directly affects cycle efficiency and steam flow. Since the higher pressure ratings are likely to require triple-pressure HRSGs, as discussed earlier, the lower end of the pressure range appears better suited for peaking service while providing reasonable efficiency during the baseload life.

Low-Temperature (LT) Economizer. A low-temperature economizer, inserted after the deaerator economizer, can be used to further the stack temperature lower (and improve efficiency) when acid condensation is not a consideration. When utilizing dual fuel systems (sulfur-bearing oils), the LT economizer may have to be bypassed. Also, a feedwater heater incorporated in the cycle would have the same effect.

Fuels

Fuel selection influences a gas turbine in the areas of equipment life and equipment availability and heat rate. Most fuels are available at the site by rail, barge, pipeline, or truck delivery. The fuel characteristics are compared in Table 5.

Natural gas is a clean, low-sulfur, cool-burning fuel with the highest heating value and is ideally suited for gas turbines. It does not require any pretreatment or storage and has the lowest requirement for NO_x control steam.

The No. 2 and No. 6 oils are hot-burning fuels, and usually contain contaminants and various amounts of sulfur which can require pre- or posttreatment. The high temperatures, combined with the corrosive effects of sulfur and erosive ef-

Table 6 Cycle configuration comparison; peaking versus base load

	PEAKING	BASE LOAD
Pressure	Intermediate	High
Pressure Levels	Single/Dual	Triple
Reheat	No	Yes
Fuel	Nat. Gas/No. 2	Nat. Gas/MBtu/No. 2
No. HRSGs	Individual	Individual
No. Turbines	Individual	Individual or Single
Supplemental Firing	Yes	Yes (1)

(1) INFLUENCES HEAT RATE

fects of contaminants, can greatly reduce the life and day-to-day availability of gas turbines; in some cases they may require up to a 5 percent derating.

MBTu fuels are medium Btu gases (300 to 400 Btu/scf, or 11.2 to 14.9 MJ/m^3) produced from any of several coal gasification processes. Because the heating value is only one third that of natural gas, the fuel flow rate must be three times higher. Significant machine modifications can be required in some machines to convert to MBtu gas.

Because of its tendency to produce large deposits of molten ash, No. 6 fuel oil is not recommended with waste heat boilers without soot blowers. For peaking duty, No. 6 may be a tolerable fuel since adequate off-line time is available for cleaning. However, because of this need for frequent (weekly) cleaning or washing, it is not recommended for base load operation. Also, due to the need for sootblowers, No. 6 oil requires larger HRSGs.

The high-temperature fuels (oils) require more NO_x suppression steam than the gaseous fuels.

Cycling Versus Base Load Duty

Because of the load growth projection in the Virginia Power service area referred to earlier, the initial requirement for power in 1991 will be for daily cycling duty. Following normal growth patterns, this will be converted to base load by the year 2000. Therefore, the requirement is for a facility that functions as an intermediate for the first half of its life and as a base-loaded unit for the last half. It may also undergo several changes in fuel throughout its life. A summary of the features considered most suitable for each application is shown in Table 6.

For the peaking case these are single, intermediate-pressure, nonreheat HRSG and steam turbine for each combustion turbine. Suitable fuels are natural gas, No. 2 fuel oil, and No. 6 fuel oil.

For intermediate loads, a multipressure, intermediate-pressure HRSG with reheat is preferred. Suitable fuels would be No. 2, natural gas, or MBtu gas.

For the base-loaded case, multipressure, high-pressure HRSGs with reheat and clean burning fuels are preferred in order to achieve optimum efficiency and minimum downtime.

As can be seen, no single configuration is considered ideal for all applications.

Diverter Damper

The use of a diverter or bypass damper between the combustion turbine and the HRSG has an influence upon unit flexibility, operability, and availability.

Although a historically high-maintenance item, dampers do allow the combustion turbine to operate when the steam cycle is down. The indicated difference in equivalent availability between a unit with dampers and one without can be between 0.5 and 2 percent. System economics must also be considered in the decision.

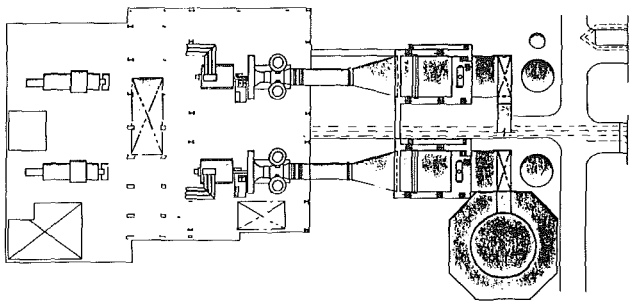

KRAFTWERK V84

Fig. 4

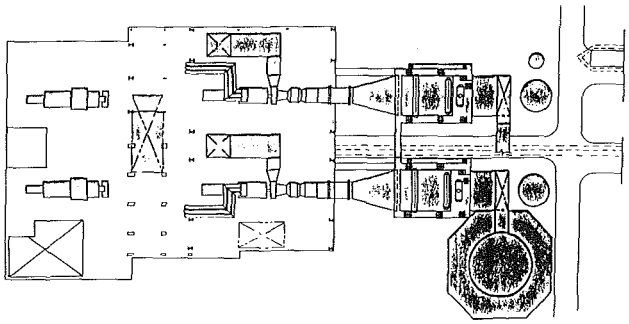

WESTINGHOUSE 501D

Fig. 5

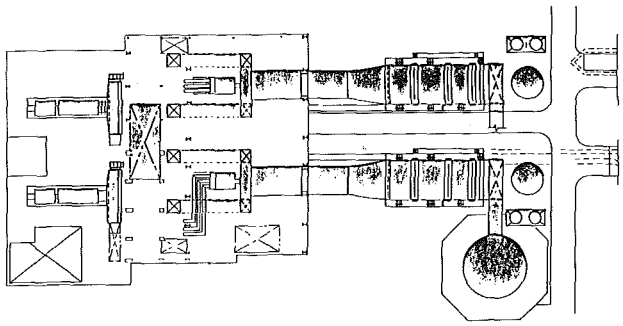

GENERAL ELECTRIC - 7F

Fig. 6

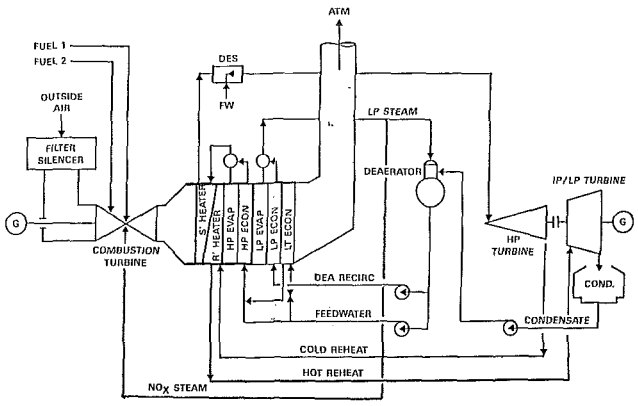

Fig. 7 Preferred cycle

Reuse of Existing Facilities

The major equipment items in the plant, including turbines, feedwater heaters, and condensers and pumps were not con-

sidered suitable for reuse by virtue of age and accumlated running time. The structures, however, including the turbine building, turbine pedestals, and boiler foundations, appear to be adequate for the size and weight of the new equipment.

Figures 4, 5, and 6 show general arrangements for two-unit combined cycles on the existing footings and foundations. The space can also accommodate three Westinghouse or Kraftwerk combustion turbines in a three-unit configuration, although this is much more crowded.

The circulating water inlet and discharge structures are also reusable after refurbishment. This eliminates river dredging and associated permits. The circulating water lines may require replacement to ensure an additional 20-year operating life.

Recommended Arrangement

The preferred arrangement is the two-combustion-turbine arrangement. Of these, the GE7F option offers several advantages; it is the only unit which can produce the 400 MW (400,000 kW), with reheat (efficiently), and without supplementary firing. Therefore, it also has the lowest combined cycle heat rate.

Figure 7 shows a preliminary cycle arrangement for the 7F.

Performance of the Integrated Gas and Steam Cycle (IGSC) for Reheat Gas Turbines

K. Takeya

H. Yasui

Engineering Research Association for Advanced Gas Turbines, Tokyo 105, Japan

In 1978, the Japanese government started a national project for energy conservation called the Moonlight Project. The Engineering Research Association for Advanced Gas Turbines was selected to research and develop an advanced gas turbine for this project. The development stages were planned as follows: first, the development of a reheat gas turbine for a pilot plant (AGTJ-100A), and second, a prototype plant (AGTJ-100B). The AGTJ-100A has been undergoing performance tests since 1984 at the Sodegaura Power Station of the Tokyo Electric Power Co., Inc. (TEPCO). The inlet gas temperature of the high-pressure turbine (HPT) of the AGTJ-100A is 1573 K, while that of the AGTJ-100B is 100 K higher. Therefore, various advanced technologies have to be applied to the AGTJ-100B HPT. Ceramic coating on the HPT blades is the most desirable of these technologies. In this paper, the present level of development, and future R & D plans for ceramic coating, are taken into consideration. Steam blade cooling is applied for the IGSC.

Introduction

Since 1978, The National Research and Development Program for Energy Conservation Technology, called the Moonlight Project, has been conducted by the Ministry of International Trade and Industry (MITI) of Japan.

Under the master program, a new combined cycle plant having a target total efficiency of 55 percent has been under development at the Engineering Research Association for Advanced Gas Turbines. This high-efficiency combined cycle plant consists of a high-efficiency reheat gas turbine and a conventional steam turbine.

As the first step, the AGTJ-100A reheat gas turbine has been developed for a pilot plant whose target combined cycle efficiency is 50 percent. The AGTJ-100A is a twin spool reheat gas turbine with an intercooler, which is a water-spray type direct heat exchanger. The high-pressure system consists of the high-pressure compressor (HPC), high-pressure combustor (HC), and high-pressure turbine (HPT). The intermediate turbine (IPT), reheat combustor (RH), low-pressure turbine (LPT), and low-pressure compressor (LPC) comprise the other spool.

In the case of the IGSC evaluation, superheated high-pressure steam is injected into the front of the HC and then superheated much higher to the HPT inlet temperature. This is the key point for the IGSC to maintain high plant thermal efficiency. See the references at the close of the paper.

Conditions of the IGSC. The reheat gas turbine inlet temperature is 1300°C for the HPT and 1175°C for the LPT, which is the same as the level in the reheat gas turbines being developed under the Moonlight Project in Japan. The cooling blade/nozzle metal temperatures are 800°C/850°C, which are also the same as in the Moonlight Project. The HPT, IPT, and LPT are all steam cooled. Furthermore, the inlet gas temperature of the RH is always kept at 800°C in order to protect it from high-temperature damage.

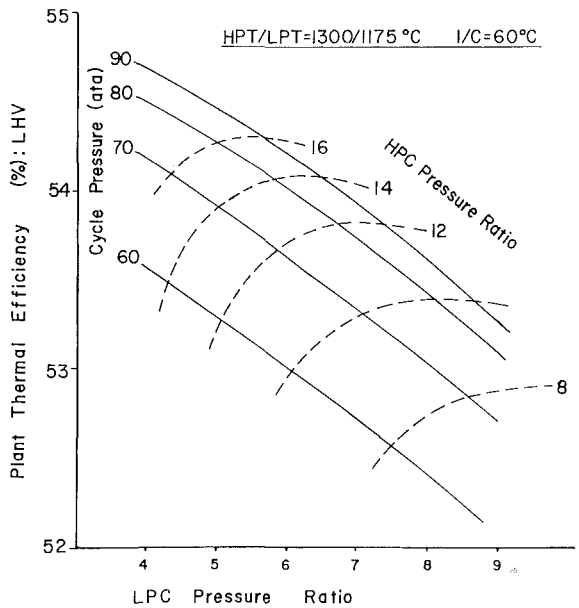

Fig. 1 Plant thermal efficiency of IGSC

Contributed by the Gas Turbine Division of THE AMERICAN SOCIETY OF MECHANICAL ENGINEERS and presented at the 32nd International Gas Turbine Conference and Exhibit, Anaheim, California, May 31–June 4, 1987. Manuscript received at ASME Headquarters April 10, 1987. Paper No. 87-GT-264.

Table 1 Assumed efficiency and pressure loss

(1)	LPC efficiency (polytropic)	91 percent
(2)	HPC efficiency (polytropic)	90 percent
(3)	HPT efficiency (polytropic)	85 percent
(4)	IPT efficiency (polytropic)	86 percent
(5)	LPT efficiency (polytropic)	89 percent
(6)	LPC inlet pressure loss	100 mmAq
(7)	LPT outlet pressure loss	400 mmAq
(8)	Intercooler pressure loss	2.0 percent
(9)	High-pressure combustor pressure loss	3.5 percent
(10)	Reheater pressure loss	2.5 percent
(11)	HP shaft mechanical loss	1.7 percent
(12)	LP shaft mechanical loss	1.0 percent
(13)	Generator loss	1.5 percent
(14)	Leakage air for seal	2.5 percent
(15)	LPC inlet air temperature	15°C
(16)	Inlet air relative humidity	60 percent
(17)	LHV of fuel (NG)	11.701 kcal/kg
(18)	Theoretical combustion air/fuel ratio	16.9
(19)	Steam turbine efficiency (adiabatic)	85 percent
(20)	Steam turbine condenser pressure	0.05 atm
(21)	Maximum steam temperature of *S/T*	566°C
(22)	Maximum steam pressure of *S/T*	169 atm
(23)	Pinch point of HRSG	20°C

Gc : Coolant flow Gg : Main gas flow

Tc : Coolant temp Tg : Main gas temp

Tm : Blade/Nozzle metal temp

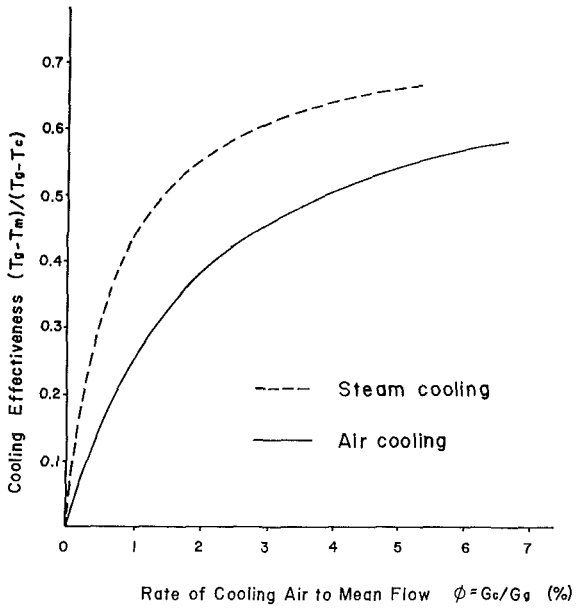

Fig. 2 Cooling effectiveness of steam and air cooling blades/nozzles

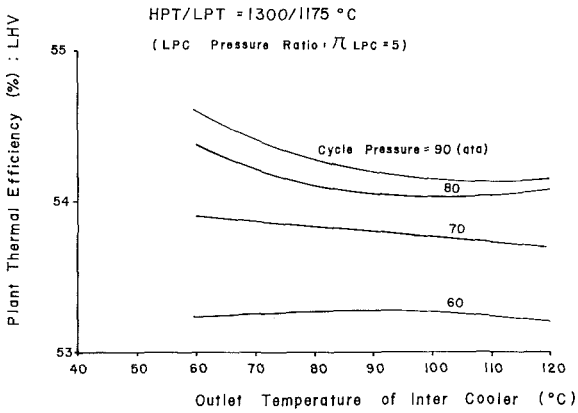

Fig. 3 Thermal efficiency influence of intercooler temperature

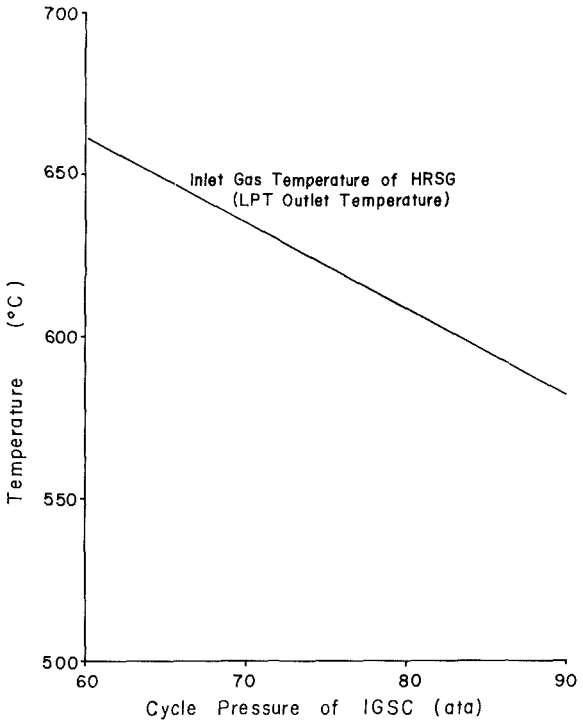

Fig. 4 Gas temperature of HRSG by cycle pressure of IGSC

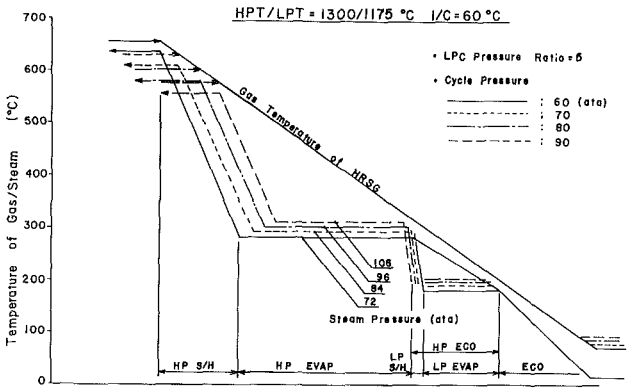

Fig. 5 Temperature characteristics of HRSG for IGSC

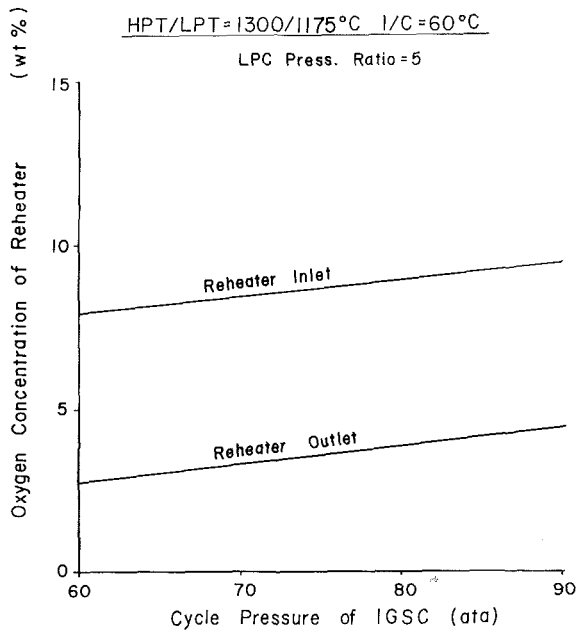

Fig. 6 Oxygen concentration of reheater

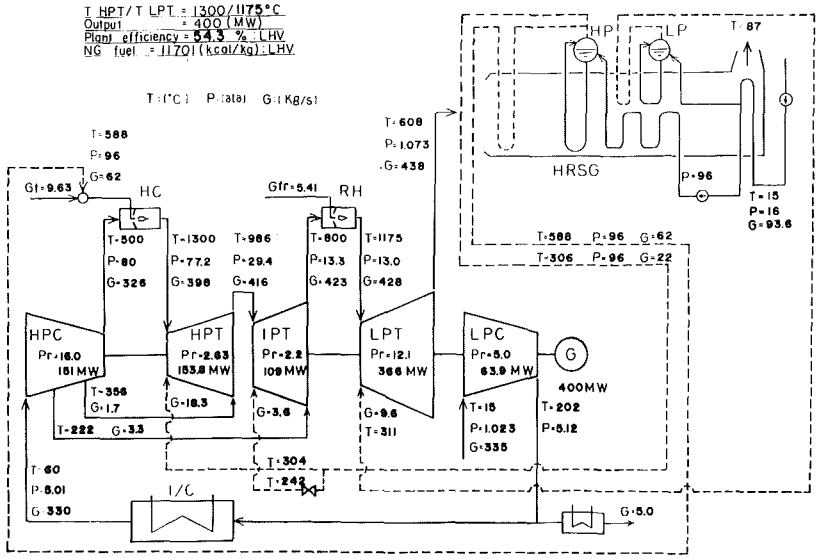

Fig. 7 Heat balance of IGSC

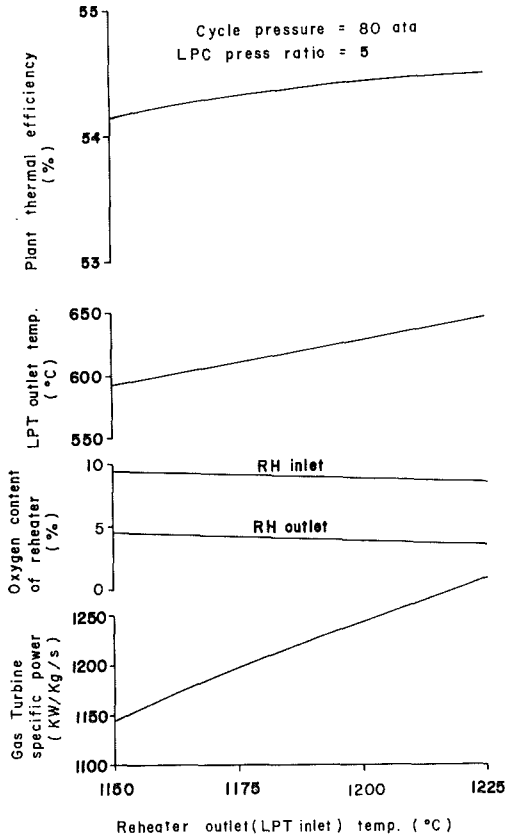

Fig. 8 Influence of reheater outlet temperature on performance of IGSC

Cycle Pressure and Thermal Efficiency of the IGSC. When the temperature conditions of the IGSC are decided on, the next question is how to choose the cycle pressure and the distribution of the pressure ratio between the LPC and HPC.

Figure 1 shows the plant thermal efficiency characteristics of the IGSC by the two parameters of cycle pressure and LPC/HPC pressure ratio. The efficiency increases as the cycle pressure increases and the LPC pressure ratio decreases.

This means that the plant thermal efficiency increases as the cycle pressure decreases, if the LPC pressure ratio decreases even further. However, the LPT outlet temperature increases as the cycle pressure decreases and the influence of the LPC pressure ratio on the LPT outlet temperature is very small. The characteristics of the LPT outlet temperature according to the cycle pressure are shown in Fig. 4. Hence, the minimum cycle pressure depends on the maximum temperature selected for the LPT outlet.

The assumed efficiency and pressure loss is shown in Table 1. The efficiency of the turbines and compressors is defined in terms of polytropic efficiency in order to prevent the influence of pressure ratio deviation.

The steam and air cooling flow to the blades and nozzles is calculated based on the model of cooling effectiveness shown in Fig. 2.

Intercooler Outlet Temperature and Thermal Efficiency of the IGSC. Although the thermal efficiency of reheat gas turbines is affected by the intercooler outlet temperature, the IGSC is not affected in this way, as shown in Fig. 3. Consequently, the design temperature of the intercooler outlet depends on the choice of maximum temperature of the HPC outlet and the materials of the HPC blade.

Heat Recovery Steam Generator. The temperature characteristics of the HRSG inlet gas according to the pressure of the IGSC are shown in Fig. 4. The temperature decreases if the cycle pressure is increased. Figure 5 shows the temperature diagram of the HRSG.

In this case, the minimum limited outlet gas temperature of the HRSG is set at 80°C and clean fuel is used, to protect against corrosion from the acid dew point.

Oxygen Concentration in Inlet Gas of Reheater. Significantly more oxygen is consumed in the high-pressure combustor in order to superheat the injected steam. Furthermore, the cooling steam of the blade/nozzle is mixed into the main gas flow, so the oxygen concentration in the inlet gas of the reheater is quite lean. The characteristics of oxygen concentration are shown in Fig. 6. It must be demonstrated whether stable burning can be achieved with only 9 wt percent oxygen. In our experience from development tests on the reheater in the Moonlight Project, the stability of burning mainly depends on the temperature of the inlet gas at a low

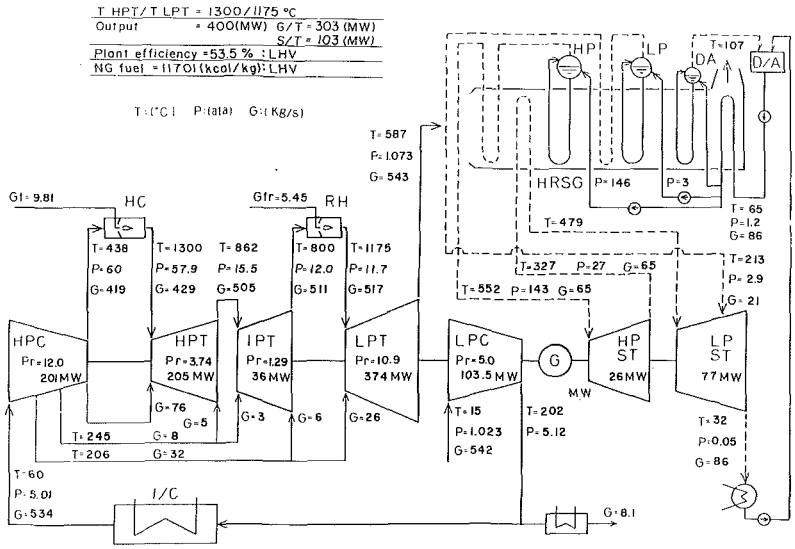

Fig. 9 Heat balance of combined cycle

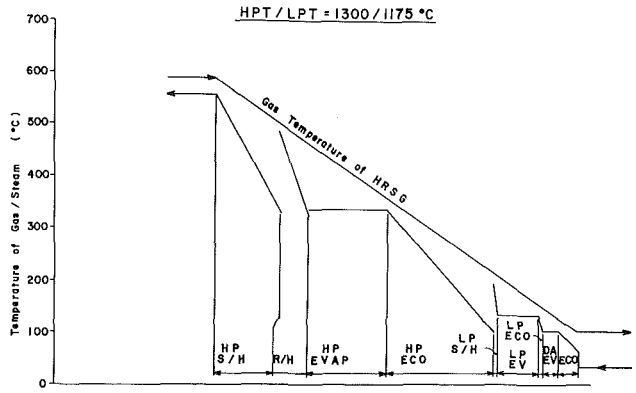

Fig. 10 Temperature characteristics of HRSG for combined cycle

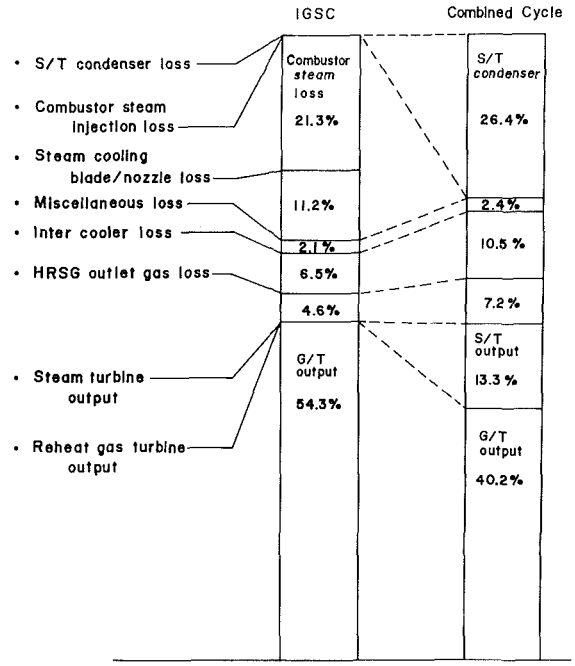

Fig. 11 Bar chart of heat energy flow

concentration of oxygen. Hence, stable burning can be maintained at an inlet gas temperature in the reheater as high as 800°C.

Heat Balance of IGSC. An example of one case is shown in Fig. 7. The conditions of heat balance were an HPT inlet temperature of 1300°C, an LPT inlet temperature of 1175°C, a cycle pressure of 80 atm, and an LPC pressure ratio of 5 in this example.

The calculated plant thermal efficiency was 54.3 percent at the LHV. In this case, the output capacity of the reheat gas turbine was 400 MW, the LPC inlet air flow was 335 kg/s, and the LPT exhaust gas flow was 438 kg/s. The value of flow was within the range of recent high-capacity conventional gas turbines, which means that the machine size of the rotating parts can be designed to the same level as in conventional gas turbines, allowing an output capacity as high as 400 MW to be realized from the aspects of fluid dynamics and structural strength.

Figure 8 shows the influence on performance of raising the reheater outlet temperature from 1150°C to 1200°C under the same pressure conditions. The plant thermal efficiency does not increase in proportion to the increase in reheater outlet temperature.

The main requirement for overcoming the lack of increase in plant thermal efficiency is an increase in the steam cooling flow to the LPT blades and nozzles.

Combined Cycle of Reheat Gas Turbines

Combined Cycle Systems. In this paper, one definition of the combined cycle is the replacement of combustor steam injection in the IGSC by a steam turbine generator; the cooling blades/nozzles of HPT, IPT, and LPT are air cooled by extracting air from the HPC instead of the steam.

In the combined cycle, the condition of the steam from the HRSG is limited to 566°C, 169 atm, even if the inlet gas temperature of the HRSG is sufficiently high.

The steam turbine is composed of a high-pressure turbine and reheat turbine, with the induction of superheated low-pressure steam to the intermediate stage of the reheat turbine. The reheated steam temperature is controlled to keep the steam dry ratio of outlet steam at more than 93 percent.

Performance of the Combined Cycle. In order to compare the performance of the combined cycle, the conditions of the

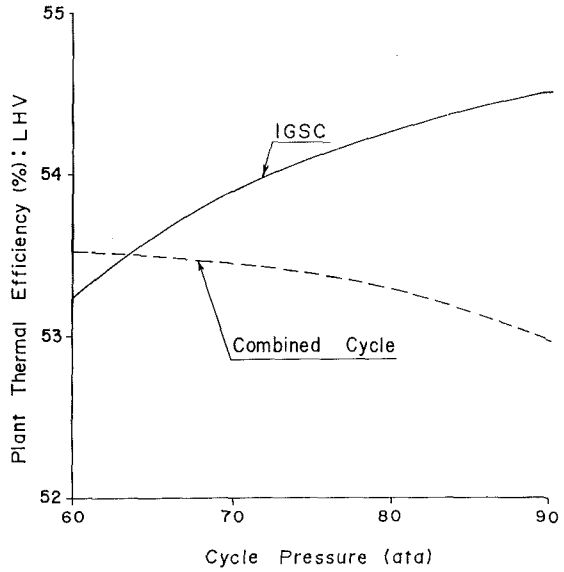

Fig. 12 Influence of combined cycle system on plant thermal efficiency

reheat gas turbines were kept the same as in the IGSC. The heat balance of the combined cycle is shown in Fig. 9. The pressure conditions chosen were a cycle pressure of 60 atm and an LPC pressure ratio of 5, which are the optimum values for performance. The inlet air flow of the LPC was 542 kg/s at 400 MW output, this output being comprised of 300 MW from the reheat gas turbines, and the remaining 100 MW from the steam turbine.

The temperature characteristics of the HRSG are shown in Fig. 10.

Conclusions

The plant thermal efficiency of the IGSC can be expected to be 54 percent, which is comparable to the conventional combined cycle. In Fig. 11, the heat loss ratios of the systems are shown.

Figure 12 shows the influence on plant thermal efficiency of the combined cycle systems. At the combined cycle system of the reheat gas turbines, the cycle pressure does not influence the plant thermal efficiency as much as the IGSC.

As described above, since the IGSC has a plant thermal efficiency equivalent to or higher than that of conventional combined cycles, it has the advantage that no steam turbine systems are required, resulting in a reduction in product costs.

References

1 Rice, I. G., "The Reheat Gas Turbine With Steam-Blade Cooling—A Means of Increasing Reheat Pressure, Output, and Combined Cycle Efficiency," ASME JOURNAL OF ENGINEERING FOR POWER, Vol. 104, Jan. 1982, pp. 9–22.

2 Mori, K., Kitajima, J., Kimura, T., and Miki, S., "Preliminary Study on Reheat Combustors for Advanced Gas Turbines," ASME JOURNAL OF ENGINEERING FOR POWER, Vol. 104, Jan. 1982, pp. 1–8.

3 Rice, I. G., "The Integrated Gas/Steam Nozzle With Steam Cooling, Part I—Application," ASME Paper No. 84-GT-134, 1984.

4 Rice, I. G., "The Integrated Gas/Steam Nozzle With Steam Cooling, Part II," ASME Paper No. 84-GT-135, 1984.

5 Messerlie, R. L., "Integration of the Brayton and Rankine Cycle to Maximize Gas Turbine Performance—A Congeneration Option," ASME Paper No. 84-GT-52, 1984.

6 Digumarthi, R., and Chang, C.-N., "Cheng-Cycle Implementation on a Small Gas Turbine Engine," ASME JOURNAL OF ENGINEERING FOR GAS TURBINES AND POWER, Vol. 106, July 1984, pp. 699–702.

7 Lloyd Jones, J., "Design and Construction of the First Commercial Cheng Cycle Series 7 Congeneration Plant," ASME Paper No. 84-IGT-122, Sept. 1985.

8 Rice, I. G., "Thermodynamic Evaluation of Gas Turbine Cogeneration Cycles: Part II—Complex Cycle Analysis," ASME JOURNAL OF ENGINEERING FOR GAS TURBINES AND POWER, Vol. 109, Jan. 1987, pp. 8–15.

9 Larson, E. D., and Williams, R. H., "Steam-Injected Gas Turbines," ASME JOURNAL OF ENGINEERING FOR GAS TURBINES AND POWER, Vol. 109, Jan. 1987, pp. 55–63.

10 Burnham, J. B., Giuliani, M. H., and Moeller, D. J., "Development, Installation, and Operating Results of a Steam Injection System (STIG™) in a General Electric LM5000 Gas Generator," ASME JOURNAL OF ENGINEERING FOR GAS TURBINES AND POWER, Vol. 109, July 1987, pp. 257–262.

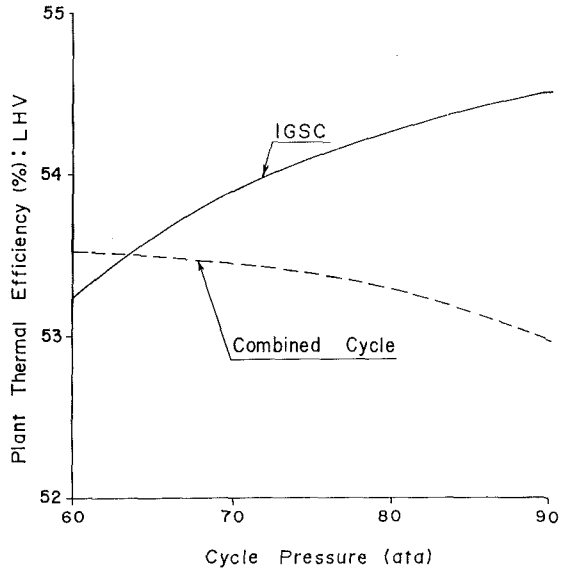

Fig. 12 Influence of combined cycle system on plant thermal efficiency

reheat gas turbines were kept the same as in the IGSC. The heat balance of the combined cycle is shown in Fig. 9. The pressure conditions chosen were a cycle pressure of 60 atm and an LPC pressure ratio of 5, which are the optimum values for performance. The inlet air flow of the LPC was 542 kg/s at 400 MW output, this output being comprised of 300 MW from the reheat gas turbines, and the remaining 100 MW from the steam turbine.

The temperature characteristics of the HRSG are shown in Fig. 10.

Conclusions

The plant thermal efficiency of the IGSC can be expected to be 54 percent, which is comparable to the conventional combined cycle. In Fig. 11, the heat loss ratios of the systems are shown.

Figure 12 shows the influence on plant thermal efficiency of the combined cycle systems. At the combined cycle system of the reheat gas turbines, the cycle pressure does not influence the plant thermal efficiency as much as the IGSC.

As described above, since the IGSC has a plant thermal efficiency equivalent to or higher than that of conventional combined cycles, it has the advantage that no steam turbine systems are required, resulting in a reduction in product costs.

References

1 Rice, I. G., "The Reheat Gas Turbine With Steam-Blade Cooling—A Means of Increasing Reheat Pressure, Output, and Combined Cycle Efficiency," ASME JOURNAL OF ENGINEERING FOR POWER, Vol. 104, Jan. 1982, pp. 9–22.

2 Mori, K., Kitajima, J., Kimura, T., and Miki, S., "Preliminary Study on Reheat Combustors for Advanced Gas Turbines," ASME JOURNAL OF ENGINEERING FOR POWER, Vol. 104, Jan. 1982, pp. 1–8.

3 Rice, I. G., "The Integrated Gas/Steam Nozzle With Steam Cooling, Part I—Application," ASME Paper No. 84-GT-134, 1984.

4 Rice, I. G., "The Integrated Gas/Steam Nozzle With Steam Cooling, Part II," ASME Paper No. 84-GT-135, 1984.

5 Messerlie, R. L., "Integration of the Brayton and Rankine Cycle to Maximize Gas Turbine Performance—A Congeneration Option," ASME Paper No. 84-GT-52, 1984.

6 Digumarthi, R., and Chang, C.-N., "Cheng-Cycle Implementation on a Small Gas Turbine Engine," ASME JOURNAL OF ENGINEERING FOR GAS TURBINES AND POWER, Vol. 106, July 1984, pp. 699–702.

7 Lloyd Jones, J., "Design and Construction of the First Commercial Cheng Cycle Series 7 Congeneration Plant," ASME Paper No. 84-IGT-122, Sept. 1985.

8 Rice, I. G., "Thermodynamic Evaluation of Gas Turbine Cogeneration Cycles: Part II—Complex Cycle Analysis," ASME JOURNAL OF ENGINEERING FOR GAS TURBINES AND POWER, Vol. 109, Jan. 1987, pp. 8–15.

9 Larson, E. D., and Williams, R. H., "Steam-Injected Gas Turbines," ASME JOURNAL OF ENGINEERING FOR GAS TURBINES AND POWER, Vol. 109, Jan. 1987, pp. 55–63.

10 Burnham, J. B., Giuliani, M. H., and Moeller, D. J., "Development, Installation, and Operating Results of a Steam Injection System (STIG™) in a General Electric LM5000 Gas Generator," ASME JOURNAL OF ENGINEERING FOR GAS TURBINES AND POWER, Vol. 109, July 1987, pp. 257–262.

DISCUSSION

Ivan G. Rice[1]

The authors propose to integrate the reheat gas turbine with the steam cycle whereby all the steam generated by the heat recovery boiler is injected directly into the gas turbine, thus eliminating the steam turbine, condenser, and associated cooling tower. A large 400-MW steam-injected reheat gas turbine, which is to be some four times larger than the largest present-day industrial simple-cycle unit, is projected. The authors are complimented on their courage in projecting this cycle. This discussion is submitted to bring out several additional points relevant to the cycle not covered by the authors and to request their comments on these points.

Discussion of Paper

It is the conclusion of this discussor, as well as the authors, that the effect of reheating the high-pressure injection steam to the full reheat temperature is appreciable, which accounts for the overall cycle improvement above that of the reheat-gas-turbine combined cycle. References [1, 2] are cited as initial studies on this subject made by this discussor in 1979. Steam injected into the compressor discharge, whether with the fuel or used as steam-blade cooling, improves overall cycle efficiency as was shown in these initial studies. At the time the 1979 papers referred to were published, it was not known just how much primary steam could be injected before the reheat combustion stability and efficiency became a problem. Tests conducted by the Japanese indicate that vitiation by full primary-steam injection can be dealt with by keeping the reheat combustor entrance temperature high—at about 800°C.

Nothing is said in the paper under discussion about NO_x pollution, but the added steam injection no doubt greatly reduces NO_x formation. The authors are requested to comment on NO_x reduction relevant to the IGSC cycle.

It is assumed, in reviewing the cycle data of Table 1, that the polytropic IPT turbine efficiency of 85 percent takes into account the diffuser loss of the high-velocity gas exit to the reheat combustor. The 2.5 percent pressure loss seems inadequate otherwise. The authors might choose to comment on this point.

Figure 1 of the paper clearly shows the effect of the intercooler heat rejection. As the intercooler LPC pressure ratio increases, the cycle efficiency falls off for any given overall cycle-pressure ratio. The authors are requested to comment on why the curves of Fig. 1 were not extended to the left to the point where the efficiency no longer improves. This point takes place at about 2 atm pressure according to this discussor's calculations [3]. There can, therefore, be a case made to intercool at this lower LPC ratio to optimize cycle efficiency.

Similarly, in regard to the 80 cycle pressure in Fig. 3, it is observed that the plant thermal efficiency rises noticeably as

[1]P.O. Box 233, Spring, TX 77383; Fellow ASME.

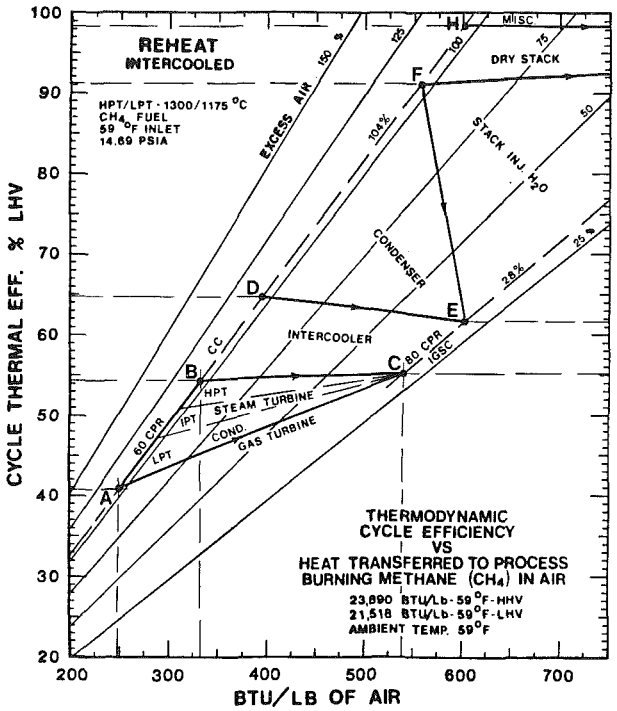

Fig. 1 Plot of percent heat distribution versus heat transferred for the Japanese combined cycle and IGSC cycle

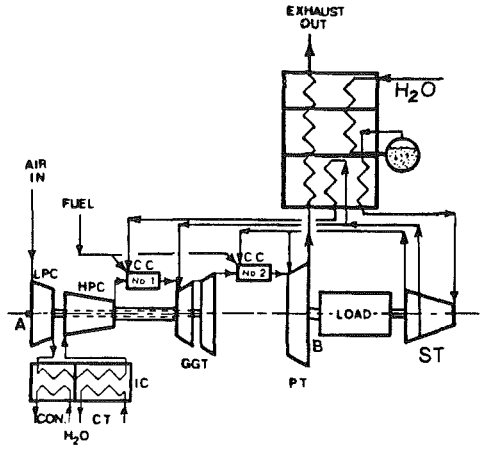

Fig. 2 Schematic diagram of intercooled reheat gas turbine IGSC cycle incorporating a topping steam turbine

the outlet temperature of the intercooler is lowered. It is wondered why the authors did not select an intercooler outlet temperature of perhaps 30°C instead of 60°C to yield a 55 percent plant efficiency.

It is interesting to note in Fig. 12 that the combined cycle peaks out at a cycle pressure ratio of about 60, whereas the IGSC cycle continues to rise—even past a cycle pressure of 80, which was the pressure selected for the example of Fig. 7.

The use of steam-blade cooling, as shown in Fig. 7, is noteworthy. The cooling effectiveness of steam versus air shown in Fig. 2 illustrates the superior cooling characteristics of steam. Therefore, steam-blade cooling should be applied to the combined cycle also.

Heat Distribution

This discusser has taken the data from Figs. 7, 9, and 11 and has plotted the distribution of heat input (cycle efficiency) against heat output in terms of Btu/lb of air and presents the resulting graph as Fig. 1 of this discussion. This graph has an advantage over the bar chart as it shows specific work and fuel input in terms of percent excess air. The development of this graphic solution is given in [3] of this discussion.

Considering the reheat gas turbine combined cycle, the gas turbine work contribution is shown as point A for the calculated 104 percent excess air. No electric-generator loss is considered. The air flow of 534 kg/s after the intercooler was used in the calculation. The continuation at constant excess air to point B represents the contribution of the steam turbine. Point B to D indicates the intercooler loss and point D to F the condenser loss. The dry stack loss is shown by proceeding from point F to point H, whereas the remainder of heat to the 100 percent line covers the miscellaneous loss of about 1.6 percent.

Taking into account the reheat-gas turbine integrated cycle, the excess air is calculated to be 28 percent based on an air flow of 330 kg/s at the intercooler exit. The gas turbine output is given as point C where the steam-turbine power of the LPT, IPT, and HPT does not exist, because all the steam generated is injected into the gas turbine. The intercooler loss is shown as point C to E. Note that the stack-injected H_2O loss point is off the graph to the right at 28 percent excess air projection (point G). The dry stack loss and miscellaneous loss points are likewise off the graph to the right. Intermediate points between A and C and B and C reflect varying degrees of excess air and condensing steam-turbine output.

It is interesting to note that the largest loss of the combined cycle, that of condenser (D to F), shifts to the stack-injected H_2O loss for the ISGC cycle. The condenser loss is dominated by the latent heat of the water condensed, and likewise the stack-injected H_2O loss is predominantly the latent heat of the injected steam at the boiler exhaust. The second largest loss occurs as intercooler loss which can be noted in Fig. 1 of this discussion. In accordance with the second law of thermodynamics, these two losses can be evaluated in terms of exergy with the prospect of rearranging the IGSC cycle to reduce these two highest losses. This will be discussed below.

Topping Steam Turbine

Reference is made to the schematic diagram, Fig. 2, of this discussion. In this arrangement a topping steam turbine is connected to the end of the load. The heat-recovery steam generator produces high-pressure, high-temperature steam at perhaps 2400 psig and 1000°F (16.6 MPa and 538°C). The gas turbine is shown to be an aero-derivative type with a cycle pressure ratio of 35 to 40. Intercooling takes place at a low compressor-pressure ratio of 2 to 2½.

The discharge steam from the topping steam turbine is divided such that about 30 percent goes to cool the gas-generator blading and about 50 percent is reheated to the 1000°F (538°C) level before being injected into the high-pressure combustor or compressor discharge. The remaining 20 percent is expanded in the topping steam turbine and is then used for the power turbine and reheat combustor cooling/injection. Selecting a cycle pressure ratio of about 40 makes it possible for the topping steam turbine to have an expansion ratio of 4—a conventional and practical arrangement. Considering a cycle pressure ratio of 80, as suggested by the authors, creates a problem for the topping steam turbine. The throttle pressure would have to be supercritical and the turbine would be rather unconventional.

A plot of cycle thermal efficiency versus LPC pressure ratio for the topping-steam-turbine arrangement is given in Fig. 3 of this discussion. This graph shows the cycle efficiency rising as the LPC pressure ratio is reduced and is similar to what the authors presented. The maximum efficiency for intercooling is seen to occur at an LPC ratio between 2 and 2½. Point A pinpoints a gas generator such as the LM5000. Point B shows the

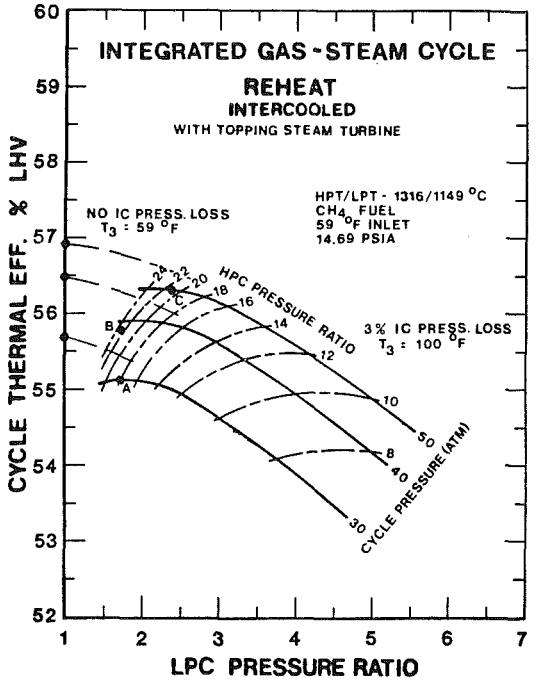

Fig 3 Graph of cycle efficiency versus LPC pressure ratio when topping steam turbine is applied

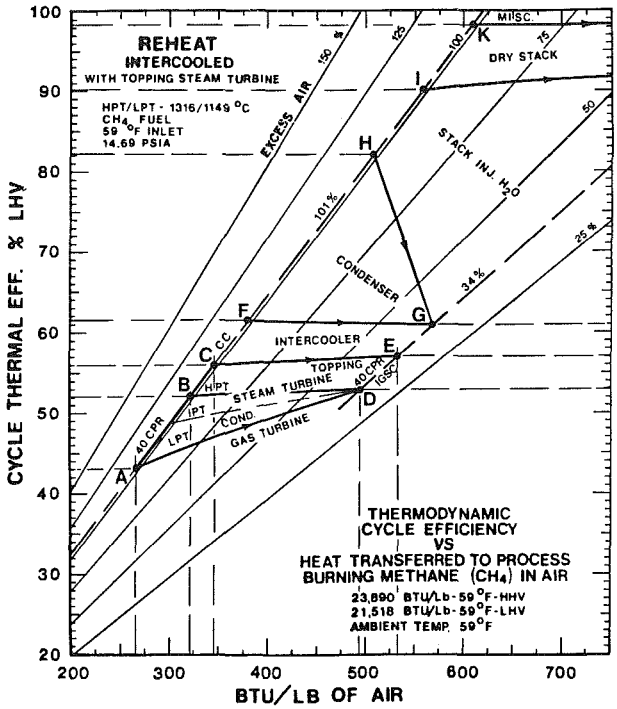

Fig. 4 Plot of percent heat distribution versus heat transferred for intercooled reheat gas turbine combined cycle and the IGSC cycle, both incorporating topping steam turbines

38 CPR engine developed by the NASA E^3 program, and point C represents a supercharged version of the E^3 engine.

Note that the cycle efficiency is greatest where there is no intercooler and where there is no parasitic pressure loss and intercooler heat rejection. Note the dots on the left vertical scale. Therefore, there remains a strong case for eliminating the intercooler—particularly where less oxygen is consumed by the first combustion whereby more oxygen is left for the reheat combustor to insure better combustion.

Figure 4 of this discussion presents a plot of percent heat input distribution versus associated cycle output values for the 40 cycle pressure-ratio arrangement. Considering the combined-cycle configuration at 101 percent excess air, point A represents the reheat gas turbine output and point A to B includes the condensing IPT and LPT steam turbine. The values from B to C give the topping power of the HPT. The intercooler loss is given by point C to point F. The condenser loss is from F to H. The steam-blade cooling loss is represented by H to I, and the dry-stack loss I to K. The top 1.6 percent covers the miscellaneous loss.

Consider now the IGSC cycle at 34 percent excess air again for a 40 cycle pressure ratio. Point D represents the gas turbine power. Point D to E gives the topping steam-turbine power. The intercooler loss is shown as point E to G. The stack injection H_2O loss goes from G to J (off the graph to the right). The dry stack loss is given as J to L (off the graph). The miscellaneous loss is again at the very top of the graph. It can be seen that the overall cycle efficiency is improved to about 57 percent over the 55 percent of the author's IGSC cycle. Refer to Fig. 1 of this discussion. The cycle efficiency increase is due to the added steam-turbine topping power and the reduced intercooler loss.

Data presented in Fig. 4 give rise to the prospect of developing a cycle whereby the reheat excess air is about 70 percent. In this instance, the steam flow to the condenser is reduced by perhaps 50 percent and the steam turbine LPT can be a far less expensive single-flow arrangement. Of course, the condenser and cooling towers would be greatly reduced also, but the flexibility to take load swings on the condenser would remain.

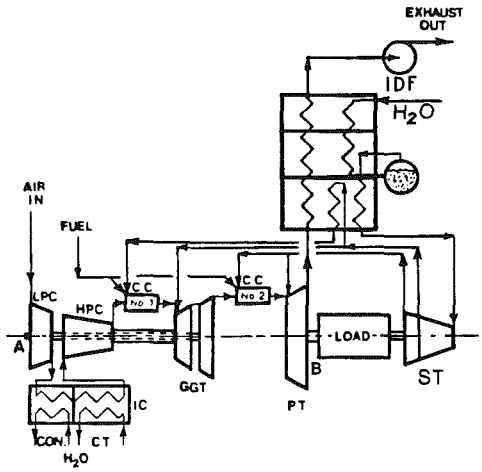

Fig. 5 Schematic diagram of the inverted IGSC cycle incorporating an exhaust induced draft fan (IDF)

Inverted Cycle

The inverted cycle has been suggested by Wilson [5] as a way to obtain incremental power from the combined cycle. Reference is made to Fig. 5 of this discussion. An induced draft fan (IDF) is placed at the heat-recovery steam-generator exit whereby the exhaust flow is compressed by the fan to a pressure of perhaps 25 in. H_2O (0.635 m of H_2O). The system operates on the differential expansion power produced and compression power required.

Considering equal expansion and compression ratios, a constant K value (ratio of specific heat) and a constant specific heat, the ratio of power generated to the power consumed is given by the following formula:

$$\frac{P_{TG}}{P_{FM}} = \frac{T_T}{T_F} \times n_T \times n_F \times E_G \times E_M \qquad (1)$$

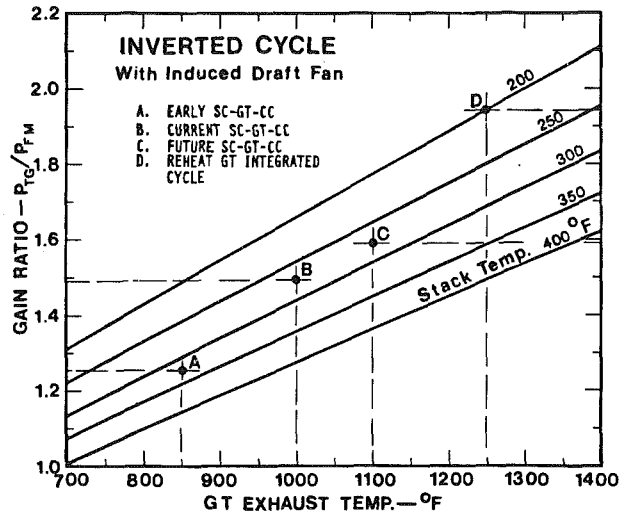

Fig. 6 Inverted cycle gain ratio versus gas turbine exhaust temperature for various boiler stack temperatures

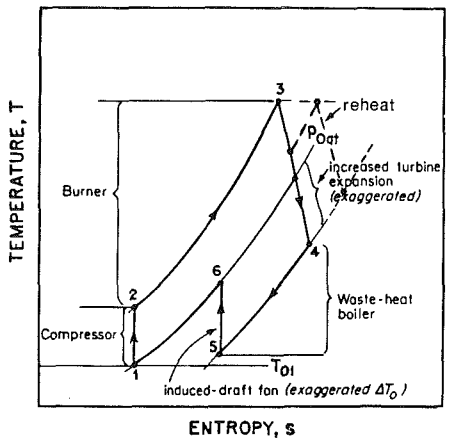

Fig. 7 Simple cycle gas turbine inverted cycle temperature-entropy diagram with dashed lines showing reheat

where: P_{TG} = incremental power of the turbine generator; P_{FM} = incremental power of the fan motor; T_T = absolute temperature of the turbine exhaust; T_F = absolute temperature of the fan inlet; n_T = turbine isentropic expansion efficiency; n_F = fan isentropic compression efficiency; E_G = generator electrical efficiency; E_M = motor electrical efficiency.

Selecting typical values for the efficiencies of 0.89, 0.89, 0.985, and 0.96, respectively, yields the following formula:

$$\text{Gain ratio} = \frac{P_{TG}}{P_{FM}} = 0.749\,\frac{T_T}{T_F} \qquad (2)$$

A plot of formula (2) for various stack temperatures is given in Fig. 6 of this discussion. In the early years there was not a very great incentive to apply this cycle which can be noted by point A. Current units, represented by point B, show possibilities where the gain ratio is about 1.5. Future simple-cycle combined cycles incorporating such new machines as the GE-7F with its 1100°F (593°C) exhaust temperature show more promise. Refer to point C and [6]. However, when the exhaust temperature reaches 1200 to 1300°F (649 to 704°C) which is the case for the reheat gas turbine, point D, either for the combined cycle or the steam injected IGSC cycle, the gain ratio reaches about 2 and the cycle becomes compelling. For example: considering a 5000 kW IDF fan, the gas turbine generator would produce 10,000 kW incremental power which would give a net gain of 5000 kW of gas turbine topping power—of course at a slightly reduced exhaust temperature.

A T-S diagram of the inverted cycle for the simple-cycle gas turbine operating with a boiler, taken from [5], is presented as Fig. 7 of this discussion. Note the increase in work area of the diagram. The reheat gas turbine offers a greater increase, which can be concluded. The magnitude of power increase and cycle efficiency increases for the reheat gas turbine cycles would be approximately a modest 1½ percent for the inverted cycle.

Alternate Heat Recovery

Figures 1 and 4 of this discussion clearly show that the greatest cycle loss takes place because of the latent heat rejection of the H_2O either in the condenser for the combined cycle or at the stack for the IGSC cycle. This loss can also be expressed as exergy when applying the second law of thermodynamics to relate to availability. The hope of improving cycle efficiency in either cycle, therefore, lies in somehow reducing this high H_2O latent heat rejection.

One possible improvement lies in attacking the condenser loss. Absorption by ammonia is reported by Kalina and Leibowitz [7] at this 1987 Annual Gas Turbine Institute Conference as a way, in effect, of lowering the stack temperature and reducing the condenser loss, thus improving the combined cycle efficiency. In the Kalina cycle the relationship of the heat transfer to the ammonia-water mixture and the Second Law efficiency also plays an important part regarding exergy.

Fuel reforming is likewise being studied as a means of reducing the latent H_2O heat rejection out the stack of the IGSC cycle by using the exhaust heat to reform either methanol or methane (CH_4) to a greater heating value by a steam and catalytic endothermic reaction. Discharge of steam out the stack is reduced in the process. Reforming of methanol has been reported by Seglem [8] and Janes [9] as a way to improve combined-cycle efficiency when applying a simple-cycle turbine. It might be possible to apply the reheat gas turbine to take advantage of the turbine's elevated exhaust temperature. The exhaust heat that is required to heat and reform the fuel would be regenerated back into the gas turbine at topping efficiency. At the same time the gas would be humidified for NO_x control.

Summary

The authors are graciously thanked for their contribution to the state-of-art by this paper and are requested to kindly comment on any work their organization is doing in the area of (*a*) reheat gas turbine cycle pressure ratios of 30 to 50 with a low LPC pressure ratio; (*b*) reduction in NO_x, (*c*) cycles applying a topping steam turbine; (*d*) cycles using the inverted cycle principle; (*e*) bottoming cycles applying the Kalina cycle; and (*f*) cycles involving CH_4 heating, humidifying and/or reforming—all aspects which have been touched upon in this discussion.

This rather bold paper is a significant step forward by the authors toward the optimization of the reheat gas turbine integrated cycle.

References

1 Rice, I. G., "Steam-Cooled Blading in a Combined Reheat-Gas-Turbine, Reheat-Steam-Turbine Cycle: Part I—Performance Evaluation," ASME Paper No. 79-JPGC-2.

2 Rice, I. G., "Steam-Cooled Blading in a Combined Reheat-Gas-Turbine, Reheat-Steam-Turbine Cycle: Part II—Design Considerations," ASME Paper No. 79-JPGC-GT-3.

3 Rice, I. G., "Evaluation of the Compression-Intercooled Reheat-Gas-Turbine Combined Cycle," ASME Paper No. 84-GT-128.

4 Rice, I. G., "Thermodynamic Evaluation of Gas Turbine Cogeneration Cycles: Part I—Heat Balance Method Analysis," ASME JOURNAL OF ENGINEERING FOR GAS TURBINES AND POWER, Vol. 109, 1987, pp. 1-7.

5 Wilson, D. G., *The Design of High-Efficiency Turbomachinery and Gas Turbines*, The MIT Press, Cambridge, MA, 1984, Chap. 3, pp. 135–139.
6 Tomlinson, R. O., et al., "GE Stag 107F Combined Cycle—Highest Efficiency Electric Utility Power Generator," American Power Conference, 1987.
7 Kalina, A., and Leibowitz, H. M., "Applying Kalina Technology to a Bottoming Cycle for Utility Combined Cycles," ASME Paper No. 87-GT-35.
8 Seglem, C. E., "Performance of Combined Cycle Power Plants Fueled by Methanol," The American Chemical Society Mid-Atlantic Meeting, 1979.
9 Janes, C. W., "Increasing Gas Turbine Efficiency Through the Use of a Waste-Heat Methanol Reactor," 8412-0513-2/79/0779-423, The American Chemical Society, 1979.

C. P. Ashworth[2]

The paper "Performance of the Integrated Gas and Steam Cycle (IGSC) for Reheat Gas Turbines" is another encouragement to those of us who believe much could be gained by getting cycles of this general type into general utility use.

I include in this general type the whole gamut of mass-steam-injected gas turbine cycles – basically cycles which expand steam with the gas in gas turbine and eliminate a separate steam turbine cycle. For simplicity, I will refer to any such concepts as steam-injected cycles, including IGSC.

My company sponsored an early development project at International Power Technology, Inc., on its patented Cheng cycle, named for IPT's founder, Dr. Dah Yu Cheng. The purpose of the project was to develop features to make the Cheng cycle attractive for utility use.

Following work with IPT, Pacific Gas and Electric and General Electric jointly funded development of a minor-modified version of its commercial LM5000 aircraft-derivative gas turbine, the steam-injected gas turbine (STIG) which boosted output and efficiency significantly.

The joint effort with General Electric also identified an intercooled STIG (ISTIG) as a very attractive further development of the LM5000 STIG. Several STIGs have been sold and we expect that market success with STIGs will lead eventually to intercooled versions.

We have also discussed with others development of topping devices for gas turbines for these kinds of cycle, something akin to superchargers except at the high-temperature part of the cycle. But our own budget constraints have prevented us so far from getting such work underway. These are intended to provide improvements to these cycles by adding small components rather than doing major gas turbine development.

We have pursued these cycles for reasons which were not mentioned in the paper. The principal reasons are:

- These cycles appear to be suitable for small units, and, consequently, suitable for innovation and high-tech improvement.
- These cycles make direct use of the products of well-funded U.S. aircraft gas turbine development.

The principal competitor or alternative to steam-injected cycles is the combined cycle, which has a separate steam turbine cycle. Combined cycles get more attention than steam-injected cycles and currently have better economy and efficiency. However, combined cycles have more components than steam-injected cycles and optimize to much larger units. Some people see this as making them ideal for utilities: "utility size," that is, units of substantial size, in the hundreds of megawatts.

I do not see large size as an advantage and do not like the concept that says things must be large to be utility size. High tech tends to come easier in smaller sizes and large size does not always bring economy. Considering that heavy truck engines are today more efficient and lower in cost per kilowatt than supercritical steam power plants, utility size for some applications may mean truck engines.

[2]Pacific Gas and Electric Company, San Francisco, CA.

The point is that steam-injected cycles should not play second fiddle to combined cycles just because the latter are good for large units. I think steam-injected cycles should be considered equally.

Currently, steam-injected cycles do not match the economy and performance of the best combined cycles, but they come close enough that utility application for them can be found. Once established, they should be judged for their potential.

Steam-injected gas turbine cycles can be made very attractive without being scaled up to large sizes. They can use aircraft-derivative gas turbines. Aircraft engines do not give the best combined cycles.

But the real plus for steam-injected gas turbine cycles is their promise and potential. The intercooled STIG promises to be at least as economic as the best combined cycle. More importantly, aircraft gas turbines are currently the most advanced state-of-the-art gas turbines in service, and hundreds of millions of dollars per year are committed to advance them further. There is simply no way for heavy industrial gas turbine development for use in combined cycles to keep up with aircraft gas turbine development short of a major commitment by a major industrial nation. In U.S. technology, aircraft gas turbines are run routinely on test stands with gas inlet temperatures hundreds of degrees hotter than industrial gas turbines used in large combined cycles. Concept assessments which do not take this difference into account are simply not making valid comparisons. It stands to reason, at least for the U.S., that the sooner steam-injected gas turbine cycles come into a competitive position in utility gas-fired generation, the sooner we will have gas-fired generation technology on a faster development track – and substantially improved products.

My view of steam-injected cycles versus combined cycles as a contest between high tech in small scale and slow tech in large scale is obviously simplistic and could prove wrong. Combined cycles are the best we have today. My concern is that if utilities do not warm up to steam-injected cycles we may be stuck on a path of scaleup, slowed-down technology improvement, and loss of competitiveness.

The paper shows just one promising advancement that can be considered for steam-injected cycles. There are many others. Some promising concepts have been disclosed to us in confidence and I cannot discuss them. Let me just briefly mention a few nonconfidential concepts to illustrate how many ways, including IGSC, there are to improve steam-injected cycles substantially.

First and foremost is the concept being pursued by General Electric and the federal Clean Coal Program to broaden the market for existing STIGs to include coal applications by an optimal coupling of STIGs with coal gasification through the innovation of hot-gas-cleanup. This concept is to be demonstrated in a $165 million project which appears to have about 80 percent of the required funding already lined up.

This concept goes together well enough that it promises the same economy with an existing STIG at 50 megawatts as a 400–500 megawatt integrated coal gasification combined-cycle plant which uses the best available combined cycle. GE seems to be ambivalent about selling turbines for either small gasification STIGs or large gasification combined cycles. But I cannot see why, given a choice, any utility would want to buy 400–500 megawatt units if it could accomplish the same costs in 50 megawatt increments.

Successful demonstration of the integrated coal gasification, hot gas cleanup, STIG would stimulate development of the intercooled STIG (ISTIG) previously mentioned.

An ISTIG without coal gasification promises a lower heating value efficiency and plant cost per kilowatt in a roughly 100 megawatt size that is fully competitive with much larger combined cycles. With gasification and hot gas cleanup,

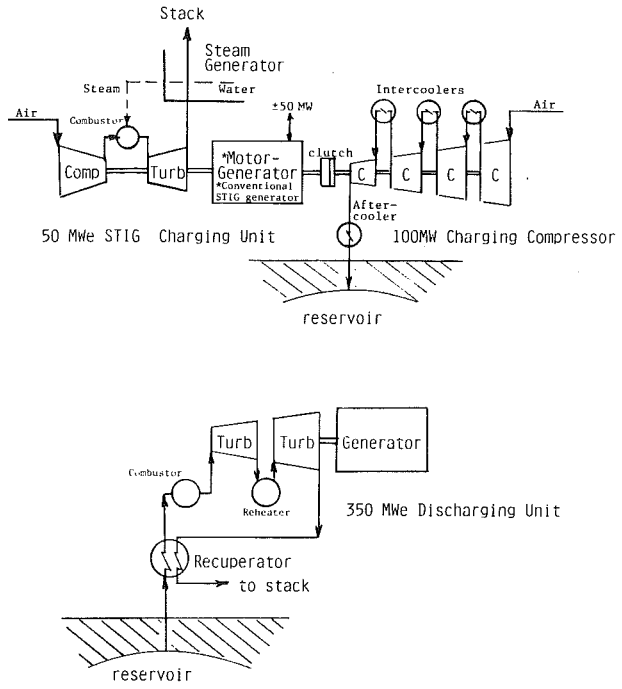

Fig. 1 Grid-augmented STIG-charged Lundberg stored-air power plant: 50 MWe input multiplied to 400 MWe output

it would be superior. However, the ISTIG is not developed and could cost as much as $100 million to develop.

There are ideas for a cheaper-to-develop ISTIG, such as modifying the existing STIG enough to permit spraying a small amount of water into the compressor for evaporative intercooling. But these ideas involve compromises and diversion of resources that have to be justified.

Let me describe another STIG concept to illustrate that large gains may be possible by innovative use of relatively established equipment. This involves the use of a conventional STIG with energy storage.

Energy storage is not just a means of putting away low cost off peak power for use on peak. A concept patented by Bob Lundberg associated with Science Applications International Corporation uses storage to multiply output and reduce cost per kilowatt of a generating plant and to enable the base plant (the commercially available STIG in this case) to operate efficiently base loaded.

Figure 1 adds to the STIG-charged Lundberg concept the ability to store energy from the grid – essentially a combination of Lundberg and conventional compressed air energy storage (CAES).

What we have on the figure is a conventional 50 MW STIG with the collector end of the generator shaft modified to deliver the torque necessary to drive, through a clutch, a 100 MW compressor for reservoir storage. Also tapped into the same reservoir is a 350 MW discharging gas turbine which has no compressor.

With the clutch open, the plant operates as a conventional 50 MW STIG. Reservoir requirements have no impact on design of the STIG; it is standard design, some of which are already in existence. If STIGs improve, improved STIGs can be used. If coal capability is needed, it can be the STIG for an IG-STIG. The STIG can be built as a separate commitment from the rest of the plant, i.e., "phased."

With the clutch closed, the charging compressor, whose discharge must match the reservoir which varies from site to site, draws 100 MW. Despite its rating being double that of the STIG and its use of intercoolers, its cost may be only half that of the STIG. Fifty MW comes from the STIG and the other 50 MW comes from the generator drawing power from the grid. The generator does not need to be modified for motoring because it does not have to be motored up to speed. Except for its rotor load angle lagging the stator instead of leading, the generator does not know the difference whether it is generating or motoring.

With the clutch open and the discharging unit running at full power, the plant output is 400 MW: 50 MW from the STIG and 350 MW from the discharging unit.

The cost/kW (discharge) of the plant can be very low if the large output of the discharge unit can be obtained at low cost (including associated wells) because this multiplies the output of the base unit (the STIG). Alternatively, cost of energy excluding cost of capital can be very low at any capacity factor if the discharge unit is efficient because energy is produced efficiently in all operating components regardless of load swings.

There is obviously a tradeoff between cost and efficiency of the discharge unit that must be optimized to determine whether and how much the concept would benefit. Let's suppose that the multiplication of output provided by storage can be made to pay. I should point out that use of underground reservoirs for storage of compressed gas is not a far-out idea. The gas side of my company makes extensive use of underground natural gas storage under conditions which appear appropriate for this concept.

If storage can be made to pay, notice what it means to the size of the base charging unit. We get a 400 MW output from a 50 MW STIG. Basing a plant like this on a larger more complex concept would not be desirable because gigawatts of output would depend on single unit reliability.

Let me conclude by saying that in the real utility world, small fossil-fuel units of advanced steam-injected cycles variety look potentially attractive for dealing with swinging loads, inflexible sources, and unregulated generation competition. I am glad to see IGSC – another concept being pursued that has much promise.

M. A. El-Masri[3]

The discusser congratulates the authors on their interesting work and would like to offer a few comments for their consideration.

The results of some recent studies by the discusser comparing Intercooled Reheat (ICRH), Nonintercooled Reheat (RH), and Brayton (BR) gas turbine combined cycles are summarized on Figs. 1-3. Those computations are for air-cooled systems with assumptions described in [1]. The study shows that the nonintercooled reheat system provides maximum efficiency, at conditions requiring a high reheat inlet temperature, but can provide excellent efficiencies with acceptable reheat inlet temperatures at very moderate Turbine Inlet Temperature (TIT). It also shows that the nonreheat (Brayton) cycle can provide efficiencies which are slightly higher than those for the ICRH system, provided the TIT is raised to the 1700-1800 K range. The Brayton cycle, however, cannot match the specific power of the ICRH cycle. The level of component technology assumed in the study of [1] is only slightly different from that used in the present papers and is consistently applied to all three cycle types. The computations were carried out using the GASCAN model [2], which accounts for cooling thermodynamic and aerodynamic losses and which has been calibrated to model current advanced engines accurately. Yet another recent study was performed by the author and others [3] in which the nonintercooled reheat cycle was compared to the Brayton cycle using the EPRI GATE program. The results showed good agreement with those of [1]. The discusser therefore invites the authors to pre-

[3]Department of Mechanical Engineering, Massachusetts Institute of Technology, Cambridge, MA 02139.

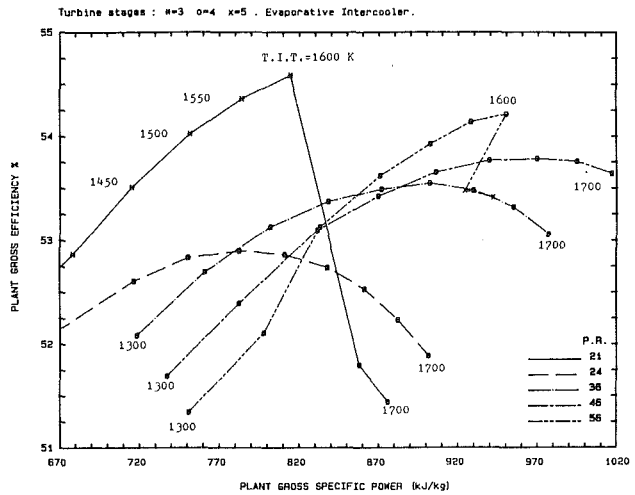

Fig. 1 Performance map for the intercooled reheat combined cycle [1]

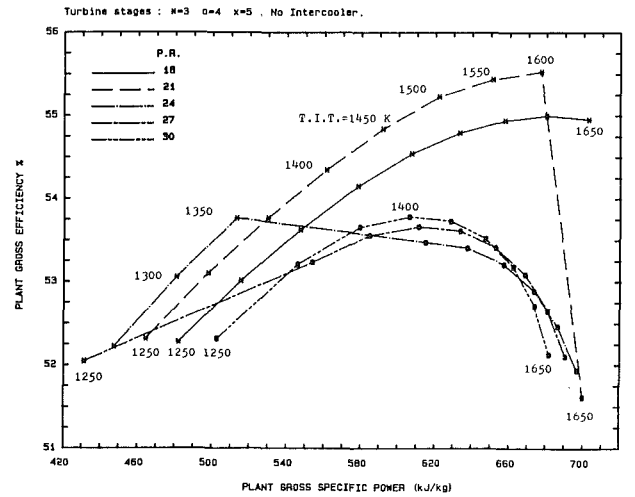

Fig. 2 Performance map for the nonintercooled reheat combined cycle [1]

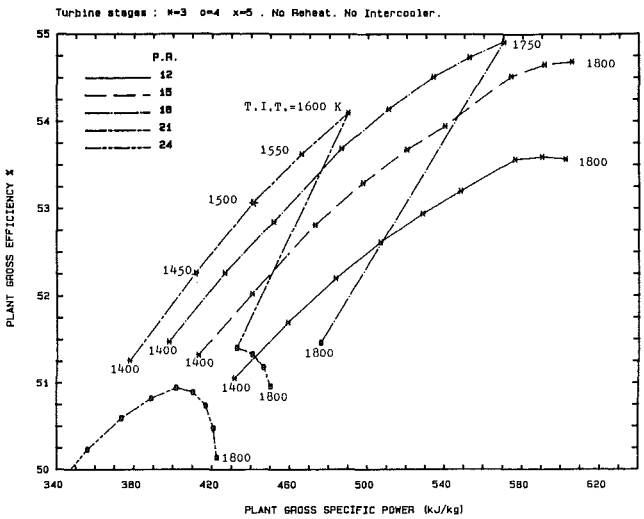

Fig. 3 Performance map for the nonreheat gas turbine combined cycle [1]

sent the performance results based upon their model and assumptions applied to Brayton cycles and nonintercoooled reheat cycles.

On the subject of the integrated cycle compared to the combined cycle, the discusser has shown from thermodynamic considerations that steam injection incurs a fundamental mixing available-work loss of 543 kJ/kg of steam [4]; this loss is not present in the combined cycle, which therefore possesses a fundamental advantage. The discusser would like to suggest that the advantage of the integrated cycle over the combined cycle that appears in the authors' calculations derives more from steam cooling than from steam injection. The authors' comments on the possibility that a combined cycle with steam cooling may be more efficient than the integrated cycle would be appreciated.

References

1 El-Masri, M. A., "Exergy Balance Analysis of the Reheat Gas Turbine Combined Cycle," *Proc. 1987 ASME/JSME Thermal Engineering Conference*, Honolulu, HI, Mar. 22–27, 1987.

2 El-Masri, M. A., "GASCAN—an Interactive Code for Thermal Analysis of Gas Turbine Systems," ASME JOURNAL OF ENGINEERING FOR GAS TURBINES AND POWER, Vol. 110, 1988, this issue.

3 Giglio, R. S., "A Thermodynamic Performance Analysis of a Combined Cycle Engine," S.M. Thesis, Dept. of Mech. Eng. MIT, Cambridge, MA, June 1986.

4 El-Masri, M. A., "A Modified, High-Efficiency, Recuperated Gas-Turbine Cycle," ASME JOURNAL OF ENGINEERING FOR GAS TURBINES AND POWER, Vol. 110, 1988, this issue.

M. Nakhamkin[4] and P. Hoffmann[5]

The paper introduces a number of theoretical and practical considerations applicable to reheat gas turbines without recuperator and with utilization of the exhaust gas heat in heat recovery steam generator (HRSG) for further steam injection before entering a high-pressure (HP) combustor.

The problems presented in the paper and theoretical approaches adopted for problem solutions are similar to those which were used by Dresser-Rand, Inc. (D-R) and Gibbs & Hill, Inc. (G&H) in the course of development of 50-MW turbomachinery for Compressed Air Energy Storage (CAES) plants.

The same problems had to be addressed in the course of both developments: selection of HP and low-pressure (LP) turbine inlet pressures and temperatures; selection of the optimal overall compression pressure ratio (OCPR) and its distribution among compressors with intercoolers; distribution of the expansion pressure ratio between HP and LP turbines.

The similarity of both developments goes even further: turbomachinery for advanced CAES plants has provision for steam injection before entering HP combustors, which is similar to the reheat gas turbine in the paper. The difference is that in the paper's gas turbine, steam is generated in HRSG, while in CAES plant cycles steam is generated in thermal energy storage (TES), which utilizes the compression heat otherwise wasted in intercoolers.

In spite of similar theoretical and technical approaches, the resulting optimized cycles are different for the paper's gas turbine and the turbomachinery for CAES applications.

These differences are consistent with specifics of these two reheat turbomachinery applications.

The following is a discussion of the reheat gas turbine presented in the paper and a parallel description of the 50-MW turbomachinery train for CAES plant with comments on similarities and differences.

[4]Chief Engineer, Gibbs & Hill, Inc.

[5]General Manager, Power Generation Projects, Turbodyne Division of Dresser-Rand, Inc.

Comparative Conceptual Analysis of Reheat Gas Turbine With 50-MW Reheat Turbomachinery for Compressed Air Energy Storage Plant

For the reheat gas turbine the thermodynamic cycle optimum parameters are determined based only on gas turbine economics. The turbomachinery train is one of the most important components of the CAES plant and its engineering required extensive research and development efforts.

The turbomachinery train optimization for CAES application was conducted using a computerized procedure which identifies the most cost effective turbomachinery train parameters based on the consideration of the overall CAES plant economics including underground storage.

Turbomachinery trains for CAES application are engineered based on the following considerations specific for CAES technology:

- Turbomachinery train and underground storage operating parameters are interrelated. Economic calculations indicated that turbomachinery train parameters have a significant impact on both turbomachinery and underground storage economics. Therefore, turbomachinery cycle optimization should be based on economics of the overall CAES power plant, including underground storage.
- Underground storage may limit or even dictate turbomachinery train parameters due to the limitations in the stored air pressure range and temperatures.
- Turbomachinery train must be flexible for adjustments to reflect specific site conditions and electrical systems characteristics.

Figure 1 shows cycle configuration for the 50-MW turbomachinery train.

The optimized turbomachinery trains for the CAES application have the following specifics as compared to gas turbines in the paper.

(A) A number of turbomachinery trains for CAES application differentiated by HP turbine inlet pressures (varying from 295 psia to 882 psia) has been developed, in order to embrace anticipated maximum CAES plant cycle compressed air pressures, dictated or limited by local underground storage conditions. Of two major performance characteristics – heat rate and specific air consumption – the latter is particularly important because it affects required underground storage volume and associated cost. In order to reduce specific air consumption, turbomachinery trains for the CAES application have a reheat, in spite of the slightly higher heat rate associated with reheat.

Comparison of inlet temperatures shows that the CAES turbomachinery has significantly lower HP and LP turbine inlet temperatures, 1000°F and 1670°F, respectively, as compared with gas turbines in the paper (2372°F and 2147°F, respectively). This is explained by the two reasons:

- The CAES turbomachinery has daily startups and cycling with associated thermal fatigue problems. Lower temperatures were selected to provide the required 25–30 years turbomachinery useful life.
- The CAES turbomachinery trains were developed with emphasis on the utilization of components with proven experience.

The HP expander with an inlet pressure of 1000°F is steam turbine derivative and has proven extensive operating experience.

The LP expander is an extension of the high-temperature expander technology. Although it utilizes proven technical procedures and approaches, extensive innovative engineering was required to increase LP expander inlet temperature from 1300°F (typical for industrial expanders) to approximately 1600–1700°F. The innovative engineering was conducted mostly in the area of the design of the cooled first-stage nozzles.

(B) For CAES turbomachinery the OCPR is significantly higher than the overall expansion pressure ratio (OEPR) due to friction and static pressure losses between compressor discharge – deep underground storage – turboexpander inlet plus pressure change in the cavern if it operates with sliding pressure (constant volume uncompensated caverns).

The difference between OCPR and OEPR can be as high as 300 psi to 600 psi, while for conventional reheat gas turbine in the paper it does not exceed 50 psi. As a result of relatively high OCPR, energy consumption by compressors is higher and, hence, much more attention should be paid to the compressor train optimization. OCPR also affects cavern volume: the higher the OCPR the lower the required cavern volume and costs.

Based on these considerations, optimum OCPRs for CAES turbomachinery are approximately the same as for the gas turbine in the paper, although for lower turboexpander inlet temperatures it should be significantly lower.

(C) High OCPR requires typically three to four compressors with intercoolers between them. Distribution of the OCPR among compressors is a subject for optimization based on the compression train capital and operating costs.

Comparative analysis of two optimized compressor trains shows that in the CAES application the optimum LP compressor pressure ratio is significantly higher than the optimum one for the gas turbine in the paper. It is explained by the fact that in the gas turbine, the HP compressor discharge temperature affects fuel consumption and heat rate, which is an important consideration, along with minimization of power required to drive compressors. In the CAES application the compressor train optimization does not affect fuel consumption and therefore, power consumption by compressors is the only valid criterion.

(D) The turbomachinery train has a recuperator which recovers some of the low-pressure turbine exhaust heat for preheating the air from the cavern. The recuperator significantly reduces negative effect of the reheat on the CAES plant heat rate. The gas turbine in the paper has HRSG for recovery of the LP turbine exhaust heat.

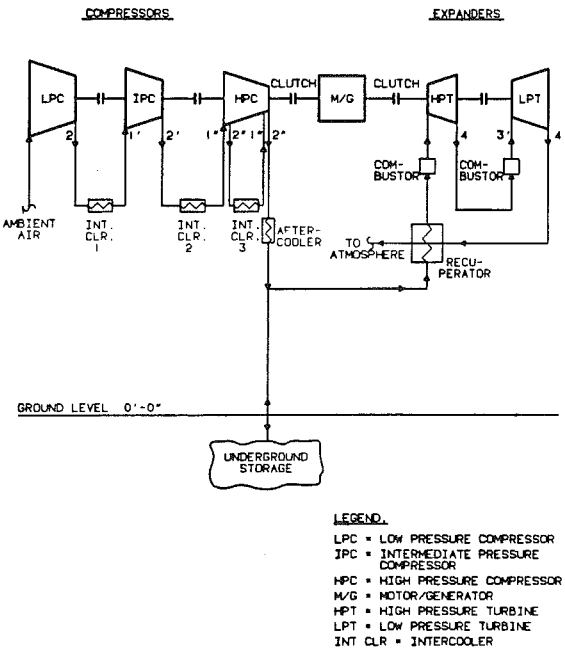

Fig. 1 Flow diagram for conventional CAES cycle

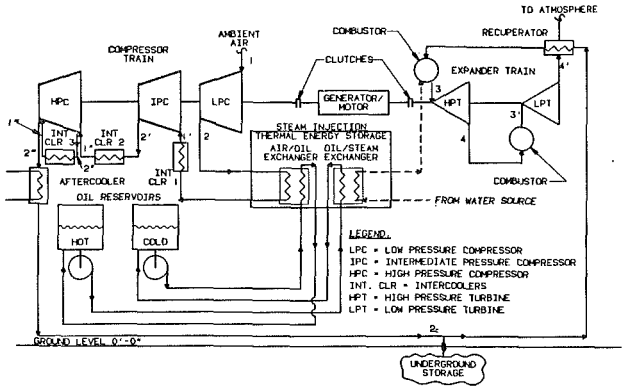

Fig. 2 Flow diagram for CAES plant concept utilizing TES for steam generation and injection into combustor

The shaft location of the major components for the gas turbine presented in the paper impacts significantly on its operational characteristics and therefore deserves special consideration. The analysis shows that schematic with HPC and HPT on one shaft and IPC, LPT, LPC, and electrical generator on another shaft has a number of advantages. Nevertheless the following potential problems associated with part load operations shall be addressed:

(*a*) Due to the relatively similar changes of pressure ratios for HPC and HPT on one shaft and IPC, LPC, and LPT on another shaft, turbine inlet temperatures have a tendency to stay high at reduced air flow. The HP inlet temperature may even exceed the inlet temperature value at design point.

(*b*) The LPC location on the generator shaft significantly limits potential air flow reduction (to avoid surge) and therefore significant turbine inlet temperature reductions are required for reduced load.

(*c*) High inlet turbine temperatures and limits on air flow reduction at part load operations taken together present technical problems which should be properly addressed.

Turbomachinery With Steam Injection

As was mentioned above, the advanced CAES plant concept utilizes turbomachinery with steam generation in TES and injection into turboexpander train. The conceptual configuration of this concept is presented in Fig. 2.

The utilization of heat generated during air compression provides additional premium fuel savings. In a CAES plant, more than 90 percent of purchased off-peak energy is rejected in intercoolers and an aftercooler during the compression mode of operation. TES absorbs the air compression heat (otherwise rejected), stores it, and then returns this heat for usage during peaking/intermediate electric power generation periods. The compression heat is utilized for generation of steam which can be combined with the compressed air and expanded in the turboexpander train to generate additional electric power. This concept has a number of advantages: improved performance and economics and reduced fuel consumption and associated emissions. The technical problems encountered in steam generation and injection portion of these two developments are similar. The major problem is an optimization of steam flow parameters (pressure and temperature) for most cost effective utilization of the compression heat. The turbomachinery equipment for a CAES plant utilizing TES is similar to that of a conventional CAES plant except for necessary adjustments to accommodate the addition of a TES system in the compression cycle and steam generation and injection in the expansion cycle.

G&H conducted the compressor train optimization using a specially developed computerized procedure. The optimized compressor train has four sections of compression similar to that of the conventional compressor trains. A four-section compression train represents the optimum combination of the capital and operating costs of all affected components and systems. The compression pressure ratio for the LP compressor is selected as 13. The balance of the required pressure ratio was evenly divided among three subsequent sections. The overall compression ratio is a subject for optimization and depends on the underground storage type and depth. Inlet air to Sections 2 through 4 is cooled in intercoolers to a temperature of 85°F.

Turboexpander trains with hardware engineered for conventional CAES plants concepts have been used for concepts with steam injection. The combustors have been adjusted to provide for the injection of the saturated steam of the required pressure (before entering HP combustor). The performance characteristics of the turboexpander trains have been adjusted to account for deviations associated with additional steam flows.

Conclusions

(A) Comparative analysis of the reheat gas turbine presented in the paper and the reheat gas turbine for CAES application indicated a number of similar problems and solutions.

(B) The major conceptual technical decisions in the paper are based on sound technical approaches.

(C) In order to assess engineering aspects and practicality of the gas turbine design, additional information is required.

(D) Special attention shall be paid to the reheat gas turbine part-load operation due to considerations presented in the discussion.

A Modified, High-Efficiency, Recuperated Gas Turbine Cycle

M. A. El-Masri
Associate Professor,
Department of Mechanical Engineering,
Massachusetts Institute of Technology,
Cambridge, MA 02139

The thermal efficiency of an intercooled/recuperated cycle may be increased by: (a) evaporatively aftercooling the compressor discharge; and (b) injecting and evaporating an additional amount of water in the recuperator. Comparative computations of such a modified cycle and intercooled/recuperated cycles carried out over a wide range of pressure ratios and turbine inlet temperatures and at two different levels of component technologies show an advantage of over five percentage points in efficiency for the modified cycle. About 60 percent of this improvement results from modification (a) and 40 percent from modification (b). The modified intercooled/recuperated cycle is compared with nonintercooled steam-injected gas turbine systems at each component technology level. The present cycle is found to be superior by about 2.75 percentage points in efficiency and to require a substantially smaller water flow rate. To assist in interpreting those differences, the method of available-work analysis is introduced and applied. This is identical to exergy analysis for systems with a pure-substance working fluid, but differs from the latter for systems using a mixture of pure substances insofar as the thermodynamic dead state is defined for the chemical and phase composition realized at the exhaust conditions of practical engineering devices and systems. This analysis is applied to the heat-recovery processes in each of the three systems considered. It shows that the substantial, fundamental available-work loss incurred by mixing steam and gases in the steam-injected system is the main reason for the superior efficiency of the precent cycle.

Introduction

The efficiency of a Brayton-cycle gas turbine may be improved by recuperators (or regenerators) which recycle a portion of the exhaust energy to preheat compressor discharge air prior to the combustor. Progress in materials technology and design methodology has enabled rotary ceramic regenerators suitable for small engines to achieve heat-exchanger effectiveness of over 93 percent, with pressure drops per steam in the 2.5–5.4 percent range and leakage rates below 4.5 percent [1]. Surface-heat-exchange recuperators, suitable for larger engines and capable of withstanding 922 K (1200°F) exhaust gases have been reported to achieve heat exchanger effectiveness in the 80–91 percent range [2]. Currently available nonintercooled recuperated gas turbine engines achieve thermal efficiencies in the 30–36 percent range [3–5]. A shipboard generator-drive intercooled/recuperated engine is reported to reach 37.8 percent, with advanced development versions projected to provide 43 percent [3].

Since the recuperator utilizes the temperature difference between the exhaust gases and the compressor discharge, its benefit to a Brayton cycle increases at low pressure ratios and high turbine inlet temperatures (TIT). Cycle calculations based upon component efficiencies, metal temperatures and turbine-cooling practice typical of axial-flow utility gas turbines showed that recuperated Brayton cycles offer maximum efficiency at pressure ratios of about 9 and TIT's about 1500 K [6]. For the assumptions of that calculation, an optimum cycle peaks at about 38.5 percent gross[1] thermal efficiency and 250 kJ/kg gross specific power. Unrecuperated Brayton cycles based upon the same set of assumptions achieve approximately 36 percent peak efficiency and 240 kJ/kg at a pressure ratio and TIT of about 26 and 1450 K, respectively [7]. The use of compressor intercooling significantly improves the performance of recuperated cycles, since the compressor work is reduced and the energy lost in the intercooling is mostly recovered by extracting more heat from the exhaust gases in the recuperator. Calculations of intercooed/recuperated cycles without shaft-arrangement constraints show gains of about 3 points in efficiency together with a specific power increase of about 55 percent over those values for the nonintercooled recuperated cycle based upon the same utility-turbine component assumptions [6]. Evaporative water-injected intercoolers were found to offer slightly superior cycle efficiencies over those for surface-heat-exchanger intercoolers, since the

Contributed by the Gas Turbine Division of THE AMERICAN SOCIETY OF MECHANICAL ENGINEERS, and presented at the 32nd International Gas Turbine Conference and Exhibit, Anaheim, California, May 31–June 4, 1987. Manuscript received at ASME Headquarters February 3, 1987. Paper No. 87-GT-13.

[1] Gross output is net cycle work before deducting mechanical losses, electrical losses, or auxiliary power requirements. Net efficiencies after those deductions would be 1–2 points lower.

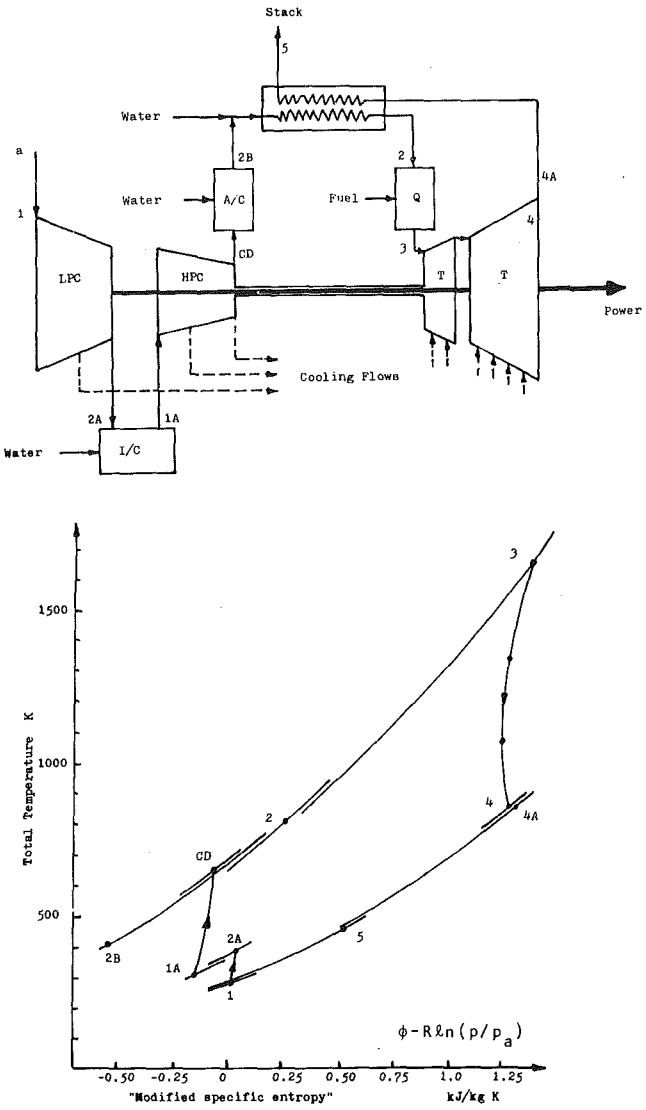

Fig. 1 Schematic of proposed system; numerical values on the bottom plot correspond to the cycle of Appendix 3

former increment the gas flow by the amount of evaporated water with negligible compression work for the liquid phase of that increment up the intercooling pressure.

The maximum amount of turbine-exhaust energy recovered by a recuperator is constrained by two fundamental factors. Firstly the temperature of the cold stream entering the recuperator from compressor discharge is typically well above economically optimum stack gas temperatures. This is true for practical intercooled cycles as well as nonintercooled systems since cycle efficiency for the former occurs at pressure ratios of about twenty, making a two-shaft arrangement with a high-pressure compressor (HPC) spool downstream of the intercooler desirable. The necessity of adequately loading the first turbine stage which drives that spool implies post-intercooling pressure ratios in the range 4–7 and compressor discharge temperatures on the order of 600 K. Underloading the first turbine stage which drives the HPC spool results in higher turbine cooling losses. Secondly since the cold stream entering the recuperator has a much lower heat capacity than the turbine exhaust stream, the temperature difference in such an imbalanced counterflow recuperator increases towards the cold end, further aggravating the problem of recovering energy from the hot stream. This heat-capacity imbalance in a modern axial-flow engine is on the order of 25 percent since the turbine exhaust flow has a higher specific heat and its mass flow is greater than that at compressor discharge by the sum of all turbine-coolant and fuel mass flows.

In the present paper, the modified intercooled/recuperated cycle illustrated in Fig. 1 is proposed and analyzed. It embodies an evaporative aftercooler at compressor discharge followed by a water-injected evaporative recuperator. The first of those features was previously proposed by Lysholm [8] and discussed by Gasparovic and Hellemans [9], who did not consider the influence of additional water injection in the recuperator on the basis that it would reduce cycle efficiency. While that may be true for uncooled gas turbines where the heat-capacity imbalance between the recuperator streams is small, the results presented below show that recuperator water injection results in further significant gains. Foote [10] proposed recuperator water injection without aftercooling.

In this paper results of calculations using the GASCAN model [11] are presented for two-shaft intercooled/recuperated cycles (ICR) with and without evaporative aftercooling and a water-injected recuperator (WIR). The results are presented at two levels of turbine-component technologies. A conservative set of component assumptions similar to those used in [6, 7] is used to represent utility turbines and an advanced set to characterize system performance for power plants based on advanced aircraft-engine component technology. Calculations of Steam-Injected Cycle (STIG) performance are also given for comparison. Those cycles offer excellent cogeneration potential and are being developed by at least two major gas turbine manufacturers [12–16]. The pro-

Nomenclature

Cp = specific heat at constant pressure, J/kg-mole K
d = indicates a differential quantity
h = specific enthalpy, J/kg-mole
h_{fg} = latent heat of vaporization, J/kg-mole
h'_{fg} = $h_{fg} + Cp_f(T_{sat} - T_a)$
i = index representing a component in a mixture
MW = molecular weight
n = mole flow rate, kg-mole/s
p = total pressure, N/m^2
Q = heat rate, W
R = universal gas constant, J/kg-mole K
s = specific entropy, J/kg-mole K
T = total temperature, K
v = specific volume, m^3/kg-mole
ϕ = the function $T_a\int^T Cp\, dT/T$, J/kg-mole K
ω = specific available work, J/kg-mole K
ω' = specific exergy = $h - T_a s$, J/kg-mole K
Ω = available-work rate, W
Ω' = exergy rate, W

Subscripts

a = ambient
c = coolant
f = liquid water
g = gas
L = lost
sat = saturated
w = water, H_2O

Abbreviations and Acronyms

HRSG = Heat Recovery Steam Generator
ICR = Intercooled/Recuperated
PR = Pressure Ratio
RH = Relative Humidity
STIG = Steam-Injected Gas Turbine
TIT = Turbine Inlet Temperature
WIR = Water-Injected Recuperator

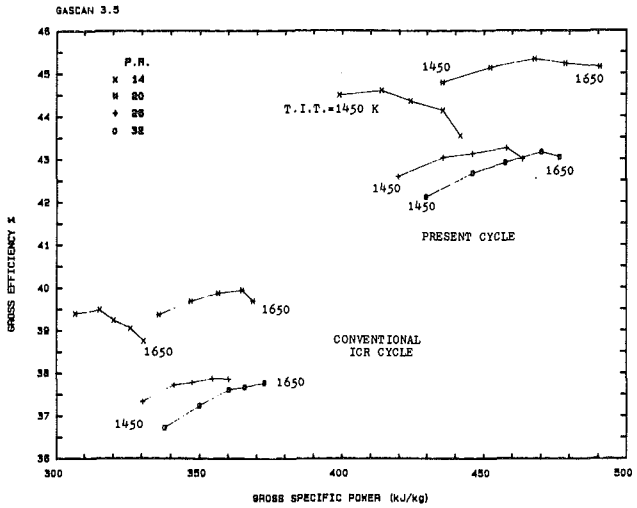

Fig. 2 Performance comparison between the present cycle and the conventional intercooled/recuperated cycle; conservative component assumptions

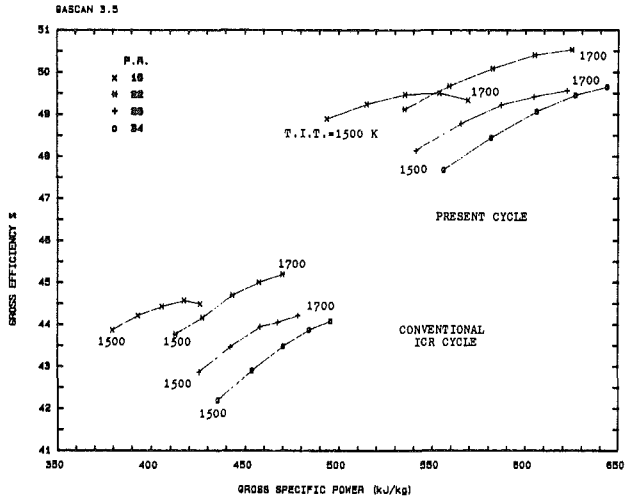

Fig. 3 Performance comparison between the present cycle and the conventional intercooled/recuperated cycle; advanced component assumptions

posed cycle is found to be superior to the STIG cycle in both efficiency and water consumption.

Cycle Computation Results

The GASCAN cycle analysis code [11] is used to obtain the present results. This is a microcomputer-based interactive code that allows flexible representation of a wide range of multishaft axial-flow-turbine systems incorporating intercoolers, recuperators, regenerators, gas turbine reheats, and steam or water injection at various cycle points. All built-in models for calculating cooling flows, their dependence on coolant and gas properties and their impact on turbine performance are semi-empirical, combining user-supplied quantities with analytically derived scaling relations [17, 18]. Provision to quantify the effects of ceramic thermal barrier coatings is included. The code generates a simplified, turbine gas-flow path. The program internal structure is completely dimensionless, with polynomials describing the properties of all relevant chemical components referred to the ISO standard ambient. Conversion from and to dimensional quantities occurs at the input/output interface in a choice of unit systems. Considerable effort has been made in writing the code to minimize the number of independent dimensionless variables needed to model system thermodynamic performance accurately, and to choose the variables used as independent inputs. Approximately one hundred independent dimensionless quantities are required for the computation of the efficiency and specific quantities for each of the present cycles. A single dimensional quantity is required for each cycle to provide a physical scale and to enable the determination of its dimensional attributes.

The key inputs used to compute the results presented are listed in Appendix 1 for both levels of assumed component technologies. A two-shaft configuration such as illustrated in Fig. 1 is used in all results. Cycles with pressure ratios below 19 have three equal-pressure-ratio turbine stages. Those above 22 have four equal-pressure-ratio stages. Cycles with pressure ratios of 19, 20, and 22 have three unequal-pressure-ratio turbine stages, since the first turbine stage is unloaded and the last stage uploaded in order to avoid negative first stage hub reactions. The maximum allowable first-stage pressure ratio is therefore reduced as TIT increases and as the maximum allowable hub velocity for that stage decreases. The latter depends on the allowable tip speed and hub-to-tip radius ratio.

It should be noted that for heavily cooled turbines, one should try to maximize stage loadings to increase the work-extraction rate relative to the heat transfer [19, 20]. This is particularly true for the first stage(s) in order to reduce the temperatures entering the subsequent stages and minimize cooling losses. In the present cycle calculations, the first turbine stage is used to drive the HPC spool; thus its loading affects the intercooling pressure ratio. In a final design analysis, a detailed tradeoff between stage loadings, cooling losses, intercooling, and recuperation losses must be performed and is not attempted here.

Figure 2 shows the performance maps for the proposed WIR/ICR cycle and the "conventional" ICR cycle for the conservative component assumptions. The proposed cycle peaks at about 45.3 percent and 470 kJ/kg at PR = 20 and TIT = 1550 K. The best ICR cycle on that map is just under 40 percent and 370 kJ/kg at PR = 20 and TIT = 1600 K. Figure 3 shows a comparison of the two systems based upon the advanced component assumptions. Here the proposed cycle peaks at about 50.5 percent and 625 kJ/kg at PR = 22 and TIT = 1700 K, whereas the best ICR cycle on that map achieves 45.2 percent and 470 kJ/kg at the same PR and TIT. Thus the advantage of the "best-case" WIR/ICR cycle over the "best case" ICR cycle of about 5.3 percentage points in efficiency (11 percent reduction in fuel consumption) together with about 30 percent increase in specific power is observed at both levels of component technology assumptions.

The results of Fig. 3 may be appreciated by referring to Figs. 4–6, where the WIR/ICR cycle is compared to the ICR cycle at several state points. Figure 4 shows the increase in turbine mass flow for the WIR cycle. The decrease in compressor discharge flow for the WIR case is because of the increased turbine flow, which requires more cooling air, and also due to the decrease in the intercooling pressure and thus the intercooler water-injection flow. The latter effect is due to the increased first-stage turbine work and the corresponding HPC spool pressure ratio. As TIT increases, the difference between mass flows at 2 and 2B, which represents the WIR water injection, increases, whereas that between CD and 2B, which represents after-cooler water injection, stays almost constant. Figures 5 and 6 show the variations in mainflow water content and temperature. The increase in water content between states 2 and 3 is the result of methane combustion. This increase is greater at higher TIT. The reduction of water content between states 3 and 4 is due to dilution with cooling air; this reduction therefore increases with TIT. The slight decrease in compressor-discharge water content as TIT increases is

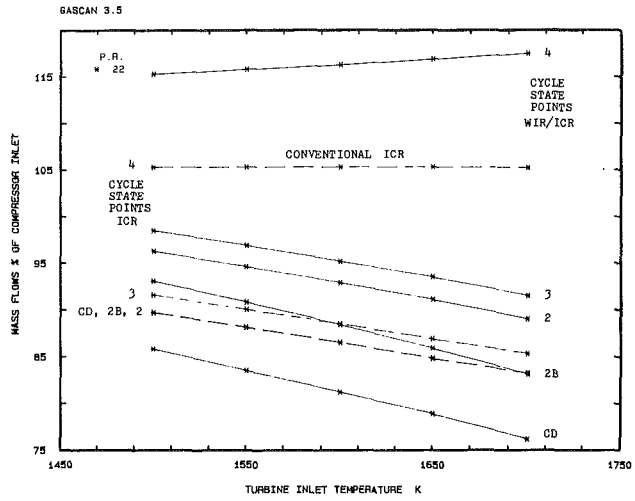

Fig. 4 Mass flows at several cycle state points; advanced component assumptions

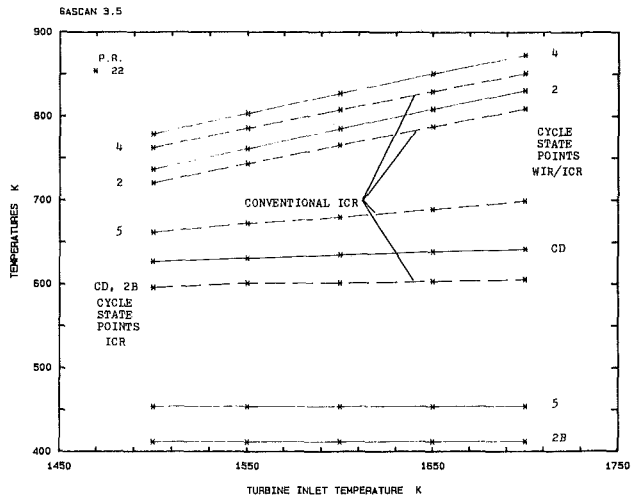

Fig. 6 Total temperature of the main gas at several cycle state points for a cycle pressure ratio of 22; advanced component assumptions

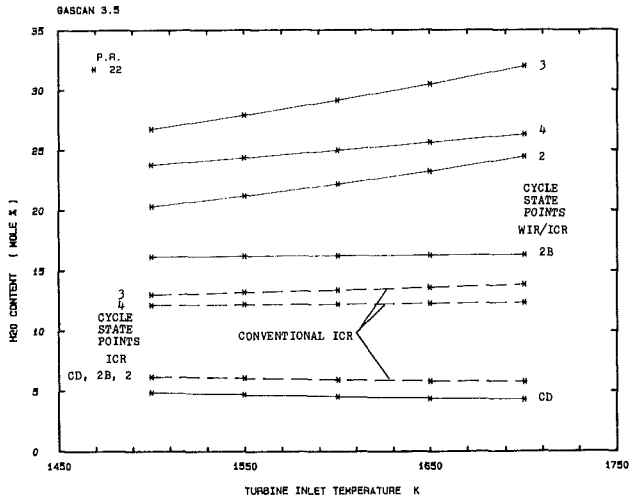

Fig. 5 Water-vapor content of the main gas at several cycle state points for a cycle pressure ratio of 22; advanced component assumptions

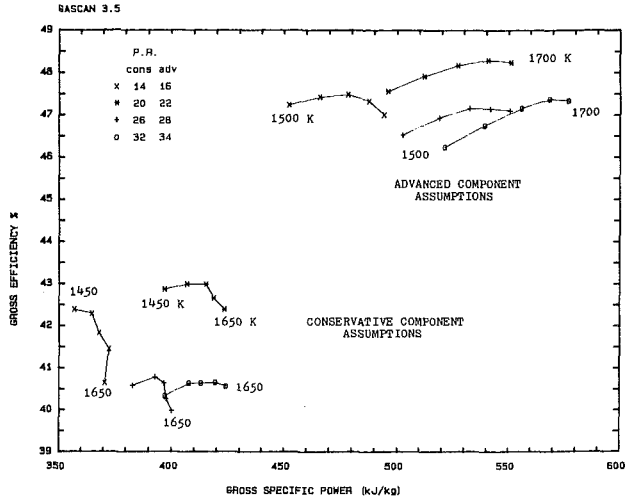

Fig. 7 Performance map for the ICR cycle with evaporative aftercooling, but without the water-injected recuperator

because of the increasing first-stage work and HPC pressure ratio which decrease the intercooling pressure.

Figure 7 shows the performance maps at both component-technology assumptions for the case where an evaporative aftercooler is used without the WIR. The "best case" efficiency in both of those cases is seen to be about 3 points above that for ICR and 2.3 points below that for the WIR/ICR cycle. This is because the aftercooler addresses the problem of providing a low-temperature cold stream to extract exhaust heat down to a lower temperature. However, this stream has insufficient heat capacity to perform this function efficiently. The WIR redresses this heat capacity imbalance.

The proposed WIR/ICR cycle invites comparison with the STIG cycle, since both use exhaust heat to generate water vapor to increase turbine massflow. The performance map for this cycle (which has no intercooler) is shown in Fig. 8 for both levels of component assumptions. For the conservative set it peaks at 42.5 percent and 450 kJ/kg at PR = 19 and TIT = 1550 K, whereas for the advanced set the peak efficiency is about 47.8 percent and 620 kJ/kg at PR = 20, TIT = 1600 K. The peak efficiency is seen to be about 2.75 points below that for the proposed WIR/ICR cycle. The specific power at peak efficiency is approximately the same for both systems.

Key results for three 60-MW engines using the WIR/ICR,

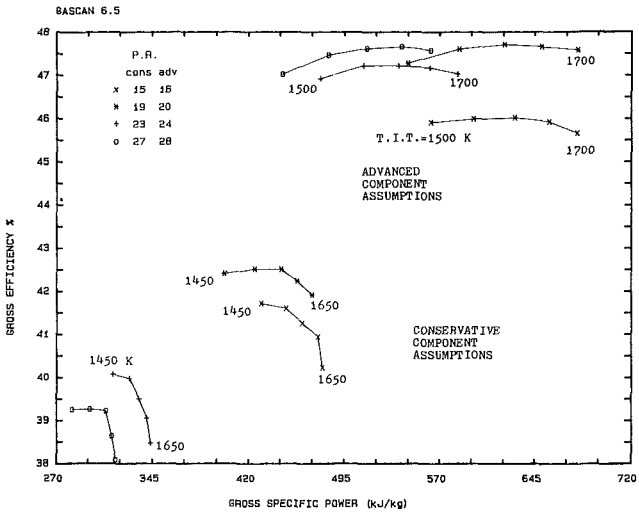

Fig. 8 Performance map for steam-injected gas turbines based upon the same two sets of component assumptions used for the modified recuperated cycle; all STIG cycles shown have nonintercooled compressors

Table 1 Comparison of three 60 MW cycles with similar advanced components

	Water-Injected Recuperator ICR Cycle	Steam-Injected Cycle	ICR Cycle
Gross power MW	60	60	60
Overall pressure ratio	22	20	22
Turbine inlet temperature K	1650	1650	1650
Gross specific power kJ/kg	605.5	649.5	457.6
Gross thermal efficiency %	50.41	47.64	45.01
Drive-shaft RPM	5060	4934	4808
Last-stage tip radius m	0.99	1.02	1.05
Compressor inlet airflow kg/s	99.1	92.4	131.1
Water supply rate kg/s	14.32	19.91	4.2
Fuel supply rate kg/s	2.37	2.51	2.65
Exhaust flow rate kg/s	115.8	114.8	137.9
Cooling air % compressor inlet	22.8	30.0	17.8
Total coolant % compressor inlet	23.3	30.0	18.4
Turbine exhaust temperature K	851	877	830
Stack temperature K	454	400	690

STIG, and ICR cycles are summarized in Table 1. All cycles have identical advanced component assumptions, TIT of 1650 K, and are close to the optima on the performance maps. The thermodynamic state points for those cycles as well as the turbine gas path for the WIR/ICR case are given in Appendix 2. The proposed WIR/ICR cycle is seen to be superior by 2.8 points in efficiency over the STIG cycle and 5.4 points over the ICR. The water consumption rate for this engine is 28 percent below that for the STIG engine. The thermodynamic analysis which follows should elucidate the fundamental reasons behind those differences.

Available-Work Thermodynamic Analysis

The energy balance of a power-plant cycle describes its overall performance in terms of energy addition, work output, and energy rejection. The energy balance embodies no quantitative measure of the processes which reduce work output and increase energy rejection since there is no provision to distinguish between work and heat, or to quantify the "quality of heat" or the losses in irreversible isenthalpic process such as throttling or viscous fluid friction. The understanding of factors affecting plant performance is improved by applying available-work-balance analysis

$$\Omega_{in} + \int \left(1 - \frac{T_a}{T}\right) dQ_{in} = \Omega_{out} + \Omega_L + W_{out} \tag{1}$$

where Ω_{in} and Ω_{out} represent the maximum work which may be extracted from all fluid streams entering and leaving the system in question. The integral of the second term is performed over the boundary of the system. Internal models of the processes occurring within the system or device can be used to further break down the available-work loss Ω_L into its origins. Such breakdowns have been given for gas turbine cycles [6, 7, 20, 21], steam bottoming cycles [22], gas turbine combustors [7], recuperators and regenerators [6], and for turbine cooling [7, 19].

For a pure substance, the available work is equal to the thermodynamic availability or exergy with respect to the ambient presssure and temperature. On the other hand when one considers a mixture of substances, the practically extricable work from the mixture may differ from its thermodynamic exergy, since the practical "dead state" of the mixture is not necessarily the thermodynamic dead state, where the mixture is separated into its ambient, pure constituents. For instance the work available from a mixture of noncondensable[2] semiperfect gases, such as in a gas turbine, is

$$\Omega = \Sigma n_i h_i - T_a \Sigma n_i \phi_i + T_a R (\Sigma n_i) \ln(p/p_a) \tag{2}$$

and exceeds the thermodynamic exergy

$$\Omega = \Sigma n_i (h_i - T_a s_i) = \Sigma n_i h_i - T_a \Sigma n_i \phi_i + T_a R \Sigma n_i \ln(p_i/p_a) \tag{3}$$

by the work necessary to separate the gases at the ambient state. Since this is not normally of interest in gas turbine engineering, the available work of the mixture is defined by equation (2).

The presence of a condensable phase in the mixture, such as water vapor, requires definition of its practical end state. If the dew point of the gas mixture is below the stack temperature, then any condensation of vapor and release of latent heat at above-ambient temperatures occurs outside the system. The latent heat and its corresponding available work are therefore unrecoverable. The available work of the mixture is thus defined by equation (2), with the water vapor simply treated as another semiperfect gaseous component with properties

$$h = \int_{T_a}^{T} Cp dT, \ \phi = \int_{T_a}^{T} Cp \frac{dT}{T} \tag{4}$$

The datum for water properties consistent with this approach as well as with LHV (lower heat value) definitions is to assign zero enthalpy to saturated steam (and all gases) at ISO ambient temperature and an enthalpy of -2468 kJ/kg to ambient liquid water.

The practical definition for available work of pure steam, on the other hand, should be referred to saturated vapor in an ideal condenser at the reference ambient temperature (288.15 K) with a corresponding saturation pressure (0.017 bar), less the work necessary to pump the condensed liquid back to the ambient pressure. Neglecting the latter term, this exceeds the maximum available work of steam in a noncondensable mixture by

$$\Delta\omega_{\text{steam,mixing}} = RT_a \ln\left(\frac{p_a}{p_{\text{sat@}Ta}}\right) \tag{5}$$

This quantity 9786 kJ/mole of steam (543 kJ/kg of steam) is the fundamental loss in available work when the steam is mixed with the turbine gas in a STIG cycle, thereby losing the opportunity to expand it to a condenser as would be possible in a combined cycle. One must note, however, that if some heat-recovery device were to extract heat from a STIG gas turbine exhaust below its dew point, this loss would be reduced.

When liquid water is evaporated into compressed gases the available work of the gas stream may increase or decrease, regardless of whether the process is thermodynamically reversible. Figure 9(*a*) shows reversible evaporation of an infinitesimal amount of saturated liquid water into a compressed air stream at 100 percent RH. Such a process occurs in the WIR. An infinitesimal amount of heat dQ is necessary to maintain the state of saturation by raising the mixture temperature by dT to the saturation temperature corresponding to the increased partial pressure of water vapor. The energy balance gives

$$dQ = nCpdT + h_{fg} dn \tag{6}$$

and the saturation condition

$$\frac{dn}{n} = \frac{dp_{\text{sat}}}{p} \tag{7}$$

may be combined with the Clausius-Clapeyron equation

$$\left(\frac{dp}{dT}\right)_{\text{sat}} = \frac{h_{fg}}{Tv_{fg}} \simeq \frac{h_{fg} p_{\text{sat}}}{RT^2} \tag{8}$$

to give

$$\frac{dQ}{dT} = n\left[Cp + \frac{n_w}{n} \frac{h_{fg}^2}{RT^2}\right] \tag{9}$$

[2] Implying noncondensable in the range of pressures and temperatures of interest to the present engineering application.

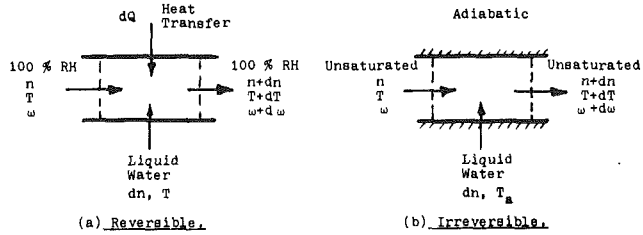

Fig. 9 Control volume for thermodynamic analysis of water injection

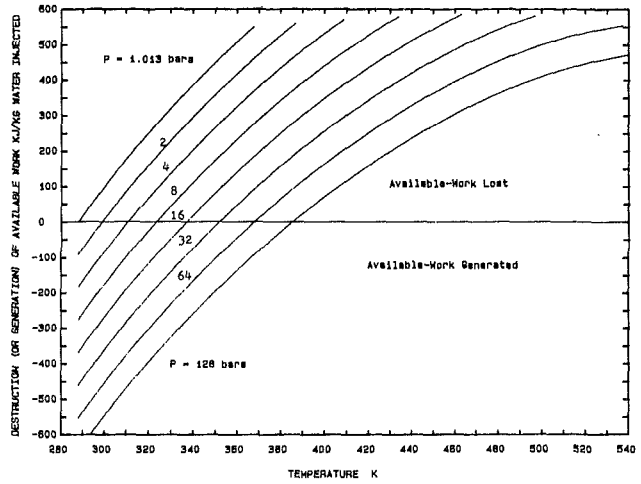

Fig. 10 The incremental loss (or generation) of available work due to the injection of an infinitesimal amount of liquid water at 288 K into an air/vapor stream at different stream temperatures and total pressures

The term in brackets is the increased "apparent specific heat" of the stream. The change in stream available work is

$$d\Omega = nd\omega + \omega dn \tag{10}$$

and the available work lost is found from equation (1)

$$d\Omega_L = dQ\left(1 - \frac{T_a}{T}\right) - d\Omega + \omega_f dn \tag{11}$$

The last term accounts for the inflow of available work due to the compressed, saturated liquid supply

$$\omega_f = Cp_f[T - T_a - T_a \ln(T/T_a)] + v_f(p - p_a) \tag{12}$$

Combining equations (6), (10), and (11) and simplifying, one may express the lost available work per mole of water injection as

$$\frac{d\Omega_L}{dn} = h_{fg}\left(1 - \frac{T_a}{T}\right) - (\omega - \omega_f) \tag{13}$$

Now consider the irreversible, adiabatic evaporation of an increment of liquid water dn injected at ambient temperature into an unsaturated, compressed, warm air stream. Such a process occurs in the intercooler and aftercooler and is illustrated in Fig. 9(b). The stream temperature change is $dT = -dnh'_{fg}/nCp$, which allows the change in stream available work to be evaluated from equation (10) and the available work lost from equation (11)

$$\frac{d\Omega_L}{dn} = h'_{fg}\left(1 - \frac{T_a}{T}\right) - (\omega - \omega_f) \tag{14}$$

showing that for cases where $h_{fg} >> Cp_f(T - Ta)$ the available work lost approaches that for the reversible case of equation (13). This loss may be negative, representing a net generation of available work by an irreversible process, as shown in Fig. 10. No violation of thermodynamic laws is involved in this case where an irreversible process actually generates available work for the system, since if one were to reseparate the water from the air, one would have to expend at least as much work as that increase. In some practical applications, such as the present gas turbine cycle, one is not interested in such a reseparation, and the air-water mixture is simply exhausted to the surroundings. It should be noted, however, that the combination of total pressure and temperature in Fig. 10 for which one obtains a net generation of available work corresponds to water mole fractions below approximately 0.017, the mole fraction for 100 percent RH at the ambient state. The realization of net available-work generation by increment water injection above this mole fraction would violate the Second Law, since that incremental amount can be reseparated without work expenditure.

An interesting consequence of this argument and of Fig. 10 is that it is possible, in principle, to construct a work-producing engine that runs on dry air and water only. Consider for instance, a gas turbine cycle consisting of isothermal compression of dry air to a pressure p followed by injection of an infinitesimal amount of water in an evaporator and isothermal expansion. All processes are allowed arbitrary heat transfer with the environment and are isothermal at T_a. Due to the larger volume flow through the turbine, the engine will produce a net work output $RT_a \ln (p/pa)$ per mole of water injection. That amount of energy is also the net heat inflow from the environment. If the water injected into the evaporator were greater than the mole fraction corresponding to 100 percent RH at ambient, the excess water would recondense during the expansion and not contribute to the work-producing flow through the turbine section downstream of its condensation. Thus whereas such an engine, which utilizes the disequilibrium between water and unsaturated air, is fundamentally possible, it is impractical since the maximum ratio of net work to compressor work is approximately 0.017, requiring unattainably low component losses. Nevertheless, this work-producing potential is exploited when water is injected in a gas turbine cycle. Figure 10 shows the desirability of carrying out water injection in a gas turbine cycle at the highest possible pressure and lowest possible temperature.

Comparative Thermodynamic Analysis of Three Cycles

Based upon the definitions of the previous section, the overall energy and available-work balances of the three cycles of Table 1 are presented in Tables 2, 3, and 4. The top section in each tables shows the streams of energy and available work supplied to the cycle. The net work is then shown, followed by and overall breakdown of the energy and available-work losses in the cycle.

In the energy balances, the stack loss represents sensible heat only. Latent heat losses are reflected by energy reductions on the supply side, i.e., the use of negative enthalpy for injected liquid water and lower heating value (LHV) for the fuel. It is interesting to observe that the processes responsible for the majority of available-work losses—combustion, turbine, recuperation, intercooling, aftercooling steam injection, pressure losses, and compression losses—are 100 percent energy efficient and appear lossless on the energy balance, with the exception of the 1 percent combustion loss. Since the fuel line enthalpy differs from its exergy by only 0.7 percent, the last column in each table represents the direct decrement to cycle net efficiency caused by each loss mechanism.

The major source of difference between the three cycles is the performance of the exhaust heat recovery system. Those differences may be understood by referring to Figs. 11, 12, and 13, which show the heat recovery temperature profiles, and to Table 5, which shows the breakdown of available-work losses in each heat-recovery system. The top section of Table 5 shows the STIG HRSG to be the most efficient energy-recovery device.

Table 2 LHV energy and available work balances for WIR/ICR cycle

GASCAN 3.5

	ENERGY		AVAILABLE WORK		
	KJ/KG al	% of Fuel Enthalpy	KJ/KG al	% of Fuel Exergy	% of Fuel Enthalpy
SUPPLY :-					
Fuel supply line	1201.015	100.000	1209.242	100.000	100.685
Atmosphere	0.000	0.000	0.000	0.000	0.000
Intercooler water	-54.990	-4.579	0.003	0.000	0.000
A/C and WIR water	-301.485	-25.103	0.255	0.021	0.021
G.T. CYCLE NET WORK	605.483	50.414	605.483	50.071	50.414
LOSSES :-					
Inlet pressure loss	0.000	0.000	0.627	0.052	0.052
Compressor	0.000	0.000	24.718	2.044	2.058
Intercooler	0.000	0.000	9.652	0.798	0.804
Aftercooler	0.000	0.000	54.777	4.530	4.561
Primary Combustor	11.993	1.000	313.790	25.949	26.127
Turbine	0.000	0.000	72.800	6.020	6.062
Exit diffuser loss	0.000	0.000	6.182	0.511	0.515
Recuperator irrevers.	0.000	0.000	73.792	6.102	6.144
Exhaust to stack	226.214	18.835	47.675	3.943	3.970

Table 3 LHV energy and available work balances for STIG cycle

GASCAN 6.5

	ENERGY		AVAILABLE WORK		
	KJ/KG al	% of Fuel Enthalpy	KJ/KG al	% of Fuel Exergy	% of Fuel Enthalpy
SUPPLY :-					
Fuel supply line	1363.344	100.000	1372.714	100.000	100.687
Atmosphere	0.000	0.000	0.000	0.000	0.000
HRSG feedwater	-531.376	-38.976	0.536	0.039	0.039
G.T. CYCLE NET WORK	649.536	47.643	649.536	47.318	47.643
LOSSES :-					
Inlet pressure loss	0.000	0.000	0.627	0.046	0.046
Compressor	0.000	0.000	22.912	1.669	1.681
Intercooler	0.000	0.000	0.000	0.000	0.000
Steam Injection	0.000	0.000	128.594	9.368	9.432
Primary Combustor	13.618	1.000	363.271	26.464	26.646
Turbine	0.000	0.000	80.399	5.857	5.897
Exit diffuser loss	0.000	0.000	6.762	0.493	0.496
Heat-recovery boiler	0.000	0.000	94.336	6.872	6.919
HRSG exhaust to stack	167.870	12.313	26.076	1.900	1.913

Table 4 LHV energy and available work balances for ICR cycle

GASCAN 3.5

	ENERGY		AVAILABLE WORK		
	KJ/KG al	% of Fuel Enthalpy	KJ/KG al	% of Fuel Exergy	% of Fuel Enthalpy
SUPPLY :-					
Fuel supply line	1016.762	100.000	1023.727	100.000	100.685
Atmosphere	0.000	0.000	0.000	0.000	0.000
Intercooler water	-79.229	-7.792	0.007	0.001	0.001
G.T. CYCLE NET WORK	457.635	45.009	457.635	44.703	45.009
LOSSES :-					
Inlet pressure loss	0.000	0.000	0.627	0.061	0.062
Compressor	0.000	0.000	24.732	2.416	2.432
Intercooler	0.000	0.000	15.926	1.556	1.566
Aftercooler	0.000	0.000	-0.000	-0.000	-0.000
Primary Combustor	10.153	1.000	268.429	26.221	26.400
Turbine	0.000	0.000	61.338	5.992	6.033
Exit diffuser loss	0.000	0.000	5.276	0.515	0.519
Recuperator irrevers.	0.000	0.000	12.795	1.250	1.258
Exhaust to stack	469.325	46.159	176.970	17.287	17.405

The ICR recuperator recovers a far smaller proportion of the turbine exhaust heat than either the STIG HRSG or the WIR system. The reason, as seen in Fig. 11, is the absence of a low-temperature heat absorber, resulting in a large stack loss. The total available work lost within that heat-recovery system, however, is less than in the other two systems as seen in Table 5. It has no mixing losses and very small heat transfer losses due to the fact that all heat transfer occurs at relatively high temperatures.

Table 5 and Fig. 12 show the STIG HRSG recovers the greatest proportion of heat from the exhaust gases, which are cooled down to the stack temperature constraint of 400 K.

Table 5 Comparison of heat recovery device performance for the cycles of Table 1

	Water-Injected Recuperator ICR Cycle	Steam-Injected Cycle	ICR Cycle
ENERGY (kW)			
Exhaust stream sensible enthalpy	79,742	86,432	84,426
Stack sensible enthalpy	22,417	15,507	61,533
Heat recycled	57,325 (71.9%)	70,925 (82.1%)	22,893 (27.1%)
AVAILABLE WORK (kW)			
Exhaust stream available work	36,435	40,314	37,854
Less extraction losses:			
Stack loss	4,724	2,409	23,202
Heat-transfer irreversibility	4,770	8,345	831
Hot-side pressure drop	412	369	465
Available-work extracted	25,679	29,191	13,356
Less re-addition losses:			
WIR Mixing	1,967	-	-
Aftercooler mixing	5,249	-	-
Steam throttling	-	784	-
Steam/air mixing	-	10,930	-
Cold-side pressure-drop	305	164	385
Available-work recycled	18,995 (52.1%)	17,313 (42.9%)	12,971 (34.3%)
Available-work lost	17,440	23,000	24,883

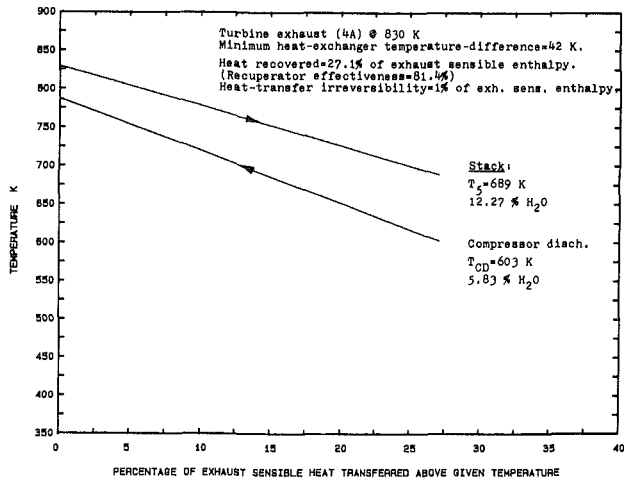

Fig. 11 Heat-recovery temperature profile for the conventional intercooled/recuperated cycle at a pressure ratio of 22 and TIT of 1650 K; advanced component assumptions

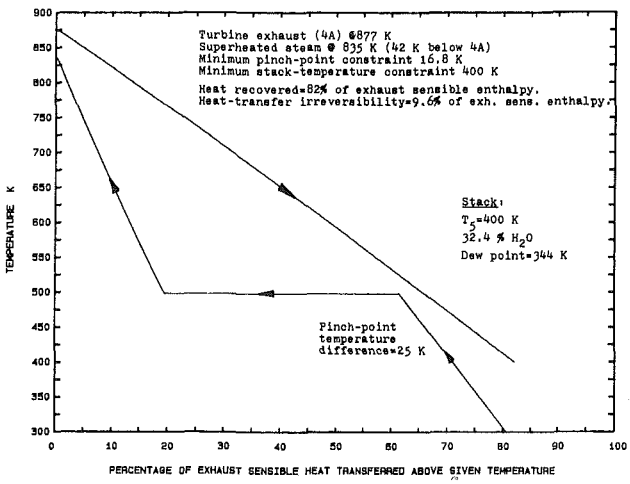

Fig. 12 Heat recovery temperature profile for the steam-injected cycle at a pressure ratio of 20 and TIT of 1650 K; advanced component assumptions

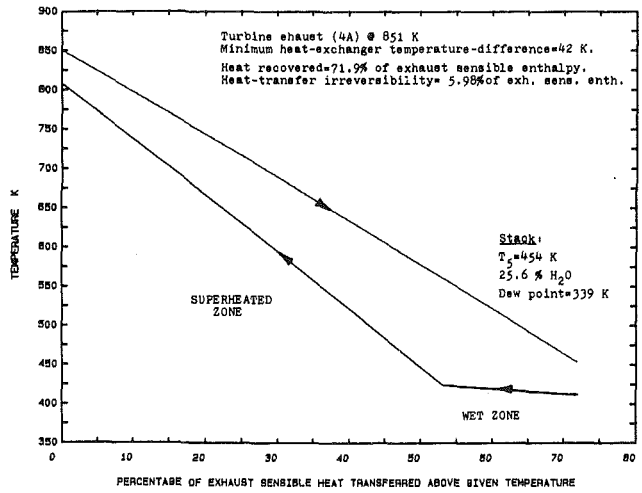

Fig. 13 Heat-recovery temperature profile for the present cycle at a pressure ratio of 22 and TIT of 1650 K; advanced component assumptions

However, due to the mismatch between the exhaust cooling and water-boiling temperature profiles, the heat transfer irreversibility is large. This, together with the high mixing loss of steam and gases, results in inferior overall performance vis-à-vis the WIR. The available-work mixing loss given in Table 5 is the sum of that corresponding to equation (5) and that arising from mixing streams of unequal temperatures. The latter is small in the present case since the temperature difference between steam (835 K) and compressor discharge (718 K) is small.

Figure 13 shows that the WIR provides a good combination of low cold-stream inlet temperature and good heat-capacity balance in the heat exchanger. This results in a much lower heat transfer irreversibility than for the HRSG as seen in Table 5. The mixing losses of injecting water into the aftercooler and WIR are also significantly lower than those for steam throttling and mixing in the STIG case. It is interesting to observe from Tables 2 and 5 together with the state points shown in Appendices 2 and 3 that the water-injection loss per unit mass of injected water is much greater for the aftercooler than for either the intercooler or WIR. This is due to the higher mean temperature in the aftercooler, which results in increased available-work losses as per Fig. 10.

Practical Considerations

The evaporative aftercooler, which provides 50-60 percent of the total efficiency gain of the proposed cycle over the ICR cycle, should not present serious design difficulties. Most impurities from the water evaporated in a flash chamber are likely to be carried through the machine to the exhaust. The water-injected recuperator, however, is more susceptible to fouling unless the water injectors are designed to produce a water mist that evaporates without impinging upon the hot walls. If that is not possible, then the system will require high-purity water or a recuperator design that lends itself to quick, periodic cleaning. One variation on the proposed system that avoids recuperator evaporation is to construct a two-stage, dry recuperator with an evaporator chamber interposed. This would have some adverse effects on system thermodynamics, in view of the discussions in section 4, but should be evaluated as a practical solution. Another concept which should be evaluated is the use of an integrated water-distillation train utilizing recuperator exhaust heat. This has been proposed for STIG systems [23], and may feasible for larger, stationary ICR/WIR cycles.

Conclusions

1 The proposed WIR/ICR cycle offers an efficiency improvement of about 5 percentage points over the ICR cycle. About 3 points derive from evaporative aftercooling and 2 points from recuperator evaporation.

2 The proposed cycle shows an efficiency improvement of about 2.75 percentage points over optimized, nonintercooled STIG systems based on identical component technologies. Water consumption for the proposed cycle is about 30 percent below that for the STIG system.

References

1 Helms, H. E., et al., "Ceramic Applications in Turbine Engines," DOE/NASA/0017-6, Allison Gas Turbines, Indianapolis, IN 46206, Oct. 1984.

2 "Regenerators for 1200 F and 90 percent Transfer," *Gas Turbine World*, Vol. 14, 1984.

3 Mills, R. G., and Karstensen, K. W., "Intercooled/Recuperated Shipboard Generator Drive Engine," ASME Paper No. 86-GT-203.

4 Lauriat, T. B., "The Avco-Lycoming TF15: A Regenerative Marine Gas Turbine," ASME Paper No. 86-GT-284.

5 *Gas Turbine World Handbook*, 1985-86, Pequot Publishing Inc.

6 El-Masri, M. A., "Exergy Analysis and Optimization of the Recuperated Gas Turbine Cycle," presented at the ASME 1986 Winter Annual Meeting, Anaheim, CA Dec. 1986.

7 El-Masri, M. A., "Exergy Analysis of Combined Cycles: Part 1—Air-Cooled Brayton-Cycle Gas Turbines," ASME JOURNAL OF ENGINEERING FOR GAS TURBINES AND POWER, Vol. 109, 1987, pp. 228-236.

8 Lysholm, A., U.S. Patent No. 2, 115, 112, 1983.

9 Gasparovic, N., and Hellemans, J. G., "Gas Turbines With Heat Exchanger and Water Injection in the Compressed Air," *Proc. Instn. Mech. Engrs.*, Vol. 185, 1971.

10 Foote, W. R., U. S. Patent No. 2,869,324, 1959.

11 El-Masri, M. A., "GASCAN—An Interactive Code for Thermal Analysis of Gas Turbine Systems," ASME JOURNAL OF ENGINEERING FOR GAS TURBINES AND POWER, Vol. 110, 1988, this issue.

12 Brown, D. H., and Cohn, A., "An Evaluation of Steam Injected Combustion Turbine Systems," ASME JOURNAL OF ENGINEERING FOR POWER, Vol. 103, pp. 13-19.

13 Leibowitz, H., and Tabb, E., "The Integrated Approach to a Gas Turbine Topping Cycle Cogeneration System," ASME JOURNAL OF ENGINEERING FOR GAS TURBINES AND POWER, Vol. 106, 1984, pp. 731-736.

14 Burnham, J. B., Giuliani, M. H., and Moeller, D. J., "Development, Installation and Operating Results of a Steam Injector," ASME JOURNAL OF ENGINEERING FOR GAS TURBINES AND POWER, Vol. 109, July 1987.

15 Digumarthi, R., and Chang, C. N., "Cheng-Cycle Implementation on a Small Gas Turbine Engine," ASME JOURNAL OF ENGINEERING FOR GAS TURBINES AND POWER, Vol. 106, 1984, pp. 699-702.

16 Jones, J. L., Flynn, B. R., and Strother, J. R., "Operating Flexibility and Economic Benefits of a Dual Fluid Cycle 501KB Gas Turbine Engine in Cogeneration Applications," ASME Paper No. 82-GT-298.

17 El-Masri, M. A., and Pourkey, F., "Prediction of Cooling Flow Requirements for Advanced Utility Gas Turbines; Part 1: Analysis and Scaling of the Effectiveness Curve," presented at the ASME 1986 Winter Annual Meeting, Anaheim, CA, Dec. 1986.

18 El-Masri, M. A., "Prediction of Cooling Flow Requirements for Advanced Utility Gas Turbines; Part 2: Influence of Ceramic Thermal Barrier Coatings," presented at the ASME 1986 Winter Annual Meeting, Anaheim, CA Dec. 1986.

19 El-Masri, M. A., "On Thermodynamics of Gas Turbine Cycles; Part 2: A Model for Expansion in Cooled Turbines," ASME JOURNAL OF ENGINEERING FOR GAS TURBINES AND POWER, Vol. 108, 1986, pp. 151-159.

20 El-Masri, M. A., "Exergy-Balance Analysis of the Reheat Gas Turbine Combined Cycle," presented at the 1987 Joint ASME-JSME Thermal Engineering Conference, Honolulu, HI, Apr. 1987.

21 El-Masri, M. A., "On Thermodynamics of Gas Turbine Cycles; Part 1: Second Law Analysis of Combined Cycles," ASME JOURNAL OF ENGINEERING FOR GAS TURBINES AND POWER, Vol. 107, 1985, pp. 880-889.

22 Chin, Wo, W., and El-Masri, M. A., "Exergy Analysis of Combined Cycles; Part 2—Analysis and Optimization of Two-Pressure Steam Bottoming Cycles," ASME JOURNAL OF ENGINEERING FOR GAS TURBINES AND POWER, Vol. 109, 1987, pp. 237-243.

23 Cerri, G., and Arsuffi, G., "Calculation Procedure for Steam Injected Gas Turbine Cycles With Autonomous Distilled Water Production (1)," ASME Paper No. 86-GT-297.

APPENDIX 1

Assumptions Used in Results Presented

General Assumptions:

Ambient: ISO, 1.013, bar, 288.15 K, 60 percent RH
Fractional total-pressure losses:—
Inlet: 0.0075 Combustor: 0.04 Diffuser: 0.06 Intercooler: 0.03
Recuperator: air-side: 0.04, gas-side: 0.04
HRSG gas-side: 0.035, gas/steam mixer: 0.025

Minimum stack temperature: 400 K
Minimum recuperator temperature difference = 42 K
HRSG gas-superheated steam temperature difference = 42 K
Minimum HRSG pinch-point temperature difference = 16.7 K
Exit RH: Intercooler: 90 percent, aftercooler: 100 percent

CH_4 fuel, standard enthalpy of reaction = 50187.34 kJ/kG LHV
Standard lower Gibbs function of reaction = 50086.97 kJ/kG
Fuel line at 20.7 bars, 288 K.
Combustion efficiency = 99 percent

Compressor polytropic efficiencies:
Conservative: LPC: 0.905 HPC: 0.905
Advanced : LPC: 0.92 HPC: 0.91

Turbine

Stage	Uncooled total-to-total efficiency, percent	Absolute rotor-exit flow angle @ pitch (deg)	Flow coefficient
1	89.5	19.48	0.50
2	91.0	9.74	0.50
3&4	92.0	4.87	0.50

All turbine stages free vortex.
Hub-to-tip radius ratio = 0.75 for the last turbine stage on each shaft.
Maximum tip speeds: conservative: 450 m/s, advanced: 530 m/s.

Gas path cooling flows calculated from effectiveness-curves specified in GASCAN by three parameters for each row. The curves for the conservative case are shown in Fig. A1. The curves for the advanced case are similar except for reducing coolant flow by 10 percent. In addition a coolant leakage of 0.4 percent (cons.) or 0.2 percent (adv.) by volume is assumed for each cooled row.

Wheelspace purge flows specified by a reference volumetric fraction of the main gas flow for each stage based upon a hub-to-tip radius ratio of 0.8. This fraction is taken as 0.6 percent (cons.) and 0.33 percent (adv.). The code adjusts purge mass flows based upon local densities and computed hub-to-tip radius ratios such that the ratios (purge flow radial velocity/hub peripheral velocity) and (wheel gap/hub radius) are maintained constant.

Cooling-flow aerodynamic penalties are computed by specifying main gas total-pressure loss parameters (Y) for each coolant flow in each stage

$$\frac{\Delta p}{p} = Y\frac{n_{c,i}}{n_g}\left(1+\frac{MW_{c,i}}{MW_g}\right)$$

In the present calculations, Y is taken as 0.25 for stators, 0.3 for rotors, 0.4 for forward wheelspaces, and 0.35 for aft wheelspaces. The corresponding effects on cooled stage efficiency for the first stage of the cycle of Appendix 3 are shown in Fig. A2.

Coolant circuit:

Number of cooling-air extraction points = number of stages.
Extraction pressures = 1.3 × inlet total pressure of corresponding stator (but ≤ compressor discharge).

Blade row	Cooling method	Gas temperature pattern factor	Maximum metal temperatures K	
			Conservative	Advanced
Stator 1	Film	0.100	1035	1120
Rotor 1	Film	0.056	1000	1100
Stator 2	F(adv.),C(cons.)	0.036	1015	1100
Rotor 2	Convection	0.025	970	1070
Stator 3,4	Convection*	0.018	1015	1100
Rotor 3,4	Convection*	0.014	950	1020

*In most cycles stages 3 and/or 4 are uncooled.

Each stator cooled from corresponding bleed, each rotor from the same source as the first stator for its spool, each wheelspace from the same source as the adjacent stator.

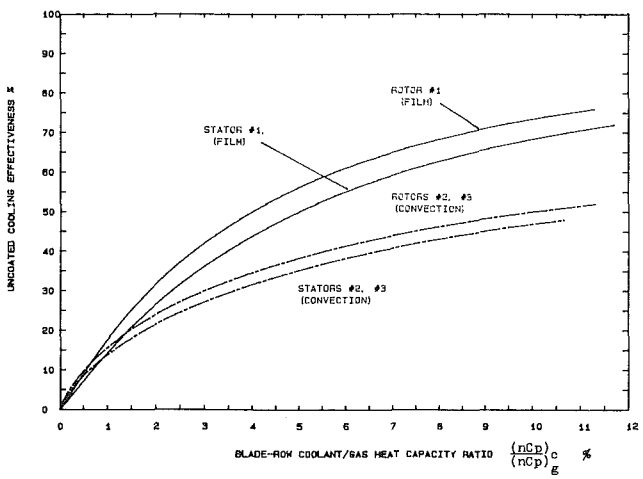

Fig. A1 The cooling-effectiveness curves for the conservative assumptions

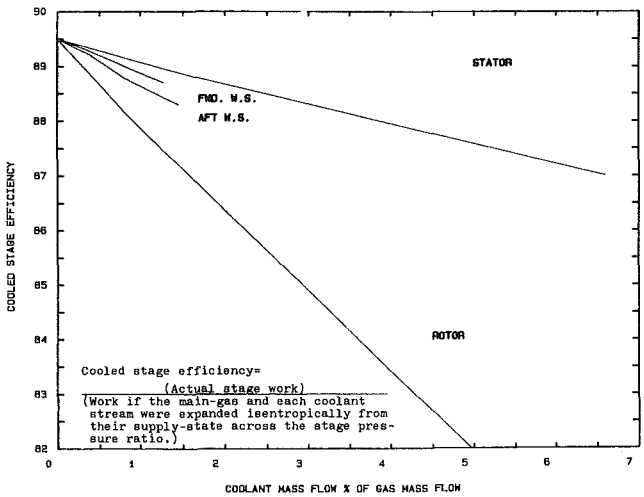

Fig. A2 The cooled stage efficiency corresponding to the values of the total-pressure loss parameters (Y) used. The plot shown is for the conditions of the first stage of the WIR/ICR cycle at PR = 22 (stage PR = 2.4) and TIT = 1650 K.

APPENDIX 2

State Points for the Cycles of Table 1 and Turbine Gas Path for the WIR/ICR Cycle of That Table

GASCAN 3.5 — State Points for the WIR/ICR Cycle of Table 1.

POINT	PRESSURE BAR	TEMPERATURE K Absolute	TEMPERATURE K Rotor-Relative	MOLE-CULAR WEIGHT	MOLE COMPOSITION % N2 etc.	O2	CO2	H2O
Air Inlet (a)	1.013	288.1		28.87	78.22	20.75	0.03	1.00
Comp. Inlet (1)	1.005	288.1		28.87	78.22	20.75	0.03	1.00
LPC Disch. (2A)	2.375	376.0		28.87	78.22	20.75	0.03	1.00
Interc. Dis(1A)	2.304	320.6		28.50	75.52	20.03	0.03	4.41
HPC Disch. (cd)	22.119	638.4		28.50	75.52	20.03	0.03	4.41
R/G Inlet (2b)	21.676	411.7		27.20	66.15	17.55	0.03	16.28
R/G Disch. (2)	21.234	808.6		26.43	60.66	16.09	0.02	23.23
Comb. Disch.(3)	20.385	1650.0		26.01	58.17	7.23	4.13	30.48
Inlet STATOR 1	20.385	1650.0		26.01	58.17	7.23	4.13	30.48
Inlet ROTOR 1	19.473	1585.2	1450.2	26.20	59.48	8.19	3.82	28.52
Inlet STATOR 2	8.494	1341.0		26.30	60.18	8.71	3.65	27.47
Inlet ROTOR 2	8.222	1305.3	1166.7	26.41	60.95	9.27	3.47	26.31
Inlet STATOR 3	3.205	1071.2		26.46	61.28	9.52	3.39	25.80
Inlet ROTOR 3	3.193	1068.4	937.7	26.47	61.35	9.57	3.38	25.70
Turb. Exit (4)	1.117	850.6		26.47	61.39	9.60	3.37	25.64
Diffuser Ex(4A)	1.054	850.6		26.47	61.39	9.60	3.37	25.64
R/G - stack (5)	1.013	453.7		26.47	61.39	9.60	3.37	25.64

GASCAN 3.5 — State Points for the ICR Cycle of Table 1.

POINT	PRESSURE BAR	TEMPERATURE K Absolute	TEMPERATURE K Rotor-Relative	MOLE-CULAR WEIGHT	MOLE COMPOSITION % N2 etc.	O2	CO2	H2O
Air Inlet (a)	1.013	288.1		28.87	78.22	20.75	0.03	1.00
Comp. Inlet (1)	1.005	288.1		28.87	78.22	20.75	0.03	1.00
LPC Disch. (2A)	3.229	413.1		28.87	78.22	20.75	0.03	1.00
Interc. Dis(1A)	3.132	332.7		28.34	74.39	19.73	0.03	5.84
HPC Disch. (CD)	22.119	603.1		28.34	74.39	19.73	0.03	5.84
R/G Disch. (2)	21.234	787.6		28.34	74.39	19.73	0.03	5.84
Comb. Disch.(3)	20.385	1650.0		27.85	71.41	10.94	4.03	13.62
Inlet STATOR 1	20.385	1650.0		27.85	71.41	10.94	4.03	13.62
Inlet ROTOR 1	19.579	1585.3	1447.1	27.88	71.62	11.54	3.76	13.08
Inlet STATOR 2	8.494	1329.1		27.90	71.73	11.87	3.61	12.79
Inlet ROTOR 2	8.245	1293.7	1156.2	27.92	71.85	12.24	3.44	12.47
Inlet STATOR 3	3.205	1053.2		27.93	71.91	12.39	3.37	12.33
Inlet ROTOR 3	3.192	1050.0	924.6	27.93	71.92	12.43	3.35	12.30
Turb. Exit (4)	1.117	829.6		27.93	71.93	12.45	3.34	12.28
Diffuser Ex(4A)	1.054	829.6		27.93	71.93	12.45	3.34	12.28
R/G - stack (5)	1.013	689.1		27.93	71.93	12.45	3.34	12.28

GASCAN 6.5 — State Points for STIG Cycle of Table 1.

POINT	PRESSURE BAR	TEMPERATURE K Absolute	TEMPERATURE K Rotor-Relative	MOLE-CULAR WEIGHT	MOLE COMPOSITION % N2 etc.	O2	CO2	H2O
Air Inlet (a)	1.013	288.1		28.87	78.22	20.75	0.03	1.00
Comp. Inlet (1)	1.005	288.1		28.87	78.22	20.75	0.03	1.00
LPC Disch. (2A)	2.282	371.4		28.87	78.22	20.75	0.03	1.00
HPC Disch. (CD)	20.108	717.7		28.87	78.22	20.75	0.03	1.00
Combustor in(2)	19.505	762.0		25.29	52.38	13.90	0.02	33.70
Comb. Disch.(3)	18.725	1650.0		24.88	50.07	4.44	4.44	41.04
Inlet STATOR 1	18.725	1650.0		24.88	50.07	4.44	4.44	41.04
Inlet ROTOR 1	17.681	1580.9	1452.7	25.24	52.60	5.91	4.05	37.45
Inlet STATOR 2	7.802	1346.4		25.43	53.95	6.69	3.83	35.52
Inlet ROTOR 2	7.528	1311.2	1181.3	25.62	55.29	7.46	3.62	33.63
Inlet STATOR 3	3.048	1089.2		25.71	55.91	7.83	3.53	32.74
Inlet ROTOR 3	3.030	1085.3	959.7	25.73	56.07	7.92	3.50	32.51
Turb. Exit (4)	1.111	876.8		25.74	56.13	7.95	3.49	32.43
Diffuser Ex(4A)	1.048	876.8		25.74	56.13	7.95	3.49	32.43
HRSG- stack (5)	1.013	399.8		25.74	56.13	7.95	3.49	32.43

Free-Vortex Turbine Gas-Path for the WIR/ICR Cycle of Table 1.

GASCAN 3.5

	ABSOLUTE Velocity M/S	ABSOLUTE Angle deg	ABSOLUTE Mach Number	RELATIVE Velocity M/S	RELATIVE Angle deg	RELATIVE Mach Number	Radius M	Reaction /Blade Velocity M/S	Static Temp. K
				ROTOR # 1 10792 RPM					
INLET :-									
Hub	802.9	74.7	1.08	451.9	62.1	0.61	0.33	0.014	1375.0
Pitch	719.1	72.9	0.95	338.6	51.4	0.45	0.37	0.276	1416.6
Tip	652.9	71.1	0.86	257.6	34.9	0.34	0.42	0.445	1446.2
EXIT :-									
Hub	228.7	22.4	0.31	496.9	64.8	0.67	0.32	362.4	1351.7
Pitch	224.3	19.5	0.30	540.7	67.0	0.73	0.37	422.8	1352.4
Tip	221.3	17.2	0.30	588.0	68.9	0.80	0.43	483.2	1352.8
				ROTOR # 2 5060 RPM					
INLET :-									
Hub	727.9	72.1	1.08	348.5	50.1	0.52	0.80	0.206	1123.7
Pitch	696.3	71.3	1.03	308.5	43.6	0.46	0.84	0.305	1139.1
Tip	667.7	70.5	0.98	275.4	35.8	0.40	0.88	0.386	1152.5
EXIT :-									
Hub	227.1	10.4	0.35	510.4	64.1	0.78	0.79	418.0	1065.7
Pitch	226.6	9.7	0.35	534.0	65.3	0.81	0.84	446.7	1065.8
Tip	226.2	9.2	0.35	558.1	66.4	0.85	0.90	475.5	1065.9
				ROTOR # 3 5060 RPM					
INLET :-									
Hub	715.0	71.2	1.19	348.7	48.7	0.58	0.78	0.127	885.1
Pitch	652.1	69.3	1.07	274.6	33.1	0.45	0.87	0.359	915.9
Tip	601.2	67.5	0.97	235.5	12.2	0.38	0.95	0.509	938.8
EXIT :-									
Hub	231.3	5.7	0.40	476.7	61.1	0.82	0.74	394.6	832.4
Pitch	231.0	4.9	0.40	532.3	64.4	0.91	0.87	460.4	832.4
Tip	230.8	4.3	0.40	590.0	67.0	1.01	0.99	526.1	832.4

Mass, Energy, and Available-Work Streams for the WIR/ICR Cycle of Table 1.

GASCAN 3.5

STREAM	THERMODYNAMIC STATE P BAR	T K	h KJ/KG	omega KJ/KG	FLUXES Enthalpy KW	Avl.Work KW	Mass KG/S
Atmosphere inlet	1.013	288.1	0.0	0.0	0.0	0.0	99.09
Compr. Inlet (1)	1.005	288.1	0.0	-0.6	0.0	-62.1	99.09
LPC into IC (2A)	2.375	376.0	89.1	82.3	8831.2	8152.6	99.09
LPC power input						8831.2	
H2O inj. in I/C	2.375	288.1	-2467.5	0.1	-5449.2	0.3	2.21
IC into HPC (1A)	2.304	320.6	33.4	71.0	3385.5	7196.1	101.30
HPC dischg. (CD)	22.119	638.4	370.2	388.9	28961.6	30428.8	78.18
HPC power input						32511.9	
H2O inj. in A/C	22.119	288.1	-2465.6	2.1	-17275.4	14.6	7.01
R/C inlet (2B)	21.676	411.7	136.6	293.7	11638.6	25015.3	85.18
H2O inj. in WIR	22.119	288.1	-2465.6	2.1	-12600.1	10.6	5.11
R/C sat. pt.(2C)	21.455	423.2	142.4	279.8	14045.3	27596.0	90.30
R/C into Comb(2)	21.234	808.6	571.2	501.2	56334.2	49424.6	90.30
Bleed port # 1	22.119	638.4	370.2	388.9	4748.0	4988.5	12.83
Bleed port # 2	11.042	519.0	241.3	265.8	1976.0	2177.0	8.19
Bleed port # 3	4.167	385.3	100.5	133.2	211.9	280.8	2.11
Fuel line	30.038	319.8	50258.2	50602.5	119013.9	119829.2	2.37
Comb. Disch. (3)	20.385	1650.0	1878.9	1490.5	174159.6	138158.9	92.69
STAGE # 1							
Main Gasflow in	20.385	1650.0	1878.9	1490.5	174159.6	138158.9	92.69
STATOR coolant	22.119	638.4	370.2	388.9	2845.3	2989.4	7.69
ROTOR coolant	22.119	638.4	370.2	388.9	1693.3	1779.1	4.57
FWD.WS coolant	22.119	638.4	370.2	388.9	209.4	220.0	0.57
AFT WS coolant	11.042	519.0	241.3	265.8	105.3	116.0	0.44
Stage power output						32722.8	
STAGE # 2							
Main Gasflow in	8.494	1341.0	1380.7	1011.0	146290.2	107118.7	105.95
STATOR coolant	11.042	519.0	241.3	265.8	1089.5	1200.3	4.52
ROTOR coolant	11.042	519.0	241.3	265.8	404.4	445.5	1.68
FWD.WS coolant	11.042	519.0	241.3	265.8	376.8	415.1	1.56
AFT WS coolant	4.167	385.3	100.5	133.2	119.0	157.7	1.18
Stage power output						35062.0	
STAGE # 3							
Main Gasflow in	3.205	1071.2	985.4	623.1	113217.8	71585.3	114.89
STATOR coolant	4.167	385.3	100.5	133.2	0.0	0.0	0.00
ROTOR coolant	11.042	519.0	241.3	265.8	0.0	0.0	0.00
FWD.WS coolant	4.167	385.3	100.5	133.2	59.0	78.2	0.59
AFT WS coolant	4.167	385.3	100.5	133.2	33.8	44.8	0.34
Stage power output						33558.3	
Turbine exit (4)	1.117	850.6	688.5	319.9	79741.5	37048.0	115.82
Diff. to R/G(4A)	1.054	850.6	688.5	314.6	79741.5	36435.4	115.82
R/G to stack (5)	1.013	453.7	193.6	40.8	22416.6	4724.4	115.82

The Design and Development of an Advanced Heavy-Duty Gas Turbine

D. E. Brandt
Manager, Gas Turbine Engineering and Development,
General Electric Company,
Schenectady, NY 12345

Significant advances in all elements of gas turbine design technologies have occurred during the past decade. These developments have created a technical climate conducive to the creation of a totally new heavy-duty gas turbine, as opposed to the uprating of an existing design. This paper discusses the features and characteristics of a new heavy-duty gas turbine that takes advantage of the latest technological advances. Discussed are the basis for design parameter selection, the operating characteristics, the materials of construction, and the component design features. Also presented are the features and performance of the unique combustion system and the results of and plans for component and prototype testing. This paper represents a comprehensive treatment of this advanced gas turbine, which is in the initial manufacturing stage in preparation for extensive factory testing followed by shipment to a customer by mid-1988.

Introduction

The General Electric MS7001F gas turbine is a totally new 3600 rpm heavy-duty design, directed at a broadly based application in the 60 Hz power generation industry. It has an introductory simple cycle ISO rating of 135.7 MW with a heat rate of 10,390 Btu/kWh (LHV) at a firing temperature of 1260°C (2300°F) on natural gas fuel. This gas turbine has been designed for both simple and combined-cycle applications, and will operate on all conventional gas turbine fuels, as well as coal-derived gas produced in an oxygen-blown integrated gasification combined-cycle (IGCC) installation. In natural gas combined-cycle applications, the total plant output will be in excess of 200 MW, with a heat rate less than 6828 Btu/kWh (LHV), depending upon the plant configuration and the type of steam cycle selected. The 593°C (1100°F) exhaust temperature allows for outstanding reheat steam conditions.

The technologies associated with the gas turbine have seen substantial advancement during the past decade. This has been driven by economic considerations, such as the rapid increase in the cost of energy, as well as the acceptance of the gas turbine as a reliable source of power. Additionally, the cycle arrangement flexibility of the gas turbine with its progressive add-on features and its comparatively low demand on investment resources has made the gas turbine a very attractive alternative when electrical capacity expansion is being considered or when a demand exists for large amounts of thermal energy in conjunction with power generation. These market forces have provided the necessary impetus to drive a substantial investment in the technologies associated with gas turbines. Materials and process developments have resulted in higher quality components due to tighter process control, higher strength alloys, and improved high-temperature coatings. Advanced analytical methods coupled to improved understanding of materials behavior have resulted in a considerable improvement in the optimization of design. Recent developments in our understanding of the combustion process have substantially improved the emissions associated with elevated firing temperatures. Advances in heat transfer, fluid flow, structural and dynamic analysis, and aerodynamics have all set the stage for a major development in the design of advanced heavy-duty gas turbines. This paper discusses the features and characteristics of a new heavy-duty gas turbine that takes advantage of these latest technological advances.

General Description

Figure 1 illustrates the general configuration of the MS7001F gas turbine. It consists of a single rotor of bolted

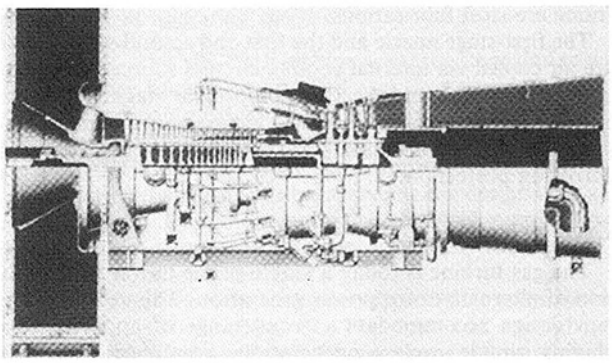

Fig. 1

Contributed by the Gas Turbine Division of THE AMERICAN SOCIETY OF MECHANICAL ENGINEERS and presented at the 32nd International Gas Turbine Conference and Exhibit, Anaheim, California, May 31–June 4, 1987. Manuscript received at ASME Headquarters February 3, 1987. Paper No. 87-GT-14.

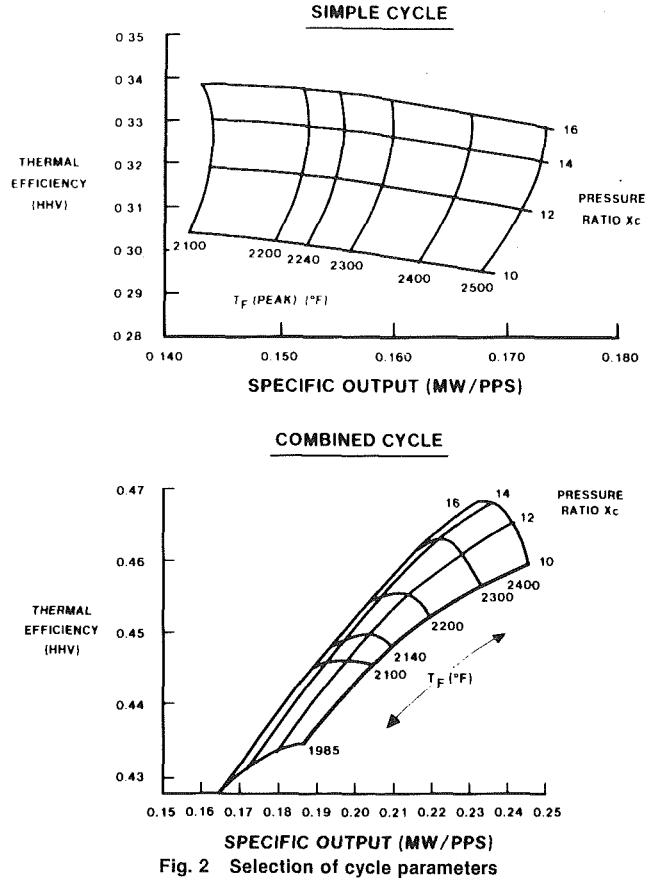

Fig. 2 Selection of cycle parameters

construction supported by two 419 mm (16.5 in.) diameter, four-element tilting pad bearings, with the output flange on the compressor end. Thrust is absorbed by a 635 mm (25 in.)×432 mm (17 in.) tilting pad thrust bearing with eight shoes on both sides of the thrust bearing runner. The thrust bearing load capability is 80,000 lb in both fore and aft directions so as to allow flexibility in simple and combined-cycle applications.

The compressor is an 18-stage axial flow design with a pressure ratio of 13.5; the turbine is a three-stage design characterized by being intermediate between full reaction and impulse. The exhaust diffuser directs the flow of exhaust gases axially into either an exhaust stack or a heat recovery boiler.

The combustion system consists of 14 combustors oriented at a 13 deg angle. Each combustor has 356 mm (14 in.) nominal diameter.

The stator casings are of horizontally split design to provide ready access to the internal parts during maintenance operations. The inlet case is grey cast iron, and the forward and aft compressor casings are of nodular cast iron, while the compressor discharge and turbine shell casings and the exhaust frame are steel fabrications.

The first-stage nozzle and the first and second-stage buckets are air cooled via internal cooling circuits sourced from compressor discharge and the 17th compressor stage. The second and third-stage nozzles are cooled via external circuits sourced from the 13th compressor stage. All buckets are coated for corrosion protection.

Cycle Selection

The gas turbine is today a viable prime mover in the selection of alternatives for power generation. This requires that a new design accommodate a broad range of applications including simple cycle, cogeneration, combined cycle, heat recovery, and IGCC. For this reason, the cycle needs to be balanced in pressure ratio to satisfy both simple and heat recovery cycle requirements.

Initial studies over a range of firing temperatures indicated that a value of 1260°C (2300°F) represented a reasonable firing temperature consistent with long component lives, advanced cooling methods, material capabilities, and effective corrosion protective coatings. Given the selection of the firing temperature, it was then necessary to select a cycle pressure ratio. Figure 2 illustrates the basis for selection of 13.5:1 as the design pressure ratio for this air-cooled machine.

When selecting cycle parameters for simple-cycle applications, it is important to provide as high a power density for the power plant as possible. In this regard the specific output is a significant measure: the greater the output per pound of air flow, the smaller the gas turbine. From Fig. 2 it can be seen that the specific work peaks at approximately 14:1 for a firing temperature of 1260°C (2300°F).

Combined-cycle applications require a cycle configuration that emphasizes thermal efficiency. Figure 2 also illustrates that at a firing temperature of 1260°C (2300°F), the highest efficiency is obtained at a pressure ratio of 13.5:1 in combined cycle application.

With the firing temperature and pressure ratio established, optimal compressor flow can now be determined. Of major consideration in this decision is the exit annulus area of the turbine. Once a successful design is conceptualized for the first turbine stage at a specific firing temperature, it becomes necessary to determine just how large a last-stage bucket can be, while maintaining mechanical integrity and aerodynamic performance. The MS7001F utilizes GTD-111 as the alloy for all three turbine buckets. GTD-111 is a derivative of René 80 with improved hot corrosion resistance. It also has a 50 percent improved creep strength and a 20 percent improvement in 649°C (1200°F) LCF capability over U-500. The strength of GTD-111, together with a new aerodynamic turbine design with a moderate exit Mach number, established the flow at 408 kg/s (900 lb/sec). The net result is a turbine efficiency which is significantly higher than that of the MS7001E turbine.

Gas Turbine Design

Compressor. The compressor for the MS7001F is an axial flow, 18-stage compressor with extraction provisions at stages 5 and 13. The compressor aerodynamic and mechanical design closely follows that of the 17-stage MS7001E (633 lb/sec, 3600 rpm), but with an additional zero stage; for convenience in maintaining this relationship, the MS7001F compressor stages are numbered 0 through 17 rather than 1 through 18.

The MS7001F compressor was developed by first applying a scale factor to the diameters of the MS7001E, then increasing the annulus area an additional amount to achieve the desired flow, and lastly adding a zero stage. As a result, the MS7001F is aerodynamically similar to the MS7001E, and most of the blading is interchangeable with the MS7001E except for length. Stages 0 and 1 have been designed for operation in transonic flow using design practices applied by the aircraft gas turbine designers. As a result of using this conservative design approach, variable stators in addition to variable inlet guide vanes are not required for surge control. The MS7001F compressor contains three exit guide vane rows to straighten the flow entering the compressor diffuser in order to enhance its performance.

Surge control of the compressor is accomplished through variable inlet guide vanes (VIGV) and selective bleed at the 13th stage. When the unit is started, the VIGV are at their minimum setting, and they are controlled along a prescribed schedule as a function of corrected speed as the unit accelerates. At 100 percent speed the VIGV are full open for simple-cycle applications; for combined-cycle applications,

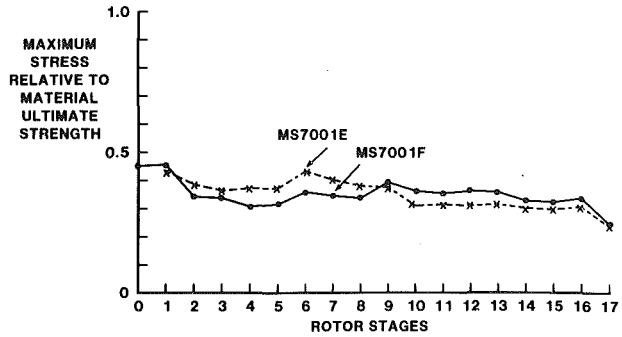

Fig. 3 MS7001E/MS7001F compressor rotor blade relative stress comparison

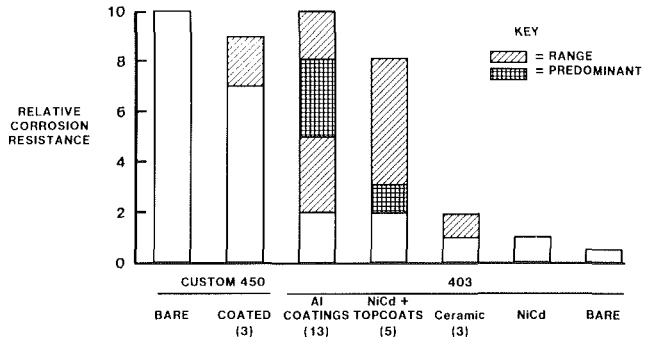

Fig. 4 Corrosion resistance; acidic laboratory tests

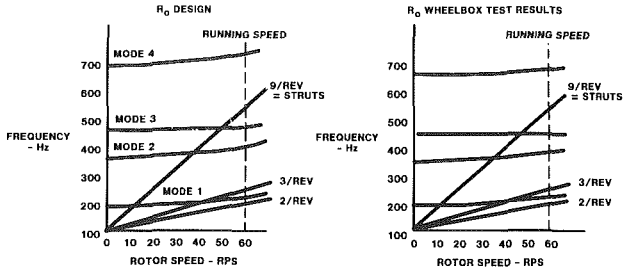

Fig. 5 Campbell diagram

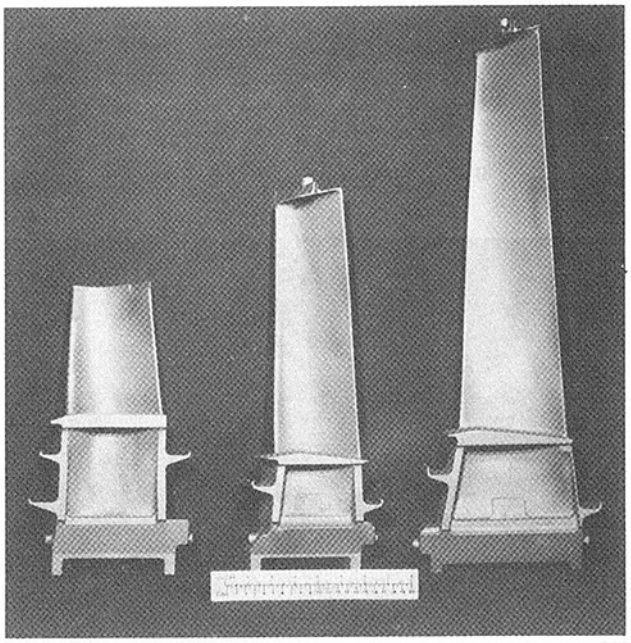

Fig. 6 Buckets

they are at an intermediate setting and then open as a function of load and exhaust temperature to maintain maximum thermal efficiency. The 13th stage bleed valves close during start-up when the generator breaker closes.

The low stage loading, which has resulted in a very rugged MS7001E compressor, is retained in the MS7001F. This has resulted in retention of a very high level of compressor efficiency in the MS7001F.

Higher strength alloys have been applied in order to accommodate the increased compressor blade stresses. Custom 450 stainless steel has been selected for the VIGV and stages 0 through 8. A higher strength version of AISI 403 with columbium addition is the alloy of choice in stages 9 through the exit guide vanes. The net result of the application of these higher strength alloys is that the applied stress/yield strength ratio is equivalent to that of the MS7001E (Fig. 3). The application of Custom 450 will have an additional benefit in corrosive environments. Field and laboratory testing of this alloy in very acidic salt environments (pH = 4) has demonstrated that it can be applied without coatings for corrosion protection. In these tests a variety of coatings was applied to AISI 403 and Custom 450 and compared with uncoated Custom 450. The field tests were performed on MS7001E machines operating in industrial environments that had proven to be very aggressive to NiCd-coated AISI 403. Uncoated Custom 450 demonstrated a clear superiority over any other non-Custom 450-based system, as well as coated Custom 450 (see Fig. 4). Those coated systems, which appeared to be equivalent to bare Custom 450 in the laboratory tests (Fig. 4), did not hold up in the field tests. Erosion was the main cause of coating failure. Of particular interest is the result wherein coated Custom 450 resulted in shorter lives than bare Custom 450. The mechanics causing this dichotomy are not understood at this time and require further study.

The dynamic behavior of compressor blading is of great concern to the compressor designer. For this reason, full-scale wheel-box testing of the stage zero blading was performed before the final design was committed to manufacturing. This testing was accomplished in General Electric's Gas Turbine Development Laboratory low-pressure wheelbox facility. This facility permits the testing of fully bladed, full-scale rotors up to 4.3 m (170 in.) diameter at rated machine speeds and pressures as low as 2 psia. The blades are instrumented to determine their dynamic response while being excited by air jets as a dynamic stimulus. Extensive efforts have been applied over the last decade to develop advanced computer-based predictive techniques that will accurately predict the dynamic response of complex unshrouded compressor and turbine blading. The results of this effort are demonstrated in Fig. 5, where the predicted and measured Campbell Diagrams are compared for the 0 stage compressor blading. Not only is the prediction exceptionally accurate, but it is clear that dynamic responses of the blade are well clear of the forcing functions of significance at operating speed.

Turbine. The MS7001F turbine is a three-stage design with the first-stage bucket unshrouded and the second and third-stage buckets equipped with integral Z form tip shrouds. This newly designed turbine is 2 percent higher in efficiency than the MS7001E turbine. Unlike the compressor, the MS7001F turbine represents a totally new aerodynamic design with zero exit swirl at full load and a moderate exit Mach number. As a result of this conservative design approach, the turbine is capable of significant uprating.

Each of the three rotor stages consists of 92 investment-cast buckets of GTD-111 (Fig. 6). The first and second-stage nozzles are constructed of 24 two-vane investment-cast FSX-414 segments, and the third-stage nozzle of 20 three-vane

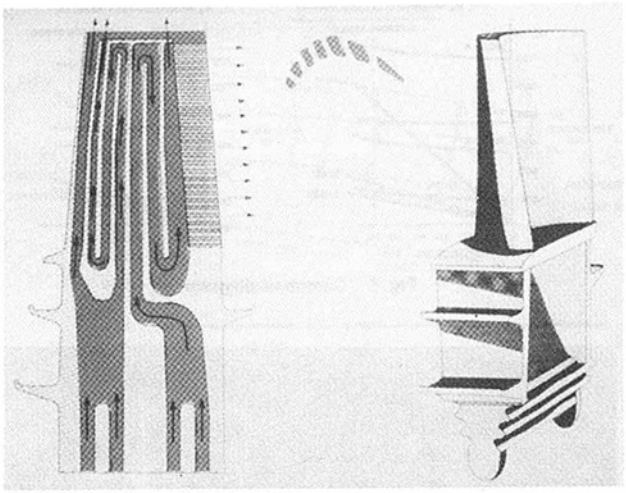

Fig. 7 First-stage bucket cooling passages

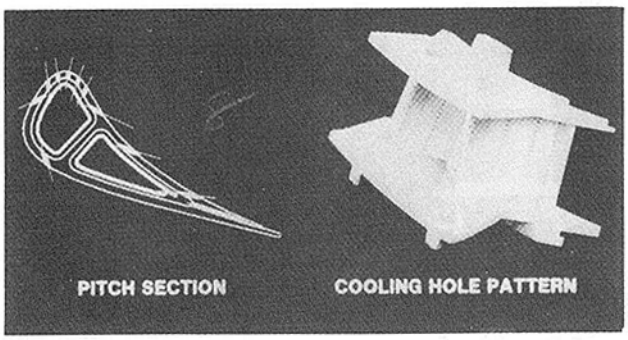

Fig. 8 First-stage nozzle cooling

investment-cast FSX-414 segments. The first and second-stage buckets and all three nozzle stages are air cooled. The first-stage bucket is convectively cooled via serpentine passages with turbulence promoters formed by coring techniques during the casting process (Fig. 7). The cooling air leaves the bucket through holes in the tip as well as in the trailing edge. The second-stage bucket is cooled by convective heat transfer using STEM (Shaped Tube Electrode Machining) drilled radial holes with all cooling air exiting through the tip. The first-stage nozzle contains a forward and aft cavity in the vane, and is cooled by a combination of film, impingement, and convection techniques (Fig. 8) in both the vane and sidewall regions. There is a total of 575 holes in each of the 24 segments. The second-stage nozzle is cooled by a combination of impingement and convection techniques while the third-stage nozzle is cooled by convection. The advanced cooling techniques applied in the MS7001F turbine components are the result of extensive aircraft engine development, as well as correlative field testing performed on cooled components in current production heavy-duty machines. In addition, hot cascade tests were performed on MS7001F first-stage components to validate the heat transfer design assumptions. The efficient use of cooling air made possible by the advanced cooling methods applied is further enhanced by the reduced vane surface area of the first-stage nozzle, achieved by low solidity. The particular vane shape selected has also been developed for aircraft engines, and is illustrated in Fig. 8.

In order to enhance further the excellent hot corrosion and oxidation resistance of GTD-111, all three stages of buckets are coated. The first-stage coating is a patented alloy of Co, Cr, Al, and Y, applied by the PLASMAGUARD™ low-pressure plasma spray method. The second-stage bucket is coated with a patented alloy of Co, Cr, and Y, also applied by the PLASMAGUARD™ low-pressure plasma spray method. The third-stage bucket is coated with a high-Cr coating, which is applied by a pack process and is subsequently given a diffusion heat treatment. The first-stage coating possesses outstanding high-temperature hot corrosion resistance with a 3× improvement over uncoated GTD-111. The second-stage coating has been specifically developed to provide exceptional resistance to both high and low-temperature hot corrosion. The high Cr coating of the third stage focuses principally on providing protection against low-temperature hot corrosion.

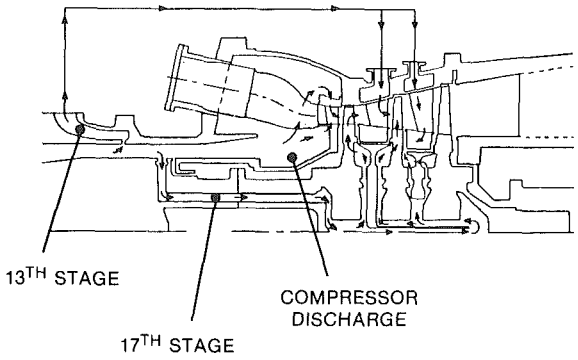

Fig. 9 Cooling circuit

The buckets of all three stages are designed with long shanks and integral cover plates. These shanks provide for isolation of the gas path from the wheel rim and for mechanical damping of the bucket system via seal/damping pins located under the platform and in the cover plate edges. This system, in combination with the interlocking bucket tip Z shrouds, has proven very effective and durable in similar designs found in the MS7001E and other production machines. Careful attention has been given in designing the bucket shank regarding the transition between the bucket airfoil root and the dovetail to assure that high stresses are avoided due to structural discontinuities.

The first and second-stage stationary shrouds are two-piece designs where the gas side inner shroud is separate from the supporting outer shroud in order to provide freedom for expansion/contraction for improved low cycle fatigue (LCF) life. The first-stage shroud is cooled by impingement, film, and convective means.

The cooling circuit for the turbine components consists of both internal and external circuits (Fig. 9). The first and second-stage buckets, the first-stage nozzle, and the first-stage shroud are cooled by an internal cooling air circuit, while the second and third-stage nozzles are cooled by an external cooling air circuit. The internal circuit is supplied by 17th stage and by compressor discharge air, and the external circuit by 13th stage extraction air. The first-stage nozzle and shroud cooling air is supplied from the compressor discharge plenum housing the combustion transition pieces. The bucket cooling is supplied by air flowing radially inward at the 17th stage compressor wheel, thence through 15 holes drilled axially through the distance piece, and then over the forward face of the first-stage turbine wheel. The bucket cooling air then flows through the bore of the first-stage turbine wheel into the chamber between the first and second-stage wheels to the root of the first and second-stage buckets. This circuit also provides air to heat the bores of the second and third-stage wheels and to purge the wheelspaces, as shown in Fig. 9. The external circuit consists of piping between the 13th stage extraction belt and the turbine shell, as shown in Fig. 9.

Combustor. The MS7001F combustion system consists of 14 combustion chambers with 356 mm (14 in.) nominal

™Trademark of General Electric Company.

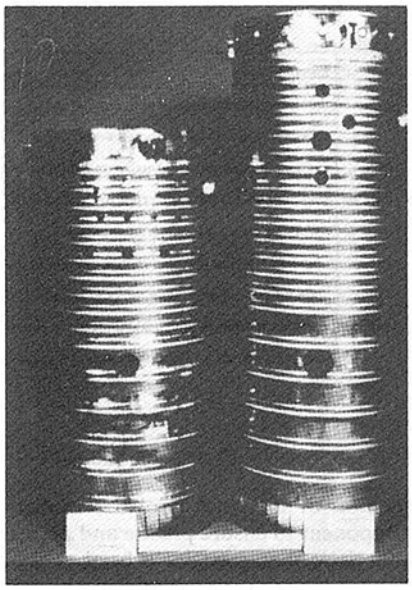

Fig. 10 Combustion liner

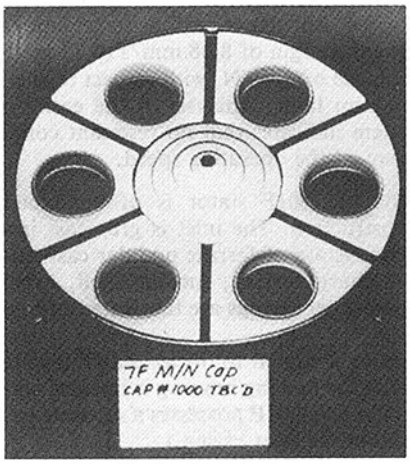

Fig. 11 Combustion liner cap

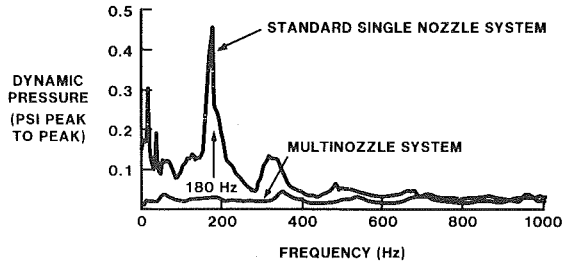

Fig. 12 Multi and single-fuel nozzle combustion noise

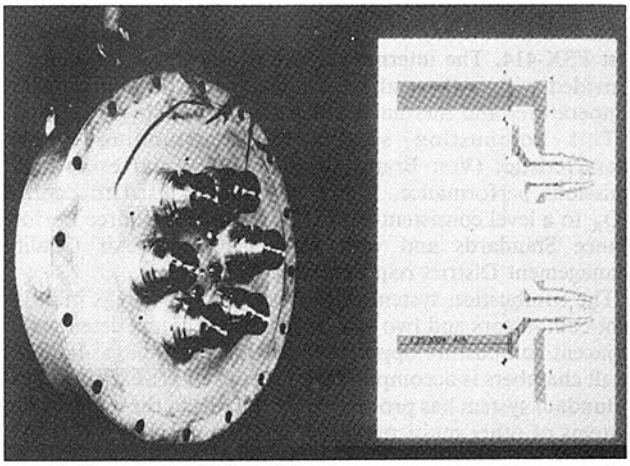

Fig. 13 Fuel nozzle/combustion cover assembly

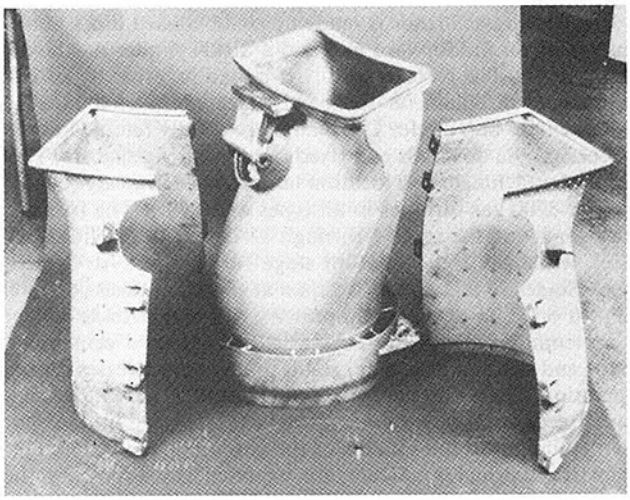

Fig. 14 Transition piece

diameter combustion liners. Transition pieces conduct the combustion gases to the first-stage nozzle.

The liners are constructed in a manner identical to the MS7001E liners (Fig. 10) but are 30 percent thicker and 213 mm (8.4 in.) shorter. This particular design provides for extensive and effective film cooling of the liner wall, as well as penetrations for combustion and dilution air and for cross-fire tube connections. The MS7001F liners are constructed of Hastelloy-X material, as are the other product line liners, with the addition of HS-188 in the lower 282 mm (11.1 in.) portion and the application of thermal barrier coating to the internal surface. These additions provide for improved high-temperature strength and a reduction of metal temperatures and thermal gradients. A flow sleeve surrounds the liner to provide a controlled flow path for the combustion, dilution, and cooling air.

The liner cap represents a change over the MS7001E design in that it provides for six fuel nozzles in lieu of one (Fig. 11). This multifuel nozzle arrangement was selected as a result of the superior field experience with a prototype multifuel nozzle system on an operating MS7001B/C gas turbine in utility service with water injection for NO_X control [1]. This test, confirmed by extensive laboratory full-scale combustion tests, clearly demonstrated the reduced combustion noise (dynamic pressure) level achieved when operating with multifuel, as opposed to single-fuel nozzle systems (Fig. 12). The noise reduction resulting from replacing the single nozzle with a multinozzle system reduced the combustion system wear to the point where combustion inspection intervals of the tested machine could have been extended from 3000 to 12,000 hr. Additionally, the application of the multifuel nozzle concept results in a shorter flame, contributing to the MS7001F combustion system being 23 in. shorter than the MS7001E system. The six fuel nozzles are mounted directly on the combustion end cover such that no more piping connections are required than if a single-fuel nozzle were employed. This is accomplished through manifolding integral with the cover (Fig. 13).

The transition piece is constructed of two major assemblies (Fig. 14). The inner transition piece is surrounded by a per-

forated sleeve with the same general shape as the transition piece. This perforated sleeve forms an impingement cooling shell causing jets of compressor discharge air to be directed onto the transition piece body. The air, after impinging on the transition piece body, then flows forward in the space between the impingement sleeve and transition piece into the annulus between the flow sleeve and the combustion liner. It then joins additional air flowing through bypass holes provided in the flow sleeve to provide the air for the combustion/cooling/dilution processes. The aft frame of the transition piece is cooled through the action of compressor discharge air flowing through holes drilled such that the air enters the main gas stream as a film on the inside surface of the aft frame. The impingement sleeve is fabricated of AISI-304 stainless steel, the transition piece body of Nimonic 263, and the aft frame of cast FSX-414. The internal surface of the transition piece is provided with a thermal barrier coating to minimize metal temperatures and thermal gradients.

This combustion system has outstanding smoke characteristics (Von Brand number of 99) and exceptional emissions performance. Water or steam is used to control NO_X to a level consistent with U.S. EPA New Source Performance Standards and with most California Air Quality Management District requirements.

The combustion system possesses two spark plugs in adjacent combustors and two sets of redundant flame detectors in adjacent combustors opposite from the spark plugs. Ignition in all chambers is accomplished by means of cross firing. This redundant system has proven highly reliable in the combustion systems of other multicombustor configurations.

Rotor. The MS7001F rotor is of bolted disk and shaft construction and consists of two major groups: the compressor and turbine.

The compressor rotor is made up of 16 bladed disks plus a stub shaft on the forward end and a disk/cylinder on the aft end (Fig. 1). The rotor assembly is bolted together by fifteen 76.2 mm (3 in.) diameter 12 Cr bolts located on a 940 mm (37 in.) diameter bolt circle. The blades are solidly retained in the wheel rims via dovetails and fixed in position via spacers. This form of attachment and location has proven extremely reliable in over 3700 gas turbines in all types of service. The forward stub shaft and the stage 1 through 15 disks are of NiCrMoV steel, while the 16th and 17th stage forgings are of CrMoV steel. Stages 14 and 16 are hot spun at speeds in excess of 5000 rpm in order to develop compressive residual stresses which, when combined with the normal stresses due to centrifugal loads and thermal gradients, result in low bore stresses during operation. These parts are also spun at $-40°C$ ($-40°F$) to ensure freedom from detrimental defects. This additional hot spin is limited to the aft end of the compressor, where larger transient thermal gradients are experienced, following the same practices applied in the MS7001E gas turbine.

The turbine rotor is constructed of three M-152 (12 CrNiMoV steel) alloy wheels separated by spacers of the same alloy and with an aft bearing shaft of CrMoV steel. These are all bolted to the distance piece, also of CrMoV steel. The wheels and the forward spacer are hot and cold spun in a fashion similar to that described above for compressor disks. The main turbine bolting is of 12 Cr alloy and consists of twelve 76.2 mm (3 in.) bolts at a 1.12 m (44 in.) diameter bolt circle. The distance piece is joined to the first turbine wheel by thirty 50.8 mm (2 in.) diameter bolts of 12 Cr alloy on a 1.12 m (44 in.) diameter bolt circle. The compressor and turbine rotors are joined at the marriage joint by thirty 50.8 mm (2 in.) diameter bolts of IN-718 alloy operating on a 1.12 m (44 in.) diameter bolt circle. The turbine buckets are held in the wheel rim by means of fir tree dovetails. They are retained in position by a 360 deg lock wire, which nests in grooves machined in both the bucket and the wheel. This positive, yet easily removed, system has been in use in all MS6001 machines produced.

The construction of the rotor provides rabbetted fits between each component to ensure precise and permanent alignment. The bolt circle diameters have been made as large as possible, without interfering with blade and bucket dovetails, to produce a very rigid rotor. Only rigid body (rotor deflection energies less than 60 percent of system energies) modes exist below 100 percent speed. The first flex mode is at 137 percent of operating speed. Imbalance response calculations indicate a 100 percent speed margin of 8.38 mm/s (0.33 in./sec), with a midspan imbalance of 4 W/N, with respect to the 12.7 mm/s (0.5 in./sec) alarm limit. Analysis of the entire rotor/bearing/stator system indicates that no resonant condition exists within 6 percent of the operating speed.

Stator. The MS7001F stator is of combined cast and fabricated construction. The inlet is grey cast iron, and the compressor casings are of ferritic nodular cast iron while the compressor discharge casing, turbine shell, exhaust frame, and combustion outer casings are fabricated of SA516 carbon steel.

The inlet casing is similar to the MS9001E (885 lb/sec, 3000 rpm) except that the bearing housing is integral with the lower half casting. (The MS9001E possesses a separate bearing housing located within the inlet casing.)

The turbine shell supports the second and third-stage nozzles cantilevered from the first, second, and third-stage shrouds in a fashion identical with the MS7001E designs. The first-stage nozzle is also supported in a fashion identical to these machines. It is held at its outer diameter in a retaining ring assembled to the turbine shell and supported at its inner diameter by the compressor discharge casing.

The exhaust frame assembly supports the aft bearing as well as the AISI-347 exhaust diffuser. It is cooled by air supplied from an off-base blower as is the practice with the MS7001E family of gas turbines.

The gas turbine support system consists of four support legs and two gib blocks. The forward support legs are fixed, while the aft support legs are pivotal. With this design, the axial growth of both the rotor and stator is aft from the thrust bearing/forward support leg system. One gib is integral with the forward compressor casing and the other integral with the exhaust frame; both are located on the vertical center plane of the unit. This method of support, together with the integral No. 1 bearing and the centerline supported No. 2 bearing, assures precise internal and external alignment control under all operating conditions.

Table 1 MS7001F controls and accessory skids

SKID	SIZE	FUNCTION
LUBE OIL	11' x 34'	SUPPLIES COOLED & FILTERED LUBE, SEALING AND HYDRAULIC OIL TO TURBINE & GENERATOR, CONTAINS FUEL GAS STOP & CONTROL VALVES
LIQUID FUEL	11' x 31'	SUPPLIES FILTERED LIQUID FUEL TO GAS TURBINE
ATOMIZING AIR	11' x 16'	SUPPLIES ATOMIZING AIR FOR COMBUSTION
COOLING FAN	11' x 16'	SUPPLIES VENTILATION AND EXHAUST FRAME COOLING AIR
COOLING WATER (2)	11' x 38'	SUPPLIES COOLING WATER FOR LUBE OIL, ATOMIZING AIR, & GENERATOR
WATER INJECTION	11' x 28'	SUPPLIES TREATED WATER FOR NO_X CONTROL
STARTING	7' x 10'	CONTAINS STARTING MOTOR & TORQUE CONVERTER
AIR PROCESSING	5' x 8'	SUPPLIES AIR TO PULSE-CLEAN THE INLET FILTERS
CONTROL CAB	11' x 11'	CONTAINS THE TURBINE & GENERATOR CONTROL PANELS AND DC SUPPLY
EXCITATION	10' x 13'	SUPPLIES & REGULATES THE GENERATOR FIELD CURRENT

Accessory Design

The MS7001F accessories are all electrical motor driven. Each major system is designed to be installed on a separate skid, except the fuel gas stop ratio valve, which is installed on

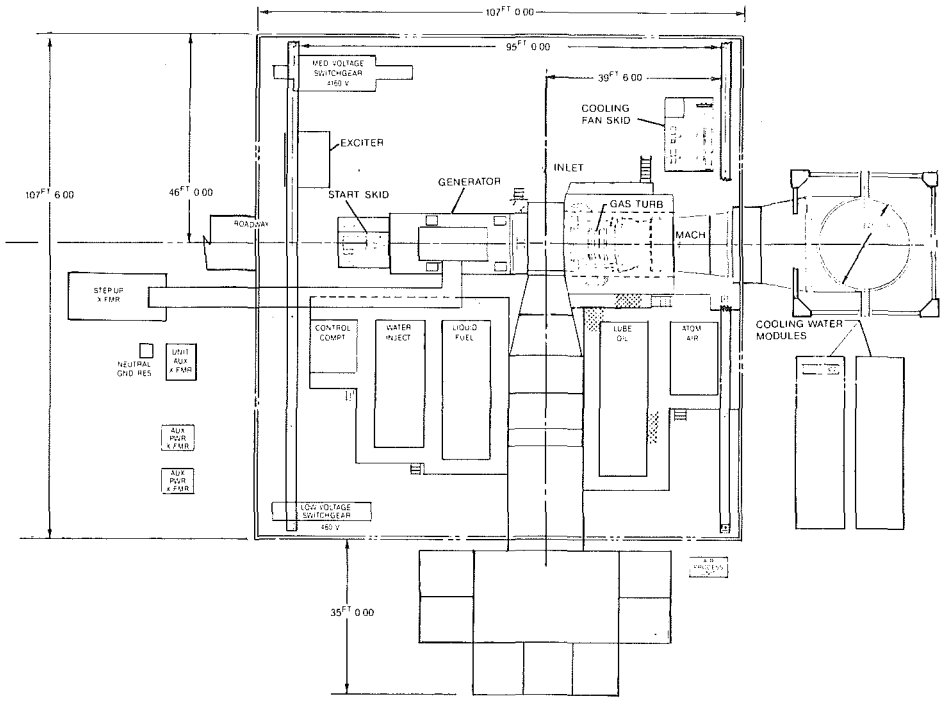

Fig. 15 Power plant arrangement concept

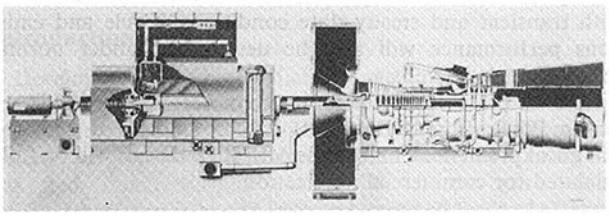

Fig. 16 MS7001F arrangement

the lube oil skid. The skids, together with their functions, are listed in Table 1.

The decision to use separate skids for each system was made to provide the greatest plant arrangement flexibility, the easiest maintenance accessibility, and improved reliability. The skids are designed for indoor or outdoor construction. When supplied with lagging, all panels are hinged so that the sides can be completely opened to facilitate servicing and observation. In addition the lagging can be simply lifted from the skid in a straight pull after unbolting it from the base. Nothing is mounted to the inside of the lagging except the vent fan. All gages can be conveniently read from the outside of the skid without restriction.

With respect to maintenance, sufficient space is provided so that any component may be serviced directly without having to remove piping or other components. Filters and coolers are oriented vertically so that they can be serviced by vertical pulls. All components and flanges are located outside the skid base so that this constrained area need not be accessed for any service or maintenance function.

A typical plant arrangement is shown in Fig. 15. In this arrangement, the skids and the turbine/generator are located on grade with a side inlet. Other inlet configurations are available including overhead and underneath. Customer preference will dictate this, as well as other configurations, with the prime concern being ready crane coverage without the necessity of removing or avoiding ducting and machinery. The flexibility of self-contained skids also allows arrangements to suit customer needs and to provide sufficient lay down space for overhaul. All accessory systems, except for the starting skid, may be placed in a basement so that a classic turbine hall configuration can be accomplished.

The gas turbine is coupled to the hydrogen-cooled generator using a rigid coupling. The 2200 hp starting motor is connected to the generator collector end through a torque converter (Fig. 16). A normal start cycle for this configuration is 12 min to full-speed no-load, followed by 18 min to full load, for a total startup time of 30 min. Two combined-cycle arrangements are available, single shaft and multishaft. In the single-shaft arrangement, the steam turbine is interposed between the gas turbine and the generator. In this arrangement, it is only necessary to remove the starting skid to service the generator, the steam turbine being left in place. In the multishaft arrangements, one or more gas turbines are utilized to generate steam to drive a single steam turbine which drives a generator that is divorced from that driven by the gas turbine.

Test Program

The design of the MS7001F gas turbine is supported by a three-phase test program:

Phase I – Fundamental studies and component tests
Phase II – Factory prototype test
Phase III – Field prototype test

The Phase I effort has included the development and application of advanced analytical methods and computer techniques in order to predict accurately three-dimensional viscous fluid dynamics, boundary layer heat transfer, dynamic response of blading, dynamic response of complex systems, and complex material behavior. Where practical, the results of these advanced analytical tools were checked on models and components to ensure the accuracy of the predictions. One example was cited in reference to the "0" compressor blade dynamic response (Fig. 5). Other examples include hot cascade testing of the first-stage nozzle and liquid crystal studies of the first-stage nozzle and bucket to verify heat transfer assumptions, flow testing of the rotor cooling circuit and other components, materials behavior testing under calculated strain/time/temperature cycles, dynamic response wheelbox

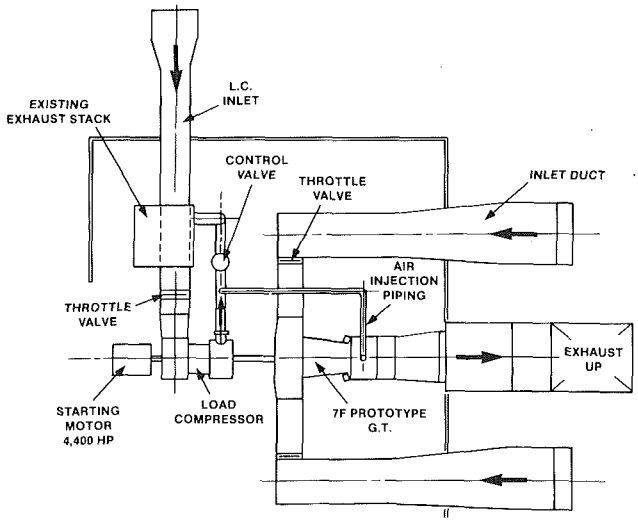

Fig. 17 Factory prototype test arrangement

Table 2 MS7001F prototype test instrumentation

	FACTORY TEST	FIELD TEST
COMPRESSOR		
DYNAMIC PRESSURE/STRAIN	106	40
TEMPERATURE	230	50
PRESSURE	248	35
COMBUSTOR		
DYNAMIC PRESSURE/STRAIN	82	20
TEMPERATURE	310	200
PRESSURE	148	70
TURBINE		
DYNAMIC STRAIN	36	60
TEMPERATURE	1256	700
PRESSURE	321	240
BEARINGS		
TEMPERATURE	57	50
PRESSURE	14	20
ACCESSORIES		
DYNAMIC STRAIN	10	30
TEMPERATURE	54	100
PRESSURE	120	160

testing of all turbine buckets, exhaust system flow testing, and maintainability studies. A major development effort was involved in all aspects of the combustor design. The multicombustor concept allows full machine conditions to be applied to an individual combustor under laboratory conditions. This has permitted complete and thorough development of the MS7001F combustor prior to actually operating the machine. Because of this, great confidence in both the aerodynamic performance, mechanical integrity, and emission performance of this key system was demonstrated early in the program.

Also incorporated in the Phase I effort has been field testing of selected materials and configurations in order to gain both manufacturing and operating experience. Included in this effort has been the field testing of impingement-cooled transition pieces, application of N-263 in transition pieces, advanced bucket coating systems, thermal barrier coatings, and new compressor blade materials.

The Phase II test effort is largely aimed at verifying the compressor performance and obtaining component and system performance and operating data. During this phase, a full compressor map will be determined, including surge margin. Also, during this phase, extensive rotor and stator instrumentation will be included to measure temperatures, pressures, hot gas path profiles, blading dynamic behavior, and system dynamic behavior.

The test configuration for this phase is illustrated in Fig. 17. The load is provided by a 17-stage MS7001E axial flow compressor, which is capable of absorbing 80 percent of the MS7001F output. Full rated firing temperature will be achieved by throttling the machine flow at the compressor inlet. The MS7001F compressor will be mapped, and the surge margin confirmed, by a combination of means including variable speed operation, variable flow through inlet guide vane, and throttling modulation and variable pressure ratio through injection of load compressor flow into the compressor discharge upstream of the combustor. Stage-by-stage, as well as overall, performance will be determined.

The Phase II test period is planned for one-year duration.

The Phase III test involves a full-load test at a customer site. In preparation for this, the factory prototype unit will be refurbished with a new rotor. The new Phase III rotor will have more extensive turbine-end instrumentation and less extensive compressor instrumentation than the Phase II rotor (see Table 2). The primary objective of the Phase III test is to verify all design and performance parameters, exclusive of developing a full-range compressor map, which will be accomplished in Phase II. Metal, cooling circuit, and gas path temperatures; cooling circuit and cycle pressures; component and system dynamic behavior will all be determined under both transient and steady-state conditions. Cycle and emissions performance will also be determined under normal steady-state conditions.

Each of the component and system data bases developed during Phase II and Phase III will be compared with the analytical predictions before the MS7001F design will be fully validated for commercial application.

Closure

This paper has presented the design approach, configuration, and application of a totally new heavy-duty gas turbine. The development of this turbine system has absorbed well over 300 man-years of direct design effort plus extensive supporting developmental effort. It will have involved some nine years from the gleam in the engineer's eye to the production of economical and reliable power on the first customers' grid. It has been nurtured during a period of uncertain energy cost, increasingly tighter environmental standards, and lagging load growth. However, it appears that, even as it is making its debut, an awareness is developing in both developed and developing societies that efficient, clean, and reliable power generation is essential to healthy economies. From this realization, then, the MS7001F is being introduced with the confidence that its contribution to progress in power generation will be firmly established.

References

1 "High Reliability Gas Turbine Combustion Project," Electric Power Research Institute, EPRI AP-3885, Project 1801-1, Final Report, May 1985.

2 "GE SPEEDTRONIC™ Mark IV Control System," 1984 State of the Art Seminar, GER-3426 (available from the General Electric Company, Turbine Business Operation, Schenectady, NY).

S. Aoki

K. Teshima

M. Arai

Engineering Research Association for Advanced Gas Turbines, Tokyo 105, Japan

H. Yamao

Research and Development Center, Mitsubishi Heavy Industries, Ltd., Tokyo, Japan

Results From the Phase II Test Using the High-Temperature Developing Unit (HTDU)

Phase II of the high-temperature turbine test was performed using the High-Temperature Developing Unit (HTDU). This unit has the same two stages as the high-pressure turbine of the AGTJ-100A reheat system. The purpose of the Phase II test was to investigate the potential of candidate technologies that may be applied to the advanced engine, the AGTJ-100B. Cooling characteristics of several cooling schemes for the first stage blades, and the performance of thermal barrier coating employed on the first stage nozzles and blades, were investigated. This paper presents the Phase II test results.

Introduction

Development of a high-efficiency gas turbine, sponsored by the Ministry of International Trade and Industry of Japan, was begun in 1978 [1]. This gas turbine had a final thermal efficiency target of over 55 percent (LHV base) as a combined gas and steam turbine plant. The reheat gas turbine AGTJ-100A, which has an interim combined thermal efficiency of 50 percent target, has been constructed and is now being tested at the Sodegaura Power Station of the Tokyo Electric Power Company.

Among the components of the AGTJ-100A, the high-pressure turbine is operated under the most severe conditions, with a turbine inlet average temperature of 1300°C and a pressure of 54.4 atm, both of which greatly exceed those of existing heavy-duty industrial gas turbines. Hence a high-temperature turbine testing program was established in order to demonstrate the performance and reliability of the high-pressure turbine of the AGTJ-100A. These Phase I tests were conducted during the three months from Dec. 1982 to Feb. 1983, in the gas turbine laboratory of Mitsubishi Heavy Industries' Takasago Machinery Works. Both the aerodynamic and cooling characteristics of the high-pressure turbine were obtained [2, 3].

The Phase II tests were performed during the two-month period of Oct. and Nov., 1984. The objectives of these tests were to study the potential of the different cooling systems to achieve a higher turbine inlet temperature and to verify the performance of thermal barrier coatings employed on the airfoil surfaces. The advanced engine, named AGTJ-100B, has as a design goal a turbine inlet temperature of 1400°C. Thus, blade and nozzle cooling schemes with enhanced cooling characteristics must be utilized to meet the 100°C higher inlet gas temperature relative to the AGTJ-100A design. Against this background, research on advanced cooling schemes, thermal barrier coatings, and new blade material having a high creep strength have been conducted in the Phase II tests, all at turbine inlet temperatures of 1300°C or lower.

In the Phase II test, the number of measuring points was increased to 400 to obtain more detailed information on the cooling characteristics of the nozzles and blades. In addition to the increased number of measuring points, infrared thermometry and a tip clearance measuring device were used to obtain surface metal temperatures of the leading edges of the first stage blades and the tip clearance of the first stage blades, respectively.

This paper presents the results of the Phase II test.

Test Facility and Instrumentation

High-Temperature Developing Unit. The tests were conducted at the gas turbine test facility of Mitsubishi Heavy Industries, Ltd., Takasago Machinery Works. A schematic drawing of the test facility is shown in Fig. 1.

The air source compressor had a pressure ratio of 16 and a

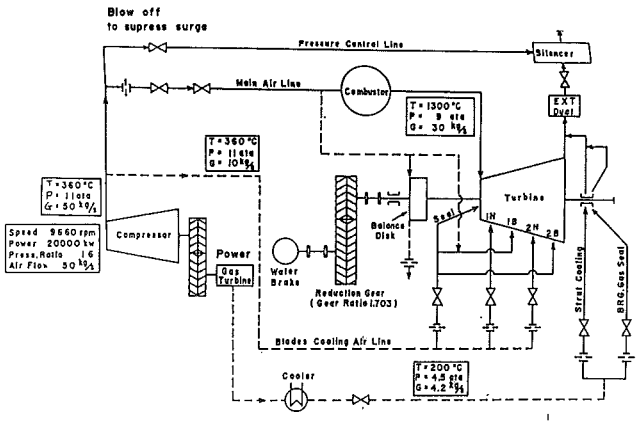

Fig. 1 Schematic drawing of the test facility

Contributed by the Gas Turbine Division of THE AMERICAN SOCIETY OF MECHANICAL ENGINEERS and presented at the 32nd International Gas Turbine Conference and Exhibit, Anaheim, California, May 31–June 4, 1987. Manuscript received at ASME Headquarters February 24, 1987. Paper No. 87-GT-254.

mass flow rate of 50 kg/s, and was driven by a gas turbine with an output of 30,000 kW. The main air flow was supplied at a temperature of 360°C and a pressure of 11 atm. Three cooling air lines were branched from the main air lines: one for the first stage nozzle cooling, another for the second stage nozzle cooling, and the last for rotating blade cooling. The air flow rate of each line was adjusted to the required value using control valves. The power generated by the test turbine was absorbed and measured by a water brake through a reduction gear. Figures 2 and 3 show a cross-sectional view and an overall view of the HTDU, respectively.

Instrumentation. Each leading edge of the two first stage nozzles was fitted at its midheight position with total pressure probes, and each leading edge of the two second stage nozzles was fitted at five positions in the radial direction with total pressure probes and sheath-type thermocouples.

At the turbine exit, a multipoint kiel type total pressure probe, a total temperature probe, and a yaw meter were fitted. Each of these probes had five measuring points in the radial direction. The measuring locations are shown in Fig. 4.

Metal temperatures of the nozzles and blades were measured by 0.5 mm sheath-type thermocouples embedded into the wall at midheight. There were three measuring points for each nozzle and blade, except for the second stage nozzle, which had five points in a radial direction. Output signals from the thermocouples were transmitted to a data processing scheme through a 50 channel slip ring. The first stage nozzle with a film cooling scheme was fitted with five static pressure taps at the midheight position.

In addition to the instrumentation described above, infrared thermometry and a tip clearance measurement device were used in the Phase II test. Figure 5 shows these mounted on the HTDU. Infrared thermometry was used to measure surface metal temperatures of the first stage blades. Tip clearance of the first stage blade was measured at one circumferential location by using a proximity-type tip clearance measuring device.

Air-Cooled Nozzles and Blades

The first stage nozzle was the type typically used in high-temperature air-cooled gas turbines. The nozzle had two cavities with cross-flow impingement cooling augmented by film external cooling at the leading edge, the pressure surface, and the suction surface. Pedestals in the internal trailing edge region were supplied with coolant flow from the aft cavity and spent cooling air was discharged from the trailing edge. Thermal barrier coatings (TBC) were employed on some of the nozzles. The thickness of the coatings was either 0.3 mm or 0.4 mm (see Table 1).

Three different cooling schemes were applied to the first stage blades. They were: (1) the insert type cooling scheme (original blade), (2) the return flow type cooling scheme, and (3) the pin fin cooling scheme. The blades with the insert type cooling scheme had one cavity with cross-flow impingement cooling augmented by film cooling at the leading edge. The blades with the return flow type cooling scheme were cooled by an internal serpentine type arrangement, with axial holes through the trailing edge. The blades with the pin fin cooling scheme had one radial coolant passage for convection cooling. Impingement and film cooling were adopted at the leading

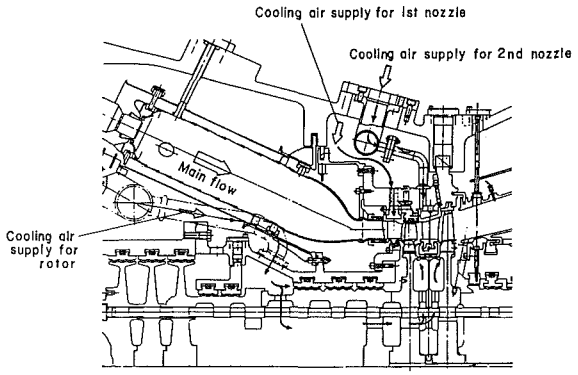

Fig. 2 Cross-sectional view of the HTDU

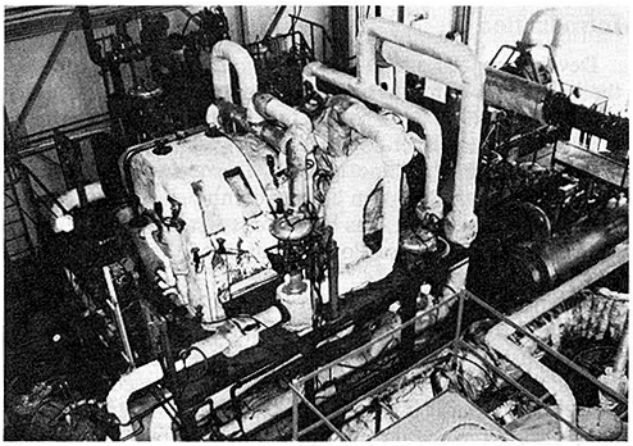

Fig. 3 Overall view of the HTDU

Nomenclature

G = mass flow rate, kg/s
ΔH = enthalpy drop, J/kg
N = shaft speed, rpm
P = pressure, atm
R = gas constant, J/kg•°C
T = temperature, °C
δ = ratio of inlet pressure to standard pressure

ϵ_{cr} = function of $\kappa = \frac{\kappa_{st}}{\kappa}$

$$\cdot \frac{\left(\frac{\kappa+1}{2}\right)^{\frac{\kappa}{\kappa-1}}}{\left(\frac{\kappa_{st}+1}{2}\right)^{\frac{\kappa_{st}}{\kappa_{st}-1}}}$$

$\Delta\eta$ = difference in turbine efficiency
η_t = turbine efficiency
θ_{cr} = squared ratio of critical velocity at turbine inlet to critical velocity at standard condition
κ = ratio of specific heat
π_t = total pressure ratio

$$\phi_{cr} = \frac{1}{\eta_t}\left\{1-\left(\frac{\kappa_{st-1}}{\kappa-1}\right)\left(\frac{\kappa+1}{\kappa_{st+1}}\right)\cdot\left(1-\eta_t^{\frac{1-\kappa}{\kappa}}\right)\right\}\frac{\kappa_{st}}{1-\kappa_{st}}$$

Subscripts

c = cooling air
DP = design point condition
g = gas
o = inlet gas, coolant, or leakage air into the flow path
in = turbine inlet condition
is = isentropic condition
M = metal
m = mean value
ref = reference condition (Gc/Gg is the value obtained on the HGT equivalent to design condition)
LE = leading edge
PS = pressure surface
SS = suction surface
st = standard condition
T = total condition
0 = turbine inlet
1 = nozzle exit
2 = blade exit

edge. Thermal barrier coatings were employed on some of the blades. The thickness of the coatings was either 0.3 mm or 0.4 mm.

The second stage nozzle had no film cooling. The cooling air, after being spent for impingement and convection cooling, was discharged from the trailing edge.

For the second stage blades, a return flow type cooling scheme was used. These blades were cooled by a simple internal serpentine type arrangement. The cooling air, after being spent for convection cooling, was discharged from the trailing edge.

The features of the nozzles and blades are summarized in Table 1.

A photograph of the first stage blades of the return flow type cooling scheme with TBC is shown in Fig. 6.

Figure 7 shows circumferential locations of the first stage blades having various cooling schemes and TBC.

Tests and Data Analysis

Procedure. The test was conducted under equivalent design conditions, shown in Table 2, to evaluate the aerodynamic and cooling characteristics of the turbine.

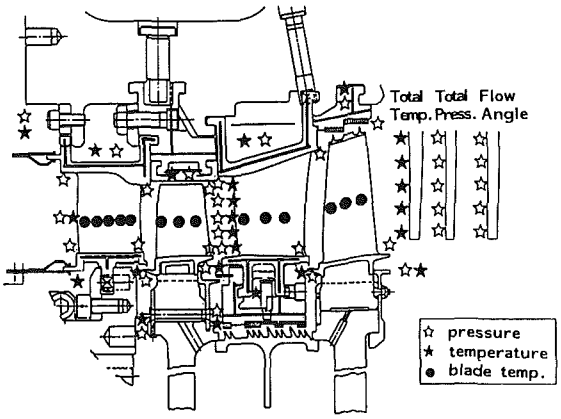

Fig. 4 Measuring locations

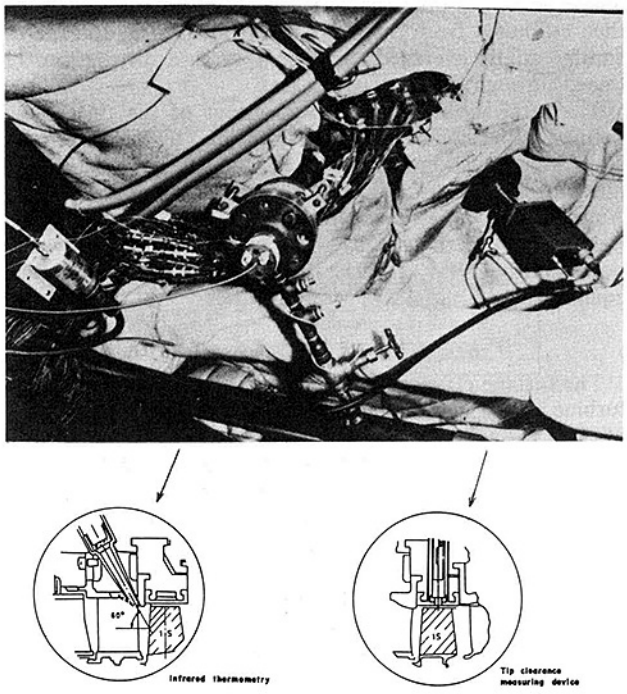

Fig. 5 Infrared thermometry and tip clearance measuring device mounted on HTDU

1 Hot Gas Tests (HGT). These tests were carried out at lower turbine inlet temperatures than the design value of AGTJ-100A. This is because these moderate gas temperatures allow for testing at a lower cooling flow rate rather than at the design value. For the aerodynamic test, equivalent shaft speeds were varied from 60 to 100 percent of the design values. The overall pressure ratio of the turbine was varied from 2.4 to 4.4, while turbine inlet temperatures were varied from 750°C to 1100°C. For evaluating cooling characteristics, the cooling air flow rates for each nozzle and blade were varied from 40 to 150 percent of the design value, while maintaining the turbine inlet temperature at about 900°C.

2 Demonstration Tests (DT). These tests were carried out at the design turbine inlet temperature of the AGTJ-100A, namely 1300°C, to demonstrate the aerodynamic performance and cooling characteristics of the high-pressure turbine. The equivalent speeds were varied from 70 to 100 percent of the design speed, while maintaining the pressure ratio and cooling flow rate at the design values.

Table 1 Features of nozzles and blades

Blade	Number of Blades	Material	Cooling system	Note
1st Nozzle Row	48	IN939	·Impingement cooling ·Film external cooling	same as AGTJ-100A
	3	IN939		with 0.3mm TBC *1
	1	IN939		with 0.4mm TBC
	2	IN939		with 0.3mm TBC and film cooling holes drilled by laser beam
1st Blade Row	61	MAR-M247CC *2	Insert *4	same as AGTJ-100A
	5	MAR-M247CC	Insert	with 0.3mm TBC
	2	MAR-M247CC	Return flow *5	
	4	MAR-M247CC	Return flow	with 0.3mm TBC
	3	MAR-M247CC	Pin fin *6	
	3	MAR-M247CC	Pin fin	with 0.3mm TBC
	1	TM321CC	Insert	
	2	TM321CC	Insert	with 0.3mm TBC
	1	TM321CC	Insert	with 0.4mm TBC
	3	MAR-M247DS *3	Insert	same as AGTJ-100A
	3	MAR-M247DS	Insert	with 0.3mm TBC
	2	TMD-5DS	Insert	same as AGTJ-100A
	2	TMD-5DS	Insert	with 0.3mm TBC
2nd Nozzle Row	60	IN939	Insert *7	same as AGTJ-100A
2nd Blade Row	94	MAR-M247CC	Return flow	same as AGTJ-100A

*1 THERMAL BARRIER COATING
*2 CONVENTIONAL CASTING
*3 DIRECTIONAL SOLIDIFICATION
*4 Impingement cooling Film external cooling
*5 Convection cooling Film external cooling
*6 Convection cooling with pin fin Film external cooling
*7 Impingement cooling Convection cooling

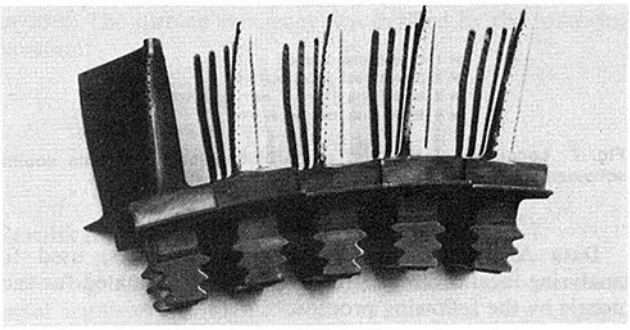

Fig. 6 First stage blades having return flow cooling scheme with/without TBC

Table 2 Equivalent design conditions

	Test Mode	Hot Gas Test (HGT)	Demonstration Test (DT)	AGTJ-100A
Equivalent Condition	Inlet total temp. (°C)	900	1300	1300
	Inlet total press. (ata)	9.0	9.0	54.44
	Inlet gas flow (kg/s)	32.6	28.1	167.3
	Speed (rpm)	7236	8380	8500
	Pressure ratio	4.06	4.06	4.03
	Work (kW)	12426	14390	88059
	Cooling air flow rate	40~150% of design flow rate	Design flow rate	Design flow rate

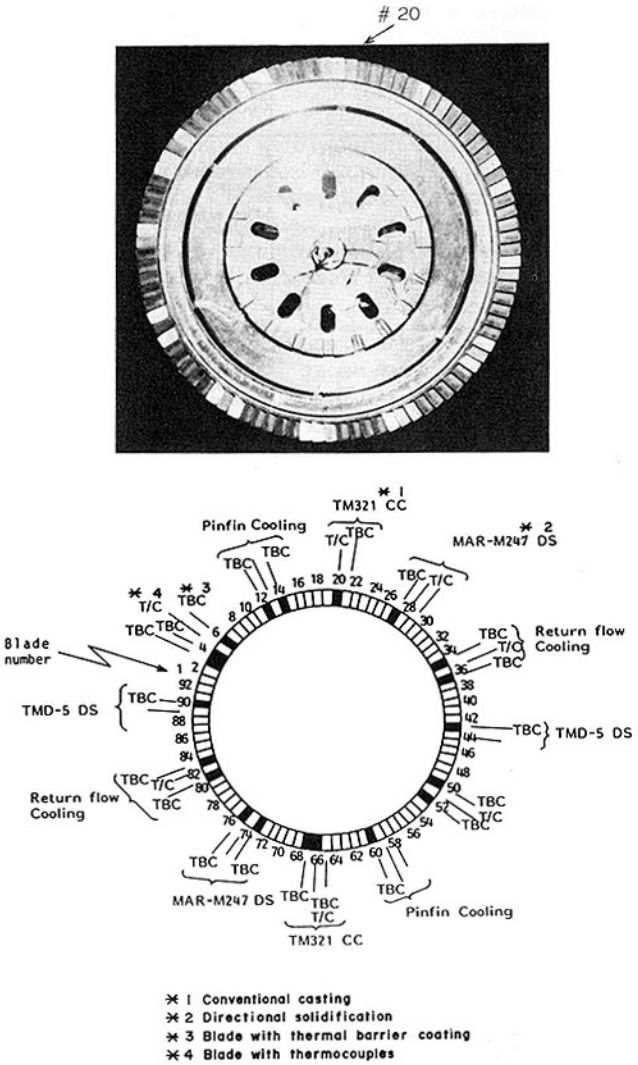

Fig. 7 Locations of the first stage blades having various cooling schemes and TBC

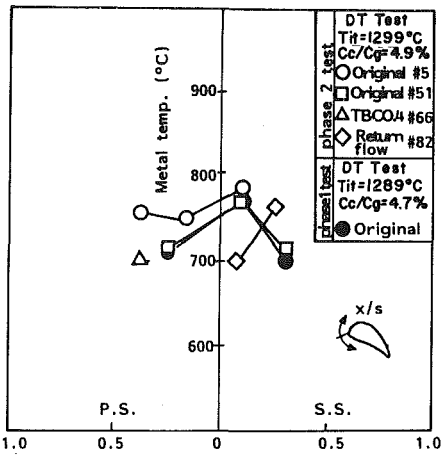

Fig. 8 Measured metal temperature distribution of various types of the first stage blade

Data Analysis. The local gas temperatures, used for analyzing local cooling effectiveness, were estimated for each nozzle by the following procedure:

For the first stage nozzle, the local inlet temperature was estimated from the mean gas temperature obtained from the enthalpy balance, and the combustor exit radial temperature distribution obtained from the previously performed combustor test.

In the case of the second stage nozzle, the temperature measured by the thermocouple was used after compensating for heat conduction error, since it had no leading edge film cooling system and the radiation error appeared to be small as a result of the moderate gas temperature.

The estimation of the blade relative local gas temperatures is very difficult in the high-temperature turbine test. This is because there are pronounced variations in the gas temperature at the combustor exit and mixing of both cooling and leakage air into the turbine flow path.

The blade inlet relative total temperatures at the midheight position of the first and second stage blades were estimated by the following procedure: (1) Firstly, the internal gas conditions of the turbine under the test condition were analyzed by the turbine one-dimensional performance calculation, using the estimated turbine inlet mean gas temperature, the inlet mass flow rate, cooling flows, leakage flows, and the inlet total pressure. (2) Next, the blade relative inlet gas temperature was obtained. (3) The local gas temperature was then estimated from the mean gas temperature, and the circumferentially averaged radial temperature distribution obtained through the combustion test.

The total aerodynamic power output of the turbine was defined as the sum of the power measured by the water brake W_{WB}, the reduction gear loss L_{RG}, the bearing loss L_{BG}, the pumping loss due to cooling air L_p, and the windage loss L_{WD}. Among these values, the pumping loss and disk windage loss were estimated analytically. The turbine total aerodynamic power output W_{TOTAL} was then defined by the following equation:

$$W_{\mathrm{TOTAL}} = W_{WB} + L_{RG} + L_{BG} + L_p + L_{WD}$$

The turbine efficiency, which is defined by the ratio of the turbine adiabatic work to actual power output, is rather complicated for an air-cooled turbine owing to the cooling flows. In this paper, the turbine total adiabatic work is defined as the sum of the isentropic expansion work of flows mixing into the turbine flow path. The mean turbine inlet gas temperature was estimated from the enthalpy balance using the mass flow rate of air and fuel entering the combustor. For burning efficiencies, data obtained from laboratory combustion tests conducted beforehand were used. The turbine inlet pressure was calculated from the measured pressure in the combustor casing and the pressure loss coefficient of the combustor obtained from laboratory tests. The amount of cooling flow and leakage air mixing into the turbine flow path was estimated

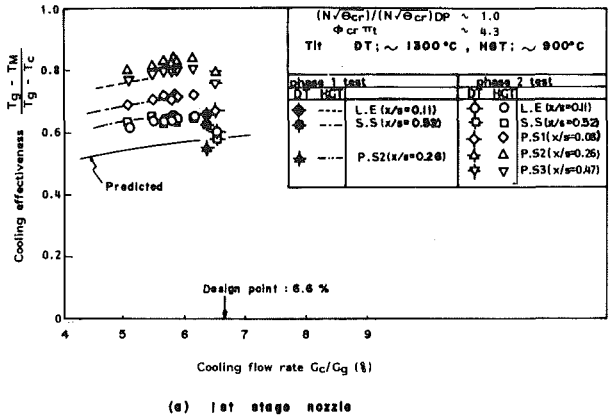

(a) 1st stage nozzle

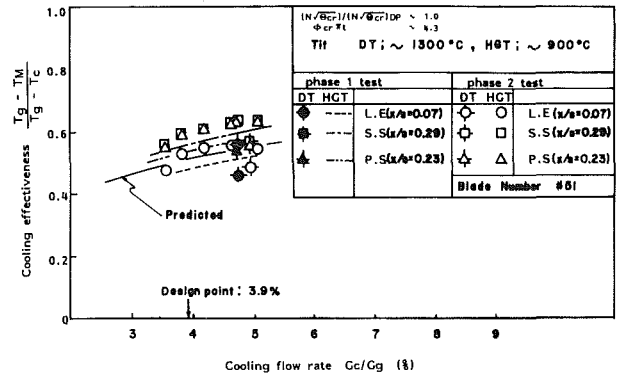

(b) 1st stage blade

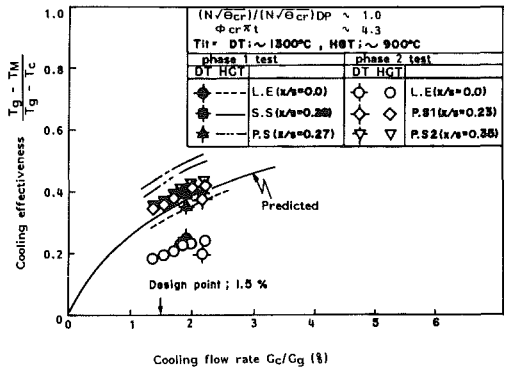

(c) 2nd stage nozzle

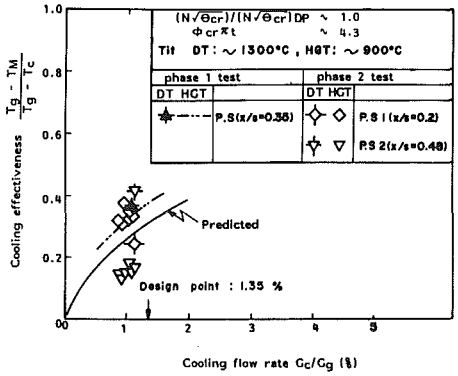

(d) 2nd stage blade

Fig. 9 Local cooling effectiveness for nozzles and blades with cooling flow rate

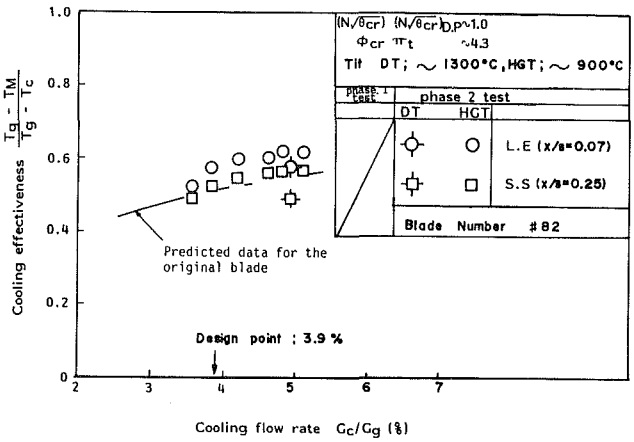

Fig. 10 Local cooling effectiveness for the first stage blade having return flow-type cooling scheme with cooling flow rate

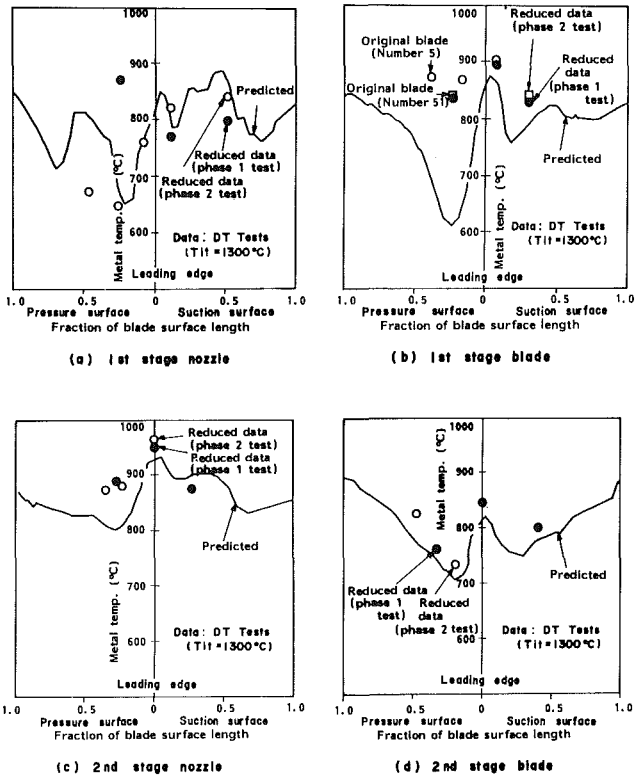

(a) 1st stage nozzle (b) 1st stage blade

(c) 2nd stage nozzle (d) 2nd stage blade

Fig. 11 Comparison of measured metal temperatures with predicted metal temperature distribution for nozzles and blades

by flow network calculations using estimated gaps between parts together with measured pressures and temperatures in cavities. The turbine efficiency was defined by the following equation:

$$\eta_t = \frac{W_{\text{TOTAL}}}{\sum_i Gi(\Delta H_{is})i}$$

Results and Discussions

Cooling Characteristics. Figure 8 shows the measured metal temperatures at midheight of the first stage blades. Original blades without TBC, an original blade with TBC, and a return flow cooling-type blade are compared. The thickness

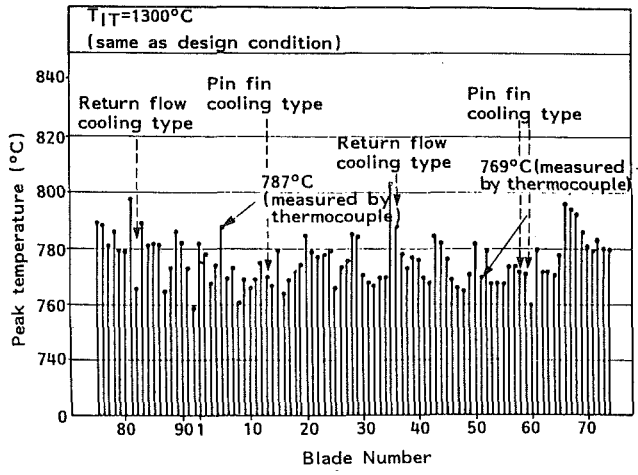

Fig. 12 Peak temperature of each first stage blade measured by infrared thermometry

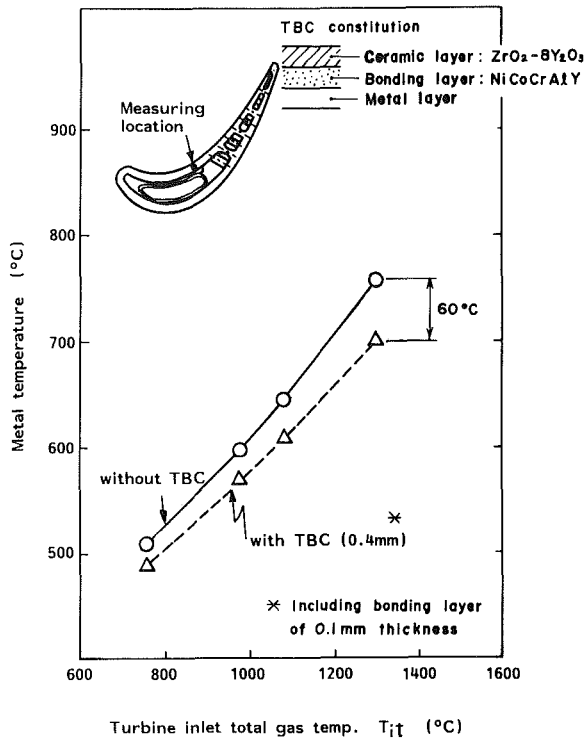

Fig. 13 Metal temperature reduction of the first stage blade with TBC

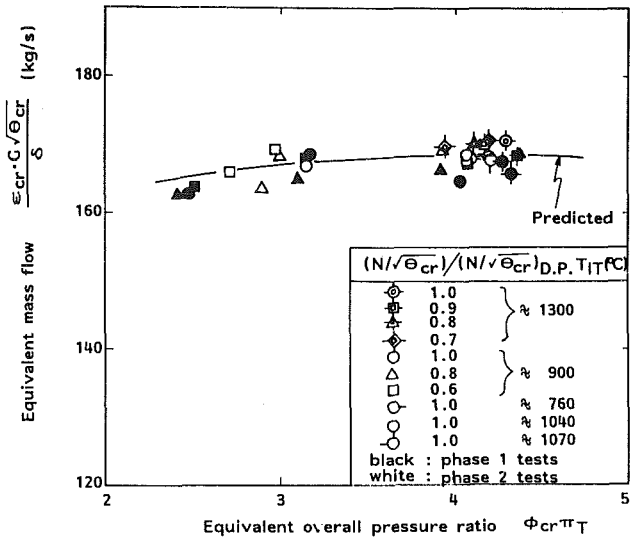

Fig. 14 Equivalent mass flow characteristics of the turbine

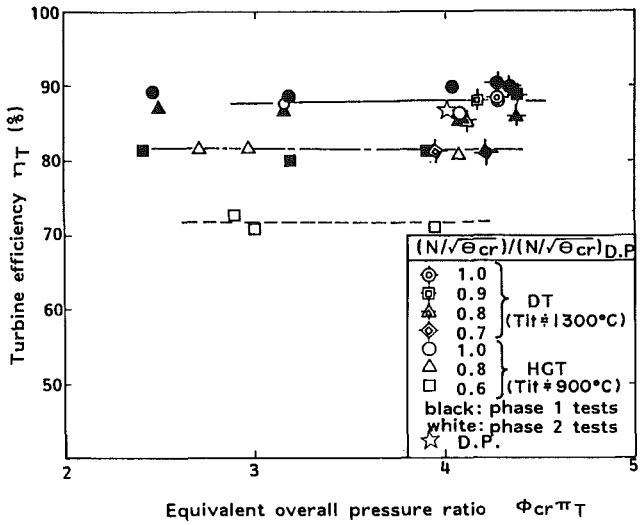

Fig. 15 Variation in turbine efficiency with equivalent overall pressure ratio

of the TBC is 0.4 mm. The measured temperatures of the original blade obtained from the Phase I test are also shown in Fig. 8.

As shown in Fig. 8, the measured temperatures of the original #51 blade agree well with those obtained in the Phase I test. Small discrepancies exist between the original #5 blade and those of the original #51 blade. TBC shows some effect in reducing the metal temperatures. The measured temperature distribution of the original blades and return flow-type cooling blade are quite different from each other. However, the measured temperature level is almost the same.

The local cooling effectivenesses with the cooling flow rates are shown in Fig. 9 for each nozzle and blade. There is a substantial difference between the local cooling effectiveness obtained from the Hot Gas Test at 900°C and that obtained in the Demonstration Test at 1300°C (see Table 2). One possible reason for the discrepancy is a lack of accuracy in the estimation of the turbine inlet gas temperature. As shown in Fig. 10, the local cooling effectiveness of the return flow type blade is similar to that of the original blade.

Figure 11 shows a comparison of the predicted metal temperature distribution with the measured data for the DT condition. As shown in Fig. 11(*a*), the measured metal temperatures of the suction side of the first stage nozzle agree well with the predicted values. However, the measured temperatures on the pressure surface do not agree with those of the Phase I test. From a comparison with the predicted value, it can be concluded that one point on the pressure surface of the Phase I test was not valid.

Figure 11(*b*) shows a comparison of measured metal temperature distribution with the predicted value for the first stage blades. Data obtained from the Phase I test will also be plotted in the figure. Repeatability is good. However, agreement between the measured data and the predicted values is not good, especially on the pressure surface. One reason for the discrepancy is a low impingement cooling effectiveness due to an inclined jet.

Figure 11(*c*) shows the measured metal temperatures and the predicted temperature distribution for the second stage nozzle. Repeatability is good. Although some discrepancy exists between the measured data and the predicted data on the

pressure surface, agreement is relatively good for the suction surface data.

Figure 11(*d*) shows a comparison of measured data and the predicted data for the second stage blades. Agreement is good for both blade surfaces.

Figure 12 shows the measured leading edge surface metal temperature using an infrared thermometry. As some of the blades employ thermal barrier coating on their external surface, the measured temperatures are highly scattered. The measured temperatures using thermocouples are also shown in the figure. The temperatures measured by the infrared thermometry are close to those measured by the thermocouples. However, the estimated temperature difference between the surface and the location of thermocouple is about 20°C. This difference is not seen in Fig. 12, and the error may be due to the low emissivities of the blade surfaces.

Thermal Barrier Coating. Some of the first stage nozzles and blades had thermal barrier coating applied to their external surfaces. The coating consisted of a NiCoCrAlY bond coating and a ZrO_2-Y_2O_3 ceramic coating, which were plasma-sprayed onto the blade surfaces. The thickness of bond coating was 0.1 mm; the thickness of ceramic coating was either 0.2 mm or 0.3 mm. The low thermal conductivity of the coatings reduced heat inflow from the hot gas flow to the airfoil.

Figure 13 shows a comparison of the measured temperatures of a blade with a thermal barrier coating and those of an uncoated blade. At a turbine inlet temperature of 1300°C, a metal temperature reduction of about 60°C is obtained by employing a thermal barrier coating of 0.4 mm thickness. For the first stage nozzle, a metal temperature reduction of about 40°C was obtained by a thermal barrier coating of 0.4 mm thickness, at a turbine inlet temperature of 1300°C.

Aerodynamic Performance. The turbine mass flow characteristics are shown in Fig. 14. Although the measured data are slightly scattered, agreement between the predicted data and the measured data is good.

Figure 15 shows variations of turbine efficiency with equivalent pressure ratios at equivalent shaft speeds. The measured efficiency at the equivalent design condition agrees well with the predicted value of 87.9 percent. The measured data are about 2 percent lower than those measured in the Phase I test. The reason for the efficiency drop is not clear.

Variations of turbine efficiency with the cooling air flow rate are shown in Fig. 16. The change in the efficiency is relatively small over the range of the test conditions because pumping loss is included in the total power output of the turbine.

Tip Clearance Measurement. Figure 17 shows the tip clearances of the first stage blades under several test conditions. The minimum clearance is obtained at the DT condition with a value of 0.64 mm. The turbine efficiency increases with a decrease in the tip clearance as shown in the figure.

Conclusions

Phase II testing of the high-temperature turbine using the AGTJ-100A high-pressure turbine were performed to investigate the potential of candidate technologies that may be applied to the advanced engine, the AGTJ-100B. The results of the test are summarized as follows.

1 Superiority of the blade with a return flow-type cooling scheme to the original blade with insert type cooling was not apparent.

2 The thermal barrier coatings employed on the airfoils were effective for reducing the metal temperatures of the airfoils. The metal temperature reduction of about 40°C and 60°C were obtained for the first stage nozzle and blade, respectively, by using thermal barrier coatings of 0.4 mm thickness.

3 Measured metal temperatures of the nozzles and blades, which have the same cooling scheme as those of the original AGTJ-100A, coincide with those obtained in the Phase I test, except those on pressure surfaces.

4 Measured tip clearance of the first stage blade is 0.64 mm at a turbine inlet temperature of 1300°C.

From the results of the phase II test, it was decided to employ the thermal barrier coatings on all nozzles and blades of the high-pressure turbine of the AGTJ-100B.

Acknowledgments

The Phase II test was carried out successfully, as was the Phase I test, with the cooperation of many people. The authors wish to express their appreciation to the Ministry of International Trade & Industry, the Agency of Industrial

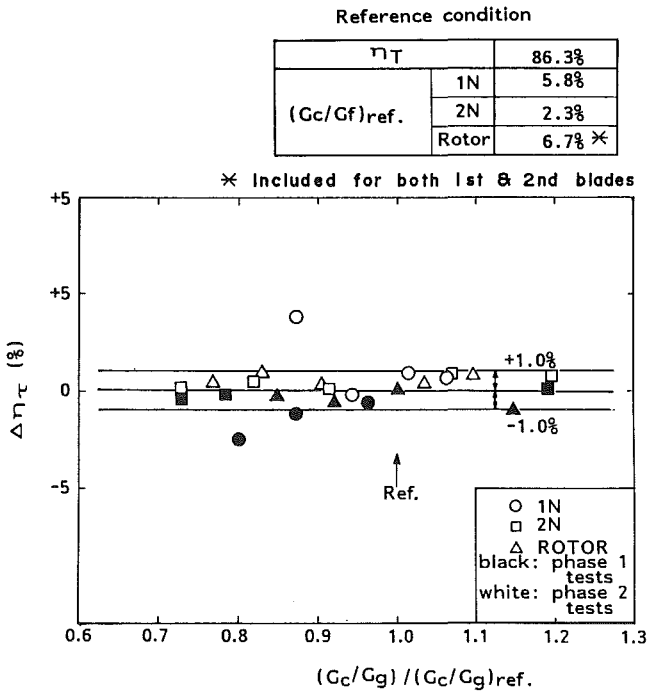

Fig. 16 Variation in turbine efficiency with cooling air flow rate

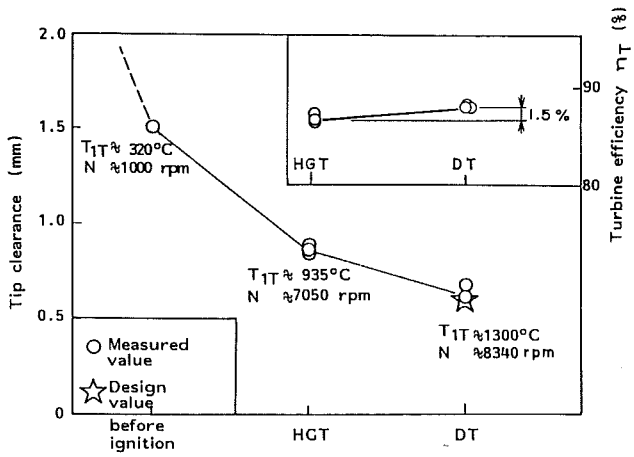

Fig. 17 Tip clearance and turbine efficiency under several test conditions

Science and Technology, and particularly to the Moonlight Project Promotion Office in Japan in charge of the planning and execution of this project. The authors would also like to express their gratitude to the members of Mitsubishi Heavy Industries, Ltd., Takasago Research and Development Center, and Takasago Machinery Works, and to Dr. K. Takeya and Mr. T. Imai (Engineering Division of the Engineering Research Association for Advanced Gas Turbines).

References

1 Hori, A., and Takeya, K., "Outline of Plan for Advanced Reheat Gas Turbine," ASME JOURNAL OF ENGINEERING FOR POWER, Vol. 103, 1981, pp. 772–775.

2 Aoki, S., et al., "Aerodynamic and Cooling Characteristics of a Full Scale High Temperature Turbine," ASME Paper No. 83-TOKYO-IGTC-116, 1983.

3 Arai, M., Teshima, K., Aoki, S., and Yamao, H., "Results From High Temperature Turbine Test on the HPT of the AGTJ-100A," ASME Paper No. 84-GT-235, 1984.

M. Arai

T. Imai

K. Teshima

A. Koga

Engineering Research Association
for Advanced Gas Turbines,
Tokyo 105, Japan

Research and Development on the HPT of the AGTJ-100B

The final target of development of the advanced gas turbine sponsored by MITI of Japan is a thermal efficiency of over 55 percent at an HPT inlet temperature of 1400°C as a combined plant. In order to attain this target, a feasibility study of the design and various R & D tasks have been conducted. This paper will first present the basic plan and then some important R & D items.

Introduction

Development of an advanced gas turbine, sponsored by the Ministry of International Trade and Industry (MITI) of Japan, was started in 1978 [1, 2]. This advanced gas turbine, which can be combined with steam turbines, has as the final target a thermal efficiency of over 55 percent (LHV base) as a combined plant.

As the interim target, a reheat gas turbine (AGTJ-100A) for the pilot plant, which will have a combined efficiency of over 50 percent, is being developed.

The AGTJ-100A has been tested at the Tokyo E. P. Co.'s Sodegaura P. S., since 1984, after the Phase I test of the High-Temperature Developing Unit (HTDU), which confirmed the performance of the High Pressure Turbine (HPT) of the AGTJ-100A, and the factory test operation, which was carried out in order to check the control system and operation.

The AGTJ-100A, as shown in [1], is a two-split shaft reheat gas turbine with an intercooler, and the high-pressure, intermediate-pressure, and low-pressure turbines are arranged in a tandem configuration. The high-pressure system is a self-balancing type gas generator, while in the low-pressure system, the intermediate-pressure turbine, low-pressure turbine, and low-pressure compressor are all connected directly to the generator.

The high-pressure compressor, combustors, high-pressure turbine, and low-pressure turbine are located in one casing, and the low-pressure compressor in another casing.

Among the components of the AGTJ-100A, the HPT is operated under extremely severe conditions: a turbine inlet mean gas temperature of 1300°C and a pressure of 55 atm. Meanwhile, the LPT has an inlet temperature (reheater exit) of 1171°C. The resulting exhaust gas temperature at 610°C allows optimum recovery efficiency of the bottoming cycle through use of the reheat triple pressure turbine as the steam turbine with pressure 169 kg/cm^2 and temperature 566/566°C, as shown in [1].

Contributed by the Gas Turbine Division of THE AMERICAN SOCIETY OF MECHANICAL ENGINEERS and presented at the 32nd International Gas Turbine Conference and Exhibit, Anaheim, California, May 31–June 4, 1987. Manuscript received at ASME Headquarters April 10, 1987. Paper No. 87-GT-263.

In parallel with the AGTJ-100A program, a reheat gas turbine (AGTJ-100B) for attaining the final target has been studied since 1978. In order to achieve a combined thermal efficiency of over 55 percent, together with an analytical investigation of the performance, various items of experimental investigation are planned and some have been carried out. Figure 1 shows the R & D schedule for the AGTJ-100B.

This paper presents the results of the analytical investigation of the performance and an outline of the planning and results for the experimental investigation.

Conceptual Design Study

The final step to 55 percent efficiency will depend on optimization of the steam cycle as gas temperatures increase. Ultimate development of the design should raise the HPT inlet temperature to 1400°C and the LPT inlet temperature to 1200°C. The exhaust temperature is approximately 650°C. This will require advanced technologies.

The hardware of the AGTJ-100B is almost the same as the

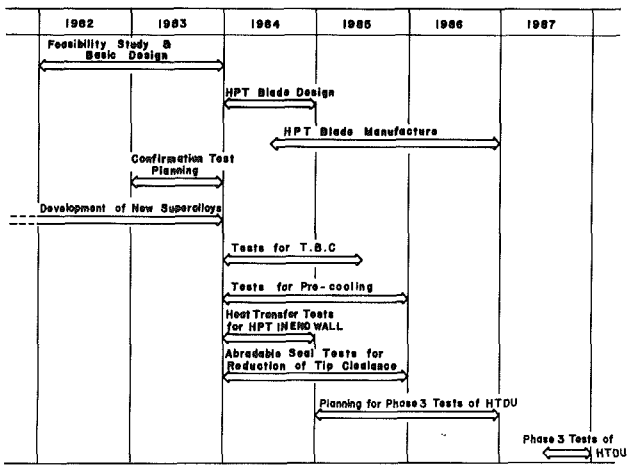

Fig. 1 R & D schedule for the AGTJ-100B

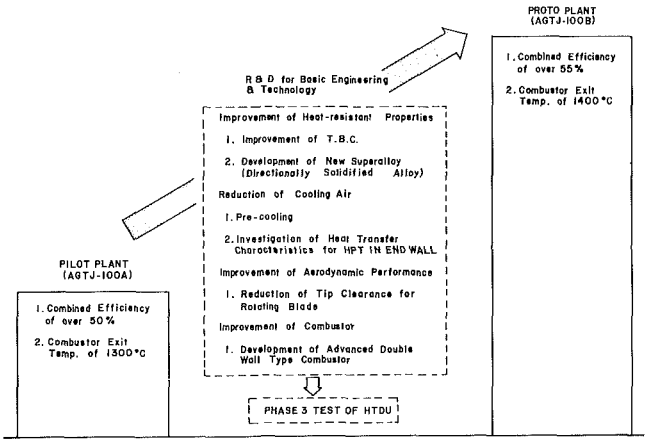

Fig. 2 Development of the AGTJ-100B

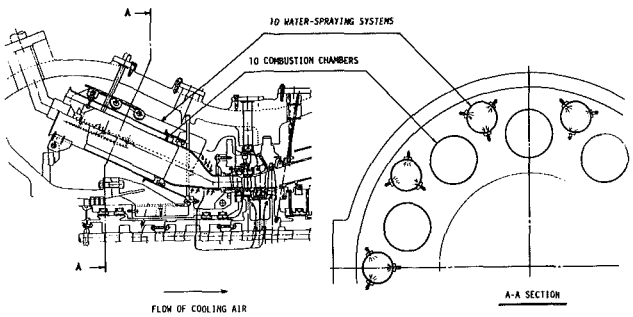

Fig. 3 Schematic of water-spraying system

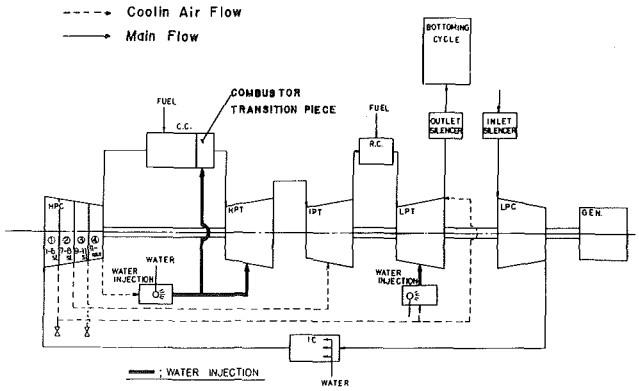

Fig. 4 Schematic of the AGTJ-100B cycle

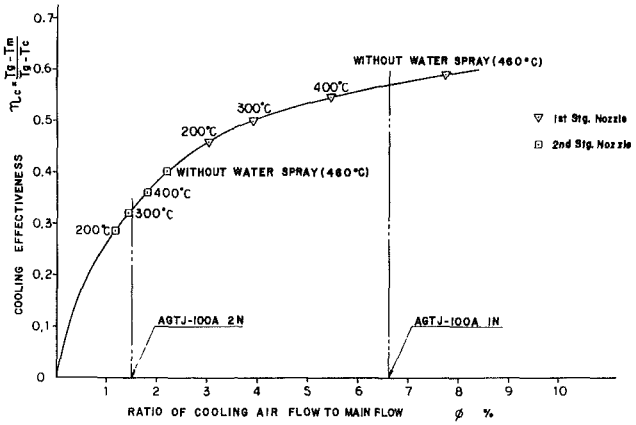

Fig. 5 Cooling characteristics of HPT nozzles

AGTJ-100A except for the high-pressure turbine system, including the combustors. To improve the HPT system, various items for development were planned, as shown in Fig. 2.

In the following paragraphs studies of the plant performance that led to the concept described above are discussed, and the design requirements of the AGTJ-100B are described.

Precooling. In order to verify performance improvement in real reheat gas turbine operation tests, it is necessary not only to raise the HPT inlet temperature without increasing the cooling air flow, but also to maintain the machine's durability. Accordingly, to keep the same durability level as the AGTJ-100A, it was decided that shaft speed of the HPT and the metal temperature of the air-cooled blades were to remain unchanged.

Especially from the point of view of existing cooling technologies, there exists a limit in improving cooling effectiveness by changing the configuration of air-cooled blades. Therefore, in order to reduce the cooling air flow without raising the mean metal temperature, precooling of the cooling air was investigated.

For the precooling method, a water-spraying system was adopted. In particular, because the supply of cooling air resulted in a large pressure loss for the HPT, it was decided to inject the smallest amount possible directly into the casing of the HP system, as shown in Fig. 3. As described in detail later, a confirmation test is planned to realize the technical development of this device. Similarly, the LPT is to have a water-injection device placed on the way from the HPC sixth stage to the LPT.

Figure 4 shows a schematic diagram of the AGTJ-100B, including the water-injection systems. In addition, the precooled air is supplied to the combustor transition pieces, various leakage air from the casings, and seal air.

Figures 5 and 6 show how precooling was able to cause reduction in the cooling air under constant gas and metal temperature.

Next the influence of decreasing the HPT cooling air flow on the combined thermal efficiency is shown in Fig. 7. According to this figure, the effectiveness is remarkable within the range between the HPC discharge condition (460°C) and the condition precooled by 400°C. This is because the effects of increasing the main flow and decreasing the pumping work of the blades due to a decrease in cooling air are superior to depressing the main flow enthalpy due to dilution.

The maximum point of thermal efficiency is near a precooling temperature of about 350°C, an improvement of about

Nomenclature

G = mass flow rate
P = pressure
T = temperature
U = velocity
ΔT = temperature drop
η = efficiency
π = pressure ratio
ϕ = flow ratio

Subscripts

a = air or condition in transition piece casing
b = blade
c = cooling air
cn = casing
g = gas
in = inlet
m = metal
w = water
1 = condition in combustion chamber casing
2 = outlet of combustion chamber

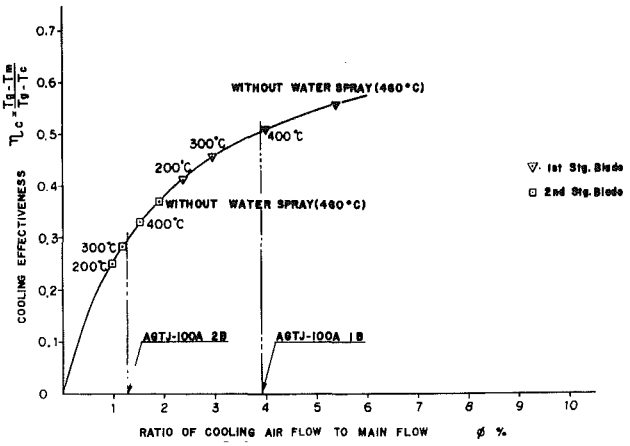

Fig. 6 Cooling characteristics of HPT blades

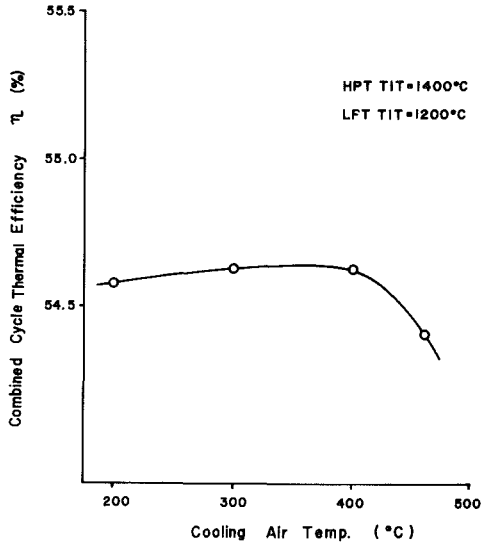

Fig. 7 Influence of precooling on combined thermal efficiency

0.23 percent. The ratio of cooling air to main flow for each HPT blade is as follows:

1st nozzle (1N)	5 percent
1st blade (1B)	4 percent
2nd nozzle (2N)	1.5 percent
2nd blade (2B)	1.3 percent

In particular, the cooling air of the first nozzle corresponds to 70 percent of the AGTJ-100A.

From these results, by precooling the HPC discharge air (460°C) to 300°C, the thermal efficiency became 54.7 percent. However, the final target (55 percent) cannot be attained with only precooling.

In addition, the same investigation was conducted for the LPT. The result showed that precooling for the LPT was ineffective to improve the combined thermal efficiency (see Fig. 8). Precooling of the cooling air for the LPT was not adopted.

Ceramic Coating. As investigated before, it is clear that a more effective improvement is needed in order to attain the final target. Thus, the application of ceramic coating onto the blade surface of the HPT was decided upon.

Figure 9 shows the influence of ceramic coating upon the cooling effectiveness. The solid line corresponds to the characteristics of the AGTJ-100A, while the dotted line indicates the characteristics of the cooling effectiveness of the ceramic coated blades (0.2 mm thickness with an MCrAlY bond coat).

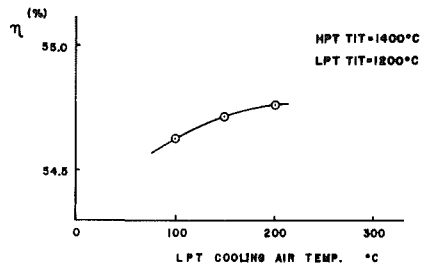

Fig. 8 Influence of precooling the LPT cooling air on combined thermal efficiency

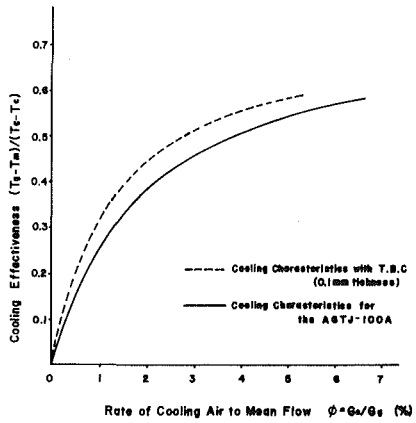

Fig. 9 Cooling effectiveness with TBC

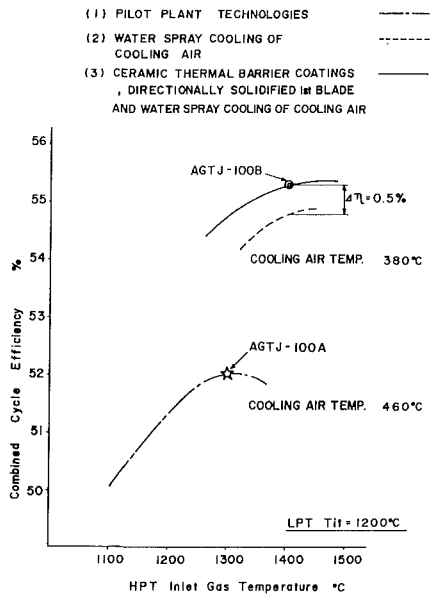

Fig. 10 Influence of ceramic coating on combined thermal efficiency

Although precooling depresses the main flow enthalpy due to dilution, the decrease in cooling air due to ceramic coating does not lead to this disadvantage. Ceramic coating is a very effective means as long as durability is adequate. Figure 10 shows the influence of ceramic coatings on the combined thermal efficiency in conditions of a HPT inlet temperature of 1400°C, a LPT inlet temperature of 1200°C, and a precooling temperature of 380°C.

This figure shows that a thermal efficiency of 55.2 percent is achieved. Hence, ceramic coating is very advantageous, but durability is a problem. Therefore, a series of confirmation tests referring to this problem was planned as described hereafter.

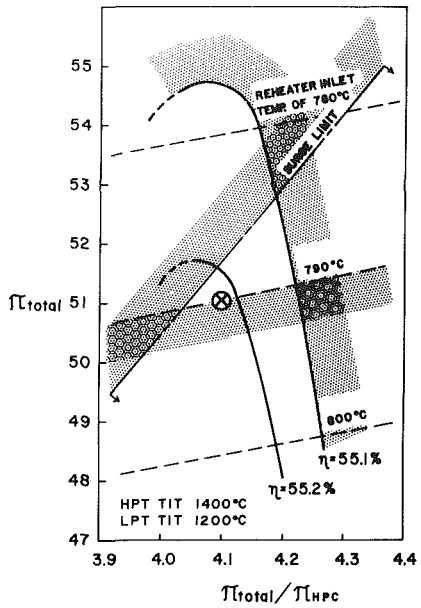

Fig. 11 Investigation of design condition

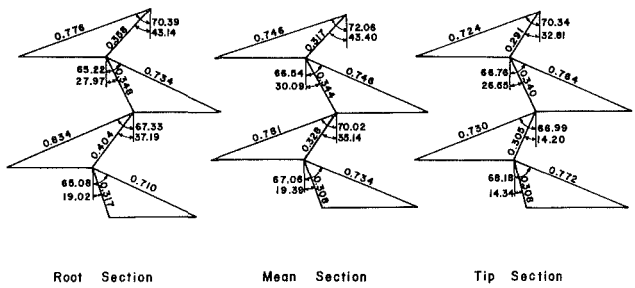

Fig. 12 Velocity triangles of the HPT

Design Requirements. In order to specify the requirements of the design condition, studies were performed on the basis of the conditions described below:

1 Cooling air for the HPT is precooled to 380°C.
2 Surfaces of the HPT nozzles and blades are ceramic coated.
3 The shaft speed of the high-pressure system is 8500 rpm.
4 The HPT inlet temperature is 1400°C.
5 The LPT inlet temperature is 1200°C.
6 The mean metal temperature of the air-cooled blades is at the same level as the AGTJ-100A.
7 The output power is 120 MW, similar to the AGTJ-100A.

In order to satisfy operating under the conditions listed above, it was planned that the HPT and the first nozzle of the IPT be newly designed and manufactured.

Results of these studies are shown in Fig. 11. From these results, the design conditions were selected under the limitations listed below:

1 The combined thermal efficiency was over 55.1 percent.
2 The surge margin was over half as much when compared with the AGTJ-100A.
3 The inlet temperature of the reheater was below 790°C.

In Fig. 11, the design condition is indicated by the mark ⊗. A description of the design conditions of the AGTJ-100B is shown in Table 1.

Design of HPT Cooled Blades. The cooled blades of the HPT were designed on the basis of the above cycle investigation.

Table 2 shows a comparison of the cooling system for the HPT between the AGTJ-100A and the AGTJ-100B.

Table 1 Specifications of the AGTJ-100B

ITEMS	REQUIREMENTS
GAS TURBINE OUTPUT	121000 kW
COMBINED EFFICIENCY	0.552
LPC PRESSURE RATIO	4.17
HPC PRESSURE RATIO	12.55
HPT INLET TEMP./LPT INLET TEMP.	1400°C/1200°C
AIR FLOW	195.2 kg/s
EXHAUST TEMP.	659 °C
LPC ADIABATIC EFFICIENCY	0.888
HPC ADIABATIC EFFICIENCY	0.875
HPT ADIABATIC EFFICIENCY	0.914
IPT ADIABATIC EFFICIENCY	0.843
LPT ADIABATIC EFFICIENCY	0.911

Table 2 Comparison of cooling system for HPT between AGTJ-100A and AGTJ-100B

	AGTJ-100A (T.I.T. 1300°C)	AGTJ-100B (T.I.T. 1400°C)
Blade Design Concept	The same technology as the existing jet engine	Thermal barrier coating (Yttria-Stabilized Zirconia)
Material 1N	IN 939	Mar M 247 C.C.
1B	Mar M 247 C.C.	TMD5 D.S.*
2N	IN 939	TM 269*
2B	Mar M 247 C.C.	Mar M 247 C.C.
Coolant	Extracted air from the HPC exit (460°C)	Extracted air from the HPC exit with water spray(380°C)
Coolant Flow Fraction (% HPT Inlet Flow)	14.1	10.0

* Newly developed super alloy

In order to cope with such severe conditions as raising the inlet temperature and decreasing the cooling air flow, the definitive feature is abolishing the film cooling system that was used for the AGTJ-100A. Therefore, it is obvious that the technology of ceramic coating holds the key to development for the AGTJ-100B.

Blade inlet and exit velocity triangles for the HPT are shown in Fig. 12. The aerodynamic and mechanical concepts are similar to the AGTJ-100A and are described in [3] in detail.

The designed blades are classified into two types of cooling configurations. They are:

Insert type
(1) 1st nozzle
(2) 1st blade A type
(3) 2nd nozzle

Return flow type
(1) 1st blade B type
(2) 2nd blade

As described above, the first blades are designed for two configurations. The best configuration will be decided upon after various confirmation tests.

At present these blades are undergoing the cascade test.

Confirmation Tests

Some technical goals to be achieved for the AGTJ-100B are evident from the conceptual design study. It is necessary to confirm these items individually by confirmation tests and also to demonstrate their integrated performance.

As precooling and ceramic coating technologies are

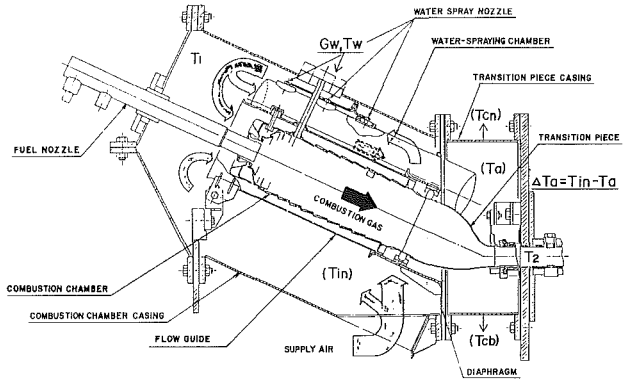

Fig. 13 Cross-sectional view of the test apparatus

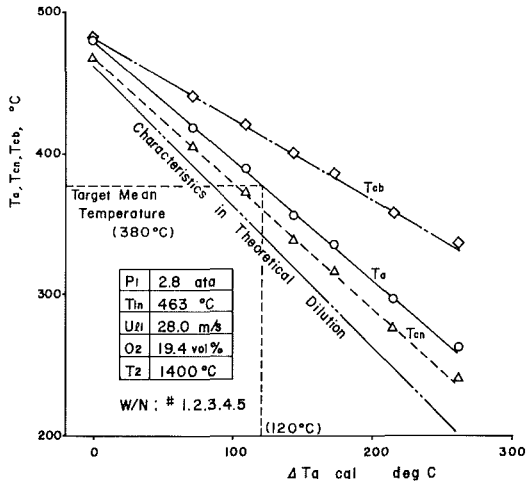

Fig. 14 Relation of temperature in transition piece casing and temperature of extracted air

predominantly important among the items listed above, the description of the outlines for confirmation tests puts emphasis on these two items.

Test for Precooling. Technical subjects for precooling the HPT cooling air by means of the water-spray system are as follows:

1 Whether the cooling air can be cooled to 380°C, along with a uniform temperature distribution.

2 Whether evaporation of the injected water is complete.

In order to confirm these phenomena, tests were performed by using a combustion chamber model of the high-pressure system (ten HP combustion chambers for the real engine).

Figure 13 shows a cross-sectional view of the test apparatus. Two sets of water spraying chambers including five water-spray nozzles for high-pressure use were attached to the combustor.

The test conditions were as follows:

1 Supply air flow was distributed at the following rate: Transition piece of combustor: casing: rotor = 40:36:24.

2 The combustor inlet temperature was 463°C.

3 The inlet combustor pressure was 2.8 atm.

4 The mean velocity in the combustion chamber was 28 m/s.

5 The exit combustor temperature was 1400°C.

The tests were performed by increasing the number of sprayed water nozzles step by step.

Figure 14 shows the temperatures in the transition piece casing and of the cooled air extracted from the casing.

"*Ta*" indicates the mean temperature in the transition piece

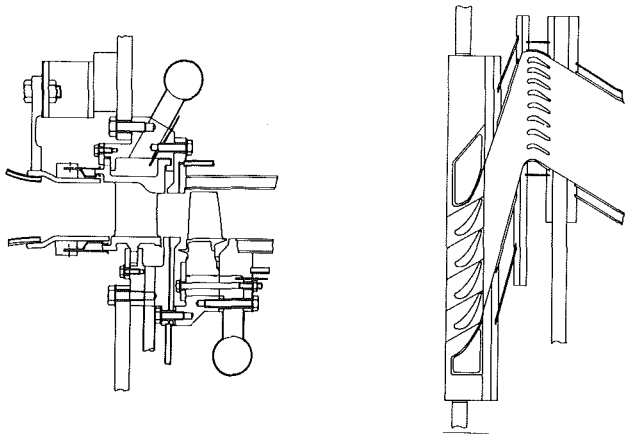

Fig. 15 Schematic of test section

casing. The number of measured temperatures in the transition piece casing is 19. "*Tcn*" indicates the temperature of the cooled air extracted from the casing for nozzle cooling. "*Tcb*" indicates the temperature of the cooled air extracted from the casing for use in the rotor (see Fig. 13 for locations of measurements). "$\Delta Tacal$" indicates a theoretical temperature drop produced by evaporation of the water spray.

From the test results, the target mean temperature in the transition piece casing (380°C) is attainable at a $\Delta Tacal$ of 120°C, but there is a problem in temperature distribution, which is due to the leakage air from the diaphragm and heat transfer from the transition piece. The difference between *Tcn* and *Tcb* is about 60°C. This should be taken into consideration when designing HPT nozzles and blades. In this condition, it was confirmed from the water drain measurement that evaporation was complete.

Test for the Thermal Barrier Coating (TBC). In order to confirm the durability of the TBC, two classes of tests were planned, and the first test has been completed.

The first step test was a thermal cycling test on a specimen simulating the temperature distribution in an actual blade. The specimens were TM-321 tubing, 25 mm in diameter and 2 mm thick, coated with an MCrAlY bond coat and ZrO_2–Y_2O_3 ceramic. In order to obtain the radial temperature gradient, the ceramic surfaces were heated in an infrared furnace while the inner surfaces of the specimens were cooled with an impinging air jet. The specimens were heated for an hour, rapidly cooled, and then rapidly reheated. The steady-state bond coat temperature ranged from 1000°C to 1200°C. These test results are described in [4]. In brief, in the case of a bond coat temperature of 1100°C (30 min/cycle), it was confirmed that the coating failed at the point where the thermocouple was embedded.

In the second step, confirmation tests in the combustor test facility are planned, and will use actual HPT first nozzles and first blades coated with TBC and be conducted under high-temperature and velocity combustion gas conditions that simulate an actual engine. The condition is a 200 thermal cycle at the maximum gas temperature of 1500°C. Figure 15 shows a schematic of the test facility. The test will be performed from Dec. 1986.

Other Tests for the AGTJ-100B. In the preceding paragraphs, two of the most important items in the confirmation tests were described. This paragraph outlines other confirmation tests for the AGTJ-100B.

In order to improve the heat-resistant property of the blade material, new superalloys have been developed from the beginning of this project [5]. Among these new superalloys, the directionally solidified (DS) superalloy (TMD-5 DS) was developed for use as a turbine blade material. Figure 16 shows

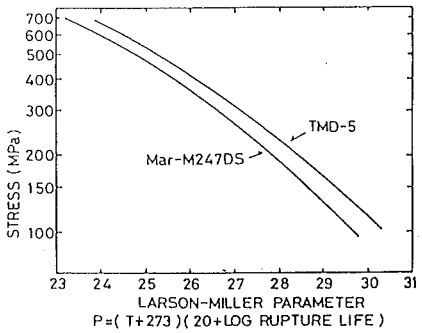

Fig. 16 Comparison of creep rupture strength between Mar-M247DS and TMD-5

a comparison of the creep rupture life between TMD-5 DS and Mar M247 used in the AGTJ-100A. It is obvious that TMD-5 DS is superior to Mar M247 and therefore will be used for the HPT first blade of the AGTJ-100B.

In order to reduce cooling air flow, the characteristics of heat transfer in the HPT first nozzle endwall were investigated. Film cooling for the HPT first nozzle of the AGTJ-100A was used. For the AGTJ-100B, the first nozzle endwall was changed to use TBC with only internal convective cooling, without film cooling. The studies on heat transfer for this endwall design were performed by referring to these test results.

In order to improve the aerodynamic performance, it is highly important to reduce the tip clearance of the rotating blade. In order to realize reduction of tip clearance, development of a new material for the abradable seal of the turbine casing and evaluation tests were performed. Promising material was developed, and the HPT tip clearance was reduced to 0.6 mm (1.0 mm for the AGTJ-100A).

Furthermore, in order to supply burning gas at a temperature of 1400°C, an Advanced Double Wall Type (A.D.W.T.) combustor was developed [6]. The burning performance was confirmed in the Phase II test by using the HTDU. This test result is shown in Fig. 17 [7].

Details of this confirmation test will be presented at another time.

Phase III Test of the HTDU

Two phases of tests using the HTDU were performed previously. The Phase I test has already been presented at the Gas Turbine Conference in Amsterdam, 1984 [3], and the Phase II test will be presented at this meeting [7].

The Phase III tests to be performed in 1987 are for the evaluation of performance and durability of the high-pressure system, incorporating the above technologies. Figure 18 shows a cross-sectional view of the test facility.

Summary

The technologies described in this paper are currently technically unproven as applicable to the industrial gas turbine. Therefore, after evaluating the test results of a series of confirmation tests step by step, the prospect of attaining the goals of the AGTJ-100B design will be improved.

We are looking forward to the realization of the AGTJ-100B.

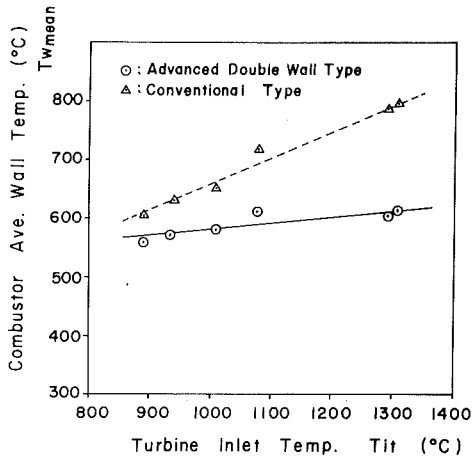

Fig. 17 Comparison of wall temperature between conventional type and A.D.W.T.

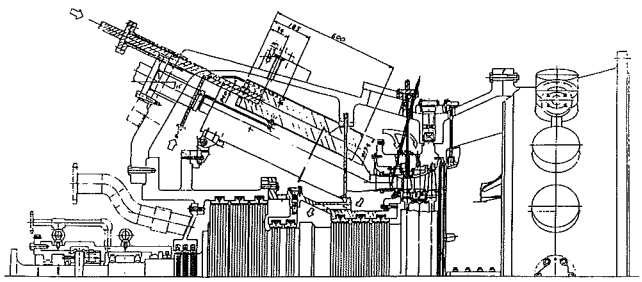

Fig. 18 Cross-sectional view of the HTDU

Acknowledgments

The authors wish to thank MITI, the Agency of Industrial Science and Technology, and especially the Moonlight Project Promotion Office in Japan for the planning and execution of this project.

The authors also appreciate the persons in Toshiba Corp., Hitachi Ltd., Mitsubishi Heavy Industries Ltd., and Kawasaki Heavy Industries Ltd., for the execution of the R & D.

References

1 Hori, A., and Takeya, K., "Outline of Plan for Advanced Reheat Gas Turbine," ASME JOURNAL OF ENGINEERING FOR POWER, Vol. 103, 1981, pp. 772–775.

2 Takeya, K., Oteki, Y., and Yasui, H., "Current Status of Advanced Reheat Gas Turbine AGTJ-100A (Part 3) Experimental Results of Shop Test," ASME Paper No. 84-GT-57, 1984.

3 Arai, M., Teshima, K., Aoki, S., and Yamao, H., "Results From High Temperature Turbine Test on the HPT of the AGTJ-100A," ASME Paper No. 84-GT-235, 1984.

4 Uchida, K., Koga, A., Teshima, K., and Arai, M., "Applications of Ceramic Coating on the Turbine Blade of the AGTJ-100B," ASME Paper No. 87-GT-00.

5 Yamazaki, M., "Nickel-Base Superalloys Developed for Advanced Gas Turbine in 'Moonlight' National Project," ASME Paper No. 83-TOKYO-IGTC-98, 1983.

6 Mori, K., Kitajima, J., Kimura, T., and Nakamura, T., "Research on High Temperature Combustor for Advanced Reheat Gas Turbine," ASME Paper No. 86-GT-281, 1986.

7 Aoki, S., Teshima, K., Arai, M., and Yamao, H., "Results From the Phase II Test of the High-Temperature Developing Unit (HTDU)," ASME JOURNAL OF ENGINEERING FOR GAS TURBINES AND POWER, Vol. 110, this issue.

Gas Turbine Safety Improvement Through Risk Analysis

T. M. Crosby

G. L. Reinman

Pratt & Whitney,
P.O. Box 109600,
West Palm Beach, FL 33410-9600

This paper is intended to provide the engineer with the information necessary to understand certain statistical methods that are used to improve system safety. It will provide an understanding of Weibull analysis, in that it describes when the Weibull distribution is appropriate, how to construct a Weibull plot, and how to use the parameters of the Weibull distribution to calculate risk. The paper will also provide the engineer with a comprehension of Monte Carlo simulation as it relates to quantifying safety risk. The basic components of Monte Carlo simulation are discussed as well as the formulation of a system model and its application in the gas turbine industry.

Introduction

The complexity of gas turbine engines and their resulting potential for presenting a multiplicity of safety hazards (Fig. 1) frequently requires that management prioritize engineering problems according to their projected impact on safety. In this way company and government resources are allocated most effectively to the areas of greatest concern (Fig. 2). At Pratt & Whitney a failure mode's impact on safety of flight is often quantified by estimating the number of incidents due to that mode. We refer to the process of calculating the expected number of incidents as "risk analysis." Risk analysis techniques have been effectively used throughout the past 12 years on the F100 engines. The F15 aircraft, which is powered by two Pratt & Whitney F100 engines, has the best twin engine fighter safety record. The F16 aircraft, powered by a single Pratt & Whitney F100 engine, has the best single engine flight safety record. These records have been made possible, in part, because of the quantitative methods used in making decisions concerning safety by the F100 program office and the Air Force.

This paper describes two of the more frequently used techniques for calculating risk from gas turbine engine failure modes: Monte Carlo simulation and Weibull-based risk analysis, and how they are used to make safety-related engineering decisions.

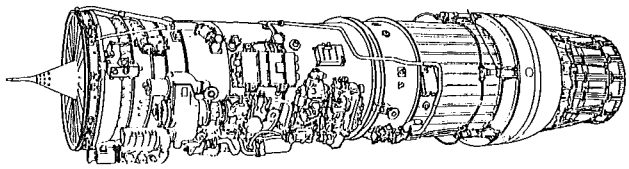

Fig. 1

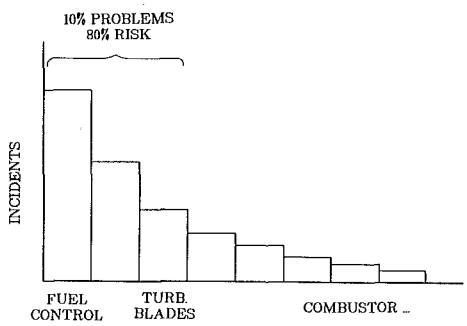

Fig. 2

Weibull-Based Risk Analyses

Weibull risk analyses are typically performed when a safety critical part presents its first few failures in a fleet of several thousand operating units. Weibull-based risk analyses typically include the following steps:

1 Performing a Weibull analysis of the failure mode (Fig. 3).

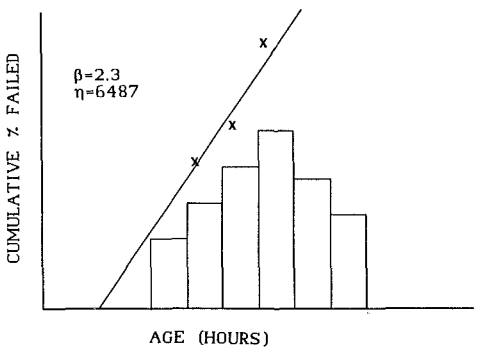

Fig. 3

Contributed by the Gas Turbine Division of THE AMERICAN SOCIETY OF MECHANICAL ENGINEERS and presented at the 32nd International Gas Turbine Conference and Exhibit, Anaheim, California, May 31–June 4, 1987. Manuscript received at ASME Headquarters February 3, 1987. Paper No. 87-GT-15.

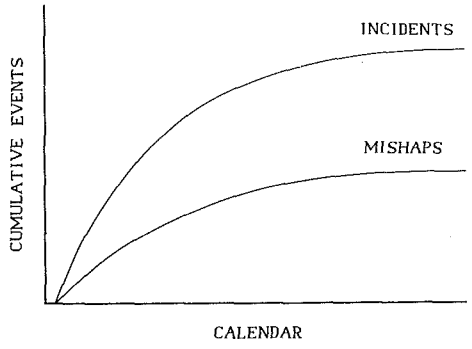

Fig. 4

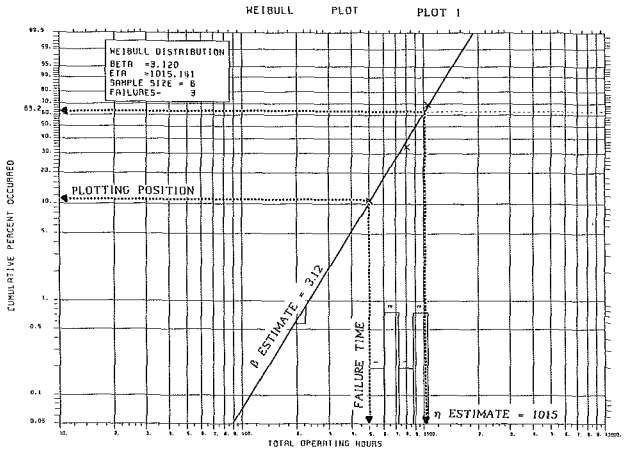

Fig. 5

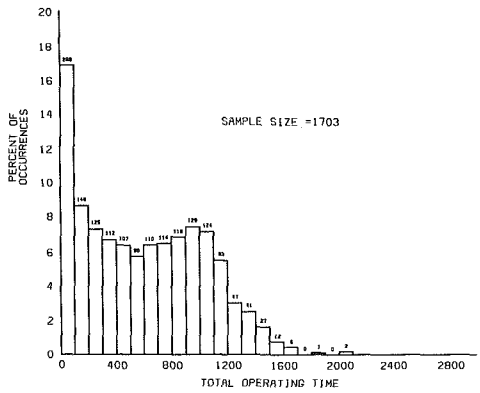

Fig. 6

Total operating hours	Average rank order No.	Plotting positions
500	1.00	0.1094
650+	—	—
700+	—	—
800	2.50	0.3437
900+	—	—
1050	4.75	0.6953

+ indicates suspension (hasn't failed yet).

2 Calculating an estimate of the expected number of failures over the calendar period of interest.

3 Calculating an estimate of the expected number of safety incidents. This is obtained by multiplying the expected number of failures by an estimate of the probability that a part failure will result in a mishap (Fig. 4).

The probability of a mishap is based on past history of the part if available. New failure mode mishap rates are determined by examining the physical hardware geometry and materials and projecting secondary damage to critical aircraft systems due to part failure. For more complex scenarios, Fault Tree analysis is utilized.

The primary data required for Weibull-based risk analysis are the age of each surviving engine in the fleet at risk and the age of each failed engine at the time of failure. "Age" here refers to the age of the part that is under consideration, and *not necessarily the age of the engine.*

With these data, a Weibull analysis can be performed using the techniques described in the USAF Weibull Analysis Handbook (Abernethy et al., 1983). In performing a Weibull analysis, the ages of failed parts as well as surviving parts are used to estimate two constants, or parameters, in the Weibull probability distribution. A cumulative probability distribution is a mathematical expression for the probability of failure before reaching any age x.

The Weibull cumulative probability distribution is

$$P(\text{failure before age } x) = 1 - e^{-(X/\eta)^{\beta}}$$

β and η are the two unknown parameters of the Weibull distribution which the data are being used to estimate. β and η have physical interpretations which will be explained along with graphic depictions of Weibull analysis in the following example.

A Weibull plot yields a variety of information about a failure mode. First, the slope of the best-fit line through the data on Weibull paper provides an estimate of the Weibull parameter beta. The parameter β, which is unitless, gives an indication of how the part failure rate changes with age. If $\beta < 1$, the failure mode has a decreasing failure rate (known as an infant mortality failure mode). If $\beta = 1$, the failure mode has a constant failure rate. If $\beta > 1$, the failure mode has an increasing failure rate (wearout failure mode). The characteristic life η is the second Weibull parameter. The characteristic life is the point at which the Weibull line crosses the 63.2 percent line (63.2 percent of the parts are expected to fail before they reach the characteristic life; see Fig. 5).

Once the Weibull analysis has been performed, the Weibull equation

$$P(\text{failure by } t) = 1 - e^{-(t/\eta)^{\beta}}$$

along with the estimates of β and η can be used to estimate the *expected* number of part failures over some period of a part's life or over some period of calendar time with the knowledge of the part's expected operating time per year. This links Weibull analysis to risk analysis.

In order to use the Weibull equation to predict risk, we need to know how each surviving part is expected to age over the *calendar period covered by the risk analysis. To do this we* need:

(*a*) the part's expected utilization rate (e.g., 30 operating hours per month);

(*b*) the times of any scheduled maintenance that would affect the failure mode (e.g., the part is replaced every 1800 cycles);

(*c*) details of any corrective action initiated in this time period (e.g., start date, completion date, effectiveness of correction action).

Also, we need to know whether a part is replaced immediately after failure with a new part, or if the part is repaired. If the part is repaired, we need to know the reliability of the repaired part relative to a new one.

Before examining the calculations involved in performing a Weibull based risk analysis, we will introduce an example: A

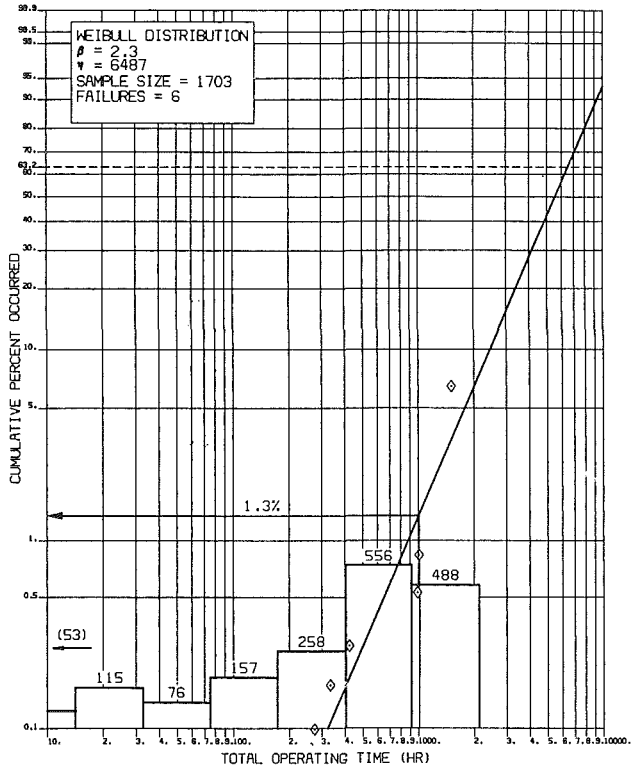

Fig. 7

gas turbine engine bearing cage had fractured in six engines with the following fracture times: 230, 334, 423, 990, 1009, and 1510 hours. Figure 6 shows a histogram of the ages of the bearings. Figure 7 shows the Weibull analysis of the bearing failures.

A risk analysis for this bearing was to be calculated over the next 12 months. Each bearing is expected to accumulate 300 operating hours over this 12-month period. Currently, the bearing cage is replaced when the bearing is returned to depot at 3000 hours. A bearing's useful life is 6000 hours. Also, a redesigned bearing that would eliminate cage fracture was being incorporated into the fleet over this one-year risk period. First we will calculate an estimate of the expected number of cage fractures without considering the effect of the redesigned bearing. Then we will determine the effect of the redesigned bearing on cage fracture risk.

First consider the way each surviving bearing cage will age over the bearing's life. A bearing cage that has accumulated 600 hours of operating time to date, for example, will be expected to accumulate 300 additional hours over the year. There will be no scheduled bearing cage replacement since that does not occur until the bearing has accumulated 3000 hours.

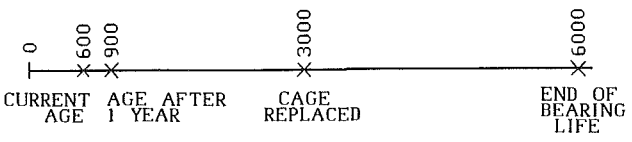

If the 600-hour-old bearing cage fractures before 900 hours it is replaced with a new cage and the bearing continues operation until the end of the one-year risk period.

In performing these risk calculations note that the probability of two or more cage fractures in a single bearing in one 300-hour interval is very small. Therefore, to calculate an estimate of the expected number of failures for the fleet we simply evaluate the probability of each bearing failing in its life interval using the Weibull equation and sum these numbers over each bearing (Gnedenko et al., 1969).

Table 1 Bearing risk after 12 months

Number of Units (N)	Current Time on Each Unit (t)	Time on Each Unit at Year's End (t+u)	F(t)	F(t+u)	Each Unit's Risk $\frac{F(t+u)-F(t)}{1-F(t)}$	Total Risk $\frac{F(t+u)-F(t)}{1-F(t)} \cdot N$
288	50	350	0.0000	0.0012	0.0012	0.3480
148	150	459	0.0002	0.0022	0.0020	0.2963
125	250	550	0.0006	0.0034	0.0029	0.3607
112	350	650	0.0012	0.0051	0.0038	0.4301
107	450	750	0.0022	0.0070	0.0049	0.5193
99	550	850	0.0034	0.0093	0.0059	0.5859
110	650	950	0.0051	0.0121	0.0070	0.7731
114	750	1050	0.0070	0.0151	0.0082	0.9325
119	850	1150	0.0093	0.0186	0.0094	1.1148
128	950	1250	0.0121	0.0225	0.0106	1.3558
124	1050	1350	0.0151	0.0268	0.0118	1.4691
93	1150	1450	0.0186	0.0315	0.0131	1.2214
47	1250	1550	0.0225	0.0366	0.0144	0.6790
41	1350	1650	0.0268	0.0422	0.0158	0.6473
27	1450	1750	0.0315	0.0481	0.0172	0.4631
12	1550	1850	0.0366	0.0545	0.0185	0.2226
6	1650	1950	0.0422	0.0613	0.0200	0.1197
0	1750	2050	0.0481	0.0685	0.0214	0.000
1	1850	2150	0.0545	0.0761	0.0228	0.0228
0	1950	2250	0.0613	0.0841	0.0243	0.0000
2	2050	2350	0.0685	0.0925	0.0258	0.0516
						Sum = 11.613

For a bearing that has accumulated 600 hours to date without failing, the probability of failure over this one-year life inteval is

$$\frac{F(900)-F(600)}{1-F(600)} \tag{1}$$

where $F(t)=1-e^{-(t/\eta)^{\beta}}$ is the cage life distribution. An estimate of this quantity is provided by the Weibull plot

$$\frac{F(900)-F(600)}{1-F(600)} = \frac{\left[1-e^{-(\frac{900}{6487})^{2.3}}\right]-\left[1-e^{-(\frac{600}{6487})^{2.3}}\right]}{1-\left[1-e^{-(\frac{600}{6487})^{2.3}}\right]} \tag{2}$$

$$=0.0066$$

Performing these calculations for each of the 1703 bearings in the fleet, and summing (Table 1) provides an estimate of the expected number of cage fractures over the one-year risk period, ignoring the effect of the redesigned bearing. In this case, the total number of cage fractures expected for the fleet is 11.6.

If the redesigned bearing is incorporated over the next 12 months, the expected number of cage fractures can be calculated by using equation (1) to calculate the probability of failure between the current age of each bearing and its expected retrofit time. The retrofit time for each bearing was estimated by adding one half of the total operating hours in one year (i.e., 150) to each bearing's current age. These are summed for each bearing to give an estimate of the risk (expected number of cage fractures) as in equation (2).

$$\text{Estimate of expected number of cage fractures} = \sum_{i=1}^{1703} \frac{e^{-(\frac{\text{AGE}_i}{6487})^{2.3}} - e^{-(\frac{\text{AGE}_i+150}{6487})^{2.3}}}{e^{-(\frac{\text{AGE}_i}{6487})^{2.3}}}$$

This was found to be 4.0. Therefore, the introduction of the redesigned bearing at 3000 hours is estimated to reduce the risk from 11.6 cage fractures to 4.0 cage fractures.

These simple formulas could not be used to calculate an estimate of the expected number of incidents when two or more cage fractures could happen with reasonably high probablity within the life of the bearing. In this event, the expected number of failures can be calculated using other formulas, or Monte Carlo simulation (Rubinstein, 1981; Law and Kelton, 1982). We have seen in this section that a Weibull analysis can be easily extended to predict the expected number of incidents or part failures over some period of the bearing's life or some

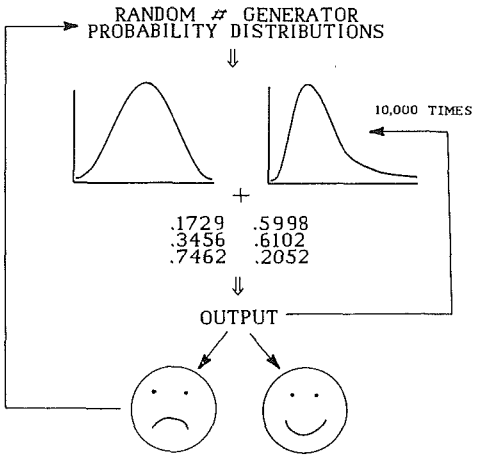

Fig. 8

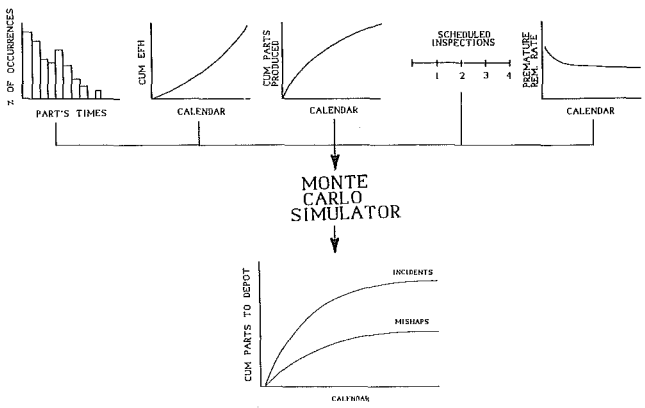

Fig. 9

period of calendar time. Once the Weibull analysis has been completed, the estimated Weibull parameters can be used along with the Weibull cumulative distribution to estimate the expected number of part failures. Frequently, however, either because of a very small amount of failure data or because an engineering-based model of a failure mode is required, Monte Carlo simulation may be used to predict risk. The next section covers this method in detail.

Use of Simulation in Risk Analysis

The calculation of risk/safety is relatively easy using Weibull analysis for the case of a population of parts with no inspections, no production schedule, and no corrective actions. In some instances, a part's service life will depend on decisions to be made in the future which will be dependent on some distribution. This is one instance when Monte Carlo simulation is useful. A Monte Carlo simulation in this context is a computer-based model of a system containing random components that is usually difficult to model analytically.

Monte Carlo simulation is a simple, fast, powerful method for solving stochastic system problems. It enables the analyst to build a computer model of failure modes and a decision plan as it affects a part's service life. Its methods can be applied to any situation with some random variables, i.e., production of gas turbine engines, tolerancing, engine test schedules, as well as wear of a particular part and its replacement. The larger the number of random variables in the model, the better the Monte Carlo simulator will work.

In writing the code for a simulator, the first necessary component is a random number generator (Fishman and Moore, 1982; Hollander and Wolfe, 1973). There are several program models that have been tested and proven to be adequately random (Crigler and Shields, 1982). Each of these methods requires an initial starting number.

The next step is to obtain or assume probability distributions for each of the random variables to be considered in the modeling. The Weibull distribution, which has already been discussed, may be one such probability distribution. Normal, lognormal, and extreme value distributions are other possibilities.

With the random number generator and the probability distributions, a model can be built. This model is then exercised for 1000, 10,000, or 100,000 trials. The number of trials is dependent on how quickly the final answer becomes stable. The statistical output may then be calibrated by comparing with "reality." If the variability in the output is large, it may be necessary to run the simulator several times with different initial starting numbers to get an estimate of the precision error of the simulator (Fig. 8).

As an example of Monte Carlo simulation, let's look at the forecasting of spare parts requirements. It would be beneficial to know approximately how many parts would have to be ordered during certain time frames so that sufficient parts will be available for engine maintenance. It would be very costly to have an engine sitting on a shop floor for 2–3 months while a spare part is being ordered or manufactured.

In order to overcome this situation, we can build a model based on past experience to predict future spare part requirements. To build one such model we used (1) the current part population times, (2) the flight hours per month accumulated by each part, (3) the number of engines produced per month in the future, (4) scheduled inspections for the part, and (5) premature part removal rate as a function of time. The Monte Carlo simulation will then process each part through time, incorporate new members, generate random inspection times (both scheduled and unscheduled), and forecast additional scheduled and unscheduled maintenance activities in the years ahead (both average values and upper bounds) (Fig. 9).

When a model of an engine flight scenario is desired for risk/safety impact, a Monte Carlo simulator is again very useful. The objective of the simulation in this case would be to identify the options available to achieve a program objective, such as no more than one safety incident in the life of the aircraft. It allows the user to combine several failure distributions for each engine mode to simulate the environment and predict what will happen to the engines in the future.

Through this methodology, the random variables can be modified during the simulation to model corrective actions, and safety impacts can be analyzed. Typically, safety considerations require corrective action based on very small samples of failure data. Here, the Weibull distribution can be very useful.

As an example of implementing corrective actions for safety benefits into the Monte Carlo simulator, we will look at diffuser case distortion. In this case, an estimate of the number of fractures due to excessive distortion occurring before the next scheduled inspection is desired.

A random sample of diffuser cases was measured for wall thickness and distortion data were taken. Weibull analysis indicated that a significant manufacturing process change had been implemented at a known earlier point in time that affected the diffuser case wall thickness and distortion. Therefore the data were split by manufacturing change date and Weibull distributions were fit to the data. In building a simulation model of distortion, we input the current diffuser case population times, inspection schedules, and cycles flown per month, in addition to the Weibull probability distributions for the case measurements on wall thickness and distortion.

Fracture life curves were used in conjunction with stress calculations to predict the maximum life of each diffuser case

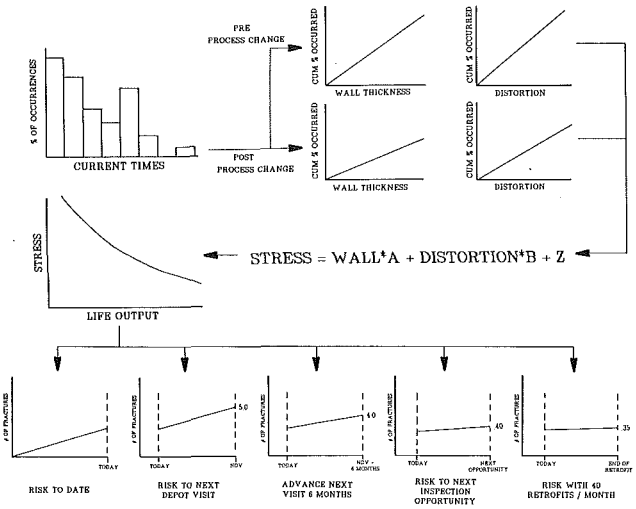

Fig. 10

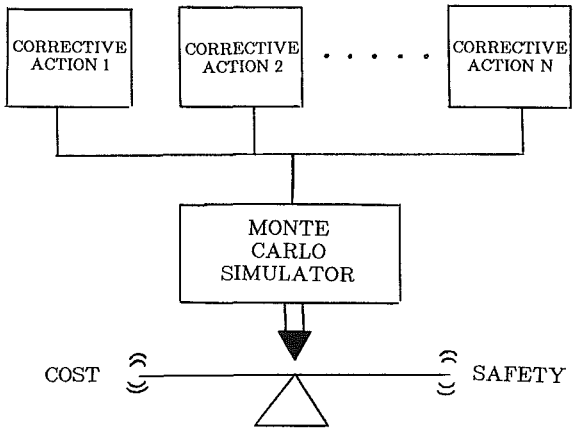

Fig. 11

based on dimensional data. The simulator would read in each engine and decide (by its serial number) what its manufacturing date was. Using a random number generator, the simulator would then pick a random wall thickness and distortion from the correct distributions (pre- or postprocess change year in question). Based on the generated dimensions, part stress was calculated. From here, the simulator would read a fracture life curve with stress and calculate the maximum life of the diffuser case before fracture. If the maximum life was prior to the diffusers case's next scheduled inspection but later than the case's current time, a fracture counter was incremented. If the maximum life was earlier than the case's current life, then the risk-to-date counter was incremented.

The risk-to-date counter is useful in calibrating the model. If this counter predicts 20 fractures to date and history shows only 1, then we need to return to the experts and correct the probability distributions, assumptions, or equations.

In the diffuser case simulation, when we were satisfied with the compatibility of the simulator output and reality, we predicted five fractures prior to the next scheduled inspection. The safety implications were not satisfactory, so it was decided to implement corrective actions into the simulator to determine which yielded a prediction that could be supported as a balance between safety and cost.

The first option considered was to move the scheduled inspections from their current time back 6 months. The simulator predicted four fractures prior to the next adjusted scheduled inspection. Although this was supportable from a cost standpoint, it still wasn't acceptable from a safety standpoint. The second option was to fix the diffuser case (eliminate distortion) as soon as the engine has returned to the depot for other maintenance. The simulator predicted 0.4 fractures. This was supportable both financially and in its safety implications. The third and final option was to fix the diffuser case before the engine was scheduled to return to shop at a rate of 40 cases per month. The simulator predicted 0.35 fractures. The safety risk did not change drastically between this option and the first access option, but the cost of this forced retrofit was significantly higher. The conclusion was therefore to support option 2: rework the diffuser cases at next opportunity. By using the Monte Carlo simulator, we were able to analyze our options and pick the one that balanced cost and safety (Fig. 10).

Closing

As has been shown, by using the two techniques presented, Weibull-based risk analysis and Monte Carlo simulation-based analysis, safety considerations can be quantitatively analyzed, potential field impact to safety risk can be minimized, and cost can be managed. These techniques have been very beneficial to Pratt & Whitney, in terms of improved safety records and in keeping maintenance costs down.

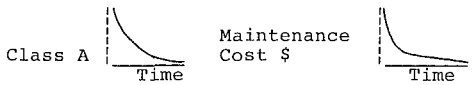

The major purpose of using risk analyses in the gas turbine industry is to provide management with quantitative groundwork for making safety decisions. Quantifying the effect of corrective actions with safety makes management's balancing of safety, cost, and supportability easier.

It is obvious that risk analysis is not possible without an adequate data base. It is necessary to keep current statistics on every engine required to assess safety risk, such as operating times on critical engine modules and components. When a strong data base is available, risk analysis is easier and more accurate since gross assumptions aren't required. When the risk analysis is fairly uncomplicated and the critical part failure scenario is best represented by a Weibull probability distribution, then a Weibull-based risk analysis is in order. The Weibull distribution will allow for a few part failures and several thousand successfully operating units. After formulating the Weibull, and estimating the parameters β and η, the Weibull equation can be used to estimate the expected number of part incidents over any period of calendar time.

If the risk analysis is more complicated, or an engineering model of a failure mode is required, or several failure modes need to be considered for a given part, then a Monte Carlo simulator may be applicable for the calculation of risk. The Monte Carlo simulator allows the user to assess various corrective actions quantitatively and choose the one which allows for the proper balance between cost and safety or supportability and safety (Fig. 11).

A Monte Carlo simulator is simple to operate once the random number generator has been obtained and the probability distributions have been defined. This type of simulation is very powerful in that virtually any flight scenario can be readily incorporated into the Monte Carlo logic, and its benefits assessed.

Both Weibull-based risk analyses and Monte Carlo simulation-based risk analysis are inexpensive, valuable managerial tools. With the integration of the computer industry into all areas of engineering, computers are readily accessible and computer time is inexpensive. Credible quan-

titative risk analyses have become a vital and necessary tool at all stages of decision making at Pratt & Whitney.

References

Abernethy, R. B., Breneman, J. E., Medlin, C. H., and Reinman, G. L., 1983, "Weibull Analysis Handbook," report AFWAL-TR-83-2079, Pratt & Whitney Aircraft, West Palm Beach, FL.

Crigler, J. A., and Shields, P. A., 1982, "Random: A Computer Program for Evaluating Pseudo-Uniform Random Numbers Generators," Naval Surface Weapons Center, Strategic Systems Department.

Fishman, G. S., and Moore, L. R., 1982, "A Statistical Evaluation of Multiplicative Congruential Random Number Generators With Modulus $2^{31}-1$," *JASA*, Vol. 77, No. 377.

Gnedenko, Belyayev, and Solvyev, 1969, *Mathematical Methods of Reliability Theory*, Academic Press, New York, pp. 101–102.

Hollander, M., and Wolfe, D. A., 1973, *Nonparametric Statistical Methods*, Wiley, New York, p. 151.

Law, A. M., and Kelton, W. D., 1982, *Simulation Modelling and Analysis*, McGraw-Hill, New York.

Rubinstein, R. Y., 1981, *Simulation and the Monte Carlo Method*, Wiley, New York.

Economic Considerations for a New Gas Turbine System in the U.S. Navy

J. C. Ness
David Taylor Naval Ship Research and Development Center, Annapolis, MD 21402
Assoc. Mem. ASME

C. B. Franks

R. L. Sadala
Advanced Technology, Inc.
Arlington, VA 22202

During the phases of a U.S. Navy acquisition program for any new system, such as a gas turbine system, various analyses are conducted to evaluate the economic and technical benefits that can be gained by the new system. It is important that the economic analyses provide a good estimation of the nonrecurring and recurring costs. For the development of a new gas turbine system, a test program to prove the system's technical and operational capability will have to be conducted and a support system will have to be developed to operate and maintain it during its life cycle. The costs of the engine development, the test program, and the support system development are considered nonrecurring or investment costs. The operation and maintenance costs over the life of the system are the recurring costs. This paper presents the life cycle cost scenario that should be used to evaluate the economics of a U.S. Navy marine gas turbine and the considerations that should be included in a Return on Investment analysis of the engine. The major cost categories discussed include engineering, logistics support, program management, and deployment support. Also, the unique considerations that would apply to marine gas turbines for Naval use are discussed along with how these considerations affect the economics of a gas turbine acquisition program. In addition, the paper identifies the funding responsibility of each cost item and provides discussion on ways to reduce the investment cost.

Introduction

In the past, many military system acquisition decisions were based on initial cost or immediate requirement. However, in many cases, operation and maintenance costs over the life of a system far exceeded its initial acquisition (development and procurement) costs. As a result, the Department of Defense has placed greater emphasis on the total cost over a system's life cycle. In recent years, Life Cycle Cost (LCC)/Return On Investment (ROI) analyses have become popular for determining the value of a new system. The LCC analysis provides an estimate of the nonrecurring (investment) cost needed to procure a new system and the recurring cost needed to operate and maintain it during its life cycle. The data from an LCC analysis are used to perform a ROI analysis. The ROI analysis provides an estimate of when a new system will pay back its investment cost. This payback is determined based on the projected reduced operating costs over the current system. Also, alternative systems can be compared to determine the most economical. In addition, the LCC/ROI analysis uses a methodology that can be developed into a budget for system acquisition and thus, reduce cost risk.

New systems are constantly being evaluated by the U.S. Navy for possible use in the future surface ships. Recent U.S. Navy combatant surface ships use the General Electric LM2500 marine gas turbine (derivative of the military TF 39 and commercial CF6-6 engines) as the main propulsion engines. The LM2500 engine was introduced on the DD 963 (USS SPRUANCE), which was commissioned in Sept. 1975, and it has served the U. S. Navy very successfully in the SPRUANCE, KIDD (DDG 993), TICONDEROGA (CG 47), and the OLIVER PERRY (FFG 7) ship classes. However, the production base for the LM2500 is declining due to its relatively old technology base and because more efficient engines are available for use today. This declining production base will increase support costs (spare parts), and likewise increase operating and maintenance costs, making new systems more economically attractive. This paper presents the cost-incurring items that should be used in LCC/ROI analyses to determine the economic feasibility of new systems. Because LCC/ROI analyses only determine the economic benefit of each system, other factors will also have to be evaluated to determine whether a system has technical advantages. This paper specifically addresses the acquisition, life cycle, and special considerations for U.S. Navy ship gas turbine systems.

Marine Gas Turbine Considerations

The gas turbine was first used and developed in aircraft and industrial applications during the 1940s. The marine applications started in the 1950s as the gas turbine improved in the areas of performance and packaging. For aircraft applica-

Contributed by the Gas Turbine Division of THE AMERICAN SOCIETY OF MECHANICAL ENGINEERS and presented at the 32nd International Gas Turbine Conference and Exhibit, Anaheim, California, May 31–June 4, 1987. Manuscript received at ASME Headquarters February 6, 1987. Paper No. 87-GT-98.

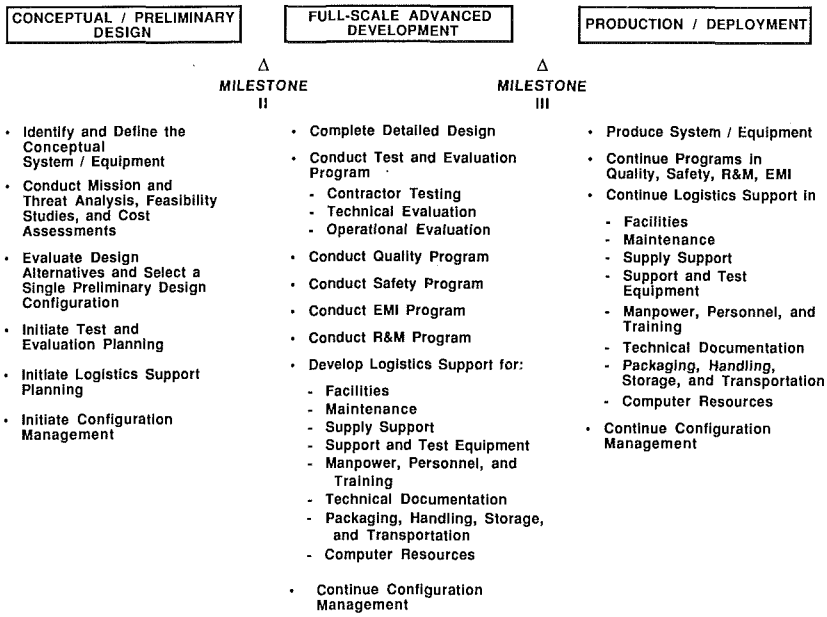

Fig. 1 NAVSEA acquisition process for a nonmajor system/equipment

tions, design emphasis is placed on the reliability of the engine to withstand numerous transients (power level changes) and reduced size and weight. For industrial applications, design emphasis is placed on reliability at constant power levels and a low fuel consumption rate. The marine application uses a combination of the technologies developed for the aircraft and industrial applications to design gas turbines with high reliability during some transient operation (but not as severe as the aircraft application) that would fit in the size and weight restrictions of the marine vessel and provide a reasonable fuel consumption rate. However, the demand for marine gas turbines is far less than for aircraft and industrial applications. Thus, there is less desire and fewer funds available for the full development of a marine gas turbine. So, as in the case of the LM2500, an existing gas turbine is modified to meet the needs of the marine application.

For U.S. Navy applications, the aircraft gas turbine derivative allows the prime mover to be developed at minimum investment cost. In addition, operation and maintenance costs are lower because technical documentation, support and test equipment, production tooling, and rework facilities are usually already available [1]. The engine acquisition cost is also lower because the parent engine production line is supported by the demand from the aircraft industry. However, this makes the marine gas turbine dependent upon the demand for the aircraft gas turbine and when this demand decreases the marine gas turbine costs for new engines and spare parts will increase. An example of this is the LM2500 marine gas turbine. The U.S. Navy to date has contracted to buy 300 to 400 engines compared to over 3000 CF6 and TF39 engines (the parent LM2500 core engine) sold. This example illustrates the dependency of the U.S. Navy's gas turbine on the demand for the parent aircraft engine.

Life Cycle Cost

In considering economic factors for an LCC analysis of a new marine gas turbine system, first a life-cycle scenario must be established that relates major phases in the acquisition process with associated costs. For the U.S. Navy, the life-cycle scenario is based on the relationship between the Naval Sea Systems Command (NAVSEA) acquisition process and the various costs incurred during that process. The NAVSEA acquisition process generally adheres to a set of guidelines that correspond to major decision points through which each project must pass. There are four phases in the life of a major system acquisition: conceptual design, preliminary design, full-scale advanced development, and production/deployment [2]. For a nonmajor system or equipment such as a new marine gas turbine system, the conceptual and preliminary design phases are combined, resulting in only three phases. A nonmajor system is defined as any system under $200 million in Research, Development, Test, and Evaluation (RDT&E) costs and/or under $1.0 billion in production costs [2]. Combining the design phases eliminates one review step, which normally occurs between the conceptual and preliminary design phases. A description of what occurs during the three phases is presented in Fig. 1.

In general, during the conceptual/preliminary design phase, funding is provided from a general pool of research and development funds. Because project funding does not actually begin until Milestone II, cost items up to that point are not usually considered and are labeled "sunk" costs. In other words, this money would be spend on system development regardless of the specific project and should not be used when performing an economic evaluation of the new system. The conceptual/preliminary design phase begins with the identification and definition of the purpose and/or mission the new system is to serve. This is followed by numerous studies, including mission and threat analyses, feasibility studies, and cost assessment. Planning for logistics support is started early in this phase. During its progression, a single preliminary design is chosen as the configuration that will meet or exceed defined requirements. Once a preliminary design reaches this stage and several plans are developed, the program is ready to be reviewed for entry into the full-scale advanced development phase.

Once Milestone II is approved, the project enters full-scale advanced development. This phase includes the detailed design, establishing logistic support, building of prototypes, and test and evaluation. When the test requirements are met and the logistics and project managerial aspects are satsified, the program is ready to be reviewed for entry into the production/development phase.

At Milestone III, the Acquisition Review Board reviews the program and decides whether to continue it into production.

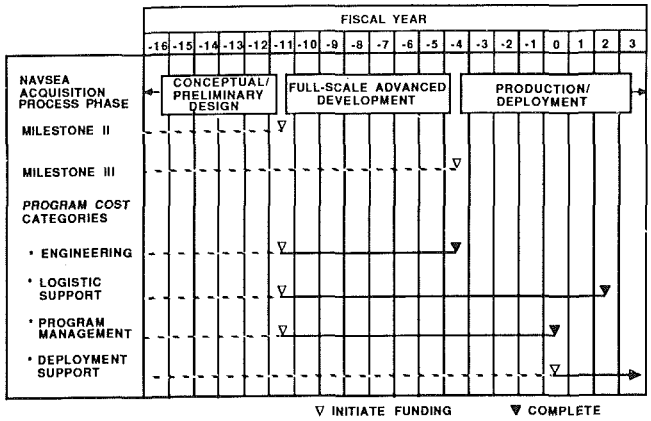

Fig. 2 Schedule of program cost categories

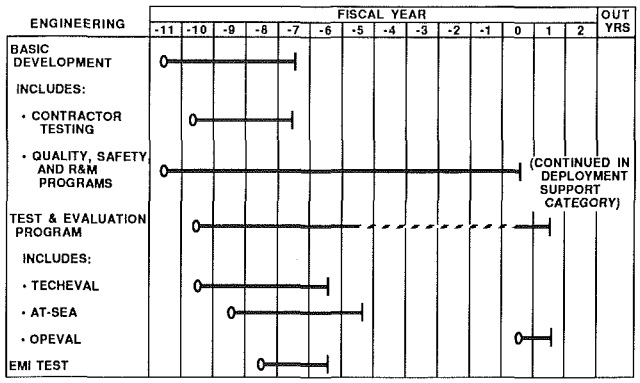

Fig. 3 Schedule of items under the engineering cost category

Approval for Full Production will be granted if the system has met all of the mission and performance requirements. However, if outstanding requirements can be met with reasonable certainty, the system can receive an Approval for Limited Production to prevent unnecessary delays in the project. During the production/deployment phase, the system is manufactured and receives its initial operational capability approval. After deployment or initial operational capability approval, the necessary engineering and logistics support programs continue through the system's life cycle.

To simplify the breakdown of cost-incurring items, four categories are introduced where each category continues through different phases of the program. These categories are used to arrange the programs, tasks, and end products in appropriately related groups. The categories are engineering, logistics support, program management, and deployment support. The engineering category encompasses all of the technically oriented programs, tasks, and end products involved in the development of the system. The logistics support category covers logistic elements from planning stages through full-scale development and production of system to the point at which the integrated logistics support becomes fully functional for the new system. The program management category covers the manpower necessary to manage the various programs in an acquisition project throughout its life cycle. Finally, the deployment support category includes all the items under the engineering, logistic support, and program management categories that incur costs after the system receives initial operational capability approval. Figure 2 shows the point at which each category will require project funds in relation to the NAVSEA acquisition project phases. The fiscal year "0" refers to the year in which the system receives initial operational capability approval. The following discussion addresses each cost category in more detail.

Engineering. During the early part of any acquisition program, the majority of the funds go into the engineering category. This category consists of basic development, Test and Evaluation, Quality, Reliability and Maintainability (R&M), Safety, and Electromagnetic Interference (EMI) programs. The schedule of these items is shown in Fig. 3. The funding for this category comes from Research, Development, Test, and Evaluation (RDT&E) funds.

Basic development includes system detailed design, component testing, and contractor establishment of quality, safety, and R&M programs. The results of basic development will be the manufacturer's final design and delivery of two or three Engineering Development Models to be used for Navy testing. For marine gas turbines, this cost can range from $70 to $120 million depending upon the amount of new design work required and the number of Engineering Development Models.

The objective of the Test and Evaluation Program is to verify that the final detailed design meets all technical and operational requirements. A Test and Evaluation Master Plan guides this program; provides the overall test thresholds; and identifies the resource requirements, schedule, and type of testing planned. Under this program, there are two types of testing: developmental (contractor testing and technical evaluation (TECHEVAL)) and operational (at-sea test, and operational evaluation (OPEVAL)) [3]. To determine the cost of the entire test and evaluation program, each one of the test programs should be evaluated separately. Contractor testing is conducted at an agreed-upon facility with a Navy representative present to observe. At this early stage of the system's development, various contractor tests may be conducted to reduce the technical risks such as endurance testing, shock testing, and EMI testing. This testing ranges in cost for a marine gas turbine from $10 to $15 million. Results of these tests are used to make necessary design changes prior to TECHEVAL and OPEVAL.

The next test is TECHEVAL, where the objectives are to verify that the system design meets the technical performance requirements and to ensure that the system is ready for OPEVAL. Also, final verification of the Integrated Logistic Support elements must be completed during TECHEVAL. The TECHEVAL site can be land-based or on board ship. Previous TECHEVALs (LM2500 and FT-9) were conducted at a Land-Based Test Site at the Naval Ship Systems Engineering Station in Philadelphia. For TECHEVAL conducted at the station, the cost can be as small as $2 million or as large as $10 million depending upon the amount of test site modifications required. The next test, at-sea, is not a Navy requirement, but because the LM2500 was the first propulsion gas turbine used on Navy ships it underwent at-sea testing to reduce operational and technical risk in an at-sea environment. For future programs, the at-sea test may not be necessary, depending upon the level of technical risk. If an at-sea test is required, it can range in cost betweeen $10 and $30 million, depending on the test ship chosen. The final test is the OPEVAL. Every effort is made during this test to ensure that the prototype resembles the planned production configuration and is installed on a ship similar to that for which it is intended. The objective of OPEVAL is to simulate normal Navy operating conditions, with a Navy crew operating and maintaining the system. If the evaluation is conducted on a fleet ship for which the engine is intended, the program cost needed is only for technical support and would be less than $0.5 million.

The Quality, Safety, and R&M programs are conducted and maintained throughout the system's life cycle by the Navy with various contractor support in accordance with respective military specifications and standards [4–7]. The system manufacturer is required to establish his part of these pro-

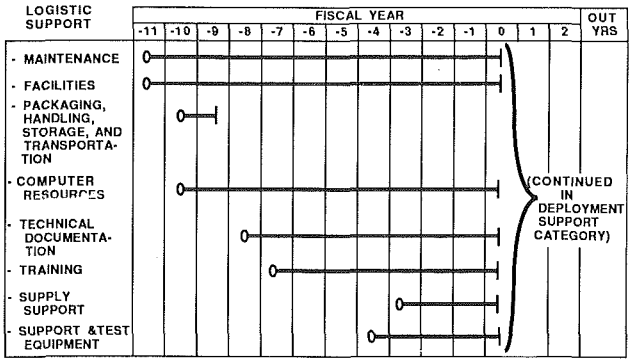

Fig. 4 Schedule of items under the logistic support cost category

grams under the contract(s) of the full-scale advanced development phase. The EMI program is a recent requirement to meet the increasing use of electronic equipment by many naval systems. The system manufacturer is responsible for ensuring the system meets the EMI requirement. The cost of these programs is included in the basic development costs.

Logistic Support. All acquisition programs require development of an integrated logistics support system that begins prior to full-scale advanced development and continues through the life of the system. In preparation for the gas turbine system entering the fleet, program expenditures for development of logistics support are started early in the full-scale advanced development phase [8]. The initial portions of the development of logistics support are funded by the RDT&E budget, and as the support system becomes established, Operation and Maintenance, Navy; Ship Construction, Navy; and Other Procurement, Navy funds are used. The gas turbine integrated logistics support encompasses the elements listed below:

- Maintenance planning
- Supply support
- Packaging, handling, storage, and transportation
- Manpower, personnel, and training
- Support and test equipment
- Facilities
- Technical documentation
- Computer resources

Figure 4 presents the logistic support cost elements and indicates when funding is required for each.

Maintenance planning consists of planning for the three levels of maintenance and conducting the Logistic Support Analysis. The Logistics Support Analysis drives all the logistic elements and insures that proper support is planned for each. Logistic Support Analysis is a systematic and comprehensive analysis constantly updated throughout the system's life cycle. The analysis generates a computerized database to analyze logistic support planned for and provided to the system. As part of this analysis, a Level of Repair Analysis is conducted. The Level of Repair Analysis describes the most effective path for repair of a failed system. Once the Logistics Support Analysis is completed, the results are used to develop a maintenance plan that identifies all the maintenance tasks and at which level they should be performed. The typical cost of maintenance planning is from $1.0 to $1.5 million.

In determining the Packaging, Handling, Storage, and Transportation logistic support requirements, output from Logistics Support Analysis is used to identify special packaging procedures and the need to develop shipping containers. Expenditures under this category cover shipping containers and transportation costs and usually range from $0.5 to $1.0 million.

The training area requires funding to establish any new or revised curricula on the operation and maintenance of the system for the Naval crew. In addition to curricula development, funding would be required for any additional materials and hardware required for conducting the course. The initial training of instructors and crew would be provided by the hardware manufacturer. Training costs normally range from $2 to $4 million.

The facilities cost encompasses the development of repair and overhaul (depot) facilities and training facilities for the new system. Development of depot facilities is started following a survey of the current repair facilities. The depot repair center is chosen based on the amount of alterations and new equipment required and the projected per overhaul cost. The cost of depot facilities development ranges from $10 to $30 million. Training facilities are developed as specified by the Navy Training Plan. If a complete engine room trainer is required including constructing a building and a full size engine room, the cost can be as high as $60 million.

Supply support and support and test equipment costs can be grouped together since both involve identification and provisioning of materials. Supply support is the continual process of providing repair parts, spares, and replenishment parts to the necessary repair and maintenance facilities. Support and test equipment is the equipment required to repair, maintain, and test the system. Ship provisioning of supply support and support and test equipment is funded by Ship Construction, Navy and Other Procurement, Navy funds and can range from $0.2 to $0.8 million per ship. Depot provisioning of supply support and support and test equipment ranges from $25 and $40 million. Intermediate level provisioning does not occur until later in the program whenever an adequate population of engines has been established. However, when established the cost can range from $2 to $5 million per facility.

Technical Documentation includes the development and documentation of all the technical data needed to support the system through its life cycle. This includes technical manuals for all levels of maintenance which describe in detail the repair and maintenance procedures for the system. The Illustrated Parts Breakdown manual identifies all the system's parts and contains drawings and illustrations of all parts of the system. The Support Equipment Recommendation Documentation is a hardward manufacturer-produced report that recommends equipment that is needed for operation, maintenance, and depot support. Provisioning Technical Documentation is a list of various types of data pertaining to the system and is used for identification, selection, and determination of initial spare part requirements. The engine Coordinated Shipboard Allowance List is a Navy-generated document for each ship that lists the on-board installed equipment; repair parts and tools; miscellaneous portable items needed for system care and upkeep; and material support needed to be self-sustaining for an estimated period of time. The Planned Maintenance System includes Maintenance Index Page, Maintenance Requirement Cards, List of Effective Pages, and the maintenance schedule. The Engineering Operating Sequencing System is a set of sequenced procedues for the system's operation and casualty control. Finally, the Personnel Qualification Standard is a list of requirements that define the minimum qualification necessary for personnel (crew) to operate or maintain a particular system. The development of the technical data can range in cost from $6 to $10 million.

Computer Resources includes any embedded hardware and software development for the new gas turbine system. These will be required for the control system of the new engine. The control system may require only development of computer software if a current marine gas turbine control system exists with sufficient hardware capability. The development of the computer resources is part of the basic development by the hardware manufacturer discussed under the engineering section.

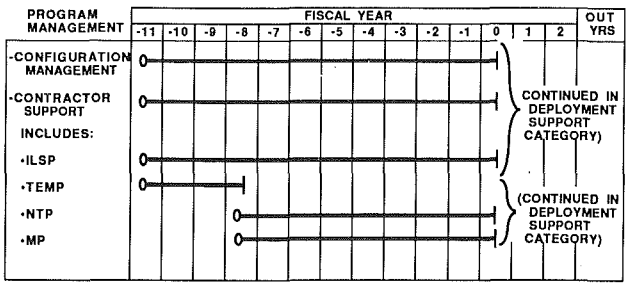

Fig. 5 Schedule of items under program management cost category

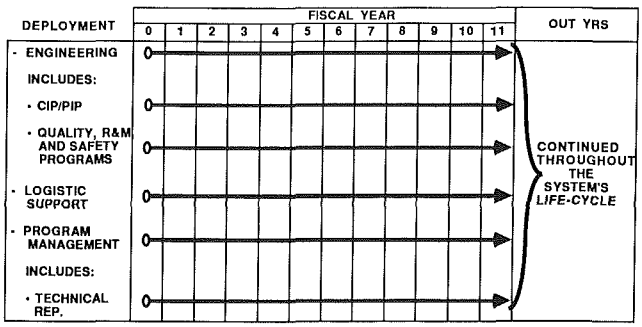

Fig. 6 Schedule of items under the deployment support cost category

Program Management. The cost elements under this category cover professional services provided by a contractor and the development of a configuration management program. Figure 5 shows the cost elements and when funding is required. The funding for this category comes from RDT&E funds. The contractor services required include the development of various plans needed to manage different aspects of the acquisition program. These plans include the Test and Evaluation Master Plan (TEMP), the Navy Training Plan (NTP), the Integrated Logistic Support Plan (ILSP), and the Maintenance Plan (MP). The contractor services also include other types of support to help the program stay within cost and on schedule. Configuration Management entails setting up and maintaining a system for tracking the functional and physical characteristics of the system and any changes to that system that may occur in its life cycle. This cost element also includes the computer resources cost for software development and equipment to establish the Configuration Management system. The costs under this category can range from $2 to $5 million.

Deployment Support. Once the system is in operation, costs are incurred to maintain it throughout its life cycle. These cost items are presented under the deployment support category. The funds for this category generally come from Operation and Maintenance, Navy and Other Procurement, Navy budgets. Figure 6 shows the scheduling of the elements under this category. The elements under this category relate directly to the three previously discussed categories. Engineering may be continued through the Component Improvement Program and Product Improvement Program (CIP/PIP). These programs are used to develop, test, and evaluate new technologies that may be applicable to the engine system. The purpose of these programs is to improve system reliability and cost effectiveness and resolve fleet problems. Logistics support is required in all areas to maintain the system's operational capability. Progam management is needed to maintain the established programs and the Configuration Management system and to obtain support of a technical representative from the manufacturer. The costs under this category are largely dependent upon the type of system being evaluated and the current or projected population of that system.

Table 1 Cost ranges per category

CATEGORY	COST RANGE
ENGINEERING	$92.0 - $175.5 MILLION
LOGISTICS SUPPORT	$44.5 - $146.5 MILLION *
PROGRAM MANAGEMENT	$ 2.0 - $ 5.0 MILLION
TOTAL INVESTMENT	$138.5 - $327.0 MILLION

* INITIAL PROVISIONING FOR SHIP AND INTERMEDIATE LEVEL FACILITIES NOT INCLUDED

Total Investment Cost

The cost categories presented involve the hardware and logistic support development for a gas turbine system. To estimate costs for the elements, historical data from the LM2500 and the FT-9 acquisition programs can be used as a data base for developing intitial estimates. Then, considering inflation rates from the time period of the LM2500 and FT-9 programs and using data from discussions with gas turbine engine manufacturers and the Navy, a cost estimate for each item can be determined.

The total investment cost (engineering, logistics, and program management cost categories) is shown in Table 1 to range from $138.5 million to over $327 million. This range does not include the investment costs for initial outfitting of ships and intermediate level maintenance facilities because the engine application will significantly affect these numbers. The cost ranges in this presentation are based on the development of a derivative aircraft gas turbine as discussed earlier. The amount of commonality with the parent gas turbine will greatly influence which end of the cost range the program approaches.

Return on Investment Considerations

Having established the basic scenario for a LCC analysis, there are other important factors that need consideration so that a ROI analysis can be performed. Throughout the full-scale advanced development phase, the LCC analysis would be based on manufacturer inputs and certain Navy requirements. However, in the Production/Deployment phase, emphasis would be turned to the ship class(es) that will utilize the new system, because the ship acquisition process affects the engine production rate, logistics support, deployment support, and overall annual fuel consumption. Therefore, the application for the new system needs addressing to perform the ROI.

Ship and Engine Acquisition Scheduling. Based on commissioning dates from [9], Tables 2 and 3 illustrate assumed retirement schedules and new ship construction schedules for frigates and destroyers/light cruisers that would be retiring from the fleet with 30 to 35 years of service life in the time period when a new gas turbine could be available for use on board ship, respectively. It is assumed that each new frigate will have two identical engine systems per ship; each new destroyer/light cruiser will have four identical engine systems per ship. This follows current practices of the U.S. Navy. Also, new ships will have a 30 year life expectancy with five overhaul periods lasting 9 months each resulting in 26 years of operational life. Engine acquisition for ship construction occurs two years prior to a particular ship's initial operational capability approval. Reference [10] has standard computational procedures for calculating spare engines that are needed

Table 2 Retirement and new replacement ship construction schedules for frigate-type ships

FISCAL YEAR	(1) FF1040 CLASS	(1) FFG-1 CLASS	(1) FF1052 CLASS	(2) FFG-7 CLASS	FFX/FFGX CLASS TOT.
1997	−1				1
98	−4				5
99	−1	−1			7
2000	−1	−4			12
01	−3	−1			16
02			−5		21
03			−13		34
04			−11		45
05			−8		53
06			−5		58
07			−4	−1	63
08				0	63
09				−1	64
10				−5	69
11				−7	76

(1) 33 YEAR SHIP LIFE

(2) 30 YEAR SHIP LIFE (ONLY FFG-7 THRU FFG-20)

Table 3 Retirement and new replacement ship construction schedules for destroyer and light cruiser-type ships

FISCAL YEAR	(1) CG-16 CLASS	(1) CG-26 CLASS	(2) DD963 CLASS	(2) DD993 CLASS	DDX/DDGX/CGX CLASS TOT.
1997	−1				1
98	−6				7
99	−2	−1			10
2000		−1			11
01		−4			15
02		−3			18
03					18
04					18
05			−1		19
06			−4		23
07			−5		28
08			−8		36
09			−7		43
10			−5		48
11				−3	51
12				−1	52

(1) 35 YEAR SHIP LIFE

(2) 30 YEAR SHIP LIFE

Table 4 Ship and engine acquisition schedules

	FFX/FFGX		DDX/DDGX/CGX			
FISCAL YEAR	SHIPS	(1) ENGINES	SHIPS	(1) ENGINES	TOTAL SHIPS	(1) TOTAL ENGINES
1995	0	2	0	4	0	6
96	0	9	0	27	0	36
97	1	4	1	13	2	17
98	4	12	6	5	10	17
99	2	9	3	17	5	26
2000	5	11	1	13	6	24
01	4	28	4	0	8	28
02	5	25	3	0	8	25
03	13	18	0	5	13	23
04	11	11	0	18	11	29
05	8	11	1	22	9	33
06	5	0	4	35	9	35
07	5	2	5	31	10	33
08	0	11	8	22	8	33
09	1	16	7	14	8	30
10	5	0	5	5	10	5
11	7	0	3	0	10	0
12	0	0	1	0	1	0
CUMULATIVE TOTALS:	76	169	52	231	128	400

(1) SPARES INCLUDED

Table 5 Example of frigate and destroyer engine system repair overhaul schedules

	FRIGATE			DESTROYER		
YEARS	ENGINE OPERATING HRS/YR	CUMULATIVE ENGINE OPERATING HRS/YR	BALANCE OF HRS REMAINING	ENGINE OPERATING HRS/YR	CUMULATIVE ENGINE OPERATING HRS/YR	BALANCE OF HRS REMAINING
0			8100.0			8100.0
1	1780.0	1780.0	6320.0	1220.4	1220.4	6879.6
2	1780.0	3560.0	4540.0	1220.4	2440.8	5659.2
3	1780.0	5340.0	2760.0	1220.4	3661.2	4438.8
4	1780.0	7120.0	980.0	1220.4	4881.6	3218.4
*5	445.0	7565.0	535.0	305.1	5186.7	2913.3
6	1780.0	#1245.0	6855.0	1220.4	6407.1	1692.9
7	1780.0	3025.0	5075.0	1220.4	7627.5	472.5
8	1780.0	4805.0	3295.0	1220.4	# 747.9	7352.1
9	1780.0	6585.0	1515.0	1220.4	1968.3	6131.7
*10	445.0	7030.0	1070.0	305.1	2273.4	5826.6
11	1780.0	# 710.0	7390.0	1220.4	3493.8	4606.2
12	1780.0	2490.0	5610.0	1220.4	4714.2	3385.8
13	1780.0	4270.0	3830.0	1220.4	5934.6	2165.4
14	1780.0	6050.0	2050.0	1220.4	7155.0	945.0
*15	445.0	6495.0	1605.0	305.1	7460.1	639.9
16	1780.0	# 175.0	7925.0	1220.4	# 580.5	7519.5
17	1780.0	1955.0	6145.0	1220.4	1800.9	6299.1
18	1780.0	3735.0	4365.0	1220.4	3021.3	5078.7
19	1780.0	5515.0	2585.0	1220.4	4241.7	3858.3
*20	445.0	5960.0	2140.0	305.1	4546.8	3553.2
21	1780.0	7740.0	360.0	1220.4	5767.2	2332.8
22	1780.0	#1420.0	6680.0	1220.4	6986.6	1112.4
23	1780.0	3200.0	4900.0	1220.4	# 108.0	7992.0
24	1780.0	4980.0	3120.0	1220.4	1328.4	6771.6
*25	445.0	5425.0	2675.0	305.1	1633.5	6466.5
26	1780.0	7205.0	895.0	1220.4	2853.9	5246.1
27	1780.0	# 885.0	7215.0	1220.4	4074.3	4025.7
28	1780.0	2665.0	5435.0	1220.4	5294.7	2805.3
29	1780.0	4445.0	3655.0	1220.4	6515.1	1584.9
30	1780.0	6225.0	1875.0	1220.4	7735.5	364.5

* – SHIP OVERHAUL

– ENGINE SYSTEM REPAIR OVERHAUL

for the new system. However, another way would be to calculate spares based on the current ratio of LM2500 spares to shipboard LM2500 engines in the inventory. Based on the above information Table 4 represents the ship and engine acquisition schedule for frigates and destroyers/light cruisers, which illustrates a future application.

Engine System Repair Overhaul. Another important area of consideration is that in operating a gas turbine-powered ship, each engine experiences different operating profiles (i.e., each engine is used at different times). However, each engine typically accumulates approximately the same total operating time. The total annual operating hours along with the mean time between removal (MTBR) (i.e., removing the engine system from the ship for depot maintenance) of the engine system are the parameters that affect the system's Repair Overhaul (ROH) Schedule. Although the MTBR of an engine system increases over the life of a ship due to increased confidence and CIP/PIP, a mature engine MTBR should be used to determine the ROH. This is because a ROI analysis will be comparing the ROH schedule for the LM2500 to that of the new system and the LM2500 is a mature engine. In using a mature MTBR, the schedule tends to be more uniform and predictable. This schedule is important since the maintenance cost for the Production/Deployment phase is determined from it. This schedule will affect the ROI analysis results.

To illustrate how to predict when an engine system requires an overhaul, Table 5 has been constructed. In determining the ROH schedules for the frigate and destroyer engine systems as shown in the table, the following assumptions are made: (1) Each ship has a life expectancy as mentioned previously; (2) the MTBR for the mature engine system is 8100 hours (h); (3) each frigate engine system operates 1780 h per year [11]; and (4) each destroyer engine system operates 1200.4 h per year [11]. As Table 5 shows, the ship overhauls are done in years 5, 10, 15, 20 and 25. During overhaul years, the engine operating hours/year are assumed to be 1/4 of the normal operating time. For the case of the frigate, its engine system is replaced five times during the life of the ship, whereas the destroyer system has only three ROHs because the engine operating time is split among four engines instead of two as in frigate. This means that the number of times in a destroyer's life the engine ROH is required to be performed is less. However, if the mature engine MTBR of 6000 h is used, the engine system is replaced seven times for the frigate and five times for the destroyer. Note, that using mature engine MTBR in either the

frigate or the destroyer case will show a usable balance of operating hours remaining for the engine system that is left in the ship when it retires.

Fuel Savings. For a new ship engine system to show any significant economic benefit it will have to have an annual fuel savings over the current systems. Previous studies [12, 13] have shown that new engine systems such as the Intercooled-Regenerative Gas Turbine could readily accomplish this requirement. The LM2500 annual fuel consumption will serve as a baseline to compare to the new engine system fuel consumption. From [11], the fuel consumption using LM2500 engines in a frigate and destroyer are approximately 48,600 and 88,000 barrels of fuel per ship per year, respectively. As an example, the Intercooled-Regenerative Engine would save on the order of 30 percent fuel [11], thus the frigate will have an approximate annual fuel consumption of 34,000 barrels of fuel and the destroyer will have and approximate annual fuel consumption of 61,600 barrels of fuel. Then, the difference between the baseline annual fuel consumption and the intercooled-regenerative annual fuel consumption is the annual fuel savings in barrels per ship. This difference in turn would be used with operational and overhaul schedules for the ship classes and fuel price to determine saving dollar amounts. The price per barrel of fuel should be based on the delivery to an operational ship at sea.

Discounting and Price Escalation. Discounting is the technique that is used for converting benefits and costs occurring over a time period to a common point in time, i.e., bringing future-year estimates into current-year dollars. Standard practice in evaluating U.S. Navy projects related to energy, such as the Intercooled-Regenerative Engine, is to assume a 10 percent discount rate [14]. As shown from previous section, the life cycle of a new engine development is quite long, possibly lasting 40 years or more. When discounting, the front-end costs play an important role because costs and savings that are realized 20 to 30 years from the beginning of development can be relatively small as compared to the up-front costs. As an example, the dollar savings that are associated with the intercooled-regenerative engine fuel savings will decrease as the dollars are discounted back to the current year. In other words, $100 spent 5 years from now for engine development would be worth $62 in current year dollars using 10 percent discounted dollars. Also, to recover this $62 in investment cost it would require $413 in fuel cost savings 20 years from now when the system is operational.

Countries exporting petroleum have collectively demonstrated an ability to control production and increase price at a higher rate than increases for other goods during the same period. Therefore, it may be of interest to increase fuel price arbitrarily in an economic evaluation by inflating the fuel price and treating it as a separate case.

ROI Discussion. The LCC data, along with an estimate for the cost of each engine and the above mentioned consideration, can be used in an ROI analysis. The ROI analysis estimates when a new system will pay back its investment cost based on its potential reduced operating cost (i.e., reduced fuel consumption) over the current system. This analysis is performed by comparing the operating and maintenance costs of the new system to that of the baseline or current system (e.g., LM2500). The amount of time it takes the new system's operating and maintenance cost savings to surpass the initial investment cost (using 10 percent discounted current year dollars) is the time required to receive a return on investment. The ROI analysis can also be used to compare two new systems to determine which system provides the maximum return over a specific time period. The cost estimates can also be used to determine required budgets and help plan the acquisition and life cycle support schedules.

General Discussion

For acquisition programs that are concerned with investment costs, there are ways to reduce some of these costs. As previously discussed, when introducing a new gas turbine system into the fleet, the basic development costs can be significantly reduced by developing a derivative of a gas turbine currently in production. These cost savings are a result of using as much common hardware to the parent gas turbine as possible, thus reducing production tooling and design costs. Also, basic development cost is further reduced by deriving the marine gas turbine from a gas turbine already in the military system. This allows the use of common parts that are already in the military supply system and usage of established depot facilities. Another example of reducing cost is to develop a system with proven state-of-the-art technology to keep the technical risk low. In this case an at-sea test may not be required, eliminating that as a cost item.

It is important to realize that the economic factors of a new system are not the only factors that determine its acceptance. Other factors such as technical advancement or satisfying a new requirement may outweigh the economic considerations. However, to determine if any technically feasible system is economically feasible, an LCC/ROI analysis needs to be performed.

Concluding Remarks

This paper has presented considerations that should be included in determining the economic benefit of a new marine gas turbine system. The analyses used to evaluate a system have been shown. The LCC analysis is an estimate of the investment and operational costs over the life cycle of the system. Also, it can be used to project budget requirements. The ROI analysis uses the LCC analysis data to project the cost and savings over the current system and determine when a payback will occur. During these analyses, there are major considerations to be examined. These considerations are summarized below:

- The demand for marine gas turbines is substantially less than for aircraft and industrial gas turbines; thus, less developmental or investment funding is available. Therefore, to minimize development cost, a derivative engine development is necessary.
- Even with a derivative engine development, the investment cost can vary significantly depending upon the amount of commonality with the parent engine.
- Engine development programs for the U.S. Navy typically can require 15 or more years before the engine is introduced into the fleet and savings are realized. Thus, the accumulation of investment cost during these years makes it difficult to show a positive ROI, especially when using discounted dollars.
- For marine gas turbines to show an economic benefit, a significant fuel savings over the current system must be achieved. Also, the application (population) of the system can significantly influence the LCC/ROI analysis.
- Historical cost data from U.S. Navy marine gas turbine programs are available for the LM2500 and FT9 engines and should be used as an initial database from which to start estimating costs.

This paper also shows that an LCC/ROI analysis should be performed at numerous stages throughout the development program. Early on in the program it is difficult to estimate costs in the out years (20-30 years in the future). Therefore, it is beneficial to develop a computer model of the LCC/ROI analysis and run various parametric cases. As the development program progresses the cost numbers can be better estimated and the computer model updated with the new program costs. If used properly, the LCC/ROI analysis can be used to reduce the cost risk of a marine gas turbine acquisition program.

Acknowledgments

The authors wish to express their appreciation to Mr. Thomas L. Bowen and Mr. Kenneth E. Tavener of David Taylor Naval Ship R&D Center, Annapolis, MD for their support.

References

1 Dix, D. M., Gissendanner, D. A., "Derivative Engines Versus New Engines: What Determines the Choice?" ASME JOURNAL OF ENGINEERING FOR GAS TURBINES AND POWER, Vol. 107, 1985, pp. 808–814.

2 Catalano, D. E., and Senio, J., "Production Approval for Shipboard Systems," 22nd Annual Technical Symposium, Association of Scientists and Engineers of the Naval Sea Systems Command, Washington, DC, 1985.

3 Toscano, M., "How to Build a Good T&E Program," 22nd Annual Technical Symposium, Association of Scientists and Engineers of the Naval Sea Systems Command, Washington, DC, 1985.

4 MIL-Q-9858A, "Quality Program Requirements," Mar. 8, 1985.

5 MIL-STD-882B, "Systems Safety Program Requirements," Mar. 30, 1984.

6 MIL-STD-785B, "Reliability Program for Systems and Equipment, Development and Production," Sept. 15, 1980.

7 MIL-STD-470A, "Maintainability Program Requirements," Jan. 3, 1983.

8 Calogero, R., and Orner, J., "The Best Laid Plans of Engineers and Logisticians Require Execution," 22nd Annual Technical Symposium, Association of Scientists and Engineers of the Naval Sea Systems Command, Washington, DC, 1985.

9 Moore, J., ed., *Jane's Fighting Ships 1985–1986*, Jane's Publishing Co., Limited, London, England.

10 DOD Instruction 4230.4. "Standard Method for Development of Spare Engine Requirements," Nov. 14, 1983.

11 "Preliminary Design of Advanced Propulsion Gas Turbine," Solicitation No. N00024-85-R-5310(S), Naval Sea Systems Command, Mar. 29, 1985.

12 Bowen, T. L., and Ness, J. C., "Regenerated Marine Gas Turbines, Part I: Cycle Selection and Performance Estimation," ASME Paper No. 82-GT-306, 1982.

13 Bowen, T. L., and Groghan, D. A., "Advanced-Cycle Gas Turbines for Naval Ship Propulsion," *Naval Engines Journal*, Vol. 96, No. 3, 1984, pp. 262–271.

14 Brown, R. J., and Yanuck, R. R., *Introduction to Life Cycle Costing*, Fairmont Press, Inc., Atlanta, GA, 1985.

Neutron and Positron Techniques for Fluid Transfer System Analysis and Remote Temperature and Stress Measurement

P. A. E. Stewart
Chief,
Advanced Projects Department,
Rolls Royce plc,
Bristol, United Kingdom

Nonintrusive radiation techniques have been routinely used, since 1970, for the determination of metal component movements and clearances within engines using high-energy x-rays. Oil system operation was first analyzed using "cold" neutrons in 1975 and, since 1980, positron-emitting isotope tomography has been developed using multiwire proportional counters to determine the X, Y, and Z coordinates of labeled oil volumes within engines. The tomographic system will allow a plane-by-plane inspection across an engine or rig to be carried out using radioisotope images overlaid by an engine general arrangement drawing. It is presently proposed that epithermal neutrons may be used for remote, noninvasive metal temperature measurement within engines or rigs. Finally, neutron diffraction may also be used for internal stress determination within compressor or turbine disks. Consideration is being given to carrying out remote stress measurements in a spinning pit or, perhaps, within an engine using this technique.

Introduction

Prior to 1970, the walls of gas turbine engines were opaque and it was not possible directly to visualize and measure the mechanical movements of internal components.

At the time, the development engineering approach was iterative through a number of successive engine tests. From test results movements were inferred, hypotheses were made, and further tests carried out to prove or disprove each hypothesis, slowly closing in on a suspected problem. The data were obtained indirectly.

What was required was a noninvasive or nonintrusive technique needing no modification to the engine. This would permit the immediate examination of an engine exhibiting a problem. Previously when an engine was stripped to install instrumentation the problem sometimes disappeared only to reappear on another engine. What was also needed was an area view of the engine to show the interrelationship of different clearances and growths in compressors, turbines, and labyrinth seals. A continual surveillance was also needed throughout the course of an engine maneuver to examine transient conditions.

In Sept. 1970, the first high-energy x-ray examination of a gas turbine engine on test was carried out at Rolls-Royce (Bristol) on an Olympus 593 engine for Concorde. The x-rays were produced by an 8 MeV radiographic electron linear accelerator or "linac," the RDL (now Viritech) Super X 1500. For the first time, large area, direct images were obtained of mechanical components. Using photogrammetric techniques, comparative measurements were taken from radiographs of the static engine and radiographs taken over a range of engine conditions. The relative movements could then be clearly identified and quantified. It was thus possible, for the first time, to visualize and measure in compressor, combustion system, and turbine areas of the engine.

Since 1970 (Stewart, 1986a), over 41,000 radiographs have been made using the Super X 1500 linac at prepared sites at Rolls-Royce Bristol, Ansty, and Hucknall and Dowty Fuel Systems Test Site at Staverton. The Super X 1500 linac has also been used at the Cell 3 High Altitude Facility at the Royal Aircraft Establishment (RAE) Pyestock. A range of specialized, high-energy x-ray, closed-circuit video systems has been developed and over 50 high-energy x-ray video examinations have been carried out. To date, 141 engines of 27 different types have been examined. Recently, in addition to the 8 MeV Super X 1500, Rolls-Royce has also purchased a 6-10 MeV Viritech Super X 3000 linac to keep pace with the increased work load. Both machines are transportable and shuttle between the Rolls-Royce work centers to serve engine projects.

The x-ray systems are mounted in mobile vehicles and the video van and radiograph development van are deployed on site. The High-Energy Dynamic Radiography system can be installed within 2 days of a requirement being notified.

Radiographic images are obtained on 35 × 43 cm film for later examination on X–Y coordinate tables at Bristol. The film is stored for use in automatic sheet film or film plate changers. The latest x-ray video systems developed by Rolls-Royce are used, as with the film, one above and one below the engine to investigate asymmetries due to internal load distributions.

Contributed by the Gas Turbine Division of THE AMERICAN SOCIETY OF MECHANICAL ENGINEERS and presented at the 32nd International Gas Turbine Conference and Exhibit, Anaheim, California, May 31-June 4, 1987. Manuscript received at ASME Headquarters February 19, 1987. Paper No. 87-GT-219.

Engine conditions that have been examined are:

- Fast and slow transients – accels and decels
- Steady state
- Shaft whirling
- Spacer bounce in compressor and turbine packs

The images are compared by pattern matching correlation techniques and digital image processing is carried out with enhancement, integration, noise reduction, contrast stretching, pseudocolor, and restoration.

X-ray film images are analyzed by skilled photogrammetrists with average accuracies of around 0.15 mm but on good edges 0.10 mm can be achieved. These are based on a 95 percent confidence of repeatability. Ellipsing of circular features limits measurement in the axial direction but radial measurement can be made over a broader field.

Examples of Applications

- Performance improvements by profiling of tip seals of turbines to reduce energy losses over the range of engine operating conditions leading to improvements in specific fuel consumption (s.f.c.).
- Understanding of thermal growths in casings and the differential expansions between disks, blades, and casings. The maximum clearances occur with a cold engine in an aircraft and a cold engine acceleration. On the other hand, a "reslam acceleration" gives the minimum clearance or worst tip interference. From the use of the x-ray technique, the cooling cycle time for the RB199 engine was found to be 10–15 min while the RB211 was 45 min.

The x-ray system also provides a greater understanding of the dimensional changes in components, with time, under engine operating conditions. For instance the "running-in" time for the RB199 has been reduced from 2.5 h to 37 min from an understanding of the movements. Similarly, the effect that module changes have on "running-in" is better understood. This gives increased performance and improved specific fuel consumption. The availability of x-ray images and their measurement cuts down the number of tenable theories on an engine problem, reducing the number of tests required and therefore the overall development time of the engine.

- Engine air system optimization from a knowledge of the behavior of internal labyrinth seals and compressor and turbine root seals. An understanding of the performance of all seals is necessary to maintain air pressure balances throughout the engine.
- Engine integrity investigations ranging from static assembly checks before test to movements of spacers in turbine and compressor packs and shaft whirling by stroboscopic x-ray techniques.

On-Line Interactive Testing. The development of this new nonintrusive approach by which it is possible to view and measure directly large areas of the engine in real time leads to a new concept of on-line interactive testing for the development engineer.

The availability of engine computer modeling, using finite element techniques, could provide a graphics image of the designed casing and blade flexures and the way in which areas of the engine structure theoretically respond to the loads and stresses encountered in service. The actual x-ray images could then be overlaid on the graphics image to identify mismatches of theory and practice. Complete cycles of engine operation could be examined in this way.

This computer-aided engineering technique could prove extremely powerful and is brought about by the application of radiation physics techniques to mechanical engineering using a range of penetrating radiations and choosing the best radiation for each specific engineering problem:

- Metal components movements may be visualized and measured using high-energy x-rays.
- Oil and fuel systems may be visualized and measured with cold neutron radiography (NR) or positron emitting isotope tomography (PET).
- Metal temperatures may be measured using epithermal neutrons.
- Metal stresses may be measured by thermal neutron diffraction.

These approaches are now examined in greater detail.

Noninvasive Analysis of Lubrication and Oil Systems on Test Using Cold Neutrons and Positron Emitting Isotopes

Lubrication systems form an important area for future improvements in gas turbine engine technology. At the present time it is difficult to visualize and measure the effectiveness of lubrication of bearings and gears and the behavior of oil jets and masses in gearboxes. The situation is analogous to that in 1970 before the advent of high-energy x-ray techniques. One problem is due to the opaque walls of the engine and gearbox casings, another is the difficulty in seeing one oil flow within or behind another.

In addition to lubrication, the function of an oil system is to act as a means of heat removal, or cooling, for the mechanical inefficiencies. If oil is allowed to stagnate alongside hot surfaces it may lacquer or carbon the surface or rise to such a temperature that it will spontaneously ignite and start an oil fire. For this reason, oil systems must be designed to minimize stagnation zones in the flow passages.

Oil system problems that may be examined using the new techniques are:

- Engine priming patterns and time to prime critical items from engine start, particularly in cold conditions (NR).
- "Oil hiding" or a maldistribution of oil in the engine; there is a need to locate and "map" the distribution of masses of oil around the system with changes in engine operating conditions (PET).
- Leackage of oil through labyrinth seals into prohibited areas within the engine, causing fires and engine breakup. This may sometimes occur after the engine has been shut down (NR or PET).
- Two phase – gas–liquid flow in delivery and scavenge systems (x-rays).
- Lubrication of bearings and ensuring the adequacy of lubrication in the presence of cooling air flows (NR and PET).
- An understanding of the oil flow dynamics within gearboxes (PET).
- The rotating components within gearboxes entrain airflow patterns, which vary with rotational speed. This induces similar oil flow patterns. The oil and air affect lubricating jets. It is necessary to know whether lubricating jets remain coherent or whether they are deflected or break up. We need to determine whether lubrication is efficient and heat removal is adequate (NR and PET).

A more detailed understanding of the efficiency of lubrication could lead to increased component life, increase in mean time between overhauls, and integrity and safety of the engine.

If oil flow patterns within gearboxes could be accurately determined in rig work together with the location, flow vectors, masses, and temperature distribution, then oil management would be improved leading to smaller, lighter gearboxes with reduced power requirement.

Oil System Analysis Using "Cold" Neutrons. The question

was raised in 1974: "Now that we can image metal components, could we perhaps image oil movements?" At the time, Rolls-Royce were fortunate in possessing an Oude Delft "Delcalix" x-ray image intensifier. This was provided with a range of phosphor screens that were interchangeable, permitting experimental work to be carried out on screens sensitive to other radiation or particles, such as gadolinium oxysulphide to neutrons.

The important question – as in all penetrating radiation applications – is to choose the radiation to enhance the information required in the image (the oil), while reducing the effect of the steel casings. Following a survey of potential radiations and particles, cold neutrons were chosen for their special properties.

Characteristics of X-Ray and Neutron Sources. A neutron is a fundamental particle with no electric charge. Neutrons are produced by reactors as part of the fission process or by neutron generators such as cyclotrons or modified linacs with suitable targets. A neutron can generally move easily through matter with little interaction and energy loss and has different properties from x-rays, which strongly interact and produce scatter.

X-rays are categorized with respect to their energy levels or penetrating power. This is usually, in x-ray machines, the accelerating voltage of the electrons before they strike the tungsten target and are brought to rest to produce x-rays. Typically x-rays of 20–60 keV are used to examine ceramics and composites, 80 keV, medically, for soft tissues, 120 keV for bones and skulls, 300–420 keV for aluminum and light steel industrial sections, and 1–10 MeV for thick sections up to 254 mm of steel. Above 12 MeV we do not use x-rays in our work at Rolls-Royce due to the possibility of creating residual radioactivity in some engine parts and possibly causing damage to electronic components. At about 15 MeV, the tungsten target and shielding of a linac become active and there are handling problems in an engine test environment. It should, perhaps, be pointed out here that when electrons strike a target, the x-rays produced have a "bremmstrahlung" or braking radiation distribution with the peak energy about 1/3 the maximum stated energy in keV or MeV (Fig. 1).

Now neutrons are similarly classified with respect to their energy level ranging from "ultra cold," through "cold" (10^{-3} to 10^{-4} eV), "thermal" (0.025 eV), "epithermal" (0.5 eV–1.0 MeV), and "fast" (1–10 MeV). The neutron distribution from a nuclear reactor is essentially Maxwellian and thus only a small proportion of the total flux are cold neutrons. It is possible to cool the source and thus move the distribution curve in order to obtain a larger cold neutron flux (Fig. 2).

In any image, for best analysis a good contrast is desirable between required and extraneous data, or signal to noise. In imaging oil within steel casings it was found that if a cold neutron energy level of 0.004 eV was chosen, e.g., the Bragg Edge for steel, then the coherent scattering cross section falls to zero. Thus the total cross section for steel falls (Fig. 3), while at that energy, neutron capture by hydrogen has risen approximately four times over the thermal neutron situation.

The resulting contrast, due to the differences in attenuation, allowed us to see clear images of oil through the steel in most areas within running engines, and measurement and analysis were facilitated.

Experimental Work to Determine the Feasibility of the Technique. In order to investigate the potential of the technique, work was carried out at the "Herald" reactor at the Atomic Weapons Research Establishment (AWRE) at Aldermaston. A residual cold neutron radiographic beam was used, which had been passed through a cold moderator to improve the cold neutron flux (Fig. 2).

The beam diameter was 20 cm and the flux level was 1×10^6 neutrons/cm^2/second (n•cm^{-2} s^{-1}). Other important factors are the beam divergence or L/D ratio, the uniformity of flux across the beam, and the gamma flux content. If the L/D is in the range of 10 to 50 then problems occur due to strong ellipsing of circular features in the image. Below 10 the images are poor. The L/D at Herald was 120.

To investigate the potential of cold neutron radiography for imaging oil-filled passages in steel casings, a strong neutron absorbing fluorescent screen of gadolinium oxysulphide was fitted to the Delcalix. A test piece comprising a range of penetrameter specimens consisting of holes drilled in steel,

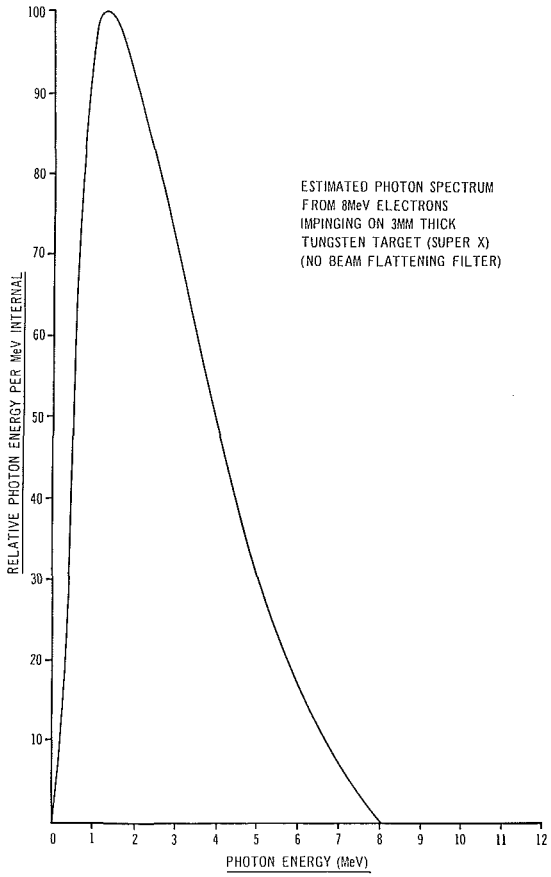

Fig. 1 Photon spectrum at 8 MeV; 3-mm-thick tungsten target

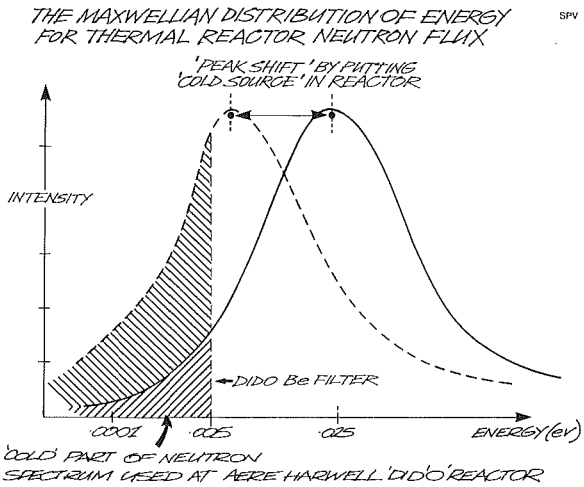

Fig. 2 The Maxwellian distribution of energy for thermal reactor neutron flux

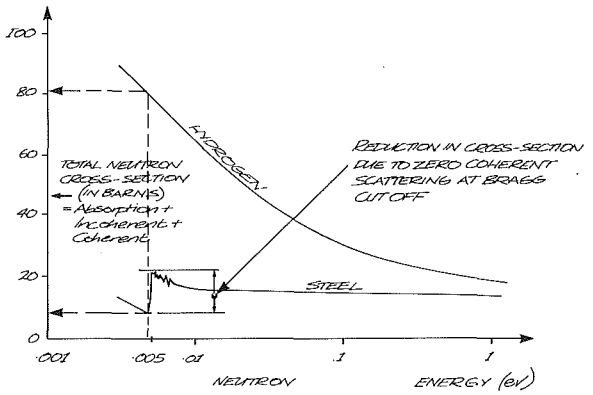

Fig. 3 Variation of cross section with neutron energy

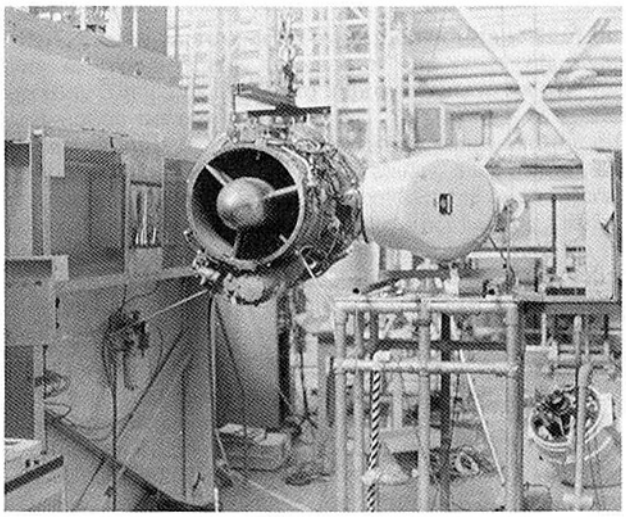

Fig. 4 Rolls-Royce Viper on Herald reactor at AWRE

filled with oil, and placed behind other thicknesses of steel was used to determine the sensitivity of the system. The holes varied from 0.08 to 1.27 cm diameter and were filled with ETO-25 gas turbine lubricating fluid. The test piece was viewed through increasing thicknesses of 25, 51, and 102 mm of steel and the penetrameter was placed at 5.0, 7.6, 10, and 30.5 cm from the face of the Delcalix to simulate gas turbine geometries. With 25 mm of steel, oil passages were visible, and the oil/air interfaces were visible. With 51 mm of steel the oil passages were still visible. Further details are given in Stewart (1980).

Finally two hypodermic syringes were filled with oil with needles of 0.508 mm and 0.610 mm. The needles were primed with oil and placed behind 2.5 cm of steel. As an example of the fine resolution of the system, the oil in the needles could be clearly distinguished on videotape images obtained from the Delcalix neutron image intensifier. Finally a Rolls-Royce "Viper" engine was placed in the neutron beam to determine visibility under static conditions (Fig. 4). The front, center, and rear bearings were examined again using the Delcalix. An oil supply line and oil priming rig were attached and priming of the center bearing oil supply carried out. Oil was clearly visible in the feed galleries within the engine as it was pumped into the bearing and was visible leaving the bearing; it then flowed back to the sump. To investigate the visibility in the gear box, oil was pumped in and was also visible. Individual oil droplets could be seen inside the gearbox. It was considered that the technique was feasible and best used for engine priming sequences. The Delcalix was used for imaging down to

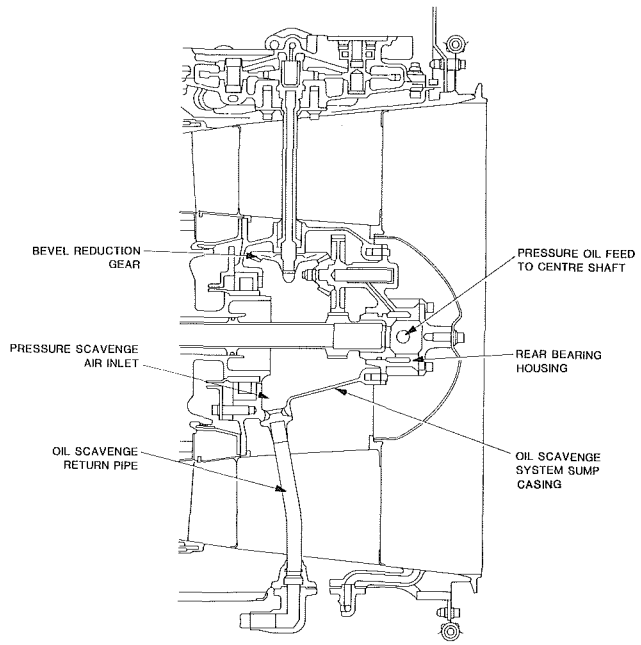

Fig. 5 Rolls-Royce Gem engine oil system: pressure scavenge

10^{-6} to 10^{-7} foot lamberts at the rear face of the scintillator with a cold neutron flux of 1×10^6 n•cm^{-2}•s^{-1}.

First Engine Test With "Real Time" NR. At this time, in the latter half of 1975, attention was being given to the oil system performance of the Gem helicopter engine. An excessive oil leakage had been encountered and the possibility of obtaining images of the oil system dynamics in the oil scavenge system sump casing (OSSSC) and oil scavenge return pipes was investigated to try to understand the cause of the problem. Unfortunately it was not considered safe to run a Rolls-Royce Gem gas turbine alongside the 5 MW Herald reactor due to the enclosed nature of the facility. The possibility of taking the neutrons out of the reactor hall by means of a flight tube was considered, but the flux thus obtained would then have been inadequate for real time imaging to be carried out.

A suitable cold neutron source existed at the "DIDO" nuclear reactor at the Atomic Energy Research Establishment (AERE) Harwell. This had a higher rating than the Herald at 25 MW thermal power compared with 5 MW. Another attractive feature was that a cold neutron beam is led out from the reactor shell and had been used for "time-of-flight" experiments. At 25 m from the shell, a small elevated experimental area was situated with a beam port of 30.5 cm (6H beam) and a cold neutron flux of 1.2×10^5 cold n•cm^{-2}•s^{-1}. This has now been improved to 3.3×10^5 n•cm^{-2} s^{-1} at the center falling to 2.5×10^5 at 15 cm from the center. The beam had a better collimation ratio ($L/D = 286$) than at Herald producing sharper, less ellipsed images. The gamma contamination at the beam center is 60 mrem per hour, which is low. This type of radiation can create a parasitic image.

The rear scavenge oil system area on the Gem engine is shown in Fig. 5. The oil supply is through the hollow center shaft and lubricates the rear bearing. Jets of oil are directed at a spur gear, which drives a bevel gear. Oil also leaves the shaft toward the center bearing. Scavenge pressure air enters the OSSSC and the design objective was that this air should pressurize the surface of the oil and return the oil to the tank via the scavenge oil return pipe and an elbow fitting.

The Gem engine was installed in the DIDO 6H experimental area (Fig. 6) and radiography and fluoroscopy (neutron video) were carried out. This was the first time that a running gas tur-

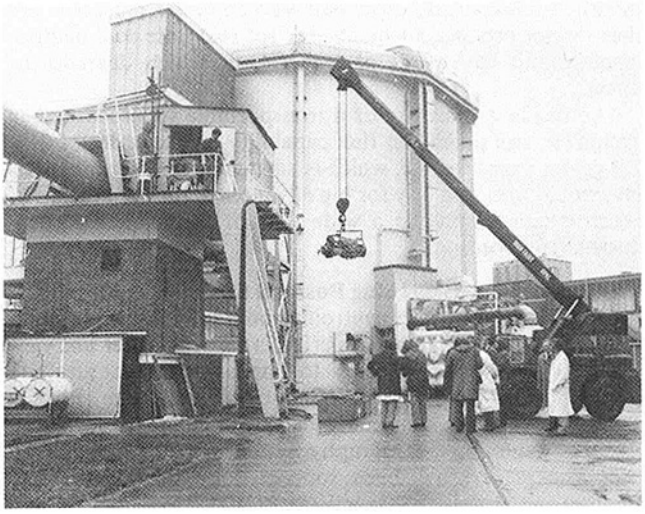

Fig. 6 Rolls-Royce Gem engine at DIDO reactor at AERE Harwell

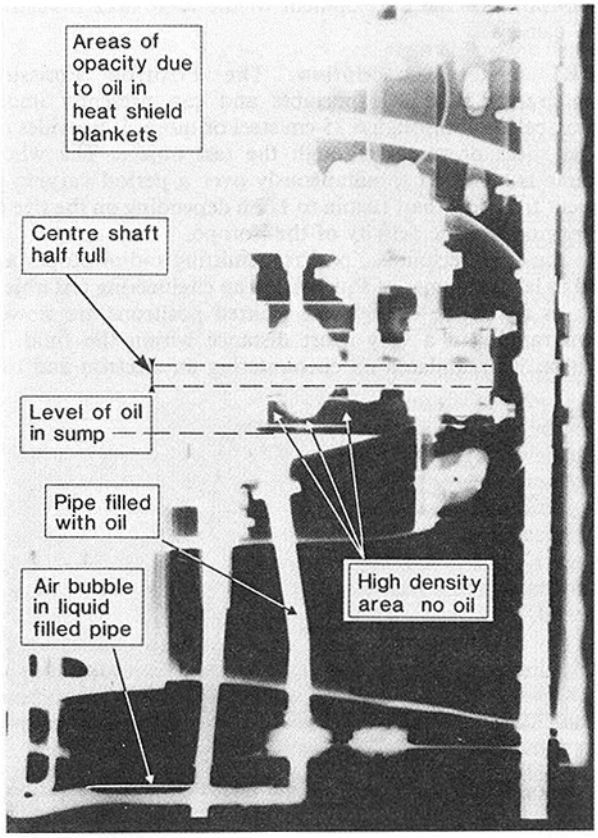

Fig. 7 Rolls-Royce Gem engine "static" neutron radiograph

bine engine had been examined using a neutron beam from a nuclear reactor for real time radiography of the performance of an oil system (1976). It was also the first large-scale engineering experiment carried out at the 6H cold neutron facility.

Analysis of Results. A radiograph was made with the engine static to determine the visibility and distribution of the oil in the rear scavenge area (Fig. 7), the area below the center shaft containing no oil. The center shaft can be seen to be half-filled with oil. (In these figures white regions represent the presence of oil whereas black regions contain no oil.) The level of oil in the sump is clearly measurable, thus giving a static volume.

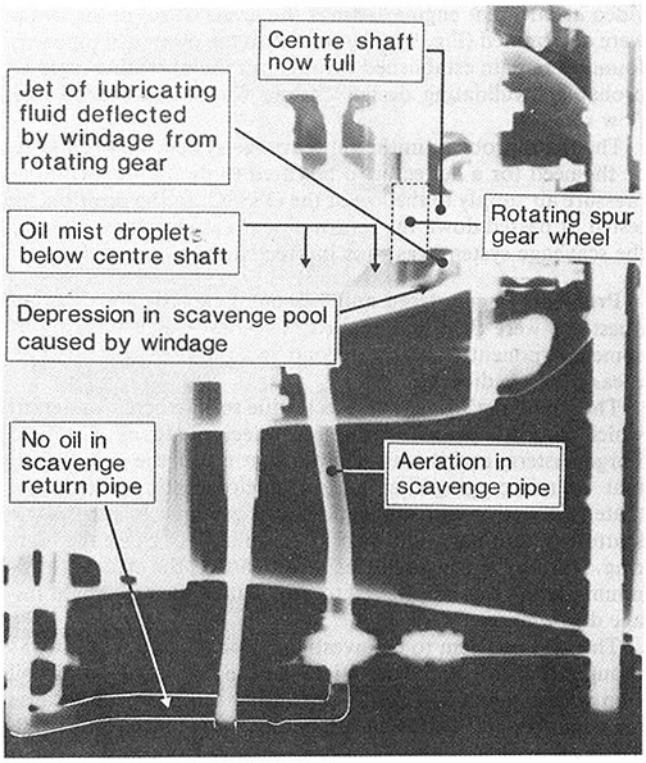

Fig. 8 Rolls-Royce Gem engine ground idle neutron radiograph

The oil in the return pipe down to the elbow is "neat," or nonaerated. In the horizontal part of the return pipe an air bubble can be seen. A large area of the radiograph toward the center and left of the engine is occluded and shows white due to an opacity in the engine.

A number of other radiographs were made with the engine running at "ground" and "flight" idle conditions.

Figure 8 shows the engine at ground idle condition. A number of features can clearly be seen. The central tube is now opaque indicating either that the tube is filled with oil or that an annulus of oil forms in the tube. One of the limitations with the neutron technique is that it is not possible to see through thick oil films on the walls of components. An oil mist with droplets estimated at 200 μm can be seen falling from the center shaft into the sump.

A jet of oil from the rear bearing area is intended to splash lubricate the spur gear, but it can be seen that windage from the rotating gear wheel has deflected the jet away leaving the gear teeth unlubricated. Corroborative evidence is obvious from the depression on the surface of the scavenge pool again caused by windage from the gear wheel.

If we now turn attention to the scavenge return pipe, it will be seen that it is not now filled with oil but has a relatively high level of aeration. A microdensitometer trace can be used to quantify the distribution and extent of aeration. It is also clear that the union produces a throttling effect on the return pipe and appears to trap oil which, on video, oscillates up and down the pipe with pressure air filling the lower horizontal pipe alone.

Finally at 73 percent flight idle the analysis of the radiograph shows the OSSSC to be totally opaque indicating that it was either filled with oil or that the oil level had risen until it encountered the rotating spur gear which had then thrown it onto the walls. The overfilling of the OSSSC led in part to the excessive oil loss from the system.

A neutron video sequence was obtained using the Delcalix and timings were obtained for center shaft filling, fall of droplets, and lubrication jet starting. From an analysis of the

video at different engine settings the levels of oil in the sump were determined (Fig. 9). The bubble in the oil return pipe was found to remain established throughout the operating regime, probably invalidating design criteria for pressure drop and flow rate.

The main problem in the oil scavenge system was found to be the need for a deflector to be fitted to direct the incoming pressure air supply to the top of the OSSSC. In the position, as tested, it passed down the return pipe preferentially to the oil; the scavenge system was thus ineffective.

Problems Encountered and Lessons Learned. Two further questions were then investigated: The first was a blurring of some components, and the second was the opacity of certain areas of the radiograph.

The "blurring" was found to be due to "Jethete" material, which is a 12 percent chromium steel made by Sheffield Forgemasters, and it was believed that either the cobalt content or microsegregation and/or agglomeration within the material together with magnetic effects gave rise to small angle scattering. Ordinary mild steel material did not cause the blurring. During the course of this investigation, the effect of cadmium plating was considered to be a source of some slight image degradation.

The next problem to be investigated was the opacity. It was thought that due to the sensitivity of the technique, a thin oil film within the engine could be causing the problem because the engine on test had been run before the test at 6H Harwell. To examine this, a new Gem engine fresh from build, with a minimum of inhibiting oil, was imaged and showed the same lack of image quality as certain of the previous modules. The jet pipe of the Gem was surrounded by a proprietary silica refractory blanket or heat shield. These "Refrasil" heat shields were then removed and the white opaque areas were clear. It was found that pinholes in the Refrasil blanket steel covers had allowed oil to seep inside and saturate the material, which then absorbed the cold neutrons.

During the course of our work at various times two neutron image intensifiers have been used coupled to video systems: originally the Oude Delft Delcalix, and later the Thomson CSF THX 1432. The performances of the Delcalix and the Thomson intensifiers are evaluated in Appendix 1 and Tables 1 and 2 and Stewart (1986b).

Summary and Conclusions. The cold neutron technique can thus be shown as a valuable means of imaging oil system performance in a dynamic engine. The technique is qualitative and quantitative. Steel thicknesses of 6.35 cm can be penetrated and the resolution is such that oil droplets down to 200 μm may be imaged in real time.

It is possible to break down the images into a number of grey scales – 8, 16, 32, or 64 – and assign pseudo or false colors using video imaging techniques. As the eye discerns color changes more efficiently than density changes this shows oil distribution in an improved manner. Another valuable technique is to store a static neutron image of the object in a digital image processor frame store and to subtract it continually from the live "running" image, leaving only the oil itself as the image.

Limitations of the system are some blurring or small angle scattering with Jethete, the obscuration of the image if quantities of oil interpose between source and imaging system, for instance, if thrown on the walls by rotating gears. However, thin films do not appear to reduce image quality.

One of the greatest problems is the present limitation of the technique for use at a nuclear reactor. Usually oil management research or gearbox rigs need large electric motors to drive them; these cannot easily be moved to a reactor. A survey was made of other neutron sources including boosted californium 252, sealed and continually pumped ion beam sources, and modified linear accelerators and Van de Graaf machines but they do not produce adequate flux for real time cold neutron imaging and have large gamma fluxes, which degrade the image.

The future availability of a transportable superconducting cyclotron with a neutron flux capability on the order of 2×10^6 cold n • cm^{-2} • s^{-1}, which is adequate for real time imaging, would open the way for big advances in the application of neutron radiography to a wide area of mechanical and industrial engineering.

Oil System Analysis Using Positron Emission Tomography. Another limitation with neutron radiography is the presentation of only a single image, in effect a vertical center line view through the engine. In order to improve data capture and display, Rolls-Royce has collaborated with the Physics Department of the University of Birmingham to develop a Positron Emission Tomography System (PET) for industrial use. The project has been supported by the Science and Engineering Research Council (SERC) as a cooperative and cofunded project with Rolls-Royce and Castrol Ltd. The SERC Rutherford-Appleton Laboratory (RAL) has been responsible for the development of the large area industrial PET camera.

PET System Description. The Positron Emission Tomography system is portable and can presently image radiolabeled oil through 6.35 cm steel or more. It provides up to 64 slices or tomes through the test object. The whole volume is recorded simultaneously over a period varying at present from less than 10 min to 1/2 h depending on the size of the engine and the activity of the isotope.

In the PET technique, positron-emitting radioisotopes are used to label volumes of fluid within an engineering test object such as an engine or rig. The emitted positrons are slowed down rapidly in a very short distance within the fluid. A positron is annihilated on encountering an electron and two

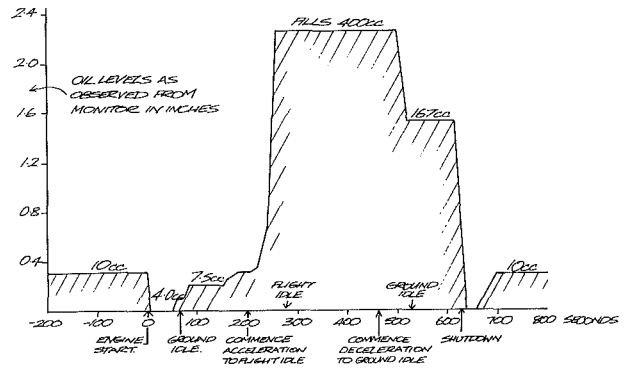

Fig. 9 Oil levels versus time for the BS360 Gem engine scavenge system sump at Harwell

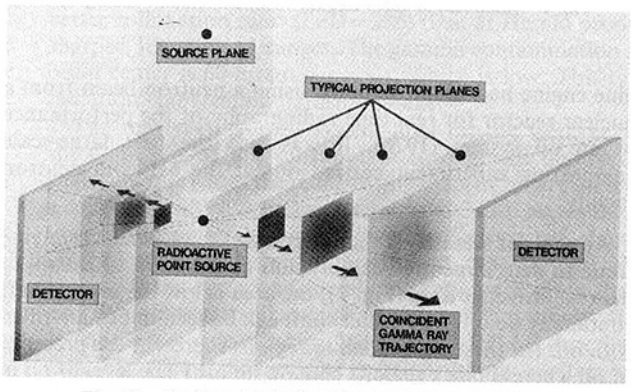

Fig. 10 Positron Emission Tomography principles

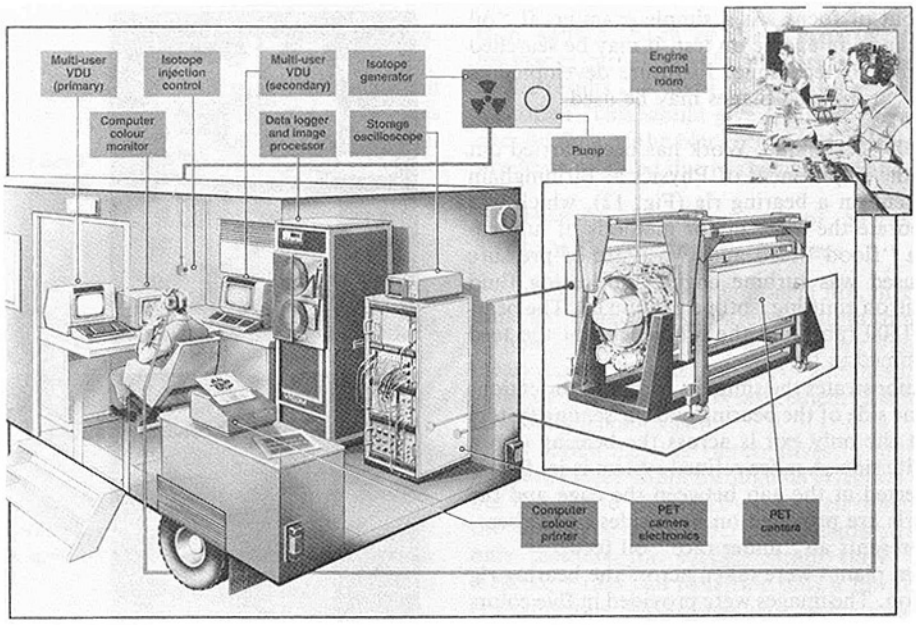

Fig. 11 Positron Emission Tomography system

511 keV gamma photons are emitted in diametrally opposite directions, colinearly (Fig. 10). If both photons are detected simultaneously in the two spatially sensitive multiwire proportional counters, the data logging system registers the X, Y, Z coordinates of both events. In this way, a data file is accumulated that can later be analyzed to generate a sequence of images representing the perceived positron activity in different planes across the engine. These images can be interpreted in terms of the volume distribution of the fluid labeled with the isotope.

The industrial application of the technique has been made possible by the development of large area multiwire proportional counters (MWPCs) by RAL. The dimensions are 96 × 64.4 × 47.9 cm with an active area of 60 × 30 cm. The weight of each counter is 350 kg. The separation of the chambers to image the gas turbine engine lubrication system is typically 50–100 cm. The spatial resolution is 2.3 mm. Two detectors are set up, one on either side of the engine under study (Fig. 11) to register the emitted radiation. An electronics system for operating and controlling the detectors has also been developed at the RAL.

The radio-isotopes injected into the oil system are gallium 68, produced by a transportable generator, or fluorine 18, which is obtained from a cyclotron operating center. In the future, if a mobile cyclotron becomes available, higher activity short-lived isotopes will be available for transient studies of the fluid system. Short-lived radioactive isotopes are chosen (^{68}Ga = 68 min and ^{18}F = 110 min) in order that radiation activity be reduced to background levels as quickly as possible after a test so that personnel have minimum exposure to radiation and levels do not build up excessively in the bulk tank and blind the detectors.

Data logging times depend on the particular application and on the quantity of radioisotope activity required for the measurement. An example described later is a test object, a bearing rig, in which 10 millicuries (mCi) of gallium 68 was used to dope 250 ml of oil in the test circuit. With this relatively low level of activity used in the early tests, about 60 min were necessary to build up the required detailed images.

Data are normally processed off line, although a VICOM image processor is being prepared to give an on-line, near real time, system. The resulting PET images contain information on the distribution of positron source activity in liquid volumes within finite slices of the object and are arrays of

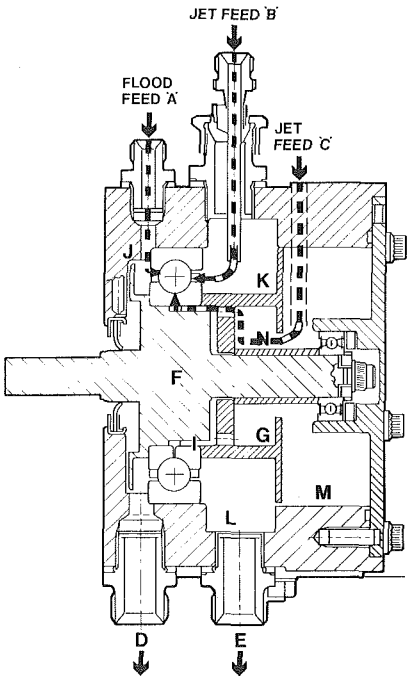

Fig. 12 Bearing rig showing oil supply paths

discrete picture elements or pixels. Typically an array of 256 × 128 pixels is used, each pixel corresponding to a 2.3 mm × 2.3 mm picture element of the image. Although the spatial resolution of the detectors is therefore 2.3 mm, quantitative analysis of the images can resolve labeled fluid volumes of dimensions less than 1 mm. Processing techniques may also be used on the images obtained to aid in their analysis and interpretation.

To help in the evaluation of the images, computer software has been written to model the three-dimensional structure of the engine and to superimpose accurately on any chosen image plane a sectional drawing of the object at that same position. The reconstructed isotope image may then be overlaid with the sectional view to identify precisely the location of the fluid in any of the 64 sectional planes. The operator may run through these sectional planes, at will, and the isotope-labeled fluid

will move into or out of focus. As a simple example, if "oil hiding" should occur in an engine on test, it may be searched for and found using this technique. In future developments horizontal, vertical, or inclined planes may be used.

Applications of the Technique. Work has been carried out by Rolls-Royce at the Department of Physics at Birmingham using the PET system on a bearing rig (Fig. 12), which was designed to incorporate the three major methods of lubrication. These were a "flood" feed and two types of pressure feed. The liquid used was turbine engine lubricating fluid doped with the positron emitting isotope gallium 68. The bearing was driven at 1500 rpm, and the efficiencies of the feed methods were examined in turn.

Flood feed A demonstrates the simplest form of lubrication. Oil is supplied to one side of the bearing and the sealing system is so arranged that the only exit is across the bearing into a drain on the opposite side. A more refined system is jet feed B in which oil is directed at the gap between the cage and the races; scavenge ports are provided on both sides of the bearing. Jet feed C represents an "under race" oil feed.

Sixteen tomogram planes were taken across the bearing rig with 5 mm separation. The images were provided in five colors to show the intensity variation within a particular image to aid interpretation. A graphic section of the bearing rig was laid over the radioisotope image at each plane.

Flood feed A (Fig. 13) could be seen to provide saturation lubrication, with large quantities of oil moving around the bearing race during operation. Jet feed B was shown to provide adequate lubrication of the bearing with most of the oil bearing forced into and across it. Jet feed C was examined and the results were totally unexpected. Close inspection of the isotope imagery revealed an oil injection vector opposite to that intended. It was concluded that the rig was misassembled. On strip it was found that the feed pipe had rotated approximately 135 deg from design position. Thus the capability of the technique in imaging oil jets and flow behavior was clearly proven and its value in fault diagnosis was shown in the first experiment.

Applications on Full Engines: Static and Dynamic. The next step in the program was to apply the PET system to a real engine. The Gem was selected due to its small size and because it exhibited an interesting oil system behavior. A module was made available by Rolls-Royce at Leavesden and doped oil was fed and imaged within the module to calibrate the system and determine appropriate activity levels, absorptions, and scattering. A full engine was then supplied and placed between the MWPCs in the laboratory (Fig. 14) and point and line sources were used for calibration of the attenuation in regions of interest, such as the center shaft and bearing regions. Quantitative information could then be derived of actual oil flow distributions at points in the engine lubrication system.

Tests are currently planned for 1987 on a running "Viper" engine to examine features of lubrication system performance and rig tests are also planned to validate new lubrication approaches. The MWPCs have been provided with acoustic enclosures to protect them from the noise fields of gas turbine engines.

Summary and Conclusions. The neutron radiography technique is very useful in qualitatively visualizing and making quantitative measurements in, for instance, the priming of engines where the flow of oil can be analyzed around a dry engine. Oil priming velocities can be determined.

The neutron radiography technique can also be useful in the measurement of oil levels in static and running engines and the locations of pockets of oil around systems. It is essentially a two-dimensional real time technique with high resolution but is not able to view one oil volume behind another.

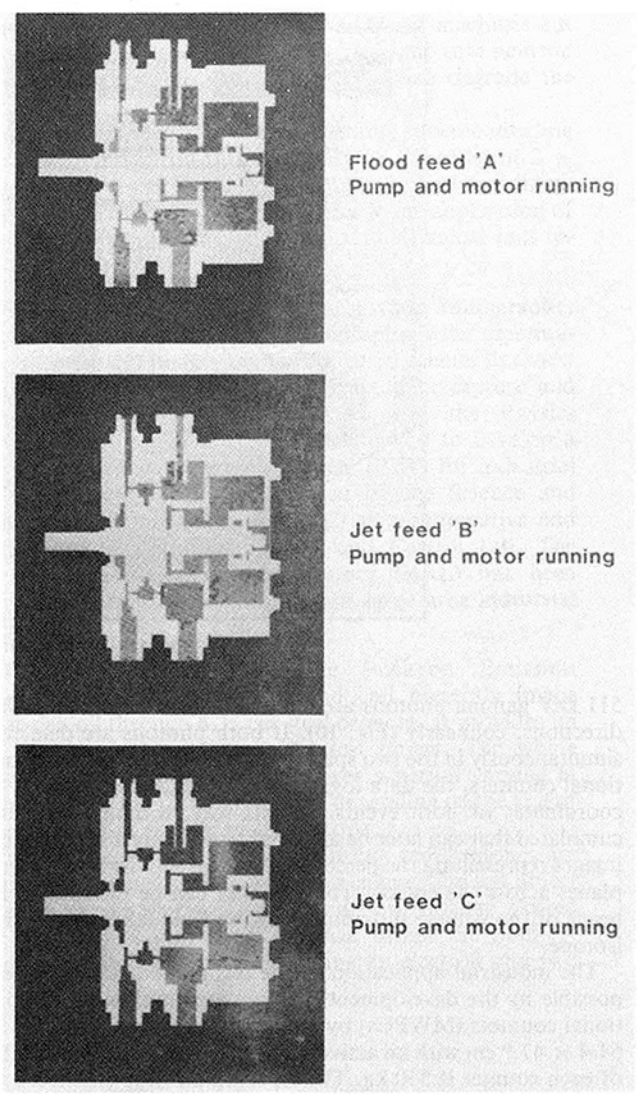

Fig. 13 Radioisotope images with computer-generated overlay

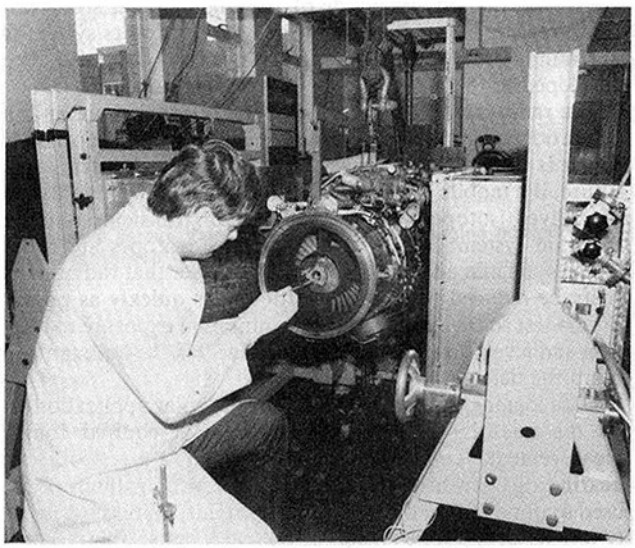

Fig. 14 Rolls-Royce Gem engine on PET system at Birmingham

Positron Emission Tomography, on the other hand, is a three-dimensional technique with a graphic overlay. The system is presently still under development. It can take up to

32 vertical slices simultaneously through an engine. At present it is not a real time system.

The resolution is presently not as good as NR with 2.3 mm full width half maximum resolution (fwhm) in the XY axes and 16 mm (fwhm) resolution in Z axis for 500 mm principal plane separation for simple geometries. The resolution within engine carcases has not yet been determined and will vary, but should be improved with system development.

Flow velocity measurements have not yet been attempted but form part of the future development program.

The neutron and PET techniques are complementary in different applications to permit noninvasive visualization and measurement of oil and fuel system dynamic performance.

Noninvasive Measurement of Metal Temperatures Using Epithermal Neutron Resonance Techniques

This radiation technique relies upon a measurement of the absorption of epithermal neutrons in the region of the narrow resonance lines for specific materials. This measurement is sensitive to target temperature due to Doppler broadening brought about by the thermal motion of target atoms. With the use of specially developed positional sensitive detectors for the epithermal neutrons, the temperature field on a suitable material can be determined over an appreciable number of pixels. Positional accuracy of $\pm$ 1 mm in measurement over an area of 15 cm^2 is possible.

Initial experiments have been carried out by Professor Fowler of Bristol University and test exposures have been made at Los Alamos using specimens of tantalum and a proprietary Rolls-Royce high-temperature alloy containing tungsten, tantalum, and hafnium (MARM002). Measurements were made using a pulsed proton beam from an accelerator striking a target. The epithermal neutrons so produced were passed from a moderator, through a collimator and cadmium filter, and then through an evacuated drift tube to an aperture and evacuated instrumented oven held at a range of temperatures from 300 K to 1000 K. The specimen was viewed through 2 cm of stainless steel simulating an engine casing. Accuracies of temperature measurement of $\pm$ 5 K in 1000 K were achieved. Due to the low flux of the Los Alamos source each measurement point took 8 h.

Additional experiments to explore other aspects of the feasibility of the technique will be carried out at the ISIS spallation neutron source at the Rutherford-Appleton Laboratories of SERC at Chilton in 1987 by Professor Fowler.

The ISIS spallation neutron source is a high-intensity pulsed neutron facility. It consists of an 800 MeV high-intensity proton synchrotron; a target station producing bursts of fast neutrons by spallation and fission in a uranium target, an array of moderators producing a variety of slow neutron energy spectra and pulse shapes, and a data collection and reduction system. It has an output of about 4×10^{16} $n \cdot s^{-1}$ and an approximate yield of 10^{14} pulsed epithermal $n \cdot s^{-1}$. Plans are in hand to enhance this performance. The ISIS is a very large installation, which is designed to fulfill a variety of experimental requirements. It is ideal for developing the epithermal neutron temperature measurement instrumentation system. However it is possible to design a high-brightness, compact, transportable source tailored more precisely to the requirements of the epithermal neutron temperature measurement system. Such a source could be a superconducting magnet cyclotron.

Utilizing the pulsed characteristics of the ISIS it may be possible, using stroboscopic techniques, simultaneously to measure surface metal temperatures on the external concave and convex surfaces and the internal air cooling passages. This could be achieved for static and rotating blades.

In order to perform this experiment, elements such as rhenium, rhodium, or platinum could be selectively plated on each surface. Each of these materials has a characteristic resonance curve to epithermal neutrons so that in the analysis of the results the shape of each curve, and its peak could be identified. This would give a pixel-by-pixel temperature map over an area of the blade. Some slight temperature correction would be required due to the incorporation of these elements.

Noninvasive Measurement of Stress Using Thermal Neutron Diffraction Techniques

In order to improve component life, there is a need to determine more precisely the stresses within rotating compressor or turbine disks. There are, however, problems in the absolute measurement of internal stress within such components. In order to carry out such measurements the technique should be noncontact/noninvasive.

In reviewing the alternatives, "ultrasonic" methods measure lattice strain through its effect on the sound velocity, but this is also affected by preferred orientation or texture in the sample. X-ray diffraction measures strain directly but can only measure the surface strain since, in the diffraction method, x-rays can penetrate only a few tens of microns into typical metals. Electromagnetic techniques are under development but many measurements are functions of strain; however, none are functions of strain alone. The neutron diffraction method measures strain directly through changes in the lattice spacing and is essentially unaffected by other properties such as texture (Allen, 1981). Work has been carried out by AERE Harwell to measure residual stresses in metals and it would appear possible to arrange a neutron source such as linear accelerator or cyclotron with a suitable target and moderator to produce a pulsed thermal neutron beam with neutron energies between 0.8 and 0.004 eV, following moderation, for diffraction stress measurement.

A typical application could be the detailed mapping of stress across the diameter of a turbine or compressor disk in a spinning pit. The neutron source could be traversed to scan along the diameter and raised or lowered to examine the web thickness. The disk could be examined at rest to determine the residual stresses and a number of predetermined rotational speeds, to determine the varying stress levels by subtraction techniques.

A linear accelerator or cyclotron with suitable neutron target and moderator could be used to provide thermal neutron pulses with a repetitive structure and which, if required, could be filtered for wavelength. The pulse duration could be variable.

A reflective fiducial market could be provided on the disk, illuminated by a laser and registered as a spatial reference on the disk by a "once-per-revolution" detector system. This signal could be used to pulse the neutron source and interrogate the same "probe volume" in the disk on each revolution. By integration of successive pulses with the disk running at a constant rpm, the signal would be integrated to provide a robust measurement as a stroboscopic technique.

The delays between laser detection and neutron pulse emission could be varied to explore other parts of the disk and map a volume. The pulse duration coupled to the rotational speed determines the probe volume.

A laser pick-off could be used if necessary to detect flexural movement of the disk, which could be a source of error. The position of the probe volume could follow the movement to ensure uniformity of measurement.

By combining this technique with surface laser interferometry a surface stress map could be obtained with thermal neutron diffraction subsurface stress measurement at critical positions.

Conclusions

This survey of the present and projected applications of

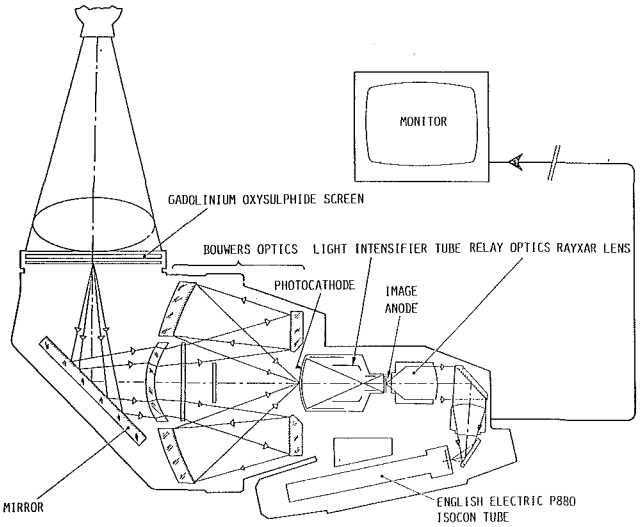

Fig. 15 Delcalix neutron image intensifier

penetrating radiation techniques to aero gas turbine research and development has shown how noninvasive methods are a powerful way of creating a "transparent engine." The objective of this approach is to abolish the need to cut holes and modify engines and to take any engine with a problem and subject it immediately to a noninvasive examination. We may select the most appropriate radiation to solve the problem, probe for and acquire the desired data through imaging or signal acquisition, and with digital image processing or knowledge-based image manipulation and pattern recognition provide the required information.

Acknowledgments

The sections of the work concerned with high energy x-radiography and neutron radiography were carried out with the support of the Procurement Executive, Ministry of Defence to whom due acknowledgment is made. The sections concerned with positron emitting isotopes and epithermal neutron temperature measurement have been carried out in conjunction with the Science and Engineering Research Council. I wish to thank Rolls-Royce for permission to present this paper.

References

Allen, A., 1981, "Measurement of Internal Stress Within Bulk Materials Using Neutron Diffraction," *NDT International*, pp. 249–254.

Stewart, P. A. E., 1980, "Cold Neutron Imaging for Gas Turbine Inspection," *Real Time Radiologic Imaging*, ASTM Special Technical Publication, 716, pp. 180–198.

Stewart, P.A.E., 1986a, "The Application of Radiation Physics and Photogrammetric Techniques for the Diagnosis and Solution of Mechanical Engineering Problems and Performance Improvements in the Development of Aero Gas Turbines at Rolls-Royce," *Advanced Instrumentation for Aero Engine Components*, AGARD Conference Proceedings No. 339, pp. 28-1 to 28-19.

Stewart, P.A.E., 1986b, "Imaging Techniques for Gas Turbine Development," *International Seminar on Laser and Opto-Electronic Technology in Industry*, SPIE Conference Proceedings, Xiamen, China, Paper No. 669-22.

APPENDIX

Real Time Neutron Video Systems

The Oude Delft Delcalix (Fig. 15) is an indirect-type intensifier with x-ray and neutron fluorescent, interchangeable input screens of 32 cm diameter. The low light level image is directed via an inclined plane mirror onto a Bouwers E4 lens system. This is comprised of concentric mirrors and has an aperture of f0.68. It is configured to transfer the image from the mirror to the front face of a single stage light intensifier with the minimum of distortion.

Table 1 Oude Delft Delcalix specification

X-ray Phosphor size	32cm	Gain	2.8×10^5
Line Pairs/cm	50.1	Sensitivity	2.5-3.0%
Spectral Sensitivity (max) 550 nm		Minimum detectable dose	0.1 r/sec
Isocon size	7.90cm		
Dynamic Range	2000:1	Max safe dose rate	500 mr/sec
Scan rate	25 fps	Magnification	1:1.5 10%
Temporal resolution	1 TV frame	Overall system accuracy	<2%
Bandwidth	7.5 mHz -3db		
TV Lines	625	Length	118.5cm
		Depth	75.4 cm
Horizontal resolution 1.2 lp/mm		Height	54.0 cm
Vertical resolution	0.91 lp/mm	Weight	95.0 kg

Table 2 Characteristics of Thomson CSF cold neutron tube THX 1432-GK-V

Input field dia normal		22 cm
Mag 1		16 cm
Mag 2		11 cm
'Cold'/Thermal neutron Transmission (Entrance window)		90%
Output screen dia		20 mm
Output phosphor		P20
QDE		95%
Limiting spatial resolution		
Normal		40 LP cm^{-1}
Mag 1		46 LP cm^{-1}
Mag 2		53 LP cm^{-1}
Conversion factor (Candela neutron sec^{-1}) Output screen luminance/ Input neutron flux	Normal	$3.2.10^{10}$
	Mag 1	$1.7.10^{-10}$
	Mag 2	$0.8.10^{-10}$
Output photon flux/ Input neutron flux	Normal	$5.2.10^6$
Length		338 mm
Diameter		285 mm
Weight		20 kg

The light intensifier tube, a tetrode, has a photocathode of 80 mm diameter and an image anode of 20 mm diameter. The gain in the green (550 nm) is approximately 100 and the brightness gain is 1400 times for green light. The tube can be switched to give 2 times or 40 percent magnification if so desired.

The image on the tube anode is then relayed via the Rayxar objective $f = 75$ mm f0.88 and thence via the two plane mirrors and the Deltamar objective $f = 104$ mm f1.4 onto the photocathode of the image isocon where it is converted into an electrical signal.

The dynamic range of the isocon is 2000:1 and is thus better than any other comparable tube. The resolution of the overall system is the multiplication of component modulation transfer functions, i.e., 9.1 lp/cm.

The Thomson CSF THX 1432 GK-V is a direct-type neutron intensifier; it has a 22 cm input field with a special glass entrance window 90 percent transparent to thermal and cold neutrons. The scintillator screen is made from gadolinium material having a large capture cross section for neutrons. The output screen is 20 mm diameter and is a P20 phosphor. The Quantum Detection Efficiency (QDE) is 95 percent and the limiting spatial resolution is normally 40 lp/cm. At magnification 1 it is 46 lp/cm and at magnification 2 it is 53 lp/cm. The normal input field of the THX 1432 is 22 cm. In Mag 1 the input field is 16 cm and in Mag 2 mode it is 11 cm.

The conversion factor is the output screen luminance (in candela$\cdot m^{-2}$) for a given input neutron flux ($n \cdot m^{-2} \cdot s^{-1}$). The conversion factor thus has units of candelas $\cdot$ $n \cdot s^{-1}$.

For normal mode the conversion factor is 3.2×10^{-10}, for Mag 1 it is 1.7×10^{-10} and for Mag 2 it is 0.8×10^{-10}. In terms of output photon flux/input neutron flux in normal mode this is 5.2×10^6.

The length of the unit is 33.8 cm, the diameter is 28.5 cm and the weight is 20 kg.

Further details of both the Delcalix and Thomson Systems are given by Stewart (1986b).

Explosive Decompression Resistance of Centrifugal Compressor O-Ring Seals: a Comparative Test Summary and Procedure

W. N. Shade
Chief Design Engineer,
Centrifugal Compressors.
Mem. ASME

D. W. Legg
Supervisor,
Research and Development.
Mem. ASME

CB Rotating Division,
Cooper Industries,
Mount Vernon, OH 43050

Explosive decompression is a phenomenon that can destroy O-ring sealing elements in high-pressure (>3.4 MPa) natural gas compressors during rapid venting to atmospheric pressure. A test rig and procedure have been developed to identify important parameters influencing O-ring seal explosive decompression failure, consistent with utilization of these seals in high-pressure centrifugal compressors. The test rig and procedure are described and comparative test results presented.

Introduction

O-rings are torus-shaped seals, commonly made from elastomeric compounds. Properly selected and installed, O-rings are reliable, yet simple, static sealing elements requiring low preload forces compared to other types of seal. O-rings are commonly used in centrifugal compressors for internal as well as external process gas, seal oil, and lubricating oil sealing. Figure 1 highlights typical O-ring seal locations in a centrifugal compressor: casing-cover joint, aerodynamic bundle perimeter, shaft seal cartridges, and bearing housings. Several of these sealing locations expose the O-rings to process gases and temperature extremes. In a number of applications, O-ring failure has caused loss of efficiency or loss of process gas to the atmosphere after only a modest period of service. Such occurrences have led to costly downtime for seal replacement and, in a few cases, minor fires. Examination of failed O-rings has revealed extensive damage such as cracks, blisters, missing segments, or foaming, all indicative of explosive decompression failure.

Permeability rates of elastomeric compounds allow high-pressure gases to diffuse and be absorbed into elastomeric materials, filling natural voids (Parker, 1982; Precision, 1982). When high pressures are released suddenly, the gas expands inside the compound, expanding the elastomer like a sponge, forming blisters or cracks on the outside surface, or even blowing off small chunks of the material (National, 1982). The severity of damage varies with pressure, gas composition, compound, size of cross section, and other factors. Damage is worse at high pressures and is rarely observed below 1.7–2.8 MPa (250–400 psi). Elevated temperature and rapid pressure drop cause increased damage, and CO_2 tends to cause more severe damage than N_2. Harder compounds and small O-ring cross sections tend to have better resistance to explosive decompression failure than softer, large section O-rings (Parker, 1973, 1982; Precision, 1982).

The phenomenon of explosive decompression is described by Hertz (1984) as one where elastomers in contact with gas at sufficient pressure become supersaturated. In this state, gas and liquid phases coexist in the elastomer, and an equilibrium shift of pressure or temperature causes bubble formation at a flaw site in the elastomer as described by Gent and Tompkins (1969). Ender (1983) identifies various degrees of elastomer damage from explosive decompression, theorizing that low solubility gases such as methane tend literally to "explode" within the seal on decompression. Gases with higher solubility might first undergo retrograde condensation, then migrate as a liquid phase through the elastomer and "boil off" the surface as a gas, causing little damage. The ability of an elastomer to perform as a pressure vessel strong enough to contain the expanding liquid depends on the shear modulus of the elastomer, which is also related to its hardness or durometer. Gent (1978) presented data suggesting that a 90 durometer (Shore A) material was resistant to explosive decompression up to about 17.2 MPa (2500 psi).

Despite selective research and testing, elastomeric compounds recommended by O-ring manufacturers have frequently been proven unsatisfactory for use in the compression of natural gas mixtures at pressures above 3.4 MPa (500 psi). Historically, testing has involved evaluation of small pieces of elastomers (not complete O-rings), simply immersed in pure gases (not mixtures), not acting as a seal (i.e., without preload), and frequently at room temperature only (Parker, 1973). For proprietary reasons, test results have usually not been published, so that machinery designers and users have had little technical information for selecting explosive decom-

Contributed by the Gas Turbine Division of THE AMERICAN SOCIETY OF MECHANICAL ENGINEERS and presented at the 32nd International Gas Turbine Conference and Exhibit, Anaheim, California, May 31–June 4, 1987. Manuscript received at ASME Headquarters February 17, 1987. Paper No. 87-GT-156.

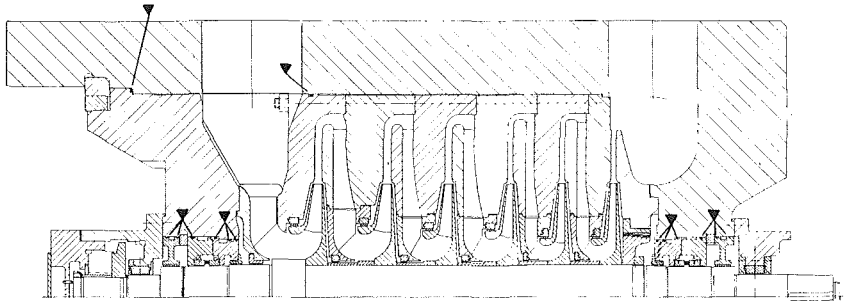

Fig. 1 Typical centrifugal compressor showing location (▾) of O-ring seals

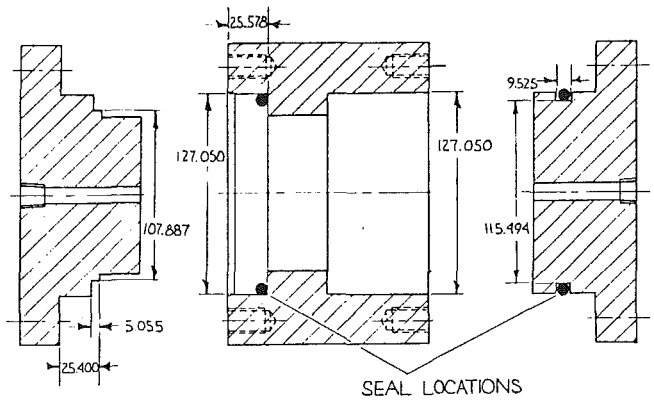

Fig. 2 O-ring pressure vessel gland geometry

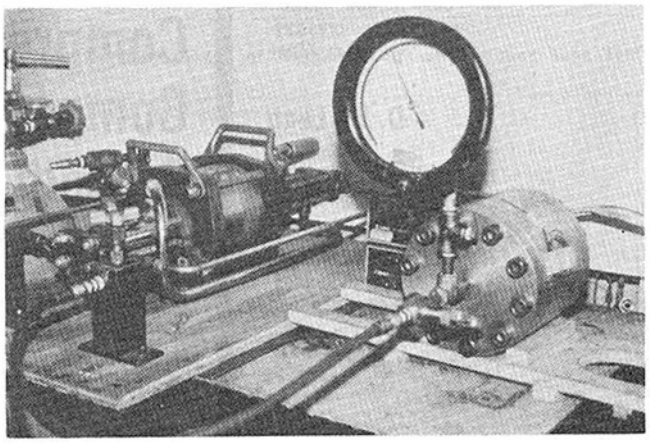

Fig. 3 O-ring pressure vessel and gas intensifier

pression resistant O-ring seals. The authors' company has established a quantitative test program to identify more clearly reliable O-ring compounds for centrifugal natural gas compressors. Primary objectives of the program are the use of commercial standard cross-section molded O-rings, installed in a properly designed gland and subjected to representative gas mixtures, pressures, and decompression or blowdown rates. The test procedure and many results are presented in this paper.

Test Apparatus and Procedure

Test Setup. This O-ring test pressure vessel is designed to accommodate two standard size 425 seals [113.67 mm (4.475 in.) i.d. × 6.985 mm (0.275 in.) cross-section diameter]. This size O-ring cross section is commonly used in compressors. The vessel is cylindrical in shape with a peripheral gland contained in one end cover and a face seal geometry machined into the opposite end cover (see Fig. 2). The design pressure for the vessel is 13.8 MPa (2000 psig) and the internal volume is 0.4 L (24.4 in.^{3}). Holes have been machined through the center of each end cover to supply and vent the test gas used to pressurize the O-ring seals. A series of interchangeable orifices is available for assembly into the gas vent line to control the rate at which the vessel is depressurized. A Haskel intensifier is used in the gas supply to provide the proper gas test pressure. The test apparatus is shown in Fig. 3. Until now two gases have been used for the testing. One is a mixture of 75 percent methane (CH_4), 15 percent carbon dioxide (CO_2), 5 percent ethane (C_2H_6), and 5 percent propane (C_3H_8). This gas is representative of natural gas mixtures frequently encountered in the gas compression industry; it should provide a fair evaluation of a seal's explosive decompression resistance. The second gas is pure nitrogen (N_2).

Volume Swell Measurements. Prior to testing, each O-ring seal is visually checked for any defects; its volume is then indirectly measured using a water displacement method. A pan balance has been modified to weigh the seal dry and submersed in a water-filled container. The seal is buoyed up in the water by a force equivalent to the quantity of water displaced. Knowing the water density at the measurement temperature, the O-ring volume can then be calculated. After this weight measurement the face and peripheral seals are assembled dry into the test vessel and the end covers are attached.

Test Procedure. The vessel is then pressurized to the proper test pressure using the Haskel intensifier. This initiates the test. After maintaining the vessel at test conditions for the desired period of time, usually 72 h, the pressure is released. This is accomplished by venting the gas through a properly sized orifice. Each decompression period is also timed. The vessel is then immediately disassembled and each seal visually inspected and abnormalities carefully documented. The seal volume measurement is repeated for the post-test seal and a volume change, or swell, calculated. This measurement is complicated by outgassing from most seals for the first several hours after the test, as evidenced by gas bubbles attached to the seal immersed in water in Fig. 4. The O-ring is observed for several hours after the test to note any visible changes, and an explosive decompression resistance rating is then selected for the test specimen. O-ring samples are subjected to only one decompression and are not reused.

Seal Segment Test. Separately, a method has been devised to evaluate short (1 in.) segments of each seal compound within the pressure vessel. Two samples of each compound are visually inspected, measured with a micrometer, and attached to a wire frame (Fig. 5). Four separate compounds can be tested at once (eight segments). The frame is mounted in the vessel, which is then pressurized as before. This method of test

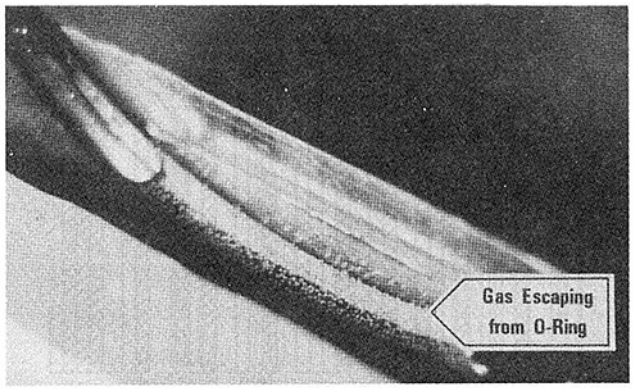

Fig. 4 Outgassing observed during post-test volume swell measurement

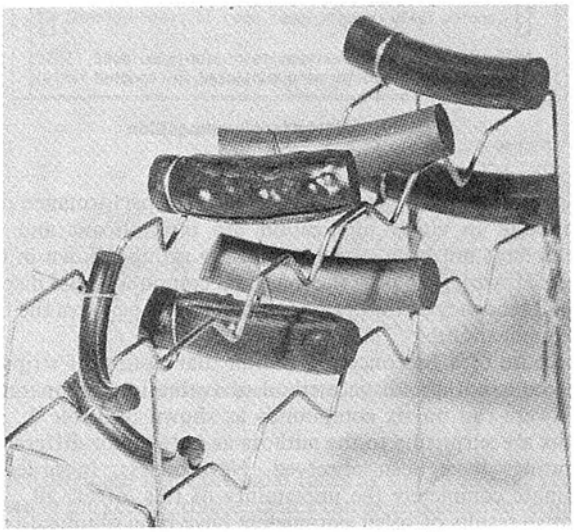

Fig. 5 O-ring segment test result

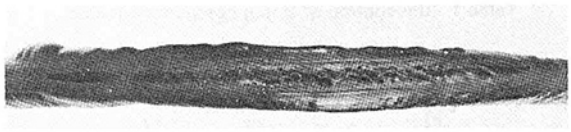

Fig. 6 CN2 seal after test (rating 1)

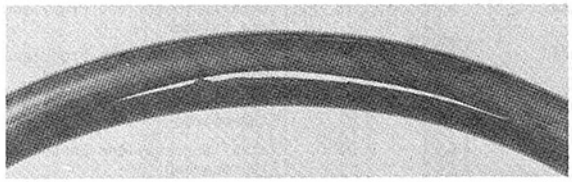

Fig. 7 TFEP1 seal after test (rating 2)

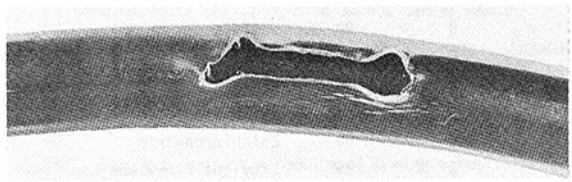

Fig. 8 TEF2 seal after test (rating 2)

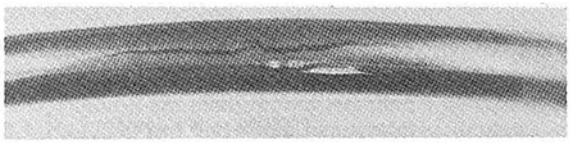

Fig. 9 TEF2 seal after test (rating 2)

subjects the entire seal segment to the pressurized gas. The vessel is depressurized in the same manner as before. The seal samples are immediately inspected and again measured with a micrometer to evaluate the amount of swell. All seals are evaluated using the rating system described below.

Explosive Decompression Resistance Rating. In order to compare the explosive decompression resistance of various compounds subjectively, a rating system has been devised. The rating for each O-ring sample is based on visual post-test observations. Explosive decompression resistance is characterized by five numbered grade levels. An O-ring sample that completes the test with no visual evidence of any defects is given a performance rating of 5. A sample that exhibits no resistance to the detrimental effects of explosive decompression, such as the one shown in Fig. 6, receives a rating of 1. Intermediate grades are used to quantify the defects observed. A rating of 4 is given if the O-ring sample exhibits fewer than three blisters (usually 3 mm diameter or smaller). Another type of appearance is characterized by the formation of a myriad of extremely tiny blisters. This type of defect is also given a resistance rating of 4. A sample that completes the test with more than three large blisters receives a resistance rating of 3. Several samples exhibiting this defect were sectioned, revealing internal cracks below these blisters. The propagation of these cracks would eventually cause the seal to rupture. Tetrafluoroethylene encapsulated seals that exhibit overloading (fine peripheral cracking) of the encapsulation are also given a rating of 3. An explosive decompression resistance rating of 2 is given to samples that exhibit splitting as shown in Fig. 7. Cracks in the tetrafluoroethylene or cord stock of the encapsulated seals (See Figs. 8 and 9) are also qualified with a rating of 2.

Results

The types of O-ring compound tested include those shown in Table 1. Described generically are 16 different compounds, comprised of seven different basic material types supplied by five different manufacturers. Nominal Shore A hardness for each compound is also indicated.

Effect of Pressure Level. Using the rating system defined previously, each test sample is rated on the basis of damage resulting from one decompression cycle. Multiple samples of some compounds are tested to verify repeatability. Table 2 lists the ratings for fourteen compounds subjected to approximately 90 s decompression following a 72 h exposure to the CO_2/natural gas mixture at 13.8 MPa (2000 psi) and room temperature. In addition, 6.9 MPa (1000 psi) ratings are shown for nine compounds, with seven tested at both pressure levels. Of these, three compounds rate lower at 13.8 MPa (2000 psi) and two are unchanged; however two compounds, which have fairly low ratings of 2 or 3 at 6.9 MPa (1000 psi), actually rate higher at 13.8 MPa (2000 psi).

At room temperature and 13.8 MPa (2000 psi) the high durometer fluorocarbon (FKM1), tetrafluoroethylene propylene (TFEP1, TFEP2), and carboxylated nitrile (CN1) compounds rate nearly perfect. The high durometer nitrile (N1, N2) and epichlorohydrin (ECO1, ECO2) compounds show light to moderate blistering, limiting their life at 13.8 MPa (2000 psi). With the exception of the TEF2 sample, which experienced cracked encapsulation caused by excessive preload,

Table 1 Description of O-ring compounds tested

COMPOUND	MANUFACTURER	HARDNESS[1] (SHORE A)	MATERIAL TYPE
FKM1	B	90	Fluorocarbon
TFEP1	C	95	Tetrafluoroethylene Propylene Base Polymer
TFEP2	A	93	Tetrafluoroethylene Propylene Base Polymer
TFEP3	A	75	Tetrafluoroethylene Propylene Base Polymer
TFEP4	A	90	Tetrafluoroethylene Propylene Base Polymer/Fiber Filled
TEF1	E	75	Tetrafluoroethylene Encapsulated Fluorocarbon
TEF2	E	75	Tetrafluoroethylene Encapsulated Fluorocarbon
CN1	B	90	Carboxylated Nitrile
CN2	C	80	Carboxylated Nitrile
N1	C	90	Nitrile
N2	B	90	Nitrile
N3	C	80	Nitrile
N4	D	75	Nitrile
ECO1	C	90	Epichlorohydrin
ECO2	B	90	Epichlorohydrin
EP1	C	85	Ethylene Propylene Copolymer

[1]The durometer hardness as measured on the Shore "A" gage. Higher numbers indicate harder material.

Table 2 Effect of pressure level

COMPOUND	PRESSURE - MPa (psi) 6.9 (1000)	13.8 (2000)
FKM1	5	4,5
TFEP1		5,5,5
TFEP2		5,5,5
TFEP3	4	3,4
TFEP4		3,3,3
TEF1		5
TEF2	2	3,3
CN1	5	5,5,5
CN2		3,3,3
N1	4	4
N2	5	3,4
N3	3	4,4
N4	3	
ECO1		4,4
ECO2	3	
EP1		3

CO_2/natural gas mixture
Room temperature
90 sec. decompression time

Table 3 Effect of sample configuration

COMPOUND	TEMPERATURE °C (°F)	CONFIGURATION O-RING	STRIP
FKM1	Room	4,5	5,5
TFEP2	Room	5,5,5	5,5
CN1	Room	5,5,5	4,5
CN2	Room	3,3,3	3,3
CN2	126.7 (260)	1	1,1
ECO1	126.7 (260)	2	2,4

CO_2/natural gas mixture
13.8 MPa (2000 psi) pressure
90 sec. decompression time

all of the compounds would have been suitable for additional pressure cycles, although the number was not investigated.

Effect of Sample Configuration. As described previously, complete O-rings are tested both as face seals and as peripheral seals. In general, differences in performance of a compound in either application are insignificant and the results have not been segregated in the ratings shown in this paper. However, four of the marginal compounds did display a slight tendency of the peripheral seal to out-perform the face seal application.

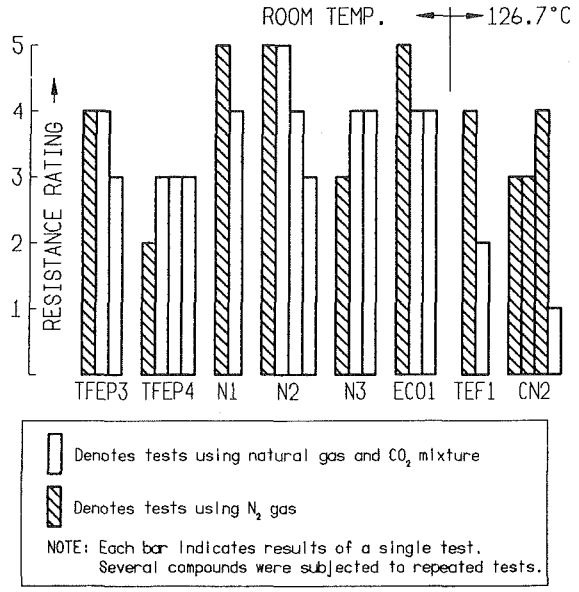

Fig. 10 Effect of gas composition

Because of a preconceived notion that testing of strips of material is not a realistic method of evaluation, comparative tests were run on six compounds as shown in Table 3. The results are surprising to the authors as only minor differences in ratings have been observed. Nevertheless, in order to eliminate completely the uncertainty of this effect, all comparative results of other parameters have been obtained from tests of complete O-rings acting as face or peripheral seals.

Effect of Gas Composition. Field experience and many references (Parker, 1973, 1982; Ender, 1983; Gent, 1978; 3M, 1986) indicate that pure CO_2 or gas mixtures containing CO_2 increase the tendency for explosive decompression failure to occur. To evaluate this effect, eight compounds were tested at identical conditions in N_2 and the CO_2/natural gas mixture. The results in Fig. 10 show that at 13.8 MPa (2000 psi) with 90 s decompression time most of the compounds rate higher in N_2, particularly at high temperature, although TFEP4 and N3 are exceptions to this trend.

Effect of Temperature. Comparative tests have been conducted on several compounds at room temperature and at 126.7°C (260°F). In the CO_2/natural gas mixture at 13.8 MPa (2000 psi) with 90 s decompression, temperature proved to be a very significant factor, as shown in Fig. 11. Although the 126.7°C (260°F) test temperature is safely within the manufacturers' published limits for static seals for each compound, the compounds rate much lower at the higher test temperature. Where no damage or only blistering occurs at room temperature, the same compounds experience longitudinal splits (Fig. 7), foaming (Fig. 6), or blowouts (Fig. 8), in just one 90 s decompression cycle from 13.8 MPa (2000 psi) at 126.7°C (260°F). None of the seal compounds shown in Fig. 11 rated higher than 2 at high temperature; they would have effectively survived few, if any, additional pressure cycles. Seal compounds that experience longitudinal splits exhibit an interesting trend wherein the splits always radiate from the compressed or loaded faces of the O-ring cross section. Peripheral seal cracks originate at the o.d. or i.d., but face seal

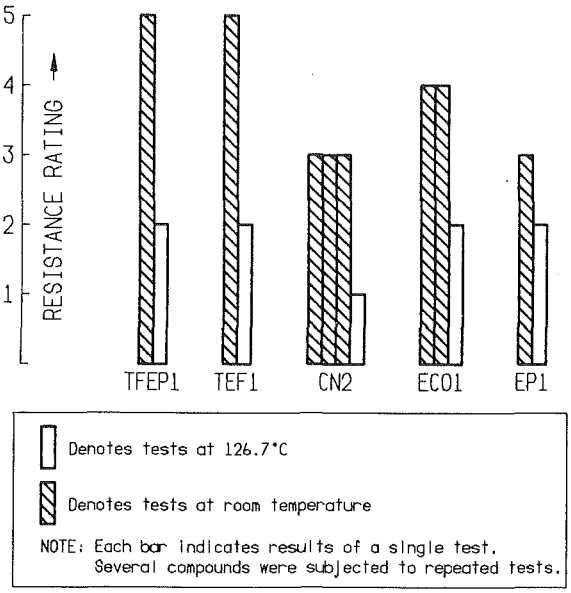

Fig. 11 Effect of temperature

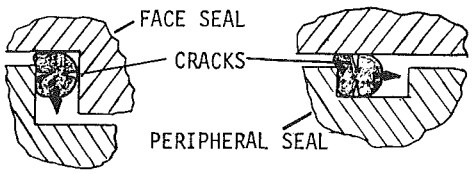

Fig. 12 O-ring expansion during decompression

cracks originate from the axial faces as shown in Fig. 12. As shown in the sketch, this tendency can be explained in terms of the direction in which the seal is free to expand during decompression. The gas pressure inside the seal overloads the seal in the direction of expansion, causing cracks in a transverse direction. High temperature contributes to this tendency because it has a softening effect on elastomers (Parker, 1982), reducing their modulus and tensile properties and therefore reducing their explosive decompression resistance.

Effect of Decompression Time. As indicated previously, decompression, or blowdown, time is a major factor in explosive decompression damage of O-ring compounds. This was confirmed by comparative tests of four compounds in the CO_2/natural gas mixture at 13.8 MPa (2000 psi) summarized in Fig. 13. The longer decompression times permit the gas trapped inside the elastomers to escape partially before the pressure differential is sufficient to burst the O-ring. This is further verified by volume swell measurements, which generally show less residual volume swell after longer decompression times. Unfortunately, 90 s decompression times, which result in major damage to many compounds, are much more typical in practice than the 780 s times, which generally result in little damage.

Volume Swell. Volume swell measurements have been made on virtually all the test samples. These measurements are difficult as gas trapped in the elastomers literally boils off with time as evidenced by the O-ring immersed in water shown in Fig. 4. This effect is minimized by making the volume swell measurements within 10 min after decompression for all samples. Space limitations make inclusion of volume swell data in this paper impractical, so only general observations are presented.

First, it is apparent that most of the elastomers experience

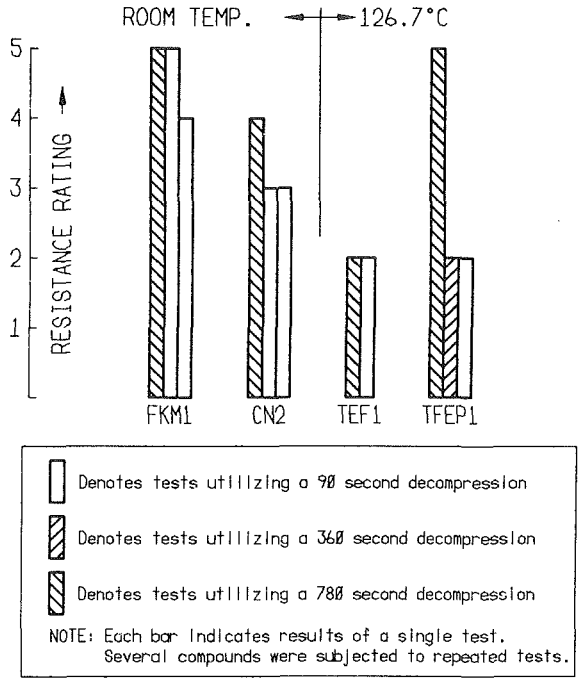

Fig. 13 Effect of decompression time

signficantly more volume swell in the CO_2/natural gas mixture than in N_2. For example, TFEP3 averages 28 percent in the CO_2/natural gas mixture, but less than 5 percent in N_2 at 13.8 MPa (2000 psi) and room temperature. Similarly, compound N_2 averages 10 percent and less than 1 percent, respectively. Secondly, less volume swell is recorded after high-temperature tests than after room temperature tests. For example, TFEP1 averages 17 percent swell at room temperature and 10 percent at 126.7°C (260°F) in the CO_2/natural gas mixture at 13.8 MPa (2000 psi). Certainly some of this difference would be attributable to gas that escapes through major elastomer fractures during decompression at the higher temperature.

Generally, no correlation has been observed between volume swell and explosive decompression resistance ratings. At 13.8 MPa (2000 psi) and room temperature in the CO_2/natural gas mixture, the best compounds in Table 3, FKM1, TFEP1, TFEP2, and CN1 have volume swell measurements averaging 7, 17, 12, and 2 pecent, respectively; while some of the marginal compounds, TEF2, CN2, and EP1, have average measurements of 13, 6, and 6 percent, respectively.

Recommendations

There are several potential factors that have not been investigated in the aforementioned testing, such as the effects of humidity, CO_2 concentration, cross-sectional diameter, and O-ring crush or preload percentage. Nevertheless some important recommendations can be made based on the data presented herein:

1 High durometer seals are recommended for best resistance to explosive decompression. In natural gas at room temperature and above 3.4 MPa (500 psi) fluorocarbon, carboxylated nitrile, and tetrafluoroethylene propylene compounds are recommended at hardness levels of 90 durometer (Shore A) or higher. Softer compounds should be avoided at high pressures.

2 Decompression times should be maximized whenever possible. As demonstrated by the test data, decompression times of 780 s are not excessive when explosive decompression

damage is to be avoided. Depressurization of compression systems should be as slow as reasonably possible in all nonemergency situations to minimize O-ring seal damage.

3 Most O-ring compounds suffer severe damage even at temperatures well below published manufacturer maxima when exposed to CO_2/natural gas mixtures at 13.8 MPa (2000 psi) and subjected to short decompression times, limiting the useful life of these seals severely.

4 O-ring seal manufacturers are encouraged to conduct more realistic testing of compounds in order to find effective solutions to this problem. Compounds should be tested as molded O-rings of realistic cross sections that are installed as seals in realistic gas mixtures at high temperature.

5 Development of an industry standard test including these features should be considered, so that results of various manufacturers' tests can be uniformly compared.

6 The influence of smaller O-ring cross sections, reduced gland expansion volumes, and backup rings should be explored in experimental apparatus similar to that described herein.

Acknowledgments

The authors wish to thank the management of CB Rotating Division of Cooper Industries for permission to publish the data presented in this paper, the five unnamed O-ring manufacturers for graciously contributing test samples, and Mr. M. Darling for his conscientious and meticulous testing efforts.

References

Ender, D. H., 1983, "Swelling of Some Oil-Field Elastomers in Carbon Dioxide, Hydrogen Sulfide, and Methane at Pressures to 4000 psi," ACS Rubber Division, 124th Meeting, Paper No. 44.

Federal-Mogul Corp., 1982, "National O-Ring Engineering Manual," Downey, CA, pp. 207–208.

Gent, A. N., and Tompkins, D. A., 1967, "Nucleation and Growth of Gas Bubbles in Elastomers," *Journal of Applied Physics*, Vol. 40, No. 6, pp. 2520–2525.

Gent, A. N., 1978, "Rubber Elasticity: Basic Concepts and Behavior," in: *Science and Technology of Rubber*, Academic Press, New York, NY, p. 17.

Hertz, D. L., Jr., 1984, "Sealing High Pressures Under Sour Conditions," ASME Paper No. 84-PET-7.

Parker Seal Co., 1973, Engineering Report 03-245, Culver City, CA.

Parker Seal Co., 1982, *Parker O-Ring Handbook ORD 5700*, Lexington, KY, pp. A2-4–A2-11, A3-9.

Precision Rubber Products Corp., 1982, *O-Ring Handbook*, Lebanon, TN, pp. 2.11, 2.12, 3.1.

3M, 1986, *Machine Design*, Vol. 58, No. 14, pp. 123–126 (Advertisement).

Solar Receiver for the Space Station Brayton Engine

H. J. Strumpf

M. G. Coombs

AiResearch—Los Angeles Division,
Allied-Signal Aerospace Company,
Torrance, CA

A study has been conducted on the preliminary design and development of a solar receiver to be used for electrical power production in a closed Brayton cycle engine on the NASA Space Station. The receiver incorporates integral thermal storage, using a eutectic mixture of LiF and CaF_2 as the thermal storage solid-to-liquid phase change material (PCM). The thermal storage is required to enable power production during the substantial eclipse period which accompanies low-earth orbits. The design comprises a cylindrical receiver cavity. The walls of the cavity are lined with a series of tubes running the length of the cavity. The Brayton cycle working fluid flows through the tubes. The PCM is enclosed in individual, sealed metallic containment canisters which are stacked and thermally connected to the working fluid tube. The material for the working fluid tubes and containment canisters is the cobalt superalloy Haynes 188.

Introduction

A study has been conducted by AiResearch – Los Angeles, a division of Allied-Signal Aerospace Company, on the design and development of a solar receiver to be used for electrical power production in a closed Brayton cycle (CBC) engine on the NASA Space Station. The study was performed for Rocketdyne Division of Rockwell International Corporation as part of Work Package-04, Phase B, of the Space Station program under NASA-Lewis Research Center.

The receiver incorporates integral thermal storage, using a eutectic mixture of LiF and CaF_2 as the thermal storage solid-to-liquid phase change material (PCM). The thermal storage is required to enable power production during the substantial eclipse period that accompanies low-earth orbits. The eutectic has a melting point of 1416°F (769°C) and a latent heat of fusion of 340 Btu/lb (790 J/g).

The CBC power unit comprises an offset parabolic concentrator that captures the solar rays and focuses the concentrated energy onto the inner surface of the receiver. This concentrated energy heats the CBC working fluid, an inert gas mixture of Xe and He with a molecular weight of 40. The heated working fluid is expanded in a turbine, driving an electrical generator and the compressor that circulates the working fluid. Cycle waste heat is rejected to a pumped-liquid radiator. The engine includes a recuperator, which increases thermal efficiency by recirculating thermal energy in the cycle.

Receiver Design

The receiver design comprises a cylindrical receiver cavity, the walls of which are lined with a series of tubes along the length of the cavity. The CBC working fluid flows through the tubes. The receiver schematic is shown in Fig. 1. The PCM is contained in a series of metal canisters. The individual containment canisters can be filled with the PCM in either the solid or liquid phase and welded shut under vacuum to form hermetically sealed units.

The containment canisters are stacked and bonded to the workding fluid tube, as shown in Fig. 2. The canisters are not bonded to each other but are separated by ceramic fiber spacers. The use of individual containment canisters for the

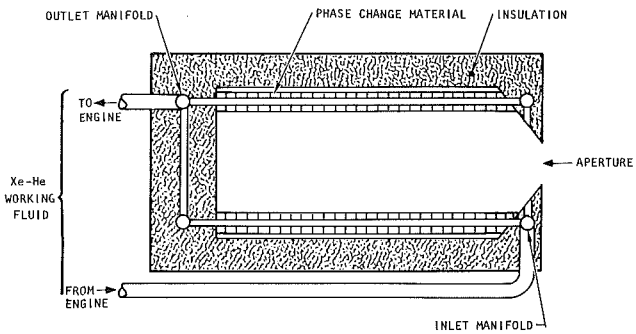

Fig. 1 Solar receiver schematic

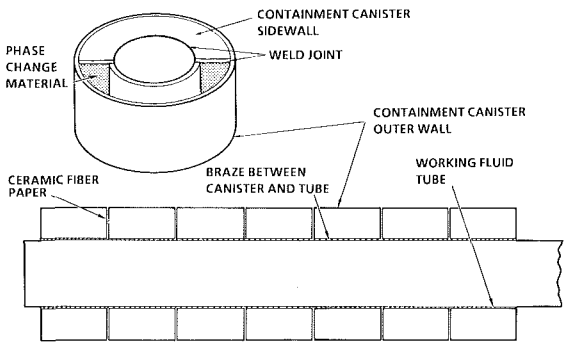

Fig. 2 Receiver tube configuration

Contributed by the Gas Turbine Division of THE AMERICAN SOCIETY OF MECHANICAL ENGINEERS and presented at the 32nd International Gas Turbine Conference and Exhibit, Anaheim, California, May 31–June 4, 1987. Manuscript received at ASME Headquarters February 24, 1987. Paper No. 87-GT-252.

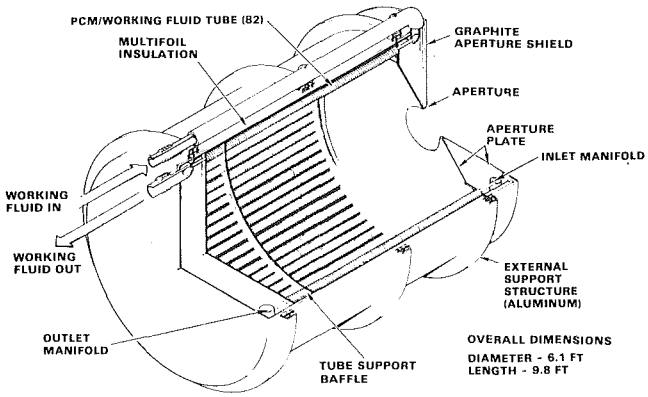

Fig. 3 AiResearch space station receiver

PCM is a key attribute of the receiver design. This configuration affords a readily fabricable and highly reliable design. Failure of a canister would affect only that individual canister and have minimal impact on receiver operation. The compartmentalization also reduces the chance of failure by localizing the void formation upon freezing (due to the lower density of the liquid as compared to the solid), minimizing the likelihood of high stress buildup.

The configuration combines three functional components—the heat receiver, the CBC heat source heat exchanger, and the thermal storage device—into a single unit. This integral design is the most straightforward approach. No heat pipes are required to distribute the heat, thus avoiding a significant increase in complexity.

Receiver operation can be described with the aid of Fig. 3. The CBC working fluid from the recuperator flows through an external duct to a toroidal manifold at the aperture end of the receiver. The manifold distributes the fluid to the individual tubes. The flow is collected in the outlet manifold and sent to the turbine.

During sunlight periods, heat is transferred through the PCM to the CBC working fluid. The PCM is also melted and heated by the solar flux. During eclipse periods, the PCM gives up its heat to the CBC working fluid and is frozen and cooled.

The cavity walls consist of a thin layer of high-temperature formed insulation. Since there is a reasonably large gap between tubes, some of the radiation entering the receiver through the aperture will impinge directly on these walls. The walls act to reradiate the incoming flux to the back side of the tubes and aid in providing a relatively uniform flux circumferentially around the tubes. The cavity walls also act as a mandrel to wrap sheets of very low conductivity multifoil insulation.

The insulated cavity is enclosed in an aluminum support structure. The tubes are supported by baffles, which are, in turn, connected to reinforced regions of the support structure. The tubes fit loosely in the baffle holes and are free to expand. The backwall of the cavity moves as the tubes expand. Tube expansion is accommodated by two external bellows.

The receiver comprises 82 tubes, 8.2 ft (2.5 m) in length, with 96 containment canisters per tube. The material for the working fluid tubes and containment canisters is the cobalt-base superalloy Haynes 188. The receiver outside dimensions are approximately 6.1 ft (1.9 m) diameter and 9.8 ft (3.0 m) long. The receiver module weighs about 3860 lb (1751 kg), with the weight breakdown shown in Table 1. Each module is appropriate for a system supplying a net electrical power of 25 kW to the user.

Table 1 Receiver weight summary

Component	Weight lb	Weight kg
Phase change material	750	340
Working fluid tubes	240	109
Containment canisters	1538	698
Inlet manifold	33	15
Outlet manifold	44	20
Ducts (including bellows and insulation)	40	18
Formed insulation mandrel	179	81
Backwall support plate	91	41
Multifoil insulation (nickel and aluminum)	259	117
Aluminum outer shell	325	147
Baffles and supports	100	45
Aperture plate	178	81
Aperture shield	85	39
Total	3862	1752

Performance Analysis

Computer Program SOLREC-TSD. Preliminary performance prediction with simplified models indicated the necessity for detailed component and flux distribution computer codes. The energy transfer among the solar input, the PCM, and the working fluid is complex and not amenable to approximate methods of analysis. An important contributing factor to this situation is the large thermal capacitance of the PCM. The continuous absorption and release of heat results in a strictly transient operation throughout an orbit. Detailed heat transfer calculations must be performed to determine the energy accumulation and heat release to the working fluid.

An additional factor, also requiring detailed analysis, is the axial redistribution of energy due to reradiation and conduction. Due to the large working fluid temperature change, wall temperature variations are inherent in the axial direction. The redistribution of heat due to the temperature variation is extremely significant during both sunlight and eclipse periods.

In order to perform the necessary calculations, a series of computer programs was assembled. Some of these programs were available, with appropriate modification, from previous AiResearch solar receiver and heat exchanger studies. Other codes were written specifically for the present effort. The assembled computer programs, called SOLREC-TSD, result in a detailed finite element description of the receiver tubes and containment canisters, including a varying solid-liquid PCM boundary location, and the interaction of these elements with solar energy focused by a concentrator. The tube/containment canister model is axisymmetric. SOLREC-TSD is exercised in a forward-marching mode as a function of time, using arbitrarily small time steps. One or more complete orbits can be followed on a real-time basis. SOLREC-TSD assumes circumferential symmetry around the receiver for fluxes and temperatures.

Orbital Variation and Control. On the low-earth orbits envisioned for the Space Station, there is a significant variation in eclipse time due to orbital precession. In addition, the value of the local insolation varies throughout the year as the

Nomenclature

CBC = closed Brayton cycle
P = Larson-Miller parameter
PCM = phase change material
S = time spent at stress and temperature, hr
T = temperature, °F
t = time to rupture, hr
σ = stress, ksi

Table 2 Orbital extremes

- Minimum insolation orbit
  - Orbital period = 91.02 min, 180 nautical miles (333 km)
  - Insolation = 1.323 kW/m^2
  - Concentrator reflectivity = 0.90 (end of life)
  - Eclipse period = 36.33 min
- Maximum insolation orbit
  - Orbital period = 93.67 min, 250 nautical miles (463 km)
  - Insolation = 1.419 kW/m^2
  - Concentrator reflectivity = 0.93 (start of life)
  - Eclipse period = 28.13 min

Table 3 Receiver conditions

	Minimum Insolation Orbit		Maximum Insolation Orbit	
Minimum receiver inlet temperature, °F (°C)	944	(507)	845	(452)
Minimum receiver outlet temperature, °F (°C)	1330	(721)	1185	(641)
Flow rate, lb/sec (kg/s)	1.8786	(0.8521)	2.7	(1.2247)
Inlet pressure, psia (kPa)	50.5	(348)	73	(503)
Maximum pressure drop, %	3.5		3.5	

earth's distance from the sun changes. These variations can be predicted with excellent precision. The real-time capability of SOLREC-TSD allows, in principle, for the tracking of the receiver over a yearly period. The computer time necessary to perform these calculations would be excessive. Instead, the following approach was taken: From arbitrary initial conditions, performance is tracked through a number of complete orbital cycles (including sunlight and eclipse periods) for non-varying orbits, until cyclic (orbital) reproducibility is attained. This is done for two sets of extreme orbital conditions, corresponding to the orbit that accepts the minimum total energy (minimum insolation orbit) and the orbit that accepts the maximum total energy (maximum insolation orbit). The conditions are listed in Table 2. The orbital extremes include an expected degradation in concentrator reflectivity: the minimum insolation orbit corresponding to the design end-of-life reflectivity of 0.90 and the maximum insolation orbit corresponding to a start-of-life reflectivity of 0.93.

The minimum insolation orbit is used to specify the requirements for the desired power level. Once designed for minimum insolation, the required power can be produced easily for higher insolation conditions. The increased insolation, however, could result in an undesirable increase in receiver and CBC working fluid temperatures. To handle the excess energy, the CBC working fluid flow rate in increased. This can be effected by selecting a flow rate prior to every orbit based on the conditions of the last orbit. The flow rate is essentially constant for a given orbit. The flow rate selection is based on orbital conditions only—orbital period, eclipse time, insolation level, etc. The desired flow is produced by adjusting the engine working fluid inventory level and pressure by means of an accumulator. A secondary control monitors the receiver outlet temperature and adjusts the inventory level as necessary.

Performance Prediction. The receiver requirements for minimum and maximum insolation orbits are presented in Table 3. The receiver outlet temperature is the minimum required for power production at the corresponding flow rate. During any given orbit, the minimum temperature is exceeded most of the time, resulting in additional electric power available to the user. Unused electric power will be dissipated by a set of resistive banks contained in a parasitic load

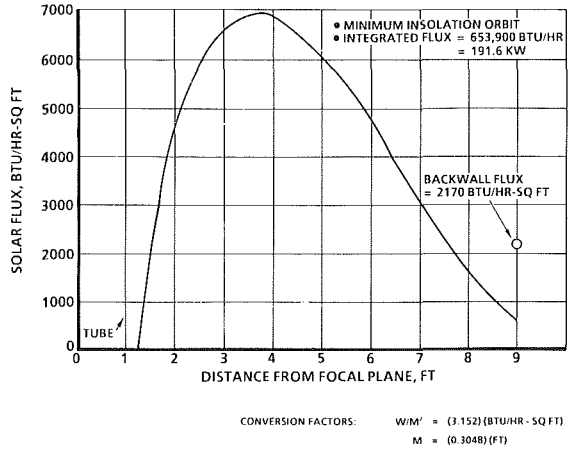

Fig. 4 Incident solar flux

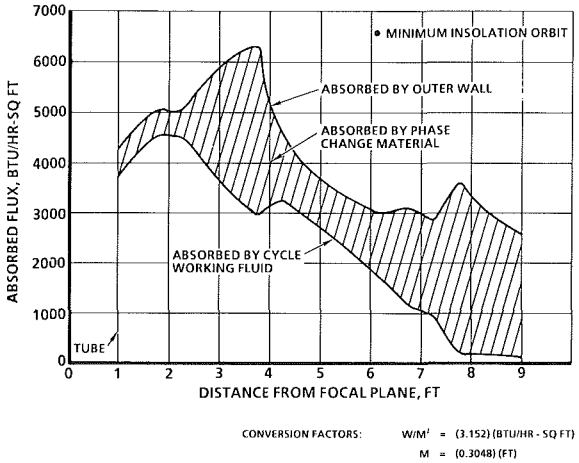

Fig. 5 Absorbed flux at sunset

regulator. The receiver inlet temperature varies as the receiver outlet temperature varies, and is not constant throughout an orbit.

As indicated in Table 3, the receiver outlet temperature selected for the minimum insolation orbit is 1330°F (721°C). This temperature was selected as a compromise between higher engine efficiency (higher temperature) and longer receiver life (lower temperature). The low receiver outlet temperature for the maximum insolation orbit is the result of the increased flow rate available from the engine inventory control scheme described above.

The predicted receiver performance for the minimum insolation orbit is based on the incident solar flux distribution shown in Fig. 4. Although not derived from any specific concentrator design, the flux distribution is typical of that obtainable from state-of-the-art offset parabolic concentrators. A total power of 191.6 kW is required in through the receiver aperture. Note that the tube inlet is offset 1 ft (0.30 m) from the aperture plane.

Absorbed flux and temperature profiles were generated as a function of time throughout the orbit. A few representative profiles ars shown here. Figure 5 presents the flux absorbed by the outer wall at sunset. This is the hottest time in the orbit. Also shown is the flux absorbed by the CBC working fluid. The difference between the absorbed wall flux and the absorbed working fluid flux is the flux absorbed by the PCM. The corresponding temperature profiles at this time are shown in Fig. 6. Also shown is the fraction of PCM in the liquid phase at any location along the tube.

Figure 7 shows the absorbed fluxes at sunrise (end of

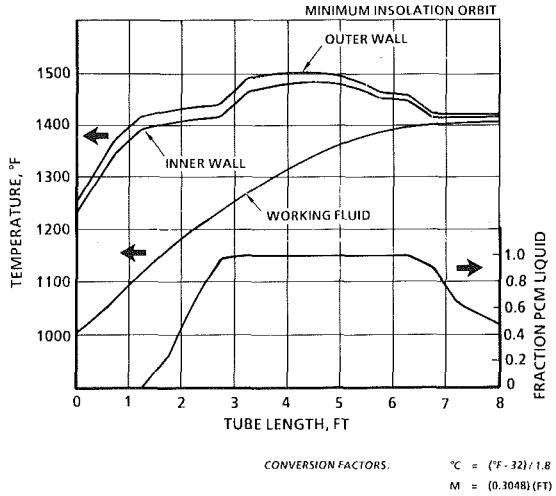

Fig. 6 Axial temperature profiles at sunset

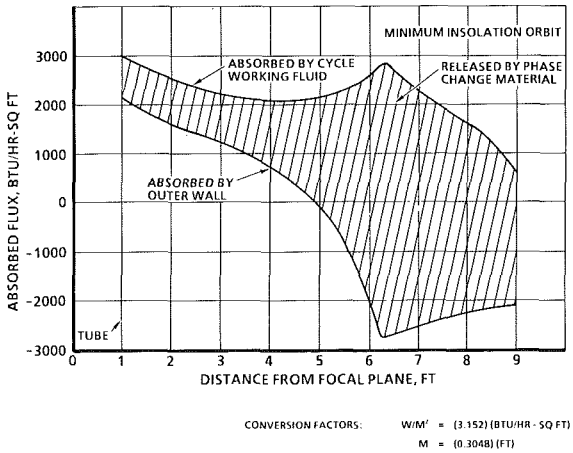

Fig. 7 Absorbed flux at sunrise

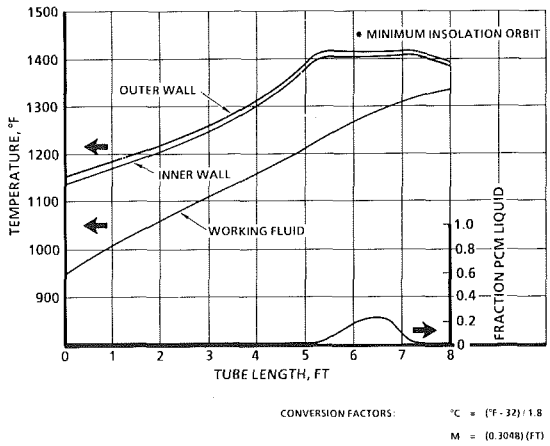

Fig. 8 Axial temperature profiles at sunrise

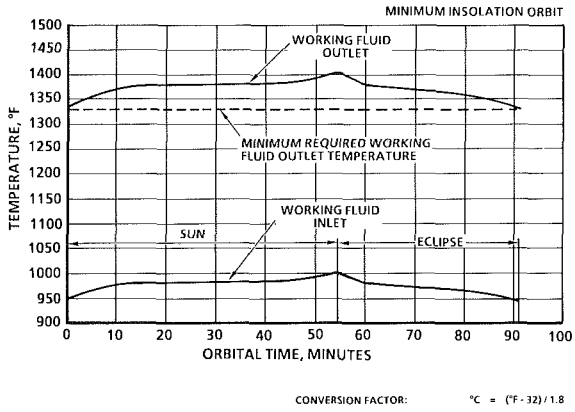

Fig. 9 Orbital temperature variations

Table 4 Energy balance (minimum insolation orbit)

	Energy, kW-hr	Percentage of total
Brayton engine minimum requirement	144.3	82.7
Aperture losses (emittance and reflection	14.3	8.2
Surface losses (through insulation and supports	12.3	7.0
Additional electric power	3.7	2.1
Total in through aperture (191.6 kW for 54.69 min)	174.6	100

eclipse). This is the coldest time in the orbit and represents the most difficult power condition. The absorbed outer wall flux is less at all locations than the absorbed working fluid flux, indicating net heat release for all PCM elements. The absorbed outer wall flux is positive at the inlet end of the tubes and negative at the outlet end of the tubes, indicating the substantial axial reradiation and conduction effects during eclipse. The corresponding temperature profiles are presented in Fig. 8. The working fluid outlet temperature is 1335°F (724°C), satisfying the required minimum of 1330°F (721°C) (see Table 3).

Temperature variations over the entire orbit are shown in Fig. 9. The working fluid outlet temperature varies from 1335° to 1407°F (724° to 764°C). The minimum required temperature is attained at all times. The energy balance is summarized in Table 4.

Receiver performance was also predicted for the maximum insolation orbit. The incident solar flux distribution is similar to the minimum insolation orbit flux distribution (Fig. 4), with all fluxes multiplied by a factor of 1.108. This factor corresponds to the appropriate local insolation and concentrator reflectivity (see Table 2). The total power in through the aperture is 212.3 kW. The absorbed flux and axial temperature profiles at sunset are shown in Figs. 10 and 11, respectively. Comparison with Fig. 6 shows that the maximum wall temperatures are lower for the maximum insolation orbit than for the minimum orbit. This is due to the increased flow rate for the maximum insolation orbit.

Temperature variations over the entire orbit are shown in Fig. 12. The working fluid outlet temperature varies from 1201° to 1375°F (649° to 746°C). The minimum required temperature is attained at all times.

Three-Dimensional Tube/Canister Analysis. The thermal model in computer program SOLREC-TSD is axisymmetric around the tube/containment canister. This results in the inherent assumption of uniform temperature circumferentially around the outer wall. To check this assumption, a detailed three-dimensional circumferential thermal model of a single canister and attached tube was prepared, as shown in Fig. 13. As indicated, the model is symmetric around the diametric plane normal to the cavity wall.

The CBC working fluid inlet temperature at the canister location along the working fluid tube and the average heat flux absorbed by the working fluid (both calculated by SOLREC-TSD) are the inputs to the thermal model. The heat flux is distributed around the front 180 deg of the outer wall and the cavity wall as a function of projected area. The back 180 deg of the outer wall exchanges heat with the cavity wall.

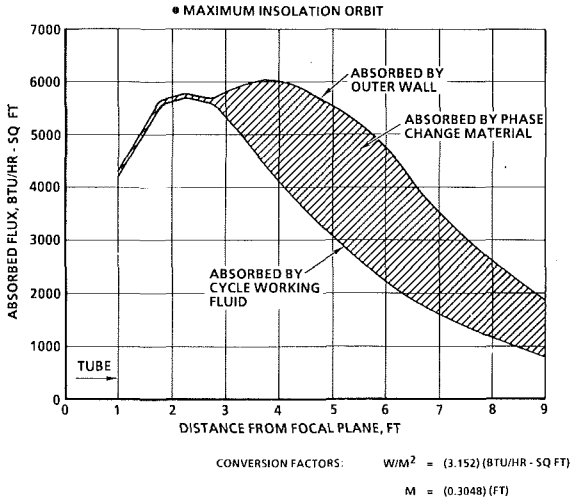

Fig. 10 Absorbed flux at sunset

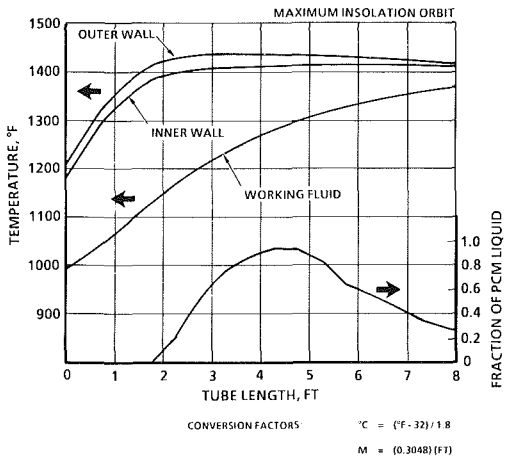

Fig. 11 Axial temperature profiles at sunset

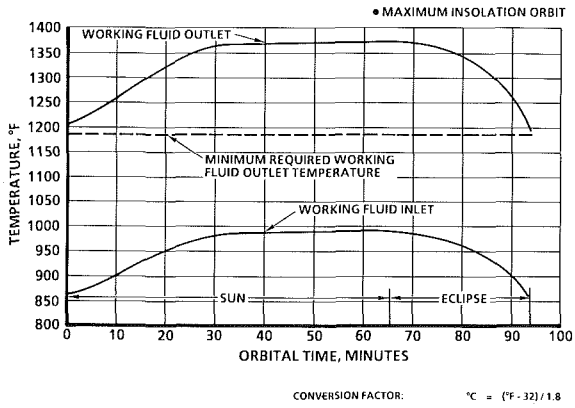

Fig. 12 Orbital temperature variations

A preliminary stress analysis identified the "critical canister" as canister number 39 from the tube inlet, at 3.25 ft (0.99 m). This is the canister that exhibits the most severe combination of stress and temperature. For this canister, the detailed thermal analysis indicates an outer wall circumferential temperature gradient varyng from ±14° to ±23°F (±8° to ±13°C) throughout a minimum insolation orbit. These gradients validate the use of computer program SOLREC-TSD, which neglects any circumferential temperature variation. It should be noted that the circumferential temperature variation is lower at canister locations closer to the tube centerline.

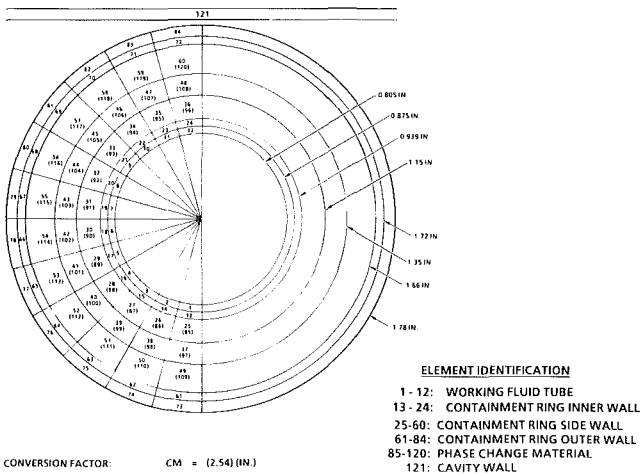

Fig. 13 Tube-canister circumferential thermal model

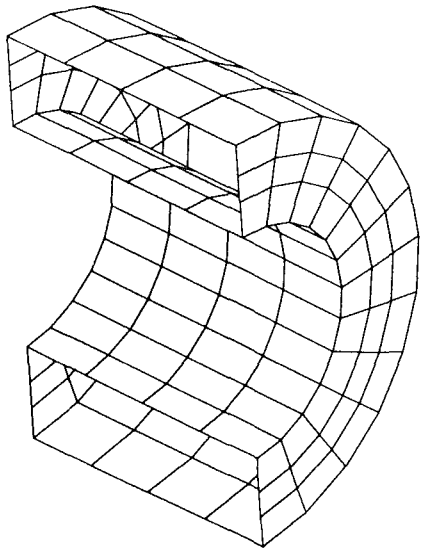

Fig. 14 Canister stress model

Canister Stress Analysis

Preliminary stress analysis indicated that the life-limiting stress factor is creep damage to the canisters. This is a result of the required 30-year life for the Space Station and the elevated operating temperatures. The creep is caused largely by thermal stresses. In order to survive 30 years of creep, the stress must be kept low. The required low stresses are far below the endurance limit of the Haynes 188 so that cyclic fatigue damage will, of necessity, be minimal.

To determine the canister creep damage and life, a detailed stress analysis procedure was developed and performed. The procedure involved the preparation of a three-dimensional stress model of a single canister, shown in Fig. 14. The canister inner wall includes the section of the attached working fluid tube. Simplifying assumptions include neglecting any axial temperature variation within the 1-in. (2.5 cm)-long canister (a few degrees at most) and neglecting the stiffening effect of the continuous working fluid tube (judged to be minor in preliminary analysis). The inputs to the stress model are the tube internal pressure and the temperature maps from the circumferential thermal model for the critical canister.

The analysis identified the critical stress location on the critical canister as the canister sidewall along the inner radius surface at the point on the diametric plane normal to the cavity wall. This point is identified as node 1 on the sidewall stress

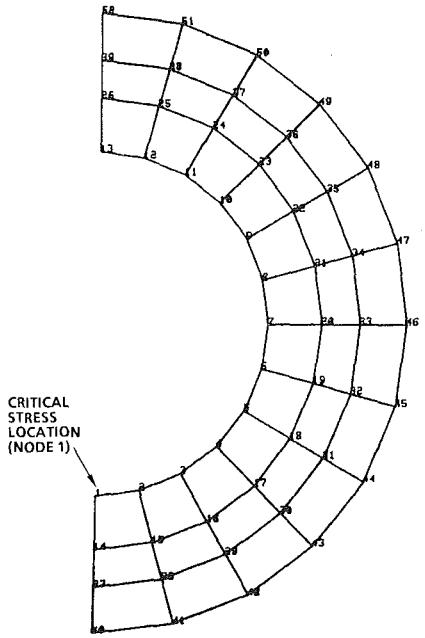

Fig. 15 Critical stress location

model shown in Fig. 15. The sidewall inner surface exhibits the maximum tensile stresses in the canister. Compressive stresses essentially do not contribute to creep damage. Node 1 always exhibits the highest temperature along the sidewall inner surface at close to the maximum stress level. There is also a variation in stress level through the thickness of the sidewall. The most highly stressed plane (sidewall inner plane) is used in the analysis.

The life of the critical canister is assumed to be a function of the creep damage at the critical stress location (node 1 inner plane). Other canisters will exhibit longer life than the critical canister.

Since creep is a volume phenomenon, the stress value at the critical stress location used in the damage analysis can be considered to redistribute partially over the region of the sidewall under tension. This tension zone occurs from the inner radius to about halfway to the outer radius. The distributed equivalent (Von Mises) stress used in the creep analysis is calculated according to

$$\text{distributed stress} = \text{direct stress} + 2/3 \text{ bending stress} \quad (1)$$

where direct stress is the average equivalent stress over the tension zone; and bending stress is the average nodal stress difference over the tension zone.

The calculated distributed stresses are approximately 8 percent less than the maximum nodal stresses. The temperature corresponding to the distributed stress is taken as the average temperature over the tension zone.

The canister life prediction is based on the cumulative creep damage over time. To determine the cumulative creep damage, stresses were predicted for the critical canister at various times during orbit. This is necessary since the stresses and temperatures vary with time. Both the minimum insolation and maximum insolation orbits were evaluated.

Due to the finite length of the time intervals, the stresses and temperatures are averaged over the interval. These interval conditions are used with the available creep rupture data (Larson–Miller curve) for Haynes 188 to predict the time to rupture t_i for each interval condition. Haynes 188 creep rupture data are available from tests up to 10,000 hr at 1600°F (871°C) and 7000 hr at 1800°F (982°C). The data were fit to the following Larson–Miller curve[1]:

$$P = 57.40716 - 8.90248 \log \sigma - 0.60035 (\log \sigma)^2 - 0.48401 (\log \sigma)^3 \quad (2)$$

where σ = stress, ksi; P = Larson–Miller parameter $= T(20 + \log t) \times 10^{-3}$; T = temperature, °F; t = time to rupture, hr.

From the predicted times to rupture, the cumulative damage for an orbit D is given by

$$D = \sum_{i=1}^{n} S_i / t_i \quad (3)$$

where n = number of conditions considered in the orbit; S_i = time spent at condition i, hr.

These calculations result in a total damage of 32.58×10^{-8} for the minimum insolation orbit and 39.91×10^{-8} for the maximum insolation orbit. It should be noted that no benefit has been taken for any stress relaxation that occurs as a function of time.

The damages from the minimum and maximum insolation orbits are averaged and the reciprocal taken to determine the number of orbits to rupture. The life is the product of the number of orbits to rupture and the average orbital period. The predicted number of orbits to rupture is 2.76×10^6, yielding a life of 484 years.

Another way of looking at the predicted life is to determine the margins with respect to the required 30-year life. These are equivalent to around 90°F (50°C) in temperature and 60 percent in stress. In other words, if every temperature throughout an orbit was 90°F (50°C) higher, the predicted life would be 30 years. Conversely, if every stress was 60 percent higher, the predicted life would also be 30 years. No other safety factors were considered in the stress analysis.

Conclusions and Summary

1 The preliminary design of the solar receiver for the Space Station Brayton engine has been completed. The configuration is straightforward and amenable to accurate analysis.

2 A series of computer programs was written and assembled to follow the performance of the receiver in real time throughout an orbit. The finite-element component description is exercised in a forward-marching, time-stepping mode.

3 Minimum and maximum insolation orbits have been identified to bracket all orbital extremes.

4 A simple flow control scheme has been devised to accommodate a range of orbital conditions.

5 Required performance has been analytically demonstrated for minimum and maximum insolation orbits.

6 A detailed procedure has been developed to predict the structural life of the critical canister.

7 The critical canister life prediction is 484 years.

8 The predicted critical canister life provides adequate margins to handle increased temperature and stresses as well as other design uncertainties and safety factors and still meet the Space Station 30-year life requirement.

Acknowledgments

The authors wish to acknowledge the significant contributions made to the study effort by K. P. Barr and R. Sharif-Razi.

[1] Conversion factors: MPa = (6.895)(ksi); °C = (°F − 32)/1.8.

STAEBL/General Composites With Hygrothermal Effects (STAEBL/GENCOM)

R. Rubinstein
Sverdrup Technology, Inc.,
Middleburg Heights, OH 44130

A computer code has been developed to perform structural optimization of turbine blades made from angle ply fiber composite laminates. Design variables available for optimization include geometric parameters such as blade thickness distribution and root chord, and composite material parameters such as ply angles and numbers of plies of each constituent material. Design constraints include resonance margins, forced response margins, maximum stress, and maximum ply combined stress. A general description of this code is given. Design optimization studies for typical blades are presented.

Introduction

The design of composite turbine blades is a very complex problem involving a large number of design variables and constraints. Even after a blade cross section is selected, the spanwise thickness distribution, root chord, ply thicknesses and angles, and blade cross-sectional stacking are all available to help meet performance constraints.

Structural optimization provides a formal, automated procedure for solving such complex design problems. Recent research at the NASA-Lewis Research Center has led to the development of STAEBL (Structural Tailoring of Engine Blades) (Fig. 1; [1, 2], which applied structural optimization techniques to turbine blade design. Capabilities have been added to STAEBL which make it a stand-alone portable computer code STAEBL/GENCOM for hygrothermal tailoring of composite turbine blades. The objective of this paper is to describe these capabilities.

STAEBL/GENCOM can be used to structurally tailor composite blades subjected to centrifugal, gas dynamic (pressure), thermal, and moisture loads. The thermal and mechanical properties are temperature and moisture dependent. Design variables include blade geometry variables such as the thickness distribution, root chord, and blade cross-sectional stacking. The blade is made of groups of plies consisting of up to seven different composite materials. Both the ply angles and the numbers of plies in each group are design variables. This allows optimization of the blade material. Constraints can be imposed on resonance margins, forced vibration response, tip displacements, and maximum root and ply combined stresses. Other program features include data transfer from finite element models and a stand-alone program version.

Contributed by the Gas Turbine Division of THE AMERICAN SOCIETY OF MECHANICAL ENGINEERS and presented at the 32nd International Gas Turbine Conference and Exhibit, Anaheim, California, May 31–June 4, 1987. Manuscript received at ASME Headquarters February 5, 1987. Paper No. 87-GT-77.

Original STAEBL Program

The original version of STAEBL was developed by Pratt & Whitney under contract to NASA-Lewis Research Center. It combines the optimization program COPES/CONMIN with a special blade geometry preprocessor and finite element analysis program as described in [1]. The optimization algorithm implemented by COPES/CONMIN is the method of feasible directions. Typical design variables include blade thickness distribution and root chord. The blade profiles are changed only by similarity transformations and stretching along the chord axis. Typical constrained quantities include resonance margins on the Campbell diagram, root stress, and root-to-chord ratios. The blade is loaded by centrifugal stresses only. In order to apply this program to composite blade design, it was modified and augmented as described in the following sections.

Hygrothermal Stress Analysis

Because STAEBL/GENCOM models the blade with

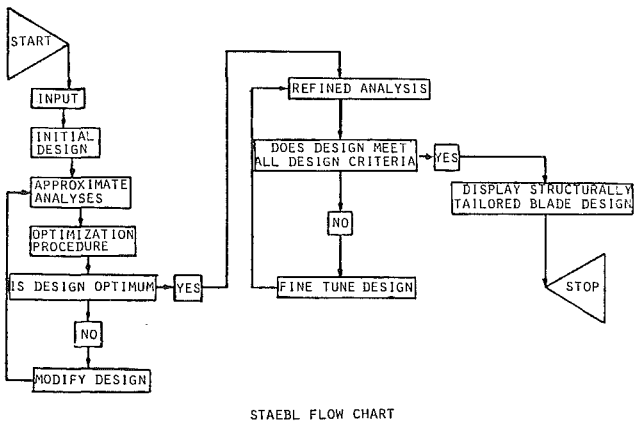

Fig. 1 Structural tailoring of engine blades (STAEBL)

triangular plate elements, the blade temperature and moisture distributions are assumed to be given at each grid point by a mean value, a through-thickness gradient, and because of different material properties through the thickness, by a through-thickness quadratic term. Two types of temperature and moisture input are allowed: The nodal quantities can be specified at each point, or they can be computed from known surface distributions using quadratic curvefits using coefficients specified by the user. Equivalent nodal thermal and hygral forces are computed in the usual way and are added to the nodal centrifugal forces. The stress recovery procedure compensates for free thermal and hygral expansion. Boundary conditions allow free expansion along the blade root.

Temperature-Dependent Mechanical and Thermal Properties

The new program version permits the elastic moduli to vary with element temperature T according to the formula

$$E = E_{\text{ref}}[(T_{GD} - T)/(T_{GD} - T_{\text{ref}})]^{1/2}$$

Since E_{ref}, T_{melt}, and T_{ref} are all user input, suitable choices for these constants should give enough accuracy for most applications. Similarly, the thermal expansion coefficient varies with temperature according to

$$\alpha = \alpha_0[(T_{GD} - T)/(T_{GD} - T_0)]^{-1/2}$$

Equivalent properties for composite materials are computed using lamination theory [3].

Temperature and Moisture-Dependent Mechanical and Thermal Properties

The elastic constants and the thermal and moisture expansion coefficients are assumed to vary with moisture and temperature according to the general formula [4]

$$P(T, M) = P(T)*((T_{GW} - T)/(T_{GD} - T_0))**\text{EXP}$$

where

T = current temperature
M = current moisture percent by weight
T_0 = reference temperature (input)
EXP = a characteristic exponent (input)
T_{GD} = a characteristic temperature (input)

and T_{GW} is defined by

$$T_{GW} = T_{GD}*(0.005M^2 - 0.1M + 1.)$$

Composite Blade Preprocessing

STAEBL/GENCOM can analyze and optimize a composite blade containing groups of plies consisting of up to seven different materials. The user supplies the ply thicknesses, fiber angles, and ply thermomechanical properties. The number of plies in each group and the ply angles are possible design variables for optimization. The program assumes that the ply layup is symmetric, and that the ply angles in each group have the same magnitude and alternating signs. The program can also handle blades made from hybrid composites as depicted in Fig. 2.

The number of plies in each group is adjusted so that the airfoil design thickness is never exceeded. The outer ply group

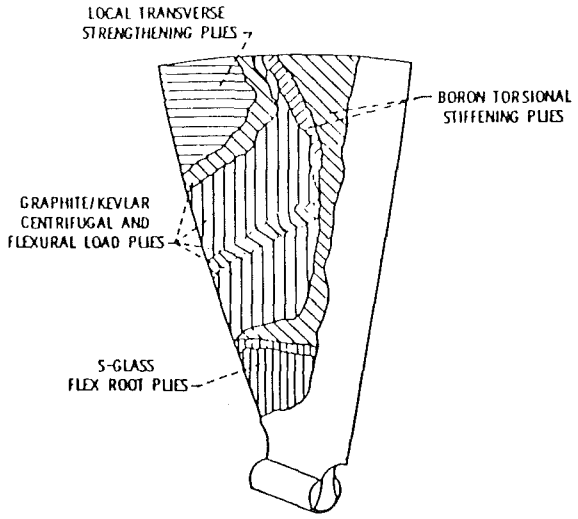

Fig. 2 Composite blade

is always present. If the design thickness is sufficient, groups of plies of constant thickness of the remaining materials are added. The number of inner plies is variable, and is adjusted so that the design thickness is achieved.

Static Pressure Loads

STAEBL/GENCOM allows input of resultant gas dynamic pressures on each element. The pressures are replaced by statically equivalent nodal forces. These forces are added to the centrifugal and thermal loads. Thus, the total static load is the resultant of centrifugal, thermal, moisture, and pressure loads.

Fatigue Life Analysis

The original STAEBL program analyzed fatigue life using the Goodman diagram. It had a hard-coded forcing function appropriate for only one specific blade. In STAEBL/GENCOM, the forcing function is a multiple of the static pressure distribution.

The required multiple of the static pressure and the static and dynamic limits on the Goodman diagram are all user input. STAEBL/GENCOM models thermal effects on fatigue life by automatically making the static and dynamic limits vary with temperature like the elastic constants.

Tip Displacement Constraints

Excessive untwist and uncamber under load could cause significant engine power losses. Composite blade design must therefore consider tip displacements. STAEBL/GENCOM allows untwist, uncamber, and tip extension to be selected as constraints on the optimal design.

Improved Execution Time and Stand-Alone Analysis Capabilities

The STAEBL program requires an aerodynamic blade

Nomenclature

E = Young's modulus
E_0 = Young's modulus at reference temperature and zero moisture
M = current moisture percentage by weight
T = current temperature
T_0 = reference temperature
T_{GD} = glass transition temperature
α = thermal expansion coefficient
α_{ref} = thermal expansion coefficient at reference temperature and zero moisture

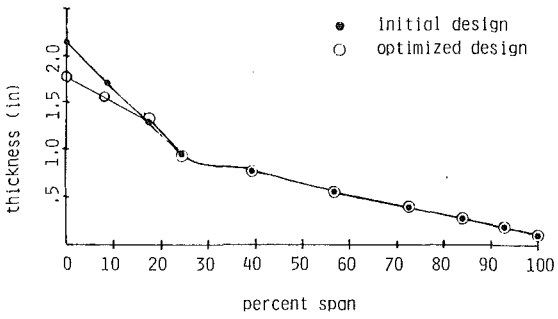

Composite Material Parameters

	Initial Design		Optimized Design	
	ply thk (in)	ply angle	ply thk (in)	ply angle
outer layer	.10	45.	.10	45.
layer 1	.10	0.	.10	0.
layer 2	.10	45.	.10	45.
core		0.		0.

Blade Weight

17.88 lb.	16.73 lb.

Fig. 3 Comparison between initial and optimized designs

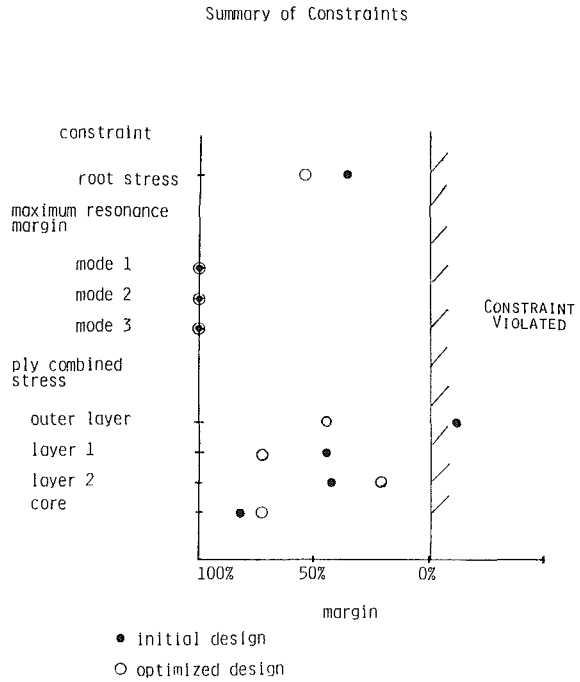

Fig. 4 Comparison between initial and optimized designs: centrifugal loads only

geometry description commonly used by blade designers. Each cross section is modeled by densely spaced points that surround the cross section. STAEBL converts this description into a finite element model based on triangular plate elements. The design perturbations generated by the feasible directions method are applied to the aerodynamic blade description. Therefore, each trial design must invoke a preprocessor to convert the aerodynamic description to a finite element description. STAEBL/GENCOM includes an option which allows direct input of a finite element model. Design perturbations are carried out directly on this model. Approximately 12 percent time savings can be obtained using this version.

The original program version invoked IMSL library routines to perform the matrix operations required by finite element analysis. The new version includes replacements for these library routines. The program can execute independently of the IMSL library and can, therefore, be used at installations where this library is not available. However, user optional calls to IMSL library are available.

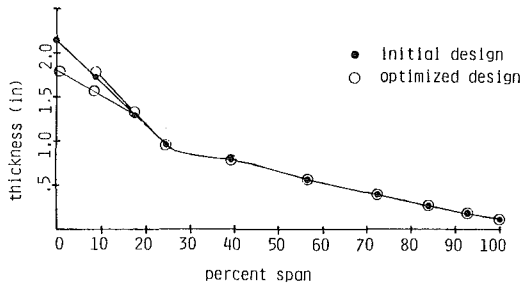

Composite Material Parameters

	Initial Design		Optimized Design	
	ply thk (in)	ply angle	ply thk (in)	ply angle
outer layer	.10	45.	.09	45.
layer 1	.10	0.	.09	0.
layer 2	.10	45.	.10	45.
core		0.		0.

Blade Weight

17.88 lb	17.45 lb

Fig. 5 Comparison between initial and optimized designs: centrifugal, thermal, and moisture loads

Offset Design Variables

Blade cross-sectional stacking is defined by the curve formed by the centers of gravity of the spanwise blade cross sections. The deviation of this curve from a straight line perpendicular to the engine axis is called "offset."

Offset has been made available as a design variable in STAEBL/GENCOM. Offset is determined by variables A, B, C, D, E, F through the equations

$$X = AZ + BZ^2 + CZ^3$$

$$Y = DZ + EZ^2 + FZ^3$$

where Z is a spanwise variable, X is transverse, and Y is chordwise.

Offset is used by blade designers to balance the centrifugal and aerodynamic pressure loads on a blade. The goal of this procedure is to reduce the static stress.

Demonstration Cases

STAEBL/GENCOM was applied to optimize the design of a sample composite blade. A propfan blade geometry was assumed, but the blade was assumed to be entirely graphite-epoxy. The composite layup consisted of an outer group of plies, two middle groups of plies, and a core group of plies. The blade geometry was that of an existing blade, and is already nearly optimal.

In a first study, the blade was subject to centrifugal loads only. The initial design violated the constraint on ply combined stress in the outer plies at the root. The initial and final blade geometries are compared graphically in Fig. 3.

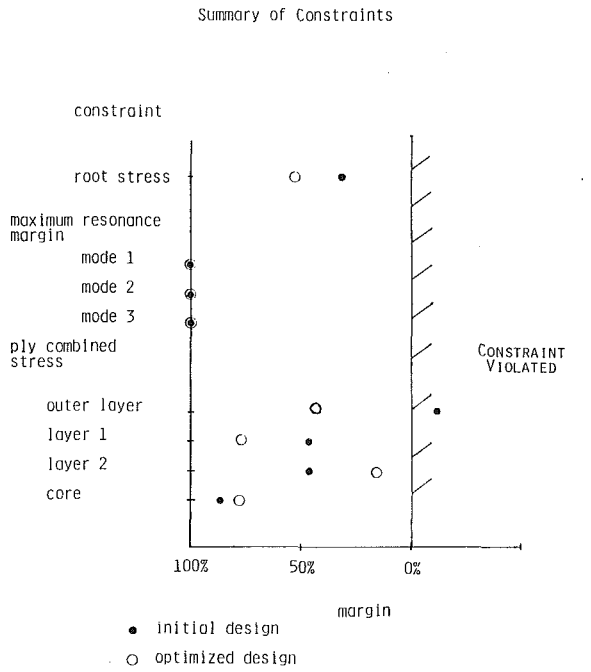

Fig. 6 Comparison between initial and optimized designs: thermal, moisture, and centrifugal loads

STAEBL/GENCOM also recommended a slight reorientation of the ply angle in the outer layer. Comparisons between the constrained variables in the initial and optimized designs appear in Fig. 4.

In a second study, the same blade was analyzed subject to centrifugal and to thermal and moisture loads believed to be representative for such blades. The optimized design weighs about 5 percent more than the design optimized for centrifugal loads alone. The initial and final designs are compared in Fig. 5, and the constrained variables are compared in Fig. 6.

The separate effects of temperature and moisture in optimal design are shown in Tables 1 and 2. These tables compare designs optimized under centrifugal loads alone, centrifugal and thermal loads, centrifugal and moisture loads, and centrifugal, thermal, and moisture loads. In this case, the thermal loads clearly have the dominant effect on the weight of the optimal design.

In order to expedite the optimization procedure, which requires analysis of a large number of trial designs, STAEBL/GENCOM uses a coarse-meshed finite element blade model. When STAEBL/GENCOM is applied in a design environment, the approximate analysis should be verified by a refined analysis. This is illustrated in the right half of Fig. 1.

Conclusions

The structural tailoring code STAEBL/GENCOM provides

Table 1 Comparison between designs optimized for different loading conditions: design variables and objective function

CENTRIFUGAL ONLY			CENTRIFUGAL AND THERMAL LOADS			CENTRIFUGAL AND MOISTURE LOADS			CENTRIFUGAL AND THERMAL AND MOISTURE LOADS		
% Span	Thk	Chd									
0	1.77	11.80	0	1.80	11.98	0	1.77	11.80	0	1.80	11.98
40	.65	13.08	40	.70	13.28	40	.65	13.09	40	.70	13.28
80	.27	7.88	80	.27	8.00	80	.27	7.88	80	.27	7.99
100	.12	3.44	100	.12	3.49	100	.12	3.44	100	.12	3.49
	Ply Thk	Ply Angle									
Outer	.09	45.0		.09	45.0		.09	45.0		.09	45.0
Layer 1	.09	0.0		.09	0.0		.09	0.0		.09	0.0
Layer 2	.10	45.0		.10	45.0		.10	45.0		.10	45.0
Core		0.0			0.0			0.0			0.0
	Blade Weight										
	16.73			17.44			16.73			17.45	

Table 2 Comparison between designs optimized for different loading conditions: response variables

CENTRIFUGAL ONLY			CENTRIFUGAL AND THERMAL LOADS			CENTRIFUGAL AND MOISTURE LOADS			CENTRIFUGAL AND THERMAL AND MOISTURE LOADS		
Natural Frequencies											
59.7	238.3	413.0	58.8	229.2	396.5	59.7	238.3	412.9	58.8	229.1	396.4
			Ply Combined Stress Margin of Safety								
Outer			.44		.45		.44			.45	
Layer 1			.74		.70		.74			.70	
Layer 2			.28		.20		.28			.21	
Core			.66		.63		.66			.63	
			Tip Displacements								
Untwist			.15		.08		.15			.08	
Uncamber			.03		.13		.03			.13	
Ext.			.03		.05		.03			.05	

an effective and practical approach to designing composite blade subject to complex mechanical and environmental loads. The large number of design variables associated with composite blade design, which include both blade geometry description variables and composite material design variables, can easily be incorporated into optimization algorithms. Both thermal and moisture effects can be modeled as part of the tailoring process. The demonstration cases demonstrate the versatility and computational capability of STAEBL/GENCOM.

References

1 Brown, K. W., Prat, T. K., and Chamis, C. C., "Structural Tailoring of Engine Blades (STAEBL)," *Proceedings of the AIAA/ASME/ASCE/AHS 24th SDM conference*, Lake Tahoe, NV, May 2-4, 1983.

2 Brown, K. W., Hirschbein, M. S., and Chamis, C. C., "Finite Element Engine Blade Structure Optimization," *Proceedings of the AIAA/ASME/ASCE/AHS 26th SDM Conference*, Orlando, FL, Apr. 15-17, 1985.

3 Chamis, C. C., and Smith, G. T., "Resin Selection Criteria for 'Tough' Composite Structures," *AIAA Journal*, Vol. 23, 1985, pp. 902-911.

4 Chamis, C. C., and Smith, G. T., "Environmental and High Strain Rate Effects on Composites for Engine Applications," *AIAA Journal*, Vol. 22, 1984, pp. 128-134.

Advanced Composite Turboprops: Modeling, Structural, and Dynamic Analyses

R. A. Aiello

S. Chi

NASA-Lewis Research Center,
Cleveland, OH 44135

This paper presents a structural and dynamic analysis of a scaled-down wind tunnel model prop-fan blade made from fiber composites. This blade is one of a series of prop-fan blades that have been tested at the Lewis Research Center wind tunnel facilities. The blade is highly swept and twisted and of the spar/shell construction. Due to the complexity of the blade geometry and its high performance, it is subjected to much higher loads and tends to be much less stable than conventional blades. The structural and dynamic analyses of the blade were performed using the NASA-Lewis COBSTRAN computer code. COBSTRAN is designed to generate the mesh and calculate the anisotropic material properties for composite blade analysis. Comparison of analytical and experimental mode shapes and frequencies are shown, verifying the model development and analysis techniques used. The methodologies and programs developed for this analysis are directly applicable to other prop-fan blades.

Introduction

As part of an overall effort to increase the propulsive efficiency of commercial aircraft engines the NASA advanced turboprop program was established. The goal of this program is to develop prop fans which can replace ducted fans without any appreciable loss in aircraft performance, but with significant gain in fuel economy. Advanced prop fans have highly swept blades, which are twisted along the span and curved about the axis of rotation. These blades will operate in a very complicated and severe aeromechanical environment.

Designs such as these have been known for some time, but the means to analyze them and the materials to build them did not exist. Today, with the development of high-speed computers and sophisticated engineering software, and the availability of composite materials, advanced turboprops can be analytically studied more thoroughly and more accurately.

The COBSTRAN (COmposite Blade STRuctural ANalyzer) code used in the analyses described in this report was developed at the NASA-Lewis Research Center and is currently being used for the design and analysis of ducted and unducted fan blades. COBSTRAN combines composite mechanics [1] with a database of fiber and matrix properties to generate material properties for use with general purpose finite element codes (MSC/NASTRAN for this case). This paper presents the results of structural and dynamic analyses, conducted at the NASA-Lewis Research Center, of a scaled-down prop-fan blade.

Contributed by the Gas Turbine Division of THE AMERICAN SOCIETY OF MECHANICAL ENGINEERS and presented at the 32nd International Gas Turbine Conference and Exhibit, Anaheim, California, May 31–June 4, 1987. Manuscript received at ASME Headquarters February 5, 1987. Paper No. 87-GT-78.

Blade Description

This wind tunnel blade model is a scaled-down version of a large advanced prop fan [2]. This blade was designed and constructed to be structurally and aeroelastically equivalent to the large-scale blade. The blade analyzed in this report is for a 2-ft-dia eight-blade turboprop. The blade is constructed of a graphite and fiberglass composite shell and a titanium spar and shank. The turboprop is designed for Mach 0.8 cruise speed at 35,000 ft altitude with a rotational blade tip speed of 800 ft/sec. The design setting angle at 3/4 blade span is 57.57 deg, and the total stage thrust is 75 lb. The blade twist and offset (relative to a radial line) also vary along the span. The variable thickness shell is made from plies of woven fiberglass cloth and unidirectional graphite fibers.

Finite Element Modeling

The finite element model for the blade was developed from coordinate descriptions defining the blade spar and shell cross-sectional geometries at 19 stations along the blade span. The midchord line of each cross section was determined from the aerodynamic profile data over a radial span of 2.52 to 12.02 in. (as shown in Fig. 1). Each midchord line was then represented by 26 grid points defining coordinate values and thicknesses.

The COBSTRAN computer code was used to generate the grid points, connectivities, and anisotropic material properties for the analysis model. COBSTRAN is designed to generate 14 grid point definitions at each radial station along the blade span. These grid point locations along the chord were selected to establish a finer mesh along the leading and trailing edges of the spar (as shown in Fig. 2). This was done to minimize the effect of the elements representing a transition of properties

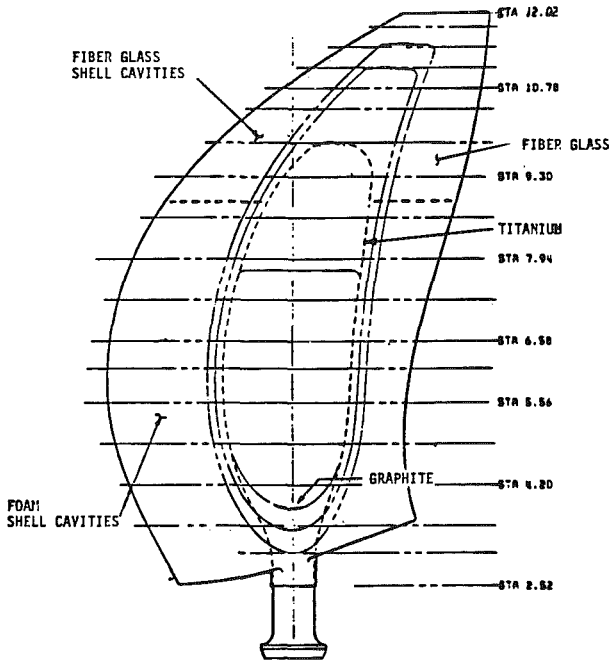

Fig. 1 Spar/shell composite blade design

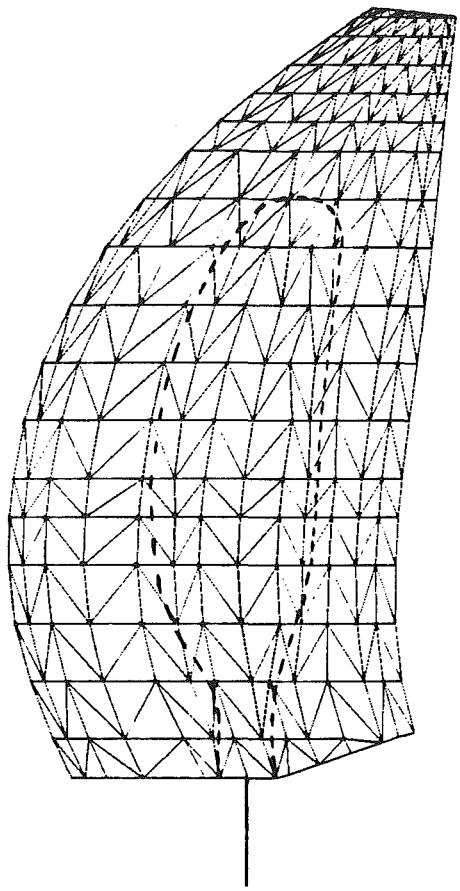

Fig. 2 Finite element model of spar/shell blade (256 nodes, 449 elements)

between the all-shell nodes and the shell/spar nodes. This is particularly necessary in COBSTRAN, which first generates composite material properties at all grid points and then averages these properties using nodes defining each element, thus generating the material properties for each element. As such, the material properties generated at grid points near the boundary between the spar and the shell will contribute to the material properties of the elements on both sides of the boundary.

The equivalent anisotropic material properties of the shell elements were generated using composite mechanics and laminate theory available in COBSTRAN. The individual ply properties were computed using micromechanics theory [1]. The stress-strain relationship at each node was calculated by laminate theory in which plane cross sections remain planar. The final developed model has 256 grid points and 449 triangular shell elements.

Generation of Ply Properties

COBSTRAN is designed to generate structural properties for unidirectional fiber composite plys from the constituent properties of the individual fibers and matrix. These constituent properties are contained in a databank within the COBSTRAN code or may be provided separately by the user in an external databank.

The structural properties normally provided to the analyst are from experimental data using the as-manufactured ply and are limited in number. COBSTRAN internally requires many more properties than are available from the manufacturer. Therefore, it is required that COBSTRAN generate these structural properties internally from its micromechanics module [1]. It is important that the ply properties generated by COBSTRAN and the limited number of as-manufactured properties agree with each other in order to produce valid modeling properties.

For this blade the as-manufactured fiberglass ply used in the design was a 0/90 deg cross-weave. The COBSTRAN representation of this cross-weave was two unidirectional plys at 90 deg to each other with each ply designated as half the thickness of the cross-weave.

A six-node plate model was used to evaluate the resultant properties of the combined plies normal to each other and compare them with the manufacturers experimental properties. Table 1 shows the comparison between selected ply properties for fiberglass/epoxy, graphite/epoxy, foam, and titanium calculated by COBSTRAN and from test results. To generate the known manufacturer's properties the input to the COBSTRAN code was modified by varying the fiber volume ratio and moduli of the fiber and matrix. The micromechanics code [1], incorporated in COBSTRAN, was not altered.

The E1 and E2 moduli of the manufacturer's cross-weave fiberglass are in the fiber directions and normal to each other. The COBSTRAN results for E1 and E2 represent the combined effects of the two layers of unidirectional fiberglass at 0/90 deg. E1 is in the 0 deg direction and E2 is in the 90 deg direction.

The graphite fiber unidirectional composite layer was represented in the COBSTRAN code by one ply of thickness equal to that of the manufacturer. The E1 modulus is in the fiber direction and the E2 modulus is normal to the fiber.

The titanium and foam, although isotropic materials, must be represented in the COBSTRAN code as fiber and matrix materials with properties determined by micromechanical analysis. This results in small inconsistencies in the E1 and E2 moduli, which are negligible to the overall analysis.

Modeling Strategy

The blade was designed with a fiberglass and graphite composite shell with an inner spar of solid titanium. The area

Table 1 Comparison of COBSTRAN generated fiber/matrix properties with manufacturer's test results

PLY STRUCTURAL MODULI – COBSTRAN vs. TEST

UNITS ksi	FIBER GLASS 0°/90° CROSS-WEAVE 0.0055 IN. THICK	PAINT 0°/90° CROSS-WEAVE 0.002 IN. THICK	GRAPHITE 0°/0° LAY-UP 0.007 IN. THICK	TITANIUM	FOAM
* E_1	3516.0	2370.0	13730.0	16000.0	9800.0
** E_1	3510.0	2370.0	13800.0	16000.0	9800.0
* E_2	3500.0	2340.0	1010.0	16000.0	9889.0
** E_2	3510.0	2370.0	1090.0	16000.0	9800.0
* E_{12}	7370.0	511.0	480.0	6190.0	4944.0
** E_{12}	7670.0	517.0	580.0	6100.0	3630.0

* COBSTRAN generated values
** Manufacturers test values

within the shell and outboard of the spar was filled with fiberglass/epoxy or foam material, depending on the spanwise location. Spar and shell were bonded with a layer of adhesive. A typical cross section is shown in Fig. 3.

The COBSTRAN option, selected for this analysis, models a blade composed of various layers of materials as a solid blade having the same structural properties as the layered blade. This method of modeling simplifies the analyses of blades with a composite shell and metal internal spar because both are treated as layered materials and equivalent homogeneous properties are determined for the combination. The finite element model is composed of two-dimensional shell elements, one element through the thickness.

The material properties at each node were determined by evaluating each node as a series of layers of fiberglass/epoxy, graphite/epoxy, adhesive and foam or titanium, as appropriate, with a symmetric stack-up through the thickness. The corresponding anisotropic stress-strain relations were calculated by laminate theory in which plane cross sections remain planar. Individual ply properties were calculated using micromechanics theory. Each node in the model contained from 8 to 176 ply layers with a different ply stack-up order depending on the location of the node on the blade.

The input to the COBSTRAN program is designed so that ply layers may be defined to exist over only specified areas of the blade expressed as a percent span and a percent chord range. Special subroutines were created for this analysis to redefine the area covered by each ply by node range rather than by percent span and percent chord range. This additional feature enhanced the procedure of modeling the ply stack-up order. Making use of this feature, and several iterations through the COBSTRAN preprocessor, resulted in each of the 256 nodes being defined by shell, adhesive, and foam or titanium as required at each nodal location.

The protective paint layer was represented by a low modulus 0/90 deg layup using specially designated fiber and matrix properties in the user-supplied external databank.

The shank of the blade was modeled using a bar element with section inertia properties adjusted for the instrumentation hole. The transition between the triangular shell elements of the blade and the bar element representing the shank was modeled using NASTRAN multipoint constraints. The root of the shank was fixed in all six degrees of freedom.

Analysis Procedures

A normal mode analysis (MSC/NASTRAN solution sequence No. 3) was performed to determine the first four

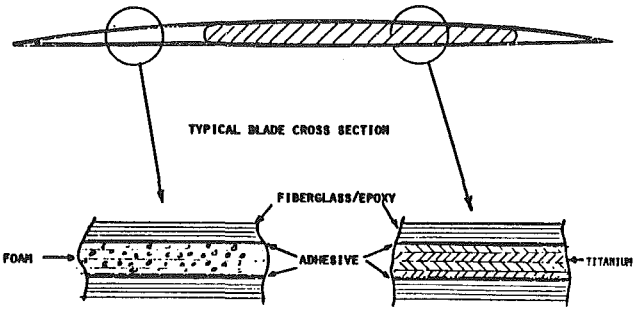

Fig. 3 Spar/shell blade cross section and modeling representation

natural frequencies and mode shapes at zero rotational speed.

Determination of steady-state deflections, natural frequencies, and mode shapes at selected rotational speeds was a more complex procedure [3]. Because of the twist and sweep of the blade, steady-state deflection calculations tend to be nonlinear. As such, the geometric nonlinear analysis capability available in MSC/NASTRAN (solution sequence No. 64) was used. This procedure requires, as a minimum, two subcases to account for differential stiffness. Additional subcases update the stiffness matrix and geometry at each iteration. The number of additional subcases is problem dependent. For this analysis, eight additional subcases were determined to be sufficient to establish convergence of displacements and incremental strain energy.

In order to perform this nonlinear analysis accurately and efficiently, three independent modifications (DMAP alters) were made to solution sequence No. 64 as follows:

(*a*) During the iteration process the stiffness matrix tended to become singular due to very small values of stiffness caused by the untwisting of the blade. To prevent this numerical instability the value of the stiffness matrix representing rotational stiffness about the axis normal to the span axis and lying in the plane of rotation was arbitrarily increased by a small value for the first seven iterations. This additional stiffness was then excluded from the eighth and final iteration so as not to influence the stiffness matrix used in the subsequent eigenvalue analysis.

(*b*) An important effect in the normal mode analysis of structures in a centrifugal force field is the increase in the magnitude of the force vector resulting from the vibratory translation of the nodal masses in the plane of rotation. Although the stiffness matrix is corrected for the static effects of the centrifugal force, the dynamic effects of the blade vibrating in the centrifugal force field are not evaluated in NASTRAN prior to eigenvalue and eigenvector extraction.

To compensate for these in-plane forces, which are proportional to the in-plane translations, the stiffness matrix is modified by treating the forces as negative stiffness values. Therefore, the modification made was to reduce the diagonal terms of the stiffness matrix associated with the translational degrees of freedom in the plane of rotation by a value of $(m \times \omega^2)$.

(*c*) To provide for computational and logistic efficiency in the extraction of eigenvalues and eigenvectors at selected rotational speeds, solution sequence No. 64 was modified to generate these values directly. The previous method required storing the updated stiffness and mass matrices and making an additional MSC/NASTRAN run for normal mode analysis at each rotational speed.

This blade was also evaluated considering other design specifications such as a protective paint layer, an instrumentation hole through the shank, and airloads. Comparative results are shown in Table 2. The model selected for final

Table 2 Natural frequencies (Hz) at 7484 rpm—airloads at 35,000 ft altitude

FREQUENCY SENSITIVITY TO STRUCTURAL AND LOAD CONSIDERATIONS

MODE	With Airloads With Point With Shank Hole	Without Airloads With Point With Shank Hole	With Airloads Without Point With Shank Hole	With Airloads With Point Without Shank Hole	With Airloads Without Point Without Shank Hole
1	202.30	202.04	205.13	202.15	207.5
2	366.28	366.34	374.16	367.07	376.0
3	461.41	459.83	462.08	460.07	468.6
4	623.32	626.27	634.05	626.40	642.5
5	-----	780.39	786.05	780.67	782.3

* Independent finite element analysis

Table 3 Comparison of calculated frequencies versus holographic test frequencies (Hz)

EFFECTS OF MATERIAL PROPERTY COMBINATIONS ON FREE FREQUENCIES

MODE	Element Properties Used in Analysis			Holographic Test Frequencies
	Bending	Membrane and Bending	Membrane, Bending and Transverse Shear	
1	154	158	147	155
2	338	339	334	326
3	373	369	364	377
4	585	571	561	545
5	655	650	635	638
6	1011	1005	986	921

analysis was the one with the protective paint layer and the hole in the shank. This model was chosen since it was most representative of the fabricated blade.

COBSTRAN calculates the membrane, bending, transverse shear, and membrane/bending coupling properties at each node. A user-selected option allows for the output of these properties either separately or by combining the membrane and bending properties into one material property matrix for each element, depending on the capability of the finite element analysis method used. Since MSC/NASTRAN accepts the independent input of each of these properties and because of the ease with which they can be presented by COBSTRAN, a study was made of the sensitivity of the blade analysis to the incorporation of these properties singly and combined. The results of this study are shown in Table 3.

The determination of ply stresses, strains, and failure criteria is made possible by use of the postprocessing feature of the COBSTRAN program. COBSTRAN accepts the element stress output from MSC/NASTRAN and calculates the stresses and corresponding membrane forces and bending moments at each node in the structural coordinate system. From these loads, using laminate theory, the resultant stresses, strains, and failure criteria are calculated for each ply layer at each node in the ply coordinate system.

Results and Discussion

Linear Dynamic Characteristics. A normal mode analysis

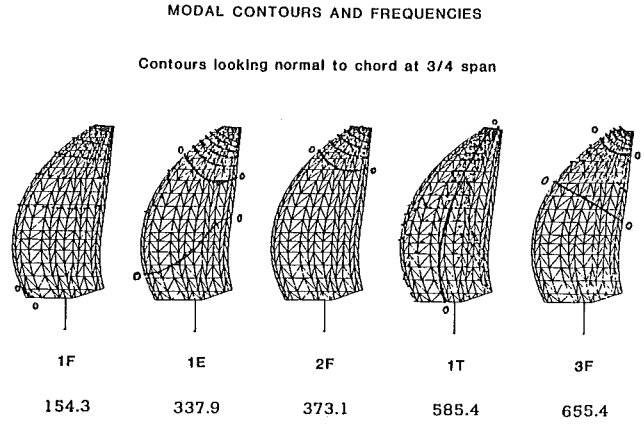

Fig. 4 Calculated frequencies (Hz) and modal contours at zero rpm

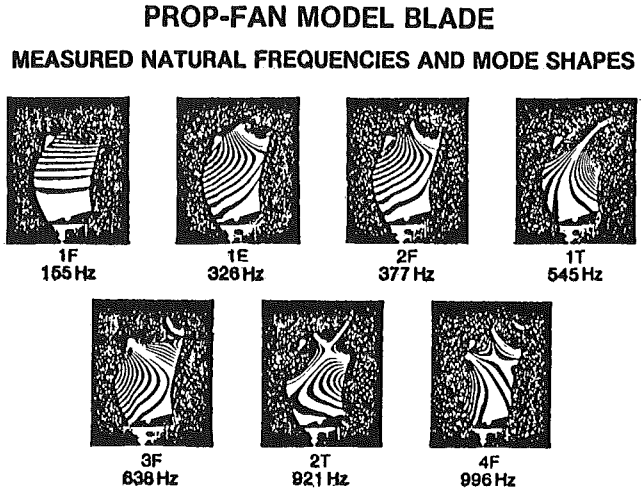

Fig. 5 Holographic frequencies (Hz) and modal contours at zero rpm

(MSC/NASTRAN solution sequence No. 3) was performed to determine the first five natural frequencies and mode shapes at zero rotational speed. Figure 4 shows the analytical natural frequencies and mode shapes. Figure 5 shows the same results from the holographic test measurements in which the blade was excited acoustically. There is excellent agreement between the two cases for both frequencies and mode shapes.

The normalized strain on the surface of the blade was also computed for the third mode. Figure 6 shows the strain gage locations on the experimental blade. Comparisons of third mode of vibration strain values calculated by COBSTRAN with the values measured [4] for the third mode are shown in Table 4.

Nonlinear Dynamic Characteristics. The frequencies and mode shapes at selected rotational speeds were determined using MSC/NASTRAN solution sequences 64, the three DMAP alterations described previously, and solution sequence 63.

A series of geometric-nonlinear analyses was performed at two blade orientations. The blade chord at 3/4 span was set at angles of 57.57 and 38.5 deg with respect to the plane of rotation. The analysis for each orientation was then done at five different rotational speeds (3000, 5000, 7000, 8000, 9000 rpm). Frequencies calculated at different rotational speeds, propeller order excitation frequencies, and the frequencies determined by spectral analysis of strain gage data from NASA-Lewis 9×15 Wind Tunnel tests are shown in the frequency versus rotational speed diagram (Fig. 7). As can be seen, the calculated frequencies are in very good agreement with those reduced from the strain gage data.

Table 4 Normalized strains at third mode of vibration

COMPARISON OF PREDICTED VS. MEASURED NORNALIZED SURFACE STRAINS

*Gage No.	Measured Data	COBSTRAN Analysis
1	.152	.106
3	.386	.340
4	1.000	1.000
5	.519	.650
6	.122	.144
E	.377	.440
F	.152	.138

* See Figure 6 for gage locations

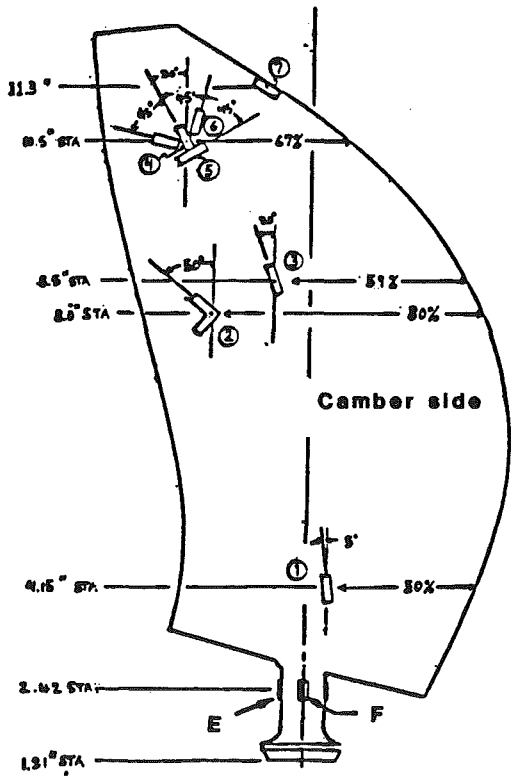

NOTE: Gages E and F shown out of true circumferential position

Fig. 6 Location and orientation of strain gages on camber/convex surface

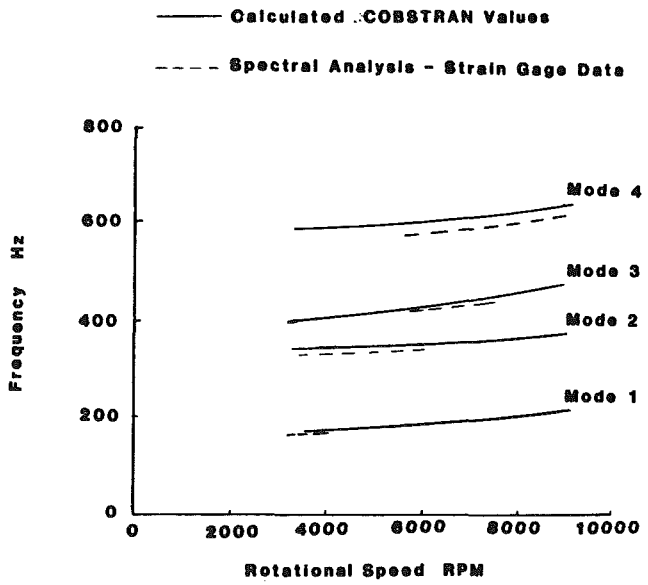

Fig. 7 Calculated and test frequencies versus rotational speed

Summary and Conclusions

A finite element model of the complex structure (spar/shell composite blade) was efficiently developed for the prop-fan blade. The analysis techniques used were validated by the good agreement of stationary frequencies and mode shapes between holographic tests and analytical results. Also, the model was further validated by the good analytical agreement of the frequencies at 7484 rpm between this study and an independent source [5]. The structural analysis procedures were further confirmed by the good agreement between the measured and calculated strains at the third mode of vibration. In addition to the model that was developed, the procedures and methodologies of developing finite element models for thin, swept, and twisted blades were verified by the good agreement of frequencies and mode shapes between test and analysis results. These results collectively demonstrate the accuracy and effectiveness of COBSTRAN computationally

to simulate the complex structural/dynamic response of composite structural components with intricate internal geometry and made from combining a variety of different materials.

References

1 Chamis, C. C., "Computer Code for the Analysis of Multilayered Fiber Composites—Users Manual," NASA TN D-7013, 1971.

2 Hirschbein, M., et al., "Structural and Aeroelastic Analysis of SR-7L Propfan," NASA TM-86877, 1985.

3 Aiello, R. A., and Chamis, C. C., "Large Displacement and Stability Analysis of Nonlinear Propeller Structures," NASA TM-82850, 1982.

4 Mehmed, O., SR7A Prop-Fan Model Blade S/N 16; Vibration Test Results and Blade Strain Gage Limits for SR7A, 1983.

5 "SR7A Aeroelastic Model Blade Design Report," Hamilton Standard Div. of United Tech. Corp., NASA-Lewis Research Center, Contract No. NAS3-23051.